ISSN 0021-9673

VOL. 517 SEPTEMBER 26, 1990
COMPLETE IN ONE ISSUE

J. Calvin Giddings Honour Volume

JOURNAL OF CHROMATOGRAPHY

INTERNATIONAL JOURNAL ON CHROMATOGRAPHY, ELECTROPHORESIS AND RELATED METHODS

SPECIAL VOLUMES

ELSEVIER

JOURNAL OF CHROMATOGRAPHY

Scope. The *Journal of Chromatography* publishes papers on all aspects of chromatography, electrophoresis and related methods. Contributions consist mainly of research papers dealing with chromatographic theory, instrumental development and their applications. The section *Biomedical Applications*, which is under separate editorship, deals with the following aspects: developments in and applications of chromatographic and electrophoretic techniques related to clinical diagnosis or alterations during medical treatment; screening and profiling of body fluids or tissues with special reference to metabolic disorders; results from basic medical research with direct consequences in clinical practice; drug level monitoring and pharmacokinetic studies; clinical toxicology; analytical studies in occupational medicine.

Submission of Papers. Manuscripts (in English; *four* copies are required) should be submitted to: The Editor of *Journal of Chromatography*, P.O. Box 681, 1000 AR Amsterdam, The Netherlands, or to: The Editor of *Journal of Chromatography, Biomedical Applications*, P.O. Box 681, 1000 AR Amsterdam, The Netherlands. Review articles are invited or proposed by letter to the Editors. An outline of the proposed review should first be forwarded to the Editors for preliminary discussion prior to preparation. Submission of an article is understood to imply that the article is original and unpublished and is not being considered for publication elsewhere. For copyright regulations, see below.

Subscription Orders. Subscription orders should be sent to: Elsevier Science Publishers B.V., P.O. Box 211, 1000 AE Amsterdam, The Netherlands, Tel. 5803 911, Telex 18582 ESPA NL. The *Journal of Chromatography* and the *Biomedical Applications* section can be subscribed to separately.

Publication. The *Journal of Chromatography* (incl. *Biomedical Applications*) has 37 volumes in 1990. The subscription prices for 1990 are:

J. Chromatogr. (incl. *Cum. Indexes, Vols. 451–500*) + *Biomed. Appl.* (Vols. 498–534):
Dfl. 6734.00 plus Dfl. 1036.00 (p.p.h.) (total *ca.* US$ 3885.00)

J. Chromatogr. (incl. *Cum. Indexes, Vols. 451–500*) only (Vols. 498–524):
Dfl. 5616.00 plus Dfl. 756.00 (p.p.h.) (total *ca.* US$ 3186.00)

Biomed. Appl. only (Vols. 525–534):
Dfl. 2080.00 plus Dfl. 280.00 (p.p.h.) (total *ca.* US$ 1180.00).

Our p.p.h. (postage, package and handling) charge includes surface delivery of all issues, except to subscribers in Argentina, Australia, Brasil, Canada, China, Hong Kong, India, Israel, Malaysia, Mexico, New Zealand, Pakistan, Singapore, South Africa, South Korea, Taiwan, Thailand and the U.S.A. who receive all issues by air delivery (S.A.L. — Surface Air Lifted) at no extra cost. For Japan, air delivery requires 50% additional charge; for all other countries airmail and S.A.L. charges are available upon request. Back volumes of the *Journal of Chromatography* (Vols. 1–497) are available at Dfl. 195.00 (plus postage). Claims for missing issues will be honoured, free of charge, within three months after publication of the issue. Customers in the U.S.A. and Canada wishing information on this and other Elsevier journals, please contact Journal Information Center, Elsevier Science Publishing Co. Inc., 655 Avenue of the Americas, New York, NY 10010. Tel. (212) 633-3750.

Abstracts/Contents Lists published in Analytical Abstracts, ASCA, Biochemical Abstracts, Biological Abstracts, Chemical Abstracts, Chemical Titles, Chromatography Abstracts, Clinical Chemistry Lookout, Current Contents/Life Sciences, Current Contents/Physical, Chemical & Earth Sciences, Deep-Sea Research/Part B: Oceanographic Literature Review, Excerpta Medica, Index Medicus, Mass Spectrometry Bulletin, PASCAL-CNRS, Pharmaceutical Abstracts, Referativnyi Zhurnal, Science Citation Index and Trends in Biotechnology.

See inside back cover for Publication Schedule, Information for Authors and information on Advertisements.

0021-9673/90/$03.50

This issue is printed on acid-free paper.

Printed in The Netherlands

For contents see p. VII

JOURNAL OF CHROMATOGRAPHY

VOL. 517 (1990)

JOURNAL *of* CHROMATOGRAPHY

INTERNATIONAL JOURNAL ON CHROMATOGRAPHY,
ELECTROPHORESIS AND RELATED METHODS

SPECIAL VOLUMES

ELSEVIER
AMSTERDAM — OXFORD — NEW YORK — TOKYO

J. Chromatogr., Vol. 517 (1990)

0021-9673/90/$03.50

Printed in The Netherlands

SPECIAL VOLUME

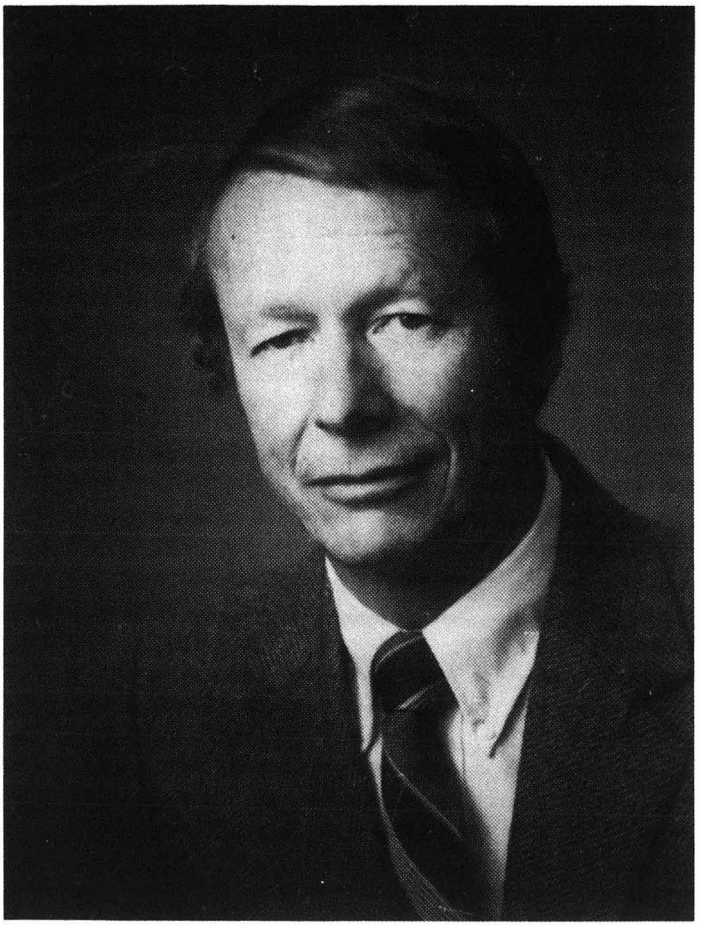

HONOUR VOLUME

on the occasion of the 60th birthday of

J. CALVIN GIDDINGS

Guest Editor

L. S. ETTRE

(Norwalk, CT)

CONTENTS

HONOUR VOLUME ON THE OCCASION OF THE 60TH BIRTHDAY OF J. CALVIN GIDDINGS

In articles with more than one author, the name of the author to whom correspondence should be addressed is indicated in the article heading by a 6-pointed asterisk (*)

Journal of Chromatography, 517 (1990) 1–2
Elsevier Science Publishers B.V., Amsterdam

PREFACE

The magnificent Wasatch Mountains rise precipitously 6000 feet above the floor of Utah valley. At one time, effluent from the many glaciers covering the range collected in the valley and filled the mighty Lake Bonneville. In modern times the valley is arid. Its population lives by the grace of the mountains as the water collected by its high peaks in the form of snow and rain is delivered to the lowland via a multitude of roaring creeks.

John Calvin Giddings was born in the shadow of these mountains on September 26, 1930. From early childhood on, the proximity to untamed nature with its many challenges became an important factor in shaping his interests and his approach to problem solving.

Cal's schooling took place along the Wasatch front, where he earned a bachelor's degree at Brigham Young University in Provo and a doctorate at the University of Utah in Salt Lake City. At the University of Utah he came under the tutelage of Henry Eyring who, in his persuasive way, convinced his young graduate student to elaborate on some recent thoughts he had had regarding the mechanisms underlying the chromatographic process. Although this study became only a small part of Cal's Ph.D. thesis, it was certainly a seed planted in fertile soil.

The years of postdoctoral work with J. S. Hirschfelder at Wisconsin were mainly devoted to expanding the theory of flames, and it was not until Cal returned to the Wasatch front, and an Assistant Professorship at the University of Utah, that his attention became fully focussed on the theory of chromatography. The period from 1957 to 1965 saw several important developments, such as the application of the random walk concept to retention and zone broadening, and the formulation of the non-equilibrium theory. By treating the plate height as the variance in migration created within a zone during its transport along the separation coordinate, it was possible to express the broadening as the sum of a variety of discrete plate height contributions. Models were developed and tested for a large number of broadening mechanisms present in different forms of chromatography. With these models in hand, principles for optimizing the chromatographic process were formulated which strongly suggested that a gain in efficiency should result from a reduction in the stationary phase particle size, and which therefore paved the way for the introduction of high-performance liquid chromatography. Much of the insight gained during this period was summarized in the book *Dynamics of Chromatography* that apeared in 1965 and quickly sold out.

During the mid-1960s, Cal turned his attention to gas chromatography, and particularly to the effects of pressure and temperature on the solubilizing power of a carrier gas. His pioneering work on pressure-programmed differential sample solubilization and "dense gas chromatography" became the precursor of today's supercritical fluid chromatography.

While the dense gas studies extended the operating range for the highly efficient gas chromatography technique to moderately large molecules, they most certainly provided no help in the fractionation of large macromolecules and particles. The search for an elution technique which could also handle colloidal samples led him in 1965 to formulate an entirely new separation principle which he termed field-flow fractionation (FFF). From that time until the present he has devoted most of his

scientific attention to the analysis of retention and zone broadening mechanisms for several of the fields applicable to FFF and to developing optimization strategies for his very versatile technique.

Cal's work in FFF has drawn scientists from all over the world to the FFF Research Center at the University of Utah. Last year, this organization hosted the *First International Symposium on Field-Flow Fractionation* with participants from twenty nations.

It would be reasonable to assume that all this creative activity had left no time for other pursuits. Reasonable, maybe, but entirely wrong. The mountains nearby have never ceased to exercise their attraction on Cal, who already as a student had developed significant skills in skiing their deep powder snow and scaling their smooth granite rock.

As one of the pioneers of ski mountaineering in the Wasatch and as a climber with several first ascents to his credit, he was a natural choice to serve a term as president of the Wasatch Mountain Club. It was during his tenure in this capacity that he began active work to preserve the wilderness quality of the Wasatch and other mountain ranges in the West. In addition to wilderness issues, his conservation concerns soon expanded to include overpopulation, air and water pollution, as well as problems presented by the rapid global increase in nuclear waste products and the persistent threat of nuclear war. His writings on these issues first appeared in several outdoor magazines and later culminated in the development of a freshman course in environmental chemistry and the publication of a widely used textbook entitled *Chemistry, Man and Environmental Change* (1973).

Of all his outdoor activities, none has appealed more to him than kayaking the raging waters of the many mountain streams in the West, and for several years he served as president of the American Whitewater Association. However, among his many daring river trips, none measures up to the expedition which he organized while on a Fulbright fellowship to Lima, Peru. This was the first expedition to successfully explore the Rio Apurímac —headwaters of the Amazon River.

Cal grew up in the shadow of the Wasatch Mountains, and he lived and worked in their vicinity for a large portion of his life. Eventually their pull became so strong that he designed and built a home in their midst, at the top of a canyon surrounded by the ubiquitous scrub oak. The year after its completion was an unusually dry period in the West, and forest fires ravaged vast areas in several states, most notably in Yellowstone Park. The Wasatch Mountains did not escape devastation, and for a period of several days in September of 1988, the scrub oak of Killyon Canyon was on fire. All residents were evacuated. With characteristic determination and tenacity, Cal defied the evacuation order and returned unseen to his threatened home where he ultimately fought alone against the elements for two days and a long night. Without this fight the home would certainly have been lost, for the flames were within a few feet of its walls, and burning embers were constantly showering its roof. By daring the authorities, he saved his home and will hopefully enjoy its tranquility for years to come.

The courage to question conventional wisdom and the dogged pursuit of goals and ideas are hallmarks of Cal's scientific and other activities. Regardless of field, these activities have often been those of a pioneer; they have opened new territories and new ways of thinking. For that, we gratefully honor Cal on his sixtieth birthday.

KARIN CALDWELL

Journal of Chromatography, 517 (1990) 3–29
Elsevier Science Publishers B.V., Amsterdam

CHROMSYMP. 1908

Plate height theory for compressible mobile phase fluids and its application to gas, liquid and supercritical fluid chromatography

DONALD P. POE*
Department of Chemistry, University of Minnesota, Duluth, MN 55812 (U.S.A.)
and
DANIEL E. MARTIRE
Department of Chemistry, Georgetown University, Washington, DC 20057 (U.S.A.)

ABSTRACT

General expressions for apparent plate height are derived in terms of temporal and spatial average values of local plate height, solute capacity factor and mobile phase density. The general expressions are applied to the appropriate expressions for gas chromatography, liquid chromatography and supercritical fluid chromatography with open tubular and packed columns. For gas chromatography, the equations reduce to the equations presented earlier by Giddings. For liquid chromatography, the equations reduce to those for local plate height. Predicted results for supercritical fluid chromatography are compared to experimental results reported in the literature.

INTRODUCTION

The deleterious effect of large pressure gradients on column efficiency in chromatography with compressible mobile phase fluids has been a long-recognized problem. The effect is associated with the fact that, as a solute band traverses a chromatographic column, it experiences varying conditions of mobile phase pressure and velocity, and the apparent plate height at the outlet may be significantly greater than the local plate height at any point in the column. In near-ideal gas chromatography (GC) (He or N_2 mobile phase and pressures less than 10 atm) this effect may be measurable but it is never very great. Giddings *et al.*[1] provided the fundamental theoretical treatment of this effect for gas chromatography, showing that the effect was due entirely to expansion of the mobile phase fluid. They showed that, assuming ideal gas behavior, the ratio of apparent plate height to local plate height reaches a maximum value of 9/8 as the ratio of inlet to outlet pressures approaches infinity. In liquid chromatography (LC), the compressibility of the mobile phase is so small that the effect of pressure drop on column efficiency is negligible.

0021-9673/90/$03.50

The situation for supercritical fluid chromatography (SFC) is quite different. Density gradients associated with large pressure drops may cause excessive band broadening, especially for strongly retained solutes. For example, in one study[2] the peak widths for some aromatic hydrocarbons were 2–4 times greater for a packed column operated under a large density gradient ($\Delta\rho = 0.18$ g/cm^3) than for the same column operated under a smaller density gradient ($\Delta\rho = 0.06$ g/cm^3). This dependence of column efficiency on density gradients can place significant limits on the resolving power of packed columns when high density gradients are produced. There have been a few detailed studies of this effect in packed column SFC[2,3] as well as in SFC with open tubular columns[4,5], but so far a rigorous theoretical treatment of the phenomenon has been lacking. It is our intention to provide such a treatment with this paper.

Subsequent to the initial investigations by Giddings *et al.*[1], Giddings[6,7] developed the theory into a more general form represented by the relation

$$\hat{H} = L\int(H/u_s^2)\mathrm{d}z/[\int(1/u_s)\mathrm{d}z]^2 \tag{1}$$

where $\hat{H}$ is the apparent plate height measured at the column outlet, L the column length, and H and u_s are the local values of plate height and solute zone velocity, respectively. Under conditions of near-ideal gas chromatography, where the capacity factor is virtually constant, eqn. 1 can be evaluated as a function of the pressure drop[6]. If however the capacity factor varies with the position in the column, as is commonly the case in SFC, the situation is more complex. Capacity factor is not a simple function of pressure. Recent advances in retention theory suggest that mobile phase density (or more specifically, reduced density) is a fundamental property affecting retention in gas chromatography (GC), LC and SFC[8]. Moreover, Martire[9] has recently derived general equations for the spatial and temporal density distribution functions, average densities and column profiles of the mobile phase fluid, as well as for the apparent capacity factors and column profiles of the solute components. It appears desirable then to rewrite eqn. 1 in terms of mobile phase density and density-dependent terms. Such an expression would be generally applicable to GC, LC and SFC, but would find its primary application in the area of SFC.

FLOW-RELATED QUANTITIES IN SFC

Because of the high compressibility and non-ideal behavior of supercritical fluids, careful definition of flow-rates and related quantities is extremely important to successful treatment of plate theory in SFC. Martire[9] has presented a general treatment of spatial and temporal aspects of column parameters applicable to GC, LC and SFC. Here we extend that treatment primarily to provide the specific tools needed for treatment of plate height theory. Throughout the following discussion we shall assume isothermal conditions and constant mass flow-rate of the mobile phase during a given separation experiment. This is achieved in practice by maintaining fixed pressures at the inlet and outlet of the column. With these restrictions a steady-state condition will be achieved so that the mass flow-rate, $\dot{m}$, remains constant along the length of the column. Radial variations, which may be significant under certain conditions[10], are ignored.

Superficial velocity and flow-rate

The volumetric flow-rate, $\dot{V}$, which is commonly measured experimentally, is related to mass flow-rate $\dot{m}$ by the simple relation

$$\dot{m} = \dot{V}\rho$$

where ρ is the density of the mobile phase. Horváth and Lin[11] define the superficial velocity u_0 as

$$u_0 = (1/\boldsymbol{A})\dot{V}$$

where $\boldsymbol{A}$ is the cross-sectional area of the tube. This is the velocity calculated from the volumetric flow-rate assuming a tube with no packing. The superficial specific mass flow-rate is then

$$F_0 = \dot{m}/\boldsymbol{A}$$

F_0 is thus the mass flow-rate per unit area assuming no packing is present. It follows from the preceding equations that

$$F_0 = u_0\rho$$

Mobile zone (excluded) velocity and flow-rate

The mobile zone, or excluded, velocity u_e is

$$u_e = u_0/\varepsilon_e$$

where $\varepsilon_e = V_e/V$ is the interparticle porosity and V_e and V are the interparticle volume and empty column volume, respectively. The excluded velocity is taken as the actual linear velocity along the column axis of the moving mobile phase between the particles, or the mobile zone. When microporous packings such as porous silica are used, the intraparticulate mobile phase is assumed to be stagnant. Likewise, the excluded specific mass flow-rate F_e may be defined as

$$F_e = F_0/\varepsilon_e$$

and it follows that

$$F_e = u_e\rho$$

The solute velocity u_s is related to the mobile zone velocity and zone capacity factor k'' by the equation

$$u_s = u_e/(1 + k'') = F_e/(1 + k'')\rho$$

where k'' is the ratio of moles of solute in the stationary zone (stagnant mobile phase plus stationary phase) to moles of solute in the mobile zone (excluded mobile phase).

Mobile phase velocity and flow-rate

The mobile phase velocity u_m, which is the average linear velocity of a mobile phase molecule or of a fully permeating, unsorbed solute, is

$$u_m = u_0/\varepsilon_t$$

where $\varepsilon_t = (V_e + V_i)/V$ is the total porosity and V_i is the intraparticle volume. This is the velocity which is typically measured experimentally. The corresponding mobile phase specific mass flow-rate F_m is then

$$F_m = F_0/\varepsilon_t = u_m\rho$$

and the solute velocity is

$$u_s = u_m/(1 + k') = F_m/(1 + k')\rho$$

where k' is the phase capacity factor, which is the ratio of moles of solute in the stationary phase to moles of solute in mobile phase.

Reduced flow-rates

In order to facilitate the use of reduced densities in the treatment which follows, two reduced mass flow-rate terms are introduced. The reduced superficial specific mass flow-rate F_{0R} is defined

$$F_{0R} = F_0/\rho_{ref} = u_0\rho_R$$

where ρ_{ref} is the reference density of the mobile phase fluid, and $\rho_R = \rho/\rho_{ref}$ is the reduced density. In GC and LC, the mobile phase density at 1 bar or 1 atm is used as the reference density. In SFC, we shall use the critical density of the mobile phase fluid as the reference density. Likewise, the reduced excluded specific mass flow-rate F_{eR} is defined

$$F_{eR} = F_e/\rho_{ref} = u_e\rho_R$$

and the reduced mobile phase specific mass flow-rate F_{mR} is

$$F_{mR} = F_m/\rho_{ref} = u_m\rho_R$$

For a column of fixed diameter and porosity, F_{0R}, F_{eR} and F_{mR} are constant under isothermal, steady state conditions, and represent the linear velocity which the mobile phase or mobile zone would have at the specified mass flow-rate if it were at its reference density.

Retention time for an unretained, excluded solute

For a packed column, the mass of excluded mobile phase m_e (that which is moving) is

$$m_e = V_e<\rho>_z = \varepsilon_e V<\rho>_z$$

where $<\rho>_z$ is the spatial average density[9]. The time to elute one column volume t_u is

$$t_u = m_e/\dot{m} = \varepsilon_e V <\rho>_z/\dot{m}$$

Incorporating the relations $\dot{m} = F_0 \boldsymbol{A}$ and $F_0 = F_e \varepsilon_e$, we obtain

$$t_u = L<\rho>_z/F_e = L<\rho_R>_z/F_{eR}$$

where L is the length of the column.

For an open tubular column

$$t_u = V<\rho>_z/\dot{m} = L<\rho>_z/F_0 = L<\rho_R>_z/F_{0R}$$

Average linear velocity

In some cases the average linear velocity of the mobile phase may be impossible to measure experimentally due to lack of a suitable unretained solute. The above equations for t_u allow for its calculation. For a packed column, the average excluded velocity $<u_e>$ is

$$<u_e> = L/t_u = \dot{m}/(\varepsilon_e \boldsymbol{A} <\rho>_z) = F_e/<\rho>_z = F_{eR}/<\rho_R>_z$$

For an open tubular column, $u = u_0 = u_e$, and

$$<u> = \dot{m}/(\boldsymbol{A}<\rho>_z) = F_0/<\rho>_z = F_{0R}/<\rho_R>_z$$

Noting that $D_t(\rho) = \rho D_z(\rho)$, it can be shown that $<1/\rho>_t = 1/<\rho>_z$, and

$$<u>_t = <F/\rho>_t = F/<\rho>_z$$

Thus it is seen that the average velocity which is usually reported as L/t_u is the temporal average velocity.

Reduced velocity

For efficiency studies involving packed columns, reduced velocity is best defined in terms of the excluded reduced velocity, v_e, that is,

$$v_e = u_e d_p/D_m$$

where d_p is the particle diameter and D_m is the diffusion coefficient of the solute in the mobile phase. Therefore, for a packed column,

$$v_e = F_e d_p/(\rho D_m) = F_{eR} d_p/(\rho_R D_m)$$

For an open-tubular column of diameter d_c,

$$v = u d_c/D_m = F_0 d_c/(\rho D_m) = F_{0R} d_c/(\rho_R D_m)$$

To the extent that the product of density times diffusion coefficient for gases and supercritical fluids is roughly constant[12], so is then the reduced velocity also approximately constant. While this product is constant in gas mixtures at low pressures, some variation is observed at high pressures. Studies on the behavior of the ratio $\rho D/\rho_0 D_0$, where the subscript 0 refers to low pressure values, show that at high pressures (in or near the supercritical region) the value of $\rho D/\rho_0 D_0$ changes in a fashion that is not accurately predicted by Enskog–Thorne theory for dense gas mixtures[13,14]. The product of ρD_m for benzene and some alkylbenzenes in supercritical carbon dioxide[13] at 40°C is less than unity at low density ($0.1 < \rho < 0.6$ g/cm^3) and increases to approximately unity at a CO_2 density of about 0.6 g/cm^3, above which it remains nearly constant. Similar behavior is observed for naphthalene under the same conditions[15], with ρD_m changing from 0.00072 to 0.00097 g cm^{-1} s^{-1} for CO_2 densities from 0.28–0.60 g/cm^3. Therefore the variation in reduced velocity with density can be significant at low densities. This variation notwithstanding, the assumption that v is constant can greatly simplify the equations for apparent plate height (*vide infra*). The question of whether this assumption leads to significant errors will be addressed later in this paper.

PLATE HEIGHT THEORY

The fundamental theory for relating apparent plate height to local plate height for non-uniform columns has been developed by Giddings[6,7]. The apparent (not local) plate height at any point in the column is defined as $\hat{H} = z(\tau^2/t^2)$, where z is distance travelled, τ is the standard deviation of the band in time units, and t is elapsed time. Normally $\hat{H}$ is measured at the outlet, where L, τ and t refer to column length, standard deviation of the eluting band and retention time, respectively. If the column is divided into infinitesimally small segments, the local plate height for each segment is $H_i = L_i\tau_i^2/t_i^2$, where L_i is the length of the segment, τ_i^2 the contribution to variance within that segment, and t_i the time required for the solute band to traverse that segment. Noting that the addition rules for τ and t differ ($\tau^2 = \Sigma\tau_i^2$ and $t = \Sigma t_i$), Giddings showed that

$$\hat{H} = L\Sigma\tau_i^2/(\Sigma t_i)^2$$

and performing the appropriate transformations, obtained the general relation presented above in eqn. 1.

Under usual conditions the column is assumed to be uniform with respect to tube diameter, stationary film thickness, particle diameter, packing structure and other stationary phase parameters. For compressible mobile phases, however, a pressure or density gradient is inevitably present, which results in variations in both the solute zone velocity and local plate height. As noted above, we desire the equivalent expression to eqn. 1 expressed in terms of density.

We begin by recalling that $u_s = F/(1 + k)\rho$, where F and k represent either F_e and k'', or F_m and k'. Under isothermal conditions and constant mass flow-rate, eqn. 1 can therefore be written as

$$\hat{H} = L[\int_0^L H(1 + k)^2\rho^2 dz]/[\int_0^L (1 + k)\rho dz]^2 \qquad (2)$$

The variable terms in H can all be expressed as functions of mobile phase density. The final step then in achieving the desired equation requires a transformation of variable from z to ρ, for which we invoke the relation $dz = D_z(\rho)d\rho$, where $D_z(\rho) = (\rho/\eta)(\delta P/\delta\rho)_T$ is the spatial distribution function relating z and ρ for the mobile phase fluid[9] (η, P and T represent viscosity, pressure and temperature, respectively). Dividing numerator and denominator in eqn. 2 by $L^2 = [\int dz]^2$, and substituting $dz = D_z(\rho)d\rho$, we obtain

$$\hat{H} = <H(1 + k)^2\rho^2>_z/<(1 + k)\rho>_z^2 \quad (3a)$$

which is the desired expression, where, once again, k represents either k' or k'', and the brackets $< >_z$ represent the spatial average of the enclosed terms. An expression which is equivalent to eqn. 3a involving both temporal and spatial average quantities is

$$\hat{H} = <H(1 + k)^2\rho>_t/<1 + k>_t^2<\rho>_z \quad (3b)$$

which is arrived at by an alternative approach in the Appendix.

Dividing eqns. 3a and 3b by d_c (column diameter) or d_p (particle diameter) yields the equivalent expressions for apparent reduced plate height $\hat{h}$,

$$\hat{h} = <h(1 + k)^2\rho^2>_z/<1 + k)\rho>_z^2 \quad (4a)$$

and

$$\hat{h} = <h(1 + k)^2\rho>_t/<1 + k>_t^2<\rho>_z \quad (4b)$$

The significant contribution of these equations is that they provide a usable form of Giddings' general expression which is directly applicable to GC, LC and SFC.

APPLICATIONS AND DISCUSSION

In the following discussion we will demonstrate how eqns. 3 and 4 may be used to predict the impact of solute zone velocity gradients in GC, LC and SFC. Because the most significant area of application is expected to be in SFC, that case will be treated in greatest detail.

Plate height equations

For chromatography with open tubular columns, the Golay equation[16] describes plate height exactly under conditions of laminar flow. For packed columns numerous variations of the van Deemter equation have been proposed[11,17–19]. For LC and SFC in columns packed with microparticulate porous silica stationary phases, we employ the equations developed by Knox and Scott[17] and by Horváth and Lin[18]. For GC, in which the stationary phase is a distinct liquid phase on a solid support, we employ the coupled form of the equation proposed by Giddings[19]. We shall refer to these as the Golay, Knox, Horváth–Lin and Giddings equations, respectively. These four equations may be written in general form as follows.

The Golay equation:

$$H = (A/F)f_1(\rho) + Bd_c^2Ff_2(\rho) + CFf_3(\rho) \quad (5a)$$

TABLE I

TERMS IN EQUATIONS FOR LOCAL PLATE HEIGHT

Equation	*Constant terms*[a]			*Density-dependent terms*[a]		
	A	*B*	*C*	$f_1(\rho)$	$f_2(\rho)$	$f_3(\rho)$
Golay	2	1/96	2/3	$D_m\rho$	$(1 + 6k' + 11k'^2)/[(1 + k')^2 D_m\rho]$	$d_f^2 k'/[(1 + k')^2 D_s\rho]$
Knox[b]	2γ	Constant	$(1 - \phi_K)/(30\gamma_{sm}\phi_K)$	$D_m\rho$	$(D_m\rho)^{-1/3}$	$k''^2/[(1 + k'')^2 D_m\rho]$
Simplified Horváth–Lin	2γ	$2\lambda/\omega$	$\theta/[30\phi(1 + \phi^2)]$	$D_m\rho$	$(D_m\rho)^{-1/3}$	$(\phi + k' + \phi k')^2/[(1 + k')^2 D_m\rho]$
Horváth–Lin[c]	2γ	2λ	$\theta/[30\phi(1 + \phi)^2]$	$D_m\rho$	$(D_m\rho)^{-1/3}$	$(\phi + k' + \phi k')^2/[(1 + k')^2 D_m\rho]$
Giddings	2γ	2λ	q	$D_m\rho$	$(D_m\rho)^{-1}$	$d_f^2 k'/[(1 + k')^2 D_s\rho]$

[a] See glossary of symbols for definitions of terms.

[b] This is a simplified form of the Knox equation. See text.

[c] In Horváth–Lin equation: $D = \kappa/(1 + \phi)^2$; $f_4(\rho) = (\phi + k' + \phi k')^2/[(1 + k')^2 (D_m\rho)^{2/3}]$.

The Knox (or simplified Horváth–Lin) equation:

$$H = (A/F_e)f_1(\rho) + Bd_p^{4/3}F_e^{1/3}f_2(\rho) + Cd_p^2F_ef_3(\rho) \quad (5b)$$

The Horváth–Lin equation:

$$H = (A/F_e)f_1(\rho) + Bd_p/[1 + \omega/(d_pF_e)^{1/3}f_2(\rho)] + \\ + Cd_p^2F_ef_3(\rho) + Dd_p^{5/3}F_e^{2/3}f_4(\rho) \quad (5c)$$

The Giddings equation:

$$H = (A/F_e)f_1(\rho) + Bd_p/\{1 + B/[\omega d_pF_ef_2(\rho)]\} + CF_ef_3(\rho) \quad (5d)$$

The factors A–D contain constant column parameters, while $f_i(\rho)$ contain terms which may show some dependence on mobile phase density, including D_m, k, d_f (stationary phase film thickness) and D_s (solute diffusion coefficient in the stationary phase). The expressions for the various parameters are given in Table I. Note in particular that the product $D_m\rho$ or $D_s\rho$ appears in each expression for $f_i(\rho)$. γ, λ, κ, q, ω, θ, ϕ and ϕ_K are column constants as defined in refs. 7, 17 and 18 (see Symbols section). We have neglected terms involving adsorption kinetics.

The terms in the Knox equation given in Table I represent a simplified form of the equation. The complete A term given by Knox and Scott is

$$2(\gamma_m + k'\gamma_sD_s/D_m)\rho D_m/F_e$$

where γ_m and γ_s are the obstruction factors to solute diffusion in the mobile and stationary phases. Likewise, the more general form of the C term is

$$(F_ed_p^2/30)\{k''/[(1 + k'')^2\rho D_{sz}]\}$$

where D_{sz} is the diffusion coefficient of the solute in the stationary zone, and is a complex function of k'', ϕ_K, γ_{sm}, D_m, γ_s and D_s, where γ_{sm} is the obstruction factor in the stagnant mobile phase[17]. If we assume that $D_s/D_m \ll 1$, the A and C terms in the Knox equation simplify to the expressions given in Table I. This assumption is reasonable for GC, and probably for SFC, where diffusivities in the mobile phase are relatively large. In LC, where D_s/D_m may be closer to unity[17,20], the more general form of the Knox equation may provide a better description of band spreading processes.

At sufficiently low reduced velocities, which are of practical interest, the B term of the Horváth–Lin equation is simplified and the D term becomes negligible[18], so that the Horváth–Lin equation reduces to a form similar to the Knox equation, both represented by eqn. 5b. The A and B terms in the Knox and simplified Horváth–Lin equations are identical with the minor difference that Horváth and Lin have provided an explicit expression for the constant B. The major difference appears to be in the C term, given by the expressions

Knox: $(1/30\gamma_{sm}\phi_K)[k''/(1 + k'')]^2(1 - \phi_K)v_e$

Horváth–Lin: $[\theta/30\phi(1 + \phi)^2][(\phi + k' + \phi k')/(1 + k')]^2v_e$

The apparent difference between these terms arises from the definition of the ϕ and ϕ_K terms. Knox's $\phi_K = V_{sm}/V_m$, whereas Horváth and Lin's $\phi = \phi_{sm}V_{sm}/V_{mz}$, where V_{sm}, V_{mz} and V_m are the volumes of stagnant mobile phase, excluded mobile phase or mobile zone and total mobile phase, respectively. ϕ_{sm} is the fraction of the stagnant mobile phase which is accessible to the solute. For a fully permeating solute ($\phi_{sm} = 1$), $\phi_K = \phi/(1 + \phi)$, and given that[17] $k'' = (k' + \phi_K)/(1 - \phi_K)$, it can be shown that

$$[k''/(1 + k'')]^2(1 - \phi_K)/\gamma_{sm}\phi_K = [\theta/\varepsilon_i\phi(1 + \phi)^2][(\phi + k' + \phi k')/(1 + k')]^2$$

The tortuosity factor used by Horváth and Lin is $\theta = \varepsilon_i/\gamma_{sm}$, where ε_i is the intraparticle porosity[11]. Thus for the conditions, (1) the solute is fully permeating, and (2) $D_s/D_m \approx 0$, the Knox equation is essentially identical to the simplified form of the Horváth–Lin equation, the C term differing only by the constant factor ε_i.

The corresponding expressions for apparent plate height are obtained by application of eqn. 3 or 4 to eqns. 5a–d for local plate height. We prefer to use the form involving temporal averages because certain chromatographic parameters, including capacity factor, are typically measured as temporal average quantities.
For the Golay equation:

$$\hat{H} = (1/G4)[(A/F)<g_3(\rho) \cdot f_1(\rho)>_t + Bd_cF<g_3(\rho) \cdot f_2(\rho)>_t + \\ + CF<g_3(\rho) \cdot f_3(\rho)>_t] \quad (6a)$$

The Knox (or simplified Horváth–Lin) equation:

$$\hat{H} = (1/G4)[(A/F_e)<g_3(\rho) \cdot f_1(\rho)>_t + (Bd_p^{4/3}/F_e^{1/3})<g_3(\rho) \cdot f_2(\rho)>_t + \\ + Cd_p^2F_e<g_3(\rho) \cdot f_3(\rho)>_t] \quad (6b)$$

The Horváth–Lin equation:

$$\hat{H} = (1/G4)\{(A/F_e)<g_3(\rho) \cdot f_1(\rho)>_t + Bd_p<g_3(\rho)/[1 + \omega/(d_pF_ef_2(\rho))^{1/3}]>_t + \\ + Cd_p^2F_e<g_3(\rho) \cdot f_3(\rho)>_t + Dd_p^{5/3}F_e^{2/3}<g_3(\rho) \cdot f_4(\rho)>_t\} \quad (6c)$$

The Giddings equation:

$$\hat{H} = (1/G4)\{(A/F_e)<g_3(\rho) \cdot f_1(\rho)>_t + Bd_p<g_3(\rho)/[1 + B/(\omega d_pF_ef_2(\rho))]>_t + \\ + CF_e<g_3(\rho) \cdot f_3(\rho)>_t\} \quad (6d)$$

where $G4 = <1 + k>_t^2<\rho>_z$ and $g_3(\rho) = (1 + k)^2\rho$. In general, $k = k'$ except in the Knox version of eqn. 6b, where $k = k''$.

We will show that in many situations the above expressions can be greatly simplified to yield more familiar results. In near-ideal gas chromatography, k is nearly independent of density and may be treated as a constant. At high mobile phase densities, the product $D_m\rho$ is approximately constant. Finally, although there is

evidence that high mobile phase densities may cause swelling of the stationary phase[21], we shall assume that d_f and D_s remain constant for the purpose of generating approximate expressions for apparent plate height.

Gas–liquid chromatography

GC is most commonly performed under near-ideal conditions with inlet pressures not exceeding 5 atm and an outlet pressure at ambient atmospheric pressure. Based on a review of available data on diffusivity of moderately large organic solutes in gases such as He and N_2, Giddings[22] concluded that $D_m\rho$ remains constant at pressures up to about 20 atm, consistent with the prediction of Chapman–Enskog theory[23]. The capacity factor varies only slightly with mobile phase density at these low pressures. Data for isooctane and several other compounds on squalane show that for N_2 as carrier gas at an inlet pressure of 5 bar and an outlet pressure of 1 bar, the variation in k' from inlet to outlet is about 5% compared to a five-fold change in density[24]. With this rather small variation in k', eqn. 3a may be approximated by

$$\hat{H} = <H\rho^2>_z/<\rho>_z^2 \tag{7}$$

which upon application to eqn. 5a or 5d, assuming that k', d_f, D_s and $D_m\rho$ are constant, yields

$$\hat{H} = (<\rho^2>_z/<\rho>_z^2)(H_L + H_M) + C'F_e<\rho>_z^{-1} \tag{8}$$

where H_L and H_M represent the longitudinal diffusion (A) term and mobile phase mixing (B) term, respectively, as they appear in eqns. 5a and 5d and $C' = Cf_3(\rho)\rho$, which is constant. For an ideal gas it can be shown that

$$<\rho^2>_z/<\rho>_z^2 = J_2^4(\rho)/[J_2^3(\rho)]^2 = (9/8)(\Gamma^4 - 1)(\Gamma^2 - 1)/(\Gamma^3 - 1)^2$$

and

$$1/<\rho>_z = J_3^2(\rho) = (3/2)[(\Gamma^2 - 1)/(\Gamma^3 - 1)](\rho_{out})^{-1}$$

where $\Gamma = \rho_{in}/\rho_{out}$, and, in general, $J_n^m(\rho) = (n/m)(\Gamma^m - 1)/(\Gamma^n - 1)$. Noting that for an ideal gas $\rho_{in}/\rho_{out} = P_{in}/P_{out}$, eqn. 8 is identical to the expression reported by Giddings *et al.*[1]. At higher pressures and with non-ideal carrier gases, where the variation in capacity factor can be quite large, it may be necessary to invoke eqn. 6. This situation is treated in the section on SFC.

Liquid chromatography

Because of the low compressibility of liquids, the case for liquid chromatography appears to be trivial, *i.e.*, the large pressure drops which are common in high-performance liquid chromatography (HPLC) provide little if any contribution to band spreading. In this section we provide general arguments as to why this should be the case for HPLC with packed columns, and estimate the effect under extreme conditions.

Under ordinary HPLC operating conditions with high-pressure pumps and

microparticulate packings, the inlet and outlet densities will differ no more than about 5%, and under these circumstances[9]

$$<\rho>_t \approx <\rho>_z \approx (\rho_{in} + \rho_{out})/2 \tag{9}$$

Likewise, the capacity factor in LC is nearly independent of the operating pressure[25]. For the moment let us also assume that $D_m\rho$ is constant. Therefore eqn. 7 is appropriate, which when applied to eqn. 5 for columns with porous silica packings, yields

$$\hat{H} \approx (<\rho^2>_z/<\rho>_z^2)H \tag{10}$$

where H represents the entire right-hand side of eqn. 5b or 5c. Now it can be shown that

$$<\rho^2>_z/<\rho>_z^2 = <\rho>_t/<\rho>_z$$

which, based on earlier observations[9], is approximately unity under normal LC conditions. Thus it appears that in LC the apparent plate height may be adequately described by the equation for local plate height using simple averages for density and related quantities.

The conclusion just reached is in agreement with the observation that there has been no general concern raised about the effect of pressure drop on resolution in liquid chromatography. A further test of this conclusion is provided by evaluating the effect of pressure drop in an extreme situation. For this purpose we use published data for the elution of benzyl acetate in a mobile phase of 5% ethyl acetate in *n*-hexane in a 25 × 0.46 cm I.D. column packed with silica gel (Partisil 10 with a 7.8 μm particle diameter)[26]. This solvent system was chosen by the authors of the cited study in part because of the relatively high compressibility of *n*-hexane, a property which should also contribute to gradient-induced band spreading. Based on data provided in Table II of ref. 26, this system would yield a flow-rate of approximately 25 ml/min at an inlet pressure of 40 MPa (400 bar). Assuming an interparticle porosity of 0.4 and based on $\rho_{ref} = \rho_{out} = 0.6603$ g cm^{-3} for *n*-hexane (density at 1 bar, ignoring the presence of ethyl acetate) at 25°C, this flow-rate corresponds to $F_{eR} = 6.52$ cm s^{-1}, which is equal to the excluded linear velocity at the outlet. The local and apparent plate heights under these conditions were estimated from the simplified Horváth–Lin version of eqns. 5b and 6b, respectively. This required the estimation of various pressure-dependent parameters as described below. For a more precise treatment of the pressure dependence of density and viscosity, the reader is referred to other published work[12,25].

(1) Approximate expressions for the spatial and temporal distribution functions, which are $D_z(\rho) = (1/\eta)(\rho^{-1}\delta\rho/\delta P)_T^{-1}$ and $D_t(\rho) = (\rho/\eta)(\rho^{-1}\delta\rho/\delta P)_T^{-1}$, were obtained by assuming that viscosity and compressibility are independent of pressure, yielding $D_z(\rho) = \rho$ and $D_t(\rho) = \rho^2$, the same expressions as for an ideal gas.

(2) The isothermal compressibility for *n*-hexane was assumed to remain constant at the handbook value[27] of $1.67 \cdot 10^{-3}$ MPa^{-1}, the value at 1 atm. In fact, the compressibility decreases by about 25% at 40 MPa. Our calculation would therefore predict a slightly greater change in density than would actually occur, which would in

turn exaggerate the effect of pressure drop on plate height. Defining the reference density ρ_{ref} as the density at 1 bar, $\rho_{R,out} = 1$, an inlet pressure of 40 MPa corresponds to $\rho_{R,in} = 1.0651$, or $\Delta\rho_R = \rho_{R,in} - \rho_{R,out} = 0.0651$.

(3) The effect of density on capacity factor was estimated from the k' *vs.* P_{in} data provided in Table VI of ref. 26 and the isothermal compressibility of *n*-hexane, yielding the following relation for pressures from 0.1 to 40 MPa:

$$k' = k'^0 - 2[0.00343\ \text{MPa}^{-1}/(\rho^{-1}\delta\rho/\delta P)]\Delta\rho_R$$
$$= k'^0 - 4.11\Delta\rho_R$$

where $k'^0 = 1.526$ is the value at 1 bar. The factor 0.00343 MPa^{-1} is the slope for the dependence of k' on P_{in}. This factor is doubled because the average column pressure would be about one-half of P_{in}. Thus the average column pressures studied in ref. 26 never exceeded 20 MPa, and the above relation represents an extrapolation to 40 MPa. At an inlet pressure of 40 MPa, then, $k' = 1.295$ at the inlet, and the column-averaged value is 1.410, which is consistent with the value of 1.389 calculated from the regression equation given by Katz *et al.*[26]. Note that the change in k' from inlet to outlet is about 18%. Katz *et al.*[26] attributed this to an increase in column temperature at higher pressures, even for a thermostated column. Thus one extreme is to assume that k' remains constant throughout the column (*i.e.*, it is independent of density), which would contribute nothing to gradient-induced band spreading. The other extreme, which we have adopted here, is to assume that the column is efficiently thermostated, and that the change in k' is due to the density gradient in the column. The truth probably lies between these two extremes, so that our assumption again has the result of exaggerating the effect of pressure drop on band spreading.

(4) The effect of mobile phase density on the diffusion coefficient (D_m) of ethyl acetate was estimated from D_m *vs.* P data[28] to yield the expression

$$D_m = D_m^0 - [2.14 \cdot 10^{-7}\ \text{cm}^2\ \text{s}^{-1}\ \text{Pa}^{-1}/(\rho^{-1}\delta\rho/\delta P)_T]\Delta\rho_R$$
$$= D_m^0 - (1.28 \cdot 10^{-4})\Delta\rho_R$$

where $D_m^0 = 3.097 \cdot 10^{-5}\ \text{cm}^2\ \text{s}^{-1}$ is the value at 1 bar.

Based on the approximations outlined above, the spatial averages of the expressions in the equation obtained by application of eqn. 3a to eqn. 5b (*i.e.*, the spatial average analogue to eqn. 6b) were evaluated by numerical integration to a precision of 1 part in 10^5, and a value for $\hat{H}$ was obtained for the conditions stated above ($P_{in} = 40$ MPa) using the values of the column constants stated earlier. A corresponding value for local plate height was calculated from eqn. 5b using spatial average values for ρ_R, k' and D_m, which are the simple average values that would be routinely observed or calculated. The resulting values were $\hat{H} = 7.274 \cdot 10^{-3}$ cm and $H = 7.256 \cdot 10^{-3}$ cm, a difference of less than 0.3%. This calculation was based on rather extreme operating conditions; results for lower inlet pressures and flow-rates produced even smaller differences between $\hat{H}$ and H. Thus the theory correctly predicts what is generally observed in practice, that for an LC column operated isothermally at a constant mass flow-rate, the effect of pressure drop on plate height is insignificant.

TABLE II

SELECTED DATA FOR NAPHTHALENE MODEL

For CO_2 mobile phase at 40°C on 5.0-μm reversed-phase silica, 15 × 0.46 cm I.D. column. Ln $k' = 6.34 - 9.49\rho_R + 2.35\rho_R^2$. See eqn. 12 and related discussion for definitions of h_{est}, $\hat{h}_{est}$, $G3$, $G4$ and $F2$.

$<\rho_R>_t$	F_{eR} cm/s	$<v_e>_t$	ΔP bar	P_{avg} bar	P_{out} bar	$<k'>_t$	k'_{out}	$\hat{h}$	$\hat{h}/h_{est}$	$\hat{h}/\hat{h}_{est}$	$<\rho>_t/<\rho>_z$	$G3/G4$	$F2/G4$
1.20	0.50	1.24	4.0	94.0	92.0	0.191	0.257	2.93	1.00	1.00	1.00	1.00	0.92
1.20	1.00	2.49	8.1	94.0	90.0	0.203	0.394	2.68	1.00	1.00	1.00	1.00	0.94
1.20	1.50	3.74	12.4	94.2	87.9	0.224	0.660	2.70	1.00	1.00	1.01	1.00	0.97
1.20	2.00	5.01	16.8	94.3	85.9	0.262	1.183	2.79	1.01	1.00	1.02	1.00	1.04
1.20	3.00	7.60	25.7	94.3	81.5	0.405	3.284	3.17	1.06	1.01	1.05	1.03	1.39
1.20	4.00	10.26	34.9	93.9	76.5	0.671	7.306	4.11	1.26	1.05	1.08	1.15	2.14
1.20	5.00	12.98	44.7	92.9	70.5	1.066	14.070	5.78	1.61	1.11	1.12	1.35	3.17
1.20	6.00	15.76	55.5	91.0	63.3	1.681	26.358	8.32	2.10	1.20	1.16	1.61	4.37
1.20	7.01	18.59	67.9	88.0	54.0	2.594	49.874	11.79	2.70	1.32	1.21	1.88	5.53
1.20	8.00	21.43	83.7	82.9	41.1	3.914	101.403	16.51	3.45	1.52	1.27	2.11	6.49
1.30	0.50	1.23	4.0	97.8	95.8	0.132	0.156	2.93	1.00	1.00	1.00	1.00	0.84
1.30	1.00	2.47	8.0	97.9	93.9	0.134	0.193	2.67	1.00	1.00	1.00	1.00	0.84
1.30	1.50	3.70	12.1	98.2	92.2	0.139	0.258	2.68	1.00	1.00	1.00	1.00	0.85
1.30	2.00	4.95	16.3	98.6	90.4	0.146	0.376	2.75	1.00	1.00	1.01	1.00	0.86
1.30	3.00	7.47	25.3	99.2	86.6	0.182	1.025	2.92	1.00	1.00	1.02	1.00	0.92
1.30	4.00	10.04	34.4	99.7	82.5	0.261	2.683	3.20	1.03	1.01	1.04	1.01	1.12
1.30	5.00	12.67	43.7	100.0	78.2	0.417	5.893	3.88	1.17	1.03	1.06	1.08	1.63
1.30	6.00	15.34	53.4	99.8	73.1	0.657	11.148	5.25	1.45	1.09	1.09	1.24	2.47
1.30	7.00	18.07	64.0	98.8	66.8	1.026	20.218	7.59	1.92	1.17	1.12	1.48	3.62
1.30	8.01	20.86	75.5	96.8	59.0	1.571	36.474	11.05	2.55	1.28	1.16	1.77	4.91

1.40	0.50	1.23	4.2	104.1	102.0	0.097	0.105	2.92	1.00	1.00	1.00	1.00	0.79
1.40	1.00	2.47	8.4	104.2	100.1	0.096	0.115	2.66	1.00	1.00	1.00	1.00	0.79
1.40	1.50	3.70	12.6	104.6	98.3	0.097	0.130	2.67	1.00	1.00	1.00	1.00	0.79
1.40	2.00	4.94	16.7	104.6	96.3	0.098	0.150	2.73	1.00	1.00	1.00	1.00	0.79
1.40	3.00	7.42	25.2	105.6	93.0	0.103	0.232	2.88	1.00	1.00	1.01	1.00	0.80
1.40	4.00	9.93	34.1	106.7	89.7	0.113	0.464	3.02	1.00	1.00	1.01	1.00	0.81
1.40	5.00	12.47	43.5	107.8	86.0	0.139	1.207	3.18	1.01	1.00	1.02	1.00	0.86
1.40	6.00	15.06	52.8	108.7	82.2	0.200	3.032	3.45	1.04	1.01	1.04	1.01	1.03
1.40	7.00	17.70	62.4	109.4	78.2	0.305	6.137	4.08	1.15	1.03	1.06	1.07	1.42
1.40	8.00	20.37	72.4	109.5	73.3	0.474	11.245	5.43	1.43	1.09	1.08	1.20	2.14
1.60	0.50	1.26	4.7	132.1	129.7	0.059	0.060	2.91	1.00	1.00	1.00	1.00	0.73
1.60	1.00	2.52	9.5	132.2	127.5	0.059	0.062	2.66	1.00	1.00	1.00	1.00	0.73
1.60	1.50	3.78	14.2	132.5	125.4	0.059	0.063	2.67	1.00	1.00	1.00	1.00	0.73
1.60	2.00	5.03	18.9	132.9	123.5	0.059	0.064	2.72	1.00	1.00	1.00	1.00	0.73
1.60	3.00	7.55	28.4	133.3	119.1	0.059	0.068	2.86	1.00	1.00	1.00	1.00	0.73
1.60	4.00	10.08	37.8	133.8	114.9	0.059	0.073	3.00	1.00	1.00	1.00	1.00	0.73
1.60	5.00	12.59	47.1	133.8	110.2	0.060	0.080	3.12	1.00	1.00	1.00	1.00	0.73
1.60	6.00	15.09	56.5	134.6	106.4	0.061	0.089	3.24	1.00	1.00	1.00	1.00	0.74
1.60	7.00	17.62	65.9	135.7	102.8	0.061	0.101	3.35	1.00	1.00	1.00	1.00	0.74
1.60	7.99	20.14	75.2	137.2	99.6	0.062	0.117	3.45	1.00	1.00	1.00	1.00	0.74

Supercritical fluid chromatography

In SFC we commonly find significant variations in both solute capacity factor and mobile phase density, especially with packed columns, so it is here that eqns. 3 and 4 should be most useful. While it is possible to generate rather large pressure drops in SFC with open tubular columns, the pressure drops under typical conditions are quite small, and the equations for apparent plate height essentially reduce to those for local plate height. Therefore we will focus our attention on results for packed columns. The effects of pressure drop in capillary SFC will be the subject of a future investigation.

To evaluate the effects of solute velocity gradients in packed columns, we employ retention data for the elution of naphthalene at 40°C with CO_2 on porous silica (reversed-phase, Perisorb RP-8)[29]. A fit of ln k' *vs.* reduced density for the reported data yields the relation

$$\ln k' = 6.34 - 9.49\rho_R + 2.35\rho_R^2$$

Values of apparent plate height were calculated using the Horváth–Lin equation (eqn. 6c) and a BASIC program written in Microsoft QuickBASIC 4.0 on a personal computer. Not all of the parameters required for the calculation of plate height were known, so for the constant column parameters we chose the values suggested in ref. 18; $\varepsilon_e = 0.4, \gamma = 0.7, \lambda = 2.5, \phi = 0.8, \theta = 2, \omega = 2$ and $\kappa = 1/15$. Unless otherwise noted, all calculations correspond to CO_2 mobile phase at 40°C with 15-cm column packed with porous silica with a particle diameter of 5 μm. Values of inlet and outlet densities coresponding to selected combinations of temporal average reduced density and reduced excluded mass flow-rate (F_{eR}) were determined based on solutions to the integrated form of Darcy's Law (eqn. A3, Appendix). Inlet and outlet pressures and values of $\eta_R^{-1}(\delta P_R/\delta\rho_R)_T$ were calculated using the Jacobsen–Stewart modification of the Benedict–Webb–Rubin equation[30–32]. The Kozeny–Carman equation was used to calculate specific permeability, and the Reynolds number at the outlet was not allowed

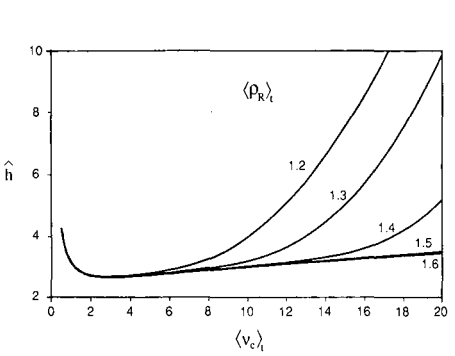

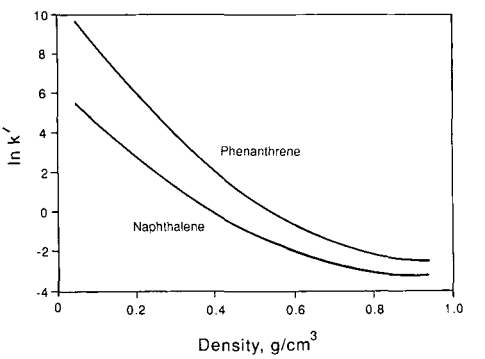

Fig. 1. Predicted effect of reduced velocity on efficiency at various average mobile phase densities for elution of naphthalene. Data calculated from eqn. 6c. Mobile phase: CO_2 at 40°C. Stationary phase: reversed-phase (octyl) porous silica, $d_p = 5$ μm. Column: 15 × 0.46 cm I.D. Solute retention: ln $k' = 6.34 - 9.49\rho_R + 2.35\rho_R^2$. See text for other solute and stationary phase parameters.

Fig. 2. Effect of mobile phase density on capacity factor for naphthalene and phenanthrene on reversed-phase (octyl) silica at 40°C. Data for naphthalene from van Wasen *et al.*[29]. Data for phenanthrene is predicted using Martire–Boehm equation[8].

to exceed 20. Reduced values of viscosity, pressure and density were employed to simplify the numerical calculations. Diffusion coefficient data for naphthalene in CO_2 at 40°C from ref. 15 were fit to a second order polynomial to yield the relation

$$D_m \cdot 10^4 \text{ cm}^2/\text{s} = 3.69 - 2.11\rho_R + 0.361\rho_R^2$$

Viscosity values were calculated from a fourth order polynomial fit to published data[30,33].

Predicted results for the effect of average operating density on efficiency with naphthalene as solute are shown in Fig. 1; selected data corresponding to these plots are presented in Table II. It is seen that the effect of pressure drop is most severe at low average column density. This is consistent with the experimental results of earlier studies[2,34]. This behavior is quite reasonable considering that at low densities $d\rho/dP$ can be quite large, leading to large changes in density and significant expansion of the mobile phase. The effect of this expansion, ignoring effects on k', is represented by $<\rho>_t/<\rho>_z$. For the data shown in Table II, values of this ratio are largest at $<\rho_R>_t = 1.20$, but they are, in general, not large enough to induce effects of the magnitude shown in Fig. 1. Second, we note that the effect of density changes on capacity factor are greatest at low carrier density (Fig. 2). A result of the latter effect is that at $<\rho_R>_t = 1.20$, $<k'>_t$ increases as v_e increases due to the lower densities and therefore higher values of k' experienced near the column outlet. The combined effects of mobile phase expansion, as measured by $<\rho>_t/<\rho>_z$, and the significant changes in capacity factor at low average carrier density, result in the very rapid rise in the $\hat{h}$ *vs.* v_e curve beyond the optimum velocity at low average carrier densities. At $<\rho_R>_t = 1.40$, the changes in the ratio $<\rho_R>_t/<\rho_R>_z$ and values of $<k'>_t$ are significantly smaller. For $<\rho_R>_t = 1.60$, where $d\rho/dP$ is relatively small, $<\rho_R>_t/<\rho_R>_z \approx 1.00$ even at high velocities, and $<k'>_t$ remains approximately equal to the value for constant density, so that the gradient-induced band broadening is negligible (Fig. 1).

A family of curves similar to those in Fig. 1 has been reported for the elution of phenanthrene at 50°C at much higher average pressures[2]. We were able to reproduce this behavior at higher pressures also by (1) adjusting the parameters in our equations for capacity factor and diffusion coefficient to yield the values reported in ref. 2 for phenanthrene at 50°C, and (2) using a particle size of 2 μm in a 15-cm column. One effect of raising the temperature is that the maximum compressibility of CO_2 occurs at higher pressure. The smaller particle size results in a larger pressure drop. The combined effect (higher temperature, smaller particle size) is to induce significant changes in k' at higher average operating pressures. Thus our equations are consistent with expected and observed behavior in this respect.

To evaluate the effect of k' on efficiency, we made an estimate of the parameters for phenanthrene in the equation

$$\ln k' = \ln k'^0 - a\rho_R + b\rho_R^2$$

where k'^0 is the capacity factor under ideal GC conditions. Although the theory behind this equation strictly applies to *absorption* chromatography[9], it should serve as a reasonable basis for estimating the effect of solute properties on coefficients a and b, since these are largely mobile phase parameters. Accordingly, estimates of a and b were

TABLE III

SELECTED DATA FOR PHENANTHRENE MODEL

For CO_2 mobile phase at 40°C on 5.0-μm reversed-phase silica, 15 × 0.46 cm I.D. column. Ln $k' = 11 - 13.32\rho_R + 3.30\rho_R^2$. See eqn. 12 and related discussion for definitions of h_{est}, $\hat{h}_{est}$, $G3$, $G4$ and $F2$.

$<\rho_R>_t$	F_{eR} cm/s	$<v_e>_t$	ΔP bar	P_{avg} bar	P_{out} bar	$<k'>_t$	k'_{out}	$\hat{h}$	$\hat{h}/h_{est}$	$\hat{h}/\hat{h}_{est}$	$<\rho>_t/<\rho>_z$	$G3/G4$	$F2/G4$
1.20	0.50	1.50	4.0	94.0	92.0	0.811	1.218	2.87	1.00	1.00	1.00	1.00	1.58
1.20	1.00	3.01	8.1	94.0	90.0	0.903	2.219	2.84	1.03	1.00	1.00	1.03	1.73
1.20	1.50	4.53	12.4	94.2	87.9	1.087	4.572	3.21	1.12	1.00	1.01	1.10	2.13
1.20	2.00	6.07	16.8	94.3	85.9	1.479	10.353	4.24	1.39	1.01	1.02	1.33	3.14
1.20	3.00	9.20	25.7	94.3	81.5	3.390	43.378	9.49	2.70	1.05	1.05	2.44	7.33
1.20	4.00	12.42	34.9	93.9	76.5	8.164	133.224	16.08	3.99	1.11	1.08	3.49	11.06
1.20	5.00	15.72	44.7	92.9	70.5	17.415	334.158	21.35	4.75	1.18	1.12	3.96	12.72
1.20	6.00	19.08	55.5	91.0	63.3	35.638	806.290	26.17	5.30	1.27	1.16	4.12	13.32
1.20	7.01	22.51	67.9	88.0	54.0	70.070	1973.225	31.94	5.96	1.41	1.21	4.20	13.57
1.20	8.00	25.94	83.7	82.9	41.1	134.705	5341.630	40.95	7.11	1.66	1.27	4.27	13.81
1.30	0.50	1.49	4.0	97.8	95.8	0.479	0.602	2.84	1.00	1.00	1.00	1.00	1.27
1.30	1.00	2.99	8.0	97.9	93.9	0.494	0.815	2.72	1.00	1.00	1.00	1.00	1.29
1.30	1.50	4.48	12.1	98.2	92.2	0.525	1.227	2.82	1.01	1.00	1.00	1.01	1.35
1.30	2.00	5.99	16.3	98.6	90.4	0.581	2.076	3.00	1.03	1.00	1.01	1.02	1.47
1.30	3.00	9.04	25.3	99.2	86.6	0.898	8.469	4.23	1.31	1.01	1.02	1.25	2.53
1.30	4.00	12.15	34.4	99.7	82.5	1.866	32.667	9.63	2.62	1.05	1.04	2.30	6.54
1.30	5.00	15.34	43.7	100.0	78.2	4.404	98.529	18.92	4.48	1.11	1.06	3.80	11.90
1.30	6.00	18.58	53.4	99.8	73.1	9.446	241.036	26.74	5.65	1.17	1.09	4.64	14.86
1.30	7.00	21.87	64.0	98.8	66.8	19.246	555.762	33.02	6.35	1.26	1.12	4.95	15.97
1.30	8.01	25.26	75.5	96.8	59.0	37.439	1271.932	39.39	7.00	1.37	1.16	5.04	16.28

1.40	0.50	1.49	4.2	104.1	102.0	0.309	0.347	2.83	1.00	1.00	1.00	1.00	1.07
1.40	1.00	2.99	8.4	104.2	100.1	0.308	0.394	2.69	1.00	1.00	1.00	1.00	1.07
1.40	1.50	4.48	12.6	104.6	98.3	0.314	0.469	2.76	1.00	1.00	1.00	1.00	1.08
1.40	2.00	5.98	16.7	104.6	96.3	0.320	0.571	2.86	1.00	1.00	1.00	1.00	1.09
1.40	3.00	8.99	25.2	105.6	93.0	0.350	1.051	3.08	1.01	1.00	1.01	1.00	1.15
1.40	4.00	12.02	34.1	106.7	89.7	0.422	2.787	3.44	1.04	1.00	1.01	1.03	1.35
1.40	5.00	15.10	43.5	107.8	86.0	0.656	10.658	5.05	1.41	1.02	1.02	1.29	2.51
1.40	6.00	18.24	52.8	108.7	82.2	1.406	38.783	12.82	3.13	1.07	1.04	2.58	7.33
1.40	7.00	21.42	62.4	109.4	78.2	3.128	104.300	25.91	5.52	1.13	1.06	4.43	13.84
1.40	8.00	24.66	72.4	109.5	73.3	6.636	243.970	37.72	7.15	1.20	1.08	5.63	18.01
1.60	0.50	1.52	4.7	132.1	129.7	0.155	0.160	2.80	1.00	1.00	1.00	1.00	0.87
1.60	1.00	3.05	9.5	132.2	127.5	0.155	0.165	2.67	1.00	1.00	1.00	1.00	0.87
1.60	1.50	4.57	14.2	132.5	125.4	0.155	0.170	2.73	1.00	1.00	1.00	1.00	0.87
1.60	2.00	6.09	18.9	132.9	123.5	0.154	0.175	2.81	1.00	1.00	1.00	1.00	0.87
1.60	3.00	9.14	28.4	133.3	119.1	0.155	0.190	2.99	1.00	1.00	1.00	1.00	0.87
1.60	4.00	12.20	37.8	133.8	114.9	0.157	0.209	3.16	1.00	1.00	1.00	1.00	0.87
1.60	5.00	15.24	47.1	133.8	110.2	0.160	0.238	3.32	1.00	1.00	1.00	1.00	0.88
1.60	6.00	18.26	56.5	134.6	106.4	0.162	0.275	3.46	1.00	1.00	1.00	1.00	0.88
1.60	7.00	21.33	65.9	135.7	102.8	0.165	0.327	3.60	1.00	1.00	1.00	1.00	0.89
1.60	7.99	24.39	75.2	137.2	99.6	0.169	0.405	3.73	1.00	1.00	1.00	1.00	0.89

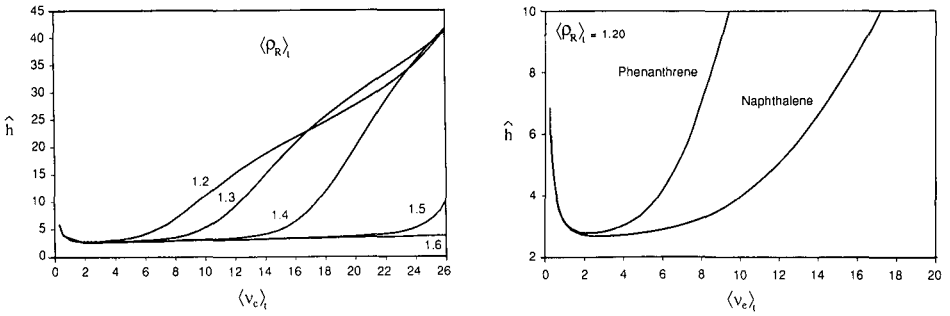

Fig. 3. Predicted effect of reduced velocity on efficiency at various average mobile phase densities for elution of phenanthrene. Ln $k' = 11 - 13.32\rho_R + 3.30\rho_R^2$. Other conditions as in Fig. 1.

Fig. 4. Predicted effect of solute on efficiency at $<\rho_R> = 1.2$. Conditions as in Fig. 1.

made by multiplying each by the ratio of the Van der Waals volume of phenanthrene to that of naphthalene, yielding $a = 13.32$ and $b = 3.30$. The value of ln k'^0 was then increased to 11, the smallest integral value for which the ln k' *vs.* ρ_R curve for phenanthrene does not intersect that for naphthalene (Fig. 2). The diffusion coefficient for phenanthrene was estimated by applying a factor of 0.826 to the values for naphthalene, which is the ratio of D_m values for phenanthrene to naphthalene at 240 bar and 50°C[2]. Plots of $\hat{h}$ *vs.* $<v_e>_t$ are shown in Fig. 3, with corresponding data presented in Table III. Two aspects about these curves are immediately obvious. First is that, at a given average density, $\hat{h}$ for phenanthrene rises much more rapidly than it does for naphthalene (Fig. 4). This is expected because of the larger values of capacity factor. On the basis of the approximate expressions

$$\hat{H} \approx H<(1 + k')^2\rho_R^2>_z/<(1 + k')\rho_R>_z^2 =$$

$$= H<1 + k')^2\rho_R>_t/(<1 + k'>_t^2<\rho_R>_z) \quad (11)$$

which we examine below, $\hat{H}$ should increase with k', since the expression has the form of the average of the square divided by the square of the average. This is consistent with the experimental results obtained by Schoenmakers and Uunk[34], who observed much greater losses in efficiency with pressure drop for naphthalene (average $k' \approx 1.3$) and biphenyl (average $k' \approx 1.1$) than for ethylbenzene (average $k' \approx 0.3$) under identical conditions.

The second interesting aspect of the curves for phenanthrene in Fig. 3 is that, for large values of $<v_e>_t$, they change in curvature, and even intersect one another. These results are predictions based on the model and remain to be verified experimentally.

It is important to emphasize that the data presented in all of the tables and figures are based for the most part on models rather than experimental data, and as such depend on the assumptions made. This distinction is especially important with respect to the effect of solute size on mass transfer in the stationary phase. Experimental results[2] have shown that, at high average densities where gradient-induced band spreading should be insignificant, the reduced plate height curve rises more rapidly for naphthalene than for phenanthrene at reduced velocities above the

optimum. This was attributed to a combination of factors involving the effects of solute size and capacity factor on the magnitude of the C term. These factors are not taken into account in the present treatment.

We now investigate the possibility of simplifying eqn. 6c by assuming that $D_m\rho_R$, and therefore v, can be assumed to remain constant. This results in the attractively simple expression

$$\hat{h}_{est} = (G3/G4)[A/v_e + B/(1 + \omega v_e^{-1/3})] + (F2/G4)[Cv_e + Dv_e^{2/3}] \quad (12)$$

where $F2 = <(\phi + k' + \phi k')^2\rho_R>_t$
$G3 = <(1 + k')^2\rho_R>_t$
$G4 = <1 + k'>_t^2<\rho_R>_z$

The same treatment applied to eqn. 6b results in even simpler expressions. The ratios $\hat{h}/\hat{h}_{est}$ and $\hat{h}/h_{est}$ are listed in Tables II and III along with other parameters including $G3/G4$ and $F2/G4$. h_{est} is a simple estimate of the reduced plate height calculated from the local plate height equation, using $<k'>_t$ in place of k', and $<D_m\rho_R>_t$ for $D_m\rho_R$. Thus $\hat{h}/h_{est}$ is a measure of the overall effect of solute velocity gradients on efficiency. The data in Tables II and III show that $\hat{h}_{est}$ is a good approximation of $\hat{h}$ except for the combination of high velocities and low average density. Considering that the evaluation of $\hat{h}_{est}$ requires evaluation of spatial and temporal averages just as does $\hat{h}$, there appears to be little advantage in utilizing this estimate in actual calculations. However, the expression for $\hat{h}_{est}$ may serve some purpose as an aid in understanding the impact of solute velocity gradients on the different band-broadening processes.

Considering eqns. 11 and 12, and that the C and D terms in eqn. 12 should be significant only at high velocities, the ratio $G3/G4$ should provide a reasonable indicator of the onset of departure of $\hat{h}$ from the corresponding value assuming no density drop (h_{est}). In fact, we find that the departure of $G3/G4$ from unity parallels that of $\hat{h}/h_{est}$, although the latter increases more rapidly. It is useful to note that as long as $G3/G4 = 1.00$, there is no significant loss of efficiency due to solute velocity gradients. The rapid increase in $\hat{h}/h_{est}$ at higher velocities appears to be related to the relative values of the ratios $G3/G4$ and $F2/G4$. At low velocities, where only the A and B terms are important, $\hat{h}/h_{est} \approx G3/G4$. At higher velocities the C and D terms become significant, and these are multiplied by the ratio $F2/G4$. This ratio increases much more rapidly than does $G3/G4$, resulting in an additional increase in $\hat{h}/h_{est}$. Another possible indicator of the loss of efficiency might be the ratio $<\rho_R>_t/<\rho_R>_z$. In the absence of changes in k' as in near-ideal GC, this would be the case (see eqn. 8). In SFC, however, the added effect of changes in k' make this ratio a rather poor indicator of the onset of loss of resolution. Data for phenanthrene in Table III show that rather large values of $\hat{h}/h_{est}$ are attained before $<\rho_R>_t/<\rho_R>_z$ increases appreciably.

Upon further examination of the data for the naphthalene and phenanthrene models in Tables II and III, the outlet pressure appears to be a simple, reliable indicator of the onset of loss of efficiency, regardless of the average density. Loss of efficiency is experienced at $P_{out} \leq 82$ bar for the naphthalene model, and at $P_{out} \leqslant 90$ bar for the phenanthrene model. The use of outlet pressure or density as a guide to avoid loss of resolution has been noted earlier[3,34].

Figs. 5 and 6 show the effect of particle size for two columns operated at the same temporal average density and keeping all other parameters constant. Fig. 5 shows that

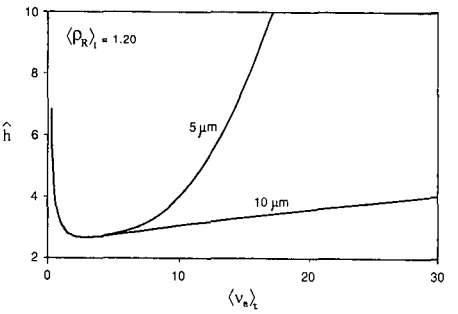

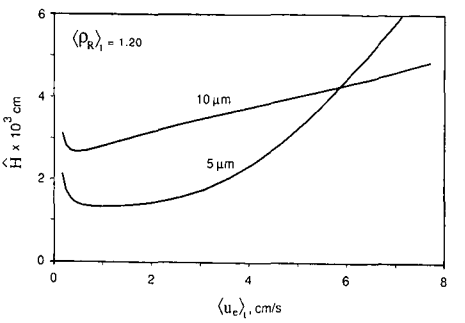

Fig. 5. Predicted effect of particle size on reduced plate height *vs.* reduced velocity curves for elution of naphthalene. Other conditions as in Fig. 1.

Fig. 6. Predicted effect of particle size on plate height *vs.* linear velocity curves for elution of naphthalene. Other conditions as in Fig. 1.

at high reduced velocities the column packed with smaller particles loses efficiency much more rapidly than the column packed with larger particles. This is due to the larger pressure drop required to operate the column with smaller particles at the same reduced velocity. Fig. 6 shows the variation in actual plate height *versus* average linear velocity. At high linear velocity, the column packed with larger particles becomes more efficient, suggesting that for fast separations it may be desirable to use larger diameter particles. These effects have also been observed experimentally[3,34].

CONCLUSIONS

We have presented a rigorous treatment which accounts for the effect of pressure drop on efficiency in column chromatography for steady state, isothermal operation, and have shown that the results predicted by theory agree in general with experiment. The band broadening which is observed when compressible mobile phase fluids experience large pressure drops in a chromatographic column is a direct result of the solute velocity gradients which are thereby induced. Accurate prediction of the gradient-induced band broadening requires a knowledge of the equation of state for the mobile phase fluid, the dependence of the solute capacity factor on mobile phase density and an explicit expression for local plate height. The dependence of solute diffusion coefficients in the mobile and stationary phases on mobile phase density must also be known. Excluding the possibility of adsorption phenomena, the major limitation to accurate prediction of plate height at this time seems to be a lack of information on the effect of mobile phase density on solute diffusion coefficients in the stationary phase or stationary zone. This limitation notwithstanding, this treatment provides the foundation for prediction of the effects of basic operating parameters such as particle or tube diameter, column length and mobile phase conditions on resolution. As such, it should prove useful for column design and optimization procedures in SFC.

ACKNOWLEDGEMENTS

This work was supported by National Science Foundation Grants CHE-8305045 and CHE-8902735, and by the Bush Sabbatical Program of the University of Minnesota, which provided partial support for D.P. while on sabbatical leave at Georgetown University. The authors also are grateful for helpful discussions with Richard Boehm and Rebecca Riester of Georgetown University, for equation of state data from Thomas Bruno of NIST at Boulder, CO, and for software routines provided by Abul Hussam (George Mason University) and Rebecca Riester.

APPENDIX

Alternative derivation of the apparent plate height equation

The basic approach taken here is similar to that used by Giddings *et al.*[1] for the effect of pressure drop on plate height in gas chromatography, but with consideration of non-ideal behavior of the mobile phase fluid, as well as the effect of mobile phase density on solute capacity factors. It is applicable to gas, liquid and supercritical fluid chromatography under conditions of constant temperature and constant mass flow-rate.

Let us define a solute zone as a region containing a fixed mass of solute. At a constant mobile phase specific mass flow-rate F_m, the width w of the solute zone, and therefore its velocity, will vary as a result of changes in mobile phase density and solute capacity factor. The velocity of the mobile phase u_m is inversely proportional to its density through the relation

$$u_m = F_m/\rho$$

The velocity of the solute is some fraction of the mobile phase velocity and is related to the capacity factor k' by the relation

$$u_s = u_m/(1 + k')$$

At any point in the column then

$$u_s = F_m/(1 + k')\rho \tag{A1}$$

Let us divide the column into increments of variable width w which correspond to the widths of a solute zone as it traverses the column. Let Δt be the average time required for a solute molecule to pass through increment j of width w_j, so that

$$w_j = u_{s,j}\Delta t$$

where $u_{s,j}$ is the velocity of the solute in increment j. During the subsequent and equal time period Δt, the solute traverses increment $j + 1$ of width w_{j+1}, and

$$w_{j+1} = (u_{s,j+1})\Delta t$$

Invoking eqn. A1,

$$w_{j+1}/w_j = u_{s,j+1}/u_{s,j} = (1 + k'_j)\rho_j/[(1 + k'_{j+1})\rho_{j+1}]$$

We now define σ_j as the *contribution* to solute zone width which occurs *within* segment j. As the solute zone moves through increment $j + 1$, the contribution σ_j to solute zone width which occurred in segment j becomes

$$\sigma_{j+1} = \sigma_j(w_{j+1}/w_j) = \sigma_j(1 + k'_j)\rho_j/[(1 + k'_{j+1})\rho_{j+1}]$$

In the absence of a velocity gradient, the variance at the outlet is

$$\sigma^2_{out} = \Sigma\sigma^2_j$$

In the presence of a gradient, noting that we can replace w_{j+1} with the width of the solute zone at the outlet, the variance becomes

$$\sigma^2_{out} = \Sigma[\sigma^2_j(1 + k'_j)^2\rho^2_j/(1 + k'_{out})^2\rho^2_{out}]$$

Letting z equal the distance travelled by the solute band, substituting $\sigma^2 = Hz$, and summing over a column of length L in the limit of infinitesimally small increments, we obtain

$$\sigma^2_{out} = \int_0^L \{(H(1 + k')^2\rho^2)/[(1 + k'_{out})^2\rho^2_{out}]\}dz$$

The standard deviation of an eluting peak in elution time τ is

$$\tau = \sigma_{out}/u_{s,out} = \sigma_{out}(1 + k'_{out})/u_{out}$$

The apparent or measured plate height $\hat{H}$ is then

$$\hat{H} = L(\tau/t_r)^2 = L\sigma^2_{out}(1 + k'_{out})^2/(u^2_{out}t^2_r) = \\ = [L/(u_{out}\rho_{out}t_r)^2] \int_0^L H(1 + k')^2\rho^2 dz \tag{A2}$$

A change in variable from z to ρ is possible using Darcy's law;

$$u_m = F_m/\rho = -(B^0/\eta)(dP/dz) = -(B^0/\eta)(\delta P/\delta\rho)_T(d\rho/dz)$$

where B^0 is specific permeability, η is viscosity and P is pressure. Rearranging, we obtain

$$dz = -(B^0\rho/F_m\eta)(\delta P/\delta\rho)_T d\rho = -(B^0/F_m)D_z(\rho)d\rho \tag{A3}$$

where $D_z(\rho)$ is the spatial distribution function for the mobile phase fluid[9]. Substituting for dz in eqn. A2,

$$\hat{H} = (B^0 L/F_m^3 t_r^2)\int H(1 + k')^2 \rho^2 D_z(\rho) d\rho \quad (A4)$$

where the integration limits are from $\rho = \rho_{out}$ at $z = L$ to $\rho = \rho_{in}$ at $z = 0$.

Also noting that dt is related to the temporal distribution function[9] $D_t(\rho)$ by the relation

$$dt = -(B^0/F_m^2) D_t(\rho) d\rho$$

and that the solute retention time $t_r = (1 + k')t_u$, where t_u is the time required to elute an unretained solute, we obtain

$$dt_r = -(B^0/F_m^2)(1 + k') D_t(\rho) d\rho$$

and

$$t_r = (B^0/F_m^2)\int (1 + k') D_t(\rho) d\rho \quad (A5)$$

Combining eqns. A4 and A5,

$$\hat{H} = (LF_m/B^0)[\int H(1 + k')^2 \rho^2 D_z(\rho) d\rho]/[\int (1 + k') D_t(\rho) d\rho]^2 \quad (A6)$$

where the integration limits are ρ_{in} to ρ_{out}. Also noting that

$$L = \int dz = (B^0/F_m)\int D_z(\rho) d\rho$$

and that $\rho D_z(\rho) = D_t(\rho)$, making the appropriate substitutions in eqn. A6, we obtain

$$\hat{H} = <H(1 + k')^2 \rho>_t / (<1 + k'>_t^2 \cdot <\rho>_z) \quad (A7)$$

or in reduced parameters

$$\hat{h} = \hat{H}/d = <h(1 + k')^2 \rho>_t / (<1 + k'>_t^2 \cdot <\rho>_z) \quad (A8)$$

where $< >_t$ and $< >_z$ represent the temporal and spatial averages, respectively, of the enclosed functions, and d is the column diameter (d_c) for open tubular columns or the particle diameter (d_p) for packed columns.

SYMBOLS

A	Area
A, B, C, D	Constants in plate height equation
B^0	Specific permeability of a packed bed
D_m, D_s, D_{sz}	Diffusion coefficient of solute, cm^2 s^{-1}: in mobile phase; in stationary phase; in stationary zone

d_c, d_p	Diameter: of column; of particle
d_f	Stationary phase film thickness
$D_t(\rho)$, $D_z(\rho)$	Density distribution function: temporal; spatial
ε_e, ε_i, ε_t	Porosity: interparticle; intraparticle; total
F, F_e, F_m, F_0	Specific mass flow-rate, g cm^{-2} s^{-1}; specific mass flow-rate: of mobile zone; of mobile phase; superficial
F_R, F_{eR}, F_{mR}, F_{0R}	Reduced specific mass flow-rate, cm/s; reduced specific mass flow-rate: of mobile zone; of mobile phase; superficial
γ, γ_m, γ_s, γ_{sm}	Obstruction factor: for longitudinal diffusion; in mobile phase; in stationary phase; in stagnant mobile phase
Γ	Ratio of inlet to outlet density
H, $\hat{H}$	Local plate height; apparent plate height
h, $\hat{h}$, $\hat{h}_{est}$, h_{est}	Reduced plate height: local; apparent; estimated apparent assuming v is constant; simple estimate of local plate height
η, η_R	Viscosity; reduced viscosity
θ	Tortuosity factor for porous particles
k', k'', k	Phase capacity factor; zone capacity factor; k' or k''
k'^0	Phase capacity factor at stated reference conditions
κ, λ, q, ω	Packing parameters
L	Length of column
m_e	Mass of excluded mobile phase
$\dot{m}$	Mass flow-rate, g/s
P, P_{in}, P_{out}	Pressure; inlet pressure; outlet pressure
v, v_e	Reduced velocity; reduced excluded velocity
ρ, ρ_{in}, ρ_{out}, ρ_{ref}	Density; inlet density; outlet density; reference density
ρ_R	Reduced density
σ, τ	Standard deviation of a solute zone: in length units; in time units
t	Time
t_r, t_u	Retention time: of a solute; of an unretained solute
T	Temperature
u_e, u_m, u_0, u_s	Linear velocity: of mobile zone; of mobile phase; superficial; of solute
V, V_e, V_i	Volume: total; interparticle; intraparticle
$\dot{V}$	Volumetric flow-rate, cm^3/s
ϕ	Ratio of intraparticle volume accessible to solute over interstitial void volume
ϕ_{sm}	Fraction of stagnant mobile phase which is accessible to solute
ϕ_K	Ratio of stagnant mobile phase volume to mobile phase volume
w	Width of a solute zone
z	Axial position in column
$< >_t$	Temporal average of function enclosed in brackets
$< >_z$	Spatial average of function enclosed in brackets

REFERENCES

1 J. C. Giddings, S. L. Seager, L. R. Stucki and G. H. Stewart, *Anal. Chem.*, 32 (1960) 867–870.
2 P. A. Mourier, M. H. Caude and R. H. Rosset, *Chromatographia*, 23 (1987) 21–25.

3 P. J. Schoenmakers, in R. M. Smith (Editor), *Supercritical Fluid Chromatography*, Royal Society, London, 1988, Ch. 4.
4 P. A. Peaden and M. L. Lee, *J. Chromatogr.*, 259 (1983) 1–16.
5 S. M. Fields and M. L. Lee, *J. Chromatogr.*, 349 (1985) 305–316.
6 J. C. Giddings, *Anal. Chem.*, 35 (1963) 353–356.
7 J. C. Giddings, *Dynamics of Chromatography, Part I, Principles and Theory*, Marcel Dekker, New York, 1965, pp. 79–82.
8 D. E. Martire and R. E. Boehm, *J. Phys. Chem.*, 91 (1987) 2433–2446.
9 D. E. Martire, *J. Chromatogr.*, 461 (1989) 165–176.
10 P. J. Schoenmakers, P. E. Rothfusz and F. C. C. J. G. Verhoeven, *J. Chromatogr.*, 395 (1987) 91–110.
11 Cs. Horváth and H.-J. Lin, *J. Chromatogr.*, 126 (1976) 401–420.
12 R. C. Reid, J. M. Prausnitz and B. R. Poling, *The Properties of Gases and Liquids*, McGraw-Hill, New York, 4th ed., 1987.
13 I. Swaid and G. M. Schneider, *Ber. Bunsenges. Phys. Chem.*, 83 (1979) 969–974.
14 Z. Balenovic, M. N. Myers and J. C. Giddings, *J. Chem. Phys.*, 52 (1970) 915–922.
15 R. Feist and G. M. Schneider, *Sep. Sci. Technol.*, 17 (1982) 261–270.
16 M. J. E. Golay, in D. H. Desty (Editor), *Gas Chromatography 1958*, Butterworths, London, 1958, Ch. 3.
17 J. H. Knox and H. P. Scott, *J. Chromatogr.*, 282 (1983) 297–313, and references cited therein.
18 Cs. Horváth and H.-J. Lin, *J. Chromatogr.*, 149 (1978) 43–70.
19 J. C. Giddings, *Dynamics of Chromatography, Part I, Principles and Theory*, Marcel Dekker, New York, 1965.
20 R. W. Stout, J. J. DeStefano and L. R. Snyder, *J. Chromatogr.*, 282 (1983) 263–286.
21 S. R. Springston, P. David, J. Steger and M. Novotny, *Anal. Chem.*, 58 (1986) 997–1002.
22 J. C. Giddings, *Dynamics of Chromatography, Part I, Principles and Theory*, Marcel Dekker, New York, 1965, p. 238.
23 S. Chapman and T. G. Cowling, *The Mathematical Theory of Non-Uniform Gases*, Cambridge University Press, Cambridge, 3rd ed., 1970, p. 258.
24 S. Wicar, J. Novak, J. Drozd and J. Janak, *J. Chromatogr.*, 142 (1977) 167–175.
25 M. M. Martin, G. Blu and G. Guiochon, *J. Chromatogr. Sci.*, 11 (1973) 641–654.
26 E. Katz, K. Ogan and R. P. W. Scott, *J. Chromatogr.*, 260 (1983) 277–295.
27 R. A. Weast (Editor), *Handbook of Chemistry and Physics*, CRC Press, Boca Raton, Florida, 65th ed., 1984.
28 E. D. Katz and R. P. W. Scott, *J. Chromatogr.*, 270 (1983) 29–50.
29 U. van Wasen, I. Swaid and G. M. Schneider, *Angew. Chem.*, 19 (1980) 575–587.
30 D. E. Martire, R. L. Riester, T. J. Bruno, A. Hussam and D. P. Poe, in preparation.
31 R. T. Jacobsen and R. J. Stewart, *J. Phys. Chem. Ref. Data*, 2 (1973) 757.
32 J. F. Ely, *Proceedings of the 63rd Gas Processors Association Convention*, Gas Processors Association, Tulsa, OK, 1984, pp. 9–22.
33 K. Stephan and K. Lucas, *Viscosity of Dense Fluids*, Plenum Press, New York and London, 1979.
34 P. J. Schoenmakers and L. G. M. Uunk, *Chromatographia*, 24 (1987) 51–57.

Journal of Chromatography, 517 (1990) 31–49
Elsevier Science Publishers B.V., Amsterdam

CHROMSYMP. 1980

Dispersion in the interstitial space of packed columns

PIERRE MAGNICO and MICHEL MARTIN*
École Supérieure de Physique et Chimie Industrielles, Laboratoire de Physique et Mécanique des Milieux Hétérogènes, URA CNRS 857, 10 rue Vauquelin, 75231 Paris Cedex 05 (France)

ABSTRACT

In order to study the dispersion mechanism occurring in the interstitial space of a porous medium, a column was packed with large (210 μm) impenetrable particles by a special dry-packing procedure, designed to obtain a permeable bed that is as uniform as possible. The experimental conditions are selected so as to eliminate as far as possible any other source of dispersion and focus essentially on that arising in the moving fluid. A linear regression analysis of the dispersion data for non-retained solutes shows that the Huber and the Horváth and Lin models fail to describe correctly the experimental results whereas the Giddings model provides a good fit to the data. The reduced plate height becomes constant and equal to 2 at high reduced velocities. It reaches a minimum value of 1 at a reduced velocity of about 3. The models and some previously published experimental data are discussed at the light of these results.

INTRODUCTION

The quality of chromatographic resolution depends on the extent of the broadening of the individual component zones as much as on the retention gap between adjacent zones. The control of this zone broadening, and hence of the dispersion of the zones as they migrate along the chromatographic column, has always been an essential goal in optimization studies of chromatographic separations. The zone dispersion in the column is due essentially to two broad classes of phenomena: (i) longitudinal molecular diffusion as a result of longitudinal solute concentration gradients and (ii) resistance to mass transfer between regions of the cross-section with different velocity components along the direction of flow. The former depends essentially on the time spent by the solute in the column. The latter can occur because of the retention of the solute on, or in, a stationary phase or because of the presence of a stagnant region of the mobile phase inside the pores of the particles. The contribution to the band broadening arising from these different sources is relatively well documented, especially when one is specifically concerned with their dependence on the carrier flow-rate. Flow non-uniformities in the cross-section of the column are also present in the interstitial space between the particles because of the shear forces

0021-9673/90/$03.50

associated with the viscous flow and of the more or less erratic path followed by the flow streamlines in the complex geometry of the porous bed. These flow inequalities contribute to the zone dispersion but the dependence of this contribution on the flow-rate is relatively complex. Several equations based on different approaches and differing mainly in the exponent of the velocity have been developed to account for this contribution. Exponents 1, 1/2 and 1/3 appear in the eddy diffusion coupling term of the models developed by Giddings[1], Huber and Hulsman[2,3] and Horváth and Lin[4], respectively. In spite of the practical importance of the corresponding term in the plate-height equation (it has a major influence on the coordinates of the minimum of the Van Deemter curve), no definitive proof of the correctness of any of these models can yet be established from experimental liquid chromatographic measurements as various and sometimes conflicting conclusions about this contribution have been derived by different authors.

It seems that these discrepancies arise mainly because the relatively slight differences between the three models are obscured by other contributions to band broadening (resistance to mass transfer in the stagnant carrier fluid within the pores of the particles or in the stationary phase, influence of retention on dispersion, extra-column band broadening) or because it was erroneously assumed that the dispersion coefficient was constant along the column whereas, in fact, a length-averaged coefficient is experimentally measured. This might be the case in liquid chromatography with packings of small particles as the relatively large pressures applied at the column inlet may affect the values of the diffusion coefficients. Further, under these conditions, the radial dissipation of the heat generated by the friction of the liquid on contact with the particles induces a radial viscosity profile and, consequently, a velocity profile which contributes to the broadening of the zones. Preliminary calculations indicate that the contribution of this effect to the plate height might increase with the fifth power of the velocity for a fully developed temperature profile[5].

The aim of this study was to determine the best model describing the physical dispersion process occurring in the interstitial space of the chromatographic packing. The experimental conditions are designed so as to focus essentially on this source of band broadening by eliminating, as far as possible any other contribution to the dispersion, except, of course, the irreducible longitudinal molecular diffusion. These conditions include the use of sieved, impervious and spherical particles, very low pressure drops, non-retained solutes and a packing procedure that provides a packing that is as regular as possible. Special attention was paid to the column arrangement to avoid any disturbing fluid instability and to the initial filling of the packing by the liquid to ensure that no air pockets remain entrapped within the packing.

THEORY

If structural heterogeneities present in the porous medium have a length scale which is small in comparison with the column length, the dispersion of the solute is described by the classical convection–diffusion equation:

$$\frac{\partial c}{\partial t} + U \cdot \frac{\partial c}{\partial x} = D \cdot \frac{\partial^2 c}{\partial x^2} \tag{1}$$

which is a combination of the phenomenological Fick's law and of the mass conservation law. Although dispersion occurs in all directions, one is concerned here only with dispersion along the longitudinal flow direction. The variable x is the distance along the column from the inlet, t the time, U the mean mobile phase velocity, c the cross-sectional average concentration of the solute and D the overall solute dispersion coefficient. In order for these terms to be defined, one has to assume the existence of a scale beyond which the porous medium is homogeneous, *i.e.*, the variables c, U, D and x are averaged over a volume known as the representative elementary volume, which must be of a small size compared with the column volume.

In the situation where one injects a continuous solution of solute with a concentration c_{max}, starting at time $t = 0$, at the inlet of the column previously filled with a solution of concentration c_{min}, which corresponds to the experimental set-up of this study, the limiting conditions for concentration in time and space are, respectively,

$$\Gamma(x,t = 0) = 0 \tag{2}$$

$$\Gamma(x = 0, t) = 1 \tag{3}$$

and, assuming a semi-infinite medium:

$$\Gamma(x \to \infty, t) = 0 \tag{4}$$

In these equations Γ is the dimensionless concentration $(c - c_{min})/(c_{max} - c_{min})$. The solution of eqn. 1 with these limiting conditions is[6]

$$\Gamma(x, t) = \frac{1}{2}\left[\operatorname{erfc}\left(\frac{x - Ut}{2\sqrt{Dt}}\right) + \exp\left(\frac{Ux}{D}\right)\operatorname{erfc}\left(\frac{x + Ut}{2\sqrt{Dt}}\right)\right] \tag{5}$$

which, when Ux/D is larger than 100, becomes, with a good approximation, equal to[6]

$$\Gamma(x, t) = \frac{1}{2}\operatorname{erfc}\left(\frac{x - Ut}{2\sqrt{Dt}}\right) \tag{6}$$

In eqns. 5 and 6, erfc represents the complementary error function. The approximation represented by eqn. 6 fully applies under the present experimental conditions where Ux/D lies in the range $2 \cdot 10^3$–$2 \cdot 10^6$ when x is taken as the column length.

The study of the dispersion of the solute reveals different properties of the medium depending on the flow-rate. When the mean velocity is very low, the solute dispersion is the same as the molecular diffusion which would be observed if a concentration gradient of the solute was established between the inlet and the outlet of the column without flow. The dispersion coefficient, D, measured is then proportional to the molecular diffusion coefficient, D_m and

$$D = \frac{D_m}{T} \tag{7}$$

The factor T is known as the tortuosity and is larger than 1. The tortuosity can be determined by measurements of the electrical conductivity of the packing. It is found that, in the porosity range encountered in bead packings, $T \approx \varepsilon^{-1/2}$, where ε is the porosity of the packing[7,8].

When the carrier flow-rate increases, the dispersion coefficient is no longer constant but becomes a function of the mean velocity. More generally, this function depends on the dimensionless reduced velocity, or Péclet number, Pe, which is the ratio of the times required to transport the solute along one particle by diffusion and by convection:

$$Pe = \frac{d_p^2/D_m}{d_p/U} = \frac{Ud_p}{D_m} \tag{8}$$

where d_p is the particle diameter and U the mean velocity.

It is convenient to express the dispersion in terms of the dispersion length, L_d:

$$L_d = D/U \tag{9}$$

This length represents half the plate height frequently used in the field of separation science.

Various equations, or models, have been proposed to represent the dependence of the dispersion length on the operational parameters and, especially, the carrier velocity. The models relevant in the context of this study are presented below assuming that there is no interaction of the solute with the packing, *i.e.*, no retention, and that the packing is made of impervious rigid spheres (no internal pores). Accordingly, dispersion will only occur in the space occupied by the carrier fluid between the particles and, apart from the molecular diffusion term arising from the existence of a longitudinal concentration gradient and expressed by the eqn. 7, is due to flow variations associated with structural heterogeneities of this space.

The Giddings model

The velocity field in a packed bed is much more complex than that in a capillary tube. Consequently, apart from the Taylor-like dispersion arising in an interstitial flow channel because of the transversal velocity variations within this channel, solute dispersion can also come from the erratic flow pattern associated with the presence of a more or less regular array of particles. These two kinds of dispersion processes can be called hydrodynamic dispersion and geometric (or mechanical) dispersion, respectively. One notes in passing that the latter process is also known as the anastomosis and, more commonly in the chromatographic literature, as the "eddy diffusion", a term which we prefer to avoid as it has mistakenly been associated in the past by some authors with the eddies induced by a turbulent flow. Clearly, the geometric dispersion mechanism appears in the laminar flow regime at low values of the Reynolds number.

The influence of these two kinds of dispersion was recognized in one of earliest models of peak broadening in chromatography by Van Deemter *et al.*[9], who simply added their respective contributions to the dispersion length. Later, this model was modified by Giddings[1], who noted that these contributions are not independent and thus additive but, instead, are coupled.

In this model, five different levels of flow heterogeneities are considered for packings of porous particles[1]. In the present study dealing with non-porous particles packed by a special procedure to ensure a packing as regular as possible, one will be concerned mainly with the trans-channel level and, to a lesser extent, with the short-range inter-channel level. The characteristic length scale of these velocity variations is assumed to be proportional to the particle diameter.

This model assumes that the dispersion due to the velocity variations is similar to a random walk process. The time corresponding to an elementary step, or correlation time, is defined as the time necessary for a solute molecule to travel from one velocity domain to another. Two mechanisms allow this transport, molecular and convection, which both have a specific correlation time. The corresponding dispersion lengths $L_{d,hydro}$ and $L_{d,geo}$ for the diffusive (hydrodynamic dispersion) and convective (geometric dispersion) mechanisms are, respectively,

$$L_{d,hydro} = C \cdot \frac{d_p^2 U}{D_m} \tag{10}$$

$$L_{d,geo} = \Lambda d_p \tag{11}$$

where Λ and C are dimensionless parameters which depend on the scale and amplitude of flow non-uniformities.

Basically, the coupling theory assumes that the total numbers of steps in the random walk is the sum of the number of steps for each of the individual processes. Then, the resultant correlation time and the resultant dispersion length appear to be the harmonic, rather than the arithmetic, sum of their respective individual contributions. Accordingly, the overall dispersion length is, combining eqns. 7, 9, 10 and 11:

$$L_d = \frac{D_m}{TU} + \frac{1}{\frac{1}{\Lambda d_p} + \frac{D_m}{C d_p^2 U}} \tag{12}$$

or

$$l_d = \frac{L_d}{d_p} = \frac{1}{TPe} + \frac{1}{\frac{1}{\Lambda} + \frac{1}{CPe}} \tag{13}$$

where l_d is the reduced dispersion length, which is half the reduced plate height. In these equations, the individual contributions of the longitudinal concentration gradient and transversal flow non-uniformities to the dispersion length have been added as they act independently to disperse the solute. At large values of the Péclet number, the dispersion is controlled by the convective mechanism and then the coupling term becomes constant while the diffusive process is dominant at lower Pe values.

The Huber model

A model based on the mass balance equation was developed by Huber and

Hulsman[2,3]. It uses a correlation obtained through dimensional analysis of experimental data by Hiby[10] to express the dispersion term arising from the flow non-uniformities, which gives

$$L_d = \frac{D_m}{TU} + \frac{1}{\frac{1}{\Lambda d_p} + \frac{D_m^{1/2}}{C d_p^{3/2} U^{1/2}}} \tag{14}$$

or

$$l_d = \frac{1}{TPe} + \frac{1}{\frac{1}{\Lambda} + \frac{1}{CPe^{1/2}}} \tag{15}$$

This equation differs from the Giddings equation by the exponent 1/2 of the Péclet number in the last term and in the numerical value of the dimensionless coefficient C.

The Horváth and Lin model

The dispersion model developed by Horváth and Lin is based on the postulate that a stagnant layer of fluid surrounds the particles and occupies a fraction of the interstitial fluid volume[4]. According to the free surface theory of Happel[11] and Pfeffer and Happel[12], the thickness of this layer is proportional to $Pe^{-1/3}$.

The model assumes that the peak broadening of a non-retained solute is due to the geometric dispersion process during the flow-dependent time spent by the solute in the streaming part of the carrier fluid, which gives for the complete dispersion length expression

$$L_d = \frac{D_m}{TU} + \frac{1}{\frac{1}{\Lambda d_p} + \frac{D_m^{1/3}}{C d_p^{4/3} U^{1/3}}} \tag{16}$$

or

$$l_d = \frac{1}{TPe} + \frac{1}{\frac{1}{\Lambda} + \frac{1}{CPe^{1/3}}} \tag{17}$$

It also differs from the Giddings equation by the exponent of the Péclet number in the second term on the right-hand side and in the numerical value of the dimensionless coefficient C. It must be clear that, in spite of the close similarity of eqns. 13 and 17, the latter is not based on a coupling effect and completely neglects the diffusive transport mechanism in the second term due to the velocity unequalities. Nevertheless, it is interesting that, if one wants to modify the Horváth and Lin model by introducing a coupling effect between the diffusive process in the stagnant layer and the convective process either in the whole interstitial fluid or only in its streaming part, by the

harmonic addition of the corresponding correlation times, one obtains an expression which has exactly the form of eqn. 14, obviously with different values of the dimensionless coefficients A and C. Moreover, as indicated by Horváth and Lin in the note added in the proof of their paper[4], the same form is found if one includes in the dispersion length expression the additional, and independent, peak broadening contribution due to diffusion into the stagnant layer by properly taking into account the flow-dependent "capacity factor" which reflects the distribution of the solute between the streaming and stagnant parts of the interstitial fluid (however, we found a term which is numerically three times smaller than that of Horváth and Lin).

More recently, Koch and Brady[13] derived the dispersion coefficient associated with the presence of a boundary layer around the particles, which, according to Acrivos and Taylor[14], is also found to have a thickness proportional to $Pe^{-1/3}$, and obtained a dispersion length expression which is a linear function of ln Pe. Such an ln U dependence was previously obtained by Saffman[15] using a different model.

The Bouchaud and Georges model

A general theory of the dispersion of solute species due to the spatial fluctuations of the velocity field has been recently developed by Bouchaud and Georges[16] by means of models with a very simple geometry. In order to study the dispersion due to flow inhomogeneities in a porous medium, they use the idealized model represented in Fig. 1, which consists of a succession of identical cells in series. In each cell, two flow paths of different lengths and permeabilities are connected in parallel. Let V and γV be the velocities in the fast and slow branches of lengths ξ and $\lambda\xi$, respectively ($\gamma < 1$). A solute molecule entering a given cell has a probability P of entering the slow branch in which its mean residence time is $<\tau>$, while the time spent in one fast branch is simply ξ/V. Assuming that the dispersion process is ergodic, *i.e.*, that the time spent in a given region is proportional to the volume of this region, a relationship is found between the probability P, $<\tau>$ and the volume fraction f of the slow branches. Using a statistical approach, Bouchaud and Georges derived a general expression for the dispersion length in terms of the first and second moments of the distribution law of the residence times in the slow paths.

A particular expression is found in the case where the residence time is unique, which corresponds to a Dirac distribution. According to this model, each path does not contribute to the dispersion, but the overall dispersion of the transit times along a large number of cells arises from combination of the paths followed by a molecule,

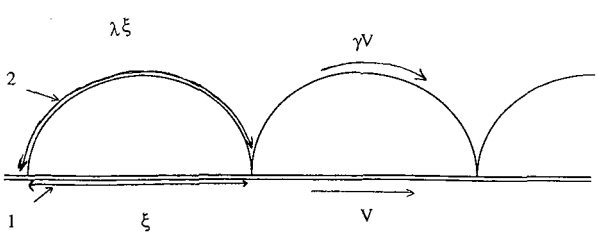

Fig. 1. Schematic model suggested by Bouchaud and Georges[16]. Two channel types (branches) are connected in parallel in one of a succession of cells connected to each other cell in series. In channel 1 of length ξ, the microscopic velocity V leads the transport process whereas, in channel 2 of length $\lambda\xi$, the local velocity γV ($\gamma < 1$) and the molecular diffusion both control the solute transport.

which is described by a binomial law. This model has been extended by Bouchaud[17] to the case where τ, the constant residence time in a slow branch, is the result of the combination of the diffusive and connective transport processes according to the harmonic coupling law:

$$\frac{1}{\tau} = \frac{2D_m}{\lambda^2 \xi^2} + \frac{\gamma V}{\lambda \xi} \tag{18}$$

Using the relationship between U, the average migration velocity of a solute molecule along the cell pattern, and V resulting from the ergodicity hypothesis, the dispersion length is found in the limit of large cell numbers and for an equal path length of the two branches ($\lambda = 1$):

$$L_d = \frac{D}{U} = \frac{1}{\dfrac{2\gamma}{\xi f(1-f)} + \dfrac{4D_m}{\xi^2 f U}} \tag{19}$$

or

$$l_d = \frac{L_d}{\xi} = \frac{1}{\dfrac{2\gamma}{f(1-f)} + \dfrac{4}{fPe}} \tag{20}$$

if the Péclet number is defined as $U\xi/D_m$. These equations do not include the longitudinal molecular diffusion term. However, regarding the more important term, in the present context, due to flow inequalities, they are similar to the corresponding Giddings' equations as far as the U dependence of the dispersion length is concerned. Clearly, this is due to the similarity of the ways in which the coupling between the diffusive and convective transports are introduced in the two approaches. However, eqns. 19 and 20, corresponding to the idealized, very simple geometric model represented in Fig. 1, show that when such a coupling occurs at a microscopic level (the individual slow branch), it manifests itself in the dispersion process at the macroscopic level. Further the Bouchaud and Georges model provides a physical meaning for the numerical coefficients which enter the dispersion equation. This is especially true for packings of porous particles.

EXPERIMENTAL

Packing procedure

A 16.6 cm × 2.4 cm I.D. column was packed with the 200–220-μm sieving fraction of glass beads by a special dry packing procedure designed to obtain a porous bed that is as regular as possible (Fig. 2). A vibrating distributor induces a constant flow of particles falling onto a short column packed with large (5 mm I.D.) glass beads, which ensures a homogeneous distribution of the particles across the whole cross-section. Then the particles pass through a set of parallel, vertical, 2.5 mm I.D. tubes, which help to keep the particles flowing homogeneously in the whole

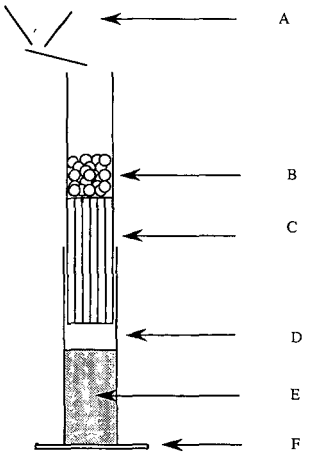

Fig. 2. Experimental set-up for column packing. A = hopper pouring the particles at a constant flow; B = packing of 5-mm glass beads; C = fixed set of 2.5 mm I.D. tubes; D = column section being packed; E = column section already packed with particles; F = support which allows the column to move and rotate around its axes.

cross-section of the packing assembly, before falling into the column to be packed. This column is moved down during the packing process in such a way as to maintain a constant falling height and avoid the formation of a longitudinal permeability gradient. At the same time, the column is rotating around its axis in order to avoid radial stratification of the packing.

Materials and methods

In order to avoid any trapping of bubbles which may significantly affect the dispersion process, the column, vertically orientated, is completely saturated with carbon dioxide, then filled upwards with water until the signal of an electrical conductivity cell monitoring the acidification of the water effluent due to the dissolution of the carbon dioxide bubbles becomes negligible. The volume of liquid in the column is of 28.5 cm^3, which gives a porosity of 38.0%. This porosity value considerably exceeds the corresponding value (26%) for a dense and perfect crystal-like arrangement of identical spheres but lies well within the range of porosities experimentally obtained when randomly packing by various techniques a very large number of particles (here about 10^7). It is believed that the packing procedure used in this study leads to a packing that is as uniform as possible.

Dispersion measurements are performed by frontal analysis of a solution of a mixture of NaCl and $CaCl_2$, rather than of a single salt solution, for eliminating ion exchange between the glass beads and the solution. A relative high concentration in the initial solution (0.5 g/l NaCl, 0.5 g/l $CaCl_2$) is used in order to avoid further adsorption and ion exchange of the solute mixture, which would otherwise lead to retention and to a significant effect on the profile, as previously observed. Then, a continuous step of solution at a different salt concentration is introduced in the column by switching the pump head of a dual-piston syringe pump (Model 919, Harvard Apparatus, South

Natick, MA, U.S.A.) by means of a four-way switching valve. The flow-rate range investigated was 33 μl/min–20 ml/min, which corresponds to Péclet numbers between 0.5 and 300. The pressure drop in the column was always less than 0.2 bar. In all instances the Reynolds number was lower than 0.4, which prevents any dispersion perturbation associated with the onset of turbulence.

The displacing solution is made more concentrated (1 g/l NaCl, 1 g/l $CaCl_2$ aqueous solution) than the initial solution to avoid the viscous fingering effect (Saffman–Taylor instability) which may occur when a more viscous solution is displaced by a less viscous solution. Further, the liquid moves upwards, rather than downwards, in order to avoid the Rayleigh–Taylor instability associated with the presence of a denser solution above a lighter one. These precautions are necessary with the relatively high concentration used in this study as these two effects have been shown to induce both an increase in the dispersion coefficient and a characteristic tailing of the elution profiles.

The concentration change of the column effluent is continuously monitored by a conductivity detector (Model 30063, Dionex, Sunnyvale, CA, U.S.A.). The temperature of the effluent is also measured in order to take into account the temperature dependence of the conductivity (2%/°C around 20°C), especially for the slowest analyses. The total dead volume of the pre- and post-column connecting capillary tubes, of the flow distributor and collector located at the column extremities and of the conductivity cell is 0.28 cm^3, *i.e.*, about 1% of the liquid volume in the column.

In the calculations, the particle diameter is assumed to be equal to 0.021 cm and $1/T$ equal to 0.6. The diffusion coefficient, D_m, is taken as equal to $1.336 \cdot 10^{-5}$ cm^2/s, which corresponds to the average of the individual coefficients of the two salts[18]. For dispersion coefficient determinations, the step between the two plateaux is normalized between 0 and 1 and measurements are performed in the 5–95% range of the front. At each time in this range, the experimental normalized concentration value gives, using eqn. 6 and the tabulated error function, the value of the reduced parameter $X = (L - Ut)/2\sqrt{Dt}$, where t is the elution time. Plotting $X\sqrt{t}$ *vs.* t gives a straight line for a Gaussian curve. The dispersion coefficient is obtained by linear regression from the intercept of this plot and the mean velocity from the slope. This mean least-square method of determination of D has the advantage of taking into account all experimental data for the front in the 5–95% range of the concentration step rather than the peak width at some more or less arbitrary selected concentration level, as classically performed in the small-pulse injection method.

RESULTS

The results obtained experimentally by this procedure are reported in Fig. 3, which shows the plot of the reduced dispersion length, l_d, *vs.* the Péclet number on a logarithmic scale. This curve has the characteristic shape of the classical Van Deemter curves with a minimum at a Péclet number of *ca.* 3 for a reduced dispersion length of about 0.5. This corresponds to a reduced plate height of 1, which is lower than that usually observed in packed chromatographic columns. Clearly, this low value is due to the use of impervious particles and to the quality of the homogeneity of the packing. With increasing Péclet number the dispersion length increases until it reaches a constant value of about 1 at large Péclet numbers.

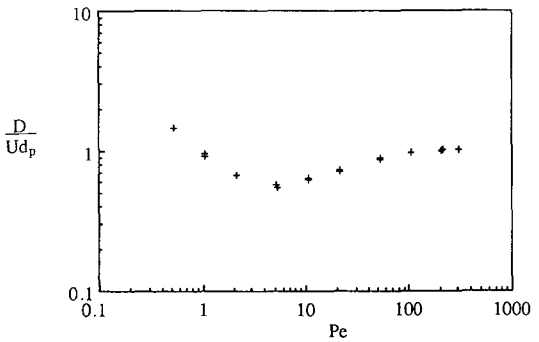

Fig. 3. Log–log plot of the reduced dispersion length *versus* Péclet number for a 16.6 cm × 2.4 cm I.D. column packed with 210-μm glass beads.

The models described above all predict a constant l_d value at large velocities, as observed, but they differ essentially in the exponent of the velocity in the hydrodynamic dispersion term of the dispersion length equation. The various equations can all be expressed by the following form:

$$\frac{D}{U} = \frac{D_m}{TU} + \frac{1}{\frac{1}{A} + \frac{1}{BU^n}} \tag{21}$$

with $n = 1/3$, $1/2$ and 1 for the Horváth and Lin, Huber and Giddings (or, equivalently, Bouchaud and Georges) models, respectively. The parameter $A = \lambda d_p$ represents the convective (geometric) dispersion process for the three models (eqns. 12, 14 and 16). It is the limiting value of the dispersion length for large velocities. The B coefficient, taking into account the hydrodynamic dispersion, differs from one model to another. Looking for a linear relationship as an easy visual, and also quantitative, test to check the validity of the agreement between experimental (D, U) data and the theoretical expressions described above, one can transform eqn. 21 as follows:

$$Y = \frac{U^n}{A} + \frac{1}{B} \tag{22}$$

where Y is defined as:

$$Y = \frac{U^{n+1}}{D - \frac{D_m}{T}} \tag{23}$$

Then a plot of Y vs. U^n should give a straight line if the corresponding model is correct. These plots are shown in Fig. 4 for the three values of n. In these plots, only data points corresponding to Péclet numbers larger than 1 are used in order to reduce the influence

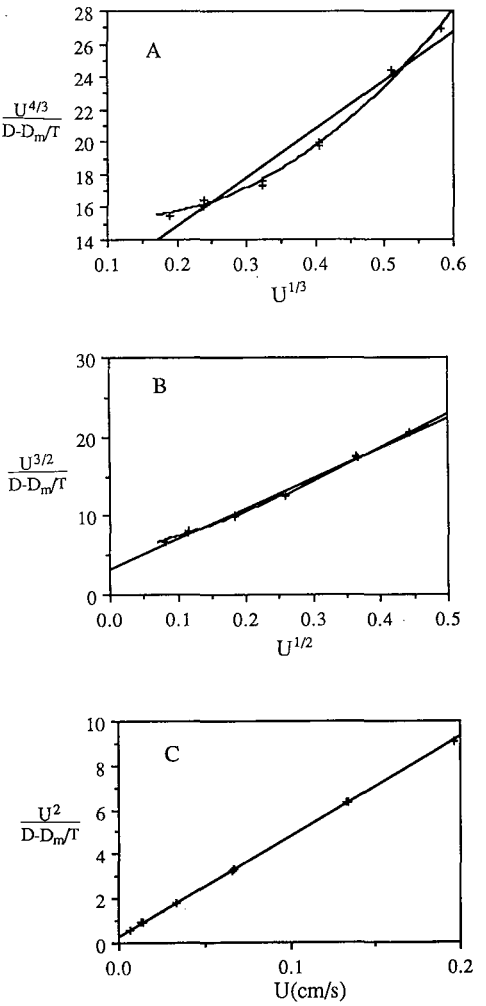

Fig. 4. Y *vs.* X plots of the experimental dispersion data with $X = U^n$ and $Y = U^{(n+1)}/(D - D_m/T)$. (A) $n = 1/3$; (B) $n = 1/2$; (C) $n = 1$. The straight lines correspond to mean least-square linear regressions. The other curves correspond to a second-degree polynomial fit.

of the uncertainties in the values of D_m and T on the denominator $(D - D_m/T)$. The best mean least-square linear fits are also indicated for each plot. Although, for the three curves, a monotonous increase of Y with U^n is observed, as expected from eqn. 22, it clearly appears that a remarkably good linear fit is obtained for $n = 1$, while the curve for $n = 1/2$ is slightly concave and at for $n = 1/3$ has a still more pronounced concavity.

As only one value of n can correctly describe the experimental data and as $n = 1$ appears to be the best of the three tested values, one cannot expect the plots for the two other n values in Fig. 4 to be straight lines. It is therefore of interest to check the

coherence of the shapes of the curves in Fig. 4, *i.e.*, to check that the observed shapes of the curves in Fig. 4A and B are in agreement with the shape that takes the theoretical variation corresponding to $n = 1$, when it is plotted according to the transformation of eqns. 22 and 23 but with another value of the parameter n (we shall take $n = 1/3$ and $n = 1/2$). For $n = 1$, eqn. 22 becomes

$$\frac{U^2}{D - \frac{D_m}{T}} = \frac{U}{A} + \frac{1}{B} \tag{24}$$

Combining eqns. 23 and 24, one obtains

$$Y = \frac{X}{A} + \frac{1}{BX^{(1-n)/n}} \tag{25}$$

with

$$X = U^n \tag{26}$$

Eqn. 25 clearly shows that the Y *vs.* X curve should not be a straight line if $n \neq 1$. When $n < 1$, it has a minimum, for:

$$X_{opt} = \left(\frac{1-n}{n} \cdot \frac{A}{B}\right)^n \tag{27}$$

The shape of the Y *vs.* X curves should therefore be concave for $n < 1$, which is indeed what is observed in Fig. 4A and B. The linear regression of the data according to eqn. 23 for $n = 1$ gives $A = 0.022$ and $B = 3.40$ (all dimensional values are in c.g.s. units). With these values, eqns. 25 and 27 give $X_{opt} = 0.24$ and $Y_{opt} = 16$ for $n = 1/3$ and $X_{opt} = 0.081$ and $Y_{opt} = 7.3$ for $n = 1/2$. Although the number of experimental points at low velocities in Fig. 4 is too small to show definite evidence of the presence of a minimum in the plots for $n = 1/3$ and $n = 1/2$, the coordinates of the minima for the two curves correspond roughly to those of points obtained at low velocity, which again agrees with the fact that the best of the three n values is 1.

Of the three n values for which dispersion models have been developed, $n = 1$ appears to be the best. One may wonder, however, if another value of n, not necessarily corresponding to a previous model, could provide a still better fit of the experimental data according to eqn. 21. This can be done by writing this equation in the form

$$Z = \ln\left(\frac{U}{D - \frac{D_m}{T}} - \frac{1}{A}\right) = \ln\left(\frac{1}{B}\right) - n \ln U \tag{28}$$

Then, a plot of Z *vs.* $\ln U$ should give a straight line, the slope of which should be equal to n. In fact, such a plot is very sensitive to the value of A which has to be stated. This is

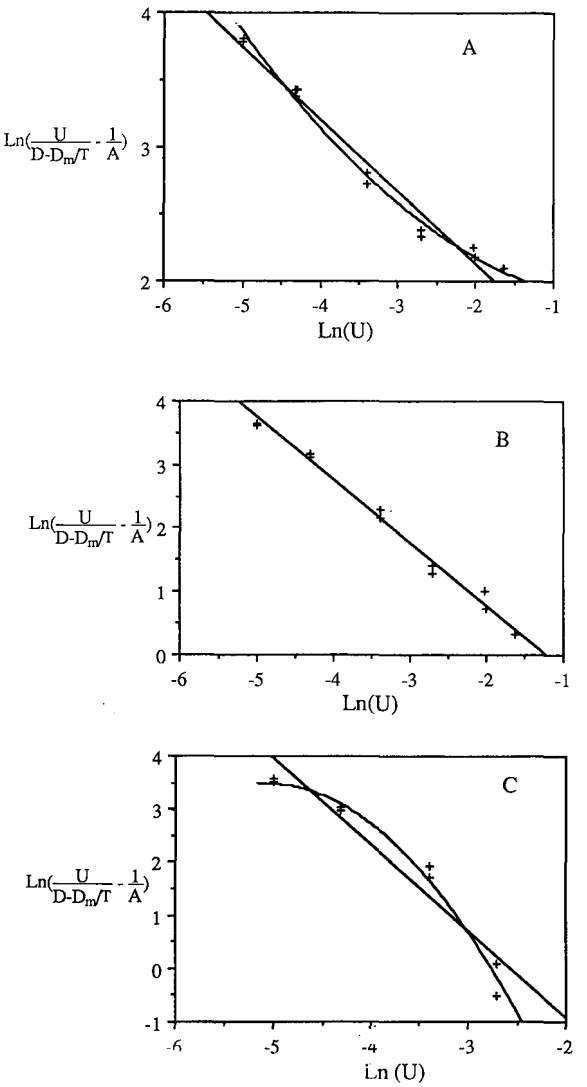

Fig. 5. Z *vs.* ln(U) plots of the experimental dispersion data with $Z = \ln [U/(D - D_m/T) - 1/A]$ for different values of $1/A$. (A) $1/A = 38.2$; (B) $1/A = 45.0$; (C) $1/A = 48.0$. The straight lines correspond to mean least-square linear regression. The other curves correspond to a second-degree polynomial fit.

demonstrated in Fig. 5, where such plots are shown for three different values of $1/A$. The first two ($1/A = 38.2$ and $1/A = 45.0$) correspond to the slopes given by the linear regression of the experimental (Y, U^n) data according to eqn. 22 for $n = 1/2$ and $n = 1$, respectively [for $n = 1/3$, one obtains $1/A = 29.8$, which gives a strongly non-linear (Z, ln U) plot, which, for this reason, is not shown in Fig. 5]. For the sake of comparison, a plot for a larger $1/A$ value ($1/A = 48$) is also shown. Fig. 5 indicates that the curve is concave for relatively low values of $1/A$, then becomes convex for larger

$1/A$ values. Eventually, it becomes linear for a given value of $1/A$. A computer search for the $1/A$ value giving the best linear fit of the data provides $1/A = 45$, which is precisely the value obtained by the procedure mentioned above for $n = 1$. With this $1/A$ value, a linear regression of the (Z, ln U) data gives, for the slope n, a value of 0.994, which, as expected, is very close to 1. Further, this $1/A$ value corresponds to a limiting dispersion length at large Péclet numbers equal to 0.022 cm, *i.e.*, to 1.06 d_p, which as can be seen in Fig. 2 is close to the experimentally obtained value, while the A values obtained by linear regression of eqn. 22 for the Horváth and Lin model ($n = 1/3$, $A = 1.60\ d_p$) and the Huber model ($n = 1/2$, $A = 1.25\ d_p$) are too large.

DISCUSSION

All these results provide a strong indication that eqn. 21 gives a correct representation of the flow dependence of the dispersion length and that the Giddings model with $n = 1$ is the most appropriate model for describing the experimental data. This suggests that, among the five different levels of flow non-uniformities distinguished by Giddings, either only one is affecting significantly the dispersion length or, if two or more of them are influencing this length, they have similar values of A/B (or, equivalently, A/C). Indeed, in the latter instance, adding two coupling terms with identical A/C values in eqn. 13 is equivalent to multiplying one coupling term by some appropriate constant. One finds, from a linear regression of the experimental data, a A value of 1.06, while the values estimated by Giddings are 0.5, 0.5 and 0.1 for the trans-channel, short-range inter-channel and long-range inter-channel effects, respectively. The B value derived by linear regression in Fig. 4C is equal to 3.40 s, corresponding to a C value in eqn. 10 of 0.103. The corresponding C values approximately estimated by Giddings for the three above effects are 0.005, 0.25 and 1, which gives A/C values of 100, 2 and 0.1, respectively, while the experimental A/C value is 10. From a comparison of these estimated and experimental values it seems that the column does not contain long-range inter-channel non-uniformities, which gives some indication of the quality of the packing procedure. However, the experimental A, C and A/C values do not correspond closely to the estimated values for either the trans-channel effect or the short-range inter-channel effect. If only one level of flow irregularities is present, as suggested above, it would have to be the trans-channel level which is present even in a crystal-like array of identical spheres. It is difficult, however, to imagine that the short-range inter-channel effect is totally absent because the packing procedure cannot be perfect. These remarks suggest, therefore, that our data reflect some combination of the trans-channel and inter-channel effects and that the A/C ratios for these two effects are not as different as the corresponding values estimated by Giddings.

It is of interest to interpret these experimental data by means of the Bouchaud and Georges model, which gives the same flow dependence of the dispersion length as the Giddings model but which is based on a simple geometric construction. This model has three parameters, f, γ and ξ, while the linear regression provides only two coefficients. If one assumes ξ is equal to the particle diameter, d_p, which seems to be a reasonable cell size to be used, then one obtains $f = 0.41$ and $\gamma = 0.11$. As γ is the velocity ratio between the two branches which have been assumed to have the same length, γ represents a permeability ratio and can be assumed to be equal to the ratio of

the squares of the diameters of the two branches, according to the Poiseuille expression. This size ratio is then found to be equal to 1/3. The Bouchaud and Georges model allows the dispersion behaviour of an extremely complex system such as a porous medium to be represented by that of a simple geometric system.

One should not be surprised that the Giddings model provides the best fit to the experimental data. Indeed, the model developed by Huber is not based on a physical model for dispersion but relies on the empirical mass transport correlation by Hiby, the accuracy of which has been questioned[19,20]. Further, this correlation is based on dispersion data obtained for Péclet numbers between 30 and 10^5. This does not allow a full description of the curvature of the l_d *vs.* *Pe* curve associated with the coupling effect for Péclet numbers between 5 and 100.

The discrepancy with the Horváth and Lin equation is even greater than that with the Huber expression. As already noted, this comes, in part, from the fact that the flow-dependent expression according to Pfeffer and Happel[12] for the stagnant boundary layer thickness, on which their equation is based, is only valid at large Péclet numbers and should therefore be used only for $Pe > 50$ (ref. 21). At lower *Pe*, the stagnant layer approaches a constant value and so should the corresponding term in the dispersion length equation. Further, the implicit approximation made in the Horváth and Lin derivation of the volume fraction of the free-streaming fluid [$1/(1 + x) = 1 - x$, where x represents the ratio of the stagnant film volume to the total fluid volume] requires that the stagnant layer is small and thus that *Pe* is large. For these reasons, the Horváth and Lin equation should not be applied for Péclet numbers lower than 50–100. However, it is seen in Fig. 3 that the convex part of the l_d *vs.* *Pe* curve, which reflects the velocity dependence of the flow non-uniformities contribution to the dispersion length, is mainly found for *Pe* values between 5 and 100. It is therefore not surprising that the Horváth and Lin equation cannot fit the experimental data satisfactorily.

Although the Giddings model provides the best fit of the experimental data in this study, one may wonder why it has not been found satisfactory in some previous similar studies with non-retained solutes and non-porous particles. In one of the first experimental proofs of the correctness of the then disputed coupling concept, Knox[22] found that the slope of the log l_d *vs.* log *Pe* curves was much smaller than 1, as a result of the coupling effect. However, he did not find a constant limiting value for l_d at large *Pe* but, instead, that l_d decreased after reaching a maximum value around $Pe =$ 5000–30 000, depending on the experimental conditions. This decrease was attributed to the onset of turbulence at large *Pe*. For all Péclet numbers, the l_d values were significantly affected by the d_c/d_p ratio of the column diameter to particle diameter, which was lower than in the present experiment. One can expect that a low d_c/d_p value will induce, first, a non-random porosity variation across the column radius, as noted by Cohen and Metzner[23] for d_c/d_p values lower than 30 in the case of newtonian fluids and, second, an important trans-column effect and, consequently, a relatively large A value. This can explain why the Knox data are better fitted by a modification of eqn. 13 obtained with an integral form in which A is constant while contributions from different C values are weighted inversely with C. Knox also found that A is of the order of magnitude of the column diameter, rather than of the particle diameter as found in this study.

In their experiments with d_c/d_p values of about 100, as in this present study,

Horváth and Lin found that (l_d, Pe) data in the Pe range 0.5–10 000 are better fitted to eqn. 17 than to eqn. 13 or 15 (ref. 4). One can note that, at large Pe, they obtained l_d values 6–7 times larger than those in Fig. 3, which indicates a significant A value. However, the A values should be the same for the three models. Therefore, this probably reflects the fact that various levels of flow non-uniformities contribute to peak broadening and that the overall dispersion length is the result of trans-channel, short-range inter-channel, long-range inter-channel and, perhaps, trans-column effects. Then the A values of each individual effect add together at large Pe. Further, l_d does not reach a constant value at Pe up to 10 000, which indicates that at least one of these effects is characterized by a very large A/C value. Indeed, it can be shown from eqn. 13 that $l_d - 1/TPe$ reaches 90% of its limiting A value when Pe is equal to $9A/C$. In addition, it must be remembered that l_d *vs.* Pe data represent average dispersion data along the column length whereas eqns. 13, 15 and 17 are local expressions of the dispersion length, *i.e.*, of half the rate of increase of the variance of the zone or front per unit column length. If the Péclet number, for instance, is not constant all along the column, then the experimentally measured dispersion coefficient reflects some average value of the dispersion length over the range of Péclet numbers scanned from the inlet to the outlet of the column. In Horváth and Lin's experiments, where the pressure drops at the largest Pe were probably of the order of magnitude of several hundred bars, the pressure dependence of the diffusion coefficient may have led significant variations of Pe along the column. Similar longitudinal gradients in Pe are correctly taken into account in gas chromatography by means of appropriate compressibility factors when they are due to the mobile phase compressibility, but they are generally neglected in liquid chromatography where the experimentally determined dispersion coefficient (or dispersion length) is plotted as a function of the Péclet number calculated using the value of the diffusion coefficient at atmospheric pressure. Such a practice has been shown to induce a significant increase in the apparent dispersion length over the true local value, especially at large Péclet numbers[24].

Finally, it is of interest, for optimization purposes, to note the minimum value of the reduced dispersion length, $l_{d,min}$ and the corresponding Péclet number, Pe_{opt}. From derivation of eqns. 13 and 21 with $n = 1$, one obtains

$$Pe_{opt} = \frac{1}{\sqrt{CT} - \frac{C}{A}} \tag{29}$$

and

$$l_{d,min} = 2\sqrt{\frac{C}{T}} - \frac{C}{AT} \tag{30}$$

The coordinates of the optimum appear to be highly sensitive to the values of C but only to a much smaller extent to the value of A. This reflects the fact that, at the relatively low Pe corresponding to this minimum, the diffusive mechanism is the most active process for relaxation of the transversal flow inequalities. With the present

values of A (1.06), C (0.103) and $1/T$ (0.6), one obtains $Pe_{opt} = 3.15$ and $l_{d,min} = 0.44$. This minimum dispersion length, which corresponds approximately to the observed minimum in Fig. 3, is about half the value obtained by Horváth and Lin and also the best reported values for high-performance liquid chromatographic (HPLC) columns (reduced plate height of 2). This indicates that there is no precisely defined lower limit for the minimum dispersion length and that it depends strongly on the quality of the packing.

CONCLUSION

The study of the dispersion of a non-retained solute in a column packed with impervious spherical particles and an appropriate data treatment of the experimentally measured values have revealed that the experimental data are correctly fitted by the Giddings coupling equation whereas they deviate from the behaviour predicted by the Huber and, especially, the Horváth and Lin expressions, in spite of the relatively small differences between these equations. This validates the physical model of the coupling of the convective and diffusive transport processes on which the Giddings equation is based.

Although the present study has dealt only with a packing of non-porous particles, this conclusion should also hold for packings of porous particles as the band broadening arising from the interstitial space is believed to be the same for these two kinds of packings.

It must be emphasized that such a conclusion can be drawn because great precautions have been taken to obtain a packing that is as regular as possible and to eliminate, as far as possible, any other source of dispersion than that arising from the flow non-uniformities in the interstitial space of the bed, especially the band broadening contributions associated with the solute retention, the porous space inside the particles, the thermal effect due to the viscous dissipation and the pressure dependence of the diffusion coefficient.

In liquid chromatographic columns packed with small porous particles, all these effects will give a more or less pronounced contribution to the overall dispersion. In addition, the usual packing procedure with these columns (filtration under pressure of a slurry of particles) probably leads to a longitudinal porosity gradient which may affect the scale and the amplitude of the flow non-uniformities and also induce a longitudinal cross-sectional average velocity gradient. Hence, the actual dispersion length is continuously changing along the column and the experimentally determined value corresponds to some average column length. This provides some explanation of the fact that HPLC experiments have not allowed the models to be distinguished. Accordingly, in kinetic optimization studies of the experimental HPLC conditions for which a relationship between dispersivity and flow velocity is required, a semi-empirical dispersion equation such as the Knox equation[25], in which the relatively complicated coupling term for the dispersion length in the interstitial space is replaced with a simple Pe^m ($m \approx 1/3$) expression, will generally be satisfactory.

ACKNOWLEDGEMENT

Fruitful discussions with Jean-Pierre Hulin are greatly appreciated.

REFERENCES

1 J. C. Giddings, *Dynamics of Chromatography*, Marcel Dekker, New York, 1965.
2 J. F. K. Huber and J. A. R. J. Hulsman, *Anal. Chim. Acta*, 38 (1967) 305.
3 J. F. K. Huber, *J. Chromatogr. Sci.*, 7 (1969) 85.
4 Cs. Horváth and H.-J. Lin, *J. Chromatogr.*, 126 (1976) 401.
5 M. Martin, unpublished results.
6 K. H. Coats and B. D. Smith, *Soc. Pet. Eng. J.*, March (1964) 73.
7 P.-Z. Wong, J. Koplik, J. P. Tomanic, *Phys. Rev. B*, 30 (1984) 6606.
8 J. N. Roberts, L. M. Schwartz, *Phys. Rev. B*, 31 (1985) 5990.
9 J. J. van Deemter, F. J. Zuiderweg and A. Klinkenberg, *Chem. Eng. Sci.*, 5 (1956) 271.
10 J. W. Hiby, in P. A. Rottenburg (Editor), *Proceedings of the Symposium on Interaction between Fluids and Particles*, Institution of Chemical Engineers, London, 1962, p. 312.
11 J. Happel, *AIChE J.*, 4 (1958) 197.
12 R. Pfeffer and J. Happel, *AIChE J.*, 10 (1964) 605.
13 D. L. Koch and J. F. Brady *J. Fluid Mech.*, 154 (1985) 399.
14 A. Acrivos and T. D. Taylor, *Phys. Fluids*, 5 (1962) 387.
15 P. G. Saffman, *J. Fluid Mech.*, 6 (1959) 321.
16 J.-P. Bouchaud and A. Georges, *C.R. Acad. Sci., II*, 307 (1988) 1431.
17 J.-P. Bouchaud, personal communication.
18 R. C. Weast (Editor), *Handbook of Chemistry and Physics*, CRC Press, Boca Raton, FL, 60th ed. 1979–80, p. F-62.
19 R. S. Deelder, *J. Chromatogr.*, 47 (1970) 307.
20 R. Tijssen, *Ph.D. Thesis*, Technical University of Delft, 1979, p. 12.
21 F. H. Arnold, H. W. Blanch and C. R. Wilke, *J. Chromatogr.*, 330 (1985) 159.
22 J. H. Knox, *Anal. Chem.*, 38 (1966) 253.
23 Y. Cohen and A. B. Metzner, *AIChE J.*, 27 (1981) 705.
24 M. Martin and G. Guiochon, *Anal. Chem.*, 55 (1983) 2302.
25 J. N. Done, G. J. Kennedy and J. H. Knox, in S. G. Perry (Editor), *Gas Chromatography 1972*, Applied Science, London, 1972, p. 145.

Journal of Chromatography, 517 (1990) 51–66
Elsevier Science Publishers B.V., Amsterdam

CHROMSYMP. 1974

Comparison of methods for the determination of the polarity and selectivity of stationary phases in gas chromatography from a thermodynamic point of view

R. V. GOLOVNYA*

A. N. Nesmeyanov Institute of Organo-Element Compounds of the U.S.S.R. Academy of Sciences, ul. Vavilova 28, Moscow (U.S.S.R.)

and

B. M. POLANUER

All-Union Institute for Genetic and Selection of Industrial Microorganisms, Ministry of Medical Industry of the U.S.S.R., 1st Dorozny pr., Moscow (U.S.S.R.)

ABSTRACT

Different scales proposed for the evaluation of polarity and selectivity in gas chromatography as relative and absolute values were compared. It is shown that the scale including six parameters, $\Delta G(X)$, $\Delta G(Y)$, $\Delta G(Z)$, $\Delta G(U)$, $\Delta G(S)$ and $\Delta G(CH_2)$, is more suitable and allows a unified system to be obtained for the polarity and selectivity of conventional stationary phases, organic and inorganic salts and polymer sorbents. The main equation for the calculation of the partial molar free energy of sorption, ΔG, is simplified for capillary gas chromatography.

INTRODUCTION

Progress in gas chromatography (GC) has greatly increased the number of available stationary phases and sorbents. Some of these stationary phases have similar or identical chemical structures and sorption properties[1,2]. The main chromatographic suppliers usually offer up to 200 stationary phases with different properties[3,4]. In recent years, new groups of stationary phases, including organic salts[5,6] and crystal hydrates of inorganic salts[7,8], have been described. Usually the selection of a suitable stationary phase for solving different problems is difficult and one needs a classification system suitable for comparison of stationary phases. The problem of a unified method for the selection and comparison of sorbents in GC still remains.

Many different approaches have been used to compare and classify different stationary phases and sorbents. All of them operate with the term "polarity". Polarity is used in GC to describe the ability of the sorbent to enter into different types of interactions with sorbates. The concepts of polarity and selectivity in GC are not

0021-9673/90/$03.50

clearly defined and are interpreted in different ways by different investigators. In our opinion, GC polarity should be defined as the capacity of the sorbent for various intermolecular interactions: dispersive, inductive, orientative and donor–acceptor[9].

The problem of polarity is still debated and many papers have been devoted to it. These can be divided into several groups. In some papers polarity is evaluated on the basis of relative parameters: values of retention indices of several test compounds[1,2,10–16], sometimes in combination with the effective molecular weights of the sorbates[17–19], or on the basis of the ratio of retention parameters of neighbouring *n*-alkanes[20–23].

Evaluation of polarity utilizing thermodynamic values has often been undertaken. Such values are the excess free energy of sorption of a methylene unit in an *n*-alkane or any other monofunctional homologous series[24–28]; the partial molar free energy of sorption of a methylene unit itself[29,30] or divided on stationary phase density[31] [$\Delta G(CH_2)$]; excess partial molar enthalpies[32] and partial molal free energies[33] of selected functional groups; and the six-parameter scale based on partial molar free energies of five test compounds and the methylene unit[9,34–36].

In this paper we compare from the thermodynamic viewpoint different methods for the evaluation of polarity in order to reveal the physical meaning of some scales. We also consider the advantages and shortcomings of the thermodynamic polarity scales. The aim of this paper is to propose a convenient quantitative thermodynamic scale for the evaluation of stationary phase polarity that will be suitable for capillary GC.

There are great differences between the definition of a "polar substance" in physical chemistry and the concept of a polar sorbate and sorbent in chromatography. In physical chemistry "polarity" is a property of one individual substance. This property is associated with the dipole moment of a molecule. The ability of this molecule to interact with other molecules and the change in their properties during interaction is not considered. Hence compounds without dipole moments are termed non-polar. In chromatography some non-polar compounds from the physico-chemical viewpoint such as benzene, *p*-dinitrobenzene, pyrazine and 1,4-dioxane are assumed to be polar sorbates. The retention times of these compounds may increase owing to complex formation and donor–acceptor interactions with some stationary phases.

In chromatography, retention is determined primarily by the energy of intermolecular interactions between the analyte substances and the liquid stationary phases or adsorbents. The partial molar free energy of solution or adsorption is essentially a total of the energies of intermolecular interactions, both non-specific, determined by physical forces, and specific electron donor–acceptor interactions of a chemical nature. When all experimental conditions are equal, a polar sorbate is retained longer on a more polar than on a less polar column[21].

It must be considered that the partial molar free energy of sorption is the result of all types of interactions. It is not possible to determine separately any part of it, dispersive, inductive, orientative or donor–acceptor. To evaluate the polarity one must use several test compounds which simulate the principal types of intermolecular interactions[9]. From this viewpoint we shall discuss some approaches to the evaluation of polarity in GC.

EVALUATION OF POLARITY USING THE METHYLENE UNIT OF A HOMOLOGOUS SERIES

n-Alkanes are capable of dispersive and weak inductive interactions. In spite of this, *n*-alkanes are used predominantly for the determination of the polarity of stationary phases, *e.g.*, their ability to enter into all types of intermolecular interactions including orientation and donor–acceptor forces. *A priori* it is assumed that the decrease in the energy of dispersive interactions of the sorbents with *n*-alkanes is proportional to their ability to enter into other types of interactions.

In initial studies it was proposed to estimate the polarity of a sorbent by using the specific retention volumes of *n*-octane or the ratio of the retentions of two neighbouring homologues of any homologous series[21]. A similar approach was proposed by Chovin and Lebbe[20]. In their scale, the polarity of β,β'-oxydipropionitrile was considered to be equal to unity (polar reference stationary phase) and the polarity of squalane was considered to be equal to zero (non-polar reference phase). The polarity (P) of a phase of interest was then calculated as follows:

$$P_x = \frac{\log (t'_{n+1}/t'_n)_{\text{squ}} - \log (t'_{n+1}/t_n)_x}{\log (t'_{n+1}/t'_n)_{\text{squ}} - \log (t'_{n+1}/t'_n)_{\beta,\beta'}} \tag{1}$$

where t'_{n+1} and t'_n are the adjusted retention times of *n*-alkanes with $n+1$ and n carbon atoms, respectively, and squ, β,β' and x refer to the stationary phases squalane, β,β'-oxydipropionitrile and the tested stationary phase x, respectively. It was mentioned that the polarity of some stationary phases might be larger than 1. The existence of stationary phases with polarities lower then zero was not considered[20].

In order to understand the physical meaning of eqn. 1, let us modify it in the following way:

$$P_x = \frac{2.3RT\log (t'_{n+1}/t'_n)_{\text{squ}} - 2.3RT\log (t'_{n+1}/t'_n)_x}{2.3RT\log (t'_{n+1}/t'_n)_{\text{squ}} - 2.3RT\log (t'_{n+1}/t'_n)_{\beta,\beta'}} \tag{2}$$

where R is the universal gas constant and T is the absolute temperature of the analysis. Eqn. 2 shows that the polarity in the scale of Chovin and Lebbe[20] is equivalent to the partial molar free energy of sorption of a methylene group for *n*-alkanes, $\Delta G(\text{CH})_2$, since $\Delta G(\text{CH})_2$ may be calculated as follows:

$$\Delta G(\text{CH}_2) = -2.3RT\log (V_{g,n+1}/V_{g,n}) \tag{3}$$

where $V_{g,n+1}$ and $V_{g,n}$ are the specific retention volumes for *n*-alkanes with $n+1$ and n carbon atoms, respectively.

If homologues are analysed under the same chromatographic conditions, eqn. 3 can be simplified to

$$\Delta G(\text{CH}_2) = -2.3RT\log (t'_{g,n+1}/t'_{g,n}) \tag{4}$$

As was demonstrated previously[9], $\Delta G(\text{CH}_2)$ is a measure of the capacity of a stationary phase for dispersive interactions.

Eqn. 2 can be transformed to the following equation using eqn. 3 or 4:

$$P_x = \frac{\Delta G(CH_2)_{squ} - \Delta G(CH_2)_x}{\Delta G(CH_2)_{squ} - \Delta G(CH_2)_{\beta,\beta'}} \tag{5}$$

In eqn. 5, the numerator is the difference in the capacity of *n*-alkanes for dispersive interactions with the stationary phase *x* and with squalane, while the denominator is the difference in the capacity of *n*-alkanes for dispersive interactions with the two reference stationary phases. Hence the scale of Chovin and Lebbe[20] really evaluates the possibility of stationary phases for dispersive interactions in relative units. On this scale a lower $\Delta G(CH_2)$ value corresponds to a higher polarity *P*. Consequently, this scale ranks stationary phase according to their capacity for dispersive interactions with *n*-alkanes. The energy of dispersive interactions depends on the polarity of the stationary phase, but will change in a non-proportional manner with capacity for orientative and donor–acceptor interactions. This correlation is not as simple as was assumed previously[20].

The scale of polarity Π_{rel}, based on a methylene group, was proposed by Sidorov[22]. The value of the polarity parameter t'_{CH_2} is defined as follows:

$$t'_{CH_2} = t'_{n+1}/t'_n \tag{6}$$

where t'_{n+1} and t'_n are the adjusted retention times of *n*-alkanes with $n+1$ and *n* carbon atoms, respectively. On the basis of t'_{CH_2}, the relative polarity Π_{rel} for the studied stationary phase was calculated using the equation

$$\Pi_{rel} = 100 \cdot \frac{[\log (t'_{CH_2})_{squ} - \log (t'_{CH_2})_x]}{\log (t'_{CH_2})_{squ}} \tag{7}$$

Considering eqns. 4 and 6, we can easily transform eqn. 7 into

$$\Pi_{rel} = \frac{\Delta G(CH_2)_{squ} - \Delta G(CH_2)_x}{\Delta G(CH_2)_{squ}} \tag{8}$$

which is similar to eqn. 5. The main difference between the polarity scales in refs. 20 and 22 is that in the latter only one reference stationary phase, squalane, is used but the practical meaning of the two scales are the same. They reflect only the energy of dispersive interactions of a methylene unit with a sorbent in relative units.

The thermodynamic polarity scale proposed by Novak *et al.*[24] also utilizes the retention of a methylene unit for ranking of stationary phases, but does not include any reference stationary phase. According the concept of "reluctance", there are differences in properties between an ideal solution and a real solution of a sorbent in a stationary phase. These differences are minimal for the solution of an *n*-alkane in a hydrocarbon stationary phase such as squalane. It was accepted that more polar stationary phases have higher values of the excess Gibbs partial molar free energy of solution for *n*-alkanes. The measurement of the total excess Gibbs partial molar free energy of sorption of molecules is difficult, and therefore polarity was defined as the

excess Gibbs partial molar free energy of sorption for a methylene group, $\Delta G^E(CH_2)$[24]. The values of $\Delta G^E(CH_2)$ can be calculated using the equation

$$\Delta G^E(CH_2) = RT \ln [(V_{g,n}/V_{g,n+1})/(P_n^0/P_{n+1}^0)] \quad (9)$$

where $V_{g,n+1}$ and $V_{g,n}$ are the specific retention volumes and P_{n+1}^0 and P_n^0 are the saturated vapour pressures of two pure liquid homologues (with $n+1$ and n carbon atoms, respectively) of any homologous series selected as test compounds.

To determine the values of the excess energies for sorption, one requires information about the vapour pressures of two test compounds at the temperature of the analysis, which are usually calculated by empirical equations of low precision. The accuracy in the determination of $\Delta G^E(CH_2)$ values is generally poor.

It was assumed that the $\Delta G(CH_2)$ value does not change for any series of homologues with $n > 5$, analysed on any stationary phase at any temperature. This assumption is not correct. Experimental data[24] show the differences in the values of the excess partial molar Gibbs free energies for sorption of homologous series. For example, on squalane $\Delta G^E(CH_2) = -35$ kcal/mol for *n*-alkanes, -17 kcal/mol for *n*-alkyl acetates and -23 kcal/mol for *n*-alkanols. An investigation of surfactants as stationary phases demonstrated that for different series of homologues the $\Delta G^E(CH_2)$ values may differ significantly. In some instances the excess partial molar Gibbs free energy for a methylene group in different homologous series may differ 5–6-fold[26,27].

Let us compare the advantages of the scales of Novak *et al.*[24] and Chovin and Lebbe[20]. For this purpose we transform eqn. 9 into

$$\Delta G^E(CH_2) = -RT \ln (V_{g,n+1}/V_{g,n}) + RT \ln (P_{n+1}^0/P_n^0) \quad (10)$$

Thus, according to eqn. 3, one can obtain from eqn. 10 the equation

$$\Delta G^E(CH_2) = \Delta G(CH_2) + RT \ln (P_{n+1}^0/P_n^0) \quad (11)$$

The second term in eqn. 11 is proportional to the ratio of the saturated vapour pressures of two pure homologues. The ratio P_{n+1}^0/P_n^0 does not depend on the type of stationary phase. Hence it becomes clear that the excess energy of sorption for a methylene group, $\Delta G^E(CH_2)$, and the partial molar Gibbs free energy of sorption, $\Delta G(CH_2)$, differ only by the constant, which depends on the vapour pressures of the test compounds and does not depend on the nature of the stationary phase. In general, the scales of Novak *et al.*[24] and Chovin and Lebbe[20] estimate the ability of a stationary phase for dispersive interactions with a methylene group.

Recently, Poole and co-workers[29,30,37] used the value of the partial molar Gibbs free energy of sorption for a methylene group, $\Delta G(CH_2)$, to measure the polarity of stationary phases and liquid organic salts. This scale, like the scale based on the excess partial molar Gibbs free energy of sorption for a methylene group[24], does not use any reference stationary phase. The $\Delta G(CH_2)$ value can be calculated easily and with high precision using, for example, eqn. 4. The $\Delta G(CH_2)$ scale[29,30] utilizes the same *a priori* assumption that the decrease in energy of dispersive interactions on a polar phase is directly proportional to the capacity of that phase for polar interactions.

Of course, the $\Delta G(CH_2)$ value is connected with the polarity of a stationary

TABLE I

ENERGETIC EQUIVALENTS OF A METHYLENE UNIT, $\Delta G(CH_2)$, AND RETENTION INDICES OF McREYNOLDS TEST COMPOUNDS[1] ON VARIOUS STATIONARY PHASES

Calculated using data in ref. 1.

Stationary phase	*b*	$-\Delta G(CH_2)$ *(J/mol)*	*I*				
			Benzene	*2-Pentanone*	*1-Butanol*	*1-Nitropropane*	*Pyridine*
Hallcomide M18 01	0.2844	2136	732	858	757	874	845
Pluronic P 85	0.2842	2135	712	676	708	803	828
Octoil S	0.2836	2130	854	980	874	1040	1034
Apiezon M	0.2833	2128	691	620	654	701	756
Polybutene 32	0.2832	2120	674	619	651	694	739
Diisooctyl adipate	0.2822	2120	731	777	753	856	839
Apiezon L	0.2821	2119	685	612	642	684	741
DEG sterate	0.2817	2116	726	764	743	841	828

phase but is not proportional to the energy of orientative and donor–acceptor interactions as was assumed in refs. 20–30. Really, the $\Delta G(CH_2)$ values estimate only the ability of a stationary phase for dispersive interactions[9]. For some stationary phases the $\Delta G(CH_2)$ values may be the same but their capacity for interactions with polar compounds may be different.

For example, in Table I are given eight stationary phases with similar values of $\Delta G(CH_2)$: hydrocarbons (Apiezons, polybutene), polyesters (Octoil S, DEG stearate) and amide (Hallcomide M18 01). One can see from Table I that the difference in the $\Delta G(CH_2)$ values for the stationary phases may be less than 20 J/mol. At the same time, the difference in retention indices of test compounds may be more than 100 index units. These stationary phases cannot be considered to be identical or even similar. The data in Table I demonstrate that the ability of a stationary phase to undergo all types of interactions cannot be measured correctly by only one parameter, the $\Delta G(CH_2)$ value. It is clear that there is no possibility of determining the chromatographic polarity of a stationary phase or sorbent using the chromatographic properties of only one type of molecule or fragment of molecule. In this instance it is impossible to evaluate by one parameter the ability of sorbent to undergo all types of intermolecular interactions with sorbates.

EVALUATION OF POLARITY USING RETENTION INDICES OF SEVERAL TEST SUBSTANCES

The polarity scale based on the sorption properties of several sorbents with different functional groups is more informative than those scales[20–30] based on only one parameter, the contribution of a methylene group to retention. For such scales of polarity one should select a number of test compounds simulating in the best way possible all intermolecular interactions: dispersive, orientative (dipole–dipole) and inductive interactions; and electron donor–acceptor interactions, including the capacity for hydrogen bonding.

This approach was used in well known classification schemes based on the

TABLE II

TEST COMPOUNDS USING FOR MEASUREMENT POLARITY ON THE McREYNOLDS SCALE

Definition	*Test compound*	*Types of interaction tested*
X	Benzene	Dispersive and π-complex formation
Y	1-Butanol	Orientative with proton-donor and proton-acceptor capabilities[a]
Z	2-Pentanone	Orientative and proton-acceptor without proton-donor capability[a]
U	1-Nitropropane	High capability for orientative interactions (dipole moment, μ = 3.6D), weak proton acceptor[a]
S	Pyridine	Weak orientative and strong proton acceptor[a]

[a] In combination with dispersive and orientative interactions.

retention indices of several test compounds proposed by Rohrschneider[10] and modified by McReynolds[1]. On this scale, polarity and selectivity may be described using five basic test compounds, benzene, 1-butanol, 1-nitropropane, 2-pentanone and pyridine. The polarity was measured by ΔI. It was also assumed that the energy of dispersive interactions of a test compound determined on squalane is the same as that on any other stationary phase. In reality there must be differences in the dispersive interactions of test compounds with different stationary phases. However, on this scale[10], this fact was not considered.

This classification system gained widespread popularity because about 200 widely used stationary phases were characterized using McReynolds constants[1]. Now about 400 stationary phases have been classified using this scale[2–4,38,40]. The principles of polarity and selectivity determination with this scale are reviewed elsewhere[39,40].

Many criteria related to McReynolds constants have been recommended. For example, in catalogues of chromatographic suppliers and handbooks the sum of the first five constants, $\sum_{i=1}^{5} \Delta I_i$, is often used to describe general polarity of stationary phases[13,19,26,27,35,38]. Similar to this parameter is the polarity index, *CP*[3,15], which can be calculated using the equation

$$CP = \frac{\frac{\sum_{1}^{5} \Delta I_{\text{stat.phase}}}{5}}{\sum_{1} \Delta I_{\text{OV-275}}} \cdot 100 \tag{12}$$

It is obvious that the scale based on the *CP* index, unlike the McReynolds scale, is restricted from both sides by squalane and OV-275.

Tarian *et al.*[14] recommended describing the polarity of a stationary phase using the parameter P_T which can be calculated as:

$$P_T = \frac{\sum_{1}^{5} \frac{I_P - I_{sq}}{I_{sq}}}{5} \cdot 100 \tag{13}$$

TABLE III

COMPARISON OF McREYNOLDS CONSTANTS AND $\Sigma\Delta I$, CP AND P_T CRITERIA FOR VARIOUS STATIONARY PHASES

Stationary phase	*X*	*Y*	*Z*	*U*	*S*	$\sum_{1}^{5}\Delta I$	*CP*	P_T
OV-22	160	188	191	283	253	1075	25	33
Triton X-200	117	289	172	266	237	1081	26	34
Polypropylene glycol 2000	128	294	173	264	226	1085	26	34
Estinox	136	257	182	285	227	1087	26	34
Trimeric acid	94	271	163	182	378	1088	26	34
Pluracol-2010	129	295	174	260	227	1091	26	34
Poly 101	115	357	151	262	214	1099	26	34
Atpet 200	108	282	186	235	289	1100	26	35
Amin 220	117	380	181	293	133	1105	26	35
Maximum difference	64	198	40	101	255	30	1	2

To compare the informativity of the McReynolds scale with the scales obtained using eqns. 12 and 13, we considered data given as examples for eight stationary phases in Table III. It is seen that maximum difference in $\sum_{i=1}^{5}\Delta I_i$ values is less than 30 i.u. for all phases (see Table III), whereas the differences in CP values, calculated by eqn. 12, are less than 2 relative units. Consequently, stationary phases with similar values of $\sum_{i=1}^{5}\Delta I_i$ and CP are not interchangeable in practice. Obviously such parameters are less informative than the McReynolds constants. The $\sum_{i=1}^{5}\Delta I_i$, CP, P_T and other similar parameters fail in the evaluation of the specific properties of a sorbent because of compensation effects.

In scales[1,10–14] which have a reference stationary phase (squalane, hydrogenated Apiezon, Apolan-87), polarity is evaluated simultaneously with the selectivity of a studied stationary phase in comparison with a reference stationary phase.

The problem of a reference stationary phase is eliminated in Evans and Haken's system of "selectivity indices"[19]. In this approach, the retention index of sorbate is divided into two parts, a dispersive index I_m and a selectivity index I^*:

$$I = I_m + I^* \tag{14}$$

The dispersive index may be calculated as the retention index of a hypothetical *n*-alkane with the same molecular mass as the sorbate:

$$I_m = \frac{M - 2.016}{0.14026} \tag{15}$$

where M is the molecular mass of the sorbate. The I_m value characterizes only the test

substance and is constant for any set of analytical conditions. The selectivity index I* depends on the type of sorbate, sorbent and analytical conditions. There is some correlation between the selectivity indices of selected sorbates and the polarity of stationary phases[19]. However, the scale[19] which uses a hypothetical *n*-alkane molecular mass cannot be interpreted thermodynamically.

The retention index percentage contribution *IP* was introduced[15] to relate the solute retention index to the sum of ten retention indices corresponding to one stationary phase:

$$IP = \frac{100\, I_P}{\sum_{P=1}^{10} I_i} \tag{16}$$

Using the *IP* parameter calculated from eqn. 16, most stationary phases were classified and separated into clusters containing groups of stationary phases with similar properties[15].

The main disadvantage of scales[1,10–19] that use ΔI and I values has been extensively discussed[9,29,30,34,36,37]. This disadvantage is connected with the great difference in the energetic equivalent of one index unit on different stationary phases[9]. The energetic equivalent of one index unit is calculated from

$$\Delta G_{\mathrm{i.u}} = \Delta G(\mathrm{CH_2})/100 = -RT \ln (t'_{n+1}/t'_n) \tag{17}$$

where t'_{n+1} and t'_n are the adjusted retention times of two neighbouring homologues.

The values of the energetic equivalent of a retention index unit at the same column temperature may vary from -24 to -5.2 J/mol[29]. This means that for two stationary phases a sorbate may have the same retention index but a different energy of sorption[9]. This fact does not allow the interpretation of ΔI values to find a physical meaning for polarity with such scales.

EVALUATION OF POLARITY OF SORBENTS USING $\Delta G'$ VALUES

Different approaches have been proposed for evaluating polarity from a thermodynamic point of view. Earlier we considered a thermodynamic scale of polarity based on the excess partial molar Gibbs free energy of sorption for a methylene group, $\Delta G^{\mathrm{E}}(\mathrm{CH_2})$ (ref. 24). It was also assumed that the polarity and selectivity of stationary phases can be defined in terms of the partial molar enthalpies of solution for certain functional groups, which were determined from the temperature dependence of the specific retention volumes of test compounds[32]. However, an evaluation of the capacity of stationary phases to retain polar substances without considering the entropy of sorption is not correct. Solution of polar compounds on polar stationary phases is accompanied not only by changes in the heat of solution but also with a decrease in the degree of freedom for the sorbate molecule. Neglecting the contribution of entropy can lead to a faulty conclusion.

This circumstance was considered by Reinbold and Risby[32]. The polarity of stationary phases was evaluated from the partial molal Gibbs free energies of sorption

for different functional groups[33]. This approach also is not correct, because the contribution of the same functional group in various molecules to the total energy of sorption may be different. The low informativity of $\Delta G_{C=O}$ and ΔG_{OH} parameters for the evaluation of the polarity of polyoxyethylene esters has been reported[35].

Considering that five McReynolds test compounds adequately simulate the main types of intermolecular interactions (Table II), it was proposed to describe the polarity of sorbents using the partial molar Gibbs free energies of sorption for these compounds[9,34]. The capacity of the stationary phases for dispersive interactions on this scale was measured by a sixth parameter, the partial molar Gibbs free energy of sorption for a methylene group[9,34].

The partial molar Gibbs free energy of solution for substances may be determined using the equation

$$\Delta G = -RT\ln(V_g T\rho/273) \tag{18}$$

where V_g is the specific retention volume of the solute and ρ is the density of the stationary phase at the column temperature T[41].

To simplify the problems relating to the determination of the specific retention volumes of all sorbates, it was recommended to calculate the partial molar Gibbs free energy of sorption using another equation:

$$\Delta G = RT\cdot\frac{(I-100n)}{100}\cdot b + RT\ln\left(\frac{V_{gn}T\rho}{273}\right) \tag{19}$$

where I is the retention index of the solute, b the natural logarithm of the ratio of the specific retention volumes or adjusted retention times of n-alkanes eluted just before and after this solute, T the column temperature and V_{gn} the specific retention volume of an n-alkane with n carbon atoms[34].

The measurement of the density of the stationary phase at the column temperature may be a problem in many instances. Therefore, it was recommended to use the value of $\Delta G'$ calculated for each test substance using eqn. 20:

$$\Delta G' = \Delta G + RT\ln\rho \tag{20a}$$

$$\Delta G' = RT\left[\frac{(I-100n)}{100}\cdot b + \ln\left(\frac{V_{gn}T}{273}\right)\right] \tag{20}$$

Such an assumption in the calculation of the values of $\Delta G'$ does not afffect the overall picture for the evaluation of the polarity of stationary phases[9,34] in comparison with ΔG values (eqn. 18), which give the correct evaluation of the polarity of the stationary phases.

The comparison of $\Delta G(CH_2)$ and five values of $\Delta G'$ for McReynolds test compounds permits the quantitative evaluation of the capacity of stationary phases for intermolecular interactions: dispersive, orientative and donor–acceptor.

The advantages of this scale[9] are the elimination of a reference stationary phase and the possibility of using retention indices and specific retention volumes of

n-alkanes from the literature. This method of calculating thermodynamic polarity is simple and may be used not only for stationary phases but also for adsorbents[9]. This scale was successfully used for the evaluation of the properties of ordinary stationary phases[36]. It was also used to investigate the ability of melted organic salts for undergo intermolecular interactions under gas chromatographic conditions[6].

CALCULATION OF POLARITY USING ENERGETIC EQUIVALENTS OF RETENTION INDICES, $\Delta G(I)$ VALUES

It is well known that the partial molar free energy of sorption is related to the retention index by a very simple relationship:

$$\Delta G = A + BI \tag{21}$$

where A and B are constants under fixed chromatographic conditions[42]. The physical meaning of constant B was considered earlier[43]. It was demonstrated that B is the energetic equivalent of an index unit. Thus BI is the energetic equivalent of the retention index of a sorbate, $\Delta G(I)$. Consequently, eqn. 21 may be transformed to[8,44]

$$\Delta G = \Delta G_{\text{i.u.}} I + A = \Delta G(I) + A \tag{22}$$

Thus, using energetic equivalents of the retention indices [$\Delta G(X)$, $\Delta G(Y)$, $\Delta G(Z)$, $\Delta G(U)$, $\Delta G(S)$] of test compounds it is possible to compare the capacity of a stationary phase to undergo different kinds of intermolecular interactions[9] but quantitative and correct evaluations are not possible because of different values of A in eqn. 22 for different stationary phases. On such a scale only the capacity for dispersive interactions may be measured quantitatively by a sixth parameter, $\Delta G(CH_2)$ calculated according eqn. 3 or 4.

In Table IV are given the values for calculating the polarity of stationary phases, molten salts and polymer sorbents. The calculation of the capacity of sorbates for different types of interactions is rough because $\Delta G(I) \neq \Delta G$.

Using $\Delta G(I)$ values for McReynolds test compounds, one can compare the properties of sorbents and stationary phases. It was mentioned previously that the retentions of sorbates on conventional stationary phases at 100°C and on porous polymers at 150–200°C are similar[40]. This assumption is confirmed by the $\Delta G(I)$ values for test compounds given in Table IV. In all instances the energetic equivalents of the index values of test compounds on porous polymers are higher.

Recently a parameter similar to the energetic equivalent of a retention index was proposed for evaluating the selectivity of stationary phases and organic salts[30], using the equation

$$I'(P) = -2.3RT[(IB)_{\text{squ}} - (IB)_{\text{SP}}] + 2.3RT(A_{\text{squ}} - A_{\text{SP}}) \tag{23}$$

where A_{squ}, A_{SP}, B_{squ} and B_{SP} are constants that may be determined from the specific retention volumes of *n*-alkanes determined on squalane (squ) and the tested stationary phase (SP), respectively.

Considering eqn. 22, we transformed eqn. 23 to

$$I'(P) = \Delta G(I)_{\text{squ}} - \Delta G(I)_{\text{SP}} + (A_{\text{squ}} - A_{\text{SP}}) \tag{24}$$

TABLE IV

CALCULATION OF POLARITY OF STATIONARY PHASES, ORGANIC SALTS AND POLYMER SORBENTS USING ENERGETIC EQUIVALENTS OF RETENTION INDICES OF TEST COMPOUNDS, $\Delta G(I)$, AT 120°C

The $\Delta G(CH_2)$ and $\Delta G(I)$ values were calculated using data from refs. 1, 6, 8, 27, 33 and 41.

Stationary phase	$-\Delta G(CH_2)$ *(J/mol)*	$-\Delta G(I)$ *(J/mol)*				
		Benzene	*2-Pentanone*	*1-Butanol*	*1-Nitropropane*	*Pyridine*
Butyl stearate	2191	15 211	15 321	15 167	16 746	16 877
Squalane	2172	14 185	12 817	13 620	14 163	15 184
Hallcomid M18	2149	15 731	18 438	16 268	18 782	18 159
Apolane 87	2140	14 429	12 844	13 487	14 215	15 499
Hallcomid M18 O	2136	15 856	18 592	16 455	19 041	18 464
Octyldecyl adipate	2130	15 593	16 381	15 891	18 000	17 745
Apiezon M	2128	14 560	13 028	13 666	14 518	15 731
Dioctyl sebacate	2125	15 411	16 113	15 624	17 686	17 473
Apiezon L	2119	14 520	12 973	13 608	14 499	15 707
DEG stearate	2116	15 177	16 574	15 515	16 828	18 839
Triton X-305	2111	19 320	22 318	19 869	24 070	23 838
Dioctyl phthalate	2097	15 629	16 280	16 301	18 629	18 168
Dexyl 400	2081	15 798	15 361	16 172	18 191	18 379
SKTFT-50	2058	14 947	15 071	17 171	18 900	17 932
PFMS-4	2058	15 627	15 194	15 997	17 994	18 180
Flexol 8N8	2053	15 381	17 332	16 244	18 729	18 030
Zinc stearate	2048	14 625	16 817	14 051	15 362	25 461
Silbor-1	1991	15 611	25 010	16 507	18 578	19 295
Versamid 940	1947	14 841	17 607	15 036	16 828	17 684
OV-7	1931	13 943	13 576	14 252	15 893	15 970
Diglycerol	1929	19 759	27 323	22 904	25 625	29 967
OV-11	1925	14 534	14 092	14 862	16 768	16 883
OV-3	1913	13 339	12 937	13 550	14 851	15 062
Tergitol NPX	1909	16 229	18 635	16 897	19 876	20 048
Triton X-100	1894	16 215	18 734	16 954	19 966	20 098
SE-30	1874	12 542	12 092	12 580	13 442	13 892
Sucrose acetate	1870	15 429	17 206	16 421	19 263	18 590
OV-101	1866	12 505	12 076	12 543	13 420	13 849
Silar 10C	1546	18 136	20 826	19 883	24 645	23 176
OV-1	1855	12 435	12 008	12 472	13 344	13 771
OV-22	1849	15 040	14 393	15 133	17 297	17 611
NPGA	1786	15 849	18 136	16 778	19 905	20 316
OV-225	1709	15 060	16 393	16 496	19 556	18 547
NPGS	1703	15 808	18 090	16 932	20 356	20 237
XE-60	1680	14 405	16 321	16 254	19 246	17 918
Carbowax 20M	1679	16 374	18 910	16 710	20 556	20 304
FFAP	1656	16 445	19 376	18 614	20 767	21 960
Carbowax 1000	1633	16 335	19 554	17 071	20 877	21 040
DEGA	1581	16 307	18 870	17 193	20 831	21 464
EGA	1573	16 112	18 393	17 009	20 565	20 958
TCEP	1338	16 675	19 364	18 454	22 482	21 599
Tetrabutylammonium picrate	1672	16 317	18 524	17 821	21 132	20 613
Tetrabutylammonium chloride	1588	16 245	28 394	16 849	22 566	21 136
$KF \cdot 2H_2O$ sorbent[a]	440	2944	3947	4435	3687	3855
Porapak Q[b]	3457	21 328	20 982	22 503	22 607	23 021
Chromosorb 102[b]	3187	19 825	19 379	20 813	21 837	21 228

[a] At 100°C.
[b] At 140°C.

One can see from eqn. 24 that the approach proposed by Poole *et al.*[30,45] is comparable to the $\Delta G(I)$ scale[8] but needs a reference stationary phase, squalane. It is more complicated because it is based on assumptions about the linear dependence of the retention volumes of *n*-alkanes on the number of carbon atoms, which is under discussion[46–48].

THERMODYNAMIC SELECTIVITY OF SORBENTS

The "selectivity" in GC, like polarity, is not clearly defined and is interpreted in different ways by different investigators. To characterize the selctivity of a sorbent this term is used in two ways: (1) to compare the capacity of an investigated sorbent to retain two sorbates (selectivity of one column); and (2) to compare capacity of two sorbents to retain one or several sorbates (selectivity of two columns). In the first instance the selectivity of the sorbents for a pair of sorbates X and Y can be calculated as the difference in their partial molar Gibbs free energies of sorption:

$$\delta(\Delta G)_{X,Y} = \Delta G_X - \Delta G_Y \tag{25}$$

It is better to measure the selectivity of a sorbent using the energetic equivalents of retention indices, $\Delta G(I)$. The partial molar Gibbs free energies of sorption are connected with the energetic equivalents of retention indices (see eqn. 17). Thus, considering that A is a constant for one sorbent under fixed analytical conditions, we obtain

$$\delta(\Delta G)_{X,Y} = \Delta G(I)_X - \Delta G(I)_Y \tag{26}$$

Let us consider the second case, the selectivity of two stationary phases, *i.e.*, their capacity to retain one substance x. The selectivity of two sorbents, S_1 and S_2, with respect to one sorbate may be measured as the difference in their partial molar Gibbs free energies of sorption:

$$\delta(\Delta G)_{S_1,S_2} = \Delta G_{S_1} - \Delta G_{S_2} \tag{27}$$

Considering, that for different stationary phases 1 and 2 the value of the constant A is usually different, the use of energetic equivalents of retention indices, $\Delta G(I)$, in this instance gives only an approximate estimation of the selectivity of the compared columns. Consequently, quantitative measurements of selectivity for one column (see eqn. 26) and the approximate estimation of the selectivity for two columns can be carried out using $\Delta G(I)$ values.

EVALUATION OF POLARITY AND SELECTIVITY OF STATIONARY PHASES IN CAPILLARY COLUMNS

Capillary columns are now widely used in GC and the determination of the polarity of stationary phases in this type of column is therefore required.

A thermodynamic approach to the polarity of capillary columns is also preferable. In this instance it is possible to use the partial molar Gibbs free energies of

sorption for several test compounds. For capillary columns, we have transformed the eqn. 18 for the calculation of ΔG to a more convenient form.

Let us define some parameters for capillary columns. The volume of the empty part of the column without stationary phase will be termed the void volume or dead volume, V_0, and the total volume of the column is V. V_L is the volume of stationary phase in the column. These parameters are calculated using the following equations:

$$V = L\pi d^2/4 \tag{28}$$

$$V_0 = L\pi(d - 2d_f)^2/4 \tag{29}$$

$$V_L = L\pi[d^2 - (d - 2d_f)^2]/4 \tag{30}$$

where d is the diameter of the capillary column, d_f the film thickness of the stationary phase in the capillary column and L the length of the capillary column. On the other hand, the dead volume of the column can be determined from the carrier gas flow-rate, ω, and the column dead time, t_0.

The specific retention volume of a sorbate X in GC is calculated using the equation

$$V_{g,X} = \frac{273t'\omega}{mT_r} \cdot j\left(1 - \frac{P^0_{H_2O}}{P_0}\right) \tag{31}$$

where t' is the adjusted retention time of a solute X, ω the carrier gas flow-rate (ml/min) measured at room temperature, T_r, m the mass of stationary phase in the column, j the gas compressibility factor, $P^0_{H_2O}$ the water vapour pressure at room temperature and P_0 the inlet gas pressure. Considering the parameters in eqn. 31, one can reach the conclusion that some of them are not related to properties of the stationary phase, and the equation may be written as

$$V_{g,X} = \frac{273t'\omega}{mT_r} \cdot j\xi \tag{32}$$

where ξ is the correction for the pressure of water vapour at room temperature if carrier gas flow-rate was measured with a bubble flow meter; $\xi = (1 - P^0_{H_2O}/P_0)$.

The partial molar Gibbs free energy of sorption of a substance X may be calculated using the equation

$$\Delta G_X = -RT\ln\left(\frac{273t'\omega T\rho j\xi}{273T_r m}\right) \tag{33}$$

We made some simplifications of eqn. 33 assuming that

$$\frac{1}{V_1} = \frac{\rho}{m} \tag{34}$$

and

$$\omega = V_0/t_0 \tag{35}$$

Thus, eqn. 33 may be transformed to

$$\Delta G = -RT\ln\left(\frac{t'}{t_0}\cdot\frac{V_0}{V_1}\cdot\frac{T}{T_r}\cdot j\xi\right) \tag{36}$$

The ratio of the adjusted retention time, t', of a solute to the retention time of an unretained compound, t_0, is the capacity factor, k', so the final expression for the calculation of the partial molar Gibbs free energy of sorption in capillary chromatography will be described by

$$\Delta G = -RT\ln\left(k'\cdot\frac{V_0}{V_1}-\frac{T}{T_r}\cdot j\xi\right) \tag{37}$$

Eqn. 37 provides an opportunity to calculate the energy of sorption using the capacity factor of a solute, k'. It is clear from eqn. 37 that to calculate the partial molar free energy of sorption of substance X it is necessary to determine the capacity factor, k', and to measure accurately the experimental conditions (column temperature, room temperature, inlet and outlet pressure of carrier gas). As a rule, using modern chromatographic equipment it is not a problem to determine these parameters. The dead volume and the volume of stationary phase in the column may be calculated from values of the column length, inner diameter, d, and stationary phase film thickness, d_f, in the capillary column. These parameters are common characteristics of columns used in capillary GC. It is seen from eqn. 37 that the calculation of the partial molar free Gibbs energy of sorption for test compounds is simpler in capillary chromatography than for packed columns. One does not need to determine the density of the stationary phase under analytical conditions, the mass of stationary phase or the carrier gas flow-rate.

Eqn. 37 can be recommended for the determination of the polarity and selectivity of stationary phases in capillary GC on the basis of the partial molar Gibbs free energies of sorption $\Delta G(X)$, $\Delta G(Y)$, $\Delta G(Z)$, $\Delta G(U)$, $\Delta G(S)$ and $\Delta G(CH_2)$ of test compounds according to the scale given in ref. 9. This scale does not use any reference stationary phase and allows stationary phases to be ranked by all main types of intermolecular interactions. If necessary, the list of test compounds may be modified or expanded. The scale[9] also may be used to measure the selectivity of one capillary column for several sorbates or the selectivity of two capillary columns for one sorbate in accordance with eqn. 24 or 25.

The scale based on eqn. 37 can describe the specificity of any liquid stationary phase and is recommended for practical use. The quantitative thermodynamic measurement of polarity proposed here gives the opportunity to create a unified scale of liquid stationary phases of both organic and inorganic origin. The six-parameter thermodynamic scale, based on eqn. 18 or eqns. 19 and 37 is more informative than all previous scales proposed for the evaluation of the polarity of sorbents in GC.

REFERENCES

1 W. O. McReynolds, *J. Chromatogr. Sci.*, 8 (1970) 695.
2 J. K. Haken, *J. Chromatogr.*, 73 (1972) 419.
3 *Chrompack General Catalog*, Chrompack, Middelburg, 1988.
4 *Alltech Associates Catalog 92*, Alltech, Deerfield, IL, 1988.
5 C. F. Poole, H. T. Butler, M. E. Coddens, S. C. Dhanesar and F. Pacholec, *J. Chromatogr.*, 289 (1984) 299.
6 K. G. Furton and C. F. Poole, *J. Chromatogr.*, 399 (1987) 47.
7 V. G. Berezkin, V. R. Alishoyev, E. N. Victorova, V. S. Gavrichev and V. M. Fateeva, *J. High Resolut. Chromatogr. Chromatogr. Commun.*, 6 (1983) 42.
8 B. M. Polanuer, R. V. Golovnya, I. L. Zhuravleva and V. K. Gordeev, *Izv. Akad. Nauk SSSR, Ser. Khim.*, (1987) 2348.
9 R. V. Golovnya and T. A. Misharina, *J. High Resolut. Chromatogr. Chromatogr. Commun.*, 3 (1980) 4 and 51.
10 L. Rohrschneider, *J. Chromatogr.*, 22 (1966) 6.
11 F. Vernon, *J. Chromatogr.*, 148 (1978) 397.
12 F. Vernon and P. L. Gopal, *J. Chromatogr.*, 150 (1978) 45.
13 G. Castello and G. D'Amato, *J. Chromatogr.*, 51 (1986) 366.
14 G. Tarian, A. Kiss, G. Kocsis, S. Meszaros and J. M. Takacs, *J. Chromatogr.*, 119 (1976) 327.
15 J. A. Garcia-Dominguez, J. Garcia-Munoz, V. Menendez, M. H. Molera and J. M. Santiuste, *J. Chromatogr.*, 393 (1987) 209.
16 L. R. Snyder, *J. Chromatogr. Sci.*, 16 (1983) 223.
17 M. Evans, *Chromatographia*, 11 (1978) 183.
18 J. K. Haken and D. Srisukh, *J. Chromatogr.*, 199 (1980) 199.
19 M. B. Evans and J. K. Haken, *J. Chromatogr.*, 406 (1987) 105.
20 P. Chovin and J. Lebbe, in J. Tranchant (Editor), *Separation Immediate et Chromatographie*, GAMS, Paris, 1961, p. 69.
21 A. B. Littlewood, *J. Chromatogr. Sci.*, 1 (1963) 16.
22 R. I. Sidorov, *Zh. Fiz. Khim.*, 56 (1982) 1057.
23 J. Sevcik and M. S. H. Lowentap, *J. Chromatogr.*, 217 (1981) 139.
24 J. Novak, J. Ruzichkova, S. Wicar and J. Janak, *Anal. Chem.*, 45 (1973) 1365.
25 P. Alessi, I. Kikis and A. Papo, *J. Chromatogr.*, 131 (1977) 31.
26 A. Voelkel, *J. Chromatogr.*, 435 (1988) 29.
27 A. Voelkel, *J. Chromatogr.*, 457 (1988) 73.
28 M. Roth and J. Novak, *J. Chromatogr.*, 234 (1982) 337.
29 B. R. Kersten, C. F. Poole and K. G. Furton, *J. Chromatogr.*, 411 (1987) 43.
30 S. K. Poole, B. R. Kersten, R. M. Pomaville and C. F. Poole, *LC · GC*, 6 (1988) 400.
31 B. R. Kersten, S. K. Poole and C. F. Poole, *J. Chromatogr.*, 468 (1989) 235.
32 B. L. Reinbold and T. H. Risby, *J. Chromatogr. Sci.*, 13 (1975) 372.
33 C. E. Fiddings, T. H. Risby and P. C. Jurs, *J. Chromatogr. Sci.*, 14 (1976) 453.
34 R. V. Golovnya, *Chromatographia*, 12 (1979) 533.
35 A. Voelkel, J. Szymanovski, J. Berger and K. Ebert, *J. Chromatogr.*, 391 (1987) 373.
36 B. V. Stolyarov and L. A. Kartseva, *Zh. Anal. Khim.*, 39 (1984) 883.
37 C. F. Poole and S. K. F. Poole, *Chem. Rev.*, 89 (1989) 377.
38 E. Leibnits and Kh. G. Shtruppe (Editors), *Prakticheskoe Rukovodstvo po Gazovoi Khromatographii (Gas Chromatography Practical Handbook)*, Mir, Moscow, 1988.
39 L. S. Ettre, *Chromatographia*, 6 (1973) 489; 7 (1974) 39 and 261.
40 W. Supina, *Packed Columns in Gas Chromatography* (in Russian), Mir, Moscow, 1977.
41 D. H. Desty and W. T. Swanton, *J. Phys. Chem.*, 65 (1966) 766.
42 S. S. Ufit, B. A. Rudenko, Zh. A. Krasnaya and V. F. Kucherov, *Dokl. Acad. Nauk SSSR*, 188 (1969) 156.
43 R. V. Golovnya and D. N. Grigoryeva, *Chromatographia*, 17 (1983) 613.
44 R. V. Golovnya and T. A. Misharina, *J. Chromatogr.*, 190 (1980) 1.
45 B. R. Kersten and C. F. Poole, *J. Chromatogr.*, 452 (1988) 191.
46 S. J. Hawkes, *Chromatographia*, 28 (1989) 237.
47 R. V. Golovnya and D. N. Grigorieva, *Chromatographia*, 18 (1984) 449.
48 A. Touabet, M. Maeck, A. Y. Badjian Habi Ahmed and B. E. Meklati, *Chromatographia*, 25 (1988) 389.
49 J. R. L. Smith, A. H. H. Tameesh and D. J. Waddington, *J. Chromatogr.*, 148 (1978) 365.

Journal of Chromatography, 517 (1990) 67–75
Elsevier Science Publishers B.V., Amsterdam

CHROM. 22 295

Cryogenic-focusing, ohmically heated on-column trap for capillary gas chromatography

STEPHEN R. SPRINGSTON

Environmental Chemistry Division, Department of Applied Science, Brookhaven National Laboratory, Upton, NY 11973 (U.S.A.)

ABSTRACT

A new method is presented for thermally desorbing solutes which have been cryogenically trapped on a capillary column. The trap heater is a thin layer of metallic gold applied to columns near their inlet. This layer is ohmically heated to initiate the separation. The temperature within the trap is related to the resistance of the gold layer. The trap is shown to not lower column performance relative to a split injection. Other advantages are discussed. Examples showing trace analyses of alkanes in air are given.

INTRODUCTION

Samples must be introduced as a narrow concentration pulse in elution chromatography, or column performance is compromised. Simplistically, the width of the pulse entering the column must be small relative to emerging peak widths. In the case of capillary gas chromatography (GC), geometric factors place stringent demands on the concentration profile delivered by the injector. A wide variety of inlet sytems capable of meeting these demands have been developed[1,2]. The sample characteristics are an important factor in selecting the appropriate injector. If an analyte of interest is present at low concentrations, the injection volume may contain less than a minimum detectable quantity. Cryogenic trapping is one method for increasing the amount of sample introduced without lowering column efficiency. Dilute components in a more volatile matrix are effectively concentrated within a cooled section of the stream. Subsequent warming of the trap initiates the separation as the narrow plug begins to migrate through the analytical column. The sample width is thus controlled by how fast the trap is heated rather than by the initial injection volume.

A variety of cryogenic sample traps have been described for capillary GC. Hopkins and Pretorius[3] demonstrated that electrically heating the trap was faster than using a heated gas stream[4]. This and other ohmically heated traps[5,6] were used to collect samples in a conductive tube connected to the analytical column. Burger and Munro[7] describe a thermal desorption system consisting of a length of metal tubing which was ohmically heated to desorb material from a 1-m fused-silica trap inside the heater, thus eliminating sample contact with heated metal. The trap was connected to the analytical column where further trapping was performed. Kolb *et*

al.[8] used cold nitrogen to concentrate the sample directly on the analytical capillary and then allowed the carrier gas to warm the trap, obviating any dead volume between the trap and column. A 10-cm section of aluminum coated fused silica was ohmically heated by Van Es *et al.*[9] to rapidly desorb samples from a 50-μm capillary passing through the heater. Input widths as short as 1 ms were reported. As with the apparatus of Kolb *et al.* trapping directly on the analytical column eliminates the dead volume of a connection.

This paper reports a simple on-column cryogenic trap that can be adapted to existing capillaries. The heating element is an integral part of the column. Samples can be concentrated and then separated without diminishing chromatographic performance. Several other unique features are described. The trap operation is demonstrated by analyzing some dilute samples of organic compounds in ambient air.

EXPERIMENTAL

A capillary column was prepared from untreated fused silica manufactured by Polymicro Technologies (Phoenix, AZ, U.S.A.). The empty capillary was purged with helium for 2 h at 250°C before statically coating with a 0.4% (w/v) solution of SE-30 (GC grade, Alltech Associates, Deerfield, IL, U.S.A) in pentane. The final column length was roughly 14 m with an internal diameter of 250 μm. This column was tested at 100°C and exhibited a coating efficiency of 93% for dodecane. The column was then split into two sections, 11.0 and 1.92 m in length.

An ohmically heated trap about 10 cm in length was fashioned on the exterior of both capillaries, starting 15 cm from the inlet of the 11.0-m column and 10 cm from the inlet of the 1.92-m column. Metallic gold was applied by depositing Liquid Bright Gold (No. 7621, Engelhardt, Hanovia Liquid Gold Division, East Newark, NJ, U.S.A.) directly on the polyimide outer coating and heating to 310°C for 20 min. Liquid Bright Gold is a true solution of gold in an organic matrix. At elevated temperatures, the organic liquid pyrolyses leaving a thin metallic film. During the heating step, the column interior was purged with helium while the exterior remained in air. The deposition and curing process was repeated three times. The resulting conductive layer is clearly visible and resists abrasion. Electrical leads were attached to the gold layer *ca.* 5 cm apart. Connections to the gold were made through electrically conductive fibers surrounding the capillary at each end of the trap. When installed, the gold layer did not contact the oven walls or the injection port.

The cryogenic focusing trap was evaluated chromatographically using a Varian VISTA 4600 GC (Varian Instruments, Walnut Creek, CA, U.S.A.) equipped with a split/splitless capillary injector. Solutes were detected by flame ionization detection (FID) with the capillary positioned flush with the flame jet tip. Chromatograms were digitally recorded using a CHROM-1 analog-to-digital board (Metrabyte, Taunton, MA, U.S.A.) operating within a PC's 286 microcomputer (PC's Ltd., Austin, TX, U.S.A.). The software controlling the data acquisition was Labtech Notebook (Laboratory Technologies Corporation, Wilmington, MA, U.S.A.). Detector sensitivity was set at $4 \cdot 10^{-12}$ A full scale. Detector output was digitized at 20 Hz. Moment analysis of the resulting data was performed with software written in Pascal (Borland International, Scotts Valley, CA, U.S.A.).

Columns were connected to the split/splitless injector and the FID system in the

normal fashion. The conductive column section was then placed in a cryogenic vessel partially filled with liquid nitrogen such that the trap was roughly 2 to 3 cm above the liquid level. The capillary entered and exited at the lid through constricted openings with most of the vapor vented well away from the column to prevent ice forming on the capillary outside the cryogenic container. Both electrical connections remained outside the vessel and were not cooled. Electrical currents through the trap were between 50 and 150 mA for these experiments. These currents required voltages between 10 to 15 V. Except for the variable-voltage power supply and switch, the entire trap assembly was located in the column oven.

Gas-phase samples containing a mixture of four normal alkanes were prepared at four different concentrations. A stock mixture containing pentane, hexane, heptane, and octane was made by adding the individual neat liquids to a 1-l flask. The liquid volumes were adjusted to produce an equimolar mixture of 2000 parts-per-million-by-volume (ppmv) of each alkane in ambient air. Single stage dilutions of the stock mixture produced samples containing 50, 100 and 200 parts-per-billion(10^9)-by-volume (ppbv) of each component. The samples were thoroughly mixed by a magnetic stirring bar.

All chromatographic separations were performed isothermally at 35°C. The injection volume was 5 μl for the 2000-ppmv stock mixture. Split injections were always used for this concentrated sample. For the three dilute mixtures, the injection volume was 1 ml. Dilute samples were injected with the split flow off for the first 90 s. The amount of each compound introduced into the capillary column is given in Table I for both injection procedures taking into account losses due to splitting. The values for the dilute samples are only an estimate, as they assume quantitative transfer of sample from the injector to the column before the split valve is opened.

The effect of sample trapping on elution profiles was investigated using the 1.92-m column. A plug injection was approximated by injecting 5 μl of the 2000-ppmv gas mixture under split conditions. By cryogenically trapping the sample and then heating the trap to initiate the separation, any decrease in performance relative to a normal split injection should be apparent. The split flow was maintained at 1.03 ml/s throughout these separations. Vapor phase injections of 5 μl were thus split 70:1 with a linear flow-rate through the column of 30 cm/s. After collecting the sample for 120 s in the cooled trap, the sample zone was rapidly heated by passing a current of 120 mA through the trap. Heating continued until all peaks were detected. Chromatograms recorded under these conditions were compared with chromatograms taken without

TABLE I

SAMPLE MASS INTRODUCED INTO CAPILLARY COLUMN ASSUMING QUANTITATIVE MASS TRANSFER FOR THE 1-ml INJECTIONS

Sample concentration	*Injection volume*	*Split*	*Solute mass (pg)*			
			C_5	C_6	C_7	C_8
2000 ppmv	5 μl	100:1	290	350	410	460
200 ppbv	1 ml	None	590	700	810	930
100 ppbv	1 ml	None	290	350	410	460
50 ppbv	1 ml	None	150	180	200	230

trapping or heating. Trapping occurred at the temperature above the liquid nitrogen, about −150°C in this experiment. During the heating step, the temperature was estimated to be above 150°C.

The dilute samples were separated on the 11.0-m column by concentrating virtually the entire sample in the trap. For these dilute mixtures, the gas phase injection volume of 1 ml was injected by syringe over a 10-s interval with the split flow off. After 90 s, the split flow valve was opened to purge the injector body of any remaining sample. At 120 s after the start of the injection, the trap was heated to initiate solute migration along the column. For comparison, a 5-μl split injection of the stock solution was separated without trapping.

Finally, measurements were made to establish whether the temperature of an electrically heated trap could be determined from its resistance. For this experiment, the trap was broken off from the column so that a miniature thermocouple, 0.013 mm diameter (Omega Engineering, Stamford, CT, U.S.A.), could be placed inside the capillary. The trap temperature could then be directly measured. The chromatographic oven was programmed from 35 to 240°C at 5°C/min while a constant voltage of 1.000 V was applied across the trap. By measuring the current through the trap, the resistance across the trap could be calculated from Ohm's law. After measuring the resistance as a function of temperature during external heating, the trap was heated ohmically by increasing the current in a stepwise fashion. With the oven held at 35°C, the resistance was again taken from simultaneous measurement of current and voltage while directly measuring the trap temperature.

RESULTS AND DISCUSSION

To ascertain the contribution to peak variance due to the cryogenic trap, the shortest possible column was studied to maximize the effects from all sources of extra-column band broadening. The separations were also performed isothermally to prevent the solute focusing encountered with temperature programming. Under such demanding conditions, the trap must be capable of rapid heating to vaporize the sample components in a narrow plug. Heating that is slow relative to the temporal length of a split injection would be readily apparent as an increase in peak variance, commonly measured as the second statistical moment. Any injection perturbations which asymmetrically distort the plug will also lead to asymmetric distortions in the

TABLE II

SECOND AND THIRD STATISTICAL MOMENTS FOR NORMAL AND TRAPPED SPLIT INJECTIONS ON A 1.92-m COLUMN

Mean ± 1 standard deviation (n = 7).

Sample	*2nd Moment · 10² (s^2)*		*3rd Moment · 10² (s^3)*	
	Normal	*Trapped*	*Normal*	*Trapped*
C_5	6.11 ± 0.49	5.33 ± 0.19	2.31 ± 0.48	1.78 ± 0.15
C_6	8.68 ± 0.59	7.81 ± 0.55	4.26 ± 0.64	3.58 ± 0.71
C_7	9.39 ± 1.81	9.95 ± 0.86	3.64 ± 2.96	5.30 ± 1.14
C_8	20.59 ± 0.55	17.56 ± 0.73	2.68 ± 0.34	2.40 ± 0.29

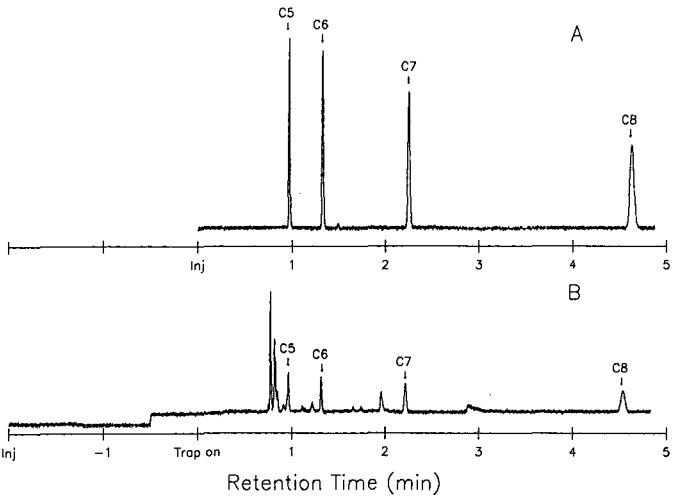

Fig. 1. Chromatograms of pentane, hexane, heptane and octane on an 11 m × 250-μm I.D. capillary column coated with 0.4% (w/v) SE-30. (A) 5 μl vapor phase injection of 2000 ppmv, split 100:1. (B) 1 ml vapor phase injection of 50 ppbv, no split, trapped for 2 min. The additional peaks are presumably due to the air dilution.

resulting solute peaks. Such peaks will have a third statistical moment greater than zero.

Split injections performed without trapping were compared with split injections which were trapped for 120 s. Mean values for the second and third statistical moments of each peak are given in Table II for normal and trapped injections. It is clear that sample trapping does not impair the peak shape relative to a normal split injection. The larger values for heptane arose from a very small impurity eluted on the tail of the peak. The precision undoubtedly suffers from the limited digitization rates[10] imposed by this equipment for these rapid elution times ($t_0 < 6$ s), but is still better than 10% relative standard deviation (R.S.D.) for the second moment and 20% R.S.D. for the third. The demands of an injector for this short column are severe. The absence of band broadening for trapped injections relative to normal split injections demonstrates the ability of this trap to rapidly vaporize solutes.

A longer column was used for separating dilute gas samples in order to provide adequate resolution between the compounds of interest and extraneous trace components present in the sample matrix. A typical split-injection separation of the sample at a concentration of 2000 ppmv is shown in Fig. 1A. In this case, a 5-μl vapor phase injection is split at a ratio of 100:1. This chromatogram is featureless except for the 4 solutes.

Fig. 1B demonstrates the trapping and subsequent analysis of a 1-ml sample at a concentration of 50 ppbv (a dilution of 40 000 from A). The gaseous sample is injected without benefit of splitting 2 min before initiating the separation. Over a 90-s period, the sample slowly passes into the column at the carrier flow-rate of 0.0123 ml/s, moving from the injector into the oven to be trapped in the cooled section of the capillary. The injection port volume cannot be quantitatively swept at this flow-rate in 90 s, therefore, the splitter valve is opened after 90 s to completely flush the port

TABLE III

FIRST STATISTICAL MOMENTS FOR AN 11.0-m COLUMN

Mean ± 1 standard deviation ($n \geq 5$).

Sample	*Split injection (2000 ppmv), first moment (s)*	*Trapped injection (50, 100, 200 ppbv), first moment (s)*
C_5	58.27 ± 0.11	57.68 ± 0.20
C_6	79.52 ± 0.23	78.83 ± 0.22
C_7	134.78 ± 0.37	133.04 ± 0.24
C_8	277.46 ± 0.35	272.12 ± 0.33

before warming the trap. The action of the valve creates a slight baseline disturbance. The separation begins when current is applied to the trap, indicated as time zero in Fig. 1B. Other components of ambient air present in the sample are also concentrated and then detected by FID. Even with these background peaks, the four components of interest are eluted at this level without significant interference.

Because these samples were prepared from ambient air, the absence of methane in the chromatograms was initially puzzling. Methane is present at a concentration of roughly 1.6–1.7 ppmv[11] in the atmosphere, or about 40 times greater than the dilute alkane samples. However, the vapor above liquid nitrogen only cools the trap to −150°C. This is well above the boiling point of methane. Thus, methane is not concentrated within the trap and is eluted as a broad peak indistinguishable from the baseline.

The reproducibility of retention times, as given by the standard deviation of the first statistical moment, is shown in Table III for split and trapped injections. The precision is comparable for the two methods. No differences were observed between the 50-, 100- and 200-ppbv samples. The mean retention times are slightly less for the trapped injections because the separation begins at the trap, about 15 cm downstream from the inlet.

A plot of peak area *vs.* sample concentration is shown in Fig. 2 for two compounds with greatly different retention ratios. The precision is indicated by error bars

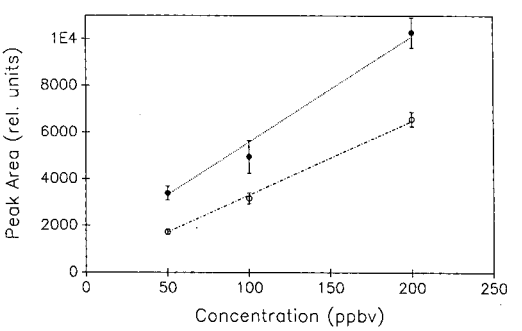

Fig. 2. Peak area *vs.* concentration for an 11 m × 250 μm I.D. capillary column coated with 0.4% (w/v) SE-30. ○ = Pentane, k = 0.305; ● = octane, k = 5.16. Samples were trapped for 2 min. Mean ± 1 standard deviation (n = 3 or 4).

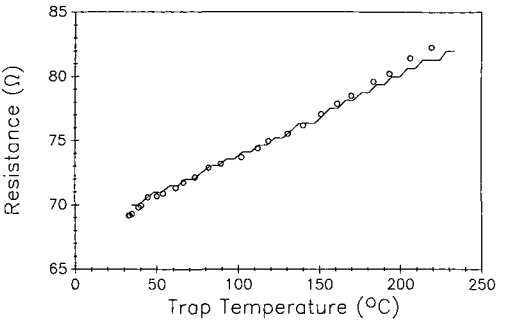

Fig. 3. Trap resistance *vs.* trap temperature. The trap temperature was measured inside the capillary. — = Trap resistance measured as trap was heated externally. O = Trap resistance measured as trap was heated ohmically.

of ± one standard deviation. If peak areas were reported relative to an internal standard the precision would improve considerably. Digitization error for these small signals also contributes to the scatter. Even so, the precision for all solutes at 50 ppbv is better than 10% R.S.D. For replicate split injections with much larger signals, the precision is 3% R.S.D.

The trap resistance varies linearly with the temperature when heated externally as shown by the line in Fig. 3. The stepwise increase is due to the digitization limitations in reading the current through the trap. The circles in Fig. 3 show how the resistance changes with temperature when the trap was ohmically heated. As expected, the correspondence between the two sets of data is quite good. This confirms that the relationship between the trap's resistance and temperature is independent of how the trap is heated. The tedious operation of inserting the thermocouple into the trap was required to establish this independence. In practice, it is not necessary to measure the temperature within the capillary directly, even for calibration. The trap temperature can be easily determined as a function of resistance by assuming the oven and the trap to be at the same temperature during calibration. Because the thermal mass of the trap is extremely low, this assumption is valid.

The relationship between trap resistance and temperature is an attractive feature of this cryogenic trap. The temperature can be determined from the voltage and current used to heat the trap. No external thermal sensor, which would cause a cold spot, is needed. With a suitable feedback system, the temperature of the trap could be easily controlled to within 5°C. This should facilitate trace level capillary column separations of volatile, thermally labile compounds such as peroxyacetic nitric anhydride (PAN)[12]. This compound can be analyzed isothermally without cryogenically cooling the column, but some means of concentrating the sample at the column head is required. The applicability of the cryogenic trap is being explored. It is reasonable to expect the sensitivity for PAN to be increased two or three orders of magnitude relative to the alkanes by substituting an electron-capture detector (ECD) for the FID. This should make it possible to perform PAN determinations in ambient air at the parts-per-trillian level.

Other trap heating profiles may also be desirable for certain samples. A multistep, or temperature-programmed trap warming would crudely prefractionate sam-

ples. The least volatile components could be retained and later removed during backflushing while heating the trap. The negligible thermal mass of the trap allows rapid cycling between the temperature limits set by the cooling chamber and the decomposition of the polyimide layer on the capillary.

Accurately controlled trap heating should be equally applicable for supercritical fluid chromatography (SFC). In this separation technique, the partition ratio of solutes also changes with temperature, however, higher temperature causes the mobile phase density to decrease and the solute partition coefficient to favor the stationary phase. Thus, unlike GC, increased temperature causes longer retention. To trap solutes in SFC, the trap would be warmed. Solute migration would commence when the trap was allowed to cool. Here, the speed of cooling is important and the low thermal mass of this trap should prove ideal. The concept of concentrating solutes within a heated zone of a capillary SFC column was suggested several years ago[13], but a suitable trap with low thermal mass was unavailable at that time. A capillary trap could also be connected upstream from a packed SFC column to concentrate samples and sharpen the concentration profile of the injection.

Phillips *et al.*[14] have described a thermal desorption modulator for GC based on an electrically conductive metallic paint. The design requirements of a modulator are similar to those of a cryogenic trap[15,16]. Conversely, the trap presented herein should be useful for multiplex chromatography. The gold layer is an excellent thermal conductor and has a thickness on the order of nanometers as opposed to 40 μm for paint[14]. In addition, the gold layer is free from any binders present in paint. These non-metallic components conduct heat poorly compared with gold and could slow the cooling cycle of a modulator. They may also possibly limit the maximum allowable modulator temperature. Thus, a cryogenic trap based on a thin layer of metallic gold has inherently faster thermal slew rates and may provide certain advantages as an injection modulator.

CONCLUSIONS

The cryogenic trap described in this paper exhibits a variety of attractive characteristics. Its low thermal mass allows rapid heating and cooling. This quality permits samples to be vaporized on a short enough time scale for isothermal analysis without contributing to band broadening. Rapid cooling should also render the trap useful for thermal modulation chromatography and SFC. Unlike some other cryogenic traps, the chromatographic stream is free from connections. All trapping occurs within the column itself. This also eliminates any sample contact with heated metal surfaces. Although a heated splitter was used for this study, gentler methods could easily be substituted.

Other positive features arise from the electrical properties of the gold layer. Because the layer is so thin, its resistance is high and it can be heated with minimal currents. Thus, only thin wire leads and voltages between 10 and 15 V are required. Such currents and voltages can be easily controlled without elaborate circuitry. Because of these features, this trap could readily be used in a fully automated system. Resistance across the trap leads varies directly with the trap temperature, in effect forming a resistance thermometer. By measuring the trap current and voltage, the trap temperature can be determined. With an appropriate feedback circuit, the tem-

perature could be accurately controlled. Since the gold layer itself poses no practical thermal limits, the trap temperature may range from that of the cryogenic bath to the maximum operating temperature of the column.

Capillaries can be equipped with the cryogenic trap after they have been coated. Thus, commercially prepared columns may be retroactively fitted with a trap. If the stationary phase cannot tolerate the required curing temperature, it should be possible to locally heat only the trap section while purging with an inert gas from the detector end. The gold layer, once applied, is quite durable and can easily be installed before coating if heating would damage the phase or column deactivation. Because the gold coating does not prevent the use of any other injection technique, all capillaries could have the thermal trap applied near the inlet before coating. The gold application step is simple and inexpensive, less than US$ 1.00 of gold solution was needed to prepare the traps described above.

ACKNOWLEDGEMENT

This research was performed under the auspices of the U.S. Department of Energy under Contract No. DE-ACO2-76CH000016.

REFERENCES

1 W. Jennings and M. F. Mehran, *J. Chromatogr. Sci.*, 24 (1986) 34.
2 J. V. Hinshaw, *J. Chromatogr. Sci.*, 26 (1988) 142.
3 B. J. Hopkins and V. Pretorius, *J. Chromatogr.*, 158 (1978) 465.
4 J. Droze, J. Novak and J. A. Rijks, *J. Chromatogr.*, 158 (1978) 471.
5 B. A. Ewels and R. D. Sacks, *Anal. Chem.*, 57 (1985) 2774.
6 L. A. Lanning, R. D. Sacks, R. F. Mouradian, S. P. Levine and J. A. Foulke, *Anal. Chem.*, 60 (1988) 1994.
7 B. V. Burger and Z. Munro, *J. Chromatogr.*, 370 (1986) 449.
8 B. Kolb, B. Liebhardt and L. S. Ettre, *Chromatographia*, 21 (1986) 305.
9 A. van Es, J. Janssen, C. Cramers and J. Rijks, *J. High Resolut. Chromatogr. Chromatogr. Commun.*, 11 (1988) 852.
10 S. N. Chesler and S. P. Cram, *Anal. Chem.*, 43 (1971) 1922.
11 B. J. Finlayson-Pitts and J. N. Pitts, Jr., *Atmospheric Chemistry*, Wiley-Interscience, New York, 1986, p. 974.
12 J. M. Roberts, R. W. Fajer and S. R. Springston, *Anal. Chem.*, 61 (1989) 771.
13 S. R. Springston, *Ph.D. Thesis*, Indiana University, Bloomington, IN, 1984, p. 46.
14 J. B. Phillips, D. Luu, J. B. Pawliszyn and G. C. Carle, *Anal Chem.*, 57 (1985) 2779.
15 J. B. Phillips, D. Luu and R. Lee, *J. Chromatogr. Sci.*, 24 (1986) 396.
16 S. Mitra and J. B. Phillips, *J. Chromatogr. Sci.*, 26 (1988) 620.

Journal of Chromatography, 517 (1990) 77–86
Elsevier Science Publishers B.V., Amsterdam

CHROMSYMP. 1881

Enhanced possibilities for identification using series-coupled capillary gas chromatographic columns

II. Retention indices as an identification tool in selectivity tuning

T. MAURER, W. ENGEWALD* and A. STEINBORN
Department of Chemistry, Analytical Centre, Karl Marx University Leipzig, Talstrasse 35, DDR 7010 Leipzig (G.D.R.)

ABSTRACT

For calculating retention (t_R) times from retention indices in series-coupled column systems with different flow-rates in the individual columns, the dependence of the dead time and of the parameters a and b of the log t_R *versus* carbon number plots for *n*-alkanes on the pressure of the medium is discussed. It is shown that the intercept a of the log t_R *versus* carbon number plots is composed additively of an easily determinable flow-independent term and a flow-dependent term. On this basis, a method was developed for the precalculation of the retention times of any substances from their retention indices under the conditions of selectivity tuning by varying the flow-rates in a system of series-coupled GC columns. The method allows statements on the presence or absence of compounds of interest by comparing calculated and measured system retention times. By repeating the identification algorithm at different pressure settings and, consequently, flow-rates, the peak shifts expected in selectivity tuning can be pursued on the one hand; on the other, a degree of certainty about the positive identification of compounds can be achieved owing to the feasible avoidance of peak overlapping, which is not possible by means of the classical retention index concept.

INTRODUCTION

High-resolution gas chromatography (HRGC) implies the optimization of the column efficiency, the selectivity and the capacity ratio. With the introduction of capillary columns, the main emphasis was laid on their high efficiency, whereas the optimization of the selectivity was not so closely observed for a long period. Only when it was recognized that many samples were more complex than had been originally thought did the necessity arise to produce capillary columns with specialized selectivity. A system with specialized selectivity can be obtained by selectivity tuning.

0021-9673/90/$03.50

Sandra *et al.*[1] suggested that in capillary GC selectivity tuning can be accomplished in on of three ways: by using tailor-made stationary phases; bu using mixed phases; or by serial coupling of columns with different stationary phases.

The last variant seems to be the most elegant method for producing a tunable selectivity because, in addition to the column length and the phase ratio, β, as variables, the very easily accessible variables temperature and/or carrier gas flow-rate can be used for setting the desired selectivity, and this method offers the chance to use standardized stationary phases with known retention properties and retention values.

However, the use of selectivity tuning for changing the selectivity in a series-coupled system places high demands on the identification in the sense of refinding the peaks in the individual chromatograms because in the case of selectivity changes it is always necessary to take account of a change in the retention sequence of components and, consequently, also of the removal of peak overlappings and the occurrence of new interferences.

Therefore, considerable experience and possibly also a certain amount of intuition are necessary for analysing complex mixtures if optimum separation is to be achieved. This especially applies to series-coupled systems in which the number of values to be varied is greater. This makes searching for a resolution optimum a very time-consuming process and it is desirable that the extent of experiments for finding this optimum should be considerably reduced by suitable simulation programs.

One precondition for optimization is the knowledge of the connection between retention and pressure of the medium or flow-rates in the column system used. This topic has been discussed in a few papers (see refs. 2 and 3 and papers cited therein). Another possibility is the use of system retention indices in directly series-coupled systems for identification[4–7]. However, these system indices have the disadvantages that they are not directly correlated with a thermodynamic value, that they are dependent on the behaviour of the flow-rates in the two columns and that the function on which their determination is based is not linear but, depending on the individual columns used, a more or less bent curve[8]. As an alternative to this we suggest that the system retention times should be calculated in advance by means of known (tabulated) retention index values of the substances on the two individual columns and that identification be achieved by comparing measured and precalculated retention times at different pressure settings of the medium.

In this way it should be possible to use with advantage the existing valuable experience with retention values for many substances on different stationary phases in the form of Kováts retention index libraries, in spite of the known disadvantages of the retention index system[2].

For this purpose, the fundamentals for the conversion of tabulated index data into retention times are presented. In the following, it will be shown how the identification of sample components (in the sense of refinding already known compounds or for establishing the presence or absence of compounds of interest) can be achieved under the conditions of selectivity tuning by comparing measured and precalculated system retention times.

EXPERIMENTAL

The schematic representation of a series-coupled system in Fig. 1 shows the values necessary for its description and their indices.

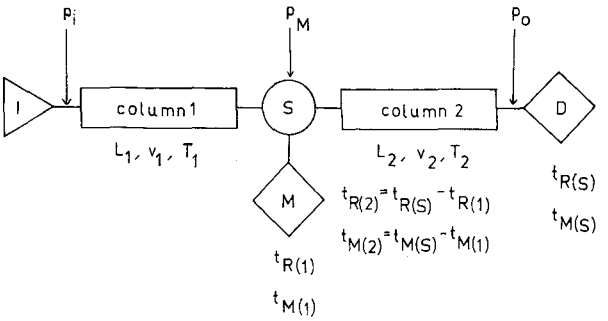

Fig. 1. Schematic diagram of the series-coupled two-column system used without intermediate trapping. I = Sample injection; S = coupling device (live T-piece) with additional carrier gas supply; M = monitor detector (FID 1); D = main detector (FID 2).

The instrument used was a Sichromat 2 (Siemens, Karlsruhe, F.R.G.), equipped with a split injector, a live T-piece and two flame ionization detectors. The carrier gas was hydrogen.

In system A (a values), column 1 was fused silica, 40 m × 0.32 mm I.D., containing WG-11 (WGA, Pfungstadt, F.R.G.) and column 2 was fused silica, 50 m × 0.32 mm I.D., containing WG-PB1 (OV-1), with temperatures and pressures as indicated in Table I. In system B (prediction), column 1[a] was glass, 67 m × 0.24 mm I.D., containing 2-[4-(4-pentylbenzoyloxy)phenyl]-5-hexylpyrimidine (PBHP)[9] and column 2 was glass, 32 m × 0.32 mm I.D., containing OV-1, with the temperatures and pressures as indicated in Fig. 4 and Table II.

RESULTS AND DISCUSSION

Dead times in series-coupled column systems

As is known, in a series-coupled column system without intermediate trapping, both the retention times (t_R) and the dead times (t_M) for the total system are composed additively of the contributions for the individual columns:

$$t_{M(S)} = t_{M(1)} + t_{M(2)} \quad (1)$$

$$t_{R(S)} = t_{R(1)} + t_{R(2)} \quad (2)$$

$$t'_{R(S)} = t'_{R(1)} + t'_{R(2)} \quad (3)$$

The dead time of a capillary separation column is dependent on its geometrical dimensions and the average linear flow-rate of the carrier gas, which is determined by the difference in the pressure existing at the inlet and the outlet of the column. The dead time can be calculated according to the following equation[3]:

$$t_M = \frac{32\, L^2 \eta(T)}{3\, r^2} \cdot \frac{p_i^3 - p_o^3}{(p_i^2 - p_o^2)^2} \quad (4)$$

[a] The column was made available by courtesy of Dr. G. Kraus of the Chemistry Department of the Martin Luther University, Halle, G.D.R.

where L is column length, $\eta(T)$ is carrier gas viscosity, r is column radius, p_i is inlet pressure and p_o is outlet pressure.

It will be useful to insert flow-dynamically ascertained values for the length or the inside diameter of the columns in eqn. 4. If the manufacturer's data on the length and inside diameter are used, they should be checked experimentally by comparing the calculated and the measured dead times under defined pressure conditions.

In principle, eqn. 4 is also valid for calculating the dead times of the individual columns in a system of series-coupled columns. In this instance, the pressure of the medium, p_M, set at the coupling piece should be inserted as the column outlet pressure of the first and as the column inlet pressure of the second separation column.

If the pressure of the medium, p_M, is increased by feeding additional carrier gas into the connecting piece, the flow-rate of the mobile phase in column 2 will increase while the flow-rate in column 1 will correspondingly be reduced. Consequently, the dead time $t_{M(1)}$ becomes greater and $t_{M(2)}$ smaller when p_M is increased (Fig. 2). Therefore, the schematic representation of the system dead time $t_{M(S)}$ as a function of the pressure of the medium shows a minimum, the position of which is dependent on the parameters of both columns.

The system dead-time curve can be described mathematically either by an approximation polynomial of the fourth degree[7] or in a simpler way by making use of eqns. 1 and 4:

$$t_{M(S)} = \frac{32\ L_1^2\eta_1(p_i^3 - p_M^3)}{3\ r_1^2(p_i^2 - p_M^2)^2} + \frac{32\ L_2^2\eta_2(p_M^3 - p_o^3)}{3\ r_2^2(p_M^2 - p_o^2)^2} \tag{5}$$

Parameters of the log t_R versus carbon number plot for n-alkanes

The possibility of calculating retention times on the basis of retention indices with the aid of the coefficients a and b of the log t_R *versus* carbon number plot was briefly dealt with in Part I[10]. However, as usually the opposite method is used, *i.e.*,

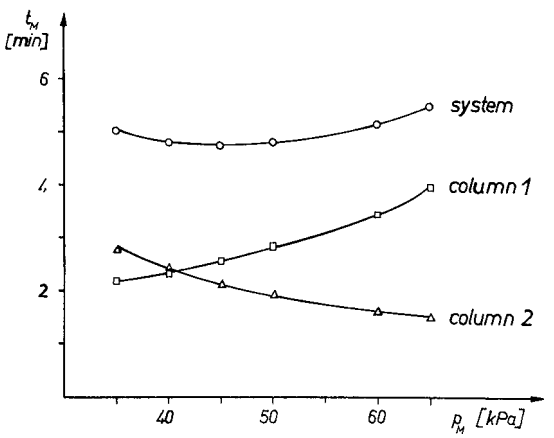

Fig. 2. Dependence of the carrier gas hold-up times $t_{M(1)}$, $t_{M(2)}$ and $t_{M(S)}$ on the pressure of the medium, obtained by using column system A. The $t_{M(1)}$ and $t_{M(S)}$ values are measured using the monitor and main detector and the $t_{M(2)}$ values are obtained according to eqn. 1.

calculating retention indices by means of retention times, the theoretical foundations of this process will be briefly described here.

The retention index concept according to Kováts is based on the, for higher *n*-alkanes, undisputed linear increase in the logarithm of the adjusted retention time (t'_R) with increase in carbon number for higher *n*-alkanes:

$$\log t'_R = a + bZ \tag{6}$$

where Z is the carbon number of the *n*-alkane used and the constants a and b are the intercept and the slope, respectively, of the *n*-alkane plot.

By means of regression methods[11], the constants a and b can be easily calculated from the retention times of an *n*-alkane mixture.

The slope $b = \log [t'_{R(Z+1)}/t'_{R(Z)}]$ is correlated with the partial molar free sorption energy of the methylene group in the *n*-alkane[12]. According to this, b is dependent on the structure of the stationary phase and on the column temperature[13] but is independent of the set flow-rate.

Nothing has been said in the literature so far about the thermodynamic importance of constant a. However, it can be easily shown that, amongst other things, the dependence of the retention times on the set flow-rate will be incorporated in constant a. For the precalculation of retention times under the conditions of selectivity tuning by varying the flow-rates, it is therefore necessary to know the dependence of the a value on the carrier gas flow-rate or a value proportional to it.

If on both sides of eqn. 6 the term $\log t_M$ is subtracted:

$$\log t'_R - \log t_M = a - \log t_M + bZ \tag{7}$$

the logarithm of the k' value of the respective *n*-alkane will be obtained on the left-hand side of eqn. 7. As this is a flow-independent value, the term $a - \log t_M$ on the right-hand side must also be independent of flow-rate. If this flow-independent "basic value" is termed a_k, the following connections are valid for an *n*-alkane of carbon number Z:

$$\log k' = a_k + b + Z \tag{8}$$
$$\log t'_R = a + b + Z \tag{9}$$
$$a = a_k + \log t_M \tag{10}$$

According to eqn. 10 a is composed additively of a flow-independent term a_k and the flow-dependent term $\log t_M$.

The validity of this relationship was examined using a C_6–C_{11} *n*-alkane mixture. The a_k values of the individual columns were determined at $p_M = 50$ kPa according to eqn. 8 from the capacity factors of the *n*-alkanes. Table I shows the high degree of agreement of the a values precalculated for various pressures of the medium with the corresponding experimental values.

Using as a basis the well known fact that the retention index (I) of any chosen substance i can be considered to be 100 times the carbon number of a hypothetical *n*-alkane with the same retention time, Haken *et al.*[14] formulated:

$$I_i = 100(\log t'_{R,i} - a)/b \tag{11}$$

TABLE I

DEPENDENCE OF THE DEAD TIMES $t_{M(1)}$ AND $t_{M(2)}$ ON THE PRESSURE OF THE MEDIUM, p_M, AND COMPARISON OF PREDICTED AND MEASURED a VALUES WITH COLUMN SYSTEM A AT $T_1 = T_2 = 100°C$ AND $p_i = 100$ kPa

p_M (kPa)	$t_{M(1)}$[a] (min)	$t_{M(2)}$[a] (min)	$a_{k(1)}$	Log $t_{M(1)}$	$a_{I(1)calc.}$	$a_{I(1)meas.}$	$a_{k(2)}$	Log $t_{M(2)}$	$a_{I(2)calc.}$	$a_{I(2)meas.}$
35	2.21	2.80		0.79	−6.14	−6.17		1.02	−4.32	−4.31
40	2.39	2.45		0.87	−6.06	−6.11		0.90	−4.44	−4.47
45	2.58	2.19		0.95	−5.98	−5.95		0.78	−4.56	−4.57
50	2.85	1.98	−6.93	1.05	−5.88	−5.88	−5.34	0.68	−4.66	−4.66
60	3.49	1.67		1.25	−5.68	−5.70		0.51	−4.83	−4.85
65	3.97	1.53		1.38	−5.55	−5.60		0.43	−4.91	−4.91

[a] Dead times $t_{M(1)}$, $t_{M(2)}$ were calculated by a regression method according to Kaiser and Rackstraw[11].

The inversion of this equation and combination with eqn. 10 results in

$$\log t'_{R,i} = a + 0.01bI_i \quad (12)$$

$$\log t'_{R,i} = a_k + \log t_M + 0.01bI_i \quad (13)$$

This offers a chance of the precalculation of retention times of any substances from their retention indices at different flow-rates, on the condition that the parameters a_k and b of the n-alkane straight line were determined at one given flow-rate.

Precalculation of system retention times at different pressure settings in a series-coupled GC system

On the basis of the fundamentals presented above for the calculation of dead time from column parameters and of retention times from tabulated retention indices, a program was developed which allows the prediction of system retention times in a series-coupled column system at different pressure settings, thus offering new possibilities both for pursuing the peak shifts required in selectivity tuning and for the reliable proof of the presence or absence of substances of interest in complex mixtures.

The program is based on the following conditions: the geometrical parameters, *i.e.*, length and inside diameter, of the separation columns used are sufficiently accurately known or have been determined according to flow-dynamic methods; the stationary phases used are standard phases with different retention properties, which can be generated in a reproducible form and for which retention index libraries are available which should be as comprehensive as possible; and on each individual column the chromatogram of an n-alkane mixture was recorded at the operating temperature and at one defined inlet and outlet pressure of the column. Fig. 3 shows the structure of the program in principle.

First, the parameters a_k and b of the n-alkane plot are calculated for both columns on the basis of the retention times of the n-alkane runs. Then the dead times for the individual columns are precalculated for the pressure settings of the coupled system for which the retention times of any substances are intended to be precalcu-

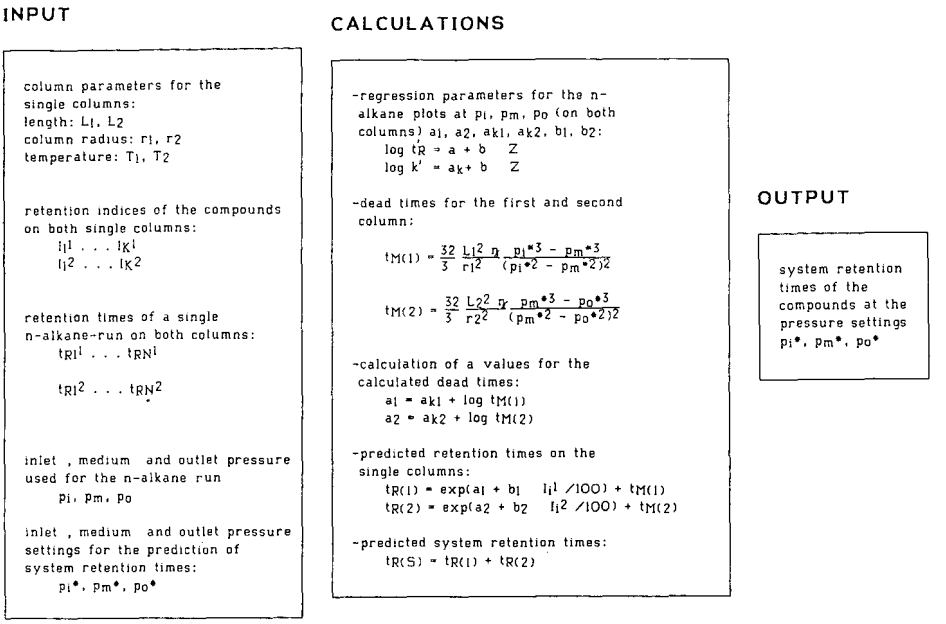

Fig. 3. Computer program for calculation of retention times for series-coupled columns.

lated. Then follows the calculation of the a values from the a_k values according to eqn. 10.

All the conditions have been given for calculating the retention times on the individual columns for all the components of interest in the mixture (whose retention indices must, of course, be known on both individual columns). The addition of these precalculated adjusted retention times to the likewise precalculated dead times for the two columns yields the system retention times to be expected for the substances of interest at the chosen pressure setting.

Fig. 4 shows the chromatogram of an alkylbenzene test mixture at different pressure settings of the medium, p_M, and constant inlet pressure, p_i.

The applied column system B is a combination of two glass capillary columns with a significantly different separation powers. The stationary phases used included a liquid-crystalline phase (PBHP[9]) in which the solute retention is determined by its geometry (shape or length to breadth ratio), and a methylsilicone (OV-1) stationary phase in which the retention is determined by the vapour pressure (boiling point) of the solute. The retention indices given in the legend to Fig. 4 demonstrate the different elution sequences resulting for the test substances used. The liquid-crystalline stationary phase has an excellent selectivity for *meta* and *para* isomers which, as is known, cannot be or can hardly be separated on non-polar stationary phases.

The chromatograms in Fig. 4 show some different selectivities of the system which can be achieved with the indicated values of the pressure of the medium, p_M, *i.e.*, with different shares of the two columns to the total selectivity of the system. A retention inversion of the *o*-xylene–isopropylbenzene pair can be observed. In

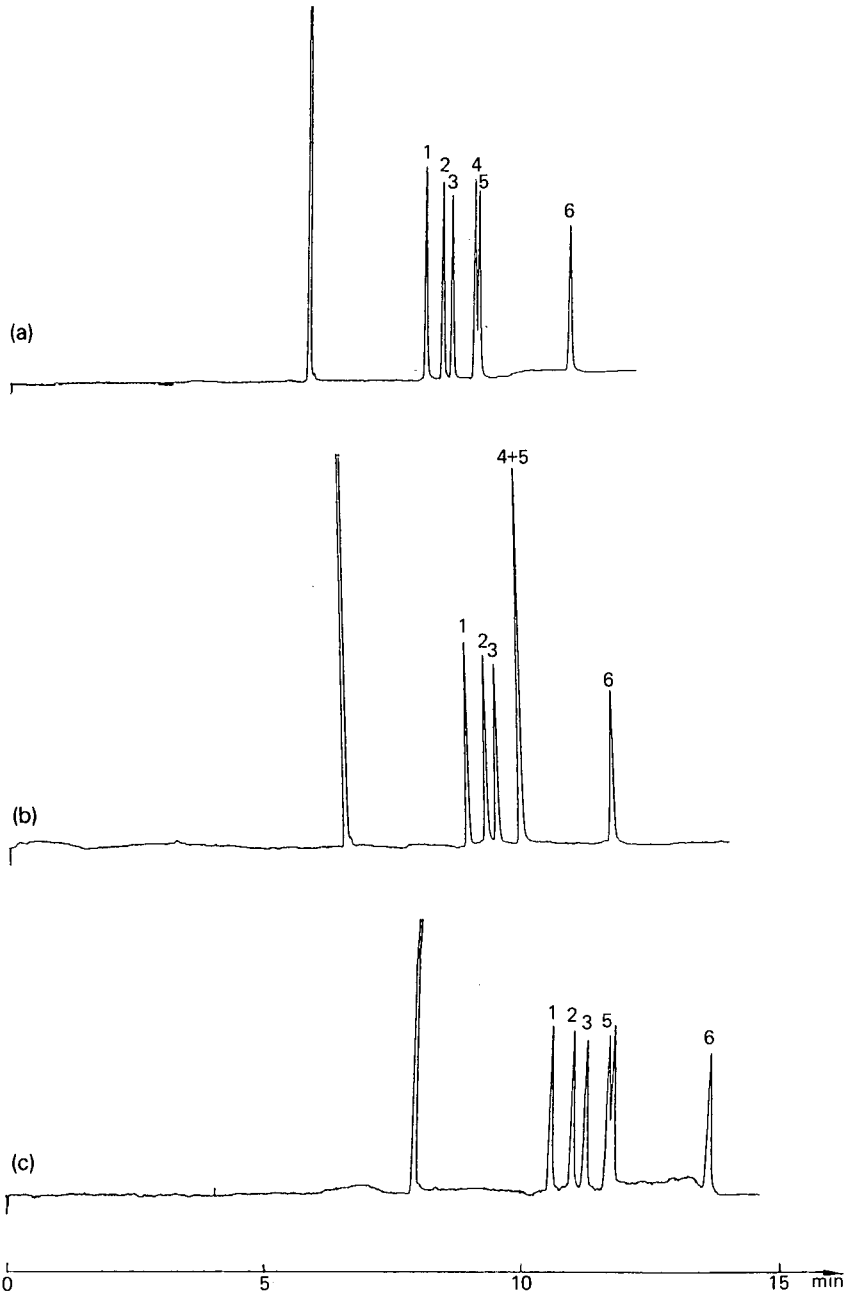

Fig. 4. Chromatograms of some alkylbenzenes obtained with column system B at $T_1 = T_2 = 90°C$ by means of the main detector. $p_i = 110$ kPa; $p_M =$ (a) 40, (b) 50 and (c) 58 kPa.

Peak No.	*Compound*	$I^{OV\text{-}1}$ *(90°C)*	I^{PBHP} *(90°C)*
1	Ethylbenzene	857.3	951.5
2	*m*-Xylene	865.2	974.1
3	*p*-Xylene	866.7	986.9
4	*o*-Xylene	887.3	1005.1
5	Isopropylbenzene	920.7	991.2
6	*tert.*-Butylbenzene	980.9	1043.9

TABLE II

COMPARISON OF PREDICTED AND MEASURED SYSTEM RETENTION TIMES, $t_{R(S)}$, FOR THE SERIES-COUPLED COLUMN SYSTEM B AT DIFFERENT PRESSURE SETTINGS OF THE MEDIUM

For experimental conditions, see Fig. 4.

Compound	p_M = 40 kPa			p_M = 50 kPa			p_M = 58 kPa		
	$t_{R(S)\ meas.}$ (min)	$t_{R(S)\ calc.}$ (min)	Δt^a (s)	$t_{R(S)\ meas.}$ (min)	$t_{R(S)\ calc.}$ (min)	Δt^a (s)	$t_{R(S)\ meas.}$ (min)	$t_{R(S)\ calc.}$ (min)	Δt^a (s)
Ethylbenzene	10.525	10.57	3	11.297	11.35	3	12.395	12.30	5
m-Xylene	10.958	10.99	2	11.759	11.71	3	13.010	12.92	5
p-Xylene	11.188	11.22	2	12.022	11.98	3	13.314	13.23	5
o-Xylene	11.765	11.83	4	12.589	12.58	1	13.938	13.90	3
Isopropylbenzene	11.869	11.95	5	12.589	12.58	1	13.826	13.80	2
tert.-Butylbenzene	14.294	14.33	2	14.993	15.06	4	16.191	16.08	6

[a] $\Delta t = t_{R\ meas.} - t_{R\ calc.}$

Table II the predicted retention times are compared with the measured retention times.

The good agreement between the precalculated and the measured values confirms the fundamental suitability of the method presented. The error in predicting the retention time is less than 2% and is partially due to the fact that for this first example the outlet pressure p_o was considered to be constant and equal to the standard pressure.

CONCLUSIONS

The method presented for the precalculation of the retention times of any substances under the conditions of selectivity tuning by varying the flow-rates in a system of series-coupled GC columns allows the identification of components expected in a mixture by comparing the precalculated and the measured system retention times.

By repeating the identification algorithm at different pressure settings and, consequently, flow-rates it is possible, on the one hand, to pursue the peak shifts expected in selectivity tuning (identification in the sense of a refinding of already known compounds under changed chromatographic conditions according to the repetition of the analysis on a second and third column with changed polarity). On the other hand, owing to the avoidability of overlapping peaks, a degree of reliability can be reached in the positive identification of compounds which is not possible with the classical retention index concept. The combination of such a GC identification system with a spectrometric detector should permit a reliable qualitative analysis in many instances.

A clear advantage of the method suggested is the unlimited applicability of already existing retention index libraries for single-column systems.

An extension of the method by including selectivity tuning by varying the column temperatures is currently under investigation. Further, there are interesting

possibilities of coupling this method with an optimization algorithm for finding the column combinations and pressure settings that allow the maximum separation of a mixture of known composition.

REFERENCES

1 P. Sandra, F. David, M. Proot, G. Dirricks, M. Verstappe and M. Verzele, *J. High Resolut. Chromatogr. Chromatogr. Commun.*, 8 (1985) 782.
2 J. V. Hinshaw and L. S. Ettre, *Chromatographia*, 21 (1986) 561, 669.
3 J. H. Purnell and P. S. Williams, *J. Chromatogr.*, 292 (1984) 197.
4 J. Krupcik, G. Guiochon and J. M. Schmitter, *J. Chromatogr.*, 213 (1981) 189.
5 T. Toth and F. Garay, in P. Sandra (Editor), *Proceedings of the 8th International Symposium on Capillary Chromatography, Riva del Garda, May 19–21, 1987*, 1987, pp. 585–595.
6 D. Repka, J. Krupcik, E. Benicka, P. A. Leclercq and J. A. Rijks, *J. Chromatogr.*, 463 (1989) 243.
7 R. E. Kaiser and R. I. Rieder, *Labor-Praxis*, 9 (1985) 1465.
8 T. Maurer, Th. Welsch and W. Engewald, *J. Chromatogr.*, 471 (1989) 245.
9 E. Matisova, E. Kovacicova, J. Garaj and G. Kraus, *Chromatographia*, 27 (1989) 494.
10 W. Engewald and T. Maurer, *J. Chromatogr.*, 520 (1990) in press.
11 R. E. Kaiser and A. J. Rackstraw, *Computer Chromatography*, Vol. 1, Hüthig, Heidelberg, 1983.
12 R. V. Golovnya, *Chromatographia*, 12 (1979) 533.
13 G. Tarjan, S. Nyiredy, M. Györ, E. R. Lombosi, T. S. Lombosi, M. V. Budahegyi, S. Y. Meszaros and J. M. Takacs, *J. Chromatogr.*, 472 (1989) 1.
14 J. K. Haken, M. S. Wainwright and R. S. Smith, *J. Chromatogr.*, 133 (1977) 1.

Journal of Chromatography, 517 (1990) 87–94
Elsevier Science Publishers B.V., Amsterdam

CHROMSYMP. 1907

Oxygen enhancement of thermal electron capture in a non-radioactive discharge source for a quadrupole mass spectrometer

W.E. WENTWORTH*, ELA DESAI D'SA and C.F. BATTEN
Chemistry Department, University of Houston, 4800 Calhoun, Houston, TX 77004 (U.S.A.)
and
EDWARD C.M. CHEN
School of Sciences and Applied Sciences, University of Houston CL, 2700 Bay Area Boulevard, Houston, TX 77058 (U.S.A.)

ABSTRACT

The electron-capture detector (ECD) is the most sensitive gas chromatographic detector available for certain compounds. In the process of developing a non-radioactive ECD based upon photoionization, we studied the enhancement of the ECD response by the addition of oxygen. This paper describes the results obtained by coupling the non-radioactive photoionization ECD to a quadrupole mass spectrometer. It describes the use of oxygen enhancement of the production of halide ions in a thermal electron-capture process. The production of the halide ions from aliphatic chloro compounds is much greater in the non-radioactive ECD than has been observed in typical radioactive ECDs. Indeed, the response to methylene chloride is equal to that of carbon tetrachloride. This result was unexpected. The exact mechanism for this enhancement is not known. The enhanced signal is smaller for bromobenzene and chlorobenzene.

INTRODUCTION

The electron-capture detector (ECD) is generally recognized as the most sensitive detector available for gas chromatography. However, it is also notorious for its difference in sensitivities[1]. For example, at room temperature, the response for carbon tetrachloride is 10^5 times that of methylene chloride[2]. One method for modifying this is to add oxygen to the carrier gas to enhance the response of the methylene chloride[3]. However, even the enhanced response of methylene chloride is less than that of carbon tetrachloride at 523 K. The enhanced response of methylene chloride does increase with decreasing temperature and would be closer to that of carbon tetrachloride at the temperature of our experiments.

We have recently described the development of a non-radioactive photoioniza-

0021-9673/90/$03.50

tion electron-capture detector (PI-ECD)[4,5]. In this paper, we describe the use of this detector as a source for a quadrupole mass spectrometer. The first objective was to merely determine the relative production of ions from various compounds. These results were as expected. However, the study was extended to determine the enhancement of electron capture and these results were quite different from that which has been observed in the conventional radioactive ECD.

In this article we describe the coupling of the chromatographic detector to a mass spctrometer and present the relative values of the normal response *versus* the enhanced responses for aliphatic and aromatic chloro and bromo compounds. Finally, we present the optimum temperatures for the use of the selective-ion mode for the halide ions and show the relationship between the O_2^- ion current and the halide ion current.

EXPERIMENTAL

The mass spectrometer and the basic atmospheric pressure ionization (API) source have been described previously[6]. In addition, an improved version of the microwave discharge ECD has been given[4,5]. The work on the oxygen enhancement was carried out with an earlier version of the microwave discharge source which will be described here. Briefly, the thermal electrons are generated through the interaction of energetic species with the carrier gas, helium–methane. The response of the detector is measured with and without oxygen. Both the halide ion intensity and the O_2^- current are measured in the selected-ion mode. The details of the data collection programs have been given earlier[6]. The mass spectrometer used in these experiments was an Extranuclear SpectraEL (Extranuclear Labs., Pittsburgh, PA, U.S.A.) having a nominal mass range of 2–400 a.m.u. It was modified to allow analysis of either positive or negative ions from an external high-pressure ionization source. The overall diagram of the various components is shown in Fig. 1. Two vertical cross sections of the actual

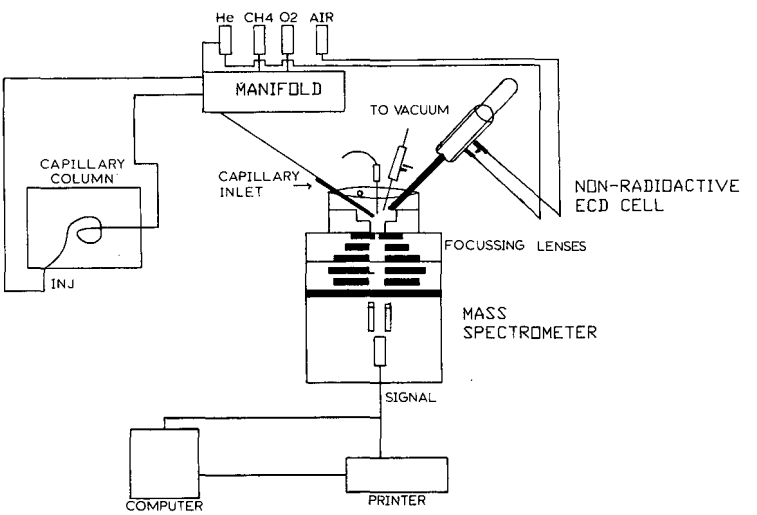

Fig. 1. Basic diagram of the experimental set up.

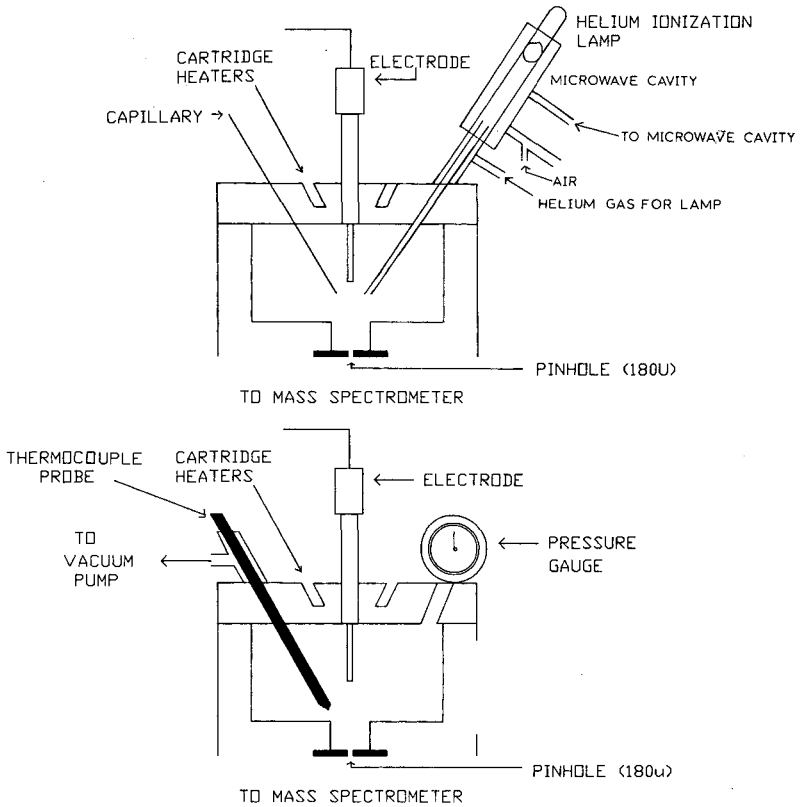

Fig. 2. Cross-sectional view of the interface; two views shown at right angles.

detector are shown in Fig. 2. The carrier gas for the chromatograph is 99.998% pure helium (Big 3 Industries, Houston, TX, U.S.A.). In Fig. 1, it can be seen that there are five entrances into the reaction zone. One serves as an inlet for the pre-mixed reactant gases to enter the reaction zone at 35°C to the horizontal plane. A second at the same angle serves as an inlet for the discharge lamp which produces the excited species. The third port serves as an inlet for the thermocouple and an exit for the gases. The fourth is an inlet for a stainless-steel electrode for the collection of electrons and the fifth is a connection to a pressure gauge.

The lamp is made of an outer quartz tube, 1/4 in. in diameter, with an entrance for the helium gas connected by means of a Kovar–Pyrex fitting and an inner quartz tube that is 18 in. in length that allows the excited species formed in the larger quartz tube to migrate down into the reaction zone. The gas flows exiting the fused-silica capillary column and the inner quartz tube intersect each other in the center of the reaction zone right above the pinhole below which stand the quadrupole of the mass spectrometer. The discharge tube is positioned inside an air-cooled microwave cavity (Opthos Instruments, Rockville, MD, U.S.A.) and is adjusted both in the position on the outer quartz tube as well as its entire length to give the minimum reflected power. The power used is generally about 40 W with a reflected power of 2 W. Helium

discharge is seen to be a very intense peach color and minor leaks in the system can easily be detected and correlated because of the change in the discharge from peach to purple, probably due to nitrogen in the air.

The high-pressure source is separated from the mass spectrometer by a 0.001-in.-thick stainless-steel disk (Optimation, Windham, NH, U.S.A.) with a pinhole aperture of 180 μm. The mass spectrometer pressure is $1 \cdot 10^{-4}$ Torr while the source pressure is about 10–20 Torr. The temperature in the ion source is measured with a thermocouple 1/16 in. in diameter (Type K Omega Engineering, Stamford, CT, U.S.A.). All of the five entrances are made leak-tight by having the lower flanges welded on to the main (top) flange of the mass spectrometer.

The data were collected as follows: the temperature of the detector was gradually raised from room temperature to 250°C and readings were taken every 15–20°C. Pure oxygen and pure methane were used as reagent gases both from Union Carbide, Linde Division (Somerset, NJ, U.S.A.). Once the optimum temperature was established, enhancement measurements were made first by taking measurements without oxygen and then taking them with oxygen. In order to remain in the linear region of the response, dilutions of the samples were made for the readings for the low-capture compounds. The gas in the reaction cell was about 20% methane and 80% helium or 20% methane, 40% helium and 40% oxygen.

The low-electron-capturing species such as methylene chloride were introduced as a solution through the gas chromatograph and the flow was adjusted to get adequate resolution of the peaks. Since actual flows at low pressures cannot be measured, they were approximated by flows at atmospheric pressure and read in terms of the number of Torr so as to be consistent from day to day.

All the compounds were reagent grade and were obtained from Baker, Fisher Scientific or Aldrich (U.S.A.). Of course, since samples are separated on the gas chromatograph, absolute purities are less significant. In addition, in the case of the enhancement values, the results are ratios and therefore any error due to purity will be cancelled out. The samples were diluted in reagent-grade hexane. All samples were injected with a 0.06-μl liquid sampling valve to obtain good reproducibility.

All of the chromatograms were taken with a DB-5 Durabond column, 30 mm × 0.32 mm I.D., with a film thickness of 1 μm at 298 K and a nominal flow-rate of 1 ml/min. The exact column conditions are not critical since the enhancement values are ratios, providing the compound under investigation is separated from its impurities.

RESULTS

The absolute responses of the PI-ECD, the enhanced responses and the enhancement ratios are given in Table I. For comparison, the enhancement ratios for a standard ECD[7] are given in the last column of Table I. Eight compounds with varying degrees of ECD sensitivity have been studied. The absolute responses are calculated from the ion counts per mole calculated using the following formula:

$$R = I_{X^-,\,\mathrm{peak}}\ W_{1/2}/\text{moles injected}$$

where R is the response, $I_{X^-,\,\mathrm{peak}}$ is the halide ion intensity at the peak, including all of

TABLE I

SENSITIZATION BY OXYGEN OF THE RESPONSE OF LOW-ELECTRON-CAPTURING COMPOUNDS IN A MICROWAVE DISCHARGE PI-ECD/COUPLED TO A MASS SPECTROMETER (MS)

The enhancement ratio is the ratio of the ion intensity with oxygen added to the ion intensity without the addition of oxygen.

Compound	*R (ion counts/mol)*		*Enhancement ratio*	
	Without oxygen	*With oxygen*	*ECD–MS*	*Standard ECD*[7]
n-C_3H_7Cl	$2.4 \cdot 10^9$	$1.4 \cdot 10^{15}$	$5.9 \cdot 10^5$	$2 \cdot 10^2$
CH_2Cl_2	$1.8 \cdot 10^{12}$	$2.9 \cdot 10^{15}$	$1.6 \cdot 10^3$	$1.1 \cdot 10^2$
$CHCl_3$	$5.9 \cdot 10^{12}$	$1.7 \cdot 10^{15}$	$2.9 \cdot 10^2$	5.0
CCl_4	$2.3 \cdot 10^{14}$	$3.4 \cdot 10^{15}$	15.0	2.0
$C_6H_5CH_2Cl$	$7.9 \cdot 10^{10}$	$3.8 \cdot 10^{15}$	$4.8 \cdot 10^4$	44.0
cis-$C_2H_2Cl_2$	$2.9 \cdot 10^9$	$8.7 \cdot 10^{14}$	$3.0 \cdot 10^2$	20.0
C_6H_5Cl	$3.8 \cdot 10^9$	$1.1 \cdot 10^{14}$	$2.9 \cdot 10^4$	15.0
C_2H_5Br	$8.7 \cdot 10^{10}$	$4.1 \cdot 10^{14}$	$4.1 \cdot 10^3$	50.0

the isotopes, and $W_{1/2}$ is the width of the peak at half height. The moles injected are calculated from the volume of the sample loop, the dilution factor, the density and the molecular weight of the sample. (In the case of the Cl^- ions a factor of 1.33 $\times$ the $^{35}Cl^-$ peak was used. In the case of the bromine compound, a factor of 2 $\times$ the $^{79}Br^-$ peak was used.) The temperature of the ECD was kept constant at 443 K for all compounds.

Although the ion intensities are generally higher at lower temperatures, residual water forms clusters with the anions and interferes with the reactions. At high temperatures no hydrates are formed and the specific ion–molecule reactions can take place.

We have carried out thermodynamic studies of the chloride, bromide, iodide, and O_2^- reactions with water at the temperature of the detector. At temperatures lower than 400 K, the release of water molecules competes with recombination but we find that the kinetic model gives the equilibrium ratios of the ions and hydrates in the temperatures region above 450 K. Thus adiabatic cooling and declustering in the pinhole are negligible under these conditions.

It is generally believed that the enhancement reaction sequences is

$$e^- + O_2 \rightleftharpoons O_2^-$$

$$O_2^- + RX \rightarrow ? + X^-$$

The normal ECD response for compounds such as methylene chloride is low because there is a significantly large activation energy for dissociative electron attachment. Thus, if an ion molecule reaction is sufficiently exothermic then the ion molecule reaction rate can be larger than the electron molecule reaction and hence there can be an enhancement. However, for compounds such as carbon tetrachloride where the rate constant for dissociative electron attachment is a maximum, the ion

molecule reaction rate should be at most equal to that for the electron molecule reaction. The neutral products of the reaction are not specified. However, one possibility is the radical ROO. Alternatively, the reaction could be one between an excited O_2^- and RX. In addition to the change from an endothermic reaction to an exothermic reaction, there must also be a change in the concentration of the reactive species. This is because the electron molecule rate constants are significantly larger than ion molecule reactions even if the reaction is exothermic. We do not know the answers to these points at present but it is known that the oxygen enhancement reaction takes place even in the radioactive ECD at atmospheric pressure.

From the data given in Table I, it is clear that the relative responses for the PI–ECD are as expected for an ECD. For example, the response for carbon tetrachloride is the greatest while that for chloropropane is the smallest. The relative values are about 10^5 which is also observed in a standard ECD. The major differences are in the enhancement ratios. The enhanced response for the PI-ECD is much greater than that for the standard ECD. The enhanced responses for all eight compounds vary by about an order of magnitude. Indeed, if chlorobenzene and ethyl bromide are excluded, then the response factors vary by slightly less than an order of magnitude. On the other hand, the enhanced response in the standard ECD still varies by three

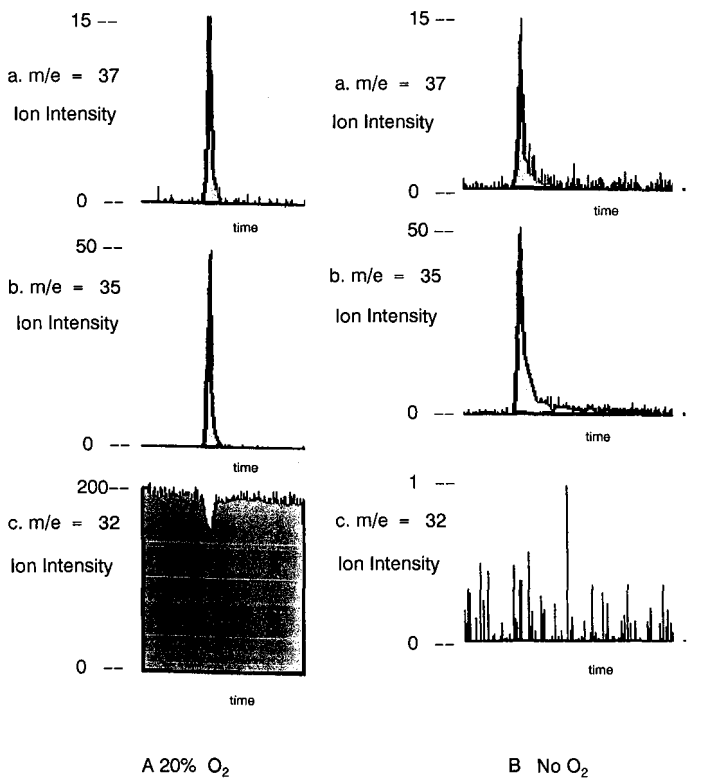

Fig. 3. Chromatograms for the injection of (A) 10 pmol of carbon tetrachloride with 20% oxygen O_2 and (B) 100 pmol of carbon tetrachloride without oxygen. Attenuations: (A) × 15 (a), × 50 (b), × 200 (c); (B) × 1. ECD temperature 441 K.

orders of magnitude. We do not understand this but recognize the value of using the PI-ECD in conjunction with a mass spectrometer as a non-selective halocarbon detector. By monitoring the intensity of the O_2^-, confirmation of the reaction can be made.

In Fig. 3 the selected-ion currents are shown for the injection of 10 pmol of carbon tetrachloride with oxygen and the injection of 100 pmol of carbon tetrachloride without oxygen. In Fig. 4, the selected-ion currents for the injection of 10 pmol of 1-chloropropane with oxygen and 10^5 pmol of 1-chloropropane without oxygen are shown. The plots are ion intensities at *m/e* 32, 35 and 37 *versus* time. It is obvious that the responses for the two compounds are about the same in the system where oxygen is added and quite different without the oxygen. In Fig. 4, the differences in the peak shapes for the chromatograms with and without oxygen should be noted. Without oxygen, the peak is not symmetrical as expected for the large amount injected. The relative intensities of the chlorine isotopes is about 3:1 when the relative attenuations are taken into account. These chromatograms show that the increase in the halide ion

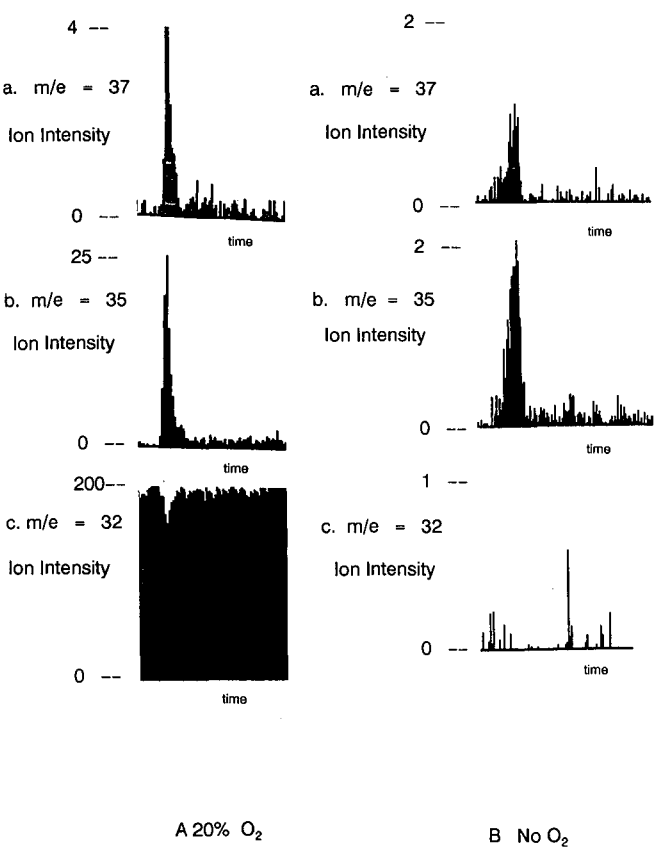

Fig. 4. Chromatograms for the injection of (A) 10 pmol of 1-chloropropane with 20% oxygen and (B) 10^6 pmol of 1-chloropropane without oxygen. Attenuations: × 4 (a), × 25 (b) and × 200 (c); (B) × 2 (a), × 4 (b) and × 1 (c). ECD temperature = 441 K.

occurs at the same time that there is a decrease in the O_2^- current. It should be noted that the decrease in the oxygen peak is less than the amount by which the chloride ions increases. No other peaks were observed in the mass spectrum as mass scans were taken during the time of elution of the gas chromatographic peak of interest.

It was also observed that the intensity of the halide ions varied linearly with the amount of compound injected.

CONCLUSIONS

The ion intensities observed in a microwave discharge PI-ECD are similar to a standard ECD when no oxygen is added to the system. When oxygen is added to the system, the production of the halide ions is enhanced. For the aliphatic chloro compounds, the enhanced response is about constant. This is different from oxygen enhancement in a standard ECD. The enhanced response of olefinic and aromatic chloro compounds is less than that for aliphatic chloro compounds. This system offers potential for the development of a chloride-specific detector by using the PI-ECD with a mass spectrometer as a gas chromatographic detector. The response can be verified by observing the decrease in the O_2^- ion.

ACKNOWLEDGEMENT

The authors acknowledge the financial support of the Robert A. Welch Foundation, Grant E095.

REFERENCES

1 A. Zlatkis and C. F. Poole (Editors), *Electron Capture-Theory and Practice in Chromatography (Journal of Chromatography Library*, Vol. 20), Elsevier, Amsterdam, 1981.
2 E. C. M. Chen and W. E. Wentworth, *J. Chromatogr.*, 68 (1972) 302.
3 E. P. Grimsrud and D. A. Miller, *Anal. Chem.*, 50 (1978) 19.
4 W. E. Wentworth, T. Limero, C. F. Batten and E. C. M. Chen, *J. Chromatogr.*, 441 (1988) 45.
5 W. E. Wentworth, T. Limero, C. F. Batten and E. C. M. Chen, *J. Chromatogr.*, 468 (1989) 215.
6 W. E. Wentworth, E. D. D'sa, C. F. Batten and E. C. M. Chen, *J. Chromatogr.*, 390 (1987) 249.
7 D. A. Miller and E. P. Grimsrud, *Anal. Chem.*, 50 (1978) 1141.

Journal of Chromatography, 517 (1990) 95–101
Elsevier Science Publishers B.V., Amsterdam

CHROMSYMP. 1941

Comparison of cuticular hydrocarbon profiles of fire ants *Solenopsis richteri* from the same colony, using capillary column gas chromatography with pattern recognition

J. H. BRILL*,[a] and W. BERTSCH
Department of Chemistry, University of Alabama, Tuscaloosa, AL 35487-0336 (U.S.A.)

ABSTRACT

The cuticular hydrocarbon profiles of workers of similar age and sub-caste of the black fire ant, *Solenopsis richteri* Forel, were examined by capillary gas chromatography and computer-based pattern recognition procedures. The data show statistically significant and reproducible differences in the hydrocarbon profiles of workers of similar age and sub-caste from the same colony.

INTRODUCTION

It is well known that cuticular hydrocarbons in insects play a role in chemical communication[1–4]. The literature on cuticular hydrocarbons is extensive. It includes the chemical characteristics of materials extracted from the genus *Solenopsis* (fire ants). The cuticular hydrocarbons of these ants are chemically characterized by the presence of alkanes, primarily homologous series of *n*-alkanes and internally branched monomethyl- and dimethylalkanes[3,4]. Studies have also been conducted to correlate gas chromatographic (GC) patterns of the cuticular hydrocarbons to variables such as colony, caste, etc.[5–8]. The primary tools for such investigations are embodied in the science of pattern recognition. Pattern recognition is a general analysis method where data sets obtained from samples are treated by appropriate algorithms for correlation to elements of individuality or to functional group properties[9–11]. In the study of cuticular hydrocarbons, gas chromatograms from different groups of insects are compared. Similarities or differences that are not easily observable by the human eye are pointed out. This process is most efficiently done by computer. Dozens of chromatograms, each consisting of a hundred components or more, can readily be processed. After suitable data pre-treatment, the pattern recognition system looks for natural groupings or clusters. The end result of such manip-

[a] Present address: Department of Chemistry, University of Missouri-Columbia, Columbia, MO 65211, U.S.A.

0021-9673/90/$03.50

ulations is the observance of specific chromatographic peaks or groups of peaks that are indicative of the individual sample sets.

In a series of previous papers, we have examined cuticular hydrocarbon patterns for two of the four species of the genus *Solenopsis*[5]. Further studies on the black fire ant (*Solenopsis richteri*) showed that statistically significant differences appeared between the GC profiles of insects from different castes and those originating from separate colonies[6–8]. The variations between different colonies are generally small. Careful examination, however, shows that somewhat larger differences can be observed between neighboring colonies[7]. It has been reported recently that harvester ants (*Pogonomyrmex barbatus*) can distinguish between neighbors and strangers[12].

In classical sample preparation methods, a large number of insects are usually extracted. The nature of this batch process tends to equalize differences that may exist between smaller sub-sets or individual insects. We have introduced a sensitive procedure that permits establishment of profiles for single insects[13]. During our studies, we have noted that individual workers from the same colony produced slight but reproducible differences in their hydrocarbon profiles.

In this last of four communications, we present evidence for statistically significant variations that cannot be ascribed to experimental error. We do not know if these observations have biological significance.

EXPERIMENTAL

Sample preparation

Individual foragers from the same colony were homogenized in a 250-μl borosilicate glass Potter-Elvehjem tissue grinder (Fisher Scientific, Norcross, GA, U.S.A.) with approximately 200 μl of redistilled *n*-hexane. After the ant was thoroughly ground up, 1 μl of internal standard (containing 250 ng/μl each of docosane, *n*-C_{22}, and dotriacontane, *n*-C_{32}, in *n*-hexane) was added to the liquid. The supernatant was transferred to a 1-ml vial. The residue was washed several times with small quantities of fresh *n*-hexane, and the washings added to the vial. Finally, the extract was made up to 200 μl with *n*-hexane (due to evaporation during the workup). A total of eight foragers of approximately the same size were treated in this manner. The experiments were repeated using foragers from five different colonies of the black fire ant.

Control

The sampling and workup procedure was also performed without the use of a forager: approximately 200 μl of *n*-hexane were placed in the tissue grinder and the homogenation step was performed by grinding the pestle in the solvent for a few minutes. The internal standard was added and the solution transferred, together with the washings, to a sample vial.

Gas chromatography

The extracts were examined by capillary GC using the splitless injection mode. The gas chromatograph was a Hewlett-Packard 5830A instrument, equipped with a Grob-type split/splitless injection port and a flame ionization detector. The column was a 10 m × 0.25 mm I.D. glass capillary, coated with a 0.25-μm film of SE-30. This column was produced in-house, following standard procedures[8]. Initial oven temper-

ature was 40°C. Thirty seconds after injection, the injector purge was activated and the oven heated rapidly to 85°C. Thereafter, the oven was temperature-programmed to 300°C at a rate of 8°C/min. The helium carrier gas was set at a flow-rate of approximately 1 ml/min. Five replicate injections, of 1.8 μl each, were made from each sample.

The samples were also examined by GC–mass spectrometry (MS), using a Hewlett-packard 5895A GC/MS system operated in the electron impact mode (70 eV). A 15 m × 0.32 mm I.D. fused-silica capillary column, coated with a 0.10-μm film of 5% phenylmethylpolysiloxane (DB-5, J&W Scientific, Folsum, CA, U.S.A.) was used.

Data analysis

The retention times and peak areas from the integrated GC reports were submitted to a mainframe computer (UNIVAC 1100). The ARTHUR chemometrics system package that contains several pattern recognition subroutines was used to analyze the data[14]. To avoid bias, unsupervised learning procedures were used; that is, the computer was not supplied with the category (colony source of individual foragers) to which each of the gas chromatograms belonged. Seven marker peaks (consisting of the two internal standards and five peaks from the cuticular hydrocarbons) were encoded with the data set, which was then transduced into multivariate form[5,15]. The marker peaks are necessary in order to normalize chromatograms and to correct for small shifts in retention time. The raw data consisted of 41 data vectors, each comprised of 26 features. The data were then autoscaled, to prevent bias from features having greatly differing magnitudes[14], and then submitted to two graphical display routines contained in the ARTHUR package. Autoscaled data were displayed in two-dimensional space using the non-linear mapping (NLM) procedure[9]. The autoscaled data were also transformed using the Karhunen–Loeve (KL) projection, a method based on principal components analysis[9], and then plotted using combinations of the first three principal components.

RESULTS AND DISCUSSION

It has been shown in the black fire ant that hydrocarbon profiles obtained by homogenation in solvent such as *n*-hexane are nearly identical with those obtained by topical washing with the same solvent, despite the fact that one method probes primarily the surface of the insect, whereas the other extracts both the surface and the internal body parts[8,16]. The methods differ only in the total amount of hydrocarbons that can be recovered in a given period of time. Replicate analyses of small numbers of insects produce virtually identical results. We have previously described a sensitive method for examining the profiles of single insects, using a pyroprobe to generate headspace samples[13] However, in the application described herein, the headspace procedure proved unsatisfactory, since it was not possible to obtain replicate samples from a single fire ant which were suitable to run on the pyroprobe. The most satisfactory method, therefore, was solvent extraction.

To minimize or exclude extraneous effects, care was taken to eliminate extraneous variables. It has been reported that cuticular hydrocarbons of adult insects change with age[17]. Since hydrocarbons remain relatively unchanged in older adults[18], it was decided to use foragers in this study. Foragers constitute the oldest workers in the colony.

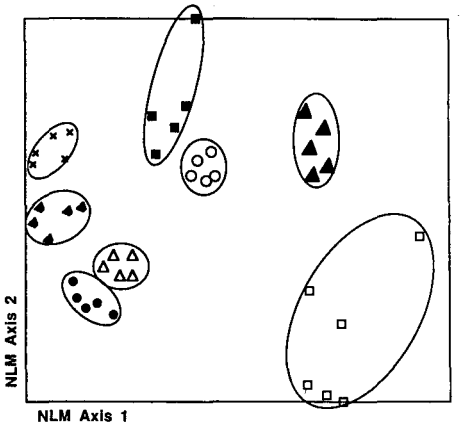

Fig. 1. Non-linear map (NLM) of the autoscaled data set obtained from hydrocarbon profiles of eight foragers, each from the same colony.

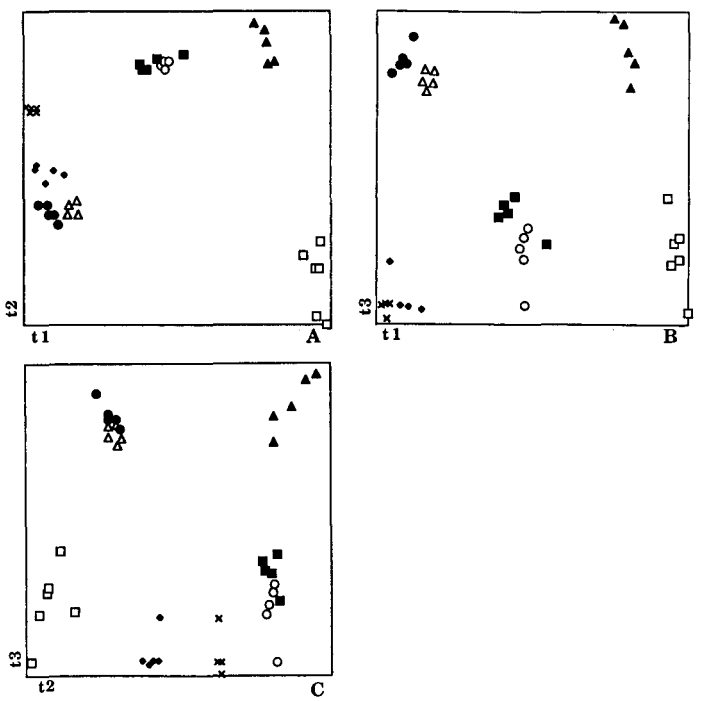

Fig. 2. Principal components (KL) plots (A–C) of the hydrocarbon profiles of eight foragers, each from the same colony. t1 = First principal component; t2 = second principal component; t3 = third principal component. The symbols are the same as in Fig. 1.

The results of these studies show statistically significant and reproducible differences in the hydrocarbon profiles of foragers from the same colony. Fig. 1 shows the NLM plot of the autoscaled data. The profiles for each of the foragers form distinct and well-defined clusters. The computer had no information concerning the different categories in the data set. The groupings observed in the NLM plot are therefore natural clusterings, which have not been enhanced by feature weighting, feature selection, or other mathematical manipulations that might lead to distortions. Only the investigator knew the categories (*i.e.*, individual foragers) to which the objects (chromatographic profiles) belonged. It is statistically significant, therefore, that these natural clusters also correspond to the various categories (individual foragers) in the data set. The cluster designated by the open squares shows a rather large spread. It is likely that the data point at the top right of the cluster is an outlier (due to an experimental error). When a sixth replicate was examined, it was located approximately at the center of the cluster, making it more likely that the aforementioned data point is an outlier.

The principal components (PC) analysis of the data set (using the KL projec-

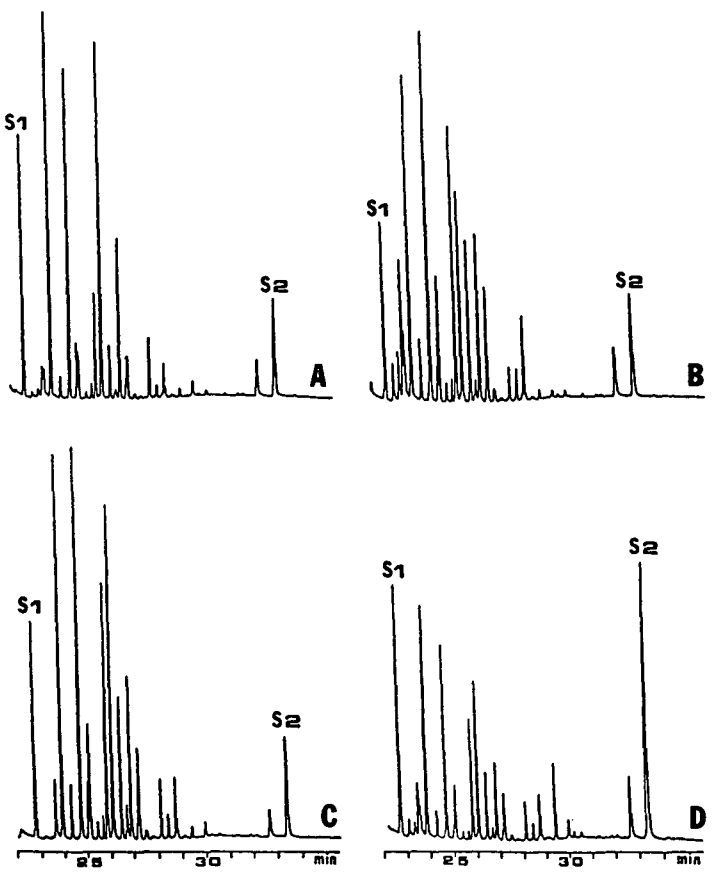

Fig. 3. Sample chromatograms of the hydrocarbon profiles of four foragers from the same colony of the black fire ant. S1 and S2 are internal standards (docosane and dotriacontane, respectively). A, B, C and D indicate the profiles of four different forgers from the same colony.

tion) also shows good correlation for each of the ant profiles, although the groupings were not as well focussed as in the NLM method. This is in accordance with previous observations[7]. Fig. 2 shows the KL plots of the autoscaled data set. Together, the first three principal components accounted for 83.7% of the explained variance in the data set. Some of the clusters in Fig. 2 show less than five objects. This is because two or more objects were "overlapping" in the two-dimensional data space, a phenomenon that sometimes occurs with linear transformation methods when projecting multi-dimensional data onto a two-dimensional space.

Sample hydrocarbon profiles of four foragers from the same colony are shown in Fig. 3. GC–MS analyses indicated that the components eluting between the two internal standards (S1 and S2) were hydrocarbons. The unusually large peak for the second internal standards (S2) relative to S1 in Fig. 3D was due to the forager possessing the same compound in its own hydrocarbon profile. Visual inspection reveals differences among the profiles of the foragers. The relative standard deviation among replicates from the same sample was less than 0.08, indicating that the reproducibility among the sample replicates was good and within expected experimented error. The observed differences in the profiles are therefore due to the samples themselves and not to sampling or instrumental errors. The control experiment was devoid of any extraneous material. When the GC profiles of foragers from several other colonies were examined, reproducible differences among the hydrocarbon profiles of foragers from the same colony were also evident.

The results of all these experiments are summarized in Table I. The chromatograms from each experiment were first normalized, to eliminate any bias caused by differences in sample size. Then the variation (relative standard deviation, R.S.D.) in the normalized peak area for each of the 26 features was compared for each sample. The resulting 26 R.S.D. values were then averaged to obtain an average relative standard deviation for each sample, which was then compared to that for other samples, as indicated in Table I. The results for category 1 of Table I indicate that the sampling procedure is highly reproducible. In category 2, replicate analyses from the homogenate extracts of individual foragers are compared. Category 3 compares the homogenate extracts of different foragers.

These studies show detectable differences in the hydrocarbon patterns of different foragers from the same nest. It is not known whether these differences have a functional significance. Individual recognition of nestmates has been reported in some ant species where workers are few in number and maintain dominance hierarchies[19–21].

TABLE I

VARIATIONS WITHIN AND BETWEEN REPLICATES FOR DIFFERENT SAMPLE CATEGORIES

Category		*Average R.S.D.*
(1)	Internal standard mixture (control) (7 replicates)	0.13
(2)	Extract of homogenate from single fire ant workers (35 replicates)	0.12
(3)	Extracts of homogenates from different fire ant workers (35 replicates)	0.42

ACKNOWLEDGEMENTS

We would like to thank D. J. C. Fletcher for helpful discussions and T. Mar for help with the data treatment.

REFERENCES

1 R. W. Howard and G. L. Blomquist, *Ann. Rev. Entomol.*, 27 (1982) 149.
2 R. K. Vander Meer and D. P. Wojcik, *Science (Washington, D.C.)*, 218 (1982) 806.
3 J. B. Lok, E. W. Cupp and G. L. Blomquist, *Insect Biochem.*, 5 (1975) 821.
4 D. R. Nelson, C. L. Fatland, R. W. Howard, C. H. McDaniel and G. L. Blomquist, *Insect Biochem.*, 10 (1980) 409.
5 J. H. Brill, H. T. Mayfield, T. Mar and W. Bertsch, *J. Chromatogr.*, 349 (1985) 31.
6 J. H. Brill, T. Mar, H. T. Mayfield and W. Bertsch, *J. Chromatogr.*, 349 (1985) 39.
7 J. H. Brill, T. Mar and W. Bertsch, *Analyst (London)*, 111 (1986) 711.
8 J. H. Brill, *Dissertation*, University of Alabama, Tuscaloosa, AL, 1985.
9 B. R. Kowalski (Editor), *Chemometrics: Theory and Applications* (*ACS Symposium Series*, No. 52), American Chemical Society, Washington, DC, 1977.
10 M. A. Sharaf, D. L. Illman and B. R. Kowalski, *Chemometrics*, Wiley, New York, 1986, p. 219.
11 D. L. Massart, B. G. M. Vandeginste, S. N. Deming, Y. Michotte and L. Kaufman, *Chemometrics: A Textbook*, Elsevier, Amsterdam, 1988, p. 371.
12 D. Gordon, *Oecologia*, 81 (1989) 198.
13 J. H. Brill and W. Bertsch, *Insect Biochem.*, 15 (1985) 49.
14 D. L. Duewar, J. R. Koskinen and B. R. Kowalski, *Documentation of ARTHUR Version 1-8-75*(*Chemometrics Society Report*, No. 2), Laboratory for Chemometrics, Department of Chemistry, University of Washington, Seattle, WA, 1975.
15 H. T. Mayfield and W. Bertsch, *Computer Appl. Lab.*, 2 (1983) 130.
16 J. H. Brill and W. Bertsch, *J. Entomol. Sci.*, 20 (1985) 435.
17 L. L. Jackson and G. L. Baker, *Lipids*, 5 (1970) 239.
18 D. J. C. Fletcher, personal communication.
19 N. R. Franks and E. Scovell, *Nature (London)*, 304 (1983) 724.
20 B. J. Cole, *Science (Washington, D.C.)*, 212 (1968) 83.
21 A. Bonavita-Cougourdan, J. L. Clement and C. Lange, *J. Entomol. Sci.*, 22 (1987) 1.

Journal of Chromatography, 517 (1990) 103–121
Elsevier Science Publishers B.V., Amsterdam

CHROMSYMP. 1952

Empirical scheme for the classification of gas chromatographic stationary phases based on solvatochromic linear solvation energy relationships

JIANJUN LI, ANDREW J. DALLAS and PETER W. CARR*
Department of Chemistry, University of Minnesota, Kolthoff and Smith Halls, 207 Pleasant Street, Minneapolis, MN 55455 (U.S.A.)

ABSTRACT

Due to the plethora of materials that have been used as stationary phases in gas chromatography it is clearly necessary to have some method for classifying phases to facilitate systematic method development. The most popular classification scheme is the Rohrschneider–McReynolds procedure which is based on the Kováts retention indices of a variety of probe solutes. Although this is a very useful approach, it is highly empirical and has been criticized on several grounds. In this work we explored the use of solvatochromic measures of solute dipolarity-polarizability (π_2^*), hydrogen bond donor acidity (α_2) and hydrogen bond acceptor basicity (β_2) to classify a variety of common capillary gas chromatographic stationary phases. Preliminary studies show that the use of only the solvatochromic parameters as explanatory variables leads to rather poor precision. However, when log capacity factors on two extreme types of phases are included among the explanatory variables quite high precision, typically an average standard deviation of less than 0.07 log units, is obtained and all columns tested were easily classified. The two reference phases should be a low-polarity phase and a high-polarity, hydrogen bond acceptor phase.

INTRODUCTION

Currently more than 200 liquid phases suitable for use as stationary phases in gas chromatography (GC) are commercially available. This huge number of materials mandates that they be classified. Consequently it is not surprising that there have been many studies aimed at identifying and quantifying their retention characteristics. The most common of these, and perhaps that which is chemically most appealing, is the multiple probe solute method developed by Rohrschneider[1–3] and later extended by McReynolds[4]. This approach has been used as the basis for choosing a small set of stationary phases that should accommodate a very wide variety of samples[5]. It is, however, based on the Kováts retention index scheme for quantifying retention.

0021-9673/90/$03.50

Among others, Poole has criticized the Kováts index based classification methods, in part because they rely on the normalization of the retention of the polar solutes relative to the retention of *n*-alkanes[6,7]. In essence, for polar stationary phases the change in the retention index of a polar solute relative to its value on a non-polar phase is due as much to the decrease in retention of the reference alkanes, relative to their retention on a non-polar phase, as it is to the increase in retention of the polar solute. Clearly this complicates the chemical interpretation of the change in retention index from phase to phase. To avoid or minimize this problem, many investigators[8] have used series of homologues other than the *n*-alkanes as the basis for retention index schemes.

Other classification schemes have been investigated[9–16]. For example, Howery and co-workers[9–11] have used factor analysis to classify GC phases. Laffort and Patte[12,13] developed the use of "solubility factors" to characterize liquid stationary phases. However, because some of these classification methods are based on retention indices or they used the retention of alkanes as a reference, they suffer from some of the problems mentioned above.

In this study we used solvatochromically based linear solvation energy relationships (LSER) to explore and rationalize retention relationships on a variety of common capillary columns that span a full polarity range. This set of columns does not cover all the possible GC phases. Most notably none of the phases has strong hydrogen bond donor properties. We choose to study the properties of fused-silica based capillary columns because they have a low ratio of surface area to phase volume and afford a less sorptive underlying solid surface relative to the porous supports used in packed columns. This helps minimize interfacial adsorption effects. It should be noted that capillary columns are not entirely free of gas–liquid interfacial adsorption effects[17–19], nor can one disregard the potential for interaction with the silica surface.

The solvatochromic parameters used in this work are the Kamlet–Taft solute dipolarity-polarizability (π_2^*), hydrogen bond donor acidity (α_2) and hydrogen bond acceptor basicity (β_2). The solute parameter is different from the solvent parameter and is differentiated from a solvent parameter by a subscript 2. The dipolarity-polarizability scale (π^* or π_2^*) is primarily a measure of the ability of a species to stabilize a neighboring dipole by virtue of its own dipolarity and secondarily by its polarizability[20,21]. It is a relative scale defined as π^* or π_2^* (cyclohexane = 0) and π^* or π_2^* (dimethyl sulfoxide = 1.00). Because aliphatic, aromatic and polyhalogenated species have very different polarizabilities it is often necessary to apply a "polarizability correction factor" (δ) to π^* or π_2^* (ref. 22). The δ parameter is conveniently defined to be 0 for aliphatics, 0.5 for polyhalogenated and 1.0 for aromatic species, whether it acts as a solvent or a solute. The α (α_2) and β (β_2) scales define the ability of a species to interact with an acceptor and a donor, respectively, via hydrogen bond formation[21,23,24]. The above are referred to as solvatochromic parameters because in general they were first established via the study of some spectroscopic property of an appropriate indicator molecule[22–24] in a variety of solvents. The solute hydrogen bond acidity and basicity parameters have been obtained by hydrogen bond complexation constants as well[25,26]. These parameters have been used to correlate, rationalize and explore the chemistry of more than 600 different chemical systems[21,27–29]. Studies of immediate relevance to this work include retention in reversed-[30–34] and normal-phase liquid chromatography[35] and gas–liquid partition coefficients in both low-molecular-weight and polymeric liquids[36–38]. In an early solvatochromic study Brady *et al.*[39]

measured the bulk phase π^* of a series of methyl and phenyl silicone oils and showed that, after correction for the configurational entropy, excellent linear correlations for the residual free energy of transfer of polar solutes from liquid to gas phase against π^* were obtained.

In this work we measured the retention of 53 solutes on 8 different polymeric phases. In a sense this approach is similar to that taken by Rohrschneider and McReynolds in their use of probe solutes. However, it markedly differs from their methodology in that a large number of polar, hydrogen bond donor and hydrogen bond acceptor solutes were used. More importantly the test solutes were chosen to span an extremely wide range in chemical characteristics. In comparison to Rohrschneider we included such extremely strong hydrogen bond donor acids as trifluoroethanol ($\alpha_2 = 0.57$) and phenol ($\alpha_2 = 0.60$) and bases as strong as dimethyl sulfoxide ($\beta_2 = 0.78$) and dimethylacetamide ($\beta_2 = 0.74$). These are considerably stronger than the strongest acids and bases used by Rohrschneider (ethanol, dioxane, methyl ethyl ketone). Our solutes encompass nearly the entire range in available dipolarity (π_2^*), hydrogen bond acidity (α_2) and hydrogen bond basicity (β_2). At the same time we were interested in the behavior within a series of homologues, so we included several members of each class. This expands the solutes set to over the 30 or so compounds needed to precisely characterize a phase by regression methods. In principle, the coefficients of any regression model can be numerically determined as soon as one has as many data points as parameters in the model. Thus we really only need data for a handful of solutes. However, we deem this approach to be chemically unacceptable. First in order for the regression coefficients to be precisely defined each parameter should be varied over a reasonably wide range. Second the explanatory variables are imprecise since in general they are obtained by measurement. In order to average out the effect of this imprecision it is necessary to use a minimum of three to four solutes per parameter. We choose to vastly over-determine the system so as to generate a high degree of statistical and chemical confidence in the meaning of the parameters. As shown in Table I, this is an extremely diverse, variegated data set. In accord with the general LSER formalism for a study in which the solute is varied while the solvent environment is fixed the appropriate LSER regression equation is:

$$SP = SP_0 + mV_I/100 + s\pi_2^* + d\delta_2 + a\alpha_2 + b\beta_2 \quad (1)$$

SP is some solute property linearly related to its energy of solvation. In chromatography, it may be taken as the logarithm of the capacity factor ($\log k'$). SP_0 is a solute independent constant. m, s, a, b and d are regression coefficients. V_I in eqn. 1 is the solute intrinsic (Van der Waals) molar volume (the same as the solvent value), computer calculated by the method of Leahy[46] or Pearlman[47], or estimated by simple additivity methods such as those of Bondi[48] or Abraham and McGowan[49]. The $mV_I/100$ term is needed to account for the endoergic (unfavorable) energy of cavity formation. A scale of 1/100 for V_I was used so that the parameter measuring the cavity term will cover roughly the same range as the other independent variables. This also makes it easier to evaluate the relative contributions of the various solute–solvent interactions to the property (SP) being studied.

When a very cohesive liquid, such as water, is used as the mobile phase the coefficient m should be large and positive leading to an increase in retention in

TABLE I

SOLUTE SOLVATOCHROMIC PARAMETERS

Compound name	*log* L^{16} [a]	$V_I/100$ [d]	π_2^* [d]	δ_2	β_2 [e]	α_2 [e]
Cyclohexane	2.913	0.598	0.00	0.0	0.00	0.00
1-Hexene	2.547	0.624	0.08	0.0	0.07	0.00
Pentane	2.162	0.553	−0.08	0.0	0.00	0.00
Hexane	2.668	0.648	−0.04	0.0	0.00	0.00
Octane	3.677	0.842	0.01	0.0	0.00	0.00
Decane	4.686	1.036	0.03	0.0	0.00	0.00
Undecane	5.191	1.134	0.04	0.0	0.00	0.00
Tetradecane	6.705	1.423	0.07	0.0	0.00	0.00
Pentadecane	7.209	1.521	0.07	0.0	0.00	0.00
Ethyl acetate	2.376	0.521	0.55	0.0	0.45	0.00
Propyl acetate	2.878	0.622	0.53	0.0	0.45	0.00
Diethyl ether	2.061	0.505	0.27	0.0	0.45[f]	0.00
Dipropyl ether	2.989	0.699	0.27	0.0	0.46	0.00
Dibutyl ether	4.001	0.893	0.24	0.0	0.46	0.00
Acetonitrile	1.560	0.271	0.75	0.0	0.42[g]	0.09
Propionitrile	1.940	0.369	0.70	0.0	0.43[g]	0.00
Acetone	1.760	0.380	0.71	0.0	0.50[f]	0.04
2-Butanone	2.287	0.477	0.67	0.0	0.48	0.03
2-Pentanone	2.755	0.574	0.65	0.0	0.48	0.03
Dimethylformamide	3.173	0.444	0.88	0.0	0.66[f]	0.00
Dimethylacetamide	3.717	0.543	0.88	0.0	0.74[g]	0.00
Dimethyl sulfoxide	3.437	0.466	1.00	0.0	0.78[f]	0.00
Propionaldehyde	1.815	0.381	0.65	0.0	0.41	0.00
Tetrahydrofuran	2.534	0.455	0.58	0.0	0.51	0.00
Triethylamine	3.077	0.704	0.14	0.0	0.67[f]	0.00
Nitromethane	1.892	0.348	0.85	0.0	0.25	0.12[g]
Nitroethane	2.367	0.455	0.80	0.0	0.25	0.00
Nitropropane	2.710	0.542	0.78	0.0	0.25	0.00
Methanol	0.922	0.205	0.40	0.0	0.41[h]	0.37[i]
Ethanol	1.485	0.305	0.40	0.0	0.44[h]	0.33[i]
1-Propanol	2.097	0.402	0.40	0.0	0.45[h]	0.33[i]
2-Propanol	1.821	0.401	0.40	0.0	0.47[h]	0.32[i]
2-Methyl-2-propanol	2.018	0.498	0.40	0.0	0.49[h]	0.32[i]
Trifluoroethanol	1.224	0.376	0.73	0.0	0.18[h]	0.57[i]
Hexafluoroisopropanol	1.392	0.546	0.65	0.0	0.03[h]	0.77[i]
Acetic acid	1.750[b]	0.323	0.60	0.0	0.45	0.55[i]
Aniline	3.993	0.562	0.73	1.0	0.50	0.26
N-Methylaniline	4.492[c]	0.660	0.73	1.0	0.47	0.12
Phenol	3.856	0.536	0.72	1.0	0.33	0.60[i]
Benzyl alcohol	4.443	0.634	0.99	1.0	0.42[h]	0.39
m-Cresol	4.329	0.634	0.68	1.0	0.34	0.58
Ethylamine	1.677	0.335	0.32	0.0	0.70	0.00
Propylamine	2.141	0.433	0.31	0.0	0.69	0.00
Butylamine	2.618	0.535	0.31	0.0	0.69	0.00
Benzene	2.803	0.491	0.59	1.0	0.13[g]	0.00
Toluene	3.344	0.592	0.55	1.0	0.14[g]	0.00
Ethylbenzene	3.765	0.668	0.53	1.0	0.12	0.00
Propylbenzene	4.221	0.769	0.51	1.0	0.12	0.00
p-Xylene	3.858	0.668	0.51	1.0	0.12	0.00
Benzaldehyde	3.935[c]	0.606	0.92	1.0	0.44	0.00
Benzonitrile	3.913[c]	0.590	0.90	1.0	0.37	0.00
N,N-Dimethylaniline	4.754	0.752	0.90	1.0	0.43	0.00
Carbon tetrachloride	2.823	0.514	0.28	0.5	0.10	0.00

[a] From ref. 40 unless otherwise indicated. [b] From ref. 41. [c] From ref. 42. [d] From refs. 21 and 43. [e] From refs. 21 and 43 unless otherwise indicated. [f] From ref. 45. [g] These are β_2^H values provided to us by Professor R. W. Taft, University of California, Irvine, CA. [h] These are β_2^H values from ref. 44. [i] From ref. 25.

a non-polar stationary phase upon an increase in solute size. Such was invariably the case in studies of reversed-phase liquid chromatography[31,33]. Abraham and co-workers[50,51] in a study of gas partition coefficients into several non-polar liquids showed that eqn. 1 did not provide an acceptable correlation. This is due in part to the fact that in studies of liquid–liquid transfer processes the energy of dispersion between the solute and the two bulk liquid phases are to a first approximation similar and largely cancel out. This cancellation cannot occur in a gas to liquid or gas to solid transfer process. Eqn. 1 does not contain any explicit dependence on the energy of dispersion although it can be shown for a wide range of solutes that there is a high degree of covariance between molar refractivity (MR) (a dispersion interaction parameter) and V_I (ref. 50). In addition detailed studies of the thermodynamics of retention in gas chromatography make it clear that there is a significant configurational entropy contribution to k'. Solvatochromic LSER regressions do not, at present, explicitly include a configurational entropy term but it too is expected to covary with V_I.

Another distinction between liquid–liquid transfer and gas–condensed phase transfer processes is the fact that the free energy of transfer of a gas to water becomes less favorable as the gas increases in size whereas in all common organic liquids the free energy of transfer becomes more favorable, that is retention increases, as the size of the gas increases[27,51]. This comes about due to the trade-off in increasingly unfavorable cavity formation and favorable dispersion energy with solute size.

Each of the solvatochromic coefficients (s, a and b) in eqn. 1 has a distinct chemical interpretation. On a phase that has no hydrogen bond donor acidity, *e.g.* hexadecane or squalane, a solute's hydrogen bond acidity and basicity should have no effect on its retention in which instance the a and b coefficients should be zero or statistically negligible. In contrast if the stationary phase were to have an active hydrogen bond donor group, such as a hydroxyl group, then one expects the b coefficient of this material to be positive. That is, an increase in solute basicity should lead to an increase in retention. By the same concept, for a highly dipolar but hydrogen bond donor inert phase one expects the s coefficient to be significant and an increase in solute dipolarity should lead to an increase in retention.

To overcome the problems inherent in eqn. 1 Abraham and co-workers[27,51] have recommended that a new solute parameter $\log L^{16}$ be used to replace V_I in eqn. 1 when dealing with gas–condensed phase processes.

$$SP = SP_0 + l \log L^{16} + s\pi_2^* + d\delta_2 + a\alpha_2 + b\beta_2 \quad (2)$$

L^{16} is the partition coefficient of the solute from the gas phase to *n*-hexadecane at 298 K. It takes into account both solute–condensed phase dispersion interactions and the work needed to create a cavity in the condensed phase. They have shown that this provides much better correlations for gas–liquid transfer processes than does eqn. 1. A similar approach was taken in this work. The initial motivation for this work was to explore the utility of the LSER given in eqn. 2 and ultimately to classify a variety of capillary columns and at the same time to see if their chemical properties as defined by the coefficients l, s, a and b could be rationalized.

EXPERIMENTAL

Unless otherwise stated, all solutes were general laboratory or analytical grade in the highest purity available. The capillary columns, which span the whole polarity scale (not including DB-23), were all a gift from J&W Scientific (Folsom, CA, U.S.A.). Their specifications and chemical structures are given in Table II. All columns used here were 15-m widebore columns. An HP-7620A gas chromatograph with heated on-column injector and flame ionization detector were used. Both the injector and the detector temperatures were kept at 250°C. Data were collected at 45, 60, 80, 115 and 150°C. The column oven temperature was stable to within 0.02°C. Helium (carrier gas) flow was adjusted as necessary to make the retention times adequate. The samples were injected either as headspace vapors (for liquid solutes) or as very dilute solutions of the solids. Sample sizes were varied to insure that the retention times were independent of the amount injected. All data were collected on an HP-3390 integrator. Corrected retention times and capacity factors were calculated referenced to the retention of methane. Data were analyzed via a multivariable linear least square regression program run on a Zenith computer.

TABLE II

PROPERTIES OF THE CAPILLARY COLUMNS USED IN THE STUDY

The polarity increases from columns 1 to 8.

Megabore column	*Phase*	*Film thickness (μm)*
1 DB-1	Methylsilicone	1.5
2 DB-5	5% Phenyl methylsilicone	1.5
3 DB-1301	6% Cyanopropylphenyl methylsilicone	1.0
4 DB-1701	14% Cyanopropylphenyl methylsilicone	1.0
5 DB-17	50% Phenyl methylsilicone	1.0
6 DB-210	50% Trifluoropropyl methylsilicone	1.0
7 DB-225	50% Cyanopropylphenyl methylsilicone	1.0
8 DB-WAX	Polyethylene glycol	1.0

RESULTS AND DISCUSSION

The results of preliminary correlations using eqn. 1 for eight different columns are shown in Table III. For brevity the results are given only at 115°C. The standard deviations and correlation coefficients shown in Table III when compared to those obtained in related studies, particularly reversed-phase liquid chromatography, indicate that these correlations are very imprecise. This is especially true of the more polar stationary phases. The correlations for the DB-WAX column are particularly poor (see below).

Even though the correlations are not as precise as we desire or can ultimately achieve (see below) the various solvatochromic coefficients m, s, a, b and d are statistically significant and should be interpreted. The coefficients m, s, b and d are

TABLE III

REGRESSION COEFFICIENTS BASED ON V_I AND SOLVATOCHROMIC PARAMETERS

Standard deviations of the coefficients are given in parentheses. Eqn. 1 is the regression equation employed.

Column	*T(°C)*	SP_0	*m*	*s*	*a*	*b*	*d*	*S.D.*[a]	r^2[b]	*n*[c]	*f*[d]
DB-1	115	−2.41	2.60	0.47	−[e]	0.46	0.51	0.17	0.9677	53	0.22
		(0.11)	(0.12)	(0.11)		(0.13)	(0.07)				
DB-5	115	−2.54	2.64	0.63	−[e]	0.44	0.49	0.19	0.9617	53	0.23
		(0.12)	(0.13)	(0.13)		(0.15)	(0.07)				
DB-1301	115	−2.78	2.69	0.89	0.31	0.42	0.44	0.21	0.9575	52[f]	0.24
		(0.14)	(0.15)	(0.14)	(0.15)	(0.16)	(0.08)				
DB-1701	115	−2.76	2.59	1.13	0.50	0.37	0.40	0.21	0.9537	53	0.26
		(0.14)	(0.15)	(0.14)	(0.16)	(0.17)	(0.08)				
DB-17	115	−2.88	2.57	1.03	−[e]	0.60	0.59	0.26	0.9390	52[f]	0.28
		(0.16)	(0.18)	(0.17)		(0.20)	(0.10)				
DB-210	115	−2.79	2.14	1.51	−[e]	0.54	0.18	0.23	0.9296	53	0.28
		(0.15)	(0.16)	(0.15)		(0.18)	(0.09)				
DB-225	115	−2.90	2.30	1.72	0.79	0.49	0.42	0.26	0.9400	53	0.31
		(0.17)	(0.18)	(0.17)	(0.19)	(0.21)	(0.10)				
DB-WAX	115	−2.83	2.11	1.73	1.79	0.64	0.55	0.31	0.9371	53	0.34
		(0.20)	(0.22)	(0.20)	(0.23)	(0.24)	(0.12)				

[a] Standard deviation of the fit.
[b] Correlation coefficient.
[c] Number of data points.
[d] Goodness-of-fit statistic[52].
[e] These coefficients were found to be not significantly different from zero and were omitted in the final fit.
[f] Propionaldehyde was excluded from DB-1301 data sets, acetic acid was excluded from DB-17, due to their being outliers at all temperatures on the respective column.

significant on all phases. The coefficients *a* is insignificant on four phases. The signs and magnitudes of *s* make chemical sense. In general *s* increases as the phase becomes more polar. This means that solute dipolarity causes a greater increase in retention on a more dipolar phase. The *m* coefficient first increases then decreases as the phase becomes more polar. This can be rationalized by viewing *m* as being the result of dispersive and inductive solute–solvent interactions, the configurational entropy and the cavity formation processes in the solvent. The *a* coefficients for the DB-1, DB-5, DB-17 and DB-210 columns are not significant. The functional groups in these phases are known to be very weak acceptors of hydrogen bonds based on their effect on the spectra of Kamlet–Taft indicators that are able to donate hydrogen bonds[53]. However, the standard deviations of the fit are too large to let us see the low basicity of these phases. In contrast, 3-cyanopropylphenyl methylsilicone has a significant basicity [β(propyl cyanide) = 0.43], thus the *a* coefficients for the three cyano phases (DB-1301, DB-1701 and DB-225) are significant and as expected increase as the percentage of the 3-cyanopropyl group increases. DB-WAX is both the most acidic [α(ethylene glycol) = 0.90] and basic [β(ethylene glycol) = 0.52] phase studied so its *a* and *b* coefficients are the largest. These coefficients agree well with the qualitative basicity, acidity, polarity and London potential of the similar phases given by Chong *et al.*[54]. Thus despite the overall poor precision of these fits all the coefficients can be rationalized.

TABLE IV

SUMMARY OF STANDARD DEVIATIONS OF THE FITS OBTAINED IN ALL STUDIES[a]

All results pertain to 45°C except where noted.

Model	*Column type*								
	DB-1	*DB-5*	*DB-1301*	*DB-1701*	*DB-17*	*DB-210*	*DB-225*	*DB-WAX*	*DB-WAX*[g]
V_I + solvatochromic parameters[a]	0.24	0.25	0.26	0.28	0.34	0.30	0.34	0.41	0.37
$\log L^{16}$ + solvatochromic parameters[b]	0.08	0.08	0.13	0.13	0.15	0.17	0.19	0.31	0.23
$\log L^{16} + \log k'_{\text{DB-WAX,115°C}}$[c]	0.08	0.08	0.12	0.13	0.18	0.33	0.13	0.15	0.09
$\log k'_{\text{DB-1,115°C}} + \log k'_{\text{DB-WAX,115°C}}$[d]	0.11	0.09	0.15	0.15	0.16	0.32	0.12	0.15	0.09
$\log L^{16} + \log k'_{\text{DB-WAX,115°C}}$[e] + solvatochromic parameters	0.06	0.06	0.10	0.08	0.09	0.09	0.07	0.15	0.04
$\log k'_{\text{DB-1,115°C}} + \log k'_{\text{DB-WAX,115°C}}$[f] + solvatochromic parameters	0.08	0.07	0.11	0.09	0.07	0.09	0.06	0.13	0.04
$\log L^{16}$ + solvatochromic parameters[b] (115°C)	0.07	0.07	0.10	0.10	0.12	0.13	0.15	0.22	0.20
$\log L^{16}$ + solvatochromic parameters[b] (80°C)	0.06	0.08	0.10	0.11	0.13	0.14	0.17	0.25	0.22
$\log L^{16}$ + solvatochromic parameters[b] (25°C)	0.10	0.09	0.16	0.15	0.16	0.18	0.21	0.37	0.24

[a] Data were regressed against eqn. 1.
[b] Data were regressed against eqn. 2.
[c] Data were regressed against eqn. 3.
[d] Data were regressed against eqn. 4.
[e] Data were regressed against eqn. 5.
[f] Data were regressed against eqn. 6.
[g] Amines were excluded from the data sets (see text).

TABLE V

REGRESSION COEFFICIENTS BASED ON log L^{16} AND SOLVATOCHROMIC PARAMETERS[a]

Eqn. 2 is the regression equation employed. Standard deviations of the coefficients are given in parentheses.

Column	*T*(°C)	SP_0	*l*	*s*	*a*	*b*	*d*	*S.D.*	*r*	*n*	*f*	R^a	$R_{crit.}$[b]
DB-1	115	−1.88	0.49	−[c]	−[c]	−[c]	0.13	0.07	0.9944	53	0.09	2.39	1.10
		(0.03)	(0.01)				(0.03)						
DB-5	115	−2.15	0.52	0.33	−[c]	−[c]	−[c]	0.07	0.9947	53	0.09	2.67	1.10
		(0.03)	(0.01)	(0.03)									
DB-1301	115	−2.37	0.53	0.52	0.47	−[c]	−[c]	0.10	0.9897	52	0.12	2.03	1.10
		(0.05)	(0.01)	(0.05)	(0.07)								
DB-1701	115	−2.37	0.51	0.75	0.66	−[c]	−[c]	0.10	0.9902	53	0.12	2.15	1.10
		(0.04)	(0.01)	(0.05)	(0.07)								
DB-17	115	−2.48	0.51	0.81	−[c]	−[c]	0.11	0.12	0.9860	52	0.14	2.06	1.07
		(0.06)	(0.02)	(0.07)			(0.05)						
DB-210	115	−2.41	0.42	1.36	−0.20	−[c]	−0.21	0.13	0.9777	53	0.16	1.76	1.14
		(0.07)	(0.02)	(0.07)	(0.10)		(0.05)						
DB-225	115	−2.58	0.46	1.48	0.93	−[c]	−[c]	0.15	0.9799	53	0.18	1.71	1.10
		(0.07)	(0.02)	(0.07)	(0.11)								
DB-WAX	115	−2.60	0.45	1.69	1.94	−[c]	−[c]	0.22	0.9679	53	0.25	1.39	1.10
		(0.10)	(0.02)	(0.10)	(0.16)								

[a] Ratio of the *f* values in Table III and Table V.

[b] $R_{crit.}$ was calculated by eqn. 5 or eqn. 6 in ref. 52 at a confidence level of 99%.

[c] These coefficients were found to be not significantly different from zero and were omitted in the final fit.

What is most important to note is the nearly monotonic deterioration in the goodness of fit as measured by either the root mean square residual (S.D.) or the correlation coefficient (r) as the phase polarity increases (see Table III). Because we will compare various models and data sets in terms of the overall standard deviations all of the important comparisons are compiled in Table IV for easy reference. In comparing the various models only the worst case results at the extreme temperature (45°C) are given in Table IV. The results at other temperatures using eqn. 2 are also given in this table.

As expected, based on the work of Abraham and co-workers[27,51], all correlations improved significantly when log L^{16} was used in place of V_I (see F test[52] in Table V). In all cases, the f ratio R is greater than $R_{crit.}$. In fact for the non-polar phases (the DB-1 and DB-5 columns) quite acceptable correlations *versus* log L^{16} were obtained. The regression coefficients (s, a and b) of the solvatochromic parameters are slightly different when eqn. 2 is used compared to eqn. 1. First, the b coefficient is insignificant for all phases, and not all of the d coefficients are significant. The l, s and a coefficients make chemical sense for the same reasons as stated for the V_I regression (eqn. 1), with the exception of the small negative a coefficient for DB-210. We also note (see Tables IV and V) that the fit quality still decreases as the phase polarity increases. Again we want to point out that the DB-WAX column gave particularly poor results. A detailed examination of the data set for this column showed that a large part of the variance for the DB-WAX phase at lower temperatures was due to the amine solutes. We note here that the amines gave very respectable peak shapes on all the other columns at all temperatures but they gave broad tailed peaks on the DB-WAX column at low temperatures. It is quite possible that the peak maximum is not a good measure of retention under these conditions and consequently the data for the amines may be invalid. However, we did not want to bias the results by deleting them from the analysis. When we do so the S.D. values for the DB-WAX phase drop to the level of the other phases as shown in the last column in Table IV.

There are two distinct categories of explanations for the lack of fit. First, our experimental k' values might be imprecise. Second, the model itself might be wrong and/or the parameters inaccurate. The lack of fit exhibited in the above sets of data is definitely not due to random experimental errors in the measurements of k'. If all or most of the variance in the fits were due to random errors in the measurement of the k' values then fits of log k' to $1/T$ (Van 't Hoff plots) should be only marginally better than fits to any model dependent correlations such as eqns. 1 and 2. In fact we examined plots of log k' *vs.* $1/T$ for each solute on each column and invariably obtained very good straight lines. The S.D. values for fits of log k' *vs.* $1/T$ for a single compound ranged from as low as 0.005 to in some cases as high as 0.04. Typically the S.D. values for this type of fit were about 0.02. These are far better than any of the results reported for regressions of log k' *vs.* either model equation. We are convinced that the average standard deviations reported in Tables III, IV and V are not due to the experimental precision in the measurement of log k'.

One possible source of model error in this study, not previously encountered in other linear solvation energy studies, is that the data (k' values) were not obtained at 25°C. We note that the solvatochromic parameters π^*, α and β are generally measured at room temperature and they are known to be at least somewhat temperature dependent[55,56]. The results given in Table IV indicate that, if anything, the fits at 45°C

are worse than the fits at higher temperatures. Thus we felt this explanation to be unlikely. This was confirmed by using the above-mentioned Van 't Hoff plots to extrapolate the log k' values to 25°C. These data were then regressed *vs.* eqn. 2. As shown in Table IV the average standard deviations at 25°C are, if anything, worse than those at higher temperatures. We must conclude that either eqn. 2 is an invalid model of retention or that the parameters are incorrect.

At this point we want to emphasize a purely empirical but very useful observation. We tested a "double" linear regression model[57], that is, retention data on two extremely different columns were used as the explanatory variables. The regression equations tested were:

$$\log k'(T) = SP_0 + l \log k'_{\text{DB-1,115°C}} + w \log k'_{\text{DB-WAX,115°C}} \quad (3)$$

$$\log k'(T) = SP_0 + l \log L^{16} + w \log k'_{\text{DB-WAX,115°C}} \quad (4)$$

where $k'_{\text{DB-1,115°C}}$ and $k'_{\text{DB-WAX,115°C}}$ denote the capacity factors on the DB-1 and DB-WAX columns obtained at a temperature of 115°C.

Refer to Table IV for a comparison to the preceding regressions. As expected there were improvements in the fits for the polar phases, but not for the phases of intermediate and low polarity. For the non-polar phase, either log L^{16} or the retention on DB-1 give about the same results. The F test shows that log L^{16} is slightly better than DB-1 for 4 data sets. Use of just the double regression cannot explain all the data, that is, the average S.D. is not yet at 0.02.

Finally we added the solvatochromic parameters as additional explanatory variables (eqns. 5 and 6).

$$\log k' = SP_0 + l \log L^{16} + w \log k'_{\text{DB-WAX,115°C}} + s\pi_2^* + d\delta_2 + a\alpha_2 + b\beta_2 \quad (5)$$

$$\log k' = SP_0 + l \log k'_{\text{DB-1,115°C}} + w \log k'_{\text{DB-WAX,115°C}} + s\pi_2^* + d\delta_2 + a\alpha_2 + b\beta_2 \quad (6)$$

The results are given in Tables VI and VII. Again see Table IV for a summary. Clearly the use of retention on two extremely different types of columns in addition to the solvatochromic parameters as explanatory variables significantly improved the goodness of fit. The average standard deviations for all the columns are now considerably better than in any of the preceding fits although they still exceed 0.02, which we feel represents the level of exhaustive fitting, as obtained in fits of log k' to $1/T$. In any case the fits are now as good as those observed in previous studies of liquid chromatography.

The improvement in the fits is purely statistical. By using retention on two extreme types of columns we have weakened the dependence of log k' on all of the solvatochromic parameters. That is, the fitting coefficients s, a and b in eqns. 5 and 6 are a good deal smaller than those in eqns. 1 and 2. Consequently the values of π_2^*, α_2 and β_2, and therefore errors in these parameters, now have less influence on the computed log k' values. Obviously experimental imprecision in the measured retentions on the DB-1 and the DB-WAX columns will be reflected in the precision of the computed log k' values.

The above is admittedly a highly empirical approach in that retention on the

TABLE VI

FINAL MULTIPLE REGRESSION RESULTS WITH log L^{16}, DB-WAX RETENTION AND SOLVATOCHROMIC PARAMETERS

Eqn. 5 is the regression equation employed. Standard deviations of the coefficients are given in parentheses.

Column	*T(°C)*	*Int.*	*l*	*w*	*s*	*a*	*b*	*d*	*S.D.*	*r*	*n*	*f*
DB-1	150	−2.07	0.43	—[a]	—[a]	—[a]	—[a]	0.15	0.09	0.9898	53	0.09
		(0.03)	(0.01)					(0.03)				
	115	−1.81	0.47	0.07	—[a]	—[a]	—[a]	0.07	0.06	0.9967	53	0.07
		(0.02)	(0.01)	(0.01)				(0.02)				
	80	−1.56	0.55	0.15	—[a]	—[a]	−0.11	—[a]	0.05	0.9980	53	0.06
		(0.03)	(0.01)	(0.01)			(0.03)					
	45	−1.28	0.66	0.22	—[a]	—[a]	−0.21	−0.11	0.06	0.9980	53	0.05
		(0.04)	(0.01)	(0.02)			(0.04)	(0.03)				
DB-5	150	−1.76	0.37	0.18	—[a]	−0.34	—[a]	—[a]	0.06	0.9942	53	0.07
		(0.04)	(0.01)	(0.02)		(0.06)						
	115	−1.53	0.41	0.22	—[a]	−0.44	−0.12	—[a]	0.05	0.9971	53	0.07
		(0.05)	(0.01)	(0.02)		(0.06)	(0.04)					
	80	−1.43	0.51	0.22	—[a]	−0.21	−0.13	—[a]	0.05	0.9978	53	0.07
		(0.05)	(0.01)	(0.02)		(0.06)	(0.04)					
	45	−1.32	0.64	0.24	—[a]	—[a]	−0.16	−0.09	0.07	0.9978	53	0.06
		(0.04)	(0.01)	(0.02)			(0.05)	(0.03)				
DB-1301	115	−1.64	0.40	0.28	—[a]	—[a]	—[a]	—[a]	0.08	0.9935	52	0.09
		(0.03)	(0.01)	(0.02)								
	80	−1.23	0.45	0.38	—[a]	—[a]	−0.13	−0.09	0.07	0.9968	52	0.08
		(0.04)	(0.01)	(0.02)			(0.05)	(0.03)				
	60	−0.96	0.49	0.46	—[a]	—[a]	−0.18	−0.16	0.08	0.9959	52	0.08
		(0.05)	(0.01)	(0.02)			(0.06)	(0.03)				
	45	−0.77	0.52	0.52	—[a]	—[a]	−0.22	−0.20	0.10	0.9949	52	0.08
		(0.06)	(0.01)	(0.02)			(0.07)	(0.04)				
DB-1701	150	−1.40	0.26	0.39	0.12	−0.34	−0.23	−0.07	0.04	0.9973	53	0.04
		(0.09)	(0.01)	(0.03)	(0.05)	(0.07)	(0.04)	(0.02)				
	115	−1.31	0.33	0.41	0.20	−0.14	−0.19	−0.11	0.05	0.9981	53	0.05
		(0.08)	(0.01)	(0.03)	(0.05)	(0.07)	(0.03)	(0.02)				
	80	−1.12	0.42	0.46	0.26	—[a]	−0.23	−0.18	0.06	0.9973	53	0.07
		(0.05)	(0.01)	(0.02)	(0.05)	—[a]	(0.05)	(0.03)				
	60	−0.82	0.45	0.55	0.19	—[a]	−0.26	−0.22	0.07	0.9967	53	0.07
		(0.07)	(0.01)	(0.03)	(0.07)		(0.06)	(0.03)				
	45	−0.89	0.53	0.50	0.35	0.29	−0.30	−0.27	0.08	0.9966	53	0.07
		(0.16)	(0.03)	(0.06)	(0.10)	(0.13)	(0.07)	(0.04)				

DB-17	150	−1.44 (0.05)	0.25 (0.01)	0.42 (0.03)	−[a]	−0.89 (0.09)	−[a]	0.08 (0.04)	0.09	0.9905	52	0.08
	115	−1.18 (0.05)	0.29 (0.01)	0.52 (0.02)	−[a]	−0.98 (0.08)	−[a]	−[a]	0.08	0.9940	52	0.09
	80	−0.91 (0.05)	0.35 (0.01)	0.59 (0.02)	−[a]	−1.03 (0.08)	−[a]	−[a]	0.08	0.9953	52	0.10
	45	−0.91 (0.17)	0.48 (0.03)	0.56 (0.06)	0.24 (0.11)	−0.85 (0.13)	−[a]	−[a]	0.09	0.9961	52	0.08
DB-210	115	−1.09 (0.13)	0.19 (0.02)	0.52 (0.05)	0.52 (0.09)	−1.19 (0.10)	−[a]	−0.27 (0.03)	0.07	0.9937	53	0.08
	80	−0.87 (0.13)	0.25 (0.02)	0.58 (0.05)	0.62 (0.09)	−1.24 (0.11)	−[a]	−0.34 (0.03)	0.07	0.9950	53	0.10
	60	−0.77 (0.15)	0.30 (0.03)	0.61 (0.06)	0.71 (0.10)	−1.22 (0.12)	−[a]	−0.39 (0.03)	0.08	0.9949	53	0.10
	45	−0.64 (0.16)	0.34 (0.03)	0.65 (0.06)	0.78 (0.11)	−1.24 (0.14)	−[a]	−0.43 (0.04)	0.09	0.9948	53	0.09
DB-225	150	−0.95 (0.13)	0.10 (0.02)	0.66 (0.05)	0.36 (0.08)	−0.51 (0.11)	−0.18 (0.06)	−0.07 (0.03)	0.07	0.9948	53	0.07
	115	−0.96 (0.11)	0.19 (0.02)	0.64 (0.04)	0.45 (0.07)	−0.29 (0.09)	−[a]	−0.08 (0.03)	0.06	0.9967	53	0.07
	80	−0.80 (0.06)	0.27 (0.01)	0.68 (0.02)	0.57 (0.05)	−[a]	−[a]	−0.12 (0.03)	0.06	0.9974	53	0.07
	45	−0.26 (0.06)	0.31 (0.01)	0.84 (0.02)	0.53 (0.05)	−[a]	−[a]	−0.19 (0.03)	0.07	0.9979	53	0.05
DB-WAX	80	0.48 (0.02)	−[a]	1.16 (0.02)	−[a]	−[a]	0.10 (0.05)	−[a]	0.07	0.9962	49	0.08
	60	0.88 (0.02)	−[a]	1.29 (0.03)	−[a]	−[a]	−[a]	−[a]	0.12	0.9891	45	0.13
	45	1.19 (0.03)	−[a]	1.39 (0.04)	−[a]	−[a]	−[a]	−[a]	0.15	0.9836	45	0.14

[a] These coefficients were found to be not significantly different from zero and were omitted in the final fit.

TABLE VII

FINAL MULTIPLE REGRESSION RESULTS WITH DUAL-COLUMN RETENTION AND SOLVATOCHROMIC PARAMETERS

Eqn. 6 is the regression equation employed. Standard deviations of the coefficients are given in parentheses.

Column	*T*(°C)	*Int.*	*l*	*w*	*s*	*a*	*b*	*d*	*S.D.*	*r*	*n*	*f*
DB-1	150	−0.41 (0.01)	0.89 (0.01)	—[a]	—[a]	—[a]	—[a]	—[a]	0.06	0.9953	53	0.06
	80	0.48 (0.01)	1.17 (0.02)	0.03 (0.01)	—[a]	—[a]	—[a]	—[a]	0.06	0.9970	53	0.08
	45	1.23 (0.03)	1.37 (0.02)	0.12 (0.02)	—[a]	—[a]	−0.23 (0.06)	−0.20 (0.03)	0.08	0.9967	53	0.07
DB-5	150	−0.37 (0.01)	0.79 (0.02)	0.09 (0.02)	—[a]	−0.26 (0.06)	—[a]	—[a]	0.06	0.9952	53	0.06
	115	−0.02 (0.01)	0.92 (0.02)	0.10 (0.01)	—[a]	−0.28 (0.05)	—[a]	—[a]	0.05	0.9977	53	0.06
	80	0.42 (0.01)	1.12 (0.02)	0.07 (0.01)	—[a]	—[a]	—[a]	—[a]	0.07	0.9966	53	0.08
	45	1.07 (0.02)	1.37 (0.02)	0.12 (0.02)	—[a]	—[a]	—[a]	−0.16 (0.03)	0.08	0.9970	53	0.07
DB-1301	115	−0.13 (0.01)	0.84 (0.02)	0.21 (0.02)	—[a]	—[a]	—[a]	—[a]	0.08	0.9935	52	0.09
	80	0.39 (0.02)	0.99 (0.03)	0.23 (0.03)	—[a]	0.16 (0.09)	—[a]	—[a]	0.09	0.9938	52	0.11
	60	0.81 (0.02)	1.09 (0.03)	0.32 (0.03)	—[a]	0.19 (0.10)	—[a]	−0.20 (0.04)	0.10	0.9943	52	0.10
	45	1.22 (0.04)	1.09 (0.03)	0.44 (0.03)		—[a]	−0.23 (0.08)	−0.27 (0.05)	0.11	0.9932	52	0.10
DB-1701	150	−0.36 (0.01)	0.50 (0.02)	0.40 (0.01)	—[a]	−0.39 (0.04)	−0.20 (0.03)	−0.09 (0.02)	0.04	0.9981	53	0.04
	115	0.04 (0.02)	0.62 (0.02)	0.45 (0.02)	—[a]	−0.26 (0.06)	−0.17 (0.04)	−0.14 (0.02)	0.05	0.9975	53	0.06
	80	0.56 (0.02)	0.81 (0.02)	0.47 (0.02)	—[a]	—[a]	−0.15 (0.05)	−0.20 (0.03)	0.07	0.9962	53	0.09
	60	0.94 (0.02)	0.89 (0.02)	0.54 (0.02)	—[a]	—[a]	−0.20 (0.05)	−0.25 (0.03)	0.08	0.9963	53	0.08
	45	1.29 (0.03)	0.95 (0.03)	0.60 (0.02)	—[a]	—[a]	−0.28 (0.06)	−0.32 (0.04)	0.09	0.9955	53	0.08

DB-17	150	−0.49 (0.01)	0.53 (0.03)	0.39 (0.02)	−[a]	−0.87 (0.09)	−[a]	−[a]	0.09	0.9907	52	0.08
	115	-0.09 (0.01)	0.62 (0.02)	0.45 (0.02)	−[a]	−0.92 (0.07)	−[a]	−[a]	0.07	0.9951	52	0.08
	80	0.39 (0.01)	0.75 (0.02)	0.50 (0.02)	−[a]	−0.96 (0.07)	−[a]	−[a]	0.07	0.9964	52	0.08
	45	1.03 (0.01)	0.92 (0.03)	0.58 (0.02)	−[a]	−0.98 (0.08)	−[a]	−[a]	0.08	0.9967	52	0.07
DB-210	115	−0.38 (0.04)	0.42 (0.04)	0.47 (0.05)	0.54 (0.08)	−1.13 (0.10)	−[a]	−0.29 (0.03)	0.07	0.9946	53	0.08
	80	0.09 (0.05)	0.55 (0.05)	0.53 (0.05)	0.62 (0.09)	−1.18 (0.11)	−[a]	−0.37 (0.03)	0.07	0.9955	53	0.09
	60	0.38 (0.05)	0.66 (0.05)	0.55 (0.06)	0.72 (0.09)	−1.15 (0.12)	−[a]	−0.43 (0.03)	0.08	0.9956	53	0.09
	45	0.66 (0.06)	0.74 (0.06)	0.58 (0.06)	0.79 (0.10)	−1.16 (0.13)	−[a]	−0.47 (0.04)	0.09	0.9955	53	0.08
DB-225	150	−0.65 (0.05)	0.27 (0.05)	0.57 (0.05)	0.34 (0.09)	−0.36 (0.11)	−[a]	−[a]	0.08	0.9936	53	0.08
	115	−0.26 (0.03)	0.42 (0.04)	0.59 (0.04)	0.48 (0.06)	−0.22 (0.08)	−[a]	−0.11 (0.02)	0.05	0.9976	53	0.06
	80	0.23 (0.02)	0.56 (0.02)	0.64 (0.02)	0.55 (0.04)	−[a]	−[a]	−0.16 (0.02)	0.05	0.9984	53	0.06
	45	0.94 (0.02)	0.64 (0.02)	0.80 (0.02)	0.50 (0.05)	−[a]	−[a]	−0.23 (0.02)	0.06	0.9984	53	0.04
DB-WAX	80	0.56 (0.03)	−0.05 (0.02)	1.24 (0.03)	−0.20 (0.06)	−[a]	0.16 (0.05)	−[a]	0.07	0.9969	49	0.08
	60	0.98 (0.05)	−0.10 (0.04)	1.43 (0.05)	−0.37 (0.10)	−[a]	0.23 (0.08)	−[a]	0.10	0.9927	45	0.11
	45	1.33 (0.06)	−0.14 (0.05)	1.58 (0.06)	−0.51 (0.12)	−[a]	0.32 (0.10)	−[a]	0.13	0.9895	45	0.11

[a] These coefficients were found to be not significantly different from zero and were omitted in the final fit.

more polar reference column depends on and correlates with the solvatochromic parameters. The degree of coveriance is not so high as to cause excessive variance inflation (see below) in the regression coefficients.

All of the results shown in Tables VI and VII are much more precise than the results given in Tables III and V. Before discussing the details of these results we should state that other pairs of "reference" columns were evaluated. There are no appreciable differences in the quality of the fits whether we use log L^{16} or the retention on DB-1. Since retention data on commercial permethyl silicone oil columns are easier to obtain than are data on hexadecane columns and for very polar solutes are less likely to show interfacial effects, we opted to use the data obtained with a DB-1 column instead of the log L^{16} data. Second, we found that the DB-WAX column was the best polar "reference" column. By this we mean that it gave good fits for all other types of columns while columns of intermediate polarity only served to correlate results for lesser and equally polar phases but failed to correlate the results for more polar columns. Thus the overall quality of the regression markedly improved as the polarity of the second reference column increased.

The above "double-reference" column empirical approach greatly complicates the chemical interpretation of the coefficients *s, d, a* and *b* in eqns. 5 and 6. This complication comes about because both the signs and the magnitude of these coefficients now have meaning only in relation to the nature of the reference columns. If retention on the non-polar reference column were utterly insensitive to solute hydrogen bond acidity and basicity then the observed *a* and *b* coefficients for eqns. 5 and 6 would depend only on the characteristics of the test column and the more polar reference column. However, *s* and *d* do vary between different non-polar references ($\log k'_{\text{DB-1,115°C}}$ and log L^{16}), thus *s* and *d* will, in general, depend upon the properties of both reference columns.

Despite the chemical complications in interpreting the solvatochromic coefficients obtained when retention data are fit to equations such as 5 and 6, the approach does lead to an empirical scheme for precise classification of phases. Phases with similar chemical structures will have similar phase coefficients (*l, w, s, d, a* and *b*). When eqn. 6 is used the most important coefficients will be *l* and *w*. Phases which chemically resemble DB-1 will have a significant *l* coefficient and a small value for *w, a* and *b*. Similarly, a phase which is *identical* to the DB-WAX column will have a large *w* coefficient and statistically negligible values for *l, s, d, a* and *b*. For intermediate polarity phases, the *l* and *w* coefficients will lie between the above two extreme cases. Solute–stationary phase interactions different from those in DB-WAX will be reflected in the respective coefficients of the solvatochromic parameters.

In order to see how the solvatochromic regression method can be used to classify columns, consider the data plotted in Fig. 1. The column type is displayed on the *x*-axis and the two most important coefficients (*l* and *w*) are plotted on the *y*-axis. Note the "I" bars indicate the precision of the *l* and *w* coefficients. Only data for 45°C are shown in the figure. It is evident that the DB-1 and DB-5 columns are numerically very similar since both *l* and *w* are identical for both columns. This is hardly surprising since DB-1 and DB-5 are chemically very similar (see Table II). We also note that the DB-1701 and DB-17 columns have both *l* and *w* values which are statistically indistinguishable. Table II indicates that these two columns ought to be chemically distinct since the DB-1701 is a 14% cyanopropylphenyl methyl silicone oil and the DB-17 is a 50%

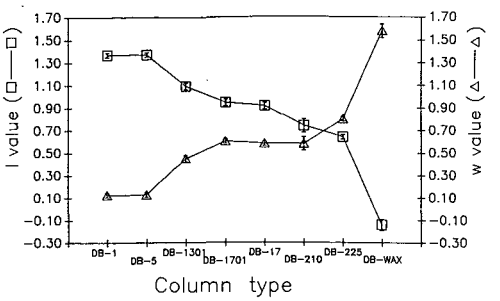

Fig. 1. Classification of columns according to *l* and *w* coefficients.

phenyl methylsilicone oil. A reviewer pointed out to us that 1701 type materials were introduced as alternatives to 17 type phases. Thus in retrospect it is interesting that such chemically different materials were classified as being so similar by our approach. However, this apparent failure to differentiate these two chemically distinct phases based on *l* and *w* is not real. Inspection of Fig. 2 which shows plots of *s*, *a*, *b* and *d versus* column type demonstrate that the DB-17 column has a very large negative *a* coefficient (−0.98) whereas the *a* value for the cyano phase is quite small, *i.e.* the basicity of the DB-1701 is much stronger than that of DB-17. In fact when all of the fitting coefficients are considered no two of these columns are seen to be chemically equivalent within the statistics of the fit. The discriminating power of the approach is related to the precision of the overall fits to the model equation. Thus any two phases whose coefficients differ by more than the indicated brackets are chemically distinct.

The effect of temperature on the two leading coefficients (*l* and *w*) is shown in Fig. 3 where results at 45, 80 and 115°C are shown. In this plot we use the two coordinates *l* and *w* to define a "phase plane". At a given temperature *l* and *w* are almost linearly related. We see the near coincidence of the DB-1 and DB-5 columns, and the DB-1701 and DB-17 columns at 45°C. At a higher temperature this similarity in terms of *l* and *w* for the pairs of columns no longer persists.

The present classification scheme is also useful in a predictive sense. Suppose that one wants to discriminate between two or more species which differ primarily in their hydrogen bond donor characteristics, the present method suggests the use of a column with the greatest overall dependence on *w* and *a*. The applicability of this idea will be explained in subsequent communications.

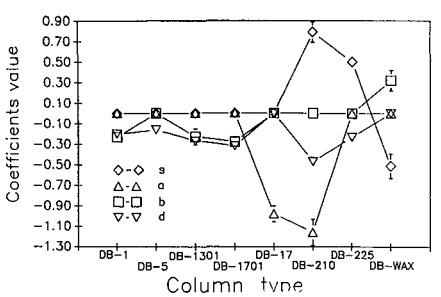

Fig. 2. Classification of columns according to solvatochromic parameter coefficients.

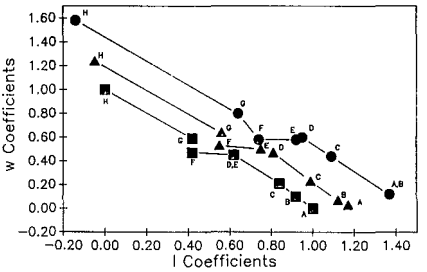

Fig. 3. Column polarity (*l* and *w* coefficients) *vs.* temperature. A = DB-1; B = DB-5; C = DB-1301; D = DB-1701; E = DB-17; F = DB-210; G = DB-225; H = DB-WAX. ● = 45°C; ▲ = 80°C; ■ = 115°C.

ACKNOWLEDGEMENT

This work was supported in part by grants to the University of Minnesota from the National Science Foundation and the Petroleum Research Foundation.

SUPPLEMENTARY MATERIAL AVAILABLE

All the log capacity factors are available either on a computer disk or on paper upon request.

REFERENCES

1 L. Rohrschneider, *J. Chromatogr.*, 22 (1966) 6.
2 L. Rohrschneider, *Adv. Chromatogr.*, 4 (1967) 333.
3 L. Rohrschneider, *J. Chromatogr.*, 39 (1969) 383.
4 W. O. McReynolds, *J. Chromatogr. Sci.*, 8 (1970) 685.
5 J. A. Yancey, *J. Chromatogr. Sci.*, 24 (1986) 117.
6 C. F. Poole and S. K. Poole, *Chem. Rev.*, 89 (1989) 377.
7 C. F. Poole, S. K. Poole, R. M. Pomaville and B. R. Kersten, *J. High Resolut. Chromatogr. Chromatogr. Commun.*, 10 (1987) 670.
8 M. B. Evans and J. K. Haken, *J. Chromatogr.*, 472 (1989) 93.
9 P. H. Weiner and D. G. Howery, *Anal. Chem.*, 44 (1972) 7.
10 P. H. Weiner, C. J. Dack and D. G. Howery, *J. Chromatogr.*, 69 (1972) 249.
11 P. H. Weiner and D. G. Howery, *Canadian J. Chem.*, 50 (1972) 448.
12 P. Laffort and F. Patte, *J. Chromatogr.*, 126 (1976) 625.
13 F. Patte, M. Etcheto and P. Laffort, *Anal. Chem.*, 54 (1982) 2239.
14 L. R. Snyder, *J. Chromatogr. Sci.*, 16 (1978) 223.
15 R. V. Golovnya and T. A. Misharina, *J. High Resolut. Chromatogr. Chromatogr. Commun.*, 3 (1980) 51.
16 M. B. Evans and J. K. Haken, *J. Chromatogr.*, 406 (1987) 105.
17 P. Farkas, L. Sojak, M. Kovac and J. Janak, *J. Chromatogr.*, 471 (1989) 251.
18 V. G. Berezkin and A. A. Korolev, *Chromatographia*, 22 (1985) 482.
19 T. Juutilainen and J. Enqvist, *J. Chromatogr.*, 279 (1983) 91.
20 M. J. Kamlet, J. L. Abboud and R. W. Taft, *J. Am. Chem. Soc.*, 99 (1977) 6027.
21 M. J. Kamlet, R. M. Doherty, M. H. Abraham, Y. Marcus and R. W. Taft, *J. Phys. Chem.*, 92 (1988) 5244.
22 R. W. Taft, J. L. Abboud and M. J. Kamlet, *J. Am. Chem. Soc.*, 103 (1981) 1080.
23 R. W. Taft and M. J. Kamlet, *J. Am. Chem. Soc.*, 98 (1976) 2886.
24 M. J. Kamlet and R. W. Taft, *J. Am. Chem. Soc.*, 98 (1976) 377.
25 M. H. Abraham, P. P. Duce, P. L. Grellier, D. V. Prior, J. J. Morris and P. J. Taylor, *Tetrahedron Lett.*, 29 (1988) 1587.

26 M. H. Abraham, P. L. Grellier, D. V. Prior, P. J. Taylor, C. Laurence and M. Berthelot, *Tetrahedron Lett.*, 30 (1989) 2571.
27 M. H. Abraham, P. L. Grellier, R. A. McGill, R. M. Doherty, M. J. Kamlet, T. N. Hall, R. W. Taft, P. W. Carr and W. J. Koros, *Polymer*, 28 (1987) 1363.
28 R. W. Taft, J.-L. M. Abboud, M. J. Kamlet and M. H. Abraham, *J. Solution Chem.*, 14 (1985) 153.
29 M. J. Kamlet and R. W. Taft, *Acta Chem. Scand.*, B 39 (1985) 611.
30 P. C. Sadek and P. W. Carr, *J. Chromatogr.*, 288 (1984) 25.
31 P. C. Sadek, P. W. Carr, R. M. Doherty, M. J. Kamlet, R. W. Taft and M. H. Abraham, *Anal. Chem.*, 57 (1985) 2971.
32 P. W. Carr, R. M. Doherty, M. J. Kamlet, R. W. Taft, W. Melander and C. Horvath, *Anal. Chem.*, 58 (1986) 2674.
33 J. H. Park, P. W. Carr, M. H. Abraham, R. W. Taft, R. M. Doherty and M. J. Kamlet, *Chromatographia*, 25 (1988) 373.
34 M. J. Kamlet, M. H. Abraham, P. W. Carr, R. M. Doherty and R. W. Taft, *J. Chem. Soc., Perkin Trans. 2*, (1988) 2087.
35 J. H. Park and P. W. Carr, *J. Chromatogr.*, 465 (1989) 123.
36 W. J. Cheong and P. W. Carr, *J. Chromatogr.*, 500 (1990) 215.
37 S. C. Rutan, P. W. Carr and R. W. Taft, *J. Phys. Chem.*, 93 (1989) 4293.
38 M. J. Kamlet, R. W. Taft, P. W. Carr and M. H. Abraham, *J. Chem. Soc. Faraday Trans. 1*, 78 (1982) 1689.
39 J. E. Brady, D. Bjorkman, C. D. Hexter and P. W. Carr, *Anal. Chem.*, 56 (1984) 278.
40 M. H. Abraham, P. L. Grellier and R. A. McGill, *J. Chem. Soc., Perkin Trans. 2*, (1987) 797.
41 M. H. Abraham, University of Surrey, personal communication, 1989.
42 Y. Zhang, A. J. Dallas and P. W. Carr, in preparation.
43 M. J. Kamlet, *Solute Solvatochromic Parameters for Use in Solubility, Partition and Toxicology Correlations*, May, 1987, unpublished work.
44 C. Laurence, M. Berthelot, M. Herbert and S. Sraidi, *J. Phys. Chem.*, 93 (1989) 3799.
45 M. H. Abraham, P. J. Grellier, D. V. Prior, R. W. Taft, J. J. Morris, P. J. Taylor, C. Laurence, M. Berthelot, R. M. Doherty, M. J. Kamlet, J. M. Abboud, K. Sraidi and G. Guiheneuf, *J. Am. Chem. Soc.*, 110 (1989) 8534.
46 D. E. Leahy, *J. Pharm. Sci.*, 75 (1986) 629.
47 R. S. Pearlman, in W. J. Dunn, J. H. Block and R. S. Pearlman (Editors), *Partition Coefficient Determination and Estimation*, Pergamon Press, New York, 1986, p. 3.
48 S. Bondi, *J. Phys. Chem.*, 68 (1964) 441.
49 M. H. Abraham and J. C. McGowan, *Chromatographia*, 24 (1987) 242.
50 M. H. Abraham and R. Fuchs, *J. Chem. Soc., Perkin Trans. 2*, (1988) 523.
51 M. H. Abraham, G. J. Buist, P. L. Grellier, R. A. McGill, R. M. Doherty, M. J. Kamlet, R. W. Taft and S. G. Maroldo, *J. Chromatogr.*, 409 (1987) 15.
52 S. Ehrenson, *J. Org. Chem.*, 44 (1979) 1783.
53 J. E. Brady, *Ph.D. Thesis*, University of Minnesota, Minneapolis, 1984.
54 E. Chong, B. deBriceno, G. Miller and S. Hawkes, *Chromatographia*, 20 (1985) 293.
55 P. Nicolet and C. Laurance, *J. Chem. Soc., Perkin Trans. 2*, (1986) 1071.
56 C. Laurance, P. Nicolet and M. Helbert, *J. Chem. Soc., Perkin Trans. 2*, (1986) 1081.
57 M. H. Abraham, M. J. Kamlet, R. W. Taft, R. M. Doherty and P. K. Weathersby, *J. Med. Chem.*, 28 (1985) 865.

Journal of Chromatography, 517 (1990) 123–129
Elsevier Science Publishers B.V., Amsterdam

CHROMSYMP. 1943

Capillary gas chromatography with graphitized carbon black

F. BRUNER*, G. CRESCENTINI, F. MANGANI and L. LATTANZI
Istituto di Scienze Chimiche, Università di Urbino, Piazza Rinascimento 6, 61029 Urbino (Italy)

ABSTRACT

The outstanding properties of fused-silica capillary columns coated with graphitized carbon black impregnated with liquid phases are described together with the details of their preparation. HETP *vs.* $\bar{u}$ curves are reported, together with some separations of industrial and environmental interest. Fast and more effective analyses may be achieved with such columns.

INTRODUCTION

The technology of capillary columns has reached highly sophisticated levels and the main research in the field of capillary gas chromatography (GC) is addressed toward two main aspects: extremely high performance in terms of HETP[1], and a search for very selective stationary phases and the development of high-temperature GC[2].

We have been studying selective stationary phases for GC through the development of columns containing graphitized carbon blacks (GCB) coated with suitable percentages and quality of stationary phases[3,4].

The success of this technique, called gas–liquid–solid chromatography (GLSC), is due to the peculiar properties of GCB and to the particular working mechanism, involving adsorption and interaction with the liquid stationary phase[3]. Further, linear elution and a low HETP are obtained for polar compounds using polar stationary phases. Very selective packed columns have been developed, which are nowadays widely used in environmental and industrial analysis[4].

In the last few years, our efforts have been devoted to the preparation of fused-silica capillary columns with the aim of coupling the high separation factors of GLSC with the large number of theoretical plates achievable in capillary chromatography. In early works[5,6] we showed that high performance and fast analysis can be achieved with these columns. In a recent paper[7] we also showed that very high reproducibility can be obtained in the preparation of these columns.

In this paper we report further progress made in the preparation of fused-silica capillary columns with GCB, which is mainly due to the use of an extremely fine particle size.

0021-9673/90/$03.50

EXPERIMENTAL

The preparation of the columns is based on a two-step procedure that can be summarized as follows: (a) preparation of a slurry where the adsorbent (GCB) and the liquid phase (SP1000) are mixed together in a suitable solvent and sonicated; (b) coating of the capillary columns by means of a static method.

Step (a) has been greatly modified with the aim of obtaining a slurry with a very fine particle size. This can be accomplished by considering that the maximum power of the sonicator is obtained when the slurry solvent is water and that a high sonication power is required when an organic solvent is used. The GCB (Carbopack B in this instance) is wet-sieved via a multi-stadium sieving cascade using water as medium. The material of finest particle size (< 20 μm) is sonicated in water by means of high-power sonicator (Model 450, Branson, Danbury, CT, U.S.A.) for 30 min. The slurry is then dried by means of a vacuum pump and methylene chloride–*n*-pentane (50:50) containing 35% (w/w) (with respect to the carbon black) of SP1000 is added. The container is shaken and sonicated again for 30 min.

The coating step (b) does not differ substantially from that described previously[4], which is a modification of the method of Xu and Vermeulen[8] (free-release static coating) for the preparation of glass capillaries. Essentially the slurry is pushed into the capillary by heating the slurry reservoir at 60°C and the solvent is then evaporated while the column is kept at a temperature higher than the boiling point of the solvent mixture[4].

Two types of column with different I.D. (0.25 and 0.53 mm) were tested. A Carlo Erba Model 5160 Mega chromatograph equipped with both split–splitless and on-column injectors and a Dani Model 8510 chromatograph equipped with a PTV injector were used. Fused-silica tubing and Carbopack B were kindly supplied by Supelco (Bellefonte, PA, U.S.A.).

RESULTS AND DISCUSSION

Fig. 1 shows scanning electron micrographs of the carbon black layer on the inner wall of the fused-silica capillary. The particle dimensions cannot be easily evaluated but they seem to be in the region of 10^{-2} μm. With the procedure described previously dimensions of about two orders of magnitude larger were obtained[4]. The graphite layer appears to be homogeneous.

In Fig. 2 the Van Deemter plots of three columns with two different inner diameters (0.53 mm for columns A and B and 0.25 mm for column C) are shown. The columns contained Carbopack B coated with SP1000 to different extents. The surface coverage values (Θ), obtained by using a method described in detail elsewhere[7], are 1.2 for column A and 4.5 for columns B and C. The obvious difference in the B term of the Van Deemter equation for columns of different diameter is shown by the large difference in both the value of the minimum HETP (H_{min}) and of the resistance to mass transfer term, C. Column B shows a lower H_{min} than column A but a higher value of C. The latter may be due to the lower homogeneity of the adsorbing layer containing a small amount of stationary phase, but the former is more difficult to explain.

The behaviour of the 0.53-mm I.D. columns is more like that of a packed than a capillary column. The only advantage of these large-bore capillary columns seems to

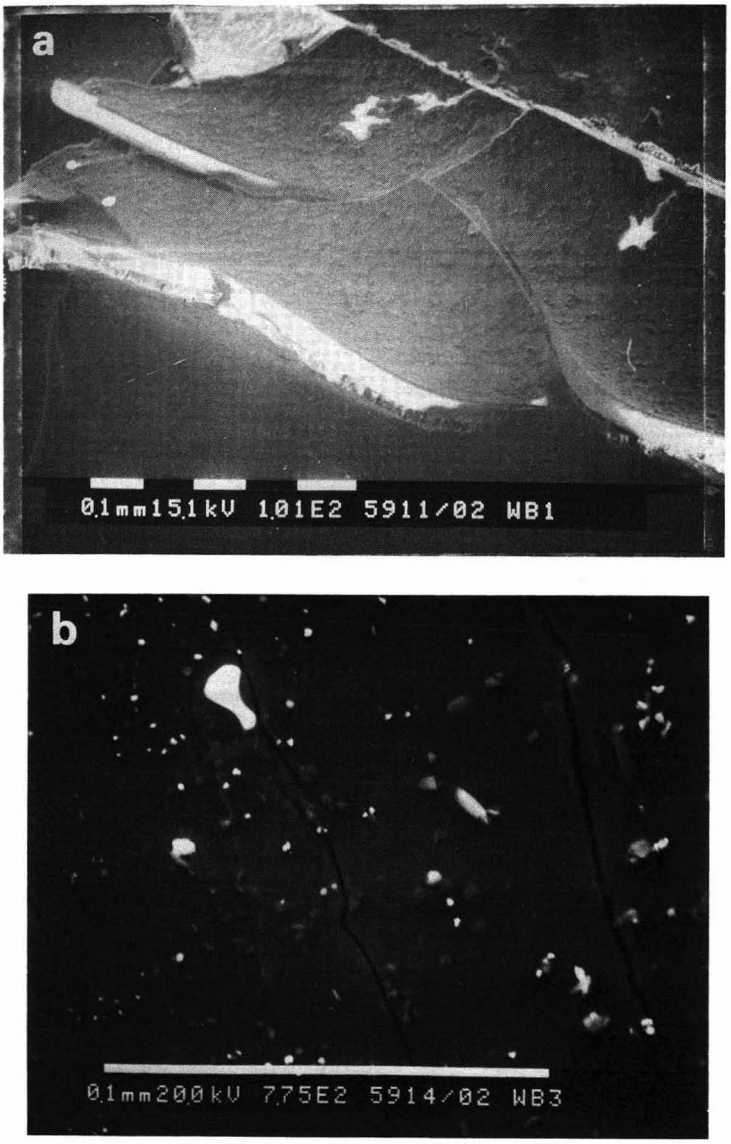

Fig. 1. Scanning electron micrographs of the inner wall of fused-silica capillary columns (C and A, see Fig. 2) coated with Carbopack B + SP1000.

be that the inlet pressure is of course much lower than for a packed column, with the possibility of making longer columns. There is also an increase in sample capacity owing to the larger surface area, which is, however, difficult to evaluate.

Further, as these columns are used in GLSC, where the mechanism is controlled by adsorption, the advantages of using wide-bore columns are even less important than in conventional capillary gas–liquid chromatography (GLC). It is concluded,

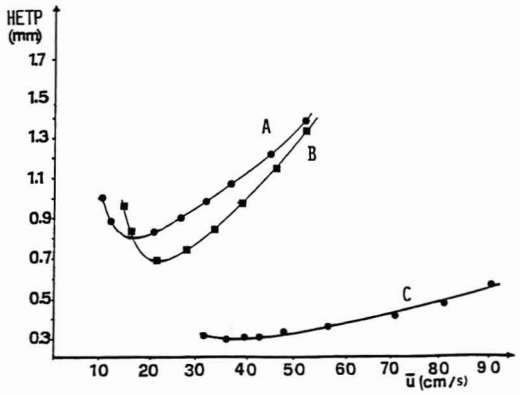

Fig. 2. Van Deemter plots obtained with three fused-silica capillary columns coated with Carbopack B + SP1000: (A) 33 m × 0.53 mm I.D.; (B) 33 m × 0.53 mm I.D.; (C) 24 m × 0.25 mm I.D. Sample, *n*-dodecane ($k' = 7$); carrier gas, hydrogen.

from a theoretical and kinetic point of view, that wide-bore columns seem not to represent progress in capillary chromatography.

Column C shows outstanding properties from the kinetic point of view. H_{min} occurs at about 40 cm/s and shows a coating efficiency of about 80% with a measured H_{min} of 0.29 mm.

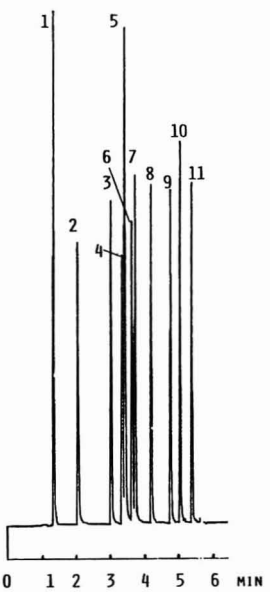

Fig. 3. Separation with a fused-silica capillary column (24 m × 0.25 mm I.D.) coated with Carbopack B + 5% SP1000. Peaks: 1 = benzene; 2 = toluene; 3 = ethylbenzene; 4 = *p*-xylene; 5 = *m*-xylene; 6 = isopropylbenzene; 7 = *o*-xylene; 8 = *n*-propylbenzene; 9 = 1,3,5-trimethylbenzene; 10 = *p*-cymene; 11 = *n*-butylbenzene. Column temperature: 1.5 min at 70°C, then heated at 20°C/min to 160°C and held to the end. Carrier gas, hydrogen; linear velocity, 40 cm/s; sample volume, 0.1 μl; splitting ratio, 1:100; flame ionization detection (FID).

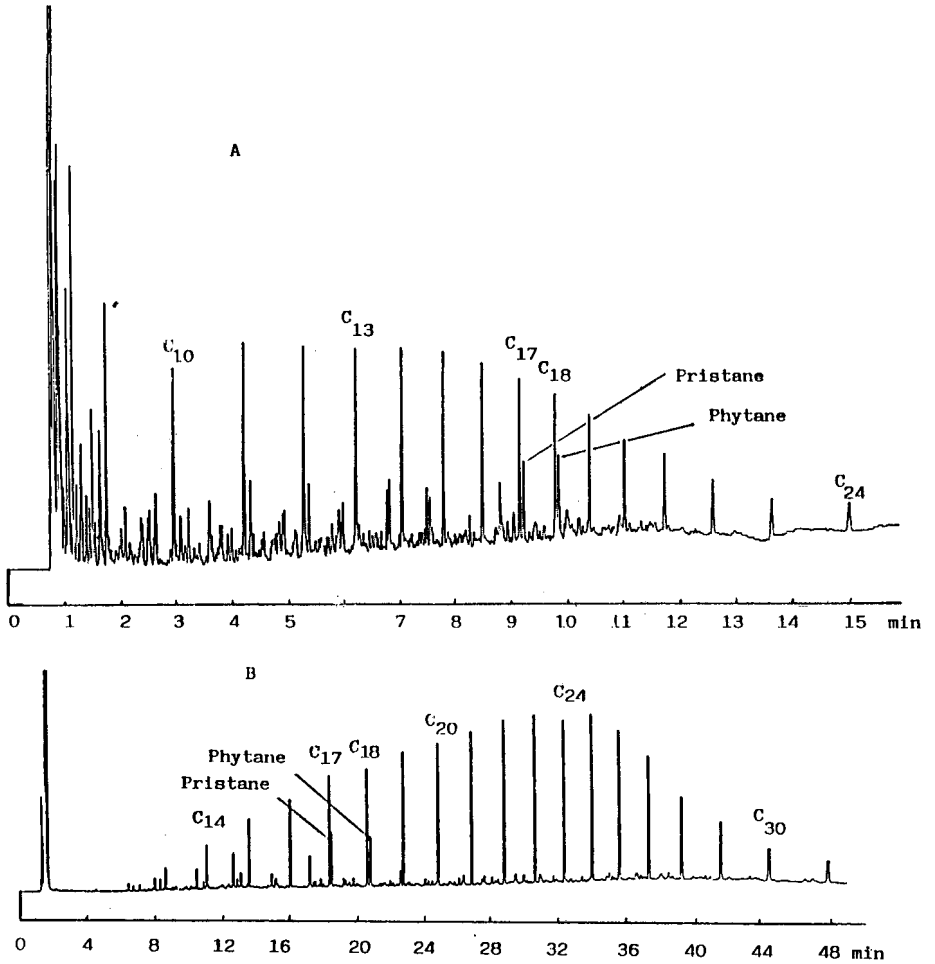

Fig. 4. (A) Separation with a fused-silica capillary column (24 m × 0.25 mm I.D.) coated with Carbopack B + SP1000. Column temperature: 2 min at 60°C, then heated at 20°C/min to 230°C and held to the end. Carrier gas, hydrogen; linear velocity, 50 cm/s; sample, 0.05 μl of Iran crude oil; splitting ratio, 1;100; FID ($8 \cdot 10^{-11}$ a.u.f.s.). (B) Separation with an SE-54 fused-silica capillary column (30 m × 0.25 mm I.D.). Column temperature, 2 min at 100°C, then heated at 5°C/min to 270°C and held to the end. Carrier gas, hydrogen; linear velocity, 42 cm/s; sample, 0.1 μl of crude shale oil; splitting ratio, 67:1; FID ($8 \cdot 10^{-11}$ a.u.f.s.).

In a theoretical treatment, Giddings[9] showed that for a highly porous and homogeneous adsorbent the C term should be as low as 10^{-7}, provided that the surface area of the adsorbent is very high (10^3 m^2/g). In practice, however, an adsorbent with both of these properties is not available, but GCB represents a good compromise, being a non-porous and homogeneous adsorbent. In this instance it is reasonable[4,9] to assume $C = 10^{-4}$. In fact, the value calculated from the Van Deemter plot is $2.2 \cdot 10^{-4}$, which is very close to the theoretical value. It should be pointed out that this value is hardly reached in GLC, so that GLSC capillary columns can yield a better resolution in a shorter time.

TABLE I

LIST OF PRIORITY POLLUTANTS SEPARATED

No.	*Compound*	*No.*	*Compound*
1	Chloromethane	19	*trans*-1,3-Dichloropropene
2	Dichlorodifluoromethane	20	Toluene
3	Bromomethane	21	Tetrachloroethylene
4	Vinyl chloride	22	*cis*-1,3-Dichloropropene
5	Trichlorofluoromethane	23	1-Chloro-2-bromopropane
6	1,1-Dichloroethylene	24	2-Chloroethyl vinyl ether
7	*trans*-1,2-Dichloroethylene	25	Bromodichloromethane
8	1,1,1-Trichloroethane	26	Ethylbenzene
9	Carbon tetrachloride	27	Chlorobenzene
10	*cis*-1,2-Dichloroethylene	28	1,1,2-Trichloroethane
11	1,1-Dichloroethane	29	Dibromochloromethane
12	Methylene chloride	30	1,4-Dichlorobutane
13	Benzene	31	Bromoform
14	Trichloroethylene	32	1,1,2,2-Tetrachloroethane
15	Chloroform	33	1,3-Dichlorobenzene
16	Bromochloromethane	34	1,4-Dichlorobenzene
17	1,2-Dichloropropane	35	1,2-Dichlorobenzene
18	1,2-Dichloroethane		

In Fig. 3 the separation of some aromatic compounds is illustrated and the high resolving power of the GLSC capillary column is shown. An almost baseline separation of the three xylenes is obtained in less than 6 min without any overlapping of possibly interfering compounds.

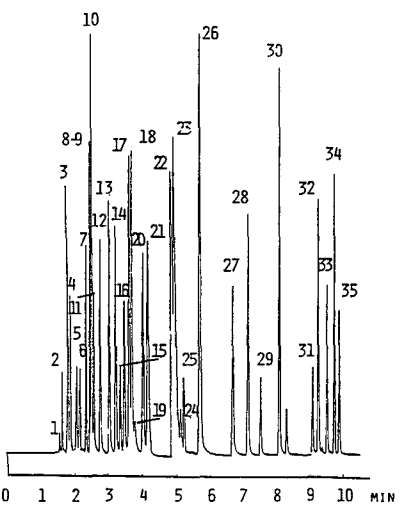

Fig. 5. Separation of 35 priority pollutants. Peak numbers as in Table I. Fused-silica capillary column (33 m × 0.53 mm I.D.) coated with Carbopack B + SP1000. Column temperature, 2 min at 30°C, then heated at 20°C/min to 200°C and held to the end. Carrier gas, hydrogen; linear velocity, 30 cm/s; sample volume, 0.1 μl; splitting ratio, 1:100; FID.

In Fig. 4 the separation of the components of a crude oil with the critical pairs *n*-C_{17}–pristane and *n*-C_{18}–phytane is shown and compared with that obtained with a GLC column with the same resolving power. The operating conditions were different as they were adjusted in each instance to obtain the best performance. The separation of interest is obtained more than twice as fast on the Carbopack B column. Of course, as our column is more retentive the overall analysis is stopped at C_{24}.

In order to show the high resolving power of these columns, a separation of 35 priority pollutants (Table I) is shown in Fig. 5. This separation, obtained in only 10 min, is one of the fastest and the most effective reported for this kind of mixture. The separations in Figs. 4 and 5 were obtained with columns A and B in Fig. 1, respectively.

In conclusion, the results given here represent the most recent achievements in GLSC with capillary columns and in our opinion provide the best demonstration that our aim of coupling a high value of α with a large number of theoretical plates has almost bean achieved. More research with the use of different stationary phases is needed in order to achieve more complete results.

REFERENCES

1 P. A. Leqlercq and C. A. Cramers, *J. High Resolut. Chromatogr. Chromatogr. Commun.*, 8 (1985) 764.
2 E. Gearaert and P. Sandra, *J. High Resolut. Chromatogr. Chromatogr. Commun.*, 8 (1985) 415.
3 F. Bruner, G. Crescentini, F. Mangani and M. Xiang, *Ann. Chim. (Rome)*, 77 (1987) 745.
4 F. Bruner, G. Crescentini, F. Mangani, P. Palma and M. Xiang, *J. Chromatogr.*, 399 (1987) 87.
5 F. Bruner, P. Ciccioli, G. Crescentini and M. T. Pistolesi, *Anal. Chem.*, 45 (1973) 1851, and references cited therein.
6 A. Di Corcia and A. Liberti, *Adv. Chromatogr.*, 14 (1976) 305, and references cited therein.
7 F. Bruner, G. Crescentini, F. Mangani and L. Lattanzi, *J. Chromatogr.*, 473 (1989) 93.
8 B. Xu and N. P. E. Vermeulen, *Chromatographia*, 18 (1984) 520.
9 J. C. Giddings, *Anal. Chem.*, 36 (1964) 1170.

Journal of Chromatography, 517 (1990) 131–142
Elsevier Science Publishers B.V., Amsterdam

CHROMSYMP. 2000

Pesticide analysis by gas chromatography with a novel atomic emission detector

PHILIP L. WYLIE*
Hewlett-Packard Co., P.O. Box 900, Rt. 41 and Starr Road, Avondale, PA 19311 (U.S.A.)
and
RIMIKO OGUCHI
Yokogawa Electric Corporation, 2-9-32 Nakacho, Musashino-shi, Tokyo 180 (Japan)

ABSTRACT

An atomic emission detector, consisting of a microwave-induced helium plasma and atomic emission spectrometer, has been used for the gas chromatographic analysis of pesticides. In principle, it is possible to detect any element in the periodic table (except helium) which can elute from a gas chromatograph. Detection limits for C, H, D, N, O, Br, Cl, F, S, Si, P, Sn and Hg were found to range from 0.1 to 75 pg/s with selectivities over carbon of 5000 or more. The gas chromatography–atomic emission detection system has been used for the detection and elemental characterization of 27 different pesticides by obtaining element-specific chromatograms for C, H, N, O, Br, Cl, F, P and S. By performing quantitative analysis for each element, it was possible to calculate the approximate empirical formulas for 20 different herbicides in two different mixtures. An extract from an apple doped with three pesticides was analyzed by gas chromatography–atomic emission detection.

INTRODUCTION

Several United States Environmental Protection Agency (EPA)-approved methods exist for the gas chromatographic (GC) analysis of pesticides including Methods 505 (ref. 1), 608 (ref. 2) and 8080 (ref. 3) (organohalide pesticides and polychlorinated biphenyls), 507 (ref. 4, 69 pesticides), 508 (ref. 5, 32 chlorinated pesticides), 515 (ref. 6, chlorinated acid herbicides), 8140 (ref. 3, organophosphorus pesticides) and 8150 (ref. 3, chlorinated herbicides). Numerous methods exist for the analysis of pesticide residues on foods. Two popular multi-residue methods are those developed by Luke[7,8] and the California Department of Food and Agriculture[9].

Four different selective detection methods are used in these methods: electron-capture detection (ECD) or electrolytic conductivity detection (ELCD) for halogenated compounds, nitrogen–phosphorus detection (NPD) for nitrogen- and phosphorus-containing pesticides, and flame photometric detection (FPD) for sulfur or phosphorus compounds.

While the above-mentioned detectors have proven to be very useful for the

0021-9673/90/$03.50

selective detection of heteroatoms in pesticides, each has certain inherent limitations. ECD is the most sensitive GC detection method for polyhalogenated compounds, but it is not very selective, responding strongly to other electronegative functional groups. Even for halogenated compounds, ECD response is not proportional to the number of halogens in a molecule and it is typically not linear beyond about two orders of magnitude. NPD sensitivity can vary over time and some types of chemical bonding can greatly reduce its sensitivity to nitrogen. For sulfur, FPD response is not linear and suffers from quenching of the signal by co-eluting compounds. Of the detection methods mentioned, ELCD is perhaps the most difficult to operate, requiring frequent maintenance and strict avoidance of contaminants.

Pesticides almost always contain heteroatoms and often have several in a single molecule. The most frequently encountered elements are C, H, O, P, S, N, Cl, Br, F and metals such as As, Hg and Zn[10]. For the analysis of complex environmental samples containing pesticides, it would be useful to have a single GC detector capable of specific element detection for any element encountered in a pesticide; indeed, a complete profile of all the elements in a pesticide molecule would greatly aid in its identification.

Detectors which combine plasma excitation with optical emission spectroscopy have been used for the selective detection of many organic and inorganic elements. Three recent reviews describe various plasma-atomic emission spectroscopy (AES) systems which have been developed as GC detectors[11–13]. Several investigators have reported analyzing pesticides using GC–plasma-AES systems[14–18].

The Hewlett-Packard (HP) 5921A atomic emission detection (AED) system used for this investigation has been described elsewhere[19–24]. The detector employs a microwave-induced helium plasma as the atomization and excitation source. This design was chosen because the energy of the helium plasma was sufficient to excite all elements in the periodic table and because it only required 100–200 ml/min of helium. In contrast, inductively coupled plasmas typically require many liters of argon or helium per minute.

This paper describes the use of this new GC–AED system for the analysis of pesticides. An objective was to show specific element detection for all of the most common elements found in pesticide formulations. Therefore a variety of insecticides and herbicides was analyzed showing specific element detection of C, H, N, O, P, F, Cl and Br. Typical detection limits and selectivities were determined for several elements.

By performing quantitative analyses on every element in an unknown molecule it should be possible to calculate its empirical formula. Several researchers have reported the results of such calculations with mixed results[24–26]. This work represents an initial investigation into the feasibility of determining complete empirical formulas for pesticides using this commercially available GC–AED system.

EXPERIMENTAL

GC–AED system

A prototype of the HP 5921A atomic emission detector was coupled to an HP 5890A gas chromatograph. Papers detailing the design and performance of the GC–AED system have appeared elsewhere[19,20].

The HP 5890A GC system was equipped with a HP 7673A automatic injector and split–splitless capillary injection port which was operated at 200–300°C, depending on the sample. Three HP columns were employed: (A) 25 m × 0.32 mm I.D. × 0.17 μm film HP-1 operated at a helium flow-rate of 1.05 ml/min (21.8 cm/s), (B) 50 m × 0.2 mm I.D. × 0.5 μm film HP-5; helium flow-rate 0.39 ml/min (21 cm/s) and (C) 25 m × 0.32 mm I.D. × 0.17 μm film HP-5; helium flow-rate 0.95 ml/min (19.7 cm/s).

Samples

Diazinon (VAP Special Products), alachlor (Monsanto), metolachlor (Ciba-Geigy), chlorpyrifos (Dow), and prometon (Ciba-Geigy) were all obtained as commercial pesticide preparations from local suppliers. They were received as 25, 45.1, 86.4, 40.7 and 25% solutions, respectively, which were diluted 1:100 in hexane or methanol. Capillary GC was performed with a 100:1 split ratio. Two herbicide mixtures containing nine and thirteen compounds, respectively, were obtained from Supelco (Bellefonte, PA, U.S.A.) as solutions of 100 μg/ml each in ethyl acetate. The herbicide mixtures were analyzed as received using a 55:1 split ratio for the detection of C, H, N, Cl, Br and S and a 12:1 split ratio for the F and O analyses.

The analysis of pesticides spiked into an apple was conducted as follows. A solution of chlorpyrifos, endosulfan I and endosulfan II was injected into a 20-g wedge-shaped apple slice so that the pesticides would be present at 680, 337 and 330 ppb[a], respectively. The apple was chopped up and blended for 3 min with 40 ml of acetonitrile in a Sorvall Omni Mixer. The solution was filtered rapidly by suction into a flask containing about 10 g of sodium chloride and the layers were allowed to separate. A 4-ml aliquot of the organic layer was evaporated to near-dryness with a stream of nitrogen and the residue was taken up in 2 ml of acetone. Analysis of the acetone solution was performed by GC-AED using 1-μl splitless injections.

RESULTS AND DISCUSSION

When extracted from water, soil or plant material, pesticides are often isolated together with numerous other synthetic and natural organic compounds. Contamination from laboratory ware (especially phthalates from plastics) and solvents is another source of concern. Element-selective detection methods such as ECD, FPD, NPD and ELCD are used for GC analysis as a way of "isolating" the halogen-, sulfur-, nitrogen- or phosphorus-containing pesticides from these contaminants. Of course, when a contaminant contains the monitored heteroatom or when the detection method (particularly ECD) is not sufficiently selective, spurious peaks arise.

Pesticides are usually very rich in heteroatoms with most having two to four elements present in addition to C and H. Using GC–AED it is possible to monitor every element in a pesticide (albeit, with varying sensitivities) providing multiple channels of corroborative data.

Table I lists several elements by groups which could be observed simultaneously along with detection limits (MDL) and selectivities which have been obtained with this system. As is commonly done for plasma detectors, the MDL values are expressed as pg/s of the element which gives a signal-to-noise ratio of 2. These values

[a] Throughout this article, the American billion (10^9) is meant.

TABLE I

TYPICAL DETECTION LIMITS AND SELECTIVITIES OBTAINED USING GC–MIP–AES

Group	*Element*	*Wavelength (nm)*	*MDL (pg/s)*	*Selectivity*
I	N	174.2	7.0	6 000
	S	180.7	1.7	150 000
	Hg	184.9	0.1	>1 000 000
	C	193.1	0.5	
II	P	177.5	1.5	25 000
III	C	247.9	2.6	
	Si	251.6	7.0	90 000
	Hg	253.7	0.1	>1 000 000
IV	Br	478.6	75	19 000
	Cl	479.5	39	25 000
	H	486.1	2.2	
	C	247.9 (2^{nd} order)	12	
V	D	656.1	2.5	600 *vs.* H
	H	656.3	3.0	
VI	F	685.6	40	30 000
VII	O	777.2	75	25 000

can be easily converted to the detection limit for a compound (in pg). The detection limit for a given element from Table I is multiplied by the GC peak width and the compound's molecular weight divided by the gram atoms of the element in the analyte. Selectivities are with respect to C except for deuterium which is relative to H.

Fig. 1 shows a multi-element-specific chromatogram of diazinon ($C_{12}H_{21}N_2O_3PS$). Three sequential chromatographic runs were required to obtain chromatograms for C, S, N, P and H. The chromatograms for C, S and N were obtained simultaneously using oxygen and hydrogen scavenger gases. While the emission line for P falls in the same region (177.5 nm), it required hydrogen as the only

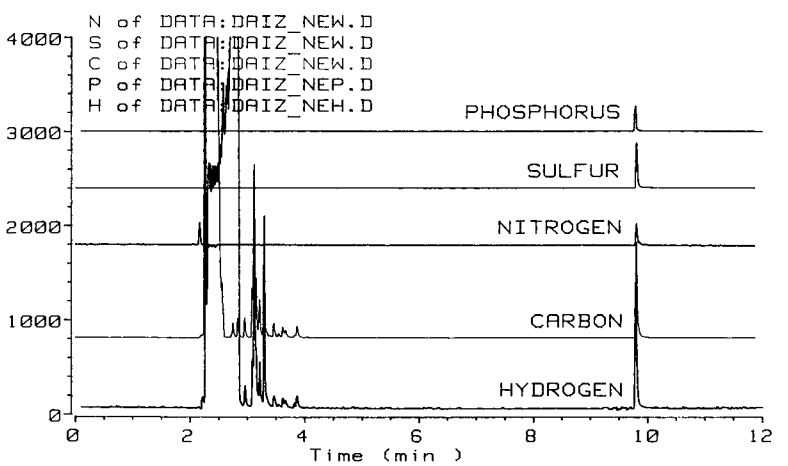

Fig. 1. GC-AED analysis of diazinon using column A. Oven temperature program: 100°C (1 min), 10°C/min to 250°C; inlet and transfer line/cavity temperatures 200°C.

scavenger gas and, therefore, had to be determined separately. The H chromatogram was obtained in a third run at 486.1 nm using only oxygen as scavenger. The three sequential runs were fully automated from the GC–AED system's controller.

Current procedures for the analysis of pesticides typically obtain only one element-specific chromatogram providing two-dimensional data (presence of the element plus retention time). In addition to the retention time, the presence of five constituent elements was confirmed using AED. Of particular interest are the chromatograms for S, N and P. Their presence combined with the retention time would usually be sufficient to identify the pesticide. Quantitation could be done using any (or all) of the elements present. This flexibility can be very useful if interfering compounds appear in one element channel but not in another.

Fig. 2 shows four element-specific traces for alachlor ($C_{14}H_{20}ClNO_2$); C, H and Cl were obtained simultaneously in a single run and N from a second run. The controller's software automatically combined data from these two injections into a single file for integration, plotting or for incorporation into a report.

At the time that diazinon and alachlor were analyzed, the experimental software did not allow the collection of oxygen-specific chromatograms. Using software modified to include oxygen detection, a mixture of prometon ($C_{10}H_{19}N_5O$), chlorpyrifos ($C_9H_{11}Cl_3NO_3PS$) and metolachlor ($C_{15}H_{22}ClNO_2$) was analyzed. A complete elemental profile was obtained in four sequential analyses; seven element-specific chromatograms (C, H, N, O, Cl, P and S) are shown in Fig. 3.

Chlorpyrifos and metolachlor were not separated on an HP-1 column (column A; *cf.* Experimental) but could be partially resolved with a 50-m HP-5 column (column B). Since the three pesticides contain different atoms, it is a trivial matter to distinguish between them. In addition to C and H prometon has N and O while metolachlor has Cl, N and O. Chlorpyrifos has all seven elements.

With less than perfect resolution, quantitation of metolachlor and chlorpyrifos would be difficult using a universal, nitrogen-specific or halogen-specific detector since both compounds would respond. However, using GC–AED, chlorpyrifos could

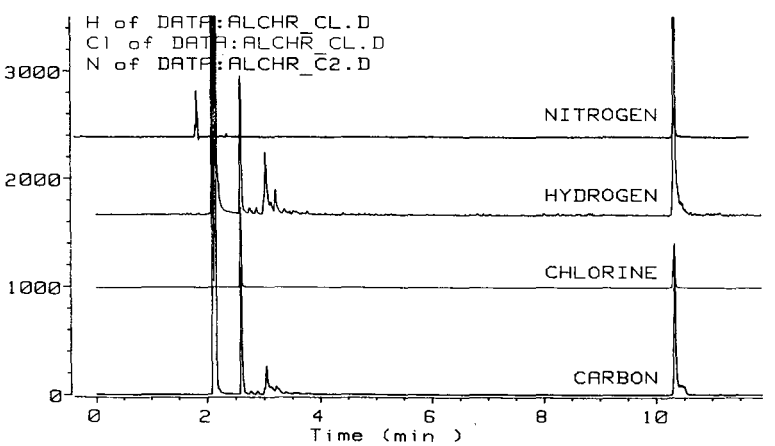

Fig. 2. GC–AED analysis of alachlor using column A. Oven temperature program: 100°C (1 min), 10°C/min to 250°C; inlet and transfer line/cavity temperatures 200°C.

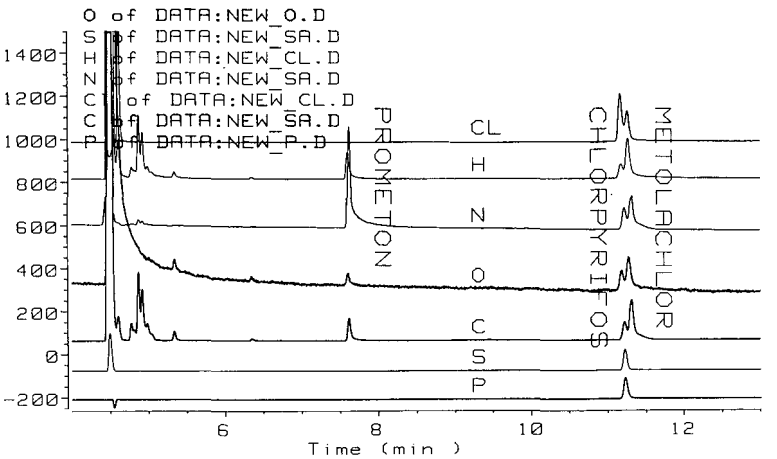

Fig. 3. GC–AED analysis of prometon, chlorpyrifos and metolachlor using column B. Oven temperature: 270°C isothermal; inlet and transfer line/cavity temperatures: 270°C and 300°C, respectively.

be quantitated using the S- or P-specific chromatograms since metolachlor gives no response on those channels. Metolachlor could then be determined by difference using the summation of the chlorpyrifos and metolachlor N signal. (Any of the five channels on which they both respond could be used.) Subtracting the known amount of chlorpyrifos would give the metolachlor amount by difference. In principle, it would not be necessary to separate the compounds at all.

A more complex mixture of 13 known herbicides (herbicide mix 1) is shown in Fig. 4 and in Table II. Eight elements are present in this mixture, including C, H, N, O, S, F, Cl and Br. The last eight peaks could easily be correlated to the known constituents by inspection. The presence or absence of peaks along with approximate peak ratios were all the information that was needed. The molecular formulas of the first five pesticides were quite similar, varying only slightly in C and H content; for these, comparison with standards was required.

Each compound was present at the 100-ng/μl level. F and O analyses were run with a 12:1 split so that 8.3 ng of each compound reached the detector. All other elements were run at a 55:1 split, delivering 1.8 ng/component to the plasma. Since AED responds to elements, not compounds, detection limits such as those in Table I are expressed in terms of the mass of an element (not molecule) which can be detected. While the amount of each herbicide reaching the detector was 1.8 ng, the amount of H detected in each of the compounds ranged from 56 pg for oxyfluorfen to 191 pg for butylate.

With a single GC detector it was possible to obtain eight different element-selective chromatograms. Of particular interest is the ability to distinguish between the halogens; neither ECD nor ELCD can do this. Since a significant number of pesticides contain either F or Br, it is helpful to detect them selectively rather than lump them together with the chlorinated pesticides.

Accurate quantitative analysis of each element should allow the analyst to calculate an empirical formula for each molecule in a mixture. Several reports have

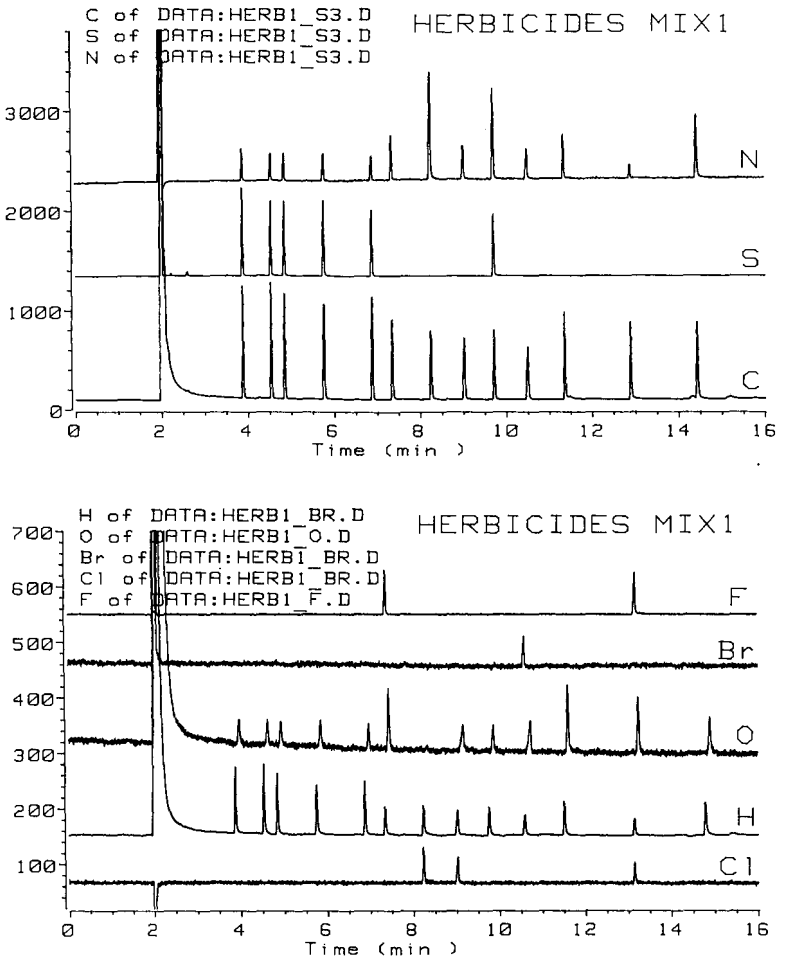

Fig. 4. GC–AED analysis of a mixture containing 13 herbicides using column C. Two plots were required to show all eight element-specific chromatograms. Compound identities and calculated elemental ratios are given in Table II. Oven temperature program: 150°C (3 min), 10°C/min to 300°C; inlet and transfer line/cavity temperatures: 280°C and 300°C, respectively.

appeared in the literature in which this has been accomplished for a limited number of elements with varying degrees of success.

Recent reports by Widmer[24] and by Sullivan and Quimby[22] have shown examples using the Hewlett-Packard GC–AED system. Widmer discussed an example for which the approximate empirical formula was generated for a compound containing C, H, O and Cl. Sullivan and Quimby used 15 different C-, H-, N- and O-containing compounds and found that approximate empirical formulas could be determined for unknowns when heteroatoms were present and certain assumptions were made about the size of the molecule. It was of interest to see if empirical formulas could be generated for the herbicides in this mixture, since between them, they contained eight different elements.

TABLE II

ELEMENTAL RATIOS CALCULATED FOR HERBICIDE MIX 1 ON THE BASIS OF GC-AED DATA (DATA WERE NORMALIZED TO KNOWN VALUES FOR C)

No.	*Herbicide molecular formula*	*Calculated elemental ratios*						
		C	*H*	*N*	*O*	*S*	*Cl*	*F*
1	EPTC $C_9H_{19}NOS$	9	15.7	0.8	1.1	0.9		
2	Butylate $C_{11}H_{23}NOS$	11	20.8	0.8	1.1	0.9		
3	Pebulate $C_{10}H_{21}NOS$	10	18.4	0.8	1.1	0.9		
4	Molinate $C_9H_{17}NOS$	9	15.1	0.9	1.0	0.9		
5	Cycloate $C_{11}H_{21}NOS$	11	17.6	0.8	1.0	0.9		
6	Trifluralin $C_{13}H_{16}N_3O_4F_3$	13	15.7	2.2	4.1			2.5
7	Atrazine $C_8H_{14}N_5Cl$	8	10.7	4.2			1.3	
8	Terbacil $C_9H_{13}N_2O_2Cl$	9	10.9	1.5	2.1		1.1	
9	Metribuzin $C_8H_{14}N_4OS$	8	11.8	3.3	1.4	I.S.		
10	Bromacil[a] $C_9H_{13}N_2O_2Br$	9	11.4	1.6	3.1			
11	Isopropalin $C_{15}H_{23}N_3O_4$	15	21.9	2.4	4.5			
12	Oxyfluorfen $C_{15}H_{11}NO_4F_3Cl$	Internal standard						
13	Hexazinone $C_{12}H_{20}N_4O_2$	12	17.7	3.0	2.4			

[a] Br was not determined.

Using oxyfluorfen as the internal standard (I.S.) (metribuzin for S), elemental ratios were calculated for the other twelve herbicides. These are summarized in Table II. No calibration was done for Br as only one Br-containing compound was present. All of the results were normalized to the known values for C.

A second mixture of 9 herbicides (herbicide mix 2; 100 ng/μl each) was analyzed under the same conditions (a minor difference is noted below) as that shown in Fig. 4. Fig. 5 shows the seven element-specific chromatograms which were obtained. Using metolachlor as the internal standard (profluralin for F), elemental ratios were calculated for each of the other herbicides. Since only one sulfur-containing compound was present, this element does not appear in the calculations. The results (normalized to carbon) are given in Table III.

The data presented in Tables II and III do not allow the determination of a precise empirical formula for most of the compounds. However, the numbers were often very close to the correct values and in every case the presence or absence of an element in an herbicide was correctly determined. It is believed that this is the first discussion of elemental ratios calculated for seven elements on the basis of GC–microwave-induced helium plasma (MIP)-AES data. These preliminary results are, in fact, very encouraging.

There are several changes in the experiment's conditions which are likely to result in even better elemental ratios. First, the herbicide mixtures were injected in the split mode which could lead to some discrimination between molecules of differing volatilities. Only one injection was made for each element group of the sample; averaging carefully integrated peak areas from multiple injections should lead to more accurate results. Second, the injection port was held at 280°C for herbicide mix 1 and 260°C for mix 2. Many pesticides are thermally labile and are known to decompose in hot injection ports. Degradation of the internal standard could lead to inaccuracies in

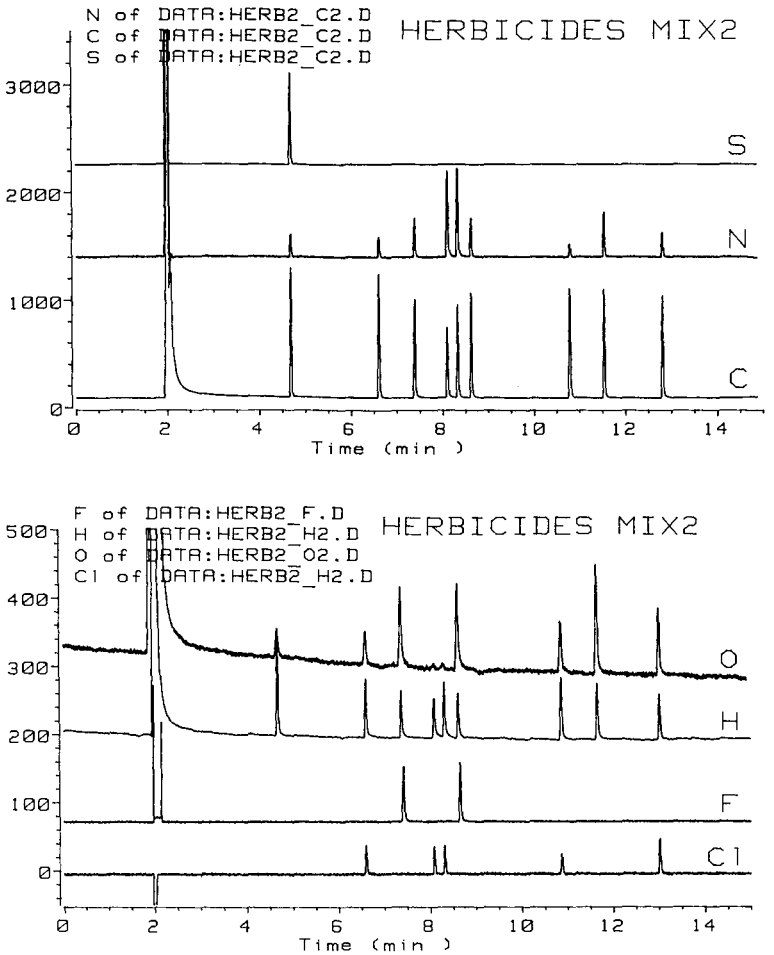

Fig. 5. GC–AED analysis of a mixture containing 9 herbicides using column C. Two plots were required to show all seven element-specific chromatograms. Compound identities and calculated elemental ratios are given in Table III. Oven temperature program: 150°C (3 min), 10°C/min to 300°C; inlet and transfer line/cavity temperatures: 260°C and 300°C, respectively.

the calculations, especially when more than one internal standard is used or if there are overlapping peaks. A possible solution for both of these potential problems is to use cool on-column injection. Calculated values for H, N and S were most often low for the 13-herbicide sample, suggesting that a different internal standard for these elements could improve the values. Widmer[24] has used multiple standards to get a closer estimation of an unknown's empirical formula.

Residue extraction experiment

In order to simulate the conditions of a real pesticide residue analysis, an apple was doped with two pesticides below the EPA action level. A solution containing chlorpyrifos ($C_9H_{11}Cl_3NO_3PS$) and endosulfan ($C_9H_6Cl_6O_3S$) was injected into a

TABLE III

ELEMENTAL RATIOS CALCULATED FOR HERBICIDE MIX 2 ON THE BASIS OF GC-AED DATA (DATA WERE NORMALIZED TO KNOWN VALUES FOR C)

No.	*Herbicide molecular formula*	*Calculated elemental ratios*					
		C	*H*	*N*	*O*	*Cl*	*F*
14	Vernolate $C_{10}H_{21}NOS$[a]	10	19.5	1.0	1.1		
15	Propachlor $C_{11}H_{14}NOCl$	11	13.3	1.0	1.0		
16	Benfluralin $C_{13}H_{16}N_3O_4F_3$	13	17.1	2.8	3.6		2.8
17	Simazine $C_7H_{12}N_5Cl$	7	11.1	4.7		0.9	
18	Propazine $C_9H_{16}N_5Cl$	9	15.0	4.6		0.9	
19	Profluralin $C_{14}H_{16}N_3O_4F_3$	14	17.7	2.8	4.4		I.S.
20	Metolachlor $C_{15}H_{22}NO_2Cl$	Internal standard					
21	Pendimethalin $C_{13}H_{19}N_3O_4$	13	19.7	3.0	4.6		
22	Oxadiazon $C_{15}H_{18}N_2O_3Cl_2$	15	18.5	2.0	3.2	1.8	

[a] Sulfur was not determined.

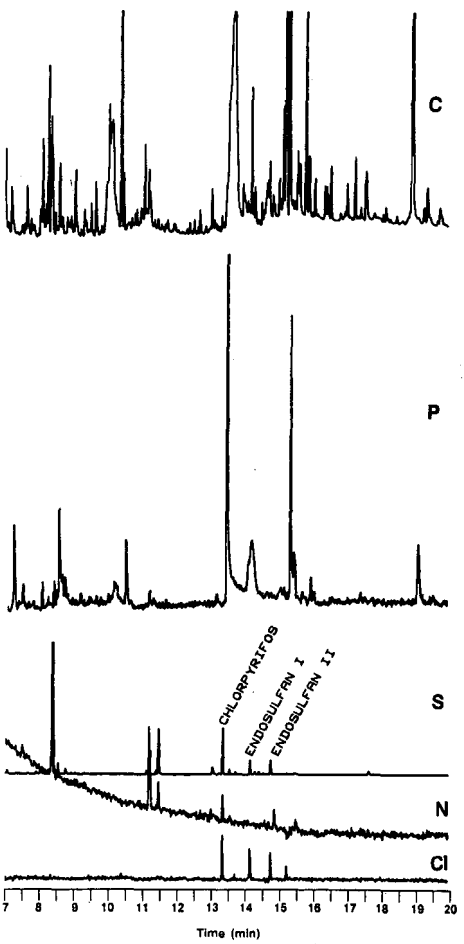

Fig. 6. GC–AED analysis of an extract from an apple doped with chlorpyrifos, endosulfan I and endosulfan II using column C. Oven temperature program: 50°C (3 min), 20°C/min to 300°C, 300°C (20 min); inlet and transfer line/cavity temperatures 300°C.

20-g wedge-shaped slice of an apple to give concentrations of 0.68 and 0.67 ppm, respectively. In apples, the EPA allows a maximum residue limit of 1.5 ppm for chlorpyrifos and 2.0 ppm for endosulfan[27]. Endosulfan was obtained as a 51:49 mixture of isomers endosulfan I and endosulfan II. In the apple their respective concentrations were 0.34 and 0.33 ppm.

Pesticides were extracted from the apple employing a slight modification of procedures used by the California Department of Food and Agriculture[9]. The carbon-selective chromatogram of the extract shown in Fig. 6 is similar to that which would be obtained from a flame ionization detector. The complexity of this chromatogram makes it clear why selective detectors are necessary for residue analyses in the absence of extensive clean-up steps.

Also shown in Fig. 6 are the element-selective chromatograms for S, N, Cl and P which were obtained from three successive injections. All of these elements are present in the chlorpyrifos peak while the endosulfan isomers show only S and Cl as expected. Oxygen was not run on this sample. In spite of the complexity of the dirty extract, these pesticides are readily seen on each of the appropriate element channels of the AED system. Coupled with the retention time, this elemental information may often be sufficient to confirm the presence of a pesticide. In other cases where similar compounds elute close together, confirmation by GC–mass spectrometry would still be required.

CONCLUSIONS

GC detectors most commonly used for pesticide methods are limited to the detection of halogens, S, N and P. ECD and ELCD cannot differentiate between F, Cl and Br. These detection methods may lack selectivity (ECD), suffer from quenching (FPD) and lack linearity (ECD and FPD). In contrast, GC–AED can, in principle, selectively detect any element in the periodic table so long as it can be analyzed by GC.

Pesticides are particularly good candidates for GC–AED analysis since they are rich in heteroatoms. Using a GC–AED system, the analyst has the choice of detecting any individual element in a molecule or of obtaining a multi-element profile.

It was possible to determine the approximate elemental composition at the low-ng level for molecules containing up to seven different elements.

The GC–AED technique shows potential as a sensitive, element-selective detector, applicable to the analysis of pesticides and many other organic and organometallic molecules. Additional work is in progress to evaluate the system for quantitative analysis and for residue analysis using a variety of pesticides doped into various fruits and vegetables. Methods for obtaining more accurate empirical formulas are also being investigated.

ACKNOWLEDGEMENT

The authors wish to thank Bruce Quimby for providing the data shown in Table I and for helpful discussions.

REFERENCES

1 *Method 505: Analysis of Organohalide Pesticides and Arochlors in Drinking Water by Microextraction and Gas Chromatography*, Physical and Chemical Methods Branch, Environmental Monitoring and Support Laboratory, U.S. Environmental Protection Agency, Cincinnati, OH, September 1986.
2 *Method 608: Organochlorine Pesticides and PCBs, Fed. Reg.*, 49, No. 209, October 26 (1984) 89.
3 *Test Methods For Evaluating Solid Waste, Vol. 1B, Laboratory Manual*, Physical/Chemical Methods, SW 846, U.S. Environmental Protection Agency, Office of Solid Waste and Emergency Response, Washington, DC, 3rd ed., November 1986.
4 *Method 507: Determination of Nitrogen- and Phosphorus-Containing Pesticides in Ground Water by Gas Chromatography with a Nitrogen-Phosphorus Detector*, Physical and Chemical Methods Branch, Environmental Monitoring and Support Laboratory, US. Environmental Protection Agency, Cincinnati, OH, September 1986.
5 *Method 508: Determination of Chlorinated Pesticides in Ground Water by Gas Chromatography with an Electron Capture Detector*, Physical and Chemical Methods Branch, Environmental Monitoring and Support Laboratory, U.S. Environmental Protection Agency, Cincinnati, OH, September 1986.
6 *Method 515: Determination of Chlorinated Herbicides in Drinking Water*, Physical and Chemical Methods Branch, Environmental Monitoring and Support Laboratory, U.S. Environmental Protection Agency, Cincinnati, OH, September 1986.
7 L. D. Sawyer, *J. Assoc. Off. Anal. Chem.*, 68 (1985) 64.
8 M. A. Luke and G. M. Doose, *Bull. Environ. Contam. Toxicol.*, 30 (1983) 110.
9 *Multi-Residue Pesticide Screens*, California Department of Food and Agriculture, Chemistry Laboratory Services Branch, Pesticide Residue Laboratories, Sacramento, CA, December 14, 1987.
10 C. R. Worthing and S. B. Walker (Editors), *The Pesticide Manual: A World Compendium*, The British Crop Protection Council, Thornton Heath, 8th ed., 1987.
11 L. Ebdon, S. Hill and R. W. Ward, *Analyst (London)*, 111 (1986) 1113.
12 P. C. Uden, *Chromatogr. Forum*, Nov./Dec. (1986) 17.
13 J. P. Matousek, B. J. Orr and M. Selby, *Prog. Anal. Atom. Spectrosc.*, 7 (1984) 275.
14 M. A. Eckhoff, T. H. Ridgway and J. A. Caruso, *Anal. Chem.*, 55 (1983) 1004.
15 T. Hanie, S. Coulombe, M. Moisan and J. Hubert, in R. M. Barnes (Editor), *Developments in Atomic Plasma Spectrochemical Analysis*, Heyden, London, 1981, pp. 337–344.
16 Y. Talmi and D. T. Bostick, *Anal. Chem.*, 47 (1975) 2145.
17 D. L. Haas and J. A. Caruso, *Anal. Chem.*, 57 (1985) 846.
18 K. E. Markides, R. J. Skelton, Jr., P. B. Farnsworth, M. L. Lee and F. J. Yang, in P. Sandra (Editor), *Proceedings of the 8th International Symposium on Capillary Chromatography, May 1987*, Huethig, Heidelberg, 1987, pp. 921–933.
19 B. D. Quimby and J. J. Sullivan, *Anal. Chem.*, 62 (1990) 1027.
20 J. J. Sullivan and B. D. Quimby, *Anal. Chem.*, 62 (1990) 1034.
21 P. L. Wylie and B. D. Quimby, *J. High Resolut. Chromatogr. Chromatogr. Commun.*, 12 (1989) 813.
22 J. J. Sullivan and B. D. Quimby, *J. High Resolut. Chromatogr. Chromatogr. Commun.*, 12 (1989) 282.
23 R. L. Firor, *Am. Lab., (Shelton, Conn.)*, May (1989) 40.
24 H. M. Widmer, *Chimia*, 43 (1989) 18.
25 P. C. Uden, K. J. Slatkavitz, R. M. Barnes and R. L. Deming, *Anal. Chim. Acta.*, 180 (1986) 401.
26 K. J. Slatkavitz, P. C. Uden, L. D. Hoey and R. M. Barnes, *J. Chromatogr.*, 302 (1984) 277.
27 *Tolerances and Exemptions from Tolerances for Pesticide Chemicals in or on Raw Agricultural Commodities*, Code of Federal Regulations 40, part 180, revised July 1, 1987, pp. 245–415.

Journal of Chromatography, 517 (1990) 143–159
Elsevier Science Publishers B.V., Amsterdam

CHROMSYMP. 1970

Turbulent flow in capillary gas chromatography — evaluation of a theoretical concept by Golay

A. J. VAN ES, J. A. RIJKS and C. A. CRAMERS*
Eindhoven University of Technology, Laboratory of Instrumental Analysis, P.O. Box 513, 5600 MB Eindhoven (The Netherlands)
with appendix by
M. J. E. GOLAY[a]
Perkin-Elmer Corporation, Norwalk, CT 06859 (U.S.A.)

ABSTRACT

Early in 1989, the late Marcel Golay derived a theory for turbulent flow capillary gas chromatography. He assumed that the flow pattern under turbulent conditions consists of a turbulent core separated from the tube wall by a very thin laminar flow layer. Further, it was assumed that the viscosity and the diffusion constant are uniform within the turbulent core. The core radius is a fraction ρ of the tube radius; the core viscosity is m times the laminar flow viscosity and the core diffusivity is assumed to be d times the laminar flow diffusion constant. Values for ρ, m and d have to be calculated from experimental data; ρ, m and d are essentially functions of Reynolds number (Re).

Using experimental data obtained in the laboratory, Golay's plate-height theory was evaluated for turbulent flow gas chromatography. In this verification an empirical relationship was used for the average turbulent diffusion constant as a function of Reynolds number and an empirical relationship for the thickness of the laminar sublayer. Further, it was assumed that $m = d$ (Reynolds' analogy). The experiments and theory agree fairly well at $Re = 6200$; at lower and higher values of Re the agreement is much poorer. The disagreement may be due to the empirical relationships used or to the postulations in the theory: Golay assumed a discontinuous change from laminar to turbulent viscosity and diffusion constants. In engineering literature often a gradual change in properties from the laminar sublayer to the turbulent and in the turbulent core is assumed.

[a] Author deceased.

0021-9673/90/$03.50

INTRODUCTION

An efficient way to increase the speed of analysis in capillary gas chromatography (GC) is to reduce the column diameter[1]. However, minimization of the column diameter is limited by the drastic reduction in the working range. With present state-of-the-art detectors this point is reached at a column diameter of about 10 μm.

The foregoing approach lowers the contribution of the velocity profile (C_m term) to the chromatographic dispersion. In addition to a reduction in column diameter, this contribution can also be lowered by changing the velocity profile.

A possible way is to coil the column into a helix, which induces a secondary flow. This effect has been extensively described by Tijssen[2] and Tijssen *et al.*[3] for GC and LC. Another way is to create turbulent flow. With turbulent flow the velocity profile is largely flattened, thus decreasing flow inequalities. Further, the effective diffusion coefficient is considerably increased by convective contributions. As a consequence, peak broadening arising in the mobile phase as a result of the velocity profile is expected to be substantially reduced. In a recent paper[4], we described an instrumental set-up that permits the study of turbulent flow capillary GC. The experimental instrumentation included previously developed sample introduction, detection and recording systems compatible with peak widths in the millisecond range [5,6].

Existing theoretical models[7–9] were evaluated experimentally. Only the Tijssen and Wittebrood theory[9] gave acceptable agreement with the experimental plate heights at various capacity factors. For unretained components reduced plate heights, $h<1$, were obtained at an average linear velocity of 15 m/s for column diameters of 320 μm. For a capacity factor $k=1$ the reduced plate height increased by a factor of 15. Therefore, it was concluded that the gain in speed of analysis by turbulent GC is limited to solutes with low capacity factors.

During these experiments, we asked M.J.E. Golay, former Extraordinary Professor in our laboratory, for expert advice concerning the several contradictionary theories on turbulent chromatography. He immediately became extremely interested in the subject. During the last months of his life he visited our laboratory several times and he derived a theory for turbulent dispersion in capillary GC. His manuscript "Calculations Relative to Turbulent Capillary Gas Chromatography" was meant to constitute his opening lecture at the 10th International Meeting on Capillary Chromatography in Riva del Garda, Italy, in May 1989. We were shocked by the message of his sudden death in his native country of Switzerland during the night of April 28–29, 1989. As a tribute to the great scientist Marcel Golay, inventor of capillary chromatography, we evaluate his postulates in this paper.

THEORY

In 1989, Golay derived a theory for turbulent dispersion in capillary GC[10] in order to explain the experimental results to be presented in the following Experimental section. He extended the theory of Tijssen and Wittebrood[9] towards general sth power velocity profile:

$$\frac{u}{\bar{u}} = \frac{s+2}{s}\left[1-\left(\frac{r}{r_0}\right)^s\right] \tag{1}$$

where u is the velocity as a function of the radial coordinate and r_0 is the column radius.

This velocity profile has proved to be a good approximation for turbulent flow, where s changes from 5 to 10 for Reynolds numbers (Re) in the range $3000 < Re < 10^5$. For turbulent dispersion this finally leads to

$$C_m = \frac{r_0^2}{D_0} \cdot \frac{4 + (4s + 16)k + (s^2 + 10s + 20)k^2}{4(s + 4)(2s + 4)(1 + k)^2} \tag{2}$$

For a parabolic velocity profile ($s = 2$), eqn. 2 reduces to the well known C_m term in the Golay–Giddings plate-height equation. For $s = 10$, eqn. 2 gives the same result as that derived by Tijssen and Wittebrood[9].

Later, Golay extended the theory in order to account for the laminar sublayer along the column wall. His original text, written in April 1989 (ref. 11), is given here in the Appendix.

The calculations are based on the assumption that the flow pattern under turbulent conditions consists of a turbulent core separated from the tube wall by a thin laminar flow layer (Fig. 1). It is also assumed that the diffusion constant and viscosity are uniform within the turbulent core. Data for the following variables have to be entered in the resulting equations:

(1) the core radius r_t as a function of the tube radius r_0:

$r_t = \rho r_0 \; ; \rho < 1;$

(2) the core viscosity μ_t as a function of the known laminar flow viscosity μ_0:

$\mu_t = m\mu_0 \; ; m > 1;$

(3) the core diffusivity D_t as a function of the known laminar flow diffusion constant D_0:

$D_t = dD_0 \; ; d > 1.$

Implied is also the postulate that ρ, m and d are essentially functions of the Reynolds

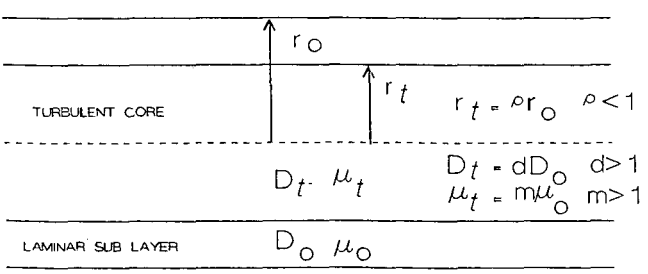

Fig. 1. Postulates made by Golay in his description of turbulent flow capillary GC.

number. Fortunately, *Re* is invariant within the tube as we pass from the high-pressure inlet side to the low-pressure outlet side.

If p_i and p_o are the inlet and outlet pressures, respectively, the gas velocity u in the laminar flow region at a distance r from the tube center ($r > r_t$) is given by

$$u = \frac{P_i^2 - p_o^2}{8p_o\mu_o L}(r_0^2 - r^2) \tag{3}$$

The velocity within the turbulent core is given by

$$u = \frac{p_i^2 - p_o^2}{8p_o L}\left(\frac{r_0^2 - r_t^2}{\mu_0} + \frac{r_t^2 - r^2}{\mu_t}\right) \tag{4}$$

The velocity profile is depicted schematically in Fig. 2.

Finally the plate height for turbulent dispersion can be written als follows[11]:
The turbulent core:

$$H_1 = \frac{2dD_0\rho^2}{u_0} + \frac{u_0 J r_0^2}{dD_0}\left(\frac{\alpha_1^2\rho^4}{4} - \frac{\alpha_1\rho^6}{3m} + \frac{\rho^8}{8m^2}\right) \tag{5}$$

where

$$J = \left[\frac{1}{1 - \left(1 - \frac{1}{m}\right)\rho^4}\right]^2$$

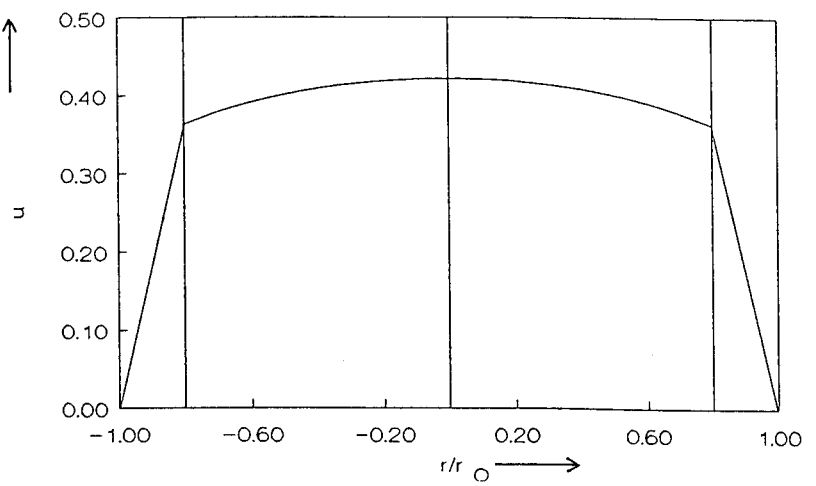

Fig. 2. Turbulent velocity profile. $m = d = 10$; $\rho = r_t/r_0 = 0.8$.

and

$$\alpha_1 = \frac{1 + 2k - 2(1+k)\rho^2 + \rho^4}{(1+k)} + \frac{2(1+k)\rho^2 - \rho^4}{(1+k)m}$$

(2) The laminar region:

$$H_2 = \frac{2D_0(1-\rho^2)}{u_0} + \frac{u_0 J r_0^2}{4D_0}\left[\frac{\alpha_2^2(1-\rho^4)}{4} - \frac{\alpha_2(1-\rho^6)}{3} + \right.$$

$$\left. + \alpha_2\beta_2(1-\rho^2) + \frac{(1-\rho^8)}{8} - \frac{\beta_2(1-\rho^4)}{2} + \beta_2^2 \ln\left(\frac{1}{\rho}\right)\right] \quad (6)$$

where

$$\alpha_2 = \frac{1 + 2k + \rho^4}{1+k} - \frac{\rho^4}{(1+k)m}$$

$$\beta_2 = \rho^4\left(\frac{1}{m} - 1\right)$$

The total plate height $H = H_1 + H_2$.

The total plate height H can only be calculated if ρ, m and d are known. In this paper, empirical relationships will be used in order to verify Golay's theory.

According to the Reynolds' analogy, mass and momentum are transported by the same mechanism (under turbulent conditions) and, therefore, it is the authors' assumption that $m = d$. The turbulent diffusion coefficient can be written as

$$\frac{D_t}{D_0} = 1 + 0.009\, Re^{0.84}\, Sc = d = m \quad (7)$$

where

D_t = average cross-sectional turbulent diffusion coefficient;
D_0 = molecular diffusion coefficient;
Sc = ν/D_0 (ν = kinematic viscosity).

Using an empirical relationship for the thickness of the laminar sublayer[12], it follows that ρ can be written as

$$\rho = 1 - \left[\frac{68.4}{(0.5Re)^{0.875}}\right] \quad (8)$$

A computer program based on eqns. 5–8 was used to calculate the plate height as a function of the Reynolds number.

Under Results and Discussion, the results will be compared with experimentally determined plate heights.

EXPERIMENTAL

Experiments under turbulent flow conditions[4] were performed with fused-silica columns of I.D. 320 μm, lengths ranging from 25 to 5 m and a stationary phase film thickness of 0.12 μm (CP SIL 5-CB; Chrompack, Middelburg, The Netherlands).

The sample introduction system consists of a pneumatically actuated Valco four-port valve (VICI AG; Valco, Schenkon, Switzerland) with an internal rotor (6 nl), which allows input band widths as low as 1 ms. The valve is mounted on top of a Carlo Erba (Milan, Italy) Model 4/60 gas chromatograph. The carrier gas (nitrogen) pressure was controlled with a Tescom (MN, U.S.A.) Model 44-1100 high-pressure regulator (up to 100 bar). A flame ionization detector could not be used as the flame was extinguished by the large carrier gas flow-rates. Therefore, a low-cell-volume (40 μl) photoionization detector (HNU Systems, Newton, MA, U.S.A.) was used throughout. The amplifier was modified to lower the time constant to about 2 ms.

Considering the high column flow-rates involved (>1 l/min), peak broadening due to the cell volume will be extremely small. As ordinary chart-speed recorders are far too slow, chromatograms were recorded on a Model 3091 digital storage oscilloscope (Nicolet, Madison, WI, U.S.A.), capable of sampling at a maximum rate of 1 MHz.

RESULTS AND DISCUSSION

Using the theory of Golay (eqns. 5–8), which accounts for a laminar sublayer, the plate height could be calculated as a function of Re for various capacity factors. Under laminar conditions ($\rho = 1, m = 1$ and $d = 1$), it can be calculated that $H_1 = 0$ and H_2 is equal to the value predicted by the Golay–Giddings equation for laminar flow.

At $Re = 6200$ the results of the Golay theory accouting for a laminar sublayer are compared with the measured plate height as a function of k in Fig. 3. A very good fit is obtained. However, just as in the other theories[9] and Golay using an sth power flow profile (eqn. 2), the fit becomes poorer at different Re numbers (see Table I). The reason is probably that in reality there is a gradual change of diffusion coefficient and viscosity from the laminar sublayer to the turbulent core. The theory assumes a discontinuous change from a molecular diffusion coefficient and viscosity to a turbulent diffusion coefficient and viscosity. More accurate diffusion and viscosity profiles have to be used. Another reason might be the empirical relationships used for ρ, m and d.

It should be noted that so far, the resistance to mass transfer in the stationary phase has been neglected. Considering the high carrier gas velocities involved (up to 15 m/s), the reliability of this assumption must be verified. The resistance to mass transfer in the stationary phase is not affected by the flow profile in the mobile phase[8,13]. Assuming a liquid diffusion coefficient $D_l \approx 10^{-5}$ cm^2/s (ref. 13), $k = 1$

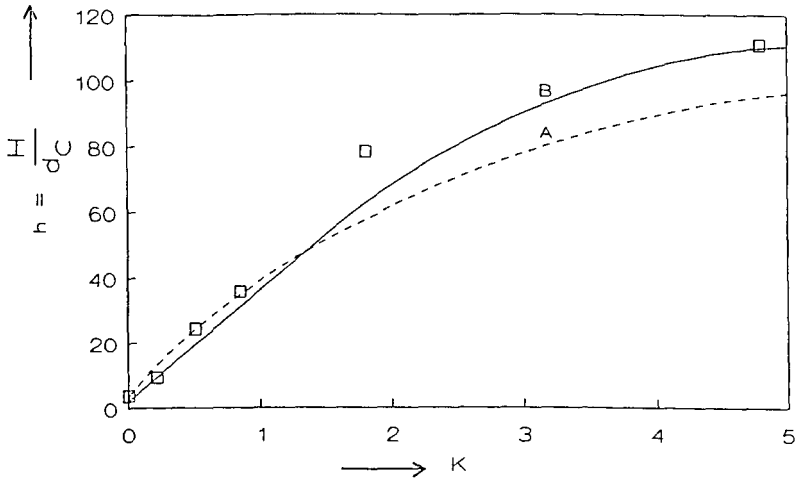

Fig. 3. Turbulent dispersion (reduced plate height, h) *versus* capacity factor (Re = 6200). □ = Experimental; A = measured according to the theory of Golay for an sth power flow profile; B = measured according to the theory of Golay accounting for a laminar sublayer.

TABLE I

REDUCED PLATE HEIGHTS, h

	Calculated h[11]		*Measured* h	
Re	$k=0$	$k=1$	$k=0$	$k=1$
3000	1.2	42	7	63
6200	0.5	44	2.6	38
10 000	0.3	46	1	22

and u = 15 m/s (Re = 10^4), the reduced plate height of the resistance to mass transfer in the stationary phase is calculated to be h_s = 0.22. This may be considered negligible with respect to the foregoing results.

APPENDIX

Calculations relative to turbulent capillary gas chromatography[a]

M. J. E. GOLAY

Perkin-Elmer Corporation, Norwalk, CT 06859 (U.S.A.)

[a] This manuscript was compiled by Dr. Golay during the first week of April 1989, with the intention that, after some experiments and calculations, he would present it at the *10th International Symposium on Capillary Chromatography, May 22–25, 1989*, in Riva del Garda. His sudden death during the night of April 28–29, 1989, prevented the fulfillment of these plans.

We base these calculations on the assumption that the flow pattern under turbulent conditions consists of a turbulent core separated from the tube wall by a very thin laminar flow layer. We assume that the diffusion constant and viscosity within the turbulent core are uniform, and our essential task will be to calculate from experimental data:

(1) the core radius, r_t, as a fraction of the tube radius, r_0:

$$r_t = \rho r_0 \; ; \; \rho < 1;$$

(2) the core viscosity, μ_t, as a function of the known laminar flow viscosity, μ_0:

$$\mu_t = m\mu_0 \; ; \; m > 1;$$

(3) the core diffusivity, D_t, as a function of the known laminar flow diffusion constant, D_0:

$$D_t = d\, D_0 \; ; \; d > 1.$$

Implied is also the postulate that ρ, m and d are essentially functions of the Reynolds number, Re; fortuitously, the Reynolds number is an invariant within the tube as we pass from the high-pressure inlet side to the low-pressure outlet side.

We shall assume that the resistance to mass transfer in the fixed phase, the term,

$$\frac{k^3}{(1+k)^2}$$

in eqn. 22a in a previous paper[14] is negligible, although it will be included in the mathematical derivations.

The pattern of the calculations will be to obtain three equations from which to calculate ρ, m and d under identical flow conditions (inclusion of the mass transfer term would require a fourth equation):

(1) the flow resistance equation;
(2) an equation connecting the observed HETP, h_0, with the postulated ρ, m and d in the absence of retention ($k = 0$);
(3) another equation connecting the observed HETP with ρ, m and d in the presence of some nominal retention, *e.g.*, $k = 1$.

The checks of the calculation should be:

(1) under the same flow conditions predict and verify h for different retentions, k;
(2) under various flow conditions observe the variations of ρ, m and d as functions of Re.

The flow resistance equation

The average carrier gas velocity, in cm s^{-1}, in a tube of length L, in cm, for the case of laminar flow, is given by

$$u_0 = \frac{p_i^2 - p_o^2}{16 p_o \mu L} \cdot r_0^2$$

where p_i and p_o are the inlet and outlet pressure and μ is the molecular dynamic viscosity, in poise (g cm^{-1} s^{-1}).

In the case of turbulent flow, designating $r_t = \rho r_0$, the radius of the turbulent core, the gas velocity in a point in the thin laminar flow region, at a distance r from the tube centre ($r > r_t$) will be given by

$$u = \frac{p_i^2 - p_o^2}{8 p_o \mu L}(r_0^2 - r^2) \tag{A1}$$

and the velocity within the turbulent core will be given by

$$u = \frac{p_i^2 - p_o^2}{8 p_o L}\left(\frac{r_0^2 - r_t^2}{\mu} + \frac{r_t^2 - r^2}{\mu_t}\right) \tag{A2}$$

The average velocity will be given by

$$u_0 = \frac{p_i^2 - p_o^2}{16 p_o L r_0^2}\left(\frac{r_0^4 - r_t^4}{\mu} + \frac{r_t^4}{\mu_t}\right) \tag{A3}$$

and the total flow will be given by

$$F_t = \pi \cdot \frac{p_i^2 - p_o^2}{16 p_o L}\left(\frac{r_0^4 - r_t^4}{\mu} + \frac{r_t^4}{\mu_t}\right) \tag{A3a}$$

$$= \pi \cdot \frac{(p_i^2 - p_o^2) r_0^4}{16 p_o \mu L}\left[1 - \left(1 - \frac{1}{m}\right)\rho^4\right] \tag{A3b}$$

As velocities, flows and the HETP (h) can be fairly accurately determined, whereas, p_i, p_0 and u cannot, the experimental procedure should consist in taking a tube of much greater length, sL, where $s \gg 1$, and, applying the same pressure differential across it, determine the velocity and flow, which are given by

$$u_L = \frac{(p_i^2 - p_o^2) r_0^2}{16 p_o \mu s L} \tag{A3c}$$

$$F_L = \pi \cdot \frac{(p_i^2 - p_o^2) r_0^4}{16 p_o \mu s L} \tag{A3d}$$

from which r_0 can be determined if required.

From eqns. A3a, b and d, we obtain

$$1 - \left(1 - \frac{1}{m}\right)\rho^4 = \frac{F_t}{sF_L} \tag{A4}$$

F_t, F_L and s are determined by direct measurements and eqn. A4 is the first of the three equations needed.

The diffusion equations – laminar flow

These equations are tedious to manipulate, and the general attack used will be first illustrated for the case of laminar flow.

We consider a chromatographic tube of length L and radius r_0 with a retentive layer of thickness Δr, with a partition coefficient C and a diffusion constant D_L. The ratio of the total sample concentration to the concentration within the gas phase will be given by

$$\frac{r_0^2 + C[(r_0 + \Delta r)^2 - r_0^2]}{r_0^2} = 1 + C\left[\left(1 + \frac{\Delta r}{r_0}\right)^2 - 1\right]$$

$$= 1 + k$$

with

$$k = C\left[\left(1 + \frac{\Delta r}{r_0}\right)^2 - 1\right]$$

or

$$\left(1 + \frac{\Delta r}{r_0}\right)^2 = 1 + \frac{k}{C} \tag{A5}$$

The velocity at any point within the tube will be given by

$$u = 2u_0\left(1 - \frac{r^2}{r_0^2}\right) \tag{A6}$$

and the average sample velocity will be

$$\bar{u} = \frac{u_0}{1 + k} \tag{A7}$$

We shall refer all calculations with respect to a system of coordinates moving with velocity $\bar{u}$ in the direction of the current, and our approach, for both the laminar

and turbulent cases, will be to postulate a general sample concentration of the form

$$f = \frac{1}{\sqrt{t}} \exp\left[- \frac{[x - e(r)]^2}{4D't} \right] \tag{A8}$$

and to apply to it the diffusion equation with the eventual aim of obtaining $e(r)$. This equation is usually given in the form

$$D\Delta^2 f = \frac{df}{dt} \tag{A9}$$

which presupposes that D is a constant throughout. When D is not eqn. A9 should properly be written as

$$D\Delta^2 f + \text{grad } D \times \text{grad } f = df/dt \tag{A9a}$$

but if D is constant within certain given zones, we may still use eqn. A9 within each zone, while introducing the boundary condition that at the interfaces of zones I and II, *e.g.*, we should have

$$D \cdot \frac{df}{dS_I} = D_1 c \cdot \frac{df}{dS_{II}} \tag{A9b}$$

where D and D_1 designate the respective diffusion constants of the two zones, S is some coordinate normal to the zones interface and c designates the ratio of concentrations which are in equilibrium across the interface.

The application of eqn. A9 to eqn. A8 yields one expression without $x - e(r)$ and one with it. The first is, after eliminating common coefficients,

$$D' = D\left[1 + \left(\frac{de}{dr} \right)^2 \right] \tag{A10}$$

and the second is

$$D\Delta^2 e(r) = -(u - \bar{u}) \tag{A11}$$

In the first expression, the dimensionless $(de/dr)^2$ represents a kind of entropy increase, and is therefore an extensive quantity which, with unity added, should be integrated throughout the tube cross-section and weighted everywhere by the appropriate diffusion times the partition coefficient when the latter differs from unity. The overall result, divided by the total effective tube cross-section, $r_0^2(1 + k)$ (π is omitted in practice), yields the desired value of D' when the flow has proceeded for some distance so that f has became substantially a Gaussian distribution for all r values.

The value of de/dr is obtained from the solutions of eqn. A11, which are

$$e(r) = -(1/D)\Delta^{-2}(u - u_0) \tag{A12}$$

for the free-flowing zone, and

$$e(r) = (1/D_1)\Delta^{-2}\bar{u} \tag{A12a}$$

for the fixed zone.

The values of de/dr obtained from this operation are, for the free-flowing inner part of the tube,

$$\frac{de}{dr} = -\frac{u_0}{2D}\left(\frac{1+2k}{1+k}\cdot r - \frac{r^3}{r_0^2}\right) \tag{A13}$$

and for the fixed phase of thickness Δr,

$$\frac{de}{dr} = \frac{u_0}{2(1+k)}\left[r - \frac{r_0^2(1+k/C)}{r}\right] \tag{A13a}$$

It can be readily verified that these expressions satisfy eqns. A12 and A12a, respectively, in addition to the boundary condition of eqn. A9b, at the interface. Further, eqn. A13a satisfies the condition $de/dr = 0$ at the end of the fixed phase zone, where $r = r_0 + \Delta r$, which results from the proper choice of $\bar{u}$ as given by eqn. A7.

Integration of $(de/dr)^2$ in the free-flowing zone yields a first contribution $\Delta D_I'$ to D':

$$\Delta D_I' = \frac{1}{1+k}\left[D + \frac{u_0^2 r_0^2}{D}\cdot\frac{1+6k+11k^2}{48(1+k)^2}\right] \tag{A14}$$

Integration and weighting of $(de/dr)^2$ in the stationary phase yields a second contribution, $\Delta D_{II}'$:

$$\Delta D_{II}' = \frac{C(u_0^2 r_0^2)}{2D_I(1+k)^3}\left[-\frac{k}{C} - \frac{3k^2}{4C^2} + \left(1 + 2\cdot\frac{k}{C} + \frac{k^2}{C^2}\right)\frac{1}{2}\cdot\ln\left(1+\frac{k}{C}\right)\right] \tag{A14a}$$

When $k/C \ll 1$, $\ln(1 + k/C)$ can be replaced by the first three terms of its development and we obtain

$$\Delta D_{II}' = \frac{1}{1+k}\left[\frac{k^3}{12(1+k)^2}\cdot\frac{u_0^2 r_0^2}{C^2 D_I}\right] \tag{A14b}$$

The parentheses in eqns. A14 and A14b correspond exactly to the parentheses on the left-hand side of eqn. 22a in a previous paper[14], except for the limitation $k/C \ll 1$, which was not included at that time.

The diffusion equation —turbulent flow

For the discussion of this case we adopt again the flow distribution of eqn. A8 and set about determining $de(r)/dr$ for the three zones:

Zone I, the turbulent core, of radius $r_t = \rho r_0$, with viscosity $\mu_t = m\mu$ and diffusivity $D_t = dD$;

Zone II, the thin laminar layer next to the tube wall;

Zone III, the stationary phase, of thickness Δr, diffusivity D_1, and with a concentration c times greater than in the free-flowing zones I and II.

The diffusion equations governing the concentration behaviour in these three zones can be solved as formerly and we obtain the following:

for Zone I, for $r < r_t$:

$$e = (1/D_t)\Delta^{-2}(u - \bar{u})$$

from which

$$\frac{de}{dr_I} = -\frac{p_i^2 - p_o^2}{32p_oD_tLr_0^2}\left[\frac{(1+2k)r_0^4 - 2(1+k)r_0^2r_t^2 + r_t^4}{(1+k)\mu}\cdot r + \right.$$

$$\left. + \frac{2(1+k)r_0^2r_t^2r - r_t^4r - (1+k)r_0^2r^3}{(1+k)\mu_t}\right] \qquad \text{(A15)}$$

Observing the boundary condition:

$$\text{for } r = r_t, \qquad D_t(de/dr_I) = D(de/dr_{II})$$

we find for Zone II, for $r_t < r < r_0$:

$$e = -(1/D)\Delta^{-2}(u - \bar{u})$$

from which

$$\frac{de}{dr_{II}} = -\frac{p_i^2 - p_o^2}{32p_oDLr_0^2}\left[\frac{(1+2k)r_0^4 + r_t^4}{(1+k)\mu}\cdot r \cdot \frac{r_t^4}{(1+k)\mu_t}\cdot r - \frac{r_0^2r^3}{\mu} + \frac{r_0^2r_t^4}{r}\left(-\frac{1}{\mu} + \frac{1}{\mu_t}\right)\right] \text{(A16)}$$

And observing the boundary condition expressed by eqn. A9b, we find for the stationary zone:

$r_0 < r < r_0 + r$:

$$\frac{de}{dr_{III}} = \frac{p_i^2 - p_o^2}{32p_oD_1L^2r_0}\left[\frac{r_0^4 - r_t^4}{(1+k)\mu}\cdot r + \frac{r_t^4}{(1+k)\mu_t}\cdot r - \right.$$

$$\left. \frac{(1+k/C)r_0^6 - (1+k/C)r_0^2r_t^4}{(1+k)\mu r} - \frac{1+k/C}{\mu_t r}\right] \qquad \text{(A17)}$$

As can be verified by inspection, the expressions given for de/dr in eqns. A15, A16 and A17 satisfy the three diffusion equations in their respective zones, plus the two boundary conditions at the I–II and II–III interfaces, plus the end condition:

$$\text{at } r = r_0 + \Delta r: \qquad (de/dr_{III}) = 0$$

the latter begin secured by our proper choice of $\bar{u}$.

When calculating the contributions of Zone I to D', we first set $r = r_0 x$ and rewrite eqn. A15:

$$\frac{de}{dr} = -\frac{(p_i^2 - p_o^2)r_0^3}{32p_o r L d D}\left[\left(\frac{1 + 2k - 2(1+k)\rho^2 + \rho^4}{(1+k)} + \frac{2(1+k)\rho^2 - \rho^4}{(1+k)m}\right)x - \frac{x^3}{m}\right]$$

or, with eqn. A3c, and denoting by α_1 the coefficient of x within the brackets:

$$\alpha_1 = \frac{1 + 2k - 2(1+k)\rho^2 + \rho^4}{(1+k)} + \frac{2(1+k)\rho^2 - \rho^4}{(1+k)m}$$

$$\frac{de}{dr_I} = -\left(\frac{su_1}{2d}\cdot\frac{r_0}{D}\right)\left(\alpha_1 x - \frac{x^3}{m}\right) \tag{A15a}$$

We calculate the contribution of Zone I to D' by applying

$$D' = D_i[1 + (de/dr)^2$$

to eqn. A15a, to obtain

$$\Delta D_I' = \frac{2}{r_I^2}\int_0^{r_i} dD\left[1 + \left(\frac{de}{dr}\right)_I^2\right] r\,dr$$

$$= \frac{2}{1+k}\cdot dD\left[\frac{\rho^2}{2} + \frac{s^2u_1^2r_0^2}{4d^2D^2}\int_0^{\rho}\left(\alpha_1 x - \frac{x^3}{m}\right)^2 x\,dx\right]$$

$$= \frac{2}{1+k}\left[dD\cdot\frac{\rho^2}{2} + \frac{s^2u_1^2r_0^2}{4dD}\left(\alpha_1^2\frac{\rho^2}{4} - \frac{\alpha_1\rho^6}{3m} + \frac{\rho^8}{8m^2}\right)\right] \tag{A18}$$

We now do likewise for Zone II and, setting again $r = r_0 x$, we rewrite eqn. A16:

$$\frac{de}{dr_{II}} = -\frac{(p_i^2 - p_o^2)r_0^3}{32p_o\mu LD}\left[\overbrace{\left(\frac{1 + 2k + \rho^4}{1+k} - \frac{\rho^4}{(1+k)m}\right)}^{\alpha_2} x - x^3 + \frac{\rho^4}{x}\underbrace{\left(-1 + \frac{1}{m}\right)}_{\beta_2}\right]$$

or, with eqn. A3c, and denoting by α_2 and β_2 the respective coefficients of x and $1/x$ within the brackets:

$$\frac{de}{dx_{II}} = -\frac{su_1r_0}{2D}[\alpha_2 x - x^3 + \beta_2(1/x)] \tag{A16a}$$

We now calculate the contribution of Zone II to D' by applying eqn. A10 to eqn. A16a to obtain:

$$\Delta D'_{II} = \frac{2}{r_1^2}\int_{r_t}^{r_0} D\left[1 + \left(\frac{de}{dr}\right)^2\right] r\,dr = \frac{2}{1+k} \cdot D\left[\frac{1-\rho^2}{2} + \frac{s^2u_1^2r_0^2}{4D^2}\int_0^L \left(\alpha_2 x - x^3 + \frac{\beta_2}{x}\right)^2 x\,dx\right]$$

$$= \frac{2}{1+k}\left\{D \cdot \frac{1-\rho^2}{2} + \frac{s^2u_1r_0^2}{4D}\left[\frac{\alpha_2^2(1-\rho^4)}{4} - \right.\right.$$

$$\left.\left. \frac{\alpha_2(1-\rho^6)}{3} + \alpha_2\beta_2(1-\rho^2) + \frac{1-\rho^8}{8} - \frac{\beta_2(1-\rho^4)}{2} + \beta_2^2 \ln(1/\rho)\right]\right\} \tag{A19}$$

Theoretically we should determine the contribution of Zone III to D', which will give us a term containing εD_1 in its denominator, but this would imply that this term is not negligible and constitutes a fourth parameter to be added to m, ρ and d, so that four equations would be required to determine all four parameters. This, however, implies the difficulty of using two columns in which the same sample has different k values but the same C^2D_1 term. At present it would appear more expeditious to make the measurements with columns having a negligible mass transfer term. Thus we would have only the difficulty of finding two columns which, for the same sample (to ensure that D_t for $k = 0$ is the same for both experiments) have appreciable k values but negligibly small terms containing $1/(C^2D_1)$. In conclusion, we form D' from the two contributions:

$$\Delta D'_I + \Delta D'_{II} = D' \tag{A20}$$

We measure D' experimentally and set the values found as equal to the quantities calculated from the known u_1, r_0 and s and from the unknown m, ρ and d and, adding these two equations derived from the cases $k = 0$, for exampe, and $k = k$ (a known k) to the flow equation, determine the three unknown quantities just said.

SYMBOLS

c	Ratio of concentrations in two zones
C	Partition coefficient
d	Factor relating core diffusivity (D_t) to laminar flow diffusion constant (D_0) ($d > 1$)

D	Diffusion constant
D_L	Diffusion constant in the stationary phase
D_t	Core diffusivity
D_0	Laminar flow diffusion constant
f	Sample concentration function
F_t	Total flow
F_L	Flow through a tube
h	Height equivalent to a theoretical plate (HETP) in general
h_0	Observed HETP
k	Capacity factor (retention factor)
L	Tube length
m	Factor relating core viscosity (μ_t) to laminar flow viscosity (μ) ($m > 1$)
p_i	Inlet pressure
p_o	Outlet pressure
r	Distance from the tube centre ($r > r_t$)
r_0	Tube radius
r_t	Core radius
Δr	Thickness of retentive layer (liquid-phase film thickness)
Re	Reynolds number
s	Factor increasing tube length ($s \gg 1$)
S	A coordinate related to the interface of zones
t	Time
u	Carrier gas velocity
u_0	Average carrier gas velocity
$\bar{u}$	Average sample velocity
u_l	Velocity in a tube
α_1, α_2	Coefficients
β_2	Coefficient
ε	A factor
μ	Molecular dynamic viscosity
μ_t	Core viscosity
μ_0	Laminar flow viscosity
ρ	Factor relating core radius (r_t) to tube radius (r_0) ($\rho < 1$)

REFERENCES

1 C. A. Cramers and P. A. Leclerq, *CRC Crit. Rev. Anal. Chem.*, 20 (1988) 117
2 R. Tijssen, *Sep. Sci.*, 13 (1978) 681.
3 R. Tijssen, N. van den Hoed and M. Kreveld, *Anal. Chem.* 59 (1987) 1007.
4 A. van Es, J. Rijks and C. Cramers. *J. Chromatogr.*, 477 (1989) 39.
5 A. van Es, J. Janssen, C. Cramers and J. Rijks, *J. High Resolut. Chromatogr. Chromatogr. Commun.*, 11 (1988) 852.
6 A. van Es, J. Janssen, R. Bally, C. Cramers and J. Rijks, *J. High Resolut. Chromatogr. Chromatogr. Commun.*, 10 (1989) 273.
7 V. Pretorius and T. Smuts, *Anal. Chem.*, 38 (1966) 274.
8 M. Martin and G. Guiochon, *Anal. Chem.*, 54 (1982) 159.
9 R. Tijssen and R. T. Wittebrood, *Chromatographia*, 5 (1972) 286.
10 M. J. E. Golay, personal communication.

11 M. J. E. Golay, unpublished paper (see Appendix).
12 R. Bird, W. Stewart and E. Lightfoot, *Transport Phenomena*, Wiley, New York, 1960.
13 C. A. Cramers, C. van Tilburg, C. Schutjes, J. Rijks, G. Rutten and R. de Nijs, in P. Sandra (Editor), *Proceedings of the 5th International Symposium on Capillary Chromatography, Riva del Garda*, Huethig, Heidelberg, 1983, p. 76.
14 M. J. E. Golay, in D. H. Desty (Editor), *Gas Chromatography 1958*, Butterworths, London, 1958, pp. 36–55.

Journal of Chromatography, 517 (1990) 161–173
Elsevier Science Publishers B.V., Amsterdam

CHROMSYMP. 1993

Use of chromatographic models for computerized optimization of coupling-point pressure in dual-column gas chromatography

T. HEVESI and J. KRUPČÍK*
Department of Analytical Chemistry, Faculty of Chemical Technology, Slovak Technical University, Radlinského 9, 812 37 Bratislava (Czechoslovakia)
and
P. SANDRA
Laboratory of Organic Chemistry, University of Ghent, Krijgslaan, 281 (S4), B-9000 Ghent (Belgium)

ABSTRACT

A novel computer-assisted procedure is presented for optimization of the coupling-point pressure (p_m) of a column for the gas chromatographic separation of multi-component samples on two capillary columns of fixed dimensions and stationary phase polarities operated at constant temperature with constant inlet (p_i) and outlet (p_o) pressures. The retention of all solutes in the system is monitored by the chromatographic model

$$k_{S,i} = k_{A,i} + x_B (k_{B,i} - k_{A,i})$$

where k is the capacity factor obtained on the polar column (A), the non-polar column (B) and on the columns coupled in series (S) and x_B is the weight factor determined from column characteristics and carrier gas pressures (p_i, p_m and p_o). The optimization procedure is monitored by a dependence of the optimization criterion (C_p) against the column coupling-point pressure (p_m):

$$C_p = f(p_m)$$

for both column series AB and BA. The optimization criterion is based on a number of peaks resolved equal to or better than the required resolution factor (primary part) in the shortest analysis time (secondary part).

Comparison of the novel optimization procedure with those based on window diagrams shows that the new model is superior as it gives unambiguously the maximum number of peaks that can be resolved under the given conditions equal to or better than the required resolution in the shortest analysis time.

0021-9673/90/$03.50

INTRODUCTION

It is well known that optimization of selectivity is the key to high-resolution gas chromatography[1–4]. For directly coupled columns, a study of selectivity tuning by variation of column length was performed by Purnell and co-workers[5–7], with particular emphasis on a correction for compressibility effects.

Selectivity optimization or tuning can be performed by coupling two columns of fixed dimensions and different polarities in series[1–4,8–15]. The overall polarity of serially coupled columns can be adjusted as required by tuning the carrier gas flow-rates through the individual columns[2–4,8,9,14,15], which was first proposed by Deans and Scott[8]; by adjusting the temperatures (isothermal, programmed temperature or a combination) of both columns[1–4,10,11,13,14] or by simultaneous tuning of carrier gas flow-rates and temperatures[2,14]. If the selectivity of two coupled capillary columns is tuned, all solutes pass through both columns and no intermediate trapping is used. The two coupled columns act as a single column, the selectivity of which is a composite of the selectivities of the individual columns. Sandra *et al.*[2] have described the selectivity tuning of two directly coupled capillary columns. They stated that a OV-1–PEG 20M tandem is less polar than a PEG 20M–OV-1 tandem. The retention is higher owing to gas compressibility effects in the polar column when this column is placed first and thus a higher polarity is obtained[2]. Equal polarities were obtained for PEG 20M–OV-1 and OV-1–PEG 20M columns in series when the corresponding carrier gas pressure drops were kept constant on changing the column order[2]. Thus, if the gas flow-rates of each column can be adjusted independently, gas compressibility effects are avoided.

For the separation of a multi-component sample, Hinshaw and Ettre[3,4] proposed optimizing the overall selectivity of two columns coupled in series and placed in one oven by tuning the carrier gas flow-rates in the individual columns and/or the oven isothermal temperatures. An optimization procedure based on a chromatographic model and on window diagrams according to Laub and Purnell[12] was used.

Computer-assisted procedures for the adjustment of optimum selectivity by tuning the intermediate pressure[14,15] or temperatures[13,14] for serially coupled columns placed in a separately heated dual oven system have been described[13–15]. The optimization procedures were based on mathematical models in which the dependences of the retention indices of all solutes on the optimized parameters were described by polynomial equations. New threshold criteria for the evaluation of the gas chromatographic (GC) separation of multi-component samples were advanced[15].

The aim of this paper is to introduce a computer-assisted procedure for the optimization of selectivity by tuning the coupling-point pressure (p_m) of two capillary columns of different polarities (A and B) coupled in series (either AB or BA) and operated at constant temperature. The optimization procedure is based on a chromatographic model which is evaluated by a threshold criterion. The validity of the optimization procedure has been verified by the separation of a mixture of 33 hydrocarbons and the new procedure is compared with the computer-assisted procedure based on window diagrams.

THEORY

It has been shown by Smuts *et al.*[16], Hinshaw and Ettre[3] and Purnell and Williams[5,7] that the capacity factor of a solute, separated in a system (S) consisting of two columns coupled in series ($k_{i,S}$), can be calculated from the capacity factors of this solute in the individual columns ($k_{i,A}$ and $k_{i,B}$):

$$k_{i,S} = x_A k_{i,A} + x_B k_{i,B} \tag{1}$$

where x_A and x_B are weight factors calculated from the following equations[3,14]:

$$x_A = \frac{t_{M,A}}{t_{M,A} + t_{M,B}} = \frac{L_A \bar{u}_B}{L_A \bar{u}_B + L_B \bar{u}_B} \tag{2}$$

and

$$x_B = \frac{t_{M,B}}{t_{M,A} + t_{M,B}} = \frac{L_B \bar{u}_A}{L_A \bar{u}_B + L_B \bar{u}_B} \tag{3}$$

hence

$$x_A + x_B = 1 \tag{4}$$

From eqns. 1–3 it follows that solute retention in columns in tandem ($k_{i,S}$) can be tuned by changing both physical and thermodynamic parameters.

From eqns. 1–3, it is obvious that the capacity factor found for a solute in columns in tandem does not depend on the column order. However, if two capillary columns of fixed lengths (L_A, L_B) and inner diameters (r_A, r_B) are coupled in series and operated with constant inlet (p_i) and outlet pressures (p_o), owing to the carrier gas compressibility different carrier gas flow-rates are established in both individual columns for column orders AB and BA.

If two columns of fixed dimensions are coupled in series, the $k_{i,S}$ value can be tuned by changing parameters that influence the carrier gas flow-rates and capacity factors in the individual columns. The carrier gas flow-rates in both individual columns can be tuned by changing the nature of the carrier gas and the inlet (p_i), column coupling-point (p_m) and outlet (p_o) pressures and temperatures (T_A, T_B). The capacity factor of a solute in the individual columns of a fixed column series can be influenced only by temperature.

Kaiser *et al.*[9] and Hinshaw and Ettre[3,4] have shown that the overall selectivity of two capillary columns coupled in series can be effectively tuned by changing the column coupling point pressure (p_m), keeping all other variables constant.

For an average carrier gas flow-rate ($\bar{u}$) in a single capillary column operated under isothermal conditions, Guiochon[17] derived the following equation:

$$\bar{u} = \frac{3}{4} \cdot \frac{K_o}{\eta L} \cdot \frac{(p_i^2 - p_o^2)^2}{p_i^3 - p_o^3} \tag{5}$$

where K_o is the column permeability, η the dynamic viscosity of the carrier gas, L the column length and p_i the inlet and p_o the outlet pressures. The permeability of a capillary column (K_o) can be calculated from the column radius (r) by[17]

$$K_o = r^2/8 \tag{6}$$

Guiochon[17] and Tóth and Garay[11] have shown that the average carrier gas flow-rates, calculated from eqns. 5 and 6, differ considerably from experimentally obtained values. As the overall selectivity of columns coupled in series strongly depends on the carrier gas flow-rates in the individual columns, these values should be known precisely. It was shown that solute retention in two columns in tandem can be predicted accurately if the permeability of the individual columns is determined experimentally instead of by calculation[11,17].

From eqn. 5, it follows that the average carrier gas flow-rate increases with increase in the driving force (P) and decrease in the resistance (R):

$$\bar{u} = \frac{P}{R} \tag{7}$$

where $P = (p_i^2 - p_o^2)^2/(p_i^3 - p_o^3)$ and $R = 4\eta L/3K_o$. Substitution of $\bar{u} = L/t_M$ into eqn. 7 gives

$$R = Pt_M/L \tag{8}$$

which can be substituted into eqns. 2 and 3 for calculation of x_A:

$$x_A = \frac{R_A L_A}{R_A L_A + (P_A/P_B)R_B L_B} \tag{9}$$

and x_B:

$$x_B = \frac{R_B L_B}{R_A L_A + (P_A/P_B)R_B L_B} \tag{10}$$

P_A/P_B can be written as

$$\frac{P_A}{P_B} = \frac{(p_i^2 - p_m^2)^2(p_m^3 - p_o^3)}{(p_i^3 - p_m^3)(p_m^2 - p_o^2)^2} \tag{11}$$

Eqn. 8 allows the resistance (R_A and R_B) to be determined from experimental data (P, t_M, L). The values of x_A and x_B can be predicted for two columns in tandem at any P_A/P_B ratio.

EXPERIMENTAL

Gas chromatographic instrumentation

The gas chromatographic system consisted of two independently controlled

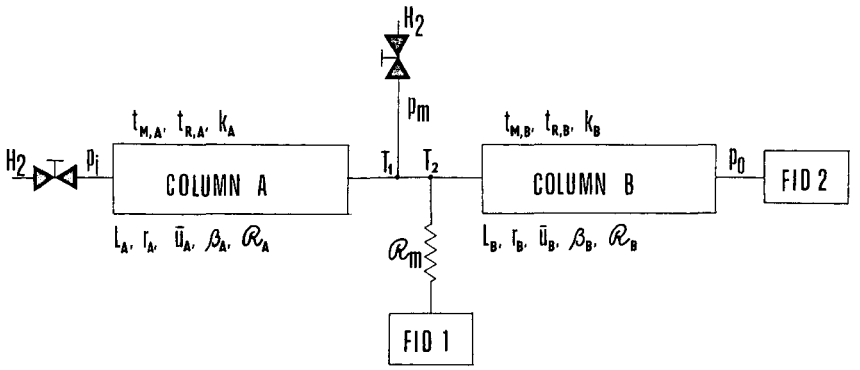

Fig. 1. Experimental set-up for a two column system with mid-point pressure tuning.

ovens (Fractovap 2350 and Fractovap 4180; Carlo Erba, Milan, Italy) interfaced with a separately heatad stainless-steel tube as described by Laub and Purnell[12]. The basic scheme of the column series polar column A (Nukol)–non-polar column B (PONA) in the order AB is shown in Fig. 1. In this work both columns were placed in the Fractovap 4180 GC oven as the oven temperature control is better than that with the Fractovap 2350 GC oven.

A sample of hydrocarbons was injected into the first column by using an all-glass inlet stream splitter port mounted in the Fractovap 2350 instrument. Two flame ionization detectors were used to monitor the solutes eluted from the first (FID 1 with the Fractovap 4180) and second (FID 2 with the Fractovap 2350) columns. The list of sample constituents with their capacity factors on individual columns is given in Table I. The inlet (p_i) and column coupling-point (p_m) pressures were controlled by a pressure controller with the Fractovap 2350 and Fractovap 4180 instruments, respectively.

The signals from FID 1 and FID 2 were recorded by an HP 3392 integrator (Hewlett-Packard, Palo Alto, CA, U.S.A.) and by a Chromatopac CR-3A computing integrator (Shimadzu, Kyoto, Japan), respectively. Two T press-fit connectors, T_1 and T_2 (MEGA, Milan, Italy), were used for coupling the columns with the pressure controller p_m and FID 1.

Capillary columns. Column A was a 60 m × 0.25 mm I.D. fused-silica capillary column coated with a 0.25-μm film of Nukol stationary phase (Supelco, Bellefonte, PA, U.S.A.). Column B was a 50 m × 0.20 mm I.D. fused-silica capillary column coated with a 0.5-μm film of immobilized polydimethylsiloxane (PONA) (Hewlett-Packard).

Operating conditions

Hydrogen was used as the carrier gas with constant inlet (p_i = 320 kPa) and outlet ($p_o \approx$ 101 kPa) pressures for the column orders AB and BA. The carrier gas flow-rates through the individual columns were changed by varying the intermediate pressure (for AB series from p_m = 250 to 290 kPa and for BA series from p_m = 210 to 250 kPa) in steps of 10 kPa. Both columns were operated isothermally with an arbitrarily chosen temperature $T_A = T_B$ = 70°C.

A sample of hydrocarbons (Table I) was diluted with *n*-pentane to 0.03% (v/v) of each compound. A 1-μl volume was injected with a 10-μl Hamilton syringe.

TABLE I

CAPACITY FACTORS FOUND FOR SAMPLE COMPONENTS AT 70°C ON POLAR (k_A) AND NON-POLAR (k_B) FUSED-SILICA CAPILLARY COLUMNS BY CORRELATING k_S AND x_B ACCORDING TO EQN. 17

Peak No.	*Compound*	k_A	k_B
1	2,3,4-Trimethylpentane	0.151	1.816
2	2,2,5-Trimethylhexane	0.138	2.330
3	*n*-Octane	0.195	2.593
4	2,3,5-Trimethylhexane	0.198	2.986
5	2,4-Dimethylheptane	0.198	3.140
6	4,4-Dimethylheptane	0.223	3.216
7	3,5-Dimethylheptane	0.233	3.497
8	3,3-Dimethylheptane	0.244	3.545
9	2,3-Dimethylheptane	0.279	4.062
10	α-3,4-Dimethylheptane[a]	0.298	4.148
11	β-3,4-Dimethylheptane[a]	0.298	4.148
12	3,4-Diethylheptane	0.406	4.752
13	Isopropylbenzene	2.689	6.152
14	*n*-Nonane	0.369	5.611
15	4,4-Dimethyloctane	0.405	6.629
16	*n*-Propylbenzene	3.369	7.633
17	2,6-Dimethyloctane	0.423	7.342
18	3,3-Dimethyloctane	0.455	7.417
19	3,4-Diethylhexane	0.501	7.649
20	2-Methyl-3-ethylhexane	0.480	7.761
21	1,3,5-Trimethylbenzene	4.250	8.545
22	1,2,4-Trimethylbenzene	5.395	10.216
23	*tert.*-Butylcyclohexane	1.058	10.319
24	1,2,3-Trimethylbenzene	7.608	12.372
25	*n*-Decane	0.709	12.066
26	*sec.*-Butylcyclohexane	1.414	13.847
27	1,3-Diethylbenzene	5.963	15.368
28	*n*-Butylbenzene	6.307	16.036
29	*n*-Butylcyclohexane	1.365	14.679
30	1,4-Diethylbenzene	6.389	16.169
31	1,2-Diethylbenzene	7.226	16.613
32	1,2-Dimethyl-4-ethylbenzene	8.641	18.988
33	*n*-Undecane	1.377	25.644

[a] α and β are diastereoisomers.

Computation

Software for the optimization procedure and also for the window method was written in Turbo Pascal language for a Toshiba T1100 Plus IBM PC/XT-compatible computer.

RESULTS AND DISCUSSION

The resistances of the individual columns (R_A and R_B) were determined at 70°C by substituting the experimental data in eqn. 8. The results obtained were R_A = 8.7 kPa min m^{-1} (σ = 0.3 kPa min m^{-1}) for column A and R_B = 7.8 kPa min m^{-1} (σ = 0.6 kPa min m^{-1}) for column B.

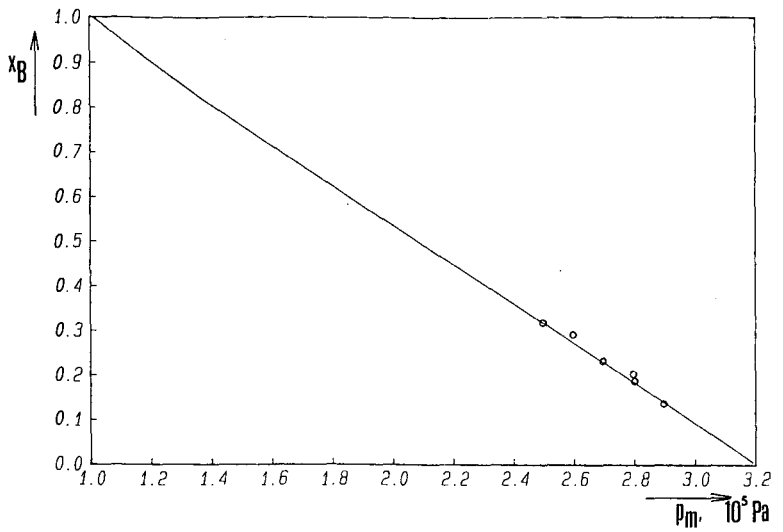

Fig. 2. Dependence of x_B on p_m, constructed for the column series AB using data calculated from eqn. 13. The circles correspond to data found for corresponding p_m values from eqn. 8.

The individual columns were then coupled in AB or BA series and operated at 70°C with constant hydrogen inlet (p_i = 320 kPa) and outlet ($p_o \approx$ 101 kPa) pressures, changing the column coupling-point pressure for series AB from p_m = 250 to 290 kPa and for series BA from p_m = 210 to 250 kPa in steps of 10 kPa.

The dependence of x_B on p_m, constructed from the corresponding data calculated with eqn. 8 for the column series AB, is shown in Fig. 2. The circles in Fig. 2 represent values of x_B found for p_m from eqn. 3 using gas hold-up times ($t_{M,A}$ and $t_{M,B}$) measured in the corresponding series using the signals from FID 1 and FID 2. The deviations between the predicted and experimental x_B values probably arise from the poor accuracy and reproducibility of pressure tuning on the available pressure controllers. Similar results were obtained for the column series BA.

From the results obtained it follows that the changes in p_m in the chosen experimental ranges lead to the changes in x_B from 0.15 to 0.35 for column series AB and from 0.40 to 0.60 for column series BA. Deans and Scott[8], Smuts *et al.*[16], Kaiser *et al.*[9] and Hinshaw and Ettre[3,4] have shown that, if necessary, x_B can be varied in a broader range both for AB and BA column series if another experimental arrangement as shown in Fig. 1 is used. It should be noted, however, that the carrier gas flow-rates ($\bar{u}_A$, $\bar{u}_B$) are usually too far from the optimum values if x_B is varied in too broad a range.

A separation of sample components can be achieved by tuning the selectivity of a column series if the sample is not too complex. In that case an optimum x_B can be found for both AB and BA column series. If the sample is very complex, however, both optimum selectivity and maximum separation power are needed. In this event a column order should be chosen that gives the highest separation power at the optimum selectivity.

A combination of eqns. 1 and 4 leads to

$$k_{i,S} = k_{i,A} + x_B(k_{i,B} - k_{i,A}) \quad (12)$$

which shows that the dependence of the overall solute capacity factor in columns in series (k_S) theoretically can vary from the value k_A (for $x_B = 0$) to the value k_B (for $x_B = 1$) both for column series AB and BA. From eqn. 12, it follows that for the elucidation of the dependence of k_S on x_B, capacity factors of the considered solute on the individual columns (k_A, k_B) can be applied. If these values are not known, they can be found by linear regression analysis of data (k_S and x_B) found for the solute on column series AB and BA. Fig. 3 shows the dependence of k_S on x_B obtained for 2-methyl-3-ethylhexane (peak No. 20). A very good correlation between k_S and x_B was obtained for both column series AB and BA, allowing Fig. 4 to be constructed, where the dependences of k_S on x_B for all sample components are shown. The plots shown in Fig. 4 were used as a basis for the computer-assisted optimization procedure with the aim of finding an x_B value (a perpendicular on the x_B axis) at which the maximum number of peaks will be resolved equally or better than required within the shortest analysis time.

The resolution factors of all peak pairs (R_{ji}) for each x_B value in the range $x_B = 0$ to $x_B = 1$ in steps of 0.001 were calculated by the following equation:

$$R_{ji}(x_B) = \frac{t_{Rj,S}(x_B) - t_{Ri,S}(x_B)}{2[\sigma_{j,S}(x_B) + \sigma_{i,S}(x_B)]} \quad (13)$$

where $t_{RS}(x_B)$ is a retention time and $\sigma_S(x_B)$ the standard deviation of a peak obtained by separating a solute in the column series with p_m which corresponds to x_B.

The retention times [$t_{RS}(x_B)$] needed in eqn. 13 were calculated from the system

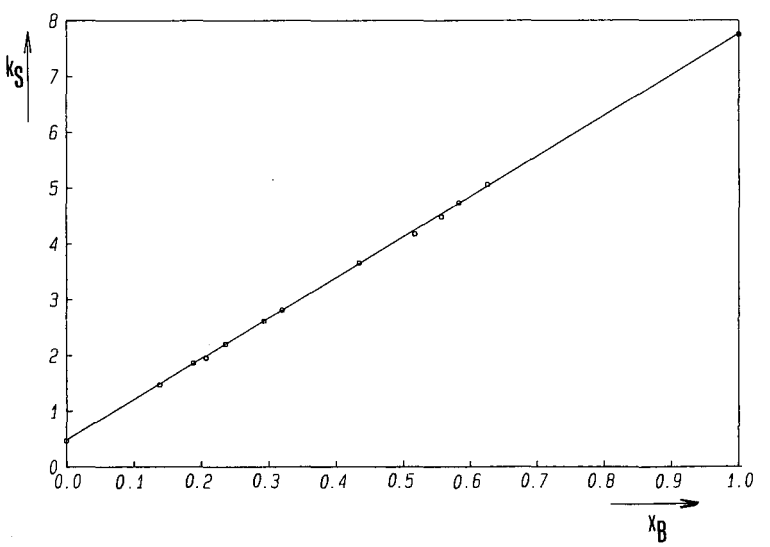

Fig. 3. Dependence of k_S on x_B for 2-methyl-3-ethylhexane (peak No. 20).

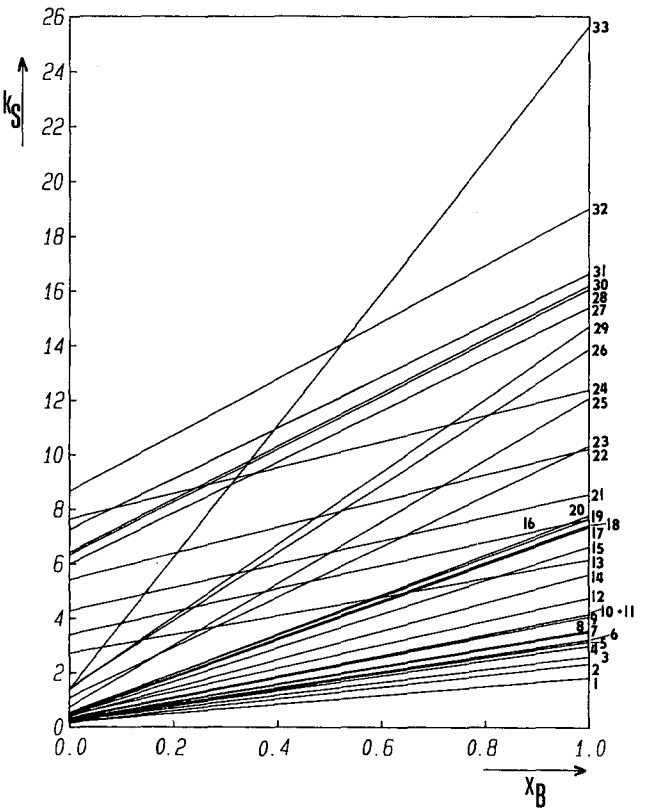

Fig. 4. Dependence of k_S on c_B for all sample constituents. For identification see Table I.

capacity factors $[k_S(x_B)]$ and gas hold-up times $[t_{MS}(x_B)]$ from the equation

$$t_{Ri,S}(x_B) = t_{M,S}(x_B)[1 + k_{i,S}(x_B)] \tag{14}$$

$t_{M,S}(x_B)$ was calculated as the sum of $t_{M,A}(x_B)$ and $t_{M,B}(x_B)$ using eqn. 8.

Correlating the standard deviations (σ_S) of all peaks obtained from all experiments in a system with the experimental variables (p_m, x_B, t_{RS}), we found that the standard deviation of any peak in a chromatogram can be predicted from the following linear equation:

$$\sigma_S = a + bt_{RS} \tag{15}$$

where a and b are coefficients which, in the experimental p_m ranges given above, did not depend on either x_B or the column order.

From the resolution factors of all peak pairs calculated from eqn. 13 at each x_B value, an optimization criterion C_p was determined from an equation already described[14,15]:

$$C_p = \sum_{1}^{n} m_i + (t_{max} - t_{R,n})/t_{max} \tag{16}$$

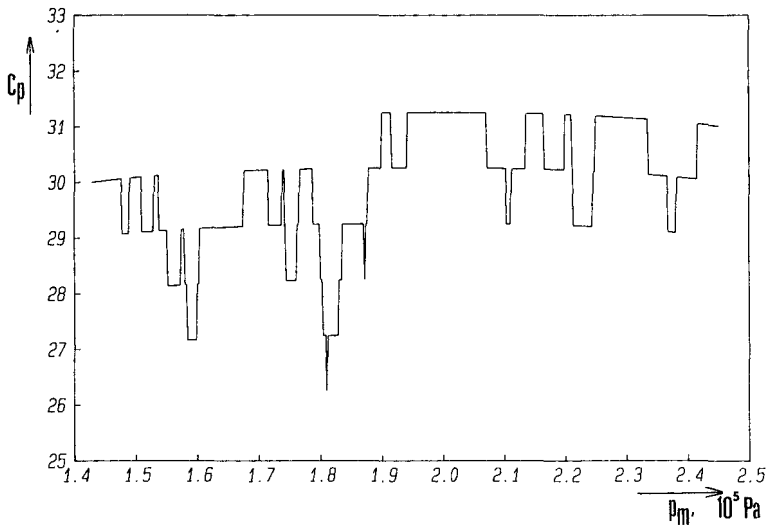

Fig. 5. Dependence of the optimization criterion (C_p) on column coupling point pressure (p_m) obtained for column series BA.

where n is the number of solutes in a sample, $m_i = 1$ if $R_{ji} > R_{ji,req}$ for $j = i \pm 1$, otherwise $m_i = 0$, $t_{R,n}$ is the retention time of the last-eluting peak and t_{max} is the maximum acceptable analysis time, which is arbitrarily chosen so that $t_{max} > t_{R,n}$. In this work $R_{ji,req} = 1.00$ and $t_{max} = 120$ min were chosen for both column series. The retention time of the last peak was read from the retention times calculated by eqn. 14 for all x_B values.

As in this work p_m was an independently variable parameter, for practical reasons p_m was used instead of x_B in the final computer-assisted optimization procedures. Moreover, as follows from eqns. 13 and 14 and from Fig. 2, it is very easy to recalculate x_B values to p_m values.

The dependence of the optimization criterion (C_p) on the coloumn coupling-point pressure is shown in Fig. 5 for column series BA. The dependence of C_p on p_m for column series AB looks like a mirror image of Fig. 5, owing to the similar column resistances and efficiencies. From these results it follows that 31 peaks can be resolved equal to or better than $R_{ji,req}$ at different p_m values with both AB and BA column orders. The second term on the right-hand side of eqn. 16 helps to localize the global optimum among the local optima, in order to choose a p_m value such that 31 peaks are sufficiently resolved within the shortest time. A maximum C_p thus corresponds to an optimum p_m. Different C_p maxima are obtained for column orders AB and BA: the maximum C_p is localized in the p_m range $2.20 \cdot 10^5$–$2.35 \cdot 10^5$ Pa for AB and of $1.95 \cdot 10^5$–$2.05 \cdot 10^5$ Pa for BA. Both optima are, however, flat and broad enough to allow the p_m value to be reset in optimum pressure ranges as the set-up reproducibility of the pressure regulator built in the Fractovap 4180 instrument is $\pm 2.5 \cdot 10^3$ Pa.

A window diagram[12] could be used as an alternative optimization procedure to localize the optimum p_m value. The basis of this is the construction of the dependences

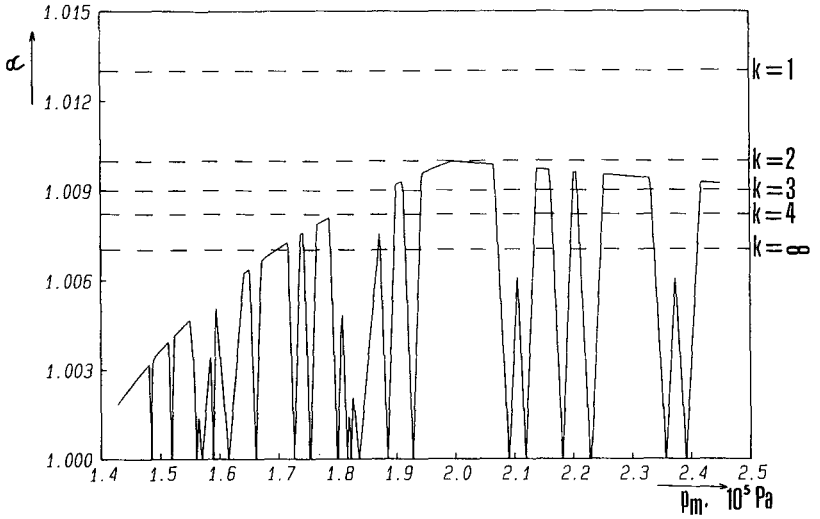

Fig. 6. Dependence of relative retentions (α) on column coupling-point pressure (p_m) obtained for column series BA (window diagram for BA column series).

of the relative retentions (α_{ji}) of all peak pairs against the column coupling-point pressure (p_m). Relative retention can be calculated, *e.g.*, from capacity factors (k):

$$\alpha_{ji} = k_j/k_i \tag{17}$$

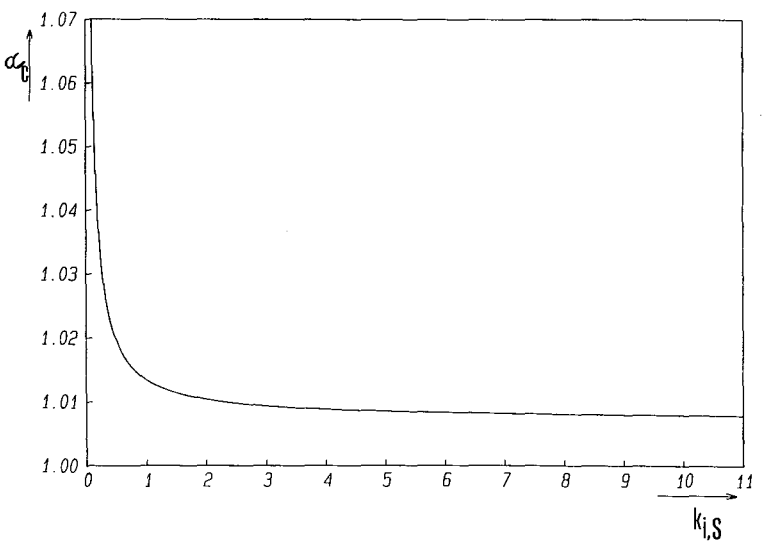

Fig. 7. Relationship between critical relative retention (α_C) corresponding to $R_{ji,req} = 1.00$ and capacity factor of the first peak in a considered pair ($k_{S,i}$) for both column series AB and BA.

Hence the window diagram could be drawn from the data taken from Fig. 4 as the dependence of α_{ji} against x_B. As p_m was the optimized parameter, window diagrams were constructed for the dependence of α_{ji} *versus* p_m. The window diagram for column series BA is given in Fig. 6. According to Laub and Purnell[12], the optimum of p_m corresponds to the tallest window. At this optimum value of p_m, the best possible separation of the least separated pairs of compounds is expected[12]. The same optimum intervals of p_m values were found from window diagrams as were found above with the proposed method both for column order AB ($2.20 \cdot 10^5$–$2.35 \cdot 10^5$ Pa) and for column order BA ($1.95 \cdot 10^5$–$2.05 \cdot 10^5$ Pa). As the maximum value of α corresponding to $p_{m,opt}$ in Fig. 6 is relatively small ($\alpha < 1.01$), from the window diagram it is not possible to deduce if peaks j and i with such a relative retention are sufficiently resolved or not, because window diagrams do not contain any information about the separation power. The value of relative retention (α_C) which corresponds to the required resolution ($R_{ji,req}$) is not constant and depends on the number of theoretical plates (n_i) and the capacity factor of the first peak (k_i) according to

$$R_{ji,req} = \frac{\sqrt{n_i}}{4} \cdot \frac{k_i}{k_i + 1} \cdot (\alpha_C - 1) \tag{18}$$

The relationship between the critical relative retention (α_C) corresponding to $R_{ji,req} = 1.00$ and the capacity factor of the first peak in a considered pair ($k_{i,S}$) is the same for both column orders AB and BA and is given in Fig. 7. From Fig. 7 it is evident that for

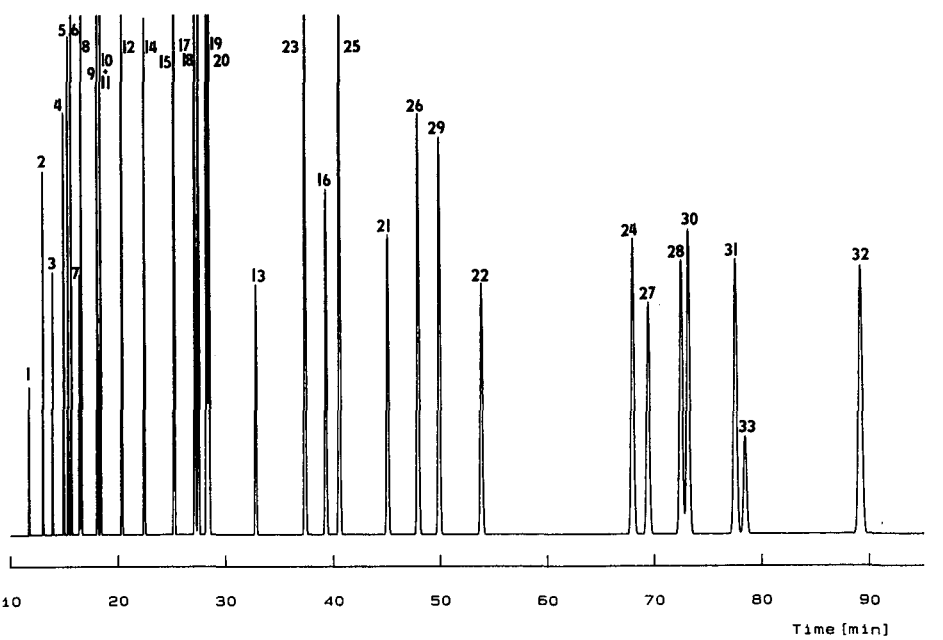

Fig. 8. Computer-simulated separation of the hydrocarbon sample for column series BA at $p_{m,opt} = 2.0 \cdot 10^5$ kPa. For peak identification see Table I.

the peak pairs eluted at very low capacity factors a relatively high α_C corresponds to $R_{ji,req} = 1.00$ and as we do not know from window diagrams at which capacity factors peak pairs are eluting, we also do not know if peaks are sufficiently resolved or not.

From the dashed lines drawn in Fig. 6 for different capacity factors (k) which correspond to α_C, it can be concludeed that the peak pair separated in the window ($p_m = 1.95 \cdot 10^5$–$2.05 \cdot 10^5$ Pa) will be resolved with $R_{ji,req} = 1.00$ only if $k_i > 2$. The use of a proper optimization criterion can help to distinguish if the peaks in the windows are sufficiently resolved or not[18].

Fig. 8 shows the chromatogram of the sample separation simulated by computer for column series BA at $p_{m,opt} = 2.0 \cdot 10^5$ Pa. All compounds in the sample, except the diastereoisomers, are resolved with $R_{j,i}$ better than 1.00 within 90 min. For the separation of diastereoisoners lower temperatures are needed[15].

ACKNOWLEDGEMENTS

We thank Dr. W. Supina (Supelco, Bellefonte, PA, U.S.A.) for the donation of a Toshiba T1100 Plus computer and a Nukol fused-silica capillary column and Mr. M. Galli (Mega, Milan, Italy) for the gift of press-fit connectors.

REFERENCES

1 R. E. Kaiser and R. I. Rieder, *J. High Resolut. Chromatogr. Chromatogr. Commun.*, 3 (1979) 416.
2 P. Sandra, F. David, M. Proot, G. Diricks, M. Verstappe and M. Verzele, *J. High Resolut. Chromatogr. Chromatogr. Commun.*, 8 (1985) 782.
3 J. V. Hinshaw and L. S. Ettre, *Chromatographia*, 21 (1986) 561.
4 J. V. Hinshaw and L. S. Ettre, *Chromatographia*, 21 (1986) 669.
5 J. H. Purnell and P. S. Williams, *J. Chromatogr.*, 321 (1985) 249.
6 J. H. Purnell, M. Rodrigues and P. S. Williams, *J. Chromatogr.*, 323 (1985) 402.
7 J. H. Purnell and P. S. Williams, *J. Chromatogr.*, 358 (1986) 39.
8 D. R. Deans and I. Scott, *Anal. Chem.*, 45 (1973) 1137.
9 R. E. Kaiser, R. I. Rieder, Lin Leming, L. Blomberg and P. Kusz, *J. High Resolut. Chromatogr. Chromatogr. Commun.*, 8 (1985) 92.
10 T. Tóth, H. van Cruchten and J. Rijks, in P. Sandra (Editor), *Proceedings of the 6th International Symposium on Capillary Chromatography*, Hüthig, Heidelberg, 1985, p. 769.
11 T. Tóth and F. Garay, in P. Sandra (Editor), *Proceedings of the Eighth International Symposium on Capillary Chromatography*, Hüthig, Heidelberg, 1987, p. 585.
12 R. J. Laub and J. H. Purnell, *J. Chromatogr.*, 112 (1975) 71.
13 D. Repka, J. Krupčík, E. Benická, P. A. Leclercq and J. A. Rijks, *J. Chromatogr.*, 463 (1989) 243.
14 D. Repka, J. Krupčík, E. Benická, F. Garay, T. Maurer and W. Engewald, in P. Sandra and G. Redant (Editors), *Proceedings of the 10th International Symposium on Capillary Chromatography*, Hüthig, Heidelberg, 1989, p. 682.
15 E. Benická, J. Krupčík, D. Repka, P. Kuljovský and R. E. Kaiser, *Anal. Chem.*, 62 (1990) 985.
16 T. W. Smuts, K. de Clerck, T. G. du Toit and T. S. Buys, *J. High Resolut. Chromatogr. Chromatogr. Commun.*, 3 (1980) 125.
17 G. Guiochon, *Chromatogr. Rev.*, 8 (1966) 1.
18 P. J. Schoenmakers, *Optimization of Chromatographic Selectivity*, Elsevier, Amsterdam, 1986, p. 202.

Journal of Chromatography, 517 (1990) 175–184
Elsevier Science Publishers B.V., Amsterdam

CHROMSYMP. 1992

Study of rapid reaction kinetics by computerized gas chromatography with stroboscopic sampling

E. KÜLLIK* and M. KALJURAND
Institute of Chemistry, Estonian Academy of Sciences, Tallinn, Estonia (U.S.S.R.)

ABSTRACT

The range of application of stroboscopic sampling is extended to two completely different chemical processes: catalysis of the conversion of alcohols to olefins in phosphoric acid (with a time resolution of 1 s and ignition of polypropylenes containing different amounts of flame retardants (with a temperature resolution of 25°C). The required frequency of analysis of the flows whose composition changes with time is considered. It is demonstrated how stroboscopy coupled with computerized chromatography can provide information that is otherwise difficult, expensive or even impossible to obtain.

INTRODUCTION

Depending on the methods used to study reaction kinetics, the chemical reactions may be classified as slow and fast. A characteristic running time for slow reactions exceeds 100 s and is shorter than 10 s for fast reactions[1]. An important parameter in this kind of study is the time resolution of kinetic curves, *i.e.*, the shortest time interval in which an analytical device used in a particular experiment needs in order to process a sampled reaction mixture. For example, using the chromatograph as an analytical device, the time resolution is determined by the sample separation time in the column (its value being usually measured in minutes). To characterize the reaction thoroughly, the reaction mixture must be sampled with a frequency determined from the Nyquist sampling theorem (also known as Kotelnikov's theorem)[2]. It is evident that for fast reaction studies, instruments with a rapid response are needed. In studying complicated macrokinetic reactions, an exact composition in the reaction components at a particular moment in time is also of interest. Chromatography can provide an excellent separation of the reaction components (reagents and products), but at the expense of separation time. Thus, common chromatographic techniques cannot be applied to rapid reaction studies.

Recently, a new technique for providing samples to the chromatograph, stroboscopic sampling, was proposed[3]. This latter enables one to overcome the

0021-9673/90/$03.50

restrictions caused by long separation times in rapid reaction studies. The principle of stroboscopic sampling is simple. The process under study is initiated many times and after each initiation a certain time interval pass. The sample is then taken from the reaction vessel and introduced into the chromatograph. By scanning the interval between initiation and sampling from zero to the end of the reaction, it is possible to record concentration curves for reactants and products with an adequate time resolution. The only requirement for effecting stroboscopic sampling is reproducibility of the process under investigation. For most chemical reactions the latter can be realized at the expense of a more or less sophisticated exerimental set-up.

The idea of stroboscopic sampling is fairly old, dating back to the beginning of the century. It has been applied successfully to many optical measurements of rapid phenomena but, to the authors' knowledge, its first application to the case when the signal carrier is mass flow was demonstrated by Kaljurand *et al.*[3]. Computerization of the experiment is crucial; although several manual kinetic experiments can be considered as "stroboscopic" (see, *e.g.*, ref. 4), human capabilities for generating precise time intervals and complicated sequences of injections (required in stroboscopic sampling) are limited.

Theoretical[5] and preliminary experimental[2,3] investigations of the stroboscopic sampling method appeared to be promising. However, for further validation of the sampling method more thorough studies are needed. In this work, the range of application of stroboscopic sampling was extended to two completely different chemical processes: catalysis of the conversion of alcohols to olefins on phosphoric acid and ignition of polypropylenes containing different amounts of flame retardants. This paper aims to demonstrate how stroboscopy coupled with contemporary computerized chromatography can provide information that is otherwise difficult, expensive or even impossible to obtain.

THEORETICAL

A change in the concentration of the volatile product of a chemical liquid-phase reaction which is carried out by the inert gas passing above the liquid is described by the following equation[6]:

$$C(t) = C_0[\exp(-at) - \exp(-kt)] \quad (1)$$

where $C(t)$ is the concentration at time t, C_0 is a constant and a and k are mass flow and chemical reaction rate constants respectively. Eqn. 1 can be used as the first approximation to describe processes in H_3PO_4 catalysis. We used eqn. 1 to calculate the time resolution necessary for the following stroboscopic experiments. According to the sampling theorem[2], a continuous function can be adequately represented by the set of function values sampled with an interval Δt if $\Delta t < 1/(2f_m)$, where f_m is the maximum frequency in the power spectrum of the function. Omitting straightforward but long Fourier transform calculations, the power spectrum of eqn. 1 can be written as follows:

$$P(f)/P_m = \{[1+(2\pi f/a)^2]\,[1+(2\pi f/k)^2]\}^{-1} \quad (2)$$

where P_m is the maximum value of the power spectrum. As follows from eqn. 2, there is no maximum frequency in the spectrum. At the expense of some small error, $P(f)/P_m$ can be considered as zero when it is less than, say, 10^{-2} and the corresponding frequency set equals f_m. Omitting again simple but time-consuming calculations, we obtain the following for two extreme cases: if $a \approx k$, then $\Delta t < 1/k$, and $a \gg k$, then $\Delta t < (ak)^{-1/2}$. Thus, taking $t = 0.1$ s (a common switching time for mechanical valves), the rate of the processes that can be studied by a given equipment is $k < 10\ s^{-1}$. On the other hand, if a more exact value is needed, say $P(f)/P_m < 10^{-4}$, then Δt should be about three times smaller.

EXPERIMENTAL

Equipment

For catalysis studies, the following chromatographic system was used. The reaction column was a 70 mm × 3 mm I.D. glass column filled with a catalyst. The analytical column was a 2 m × 3 mm I.D. metal column filled with Porasil E adsorbent, which is suitable for the separation of light olefins. Two mechanical valves (Valco C6TX) were used in the experiment. One valve performed the injection of the reagent pulses from the reagent stream supply vessel to the reactor and the other injected the products from the end of the reactor column to the top of the analytial column. The chromatograph used in this study was an LHM-80 with a flame ionization detector. The experimental set-up is described in more detail elsewhere[3].

In ignition experiments generation of the continuous reagent flow necessary to effect stroboscopic sampling is not as straightforward as with gaseous or liquid reagents because the polymer sample is a solid. According to contemporary ideas of polymer ignition, a polymer itself does not burn, but its pyrolysis products are responsible for ignition and burning. The last process provides the heat flow necessary for generation of the degradation products[7]. In our experiment, the heat flow to the sample was generated by an external oven whose temperature was set high enough to form a stream of sample degradation products but the ignition of the products was performed in the ignition reactor separated spatially from the oven where the degradation products were formed. The ignition reactor was a quartz tube (30 mm × 3 mm I.D.) and the process was initiated by passing the current impulse through the platinum wire wound around the tube, thus heating rapidly (about 80°C/s) the reagent flow inside the reactor. Sampling from the reactor to the 15 m × 0.5 mm I.D. metal capillary column coated with SE-30 liquid stationary phase (Perkin-Elmer) was performed with a laboratory-made Deans-type pneumatic switch. The pneumatic switch was controlled by a General Valve magnetic valve. By testing the valve we found that it was able to make reproducible injections with a duration as short as 50 ms. However, in this work such a short time resolution was not necessary. The chromatograph was an Intersmat IGC 121C FL with a flame ionization detector. The experimental set-up is described in more detail elsewhere[2].

Chemicals

n-Propanol and *n*-butanol used as reagents in the catalysis study were of "chemically pure" grade. For catalyst preparation, 85% phosphoric acid ("pure" grade) was used, Porasil E (Waters Assoc.) was used as a solid support for the acid. The

H_3PO_4 catalyst was prepared according to a literature procedure[8]. For ignition studies, a propylene–ethylene copolymer containing about 10% of ethylene was used. Four samples contained 0, 10, 20 and 40% of a flame retardant (Masterflam AF 709 by VAMP, Milan, Italy).

Computer and software

All experiments were controlled by an Apple IIe computer through laboratory-made interfaces and software. The built-in software-controlled relays used in Apple IIe game controllers appeared to be a convenient means for "on–off" switching valves and currents. The detector signal was digitized and read to the Apple IIe memory via a laboratory-made analogue-to-digital converter. The Apple IIe started the experiment by switching "on" the reagent sampling valve or current in the ignition reactor. Then, after a predetermined time interval, the computer took the sample from the reactor and switched all currents and valves "off". After recording the detector signal, the computer started a new cycle with different (from a previous cycle) time intervals between the reaction initiation and sampling.

RESULTS AND DISCUSSION

Catalysis on phosphoric acid

A typical set of chromatograms is shown in Fig. 1. By measuring peak areas for

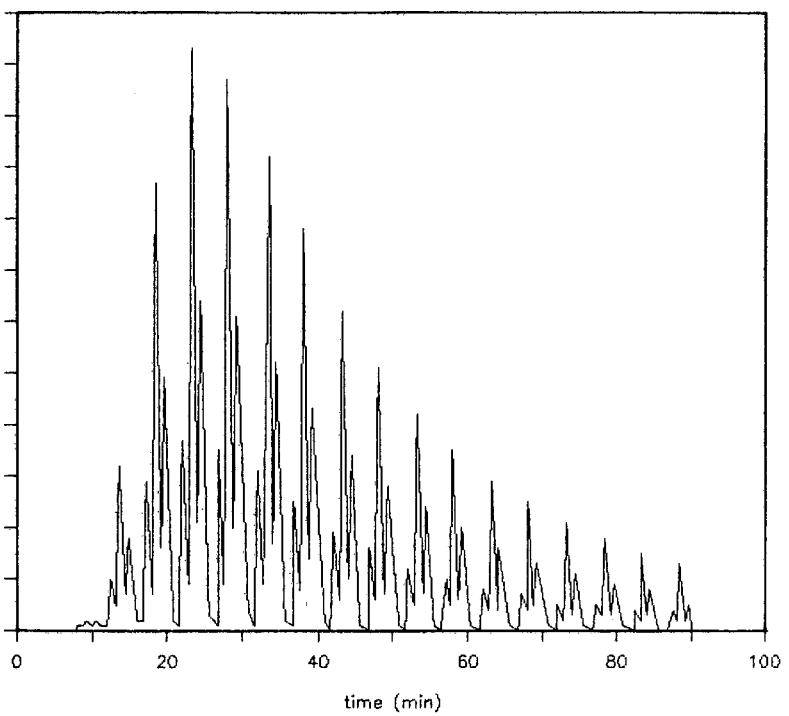

Fig. 1. Set of chromatograms of reaction products from *n*-butanol dehydration reaction. Catalyst, Porasil E covered with H_3PO_4. Time resolution, 1 s. Reactor temperature, 283°C. Identification of peaks in triplets (from left to right): 1-butene, *cis*,*trans*-2-butene and 2-methylpropene. Detector response in arbitrary units.

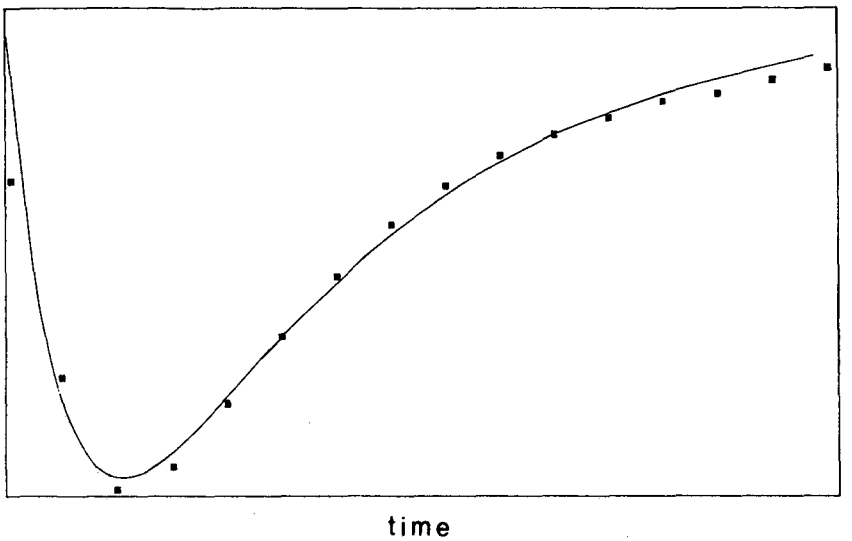

Fig. 2. Fitting of *cis*-butene peak areas (from Fig. 1) with the function in eqn. 1. Rate constants: $a = 0.940\ s^{-1}$ and $k = 0.193\ s^{-1}$. Interval between points, 1 s.

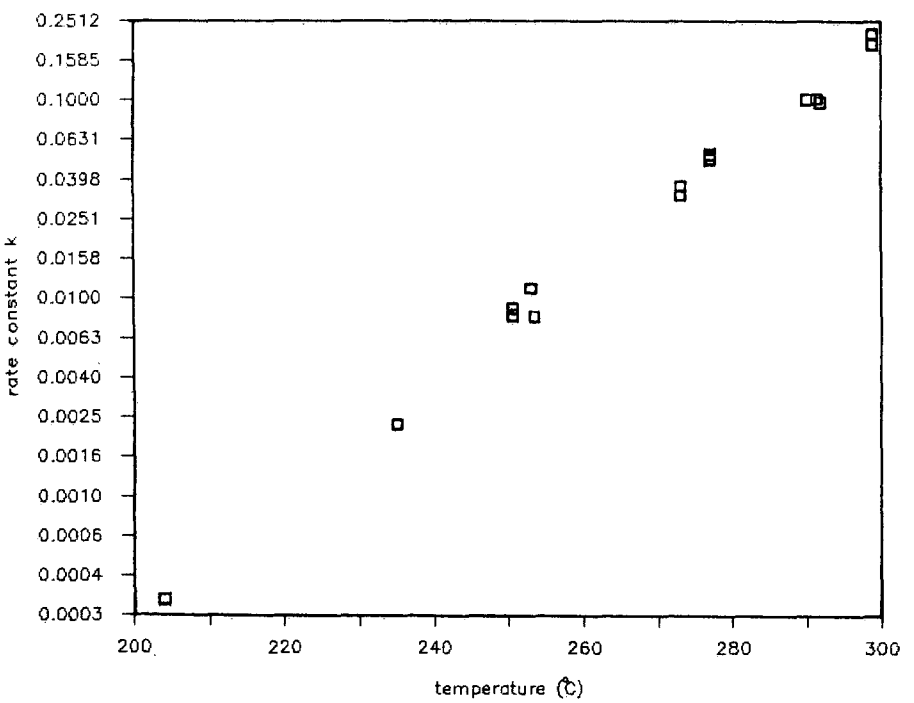

Fig. 3. Rate constant (s^{-1}) of *n*-butanol, *k*, as a function of temperature (note the logarithmic scale for *k*). The Arrhenius plot for these data gives the function $\log k = 31.01 - 18.74 \cdot 10^3/RT$ with a correlation coefficient of 0.998.

different products it is possible to construct concentration curves for different products and fit the curves to the model in eqn. 1 by the least-squares method. To minimize the difference between the experimental values and the theoretical model, we used both a random search for the best fit and the gradient method. Both procedures are standard in computational mathematics. An example of the best fit obtained is show in Fig. 2. As can be seen, the fit is perfect for the falling part of the curve but problems arise with the rising part of the curve. The error depends strongly on how many experimental points from the beginning of the curve are used for fitting. Hence the model in eqn. 1 is not the best one to describe catalysis in our system and more exact models must be sought. A discussion of the different models that can be used to describe the processes in the reactor is the topic of another paper[9]. However, for the purpose of this paper, the model in eqn. 1 is suitable.

By fitting eqn. 1 to the experimental data we obtain two rate constants, but from the results obtained it is not possible to decide which of the constants is a and which is k. From theory[6], it follows that a depends linearly on the inert carrier gas velocity and is independent of temperature. For k as a chemical reaction rate contstant the opposite applies. Hence by varying the temperature and the carrier gas velocity it is possible to differentiate between rate constants obtained by the least-squares fitting of experimental data. In Fig. 3, the temperature dependence of log k is presented as a function of temperature for butanol reactions. It can be seen that stroboscopic

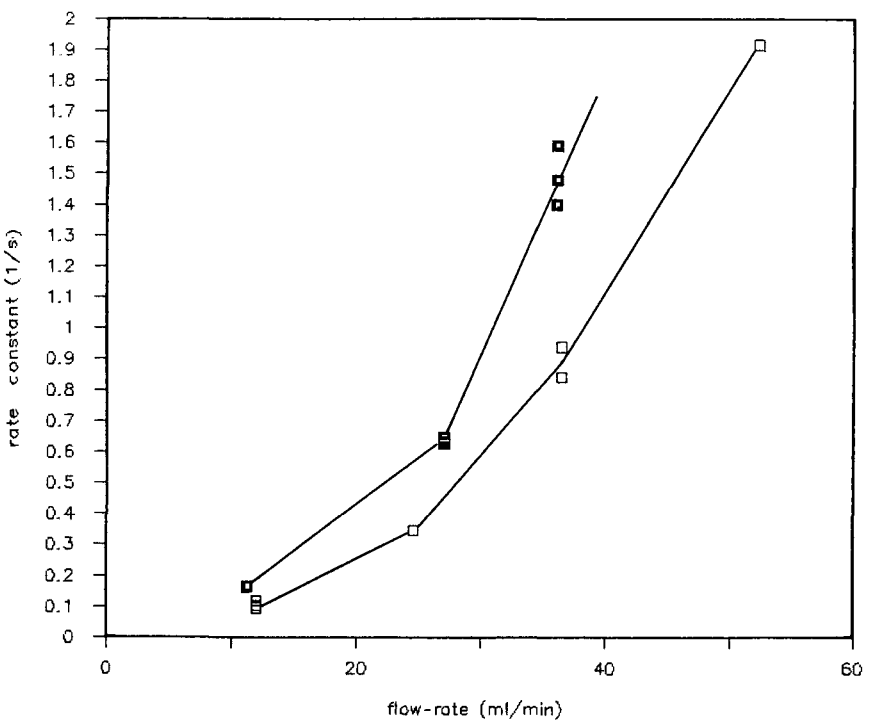

Fig. 4. Mass flow-rate constant, a, as a function of the carrier gas flow-rate through the reactor. Reactor temperature, 283°C. ■, n-Propanol ($k = 0.01$ s^{-1}); □, n-butanol ($k = 0.007$ s^{-1}).

sampling permits the measurement of reaction rate constants of more than three orders of magnitude of k and over a wide temperature range.

In Fig. 4, the dependence of a on the carrier gas velocity is presented. Evidently the function is non-linear, again demonstrating the contradiction with theory, which predicts a linear function. Hence the catalyst used in this work cannot be considered a pure H_3PO_4 liquid catalyst and the support has a strong influence on the reaction course. A complete analysis of the results of this work together with computations of the activation energies, etc., and chemical interpretation of the results will be presented elsewhere[9].

Ignition of polypropylenes

The system performance was tested by oxidation of ethanol. The reproducibility of the overall system was tested by repeating the same experiment many times and recording the product peak height at a certain temperature (450°C). The product peak height reproducibility was 0.3%. The result can be considered acceptable, taking into account that at the ignition temperature the amount of product depends critically on the reaction temperature.

According to the measurement procedure it was possible to record the temperature dependence of the product/reagent concentration curves even under conditions of very rapid self-heating. However, no temperature effects were observed in this experiment. This may be explained by a low concentration of the evolved gases in the carrier stream which, being oxidized, does not provide sufficient heat for the self-heating of the reaction environment. Therefore, in this experiment, the rapid external ballistic heating imitates conditions of self-heating during ignition.

All the samples were analysed in helium and air; 0.1-g samples, when heated at 300°C, provided a continuous and almost constant stream of evolved gases for several hours. Only at the very beginning of the sample heating did the evolution rate oscillate irregularly for the flame retardant-containing samples. Also, it was possible to observe visually extensive foaming of these samples at the experimental temperatures, which may be the reason for the irregular evolution of the degradation products from the polymer samples.

A typical set of chromatograms recorded in air as a function of temperature with a resolution of 25°C or the sample without the flame retardant is shown in Fig. 5. The first peak belongs to the lightest degradation products, probably C_1–C_3 hydrocarbons. It follows from Fig. 5 that the height of the first peak starts to increase after 500°C and the intensity of the other peaks decreases. This is the temperature at which extensive thermal degradation of the evolved products to the lightest compounds begins. The intensity of the first peak passes through a maximum and disappears at 700°C, indicating complete oxidation of the degradation products to water and carbon dioxide. As a flame ionization detector was used, the end products are invisible on the chromatograms. In helium the degradation starts above 540°C and the intensity of the first peak reaches a constant value, as expected.

The effect of the flame retardant is demonstrated in Fig. 6, in which particular temperature points are plotted for samples containing 0 and 40% of the flame retardant as a function of the polymer heating time. It follows from Fig. 6 that the flame retardant influences the heating only at the beginning. A new peak appeared in the chromatogram the intensity of which decreased rapidly and after 1 h the sample behaved like a sample with no flame retardant.

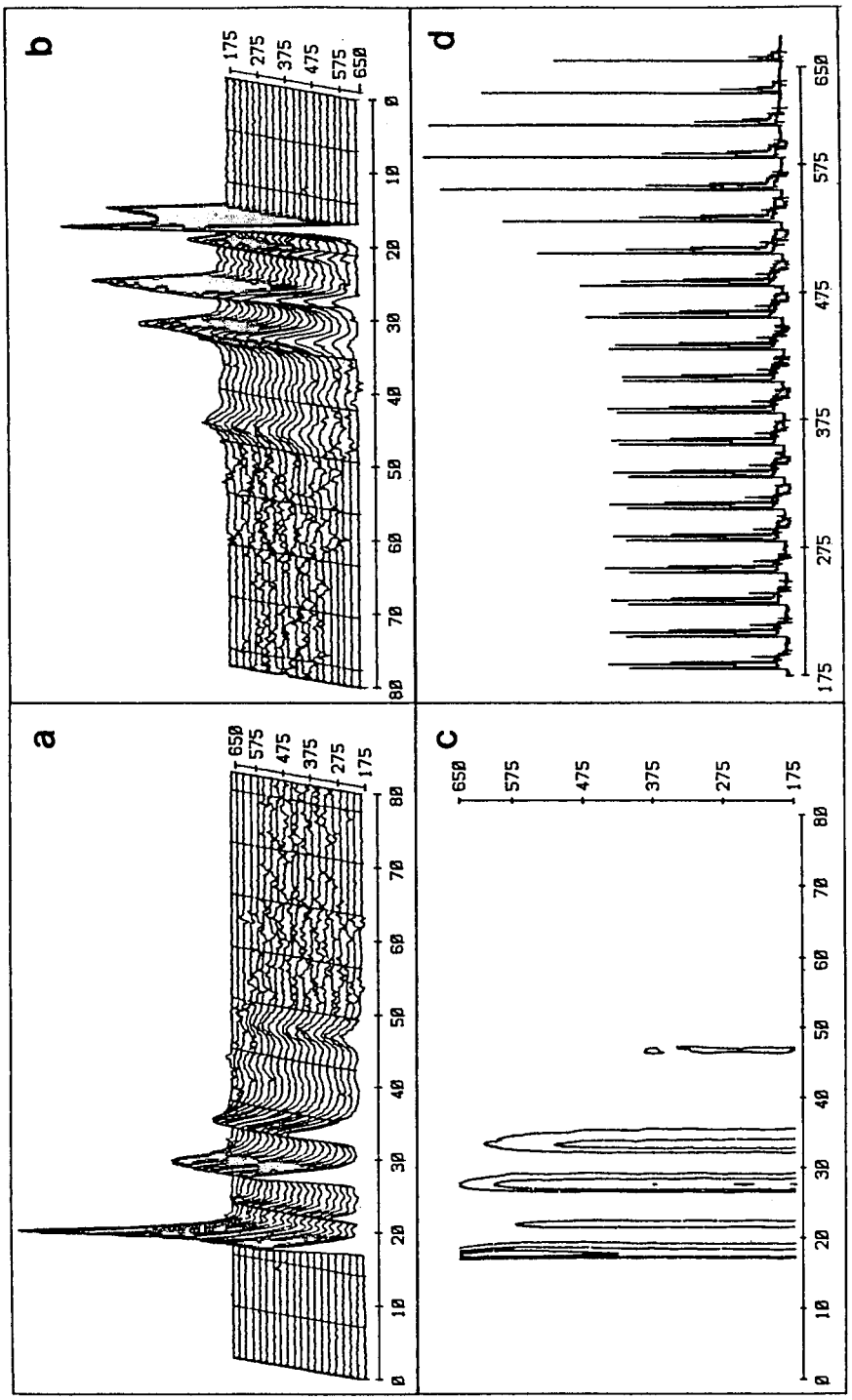

Fig. 5. Different representations of the thermochromatogram of the oxidation reaction of polypropylene degradation products. Polymer heating temperature, 300°C. (a), (b) Stack plots; (c) contour plot; (d) set of reactant chromatograms as they appear on the chart recorder. The time axis (abscissa) represents the chromatographic running time in seconds; the temperature axis (ordinate) represents the oxidation reaction running temperature with a time resolution of 25°C.

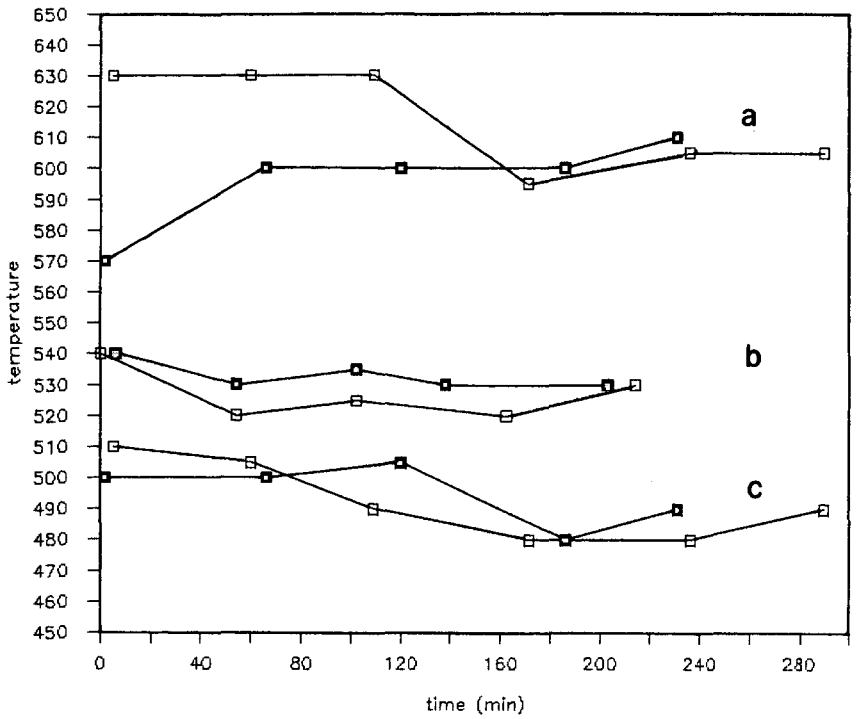

Fig. 6. Particular temperature points on polypropylene ignition thermochromatograms as a function of sample heating time. (a) Temperature of the maximum intensity of the first peak; (b) temperature of the beginning of pyrolysis of the degradation products in helium; (c) temperature of the beginning of pyrolysis of the degradation products in air. □ = 0% flame retardant; ■ = 40% flame retardant. Temperature in °C.

A more detailed analysis of ignition data together with the interpretation of the results from the viewpoint of polymer chemistry will be published in the near future.

So far gas chromatography has been used for the analysis of slow chemical reactions. Recent developments in high-speed chromatography have made possible separations in a few seconds. However, this requires the design of special fast-response chromatographic equipment[10]. As follows from the results of this work, stroboscopic sampling enables common chromatographic equipment to be used.

ACKNOWLEDGEMENTS

The authors thank A. Bureiko for performing the H_3PO_4 catalysis measurements, Dr. B. V. Stolyarov and Dr. A. N. Marinichev of Leningrad University for fruitful discussions and providing the catalyst and Dr. M. Elomaa of Helsinki University for providing the polypropylene samples and for discussions on polymer ignition problems.

REFERENCES

1 E. A. Denisoff, *Kinetics of Homogeneous Chemical Reactions* (in Russian), Vyshaya Schola, Moscow, 1988, p. 19.
2 M. Kaljurand, *Proc. Estonian AS, Chemistry*, 38 (1989) 25.
3 M. Kaljurand, M. Lamberg and E. Küllik, *Proc. Estonian AS, Chemistry*, 37 (1988) 78.
4 A. F. Shushunova and L. Y. Prokhorova, *J. Chromatogr.*, 283 (1984) 365.
5 M. Kaljurand and E. Küllik, *Computerised Multiple Input Chromatography*, Ellis Horwood, Chichester, 1989.
6 A. N. Marinitchev and B. V. Ioffe, *J. Chromatogr.*, 454 (1988) 327.
7 N. Grassie and G. Scott, *Polymer Degradation and Stabilization*, Cambridge University Press, Cambridge, 1984.
8 B. V. Ioffe, N. A. Katsanos, L. A. Kokovina, A. N. Marinitchev and B. V. Stolyarov, *Kinet. Katal.*, 28 (1987) 805.
9 A. N. Bureiko, M. Kaljurand, A. N. Marinichev and B. V. Stolyarov, *Kinet. Katal.*, in press.
10 C. A. Cramers and P. A. Leclerq, *CRC Crit. Rev. Anal. Chem.*, 20 (1988) 117.

Journal of Chromatography, 517 (1990) 185–192
Elsevier Science Publishers B.V., Amsterdam

CHROMSYMP. 1981

High-performance liquid chromatographic study of ligand-exchange reactions of fluorinated metal β-diketone chelates

TAO WANG and PETER C. UDEN*
Department of Chemistry, Lederle Graduate Research Towers, University of Massachusetts, Amherst, MA 01003 (U.S.A.)

ABSTRACT

Ligand redistribution reactions among gallium, indium, copper and nickel fluorinated β-diketonates were investigated by normal-phase high-performance liquid chromatography on a silica column. Reactions taking place at ambient temperature in tetrahydrofuran–heptane solutions were shown to proceed with statistical ligand exchange. Good chromatographic characteristics were seen for the range of initial and product gallium chelates. Although other complexes were not eluted under the conditions used, the reactions which occurred in mixed-metal systems could be inferred from examination of gallium chelate chromatograms.

INTRODUCTION

Gas chromatographic (GC) separation of neutral metal chelates is limited by requirements of adequate volatility and thermal stability[1]. High-performance liquid chromatography (HPLC), however, allows appplication to metal chelates that are less volatile or thermally stable, and provides selectivity through suitable choice of stationary and mobile phases.

HPLC of metal complexes was first reported by Huber and Kraak[2] who employed liquid–liquid partition chromatography in a ternary solvent system, consisting of water, ethanol and 2,2,4-trimethylpentane. They established conditions necessary to separate as many as six metal acetylacetonates, among them those of Be(II), Al(III), Cr(III), Fe(III), Co(III), NI(II), Cu(II), Zn(II), Zr(IV) and Ru(III). Reports in which high-performance bonded phase or liquid–solid chromatography have been applied to metal complexes have included separations of metal chelates of tetradentate β-ketoamines[3–6], metal β-diketonates[6–9], metal cluster complexes[10], organoiron complexes[11], Rh and Ir triphenylphosphine complexes[12], metal 8-hydroxyquinoline complexes[13,14], dialkyldithiocarbamates[15,16] and crown ether complexes[17]. Review papers have further detailed the research on this subject[18,19].

In addition to the application to the separation of non-volatile and thermally unstable metal chelates, HPLC can be used to study their reactions, such as ligand

0021-9673/90/$03.50

exchange between two metal chelates with different ligands. A study of ligand-exchange reactions between fluorinated gallium, indium and aluminum β-diketonate chelates has been reported by GC with microwave-induced plasma (MIP) detection[20]. However, there is the possbility that the ligand-exchange reactions did not occur in the solution, but took place at least in part, in the gaseous phase in the heated injection port of the gas chromatograph. To investigate and confirm that the ligand-exchange reactions did occur in the liquid phase, the use of HPLC was necessary.

No HPLC study of ligand-exchange reactions of fluorinated gallium β-diketonates has previously been reported. In our study, a normal-phase separation mode was used to investigate these reactions between fluorinated gallium, indium, copper and nickel β-diketonates, and to prove that they did occur in the liquid phase. The ligands tested were 1,1,1-trifluoropentane-2,4-dione (HTFA), 1,1,1-trifluoro-hexane-2,4-dione (HTFEA), 1,1,1-trifluoro-5,5-dimethylhexane-2,4-dione (HTTB) and 1,1,1-trifluoro-6-methylheptane-2,4-dione (HTIB).

EXPERIMENTAL

Instrumentation

A HPLC system (Perkin-Elmer, Norwalk, CT, U.S.A.), equipped with a Series 100 pump and a TriDet detector was employed. The mobile phase was tetrahydrofuran–heptane (specific compositions of the mobile phase are listed in Table I and in the chromatograms). UV detection was at 254 nm. The column was a Spherisorb S5W silica column (5 μm, 150 × 4.6 mm I.D.) (Keystone Scientific, Bellefonte, PA, U.S.A.). A 10-μl sample loop was used and chromatograms were recorded on an Omniscribe recorder (Houston Instruments, Austin, TX, U.S.A.).

Materials and procedures

The procedures for the preparation of $Ga(TFA)_3$ and $In(TFA)_3$ have been described[20]. $Ga(TFEA)_3$, $Ga(TTB)_3$ and $Ga(TIB)_3$ were prepared in a similar way to that for $Ga(TFA)_3$. A procedure similar to that given by Berg and Truemper[21] was used to prepare $Cu(TFA)_2$ and $Ni(TFA)_2$. This involved shaking an alcoholic solution of the ligand with a 5% nitrate solution of the corresponding metal, buffered

TABLE I

CONDITIONS OF LIGAND-EXCHANGE REACTIONS STUDIED WITH HPLC

Temperature was 25°C.

Initial chelates	*Molar ratio*	*Solvent (THF–heptane, v/v)*	*Reaction time (h)*
$Ga(TFA)_3/Ga(TIB)_3$	3:2	15:85	24
$Ga(TFA)_3/Ga(TFEA)_3$	1:1	15:85	24
$Ga(TTB)_3/Ga(TFEA)_3/Ga(TFA)_3$	7:10:14	7.5:92.5	28
$Ga(TIB)_3/In(TFA)_3$	0.5:1	13:87	330
$Ga(TTB)_3/Cu(TFA)_2$	2:5	14:86	24
$Ga(TFA)_3/Cu(TTB)_2$	1:1	15:85	16
$Ga(TTB)_3/Ni(TFA)_2$	0.5:1	13:87	330

with sodium acetate (5 g for every 100 ml of solution). After precipitation, the chelate was collected by filtration, air-dried, recrystallized from benzene, and air-dried again.

Ligand-exchange reactions were carried out by dissolving the initial metal chelates in a portion of the mobile phase and allowing the reactions to take place under the conditions described in Table I. These conditions were such that no further changes in the chromatograms obtained were observed for longer reaction times. Since the chelates were difficult to dissolve directly in the mobile phase, they were first dissolved in tetrahydrofuran (THF) and then diluted with heptane to bring the solvent compositions to those of the mobile phases employed in HPLC. The concentrations of the chelates in these solutions of reaction mixtures were in the mmol/l range. The reaction mixtures were analyzed after the time periods specified in Table I.

RESULTS AND DISCUSSION

Ligand-exchange reaction between two gallium chelates

$Ga(TFA)_3$ and $Ga(TIB)_3$ undergo ligand exchange. The equilibrium process may be described as follows:

$$Ga(TFA)_3 + Ga(TIB)_3 \rightleftharpoons Ga(TFA)_2(TIB) + Ga(TFA)(TIB)_2$$

After the reaction procedure described in Table I was carried out, the reaction mixture was chromatographed. Fig. 1 shows the separation of four resultant gallium chelates under the experimental conditions indicated. THF–heptane (3:17, v/v) proved to be a suitable mobile phase for baseline separation and good peak shape with elution in < 4 min. Peaks 1 and 4 were identified as $Ga(TIB)_3$ and $Ga(TFA)_3$, respectively, by retention-time comparison with pure chelates. Peaks 2 and 3, eluted between peaks 1 and 4, were identified as $Ga(TIB)_2(TFA)$ and $Ga(TIB)(TFA)_2$. Since a normal-phase mode was employed, chelate species with ligands of greater carbon number and molecular weight tended to be eluted earlier; the elution order of $Ga(TIB)_3 < Ga(TIB)_2(TFA) < Ga(TIB)(TFA)_2 < Ga(TFA)_3$ showed this trend. The redistribution had clearly occurred during the 24-h liquid-phase reaction; the good resolution and peak shapes obtained indicated that no discernable further redistribution occurred during the chromatographic elution process.

Ligand-exchange reaction between $Ga(TFA)_3$ and $Ga(TFEA)_3$ was then carried out under similar conditions. Fig. 2 illustrates the separation of the resulting mixture. The sequence of the peaks, based on retention-time comparison with pure chelates, was in an order similar to that in the previous redistribution reaction, and liquid-phase reaction at room temperature had certainly taken place. Again, excellent peak shape and resolution indicated no discernable on-column redistribution.

Ligand-exchange reaction among three gallium chelates

A ligand-exchange reaction between $Ga(TTB)_3$, $Ga(TFEA)_3$ and $Ga(TFA)_3$ was then carried out to serve as an example of a triple exchange among three different chelates. Following the procedure listed in Table I, the chromatogram shown in Fig. 3 was obtained with seven baseline-separated peaks. Identifications of these peaks were made by comparing retention times with those of the products obtained separately from ligand-exchange reactions between $Ga(TTB)_3$ and $Ga(TFA)_3$, between

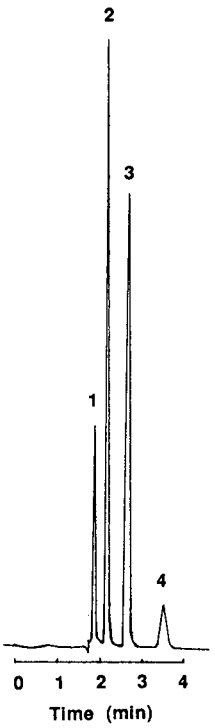

Fig. 1. HPLC separation of mixture of ligand-exchange reaction products formed from $Ga(TFA)_3$ and $Ga(TIB)_3$. Column 5 μm silica, 150 × 4.6 mm I.D.; mobile phase THF–heptane (3:17, v/v); flow-rate 1.0 ml/min; UV detection 254 nm; reaction time 24 h at 25°C. Peaks: 1 = $Ga(TIB)_3$; 2 = $Ga(TFA)(TIB)_2$; 3 = $Ga(TFA)_2(TIB)$; 4 = $Ga(TFA)_3$.

$Ga(TTB)_3$ and $Ga(TFEA)_3$, and between $Ga(TFEA)_3$ and $Ga(TFA)_3$. Peaks 3, 4 and 5 are each considered to consists of two unresolved gallium chelates. An interesting observation is that peak 3 consists of Ga(TTB)$\underline{(TFEA)_2}$ and Ga(TTB)$\underline{(TTB)(TFA)}$, the underlined parts of the two chelates being designated to show the difference between them. Since the two chelates had virtually identical retention, the two chelated ligands $\underline{(TFEA)_2}$ contribute the same overall retention as the two chelated ligands $\underline{(TTB)(TFA)}$ present together. A similar effect is also noted in peak 5, which consists of Ga$\underline{(TTB)}$(TFA)(TFA) and Ga$\underline{(TFEA)_2}$(TFA). Again the underlined parts $\underline{(TFEA)_2}$ and $\underline{(TTB)(TFA)}$ show the only difference between these two similarly retained chelates.

The complex which contained three different ligands, Ga(TTB)(TFEA)(TFA), was expected to be produced from the ligand-exchange reaction among the three chelates, $Ga(TTB)_3$, $Ga(TFEA)_3$ and $Ga(TFA)_3$. However, since it could not be produced by ligand-redistribution reactions between any two of these three chelates only, its direct identification, by retention-time comparison with such reaction products, was impossible. Therefore, retention of Ga(TTB)(TFEA)(TFA) was deduced by arguments similar to those for peaks 3 and 5. Since the only difference between

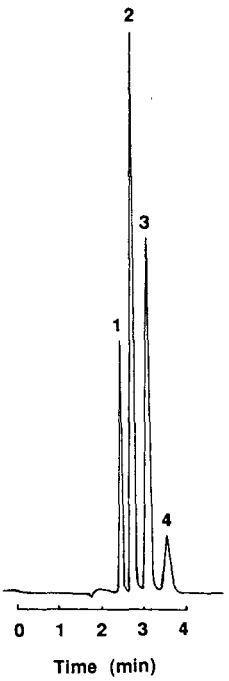

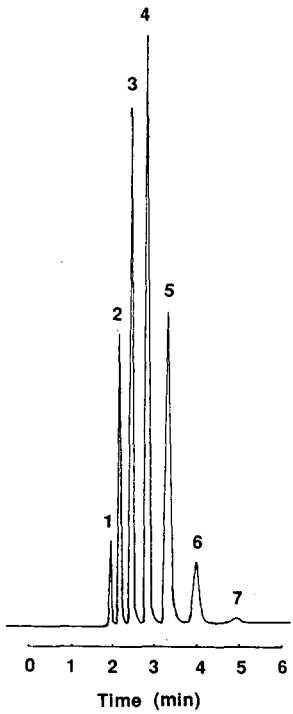

Fig. 2. HPLC separation of mixture of ligand-exchange reaction products formed from $Ga(TFA)_3$ and $Ga(TFEA)_3$. Conditions as in Fig. 1. Peaks: 1 = $Ga(TFEA)_3$; 2 = $Ga(TFA)(TFEA)_2$; 3 = $Ga(TFA)_2(TFEA)$; 4 = $Ga(TFA)_3$.

Fig. 3. HPLC separation of mixture of ligand-exchange reaction products formed from $Ga(TTB)_3$, $Ga(TFEA)_3$ and $Ga(TFA)_3$. Column 5 μm silica, 150 × 4.6 mm I.D.; mobile phase THF–heptane (7.5:92.5, v/v); flow-rate 1.0 ml/min; UV detection 254 nm; reaction time 28 h, at 25°C. Peaks: 1 = $GA(TTB)_3$; 2 = $Ga(TTB)_2(TFEA)$; 3 = $Ga(TTB)(TFEA)_2$ and $Ga(TTB)_2(TFA)$; 4 = $Ga(TFEA)_3$ and $Ga(TTB)(TFEA)(TFA)$; 5 = $Ga(TTB)(TFA)_2$ and $Ga(TFEA)_2(TFA)$; 6 = $Ga(TFEA)(TFA)_2$; 7 = $Ga(TFA)_3$.

$Ga(\underline{TFEA})_2(TFEA)$ and $Ga(\underline{TTB})(\underline{TFA})(TFEA)$ is that between the two underlined parts and since these were previously observed to give the same overall retention, peak 4 which was identified as containing $Ga(\underline{TFEA})_2(TFEA)$ [*i.e.* $Ga(TFEA)_3$], should also contain $Ga(\underline{TTB})(\underline{TFA})(TFEA)$ [which is $Ga(TTB)(TFEA)(TFA)$]. The magnitude of the response observed for peak 4 also indicated the presence of $Ga(TTB)(TFEA)(TFA)$ in addition to $Ga(TFEA)_3$; only a small peak would be expected for the latter as a result of the statistical nature of the redistribution reaction. In the reaction described, the molar ratio of $Ga(TTB)_3$, $Ga(TFEA)_3$ and $Ga(TFA)_3$ was chosen as 7:10:14, in order to present a clear redistribution chromatogram with peaks of significant scale for all species. However, for the equimolar case, the statistical response ratio, shown in parentheses (assuming identical molar absorptivities for all chelates at 254 nm), for peaks 1–7 (Fig. 3) would be predicted as peak 1 (1), peak 2 (3), peak 3 (3+3), peak 4 (9+1), peak 5 (3+3), peak 6 (3) and peak 7 (1). The lowest relative amounts of redistributed chelates are for the symmetrical complexes. Al-

though the experiment described gives skewed response data, the general trend is clearly shown as consistent with the foregoing analysis.

Ligand-exchange reactions between gallium and indium chelates

$Ga(TIB)_3$ and $In(TFA)_3$ were chosen to exemplify the HPLC study of ligand-exchange reactions between gallium and indium chelates. After allowing the two chelates to react according to the procedure listed in Table I, the reaction products were chromatographed (Fig. 4) to give four symmetrical baseline-resolved peaks. By comparing the retention times of the peaks with those obtained from ligand-exchange reaction between $Ga(TIB)_3$ and $Ga(TFA)_3$, peaks 1, 2, 3 and 4 were identified as $Ga(TIB)_3$,$Ga(TIB)_2(TFA)$, $Ga(TIB)(TFA)_2$ and $Ga(TFA)_3$, respectively. Although it has been shown by GC[20] that the mixture of ligand-exchange reaction products obtained from $Ga(TIB)^3$ and $In(TFA)_3$ did contain $In(TIB)_3$ and $In(TFA)_3$ in addition to the four gallium chelates, the indium chelates could not be eluted from the HPLC system under the conditions employed. However, the HPLC study proved that the ligand-exchange reactions between gallium and indium fluorinated β-diketone chelates did proceed in the liquid phase. Again there was no chromatographic evi-

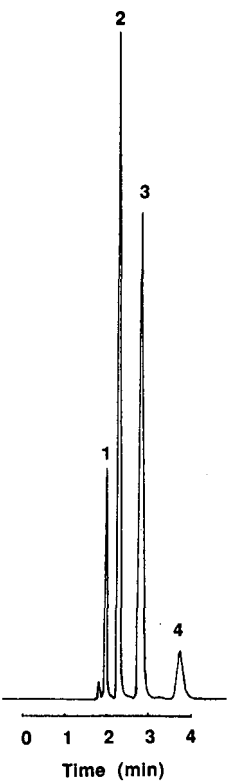

Fig. 4. HPLC separation of mixture of ligand-exchange reaction products formed from $Ga(TIB)_3$ and $In(TFA)_3$. Column 5 μm silica, 150 × 4.6 mm I.D.; mobile phase THF–heptane (13:87, v/v); flow-rate 1.0 ml/min; UV detection 254 nm; reaction time 330 h at 25°C. Peaks: 1 = $Ga(TIB)_3$; 2 = $Ga(TFA)(TIB)_2$; 3 = $Ga(TFA)_2(TIB)$; 4 = $Ga(TFA)_3$.

dence of on-column redistribution although degradation of the indium did presumably occur.

Ligand-exchange reactions between gallium and copper chelates

$Cu(TFA)_2$ was allowed to react with $Ga(TTB)_3$ in a 1:1 molar ratio according to the conditions described in Table I and the reaction products were chromatographed. Four resultant peaks are shown in Fig. 5, identified by comparing the retention times with those of the peaks obtained from the reaction between $Ga(TFA)_3$ and $Ga(TTB)_3$. Copper chelates could not be eluted under the experimental conditions employed and therefore only the gallium chelates appeared on the chromatograms.

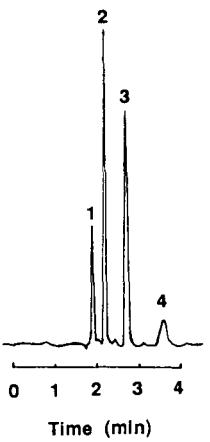

Fig. 5. HPLC separation of mixture of ligand-exchange reaction products formed from $Ga(TTB)_3$ and $Cu(TFA)_2$. Column 5 μm silica, 150 × 4.6 m I.D.; mobile phase THF–heptane (14:86, v/v); flow-rate 1.0 ml/min; UV detection 254 nm; reaction time 24 h at 25°C. Peaks: 1 = $Ga(TTB)_3$; 2 = $Ga(TFA)(TTB)_2$; 3 = $Ga(TFA)_2(TTB)$; 4 = $Ga(TFA)_3$.

$Ga(TFA)_3$ was then allowed to react with $Cu(TTB)_2$ (1:1) to yield a chromatogram which was virtually identical with that in Fig. 5. The reaction between $Cu(TFA)_2$ and $Ga(TTB)_3$ apparently proceeded to give products identical to those from the reaction between $Ga(TFA)_3$ and $Cu(TTB)_2$.

It was concluded that the ligand-exchange reactions between gallium and copper fluorinated β-diketone chelates occurred in liquid phase with no ligand distribution bias due to the difference in structure between the gallium (octahedral) and copper (tetrahedral) complexes.

Ligand-exchange reaction between gallium and nickel chelates

$Ga(TTB)_3$ was allowed to react with $Ni(TFA)_2$ (1:1) under conditions described in Table I, giving rise to a chromatogram similar to that in Fig. 5. Although the nickel chelates were not eluted from the column, the ligand-exchange reaction was shown to have occurred in the liquid phase. In this case, the reactant nickel complex was probably trimeric, but this did not appear to perturb the redistribution pattern.

CONCLUSION

This study shows that the normal-phase HPLC for these metal complexes is highly dependent upon the metal atom present. However, all of the ligand redistributions investigated were shown to have taken place in the liquid phase under the ambient temperature reaction conditions employed. The kinetics of representative ligand-redistribution reactions may be obtained from further HPLC studies.

ACKNOWLEDGEMENTS

This work was supported in part by Baxter Healthcare Inc. and by Merck, Sharp and Dohme Research Laboratories.

REFERENCES

1 P. C. Uden, *J. Chromatogr.*, 313 (1984) 3.
2 J. F. K. Huber and J. C. Kraak, *Anal. Chem.*, 44 (1972) 1554.
3 P. C. Uden, D. M. Parees and F. H. Walters, *Anal. Lett.*, 8 (1975) 795.
4 E. Gaetani, C. Laureri, A. Maugin and G. Parolari, *Anal. Chem.*, 48 (1976) 1725.
5 P. C. Uden and F. H. Walters, *Anal. Chim. Acta*, 79 (1975) 175.
6 P. C. Uden, B. D. Quimby, R. M. Barnes and W. G. Elliott, *Anal. Chim. Acta*, 101 (1978) 99.
7 P. C. Uden, I. E. Bigley and F. H. Walters, *Anal. Chim. Acta*, 100 (1978) 555.
8 R. C. Gurira and P. W. Carr, *J. Chromatogr. Sci.*, 20 (1982) 461.
9 C. A. Tollinche and T. H. Risby, *J. Chromatogr. Sci.*, 16 (1978) 448.
10 C. T. Enos, G. L. Geoffroy and T. H. Risby, *J. Chromatogr. Sci.*, 15 (1977) 83.
11 R. E. Graf and C. P. Lillya, *J. Organometal. Chem.*, 47 (1973) 413.
12 C. T. Enos, G. L. Geoffroy and T. H. Risby, *Anal. Chem.*, 48 (1976) 990.
13 C. S. Hambali and P. R. Haddad, *Chromatographia*, 13 (1980) 633.
14 P. R. Haddad and S. Valeenuwat, *J. High Resolut. Chromatogr. Chromatogr. Commun.*, 9 (1986) 127.
15 Z. G. Schwedt, *Anal. Chem.*, 288 (1978) 50.
16 P. C. Uden and I. E. Bigley, *Anal. Chim. Acta*, 94 (1977) 29.
17 A. Mangia, G. Parolari, E. Gaetani and C. F. Laureri, *Anal. Chim. Acta*, 92 (1977) 111.
18 J. W. O'Laughlin, *J. Liq. Chromatogr.*, 7(S-1) (1984) 127.
19 R. M. Cassidy, in J. F. Lawrence (Editor), *Trace Analysis*, Vol. 1, Academic Press, New York, 1981, p. 121.
20 P. C. Uden and T. Wang, *J. Anal. Atom. Spectr.*, 3 (1988) 919.
21 E. W. Berg and J. T. Truemper, *J. Phys. Chem.*, 64 (1960) 487.

Journal of Chromatography, 517 (1990) 193–207
Elsevier Science Publishers B.V., Amsterdam

CHROMSYMP. 1901

Silicas chemically bonded with multidentate phenyl groups as stationary phases in reversed-phase liquid chromatography used for non-planarity recognition of polycyclic aromatic hydrocarbons

KIYOKATSU JINNO*, KUNIHIKO YAMAMOTO, HIDEO NAGASHIMA, TAKANORI UEDA and KENJI ITOH
School of Materials Science, Toyohashi University of Technology, Toyohashi 441 (Japan)

ABSTRACT

Multidentate phenyl-bonded phases have been evaluated as stationary phases which can recognize molecular non-planarity of polycyclic aromatic hydrocarbons. The results clearly indicate that these multidentate silicas give a higher non-planarity recognition capability than that with typical octadecylsilicas such as polymeric and monomeric phases. The reason for this mechanism can be interpreted by the molecular–molecular interaction between a solute and a stationary phase and this kind of approach will open the possibility of designing new stationary phases which offer more selective or specific separations.

INTRODUCTION

As planarity recognition is directly related to the physico-chemical properties and biological activities of polycyclic aromatic hydrocarbons (PAHs)[1–3], it is necessary to have good separation and analytical methods for this recognition. Generally in the separation of PAHs by reversed-phase liquid chromatography (LC), which seems to be the most powerful and useful method, chemically bonded octadecylsilica (ODS) phases have been used as the stationary phase of choice because of their capability and applicability. ODS phases can be divided into two categories, one polymeric and the other monomeric. Polymeric phases are normally synthesized by using polyfunctional silanes in the presence of water (or sometimes even under conditions carefully controlled to exclude water) based on polymeric surface modification chemistry, whereas monomeric phases are obtained by using monofunctional silanes as the starting material. A number of papers have reported the differences in the chromatographic properties of the two types of ODS phases for PAH separations[4–10]. The conclusion was that polymeric phases have a greater capability of recognizing molecular planarity of PAHs. Non-planar molecules were eluted faster than planar molecules with polymeric phases because the phases have a "slit-like"

0021-9673/90/$03.50

structure on the surface, as described Sander and Wise[4–6]. Solid-state cross-polarization magic angle spinning nuclear magnetic resonance (CP-MAS-NMR) spectrometry of various phases clearly revealed that the molecular freedom of the polymeric phases is less than that of the monomeric phases and this limited molecular freedom induces the recognition of the molecular planarity[9,11,12], where enhancement of the retention for planar molecules would be expected. To enhance planarity recognition more, we investigated the use of dicoronylene as the stationary phase for the separation of PAHs. Dicoronylene has a very flat structure and it can retain planar and exclude non-planar solutes, so that the planarity recognition was enhanced[13,14]. However, one can consider the opposite case, in which stationary phases retain non-planar molecules to a greater extent than planar molecules, so that enhanced selectivity of planar *vs.* non-planar could be also expected.

In this work, newly synthesized phenyl-bonded stationary phases were evaluated for this non-planarity recognition of PAHs. A novel concept of the stationary phase structure has been introduced for synthesizing these phases. The phases use 'bidentate' or 'tridentate' silanes containing one reactive atom on each two or three silicon atoms that are connected through a phenyl ring. Discussions herein indicate that the design of stationary phases which offer high selectivity for particular solute groups will be possible based on the consideration of molecular–molecular interactions between solutes and stationary phase ligands.

EXPERIMENTAL

New stationary phases were synthesized using reactions developed in our laboratory[15]. Base silica was obtained from Shiseido (Yokohama, Japan). The particle diameter is *ca.* 5 μm and very low metal impurity concentrations are present. The surface area of the silica is *ca.* 270 m^2. These new materials are *p*-bis(dimethylphenyl) (BP)- and 1,3,5-tris(dimethylphenyl) (TP)-bonded silicas. For comparison, phenyl (P) and methyl (C1) bonded silicas were also synthesized. The procedures for synthesizing them are described elsewhere[15].

Typical starting silane compounds for BP and TP phases are produced by the following reactions (Me = methyl):

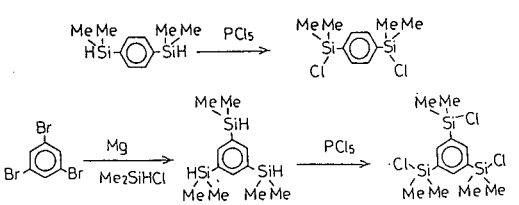

The basic difference between these phases and the generally commercially available phases is the structure on the silica surface. As shown in Fig. 1, BP and TP have a unique structure which covers the silica surface horizontally, whereas P, C1 and general ODS phases are attached vertically to the silica surface by siloxane bonding. As the bidentate or tridentate reagents can form two or three bonds to the silica surface for each molecule of silane and these multi-bonds produce a multi-membered

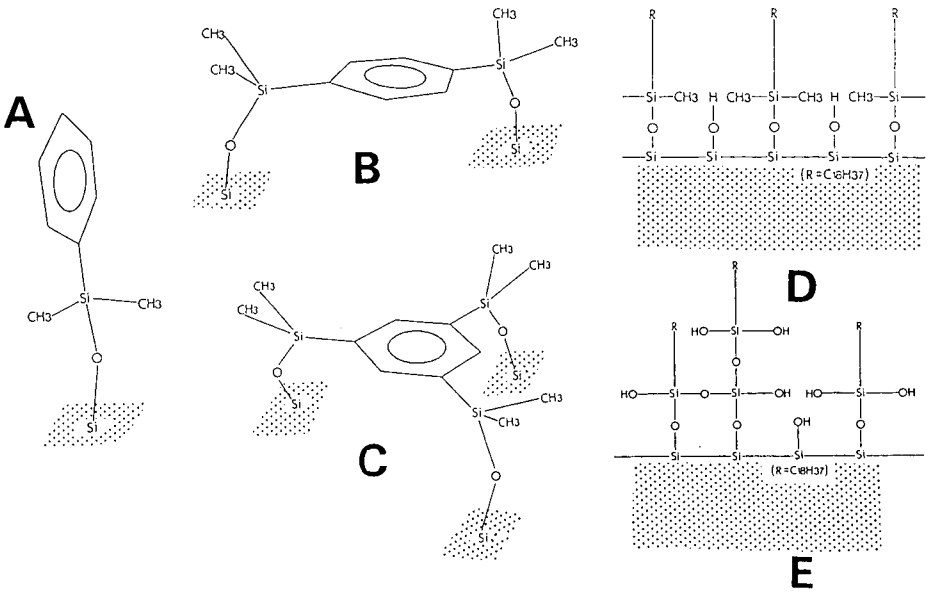

Fig. 1. Bonded-phase structures investigated. (A) P; (B) BP; (C) TP; (D) monomeric ODS; (E) polymeric ODS.

ring with the silica structure, they should lead to increased stability of the attached ligand. The materials synthesized are summarized in Table Ia, which presents the data for elemental analysis of carbon. An important consideration with the multidentate silanes is whether each silicon atom from the silane has reacted with the surface SiOH groups for a true multidentate attachment, or whether the silane connects by only one Si–O–Si bond to the surface. In order to confirm the structural differences of the three phenyl-group-bonded phases, P, BP and TP, both solution- and solid-state NMR measurements were performed.

^{13}C MAS-NMR spectra were obtained on a Model JNM GX270 FT-NMR spectrometer (JEOL, Tokyo, Japan). The magic angle was set by minimizing the line width of the side-bands of the ^{79}Br or ^{81}Br satellite transitions in KBr. For ^{13}C CP-MAS-NMR, the Hartmann–Hahn matching condition for cross-polarization was calibrated with admantane and, in order to eliminate spinning side-bands, the TOSS method was used. The measurement conditions used were basically the same as those reported by Kirkland *et al.*[16]. Solution-state NMR measurements were performed on the same NMR spectrometer.

Fig. 2 shows the ^{29}Si solution-state NMR spectra of the authentic methoxysilanes (although in the actual synthetic reactions we used chlorosilanes instead of the methoxysilanes), *i.e.*, phenyldimethylmethoxysilane for P, *p*-bis(dimethylmethoxysilyl)benzene for BP and 1,3,5-tri(dimethylmethoxysilyl)benzene for TP. The spectra indicate that they have almost identical structures with regard to the silicon atoms, because a *ca.* 10-ppm signal can be assigned to the silicon atom desired. The signal at −4 ppm is due to 1,1′,3,3′-tetramethylsiloxane as the internal standard.

The similar chemical shifts in these spectra suggest that the three silanes have the same silicon structure because the silicon atoms are connected to two methyl, one

TABLE I

STATIONARY PHASES USED IN THIS WORK

(a) Newly synthesized phases[a]

Abbrev.	*Bonded phase*	*Carbon content (wt.-%)*
P	Phenyl	8.04
BP	*p*-Bis-phenyl	7.97
TP	1,3,5-Tris-phenyl	7.46
CI	Methyl	4.46

(b) Other phases[b]

Abbrev.	*Bonded phase*	*Remarks*
DP	Diphenyl	Ref. 17
DC18	Octadecyl	Develosil-ODS, monomeric
VC18	Octadecyl	Vydac 201 TPB5-ODS, polymeric
LC18	Octadecyl	LC Packings RP-18 180JC89[c]
FC18	Octadecyl	FineSIL C18T-5[d]
CC18	Octadecyl	Capcell Pak C_{18}, monomeric[e]

[a] All phases were packed into the 150 mm × 0.53 mm I.D. fused-silica capillary by the slurry technique.

[b] All phases except LC18 were packed into the 150 mm × 0.53 mm I.D. fused-silica capillary by the slurry technique.

[c] Commercially available microcolumn (150 mm × 0.32 mm I.D.).

[d] Trifunctional phase but looks like a monomeric phase.

[e] Polymer-coated C_{18} phase.

phenyl and one methoxy group as the active site, although the tris-phenylsilane has three silicon atoms, the bis-phenylsilane has two and the phenylsilane has only one.

Fig. 3 illustrates the ^{13}C solution-state NMR spectra for these three silanes. Depending on the location of carbon atoms within these silanes, the signals around 130–150 ppm are different from each other. The spectra clearly indicate that TP and BP have two positionally different carbon atoms, whereas P has four chemically different carbon atoms, although the signal intensities do not accurately suggest the number of these carbon atoms. In Fig. 4 ^{13}C CP-MAS-NMR spectra are summarized for the three bonded silicas. Even though the signal peaks are much broader than those of the authentic silanes because these are solid-state NMR spectra, the signals are consistent with those which appeared in the solution-state spectra. The correspondence can be found by the peak numbers marked in Figs. 3 and 4.

The ^{29}Si CP-MAS-NMR spectra shown in Fig. 5 suggest some different information about the synthesized phases. The signals appearing at *ca.* 2 ppm for P, BP and TP can be assigned to silicon atoms connected to the phenyl ring and the silica surface by siloxane bonds and the two signals around −100 ppm are caused by SiOH and SiO– bondings in the substrate silica. The spectrum for P suggests that it has only one such connecting silicon atom, whereas the spectra of TP and BP indicate that they have another type of silicon atom in their structure because of the signals at *ca.* 1.6 ppm.

As Kirkland *et al.*[16] reported similar ^{29}Si NMR spectra for bidentate bonded

phases, it seems that these spectra are not unusual. The presence of the two low-field peaks could be explained by the following two assumptions: dimerization of TP and BP occurred in the synthetic reaction or different bond angles and conformations of the Si–O–Si bonds led to positionally different silicon atoms. However, it is apparent from the spectrometric data that the synthesized bonded phases are the desired materials.

For comparison, five different commercially available ODS phases, Develosil-ODS (Nomura Chemicals, Seto, Japan; DC18), Vydac 201 TPB5-ODS (Separations Group, Hesperia, CA, U.S.A.; VC18), LC Packings RP-18 (Zurich, Switzerland; LC18), FineSIL C18T-5 (Jasco, Tokyo, Japan; FC18) and Capcell Pak C_{18} (Shiseido, Yokohama, Japan; CC18), and a diphenyl (DP) phase synthesized in a previous study[17] were also evaluated. The reason for adding the DP phase for comparison is that it has been found to have some unique chromatographic properties when compared with ODS phases. These phases are listed in Table Ib.

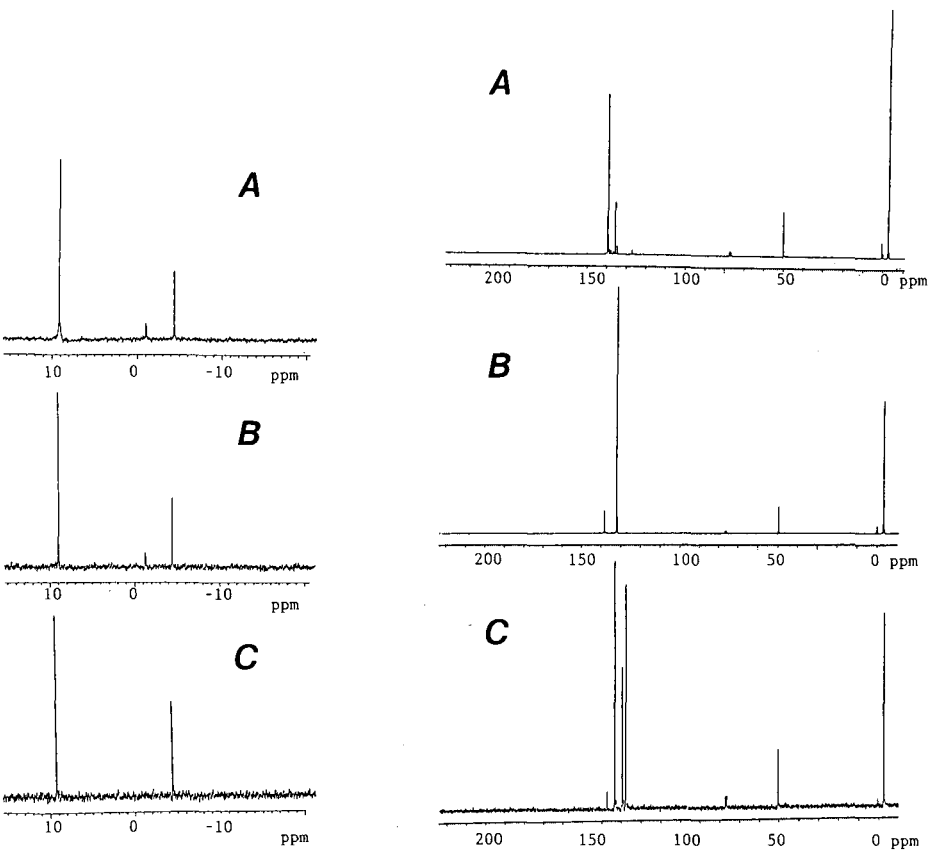

Fig. 2. ^{29}Si solution-state NMR spectra of the authentic silanes. (A) 1,3,5-Tris(dimethylmethoxysilyl) benzene; (B) *p*-bis(dimethylmethoxysilyl)benzene; (C) dimethylmethoxysilylbenzene.

Fig. 3. ^{13}C solution-state NMR spectra of the authentic silanes. (A) 1,3,5-Tris(dimethylmethoxysilyl) benzene; (B) *p*-bis(dimethylmethoxysilyl)benzene; (C) dimethylmethoxysilylbenzene.

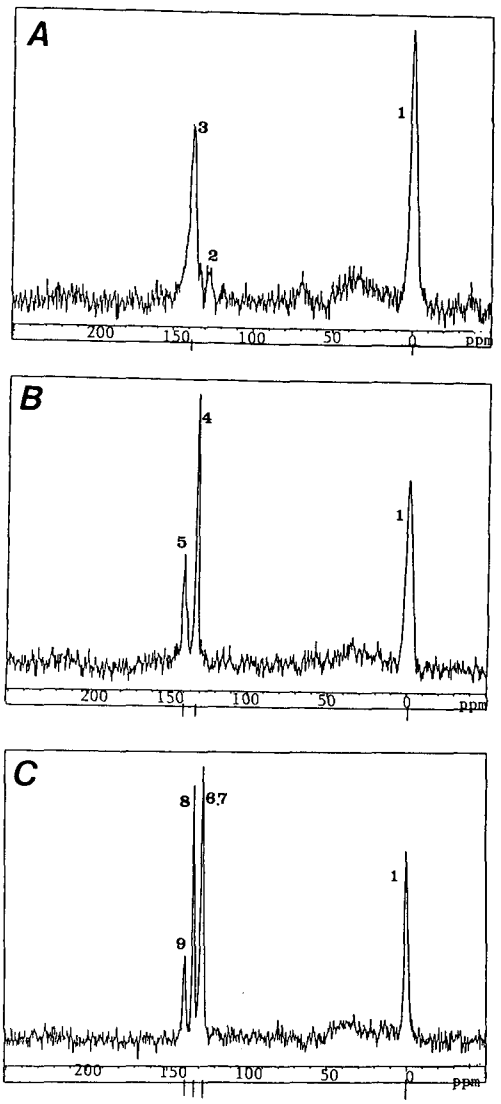

Fig. 4. ^{13}C CP-MAS solid-state NMR spectra of the chemically modified silicas. (A) TP; (B) BP; (C) P.

All the phases except LC18 were packed into fused-silica capillaries of (150 mm × 0.53 mm I.D.) by a slurry technique. LC18 was used as supplied by the manufacturer in a 150 mm × 0.32 mm I.D. fused-silica capillary.

The microcolumn LC system consisted of a microfeeder MF-2 as a pump (Azuma Electric, Tokyo, Japan), a Rheodyne (Cotati, CA, U.S.A.) Model 7513 injector and a Jasco Uvidec 100-III UV detector set at 254 nm. The mobile phases were mixtures of methanol and water and the typical flow-rate used was 2 μl/min. Chromatographic measurements were performed at least in triplicate. The retention data used

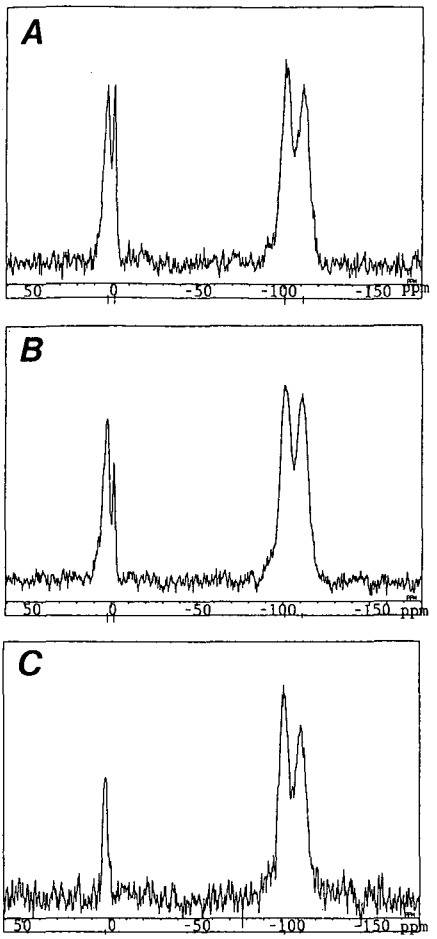

Fig. 5. ^{29}Si CP-MAS solid-state NMR spectra of the chemically modified silicas. (A) TP; (B) BP; (C) P.

for the evaluation were mean values of these experimental data. For the column dead-volume measurements, sodium nitrite solution (100 ppm) was used.

PAHs used for the evaluation were commercially available, except benzo[*a*]pyrene (BaP), tetrabenzonaphthalene (TBN) and phenanthro[3,4-*c*]phenanthrene (PhPh), which were obtained as a gift from J.C. Fetzer of Chevron Research (Richmond, CA, U.S.A.).

RESULTS AND DISCUSSION

Recognition of molecular size

To understand the basic chromatographic characteristics of the synthesized materials, the separation of four small, planar PAHs, naphthalene, anthracene, pyrene and chrysene, was attempted. The retention data obtained with methanol–water (70:30) as the mobile phase are summarized in Table II. The chromatogram obtained

TABLE II

CAPACITY FACTORS k' FOR PLANAR POLYCYCLIC AROMATIC HYDROCARBONS WITH VARIOUS BONDED PHASES

Solute	*F*	k'									
		Stationary phase									
		P	*BP*	*TP*	*DP*	*C1*	*DC18*	*VC18*	*LC18*	*FC18*	*CC18*
Naphthalene	5	1.17	1.46	1.18	0.67	0.29	4.27	1.17	2.00	1.93	3.82
Anthracene	7	2.17	3.31	2.09	1.25	0.65	13.82	4.75	5.67	5.21	11.09
Pyrene	8	2.75	4.39	2.55	1.50	0.77	21.73	7.33	8.67	7.71	16.82
Chrysene	9	3.92	6.69	3.46	2.00	1.18	39.55	19.50	13.67	12.50	28.64

on the TP phase is shown in Fig. 6. The separation capability of this phase seems very good. BP, P, C1 and six other reference phases were also evaluated. In general, the retention of these PAHs in reversed-phase LC has a high correlation with the F number proposed by Schabron *et al.*[18] in 1977[19–22] as follows:

$$\log k' = AF + B \tag{1}$$

where k' is the capacity factor of the solute, F is defined as the number of double bonds plus the number of primary or secondary carbons minus 0.5 times the number of non-aromatic rings and A and B are regression coefficients.

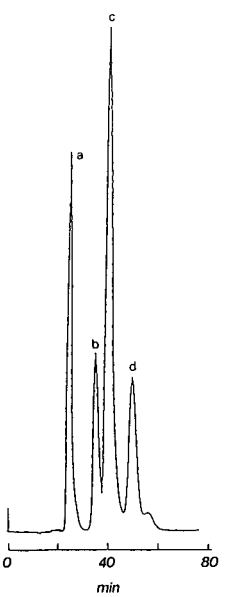

Fig. 6. Typical chromatogram for the separation of PAHs with the TP phase. Mobile phase, methanol–water (70:30); flow-rate, 2 μl/min; detection, UV (254 nm). Peaks: a = naphthalene; b = anthracene; c = pyrene; d = chrysene.

TABLE III

RESULTS OF THE REGRESSION ANALYSIS FOR THE CORRELATION BETWEEN LOG k' AND F

Log $k' = AF + B$.

Stationary phase	*A*	*B*	*r*	*F-ratio*[a]
P	0.1292	−0.5772	0.999	669
BP	0.1630	−0.6440	0.998	529
TP	0.1150	−0.4996	0.998	532
C1	0.1482	−1.2663	0.992	128
DP	0.1173	−0.7501	0.996	254
DC18	0.2393	−0.5590	0.999	1015
VC18	0.2953	−1.4159	0.994	158
LC18	0.2087	−0.7304	0.999	922
FC18	0.2015	−0.7143	0.999	1179
CC18	0.2169	−0.4953	0.999	1128

[a]Statistical significance.

Therefore, the correlation study on the data in Table II was performed by using a multiregression analysis. The results are summarized in Table III, where regression coefficients A and B, correlation coefficients r and statistical F-ratio values are given. The correlation coefficients in all instances are extremely high (> 0.992). However, close examination of the data reveals the difference between ODS phases and phenyl-bonded phases. The regression coefficients A and B in the eqn. 1 were plotted as shown in Fig. 7. Two main clusters are found: one for ODS phases and the other for

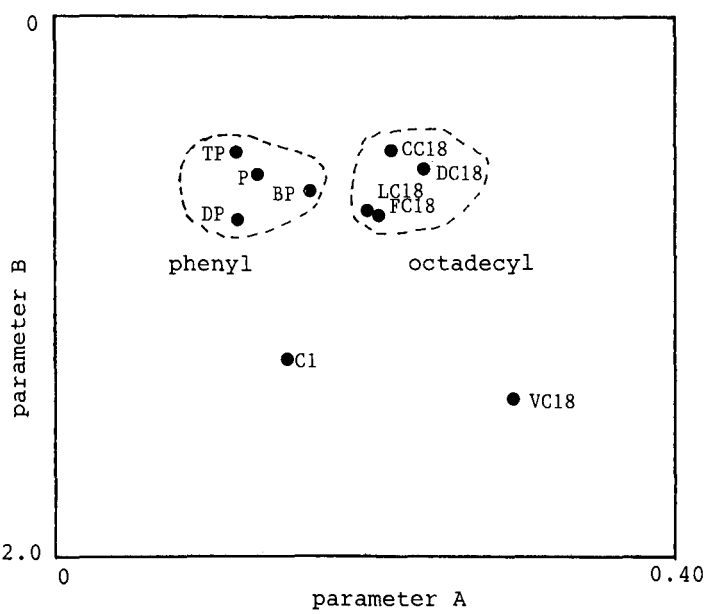

Fig. 7. Plot of parameter A *vs.* parameter B.

phenyl-bonded phases. C1 and VC18 are located far from these two groups. These two unique points can be explained as follows: VC18 has been reported to be a unique stationary phase for PAH separations[7–10] and C1 is a totally different stationary phase to the various alkyl-chain-bonded phases with regard to its surface coverage and properties. The large difference between the phenyl-bonded phases and the ODS phases should come from the retention mechanisms, where the hydrophobic interactions and π–π interactions are dominant for the former but only hydrophobic interactions are the main contributor to retention for the latter.

It is clear that, even though TP and BP have unique structures on the silica surface compared with the P and DP phases, the molecular size recognition capability of the former is similar to that of the latter but slightly different to that for the ODS phases.

Recognition of molecular planarity

Tanaka and co-workers[23–25] investigated the differences in the chromatographic properties of various ODS phases with regard to PAH planarity recognition capability, and found that ODS phases can be categorized into two main groups, one with a strong and the other with a low planarity recognition capability. They used the separation factor between triphenylene and *o*-terphenyl ($k'_{\text{triphenylene}}/k'_{o\text{-terphenyl}}$) as the indicator, where the former is a planar solute and the latter is non-planar. The ratio of the capacity factors of these two PAHs suggests that the values for polyfunctional ODS phases are larger than 2.0 and those for monofunctional phases are less than 2.0. This measure can be useful for evaluating the PAH non-planarity recognition capability of the newly synthesized materials.

TABLE IV

CAPACITY FACTORS k' FOR TRIPHENYLENE (Tri) AND *o*-TERPHENYL (Ote) AND THE SEPARATION FACTORS (α) WITH THREE MOBILE PHASE COMPOSITIONS FOR TEN STATIONARY PHASES

Mobile phases: methanol–water (80:20, 70:30 and 60:40).

Stationary phase	k'						$\alpha = k'_{Tri}/k'_{Ote}$		
	Tri			*Ote*			*80:20*	*70:30*	*60:40*
	80:20	*70:30*	*60:40*	*80:20*	*70:30*	*60:40*			
P	1.23	3.50	11.00	1.08	3.92	13.67	1.14	0.89	0.80
BP	1.53	5.58	16.58	1.27	5.50	17.33	1.20	1.01	0.96
TP	0.92	3.36	14.82	1.08	4.55	22.91	0.85	0.74	0.65
DP	0.69	1.83	5.00	0.77	2.00	5.42	0.90	0.92	0.92
C1	[a]	1.00	4.80	[a]	1.29	7.07	[a]	0.78	0.68
DC18	7.50	30.18	115.4	4.67	20.00	69.25	1.61	1.51	1.67
VC18	3.08	10.75	38.50	1.15	4.50	15.42	2.68	2.39	2.50
LC18	3.33	11.33	41.67	2.50	9.83	39.00	1.33	1.15	1.07
FC18	3.46	11.64	–[b]	2.39	8.43	–	1.45	1.38	–
CC18	–	24.82	–	–	19.00	–	–	1.31	–

[a] Not retained

[b] –, Not examined.

The experimental data obtained with the phases listed in Table I are summarized in Table IV, where the capacity factors of triphenylene and *o*-terphenyl and the separation factors with three different compositions of methanol–water mobile phases are shown. It is remarkable that the elution order of the two solutes on the ODS phases is reversed with the TP phase.

As reported by Tanaka and co-workers[23–25], polymeric VC18 gave separation factors larger than 2.0 and monomeric ODS phases gave the values between 1 and 1.7. The values in Table IV for the ODS phases are in good agreement with those reported by them[23–25]. For the phenyl-bonded phases, the separation factors are smaller than those for the ODS phases. P, BP and DP gave similar values and it appears that they do not have any recognition capability for the planarity difference between triphenylene and *o*-terphenyl. The TP phase, however, shows a unique property among the phenyl-bonded phases in its non-planarity recognition capability. The separation factors are smaller than 0.90, especially with the mobile phase methanol–water (60:40), where the value is 0.65. This means that *o*-terphenyl has an almost 50% larger retention than triphenylene.

The reason for this unique enhancement of the retention of *o*-terphenyl with the TP phase can be explained by interpretation of molecular–molecular interactions between the two solutes and the TP. In Fig. 8 a computer molecular graphics technique was applied to this problem. Fig. 8A shows that the methyl groups favour the planar solute by hydrophobic interaction and they maintain the distance between the solute and TP to reduce possibility of π–π interactions, where triphenylene can interact with the phenyl ring of the TP phase. However, as shown in Fig. 8B, *o*-terphenyl

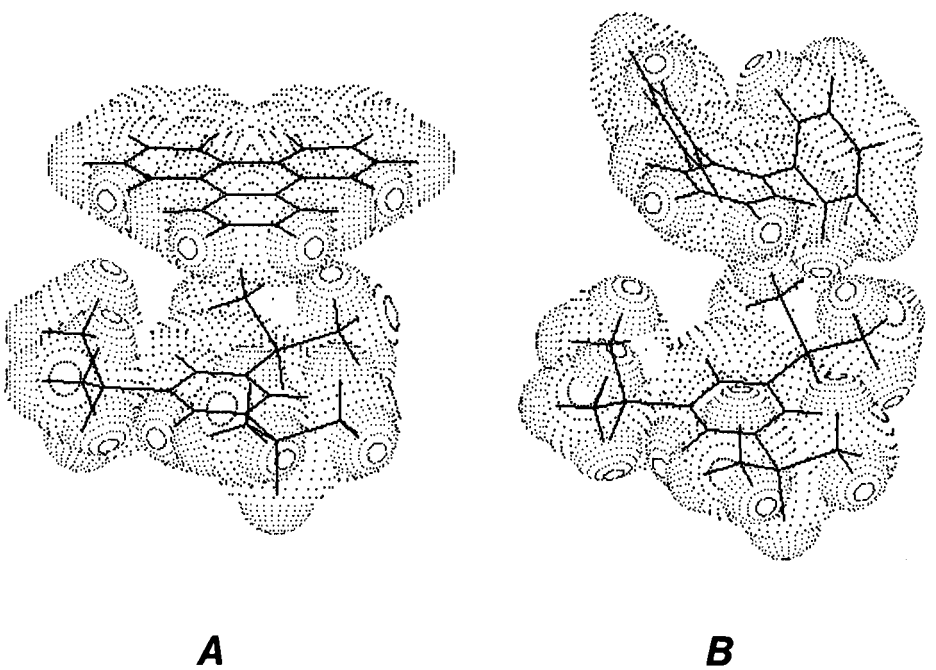

Fig. 8. Molecular–molecular interactions drawn by computer graphics. (A) Interaction between triphenylene and the TP phase; (B) interaction between *o*-terphenyl and the TP phase.

has a suitable steric structure which can interact well with the phenyl ring of the TP phase. *o*-Terphenyl has a high possibility of retention with the TP phase by two mechanisms, hydrophobic interaction of the methyl groups with two phenyl rings of the solute and π–π interaction of the phenyl ring of the phase with the central phenyl ring. This means that, in addition to the hydrophobic interaction between the methyl groups and the solute, more pronounced π–π interactions induce a larger retention of *o*-terphenyl with the TP phase than those with other phases.

This theory can also explain the small difference in the separation factors observed with C1 and with TP, where the factors with TP are smaller than those with C1. The larger absolute retention for the solutes with TP than those with C1 should also be noted.

Interpretation of the experimentally obtained data by using the concept of molecular–molecular interaction clearly explains the retention mechanism that occurs in the separation system and this kind of theoretical approach can open up the possibility of designing new stationary phases suitable for particular separation problems such as isomer separations or chiral separations.

The difference between BP and TP is also found in the experimental data. BP is more similar to the DP than the P phase with respect to the separation factor between triphenylene and *o*-terphenyl. However, other information in Table V indicates a very complicated similarity among these stationary phases. The separation factors between triphenylmethane and *o*-terphenyl are almost identical for seven phases but small differences are seen between P and DP and between BP and TP. The separation factors between *p*-terphenyl and *o*-terphenyl show some differences among the phases. VC-18 prefers to retain rod-like molecules and DC18 also has a similar but smaller preference. DP, P and C1 also have similar preference and TP and BP have intermediate preference between the former and the latter phases. Therefore, the molecular recognition properties of the stationary phases are related to each other in a complex manner.

In summary, the TP phase has a unique property of recognizing non-planar solutes in addition to a size recognition capability. Some properties are similar to those of ODS, but some are similar to those of normal phenyl- or diphenyl-bonded

TABLE V

RETENTION RATIOS AMONG TRIPHENYLMETHANE, *o*-TERPHENYL AND *p*-TERPHENYL WITH VARIOUS STATIONARY PHASES

Mobile phase: methanol–water (60:40).

Stationary phase	*Retention ratio*	
	Triphenylmethane/o-terphenyl	*p-Terphenyl/o-terphenyl*
P	1.44	1.25
BP	1.22	1.55
TP	1.22	1.53
C1	1.19	1.32
DP	1.37	1.29
DC18	1.20	2.20
VC18	1.21	4.38

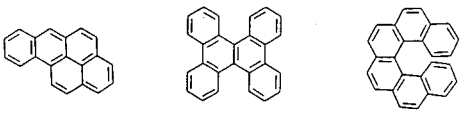

Fig. 9. Three PAHs used in the stationary phase evaluation.

phases with a characteristic non-planarity recognition capability. Differences between C1 and TP are also found.

Another useful factor for indicating the planarity recognition capability of stationary phases is the capacity factor ratio between BaP and TBN, suggested by Sander and Wise[6,10,26]. They proposed a new solute group for the evaluation of the capability of planarity recognition in reversed-phase LC, which consists of three PAHs as shown in Fig. 9. BaP is a planar molecule, TBN is bulky and rather non-planar and PhPh is more non-planar than TBN. These three PAHs can be used to categorize various ODS phases with respect to their capability to recognize molecular planarity.

In order to evaluate the capability of the new phases, measurements have been performed by using these three PAHs as test samples with methanol–water (90:10) as the mobile phase. The results are shown in Table VI. As Sander and Wise suggested that the separation factor between TBN and BaP should be lower than 0.7 for polymeric ODS phases and larger than 1.0 for monomeric phases, the experimental data in Table VI seem to be in reasonable agreement for VC18 and DC18, because the former is a polymeric and the latter a monomeric ODS phase. As the values for the TP and C1 phases are similar to that for DC18, it seems that there is no difference in properties between C1 and TP. They have similar properties with respect to molecular size discrimination to the monomeric ODS phases. However, one can calculate other separation factors between PhPh and BaP and between PhPh and TBN in order to obtain more information about these differences. The separation factors between PhPh and BaP indicate the degree of capability for molecular size and planarity recognition. There are some differences between P and TP, because the values are different from each other. ODS phases gave a more pronounced planarity recognition

TABLE VI

RETENTION DATA FOR BaP, TBN AND PhPh WITH VARIOUS STATIONARY PHASES

Mobile phase: methanol–water (90:10).

Stationary phase	*k'*			α		
	BaP	*TBN*	*PhPh*	*TBN/BaP*	*PhPh/BaP*	*PhPh/TBN*
P	0.23	0.48	0.28	2.09	1.22	0.58
TP	0.35	0.58	0.47	1.66	1.34	0.81
C1	0.13	0.24	0.18	1.85	1.38	0.75
DC18	6.06	9.86	3.60	1.63	0.59	0.37
VC18	6.79	3.64	1.43	0.54	0.21	0.39

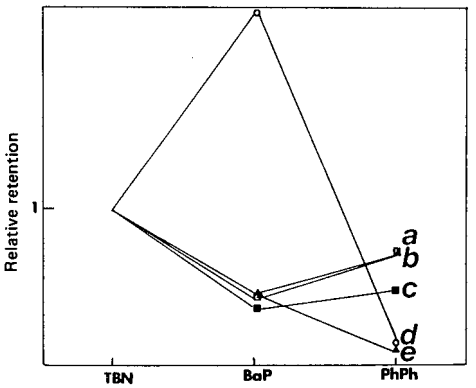

Fig. 10. Relative retentions of three PAHs with various phases. (a) TP; (b) C1; (c) P; (d) VC18; (e) DC18.

for BaP. With TP, P and C1, the retention of PhPh is larger than that of BaP. This phenomenon was also observed in the retention study on triphenylene and *o*-terphenyl. The C1 phase seems to behave similarly to TP in this instance. Therefore, hydrophobic interactions between PhPh and the methyl groups of C1 and TP may be the main contributors to the retention. The ratio for PhPh and TBN suggests some small difference between C1 and TP. As *o*-terphenyl is retained longer with TP than with C1, the same retention mechanism caused by π–π interaction should be added to this problem for the TP system. As PhPh is more non-planar than TBN, it can be concluded that TP has a much higher non-planarity recognition capability than has C1 .

Fig. 10, where the relative retentions of PhPh and BaP to TBN are plotted, illustrates the above discussion more clearly. The similarity between TP and C1 seems to be very high. However, it is possible to conclude that the TP phase is much superior to the C1 phase in chromatographic performance, because the absolute retentions with TP are higher than those with C1 and Kirkland *et al.*[16] reported that multidentate phases are more stable towards long-term usage for separations.

ACKNOWLEDGEMENTS

The authors express their sincere thanks to Y. Ohtsu of Shiseido for supplying high-purity silica gels and to J. C. Fetzer and W. R. Biggs of Chevron Research for useful discussions and the provision of some of the PAHs for evaluation. The financial support of a Grant-in-Aid for Scientific Research (C) No. 63550564 from the Japanese Ministry of Education, Science and Culture is also acknowledged.

REFERENCES

1 R. G. Harvey (Editor), *Polycyclic Hydrocarbons and Carcinogenenis* (*ACS Symposium Series*, Vol. 283), American Chemical Society, Washington, DC, 1985.
2 I. A. Smith, G. D. Berger, P. G. Seybold and M. P. Serve, *Cancer Res.*, 38 (1978) 2968.
3 G. H. Loew, J. Phillips, J. Wong, L. Hieldmeland and G. Pack, *Cancer Biochem. Biophys.*, 2 (1978) 113.
4 L. C. Sander and S. A. Wise, *Anal. Chem.* 56 (1984) 504.

5 L. C. Sander and S. A. Wise, *J. Chromatogr.*, 316 (1984) 163.
6 L. C. Sander and S. A. Wise, *Anal. Chem.*, 59 (1987) 2309.
7 K. Jinno, T. Ibuki, N. Tanaka, M. Okamoto, J. C. Fetzer, W. R. Biggs, P. R. Griffiths and J. M. Olinger, *J. Chromatogr.*, 461 (1989) 209.
8 K. Jinno, T. Nagoshi, N. Tanaka, M. Okamoto, J. C. Fetzer and W. R. Biggs, *J. Chromatogr.*, 392 (1987) 75.
9 K. Jinno, S. Shimura, N. Tanaka, K. Kimata, J. C. Fetzer and W. R. Biggs, *Chromatographia*, 27 (1989) 285.
10 L. C. Sander and S. A. Wise, *LC·GC*, 8 (1990) 378.
11 K. Jinno, *J. Chromatogr. Sci.*, 27 (1989) 729.
12 P. Shah, L. B. Rogers and J. C. Fetzer, *J. Chromatogr.*, 388 (1987) 411.
13 K. Jinno, S. Shimura, J. C. Fetzer and W. R. Biggs, *J. High Resolut. Chromatogr. Chromatogr. Commun.*, 11 (1988) 673.
14 K. Jinno, S. Shimura, J. C. Fetzer and W. R. Biggs, *Poly. Arom. Comp.*, 1 (1990) 151.
15 H. Nagashima, T. Ueda and K. Itoh, in preparation.
16 J. J. Kirkland, J. C. Glaich and R. D. Farlee, *Anal. Chem.*, 61 (1989) 2.
17 K. Jinno and M. Okamoto, *Chromatographia*, 18 (1984) 495.
18 J. F. Schabron, R. J. Hurtubise and H. F. Silver, *Anal. Chem.*, 49 (1977) 2253.
19 K. Jinno and K. Kawasaki, *Chromatographia*, 18 (1984) 44.
20 K. Jinno and K. Kawasaki, *Chromatographia*, 17 (1983) 445.
21 K. Jinno and K. Kawasaki, *J. Chromatogr.*, 316 (1984) 1.
22 K. Jinno and M. Okamoto, *Chromatographia*, 20 (1985) 112.
23 N. Tanaka, Y. Tokuda, K. Iwaguchi and M. Araki, *J. Chromatogr.*, 239 (1982) 761.
24 N. Tanaka, K. Sakagami and M. Araki, *J. Chromatogr.*, 199 (1980) 327.
25 K. Kimata, K. Iwaguchi, S. Onishi, K. Jinno, R. Eksteen, K. Hosoya, M. Araki and N. Tanaka, *J. Chromatogr. Sci.*, 27 (1989) 721.
26 L. C. Sander and S. A. Wise, *Anal. Chem.*, 61 (1989) 1749.

Journal of Chromatography, 517 (1990) 209–217
Elsevier Science Publishers B.V., Amsterdam

CHROMSYMP. 1956

Gel permeation chromatography–Fourier transform infrared study of some synthetic polymers

II. Instrumentation for the characterization of polyethylene[a]

KOICHI NISHIKIDA*
Perkin-Elmer Japan Co. Ltd., 2-8-4 Kitasaiwai, KN Bldg., Nishi-ku, Yokohama 220 (Japan)
TATSUYA HOUSAKI
Polymer Research Laboratory, Idemitsu Petrochemical Co. Ltd., 1-1 Anesaki-Kaigan, Ichihara, Chiba 299-01 (Japan)
and
MITSUHIKO MORIMOTO and TOSHIO KINOSHITA
Perkin-Elmer Japan Co. Ltd., 2-8-4 Kitasaiwai, KN Bldg., Nishi-ku, Yokohama 220 (Japan)

ABSTRACT

A high-temperature gel permeation chromatography–Fourier transform infrared (GPC–FT-IR) system was developed to characterize commercially available polyethylene. High-temperature transfer tubing was used to connect the high-temperature flow cell of an FT-IR spectrophotometer and a high-temperature GPC system. The GPC–FT-IR system was calibrated to determine the molecular weight distribution (MWD) and the short-chain branching (SCB) for high-density polyethylene (HDPE) and linear low-density polyethylene (LLDPE). The MWD and SCB of a commercial LLDPE determined using the present GPC–FT-IR system compared favourably with those measured with a solvent gradient elution fractionation technique where ^{13}C NMR spectrometry was employed to determine the SCB for the same PE.

INTRODUCTION

Gel permeation chromatography (GPC) has often been used to characterize synthetic polymers. GPC separates molecules according to size difference. The molecular weight distribution (MWD) obtained from GPC is often used to characterize synthetic polymers. In the polymer industry, GPC is commonly used to inspect

[a] For Part I, see ref. 1.

0021-9673/90/$03.50

the molecular weights (MW) and the MWD of polymers for quality control purpose[2,3].

Whereas molecular weights and distributions are convenient parameters to correlate with the physical properties of polymers, such as mechanical strength and stress cracking resistance, other properties such as branching, formation of multiple bonds and inversion of head-to-tail sequences also influence not only the chemical properties but also the physical properties of synthetic polymers[4]. Therefore, spectroscopic methods such as infrared (IR)[5] and nuclear magnetic resonance (NMR)[6] have been widely adopted as alternative methods for characterizing bulk synthetic polymers.

When an IR spectrometer is connected to a GPC system as a detector, it is possible to obtain spectroscopic information regarding the chemical composition of the polymer fraction in each elution volume instantly. Using a dispersive IR spectrometer as a GPC detector in a stop-and-go mode, Mirabella and Barrall were able to determine the chemical composition distribution of some copolymers as a function of MW. Their study showed that there is a drift of the chemical composition with respect to molecular weight, although the information obtained by their method is rather primitive compared with that obtained by complete chemical composition analysis. However, information obtained by GPC–IR still provides valuable data on chemical composition as a function of MW for certain polymer manufacturers. A Fourier transform IR (FT-IR) system is the most suitable detector for such studies, as it is capable of obtaining a full-range (4000–700 cm^{-1}) IR spectrum within 1 s without stopping the flow.

Recently, linear low-density polyethylene (LLDPE) has become commercially important, and the distribution of the short-chain branching (SCB) of LLDPE has been found to be heterogeneous. It is claimed in a recent patent application[8] that the distribution of SCB in the case of high-density polyethylene (HDPE), exhibiting a heterogeneous chemical composition, is related to the physical properties of PE such as resistance to stress cracking.

We wished to develop a GPC–FT-IR system to determine the SCB as a function of MW for commercial HDPE and LLDPE. In this paper, the details of such a GPC–FT-IR system are described, in which GPC is used to separate HDPE and LLDPE on the basis of molecular size and an FT-IR spectrophotometer is used to obtain information on the chemical structure during the GPC analysis. Several kinds of PE were included in this study.

EXPERIMENTAL

Instrumentation

A Perkin-Elmer Model 1700 FT-IR spectrometer, equipped with a narrow-band mercury–cadmium–telluride (MCT) cold detector, and a Model 7700 computer with CDS-3 software for post-run data handling and interfacing to the GPC system, was used as a detector in combination with a Waters Assoc. Model 150C high-temperature gel permeation chromatograph. A 60-cm TSK-GMH4 column (Toyo Soda) with 1,2,4-trichlorobenzene (TCB) or *o*-dichlorobenzene (ODCB) as solvent was used for polymer separation. These solvents do not show strong absorption of infrared light in the range 3000–2700 cm^{-1} (see below).

The GPC system, including autosampler, injector, column and refractive index (RI) detector, was operated at 135°C. The column eluate was directed to a heated flow cell (quartz windows, 1 mm optical path length, *ca.* 30 μl cell volume). A GPC curve typically appears *ca.* 10–15 min after injection of 1 ml of PE solution. A series of IR spectra were measured and accumulated for 15 s (seventeen scans) and each piece of accumulated data was stored as one file of time-sliced GPC data. Usually *ca.* 30 files were stored for one run, including a few files before and after the peak. It was necessary to inject 1 ml of solution to obtain a strong IR signal, although the usual GPC analysis requires the injection of smaller sample volumes.

In order to ensure that the GPC pattern is free from distortion due to the diffusion in the flow cell and overloading of the sample, the flow was returned to the built-in RI detector through a two-way heated transfer tube. The temperatures of both the flow cell and the transfer tubing were maintained at 135°C.

MWD, were calculated from GPC curves obtained with the RI and IR detectors using a universal calibration method which uses polystyrene standards[9]. In this study, the GPC curve constructed from the IR spectra, *i.e.*, the peak area of the C–H stretching vibration appearing in the range 3000–2700 cm^{-1}, was plotted against the MW of the PE fraction for each retention volume, assuming that the Lambert–Beer law holds in this region.

All the stored spectra were automatically processed by the system computer to generate a report.

Measurement of GPC–FT-IR spectra

Commercial samples of LLDPE, HDPE and high-pressure, low-density polyethylene (HP-LDPE) dissolved in TCB at a concentration of 3 mg/ml at 135°C were used. A single-beam IR spectrum was observed before PE was eluted from the column as a background spectrum and each time-sliced single-beam spectrum of the eluate was divided by this background spectrum to give the PE spectrum in the range 3000–2700 cm^{-1}. All of the IR spectra were measured at 8 cm^{-1} resolution. These time-sliced IR spectra were used to calculate the number of methyl groups per 1000 carbon atoms based on the intensity ratio between methyl and methylene groups at 2965 and 2928 cm^{-1}, respectively.

Fractionation and cross-fractionation of PE

Solvent gradient elution fractionation (SGEF) of 5 g of a commercial LLDPE-A (1-octene as co-monomer) was carried out using a column filled with 250 g of Celite (Johns Manville)[10,11]. Eight fractions were collected and each fraction was characterized by ^{13}C NMR and GPC methods. The detailed procedure for the SGEF–NMR method was described in Part I[1].

Fractionation of LLDPE-A was performed by the temperature-rising elution fractionation (TREF) technique to cross-fractionate the resin by crystallinity[12]. The two-step technique involves the deposition of LLDPE from xylene solution at 140°C on inert glass beads by gradually cooling the solution, so that the glass beads will be coated by fractions with poor solubility to xylene as the inner layers and gradually by fractions with higher solubility in the outer layers. When all of the resin had been precipitated on the glass beads, the coated polymer layer was extracted with xylene. The extraction was carried out by increasing the temperature slowly from ambient to

130°C. A 5-g amount of LLDPE gave twelve fractions. The MWD of the PE resin in each fraction was measured with the GPC system.

In order to obtain information of the number of methyl groups per 1000 carbon atoms at different MWs, each TREF eluate of LLDPE-A was fed to the GPC system and several fractions were collected from each GPC run. PE was drawn from solvent to prepare a PE film and the number of methyl groups was determined using the 1381 cm^{-1} peak intensity due to methyl groups, and their MWs were calculated from the GPC data. The experimental procedure and the three-dimensional display of the data from TREF technique have been described elsewhere[13,14].

RESULTS AND DISCUSSION

Determination of SCB as a function of MWD by the GPC–FT-IR method as compared with the SGEF–NMR method

The SCB of LLDPE is intentionally introduced by the addition of certain olefin monomers such as 1-butene, 1-hexene, 1-octene or 4-methyl-1-pentene. For example, 1-butene introduces an ethyl side-chain into PE molecules. Hence both the methyl group in this short chain and the terminal methyl group give rise to a C–H stretching vibration in the IR spectrum. As the absorptions of methyl and methylene C–H stretching vibrations appear at 2965 and 2928 cm^{-1}, respectively, the ratio of the number of methyl to methylene groups will be given by the intensity ratio of CH_3 and CH_2 absorptions, $A^{2965}(CH_3)/A^{2928}(CH_2)$. As the signal intensity of the methyl group is too weak to be recognized as a peak, the self-deconvolution technique[15] was adopted to reduce the line width and to separate the absorption of methyl groups from the intense absorption of methylene groups. The deconvoluted spectrum gives a sufficient signal intensity to be able to calculate the number of methyl groups.

In order to evaluate the branching of PEs, the numbers of methyl groups per 1000 carbon atoms, n/1000C, are calculated in the PE industry. A series of standard PE solutions were injected into the GPC system without a column and their IR spectra were measured to give A^{2965} and A^{2928} values for comparison of the n/1000C values.

These standards were obtained from 1-butene-modified LLDPE using the above-mentioned cross-fractionation method. We obtained a linear relationship between the number of methyl groups per 1000 carbons and the absorption ratio A^{2965}/A^{2928}. PE standards with similar MWs of *ca.* 100 000 were selected for this purpose in order to avoid any possible errors due to low- and high-molecular weight extremes.

As one of the two termini of the PE molecule is regarded as a methyl group and another as a vinyl group[16], the degree of SCB was equal to the calculated amounts minus one. The number of terminal methyl groups per 1000 carbon atoms, n(t)/1000C, was therefore calculated with the equation

$$n(\mathrm{t})/1000\mathrm{C} = 14\,000/M \tag{1}$$

where M is the molecular weight of PE in the eluate.

In addition, with LLDPE-A, one co-monomer molecule introduces an additional five CH_2 groups, whereas an additional CH_2 group was introduced for the 1-butene-modified LLDPE. Therefore, a proper correction should be made in order to

calculate the SCB accurately when the co-monomers of the standard and the sample LLDPE are different, as determination of the number of methyl groups depends not only the methyl group intensity but also on the methylene intensity. For instance, when 1-butene-modified LLDPE is used as a standard and 1-octene-modified LLDPE-A is analysed for SCB, the n/1000C value should be modified to take account of four extra methylene groups which lower the calculated number of methyl groups in 1-octene-modified LLDPE. With the assumption that the methylene groups in the side-chain and those in the molecular chain exhibit the same molar absorptivity, the contribution of an extra four in 1000 methylene groups (0.004) should be removed from the calibration equation. Therefore, the actual value of SCB, n/1000C(act), for 1-octene-modified LLDPE should be calculated from the observed value, n/1000C(obs), according to the equation

$$n/1000\text{C(act)} = n/1000\text{C(obs)}/\{1 - 0.004[n/1000\text{C(obs)}]\} \quad (2)$$

Fig. 1 shows the SCB as a function of MW determined with the present GPC–FT-IR method (open circles) and with the SGEF–NMR method (solid circles). The results obtained with these two independent methods coincide completely[a]. This is also true even when there is a discontinuity in the MWD of SCB near the top of the peak in the GPC curve. The results indicate that the proposed GPC–FT-IR method can be regarded as more efficient than the SGEF method. Usually the SGEF technique takes 2–3 weeks to complete, whereas the present method takes only 1 h to achieve the same results.

Characterization of LLDPE by GPC–FT-IR

As indicated in the literatures, the TREF method fractionates the PE according to the SCB[15], the SGEF method according to molecular weight[16] and the GPC method according to molecular size. As stated in the Introduction, the molecular size distribution can be approximated as the MWD, as shown in the previous section where the GPC–FT-IR method gave identical results with the SGEF–NMR method. In order to interpret the GPC–FT-IR data, we carried out the cross-fractionation of LLDPE-A by the TREF method and compared the data with those given by GPC–FT-IR.

Fig. 2 is a three-dimensional display of the relationship between the MW and SCB of LLDPE-A. Each of the twelve fractions given by the SGEF method was analysed by GPC for its MWD. Fig. 2 shows that the fraction with a small n/1000C value (1.4–2) has a narrow MWD and a higher average MW, whereas the MWD becomes wider and the average MW becomes smaller as the n/1000C value becomes larger. The average MW determined by GPC analysis of each fraction collected in the TREF method shown in Fig. 2 was plotted against the n/1000C value (Fig. 3). Fig. 3 indicates that the degree of SCB decreases as the MW of the resin increases, which

[a] The discrepancy of *ca.* one methyl group between the GPC–FT-IR and fractionation methods indicated in Part I[1] can be explained by the fact that *two* methyl groups were subtracted from the calculated values in the previous paper, instead of *one* methyl group as assumed in this paper. Also, the fourth line from the bottom of p. 527 in Part I[1] previous paper, should read, "the GPC–FT-IR method always gives one methyl *less* than the NMR method".

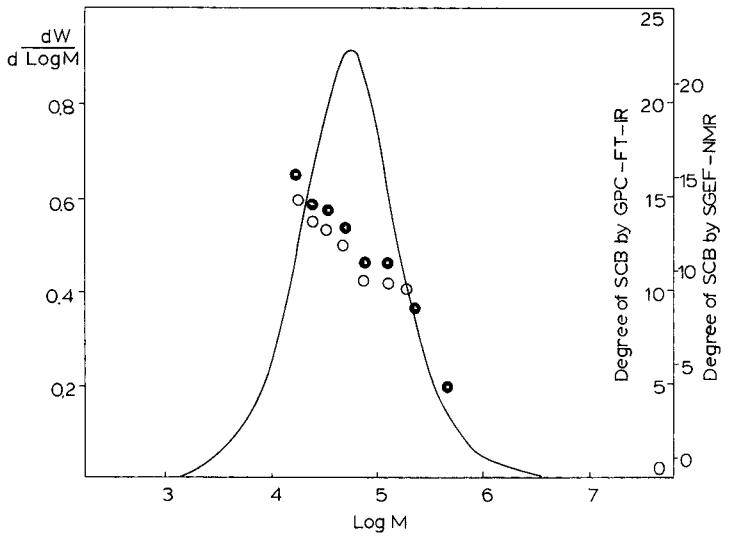

Fig. 1. Molecular weight distribution curve (solid line) detected by GPC–RI and molecular weight dependence of the degree of SCB per 1000 C as determined by (○) GPC–FT-IR and (●) SGEF–NMR methods.

illustrates a similar relationship between MW and n/1000C value to that in Fig. 1. The difference between Figs. 1 and 3 is not surprising, as the GPC–FT-IR method determines the degree of SCB for the narrow MW, whereas the TREF method determines the MWD of the PE fractions at a certain value of SCB.

Application of GPC–FT-IR method to some LLDPE and HDPE

As the present GPC–FT-IR method was found to give the same relationship between the SCB and MW as those determined from SGEF–^{13}C NMR for the 1-octene-modified LLDPE-A, we carried out the characterization of some LLDPE and HDPE samples. Although the SCB of 1-butene-modified LLDPE (LLDPE-B) decreased monotonously from 20 to 8 methyl groups per 1000 carbons with increase in molecular weight, another kind of commercial LLDPE (LLDPE-C) showed an almost constant SCB of 9.5 methyl groups per 1000 carbons over the entire MW range. According to Hosoda[16], LLDPE polymerized with $TiCl_4$ and triethylaluminium supported on $MgCl_2$ as catalysts shows a monotonous decreases in SCB with increase of MW, whereas the SCB of LLDPE, which is polymerized under homogeneous conditions with a soluble catalyst such as triethylaluminium sesquichloride and vanadium chloride, is almost independent of MW.

As HDPE is reported to have few branchings and, in addition, the branching is considered to be SCB[17,18], attempts to utilize the present GPC–FT-IR method to characterize HDPE were carried out. First, we chose NBS SRM 1475 high density polyethylene (HDPE-A) for characterization. The SCB was indeed small (average 2.8 methyl groups per 1000 carbons) and was indpendent of MW.

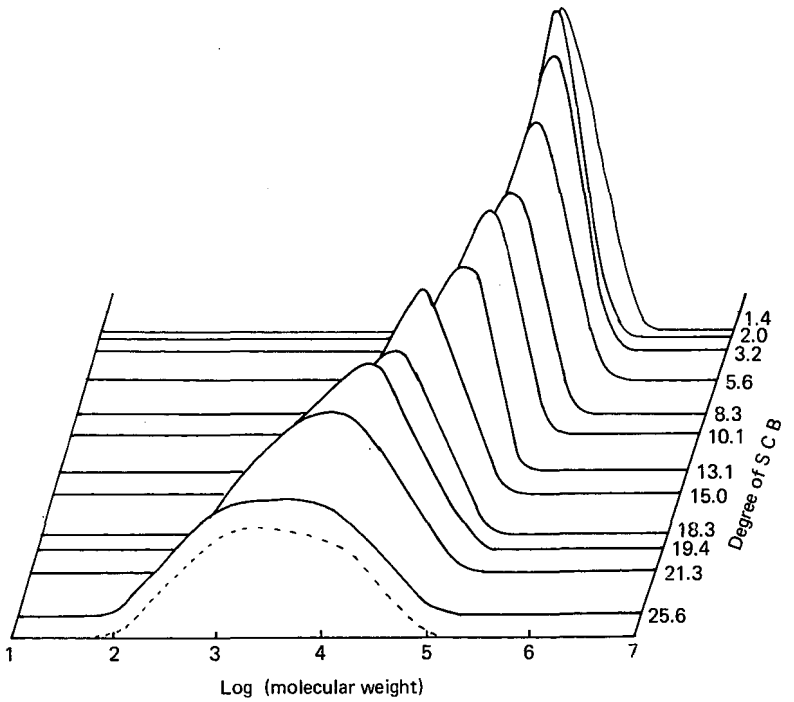

Fig. 2. Three-dimensional display of weight fractions (z-axis) cross-fractionated in terms of molecular weight (x-axis) and short-chain branching (y-axis).

Another material that we have characterized using the GPC–FT-IR method is a commercially available HDPE-B, which is used to make thin film for wrapping bags. Fig. 4 shows two peaks on the GPC curve, whereas the SCB is almost constant, with an average value of 5.2 methyl groups per 1000 carbons, over the entire MW range or increases slightly with an increase in MW. As it is abnormal to observe two peaks on the GPC curve of PE, the presence of two peaks suggests either that the material is a mixture of two different polymers or that two-step polymerization was carried out to manufacture the HDPE-B. The above-mentioned patent application[8] suggests the superiority of the physical properties of this HDPE-B from the fact that the SCB is independent of MW.

Finally we shall consider the results for HP-LDPE. As is well known, HP-LDPE has long-chain branching (LCB) in addition to SCB. As it is not possible to distinguish between LCB and SCB by IR spectroscopy, the number of methyl groups per 1000 carbon atoms was plotted against MW. It was demonstrated that the average value for HP-LDPE, *ca.* 26.9 methyl groups per 1000 carbons, is larger than those for LLDPE and HDPE and that the number of methyl groups per 1000 carbon atoms is nearly independent[16] of MW. The present results are in agreement with the chemical nature of HP-LDPE[17,18].

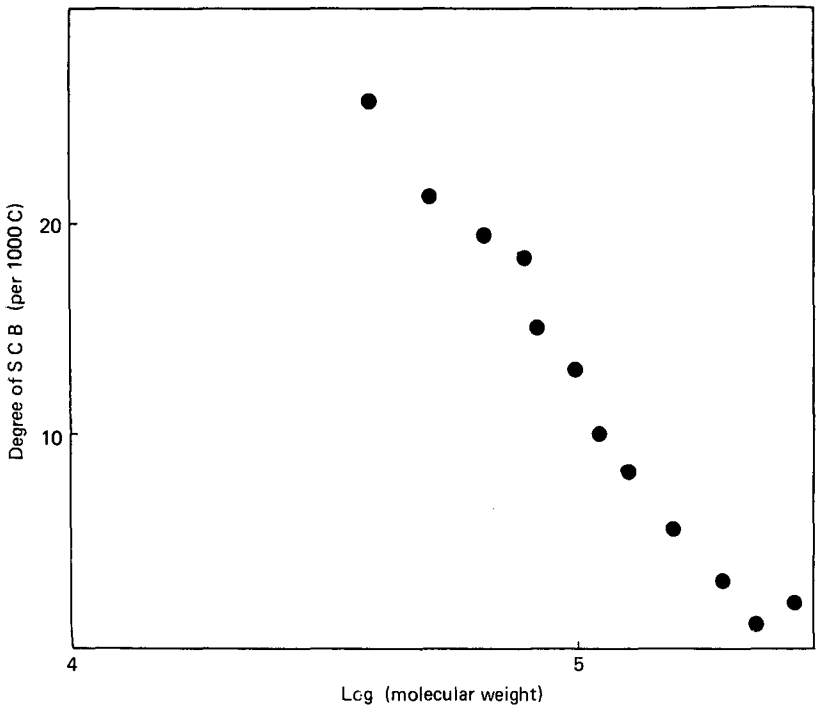

Fig. 3. Degree of short-chain branching per 1000 carbon atoms of LLDPE-A as a function of molecular weight distribution determined by the TREF method.

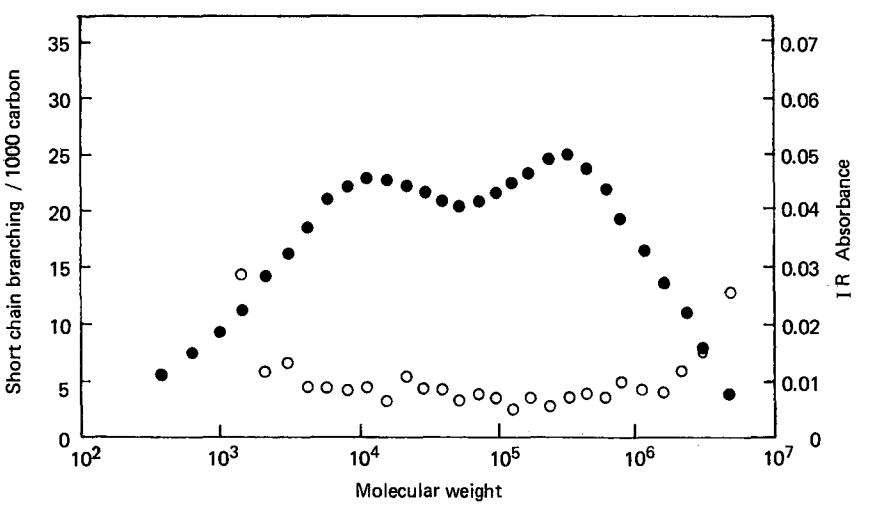

Fig. 4. Extent of short-chain branching per 1000 carbon atoms of HDPE-B as a function of molecular weight (○, left-hand ordinate) and GPC curve as measured by IR absorbance (●, right-hand ordinate).

CONCLUSION

The GPC–FT-IR method was found to be an excellent substitute for the SGEF–NMR method and can differentiate several kinds of LLDPE and HDPE according to the SCB. However, the GPC–FT-IR method, which is a two-dimensional analysis, gives only the variation of the average chemical composition, such as the ratio of co-monomer to ethylene monomer as a function of MW. Even with such a limitation, the method can differentiate several types of polyethylene for industrial purposes.

REFERENCES

1 T. Housaki, K. Satoh, K. Nishikida and M. Morimoto, *Makromol. Chem. Rapid Commun.*, 9 (1988) 525.
2 J. C. Moore, *J. Polym. Sci., Part A2*, (1964) 835.
3 L. H. Tung (Editor), *Fractionation of Synthetic Polymers*, Marcel Dekker, New York, 1977.
4 Asahi Kasei, *Jpn. Pat.*, SH060-26049 and SH060-26050 (1985).
5 D. O. Hummel, *Atlas of Polymer and Plastics Analysis, Vol. 2, Part b/I Text*, Carl Hanser Verlag, Munich, 2nd ed., 1988.
6 F. A. Bovey, *High Resolution NMR of Macromolecules*, Academic Press, New York, 1972, and references cited therein.
7 F. M. Mirabella, Jr. and E. M. Barrall, II, *J. Appl. Polym. Sci.*, 19 (1975) 2131.
8 Showa Denko, *Jpn. Pat.*, SH061-43379 (1986).
9 S. Mori, *J. Appl. Polym. Sci.*, 18 (1974) 2391.
10 L. H. Tung, *J. Polym. Sci.*, 20 (1971) 1607.
11 R. Chinag, *J. Phys. Chem.*, 69 (1965) 1636.
12 L. Wild, T. Ryle, D. Knobelock and I. Peat, *J. Polym. Sci., Polym. Phys. Ed.*, 20 (1982) 441.
13 S. Nakano and Y. Goto, *J. Appl. Polym. Sci.*, 26 (1981) 4217.
14 F. M. Mirabella, Jr. and E. A. Ford, *J. Polym. Sci., Part B*, 25 (1987) 777.
15 D. W. Maya, L. J. Bellamy, G. T. Merkin and R. W. Hannah, *Spectrochim. Acta, Part A*, 41 (1985) 335.
16 S. Hosoda, *Polym. J.*, 20 (1988) 383.
17 K. Shirayama, T. Okada and S. Kita, *J. Polym. Sci., Part A3*, (1977) 907.
18 W. D. Hoffman, G. Eckhardt, E. Brauer and F. Keller, *Acta Polym.*, 31 (1980) 233.

Journal of Chromatography, 517 (1990) 219–228
Elsevier Science Publishers B.V., Amsterdam

CHROMSYMP. 1948

Isolation and purification of lecithin by preparative high-performance liquid chromatography

JOHN V. AMARI and PHYLLIS R. BROWN*
Department of Chemistry, University of Rhode Island, Kingston, RI 02881 (U.S.A.)
CHARLES M. GRILL
Separations Technology, Inc., Wakefield, RI 02879 (U.S.A.)
and
JOSEPH G. TURCOTTE
Department of Medicinal Chemistry, University of Rhode Island, Kingston, RI 02881 (U.S.A.)

ABSTRACT

Mixed-chain, multispecies, egg yolk-derived lecithin was isolated and purified on a silica column with isocratic elution. A method development column (20 × 0.46 cm I.D.) packed with YMC 15–30 μm, 120 Å spherical silica and a mobile phase consisting of 5 m*M* ammonium acetate in acetonitrile–2-propanol–methanol–water (80:13:5:12) was used to separate the lecithin from other phospholipids. The mobile phase conditions for the method development system was adopted for two types of preparative HPLC systems: a Separations Technology SepTech NovaPrep™ 5000 system with a 20 × 1.93 cm I.D. column and a ST/800A system with a 20 × 5.00 cm I.D. Annular Expansion™ (A/E) column. The maximum load was 50 μl of crude solution (2 mg) for the method development column, 0.90 ml (35 mg) for the 20 × 1.93 cm I.D. column and 6.0 ml (240 mg) for the 20 × 5.00 cm I.D. A/E column. The flow-rates were 2, 35 and 235 ml/min, respectively. The fractions collected from the preparative systems were analyzed for purity by analytical-scale high-performance liquid chromatography and by thin-layer chromatography with selective detection with molybdenum blue for phospholipids and detection of all organic compounds by sulfuric acid. Purity of the recovered lecithin was greater than 99%.

INTRODUCTION

Natural lecithin does not exist as a discrete compound but is composed of a choline polar head and multimolecular species of varying fatty acid chain lengths and degrees of unsaturation[1] (Fig. 1). Besides being a naturally occurring emulsifier and surfactant, lecithin is also of interest as starting material for the synthesis of novel anti-viral and anti-tumor drugs[2–6]. Since purified lecithin was needed for the synthesis

0021-9673/90/$03.50

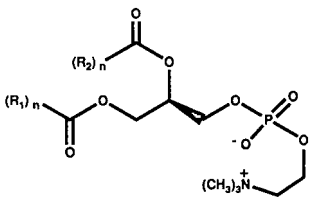

Fig. 1. Structure of lecithin.

of these drugs, we developed a method for the isolation and purification of lecithin from chicken egg yolk, where a large amount of lecithin is present.

Silica has been the sorbent most commonly used in analytical and preparative separations of phospholipids[7–26]. Patel and Sparrow[10] reported a high load when they separated lecithin from egg yolk on a preparative scale using silica packed columns and a mobile phase of chloroform–methanol–water (60:30:4). One disadvantage of this method is that ultraviolet (UV) detection can not be used, since the chloroform has high absorption at low UV wavelengths. In addition, the large volumes of chlorinated solvents required for preparative separations are detrimental to the environment and to the health of laboratory workers. Analytical separations of lecithin from other sources were developed by Jungawala *et al.*[11] with a mobile phase of acetonitrile–methanol–water (65:21:14). In 1987 this mobile phase, to which 2-propanol and trifluoroacetic acid were added, was used for preparative work[20]. Gradient elution with a mobile phase of hexane–isopropanol–water has also been reported for analytical separations[16,17,21,22] and for preparative work[25]. However, isocratic elution is preferable if large quantities of lecithin are to be isolated routinely because of the ease of operation and cost savings. UV detection is preferable to detection by refractive index. Its higher sensitivity allows better monitoring of the separation of lecithin from other phospholipids, which are present in trace amounts relative to the amount of lecithin. Since phospholipids absorb only in the region of 200 to 210 nm the mobile phase had to be transparent at 203 nm, the working wavelength of the separation.

EXPERIMENTAL

Sample preparation

Crude phospholipids were extracted from one dozen, fresh chicken egg yolks by the method of Singleton *et al.*[27]. The combined mass of the yolks was approximately 242 g. The membranous cuticle was removed by placing the yolk on a piece of screening on top of a 2-l beaker containing 600 ml of acetone. The yolk was broken and the fluid forced through the screen with a spatula. When the fluid contacted the acetone, a precipitate formed immediately. The mixture, which was allowed to stand at room temperature in the dark for 1 h, was then vacuum filtered and the solid washed with 300 ml of cold acetone. The acetone extract, which contained most of the neutral fats and pigments, was discarded. The solid was suspended in 400 ml of 95% ethanol and

stored in the dark for 2 h. The mixture was vacuum filtered and the solids washed with 100 ml 95% ethanol. The ethanol extracts were combined and dried at 30–40°C. To dissolve the phospholipids, two (100 ml) portions of petroleum ether were added to the residue. The petroleum ether solutions were combined and reduced in volume with rotary vacuum distillation by a factor of 3 to approximately 70 ml. When the solution was poured into a beaker containing 400 ml of cold acetone, a precipitate formed immediately. The mixture was allowed to stand in the dark at room temperature overnight until the solution cleared. The clear solution was decanted and the yellow solid (11.9 g) was washed with cold acetone. The phospholipids were dissolved in methylene chloride, dried and stored in the freezer under nitrogen.

Materials

All solvents and reagents (Fisher, Pittsburgh, PA, U.S.A.) used for the extraction, method development and analytical analysis were of HPLC grade. The water was doubly distilled and deionized. Each solvent was filtered through a 0.45-μm Nylon-66 filter (AllTech, Deerfield, IL, U.S.A.). For the preparative separations reagent grade solvents also from Fisher were used.

Standard egg yolk phospholipids, *i.e.* lecithin, lysophosphatidylethanolamine (LPE) and sphingomyelin (SPH) were obtained from Sigma (St. Louis, MO, U.S.A.); phosphatidylethanolamine (PE) and lysolecithin from Avanti Polar Lipids (Birmingham, AL, U.S.A.). These standards were used to characterize the phospholipids and determine retention times on the method development and analytical systems. The concentration of each standard was 1 mg/ml.

A stock solution of phospholipids from the egg yolks was prepared: 2.01 g of the egg yolk phospholipids were dissolved in 5 ml of absolute ethanol and 4.9 ml of methanol. To the alcohol solution, 0.1 ml of 10% butylated hydroxytoluene (BHT) in methanol was added as an antioxidant. The stock solution was filtered through a 0.45-μm filter. From the stock solution, 3 ml were removed and diluted with 15 ml of methanol. This working solution contained 40.3 μg of phospholipids/μl.

Method development

The chromatographic system used for the method development studies consisted of a Waters 6000A pump (Waters Division, Millipore, Milford, MA, U.S.A.), a Rheodyne 7125 injector (Rheodyne, Berkeley, CA, U.S.A.), a Knauer variable-wavelength detector set at 203 nm with a sensitivity of 0.64 a.u.f.s. (Sonntek, Woodclift Lake, NJ, U.S.A.), and a method development column 20 × 0.46 cm I.D., packed with YMC 15–30 μm, 120 Å spherical silica (Yamamura, Kyoto, Japan). The column was packed using a Haskel Pump (Haskel, Burbank, CA, U.S.A.). The isocratic mobile phase was 5 m*M* ammonium acetate in acetonitrile–2-propanol–methanol–water (80:13:5:12) at a flow-rate of 2.0 ml/min. The chromatograms were recorded on an HP 3393A integrator (Hewlett-Packard, Avondale, PA, U.S.A.) at 0.2 cm/min, and an Omniscribe recorder (Houston Instruments, Austin, TX, U.S.A.) at 0.5 cm/min. All separations were achieved at ambient temperature.

Preparative high-performance liquid chromatography (HPLC)

Two preparative systems were used for the isolation of lecithin: a SepTech NovaPrep™ 5000 (NovaPrep) and a SepTech ST/800A (800A) (Separations Tech-

nology, Wakefield, RI, U.S.A.). With the NovaPrep a ST/2001A column (20 × 1.93 cm I.D.) was used; with the 800A, a ST/3002B Annular Expansion™ (A/E) column (20 × 5.00 cm I.D.). Each column was packed with YMC 15–30 μm, 120 Å spherical silica. The NovaPrep column was packed under high pressure using a Haskel pump, while the A/E column was slurry packed.

The NovaPrep column was equilibrated with the mobile phase at a flow-rate of 35 ml/min. A Knauer variable-wavelength detector set at 203 nm, with a sensitivity of 0.64 a.u.f.s., was used to monitor the separation. The NovaPrep was under computer control, utilizing TurboPrep™ software (Separations Technology). The program was set for an equilibration time of 10 min, injection time of 0.3 min and a run time of 60 min. The working solution was manually injected with a syringe. Data were recorded on both a strip chart recorder and an HP 3393A integrator.

The 800A column was operated under manual control and the A/E column equilibrated with a mobile phase of 5 m*M* ammonium acetate in acetonitrile–2-propanol–methanol–water (80:13:5:12) for 20 min at a flow-rate of 235 ml/min (percent flow-rate 56%). The Knauer detector with the same settings was used.

Analytical analysis

Each fraction was analyzed for purity with a Waters 6000A pump, Rheodyne 7125 injector, a Schoeffel Spectro Flow Monitor SF 770 variable-wavelength detector set at 203 nm, with a sensitivity of 0.1 a.u.f.s. (Schoeffel Instrument Division, Kratos, Westwood, NJ, U.S.A.) and a 20 × 0.46 cm I.D. column containing 8–12 μm Grace silica (W. R. Grace, Baltimore, MD, U.S.A.). The flow-rate was 2.5 ml/min and the mobile phase consisted of acetonitrile–methanol–water (40:9:6).

Prior to HPLC analysis, the fractions were concentrated by rotary vacuum distillation at a temperature range of 30 to 40°C (Table I). Of each fraction 100 μl were analyzed. The fractions containing purified lecithin were pooled and the remaining solvent was removed by lyophilization. A yellowish-white solid was left, which was a mixture of the purified lecithin and ammonium acetate. The lecithin was extracted with methylene chloride. The methylene chloride solution was reduced in volume to less than 10 ml. The final traces of the solvent were removed by a stream of nitrogen. The mass of the lecithin was then determined.

Each fraction was also analyzed with thin-layer chromatography (TLC) since the spots could be detected visually. The mobile phase was composed of chloroform–methanol–water (60:30:4)[11]. The fractions were spotted on silica plates (Fisher) against the phospholipid standards and working solution. The plates were developed

TABLE I

VOLUME OF COLLECTED AND CONCENTRATED FRACTIONS

System	*Volume collected per fraction (ml)*	*Reduced volume (ml)*
Method development	4	0.5
NovaPrep 5000	70	10
ST/800A	230	40

by two methods: molybdenum blue (Sigma, St. Louis, MO, U.S.A.) which is specific for phospholipids, and sulfuric acid which visualizes all organic compounds.

RESULTS AND DISCUSSION

The mobile phase composition was optimized to provide a reasonable capacity factor for the lecithin and the best selectivity for the separation of lecithin from other phospholipids which are present in egg yolk. Since the mobile phase had little low end UV absorption, the separation of phospholipids could be monitored in the 200–206 nm region. A 1-μg/μl mixture of the standards was analyzed using the method development column. The PE and LPE, which had retention times of 4.7 and 7.8 min,

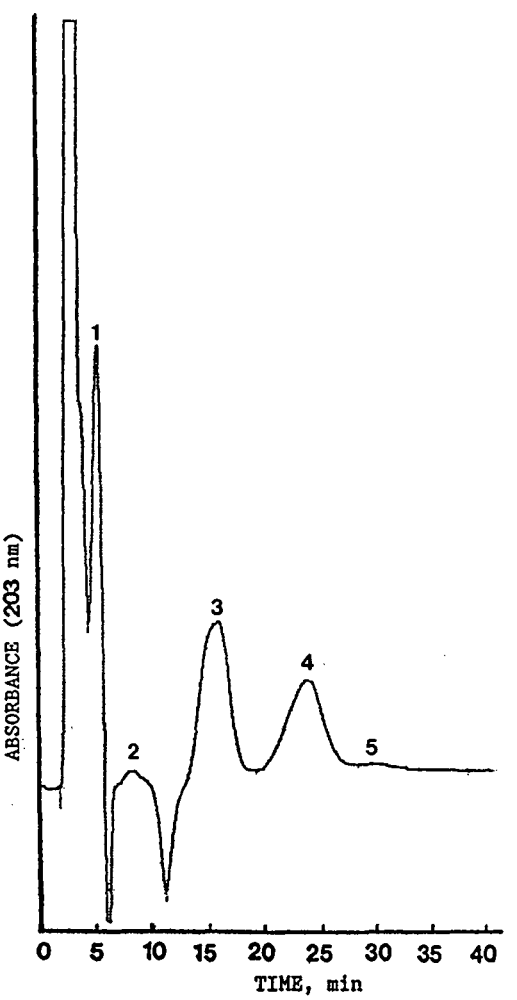

Fig. 2. Method development chromatograms of phospholipid standard mixture, 100 μl of 1 μg of each phospholipid/μl. Peak identification: 1 = PE, 2 = LPE, 3 = lecithin, 4 = SPH and 5 = lysolecithin. Conditions as given in Experimental section.

respectively, were eluted prior to lecithin (retention time of 15.6 min); the SPH was eluted afterwards at 23.8 min, as was the lysolecithin at 28.8 min (Fig. 2).

With the method development column a loading study was performed to determine the injection volume of the working solution which was optimal to obtain adequate selectivity and lecithin purity. Samples of 10, 25, 50, 75 and 100 μl were injected and fractions were collected across the lecithin peak.

The fractions were analyzed by analytical HPLC to determine the purity of the lecithin. Peaks were characterized by co-injection with the standards. The lecithin standard was eluted at 9.4 min (Fig. 3). In addition, two types of blanks were analyzed; the mobile phase before it entered the column (Before Column) and after the column (After Column) for each separation system. The fractions were also characterized by TLC using molybdenum blue spray to visualize selectively the phospholipids and sulfuric acid to detect all organic compounds.

The optimal injection volume was 50 μl (2 mg) of the working solution (Fig. 4A). Nine fractions (2 min each) were collected, concentrated and analyzed. Of the 9 fractions, 3–7 contained only lecithin with the desired purity.

When the method development system was scaled-up for each of the preparative columns, the linear velocity was kept constant. In scaling-up the volumetric flow-rate scales as the square of the column radius, the sample load scales as the column volume, while the run time scales as the column length. The loading scale-up factors for the preparative systems were 17 for the NovaPrep and 118 for the 800A (Table II).

A volume of 900 μl (35 mg) of the working solution were manually injected into the NovaPrep column. The retention time of the lecithin was 17.9 min and the run was terminated at 40 min (Fig. 4B). Seven fractions of 70 ml each were collected and concentrated to 10 ml. Fractions 1–5 contained lecithin of >99% purity. Fraction 6 was contaminated with SPH and fraction 7 contained only SPH. Representative

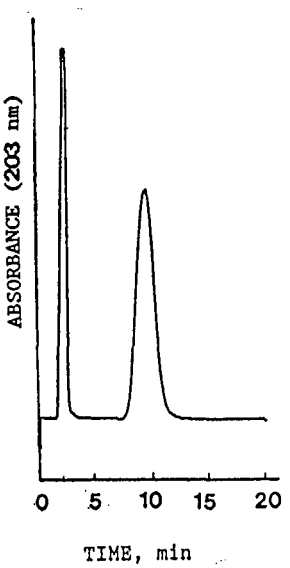

Fig. 3. Analytical chromatogram of 10 μl of 1 μg/μl lecithin standard, retention time 9.4 min. Conditions as given in Experimental section.

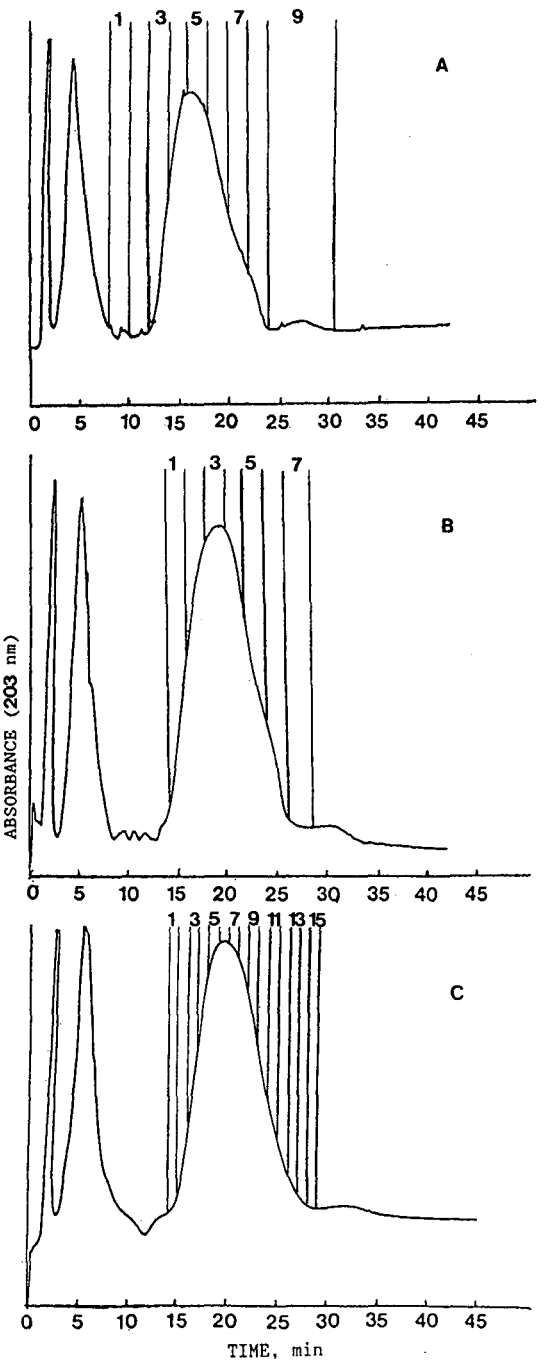

Fig. 4. Chromatograms of crude egg yolk phospholipids: (A) method development chromatogram (2 mg), (B) NovaPrep 5000 separation (35 mg), (C) ST/800A separation (241 mg). Retention time of lecithin; 14.9, 17.9 and 18.0 min, respectively. Conditions as given in Experimental section.

TABLE II

HPLC SCALE-UP

Column	*I.D. (cm)*	*Length (cm)*	*Load (g/run)*	*Flow-rate (ml/min)*	*Run time (h)*	*Solvent usage (l/run)*
ST/2020	0.46	20.00	0.002	2.0	0.83	0.10
ST/2001A	1.93	20.00	0.035	35.2	0.83	1.76
ST/3002B	5.00	20.00	0.236	236.3	0.83	11.81

analytical chromatograms of the fractions are shown in Fig. 5. Confirmation of purity was made by using TLC with two staining methods. For each fraction there was only one spot whose R_F factor corresponded to that of the standard sample of lecithin. In the pooled fractions (1–5) 25 mg of pure lecithin was recovered (72% recovery).

When 6 ml (241 mg) of the working solution were manually injected directly onto the A/E column, the lecithin was eluted at 18.0 min and the run was terminated at 43 min (Fig. 4C). Fifteen fractions of 230 ml each, 1 min in length, were manually collected. Each fraction was concentrated to 40 ml and an aliquot analyzed. Fraction 1 contained a minor component which was eluted prior to the lecithin. Fraction 13 contained only a very small amount of lecithin, whereas 14 and 15 did not have any detectable amounts of lecithin; therefore fractions 1 and 13–15 were not included in the pooled fractions. Representative chromatograms of the analyzed fractions are shown (Fig. 6). The amount of lecithin recovered was 130 mg (54% recovery).

The lecithin from each preparative system was dissolved separately in 1 ml of absolute ethanol and aliquots of 10 μl of each sample were reanalyzed. The lecithin

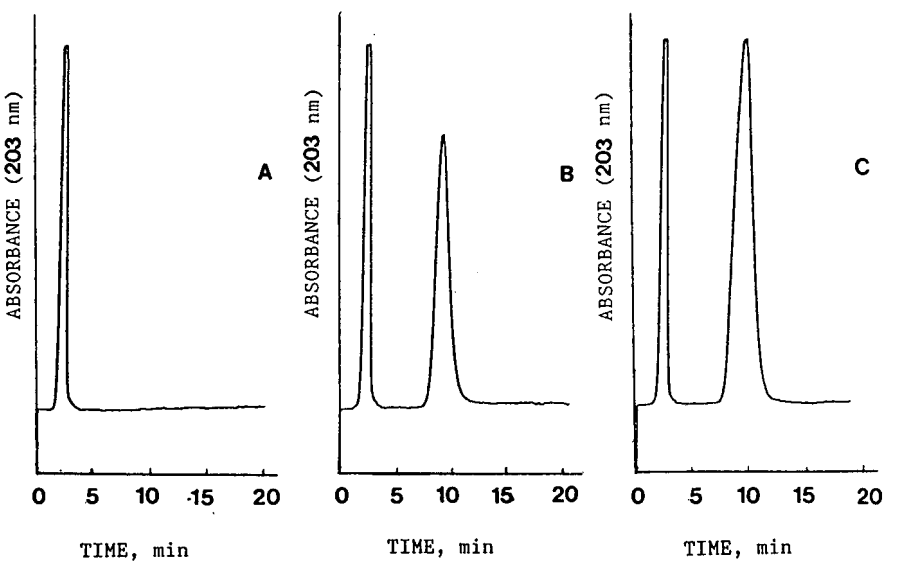

Fig. 5. Analytical HPLC of lecithin containing fractions obtained from the NovaPrep 5000: (A) mobile phase (After Column) blank, (B) fraction 1, (C) fraction 3. For conditions see Experimental section.

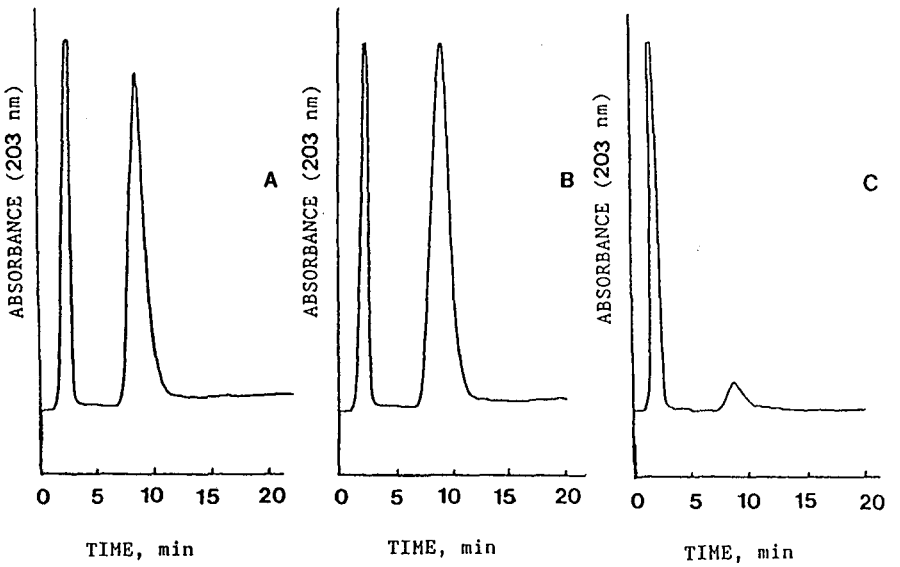

Fig. 6. Analytical HPLC of lecithin containing fractions obtained from the ST/800A: (A) fraction 2, (B) fraction 5, (C) fraction 12. For conditions see Experimental section.

both from the NovaPrep and the 800A had a purity of >99%. Development of the TLC plate with molybdenum blue revealed that only one phospholipid, lecithin, was present; development with sulfuric acid also indicated no organic components other than lecithin.

In conclusion a rapid isocratic preparative HPLC method has been developed for the isolation and purification of natural lecithin. With both preparative systems virtually identical profiles were observed, giving credence to an accurate scale-up. The capacity factors and selectivity values for all three systems are given in Table III. High purity was obtained without the use of chlorinated solvents in the mobile phase. To increase the throughput this method can be automated. In addition, it is possible to adopt these conditions for the isolation and purification of lecithin from other natural and synthetic sources or for the preparative HPLC of other phospholipids.

TABLE III

CAPACITY FACTORS (k') OF LECITHIN AND SPH AND SEPARATION FACTORS (α) OF SPH/LECITHIN

System	k'		α
	Lecithin	*SPH*	
Method development	10.3	19.2	1.9
NovaPrep 5000	12.1	20.7	1.7
ST/800A	12.1	21.5	1.8

ACKNOWLEDGEMENTS

We thank YMC, Inc. of Morris Plains, NJ, U.S.A. for donating the SiO_2 used in the method development, semi-preparative and preparative columns. We also thank Scott Lawing of SepTech for packing the method development and preparative columns. This research was supported in part by a grant from the U.S. National Institute of Allergy and Infections Diseases (AI25690), National Coorperative Drug Discovery Group for the treatment of AIDS.

REFERENCES

1 Y. J.-K. Hsieh, D. K. Welch and J. G. Turcotte, *Lipids*, 16 (1981) 761.
2 C. R. H. Raetz, M. Y. Chu, S. P. Srivastava and J. G. Turcotte, *Science (Washington, D.C.)*, 196 (1977) 303.
3 J. G. Turcotte, S. P. Srivastava, W. A. Meresak, B. A. Rizkalla, F. Louzon and T. P. Wunz, *Biochim. Biophys. Acta*, 619 (1980) 604.
4 J. G. Turcotte, S. P. Srivastava, J. M. Steim, P. Calabresi, L. M. Tibbetts and M. Y. Chu, *Biochim. Biophys. Acta*, 619 (1980) 619.
5 V. C. M. Yang, J. G. Turcotte and J. M. Steim, *Biochim. Biophys. Acta*, 68 (1982) 375.
6 M. S. Bermel, J. G. Turcotte, J. M. Steim and R. H. Notter, *J. Colloid Interf. Sci.*, 115 (1987) 167.
7 K. Aitzetmuller, *J. Liq. Chromatogr.*, 113 (1975) 231.
8 A. Kuksis and J. J. Myher, *J. Chromatogr.*, 379 (1986) 57.
9 F. G. Hegardt and L. J. Vicedo, *Revista De La Academia De Ciencias Exactas, Fisico-Quimics Y Naturales*, 29 (1974) 119.
10 K. M. Patel and J. T. Sparrow, *J. Chromatogr.*, 150 (1978) 542.
11 F. B. Jungalwala, J. E. Evans and R. H. McCluer, *Biochem. J.*, 155 (1976) 55.
12 M. L. Rainey and W. C. Purdy, *Anal. Chim. Acta*, 93 (1977) 211.
13 J. R. Nielsen, *Lipids*, 15 (1980) 481.
14 W. S. M. Geurts van Kessel, M. Tieman and R. A. Demel, *Lipids*, 16 (1981) 58.
15 R. W. Gross and B. E. Sobel, *J. Chromatogr.*, 197 (1980) 79.
16 V. L. Hanson, J. Y. Park, T. W. Osborn and R. M. Kiral, *J. Chromatogr.*, 201 (1981) 393.
17 J. R. Yandrasitz, G. Berry and S. Segal, *J. Chromatogr.*, 255 (1981) 319.
18 S.-S. Chen and A. Y. Kou, *J. Chromatogr.*, 227 (1982) 25.
19 T. L. Kaduce, K. C. Norton and A. A. Spector, *J. Lipid Res.*, 24 (1983) 1398.
20 S. Bahrami, H. Gasser and H. Redl, *J. Lipid Res.*, 28 (1987) 596.
21 W. S. M. Geurts van Kessel, W. M. A. Hax, R. A. Demel and J. DeGier, *Biochim. Biophys. Acta*, 486 (1977) 524.
22 W. M. A. Hax and W. S. M. Geurts van Kessel *J. Chromatogr.*, 142 (1977) 735.
23 R. S. Fager, S. Shapiro and B. J. Litman, *J. Lipid Res.*, 18 (1977) 704.
24 N. A. Porter, R. A. Wolf and J. R. Nixon, *Lipids*, 14 (1978) 20.
25 J. S. Ellingson and R. L. Zimmerman, *J. Lipid Res.*, 28 (1987) 1016.
26 J. Böswart, T. Schmidt, P. Kostiuk, V. Pacáková and K. Štulík, *J. Chromatogr.*, 495 (1989) 61.
27 W. S. Singleton, M. S. Gray, M. L. Brown and J. L. White, *J. Am. Oil Chem. Soc.*, 42 (1965) 53.

Journal of Chromatography, 517 (1990) 229–256
Elsevier Science Publishers B.V., Amsterdam

CHROMSYMP. 1929

Optimization of the experimental conditions in preparative liquid chromatography with touching bands

SADRODDIN GOLSHAN-SHIRAZI and GEORGES GUIOCHON*

**Department of Chemistry, University of Tennessee, Knoxville, TN 37996-1600 and Division of Analytical Chemistry, Oak Ridge National Laboratory, Oak Ridge, TN 37831-6120 (U.S.A.)*

ABSTRACT

Relationships are derived between the sample size permitting the elution of the components of a binary mixture as two touching bands and the parameters characterizing the separation and the column performance. These equations take into account the competitive interactions of the mixture components. They permit the determination of the optimum experimental conditions for maximum production rate with touching band elution.

The production rate increases monotonically with increasing inlet pressure available, provided that the column of optimum characteristics is used. For a given column, there is an optimum flow velocity and hence an optimum inlet pressure. Because of the competition between the mixture components for interaction with the stationary phase, the production rate under touching band conditions can be larger (under conditions of a predominant displacement effect) or lower (under conditions of a predominant tag-along effect) than the value derived when this competition is ignored.

INTRODUCTION

The optimization of experimental conditions for preparative chromatography is an important subject which has been actively studied in the recent years[1]. Experimentalists have tried to generalize their observations[2–5]. Various theoretical approaches have been used to derive either qualitative rules[6–10] or quantitative procedures for the calculation of optimum values of the parameters of a chromatographic separation[6–8,10]. Considerable confusion and some level of controversy are still understandably observed in an area where even the objectives are not always clarified. Depending on the type of work conducted, very different strategies are possible[11]. The preparation of small amounts of purified material needed for further investigations of its properties cannot be carried out following the same methods and principles as the industrial production of large amounts of pure compounds to be sold as drugs or fine chemicals. The time spent in developing and optimizing the separation

0021-9673/90/$03.50

is a major cost in the former instance and must itself be minimized. More subtle problems are still poorly understood. The optimum conditions for maximum production rate are very different for the first and the second component of a pair of components, especially if their relative concentration is far from unity[10]. Finally, specific requirements regarding the recovery yield and the fraction purity may affect considerably the outcome of the optimization process.

We have discussed recently the optimization of the experimental conditions for the purification of the second component of a binary mixture[7,8]. We took into account the competition between the two components for interaction with the stationary phase and the finite column efficiency. We also allowed slight band overlap by considering the cases when the required purity of the prepared product can be 99% or lower and accepting low recovery yields (*e.g.*, 60%). We showed that a considerable increase in the production rate is permitted by the use of high-performance columns at high reduced flow velocities[8,10,12].

Nevertheless, there is still great interest among practitioners in the "touching bands" case[6]. This permits the achievement of a recovery yield close to 100% and at the same time the production of nearly 100% pure compounds. The determination of the cutting time is straightforward and all the information required for the operation of the chromatograph is available from the detector signal. No separate on-line analysis of the eluate is necessary for the proper operation of the instrument. The influence of minor fluctuations in column temperature, sample size, mobile phase velocity and possibly composition has little consequence on the degree of band interference, so the control of the chromatograph is much simpler.

Knox and Pyper[6] discussed the optimization of the experimental parameters in the touching band case. They made two restrictive assumptions: first they assumed that both band profiles are right triangles and second they neglected the competition between the two components and assumed that their elution is independent of each other. These assumptions are necessary for a simple, general solution of the problem. The extent to which they affect the end result has never been investigated. Recently, Snyder and Cox[13] reformulated the equations derived by Knox and Pyper[6], multiplying the number of non-independent equations and obfuscating the issue without contributing to the solution.

The purpose of this paper is the investigation of the solution of the optimization problem in the case of touching bands for components having a Langmuir competitive isotherm and a separate assessment of the errors introduced by the two assumptions made by Knox and Pyper[6]. The problem is investigated first with the ideal model, for which an exact solution can be derived under close form[14]. Then corrections are introduced into the ideal model solution to account for the effect of the finite column efficiency, as was done in previous papers[6,8].

This paper is not intended to be a critique of the landmark paper by Knox and Pyper[6], but rather an extension of it. Within the limits of the assumptions they made, their results were correct and they provided an excellent first-order approximation. They were aware that neglecting the competitive interactions between the mixture components could not provide a better result[6]. Similarly, this paper attempts to take competitive interactions into account, but for the lack of a better model uses the Langmuir competitive isotherms. This isotherm model itself is only a first approximation, convenient for simulations, but which fits accurately the equilibrium data of few

systems[15,16]. Accordingly, our results provide a second-order approximation, not exact values of the optimum experimental conditions. The accuracy of our predictions depends on the degree of agreement between the experimental isotherms and the competitive Langmuir model.

THEORY

Touching bands with the ideal model

The ideal model of chromatography neglects the axial dispersion and assumes that the mass transfers between phases are infinitely fast, *i.e.*, it assumes that the column efficiency is infinite, whatever the mobile phase velocity. Hence the only parameter to optimize is the loading factor, which is independent of the column length. In this section, we first derive the close-form equations giving the loading factor for which touching bands is achieved, in three successive cases: (i) in the general case, (ii) when competition between the two components is ignored and (iii) when competition is ignored and the elution profiles are right triangles.

The fundamental equations

We derive the equation giving the loading factor for touching bands in the general case, then introduce the simplifications brought by the assumptions made by Knox and Pyper[6].

In the general case. We assume for the sake of simplicity that the equilibrium of the two components in the chromatographic system used is correctly described by binary Langmuir isotherms:

$$q_i = \frac{a_i C_i}{1 + b_1 C_1 + b_2 C_2} \tag{1}$$

where q_i is the amount of compound i adsorbed at equilibrium with a mobile phase where the concentrations of the components 1 and 2 are C_1 and C_2, respectively. a_i and b_i are numerical coefficients characteristic of the compounds and the chromatographic system which can be derived from the pure compound isotherms.

We have shown previously[14] that the loading factor, $L_{f,2}$, for the second component (*i.e.*, the ratio of the amount of second component in the sample injected to the column saturation capacity for this compound) which corresponds to exact separation of the two component bands, *i.e.*, to touching bands, is given by the following equation:

$$L_{f,2} = \frac{\left(\frac{\alpha - 1}{\alpha}\right)^2}{(1 + b_1 r_1 / b_2)} \tag{2}$$

where α is the relative retention of the two compounds ($\alpha = a_2/a_1 = k'_{0,2}/k'_{0,1}$) and r_1 is the positive root of the characteristic equation of the problem (ref. 8, eqn. II-3). In

practice, r_1 almost always is nearly equal to $C_{0,1}/C_{0,2}$, the ratio of the concentrations of the two components in the feed, so the loading factor for touching bands is given by

$$L_{f,2} = \frac{\left(\frac{\alpha - 1}{\alpha}\right)^2}{\left(1 + \frac{q_{s,2}C_{0,1}}{\alpha q_{s,1}C_{0,2}}\right)} = \frac{\left(\frac{\alpha - 1}{\alpha}\right)^2}{\left(1 + \frac{L_{f,1}}{\alpha L_{f,2}}\right)} \tag{3a}$$

where $q_{s,i} = a_i/b_i$, is the specific column saturation capacity. Solving eqn. 3a for $L_{f,2}$ gives

$$L_{f,2} = \left(\frac{\alpha - 1}{\alpha}\right)^2 - \frac{L_{f,1}}{\alpha} \tag{3b}$$

where $L_{f,1}$ is the loading factor for the first component. Depending on the relative concentration of the two components (*i.e.*, $C_{0,1}/C_{0,2}$), the loading factor for the second component corresponding to touching bands in the ideal model decreases from $[(\alpha - 1)/\alpha]^2$ (when $C_{0,1}$ is close to 0) to 0 (when $C_{0,2}$ is close to 0). The corresponding values of the loading factor of the first component are 0 and $(\alpha - 1)^2/\alpha$, respectively.

When the competition is ignored. In this instance we have two independent bands, the equilibrium isotherms of each compound being given by a simple one-component Langmuir isotherm. The condition for touching bands is that the band profile of the lesser retained component ends when the second component front is eluted. The first component band ends at the time $t_{e,1}$, given by[17]

$$t_{e,1} = t_p + t_{R0,1} \tag{4a}$$

where t_p is the width of the injection pulse, $t_{R0,1}$ and $t_{R0,2}$ are the limiting retention times of the two compounds at infinite dilution and t_0 is the hold-up time of the column. The retention time of the front of the second component[17], $t_{R,2}$, is

$$t_{R,2} = t_p + t_0 + (t_{R0,2} - t_0)(1 - \sqrt{L_{f,2}})^2 \tag{4b}$$

The condition for touching bands is obtained by writing $t_{e,1} = t_{R,2}$. This gives the loading factor value for the second component:

$$L_{f,2} = \left(\frac{\sqrt{\alpha} - 1}{\sqrt{\alpha}}\right)^2 \tag{5}$$

When the competition is ignored and the band profiles are right triangles. We have shown that right triangles are the asymptotic solution of the ideal model in the case of Langmuir isotherms[17]. The exact solution of the ideal model for a parabolic isotherm is also a right triangle profile[18]. This parabolic isotherm is the two-term Taylor expansion of the Langmuir isotherm. In this case, the retention time of the band front is given by[18]

$$t_{R,2} = t_p + t_0 + (t_{R0,2} - t_0)(1 - 2\sqrt{L_{f,2}}) \tag{6}$$

Writing that this retention time for the second component is equal to the elution time of the end of the first component band gives the loading factor of the second component corresponding to touching bands in this assumption:

$$L_{f,2} = \left(\frac{\alpha - 1}{\alpha}\right)^2 /4 \tag{7}$$

This equation is equivalent to that derived by Knox and Pyper[6].

Production rate and throughput. It is remarkable that both eqns. 5 and 7 are independent of the concentration of the first component in the mixture, whereas the exact eqn. 3 depends on the composition of the binary mixture.

If we assume that the cycle time is equal to the corrected retention time of the second component, $t_c = t_{R0,2} - t_0$, we obtain the following general equations for the production rate of the two components, Pr_1 and Pr_2, respectively:

$$Pr_2/(1 - \varepsilon)S = q_{s,2}uL_{f,2}/k'_{0,2} \tag{8}$$

and

$$Pr_1/(1 - \varepsilon)S = q_{s,1}uL_{f,1}/k'_{0,2} \tag{9}$$

where ε is the packing porosity, S the geometrical column cross-sectional area and u the mobile phase linear velocity. The throughput is given by

$$T/(1 - \varepsilon)S = u(q_{s,1}L_{f,1} + q_{s,2}L_{f,2})/k'_{0,2} \tag{10}$$

In the case when a different definition is chosen for the cycle time, the results of eqns. 8–10 should be multiplied by $(t_{R0,2} - t_0)/t_c$. The following discussions are based on the use of the production rate for the second component. Obviously, in the case of touching bands the production rate for the first component of a binary mixture is the product of the production rate for the second multiplied by the relative concentration of the two compounds.

Consequence of the first assumption made by Knox and Pyper

As we have shown in a previous discussion, a right triangle is the asymptotic solution of the ideal model[17]. It is a good approximation of the band profile obtained with this model for a Langmuir isotherm when the loading factor is less than 1%. We have also shown that the elution profile obtained for real columns (*i.e.*, with a finite efficiency) can be approximated by right triangles for still larger values of the loading factor, in fact as long as $bC_{Max} \leqslant 0.1$ (ref. 18).

We can expect that for low values of the relative retention, α, the value of the loading factor corresponding to touching bands is small and this first approximation has no serious influence on the result. At higher values of α, in contrast, the consequence could be more significant. Figs. 1 and 2 illustrate this effect. On both figures are plotted the individual elution profiles obtained with the loading factors given by eqn. 5 (no competition, correct Langmuir profiles) and by eqn. 7 (Knox and Pyper value, no competition, right triangles). Fig. 1 corresponds to $\alpha = 1.20$ and Fig.

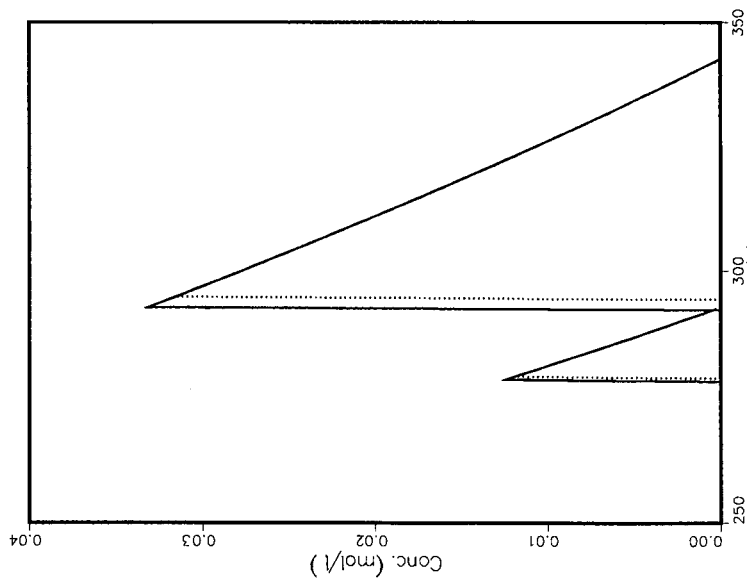

Fig. 1. Individual elution profiles of the bands of two components with non-competitive adsorption isotherms. Feed composition, 1.9; $K'_{0,1} = 6$; $\alpha = 1.2$; isotherm coefficients, $b_1 = 2.4$, $b_2 = \alpha b_1$; column length, 25 cm; phase ratio, 0.25; mobile phase velocity, 0.6 cm/s. Solid lines: exact solution of the ideal model in the touching band case for two independent Langmuir isotherms. Dotted lines: profile calculated assuming the profiles are right triangles. Sample size from eqn. 5 (solid line) or eqn. 7 (dotted line).

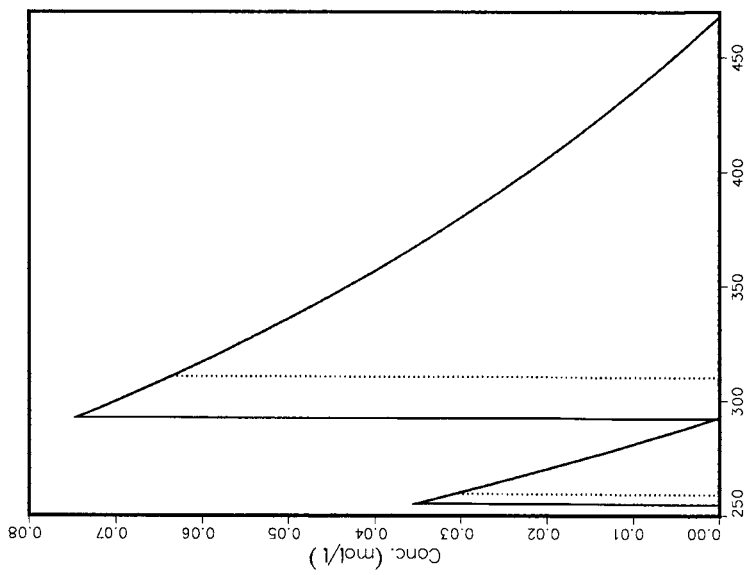

Fig. 2. Individual elution profiles of the bands of two components with non-competitive adsorption isotherms. Conditions as in Fig. 1, except $\alpha = 1.7$.

2 to $\alpha = 1.70$. In the former instance the differences are small but in the latter they are fairly important. This shows that the assumption that the band profiles are right triangles is reasonably satisfactory if the relative retention is close to unity (difficult separations). If the relative retention is large, the assumption may contribute to some extent to the large difference between the production rates predicted by the Langmuir competitive and the parabolic non-competitive models.

Consequence of the second assumption made by Knox and Pyper

A much more profound and important source of error comes from the assumption of an independent behavior of the two bands during their migration. In non-linear chromatography, the competition between the different components of the mixture cannot be neglected[4,19,20]. As long as the column is overloaded, *i.e.*, behaves non-linearly for one component, it behaves similarly for all the components whose bands interfere with the band of that compound. In agreement with the independence assumption, the loading factor for touching bands (eqns. 5 and 7) and the corresponding values of the production rates for the two compounds (eqns. 8 and 9) do not depend on the composition of the feed. This is not realistic, and eqn. 3 shows that, on the contrary, the loading factor does depend strongly on this composition when the competition is taken into account.

Comparing eqns. 3 and 7 shows that the values of the loading factors they predict are equal only for $L_{f,1}/\alpha L_{f,2} = b_1 C_{0,1}/b_2 C_{0,2} = 3$. When the ratio $L_{f,1}/\alpha L_{f,2}$ is smaller than 3 (dominant displacement effect), the loading factor corresponding to touching bands (eqn. 3) is larger than predicted by the Knox and Pyper model (eqn. 7), whereas the reverse is true for values of that ratio larger than 3 (dominant tag-along affect). If we inject the amount derived from eqn. 7, we obtain well resolved bands in the former instance and overlapping bands in the latter.

Figs. 3–5 show two chromatograms each. They have been obtained for three different feed compositions, under the same simulated experimental conditions with the sample sizes predicted by eqns. 3 and 7, respectively. In all instances, the band profiles are obtained as the analytical solutions of the ideal model for binary Langmuir isotherms[14]. Fig. 3 is obtained with a relative feed composition such that $L_{f,1}/\alpha L_{f,2}$ is smaller than 3. As expected, the sample size predicted by eqn. 3 is the larger and the sample size predicted by eqn. 7 leads to well resolved bands (resolution 1.2), whereas the nearly four times larger sample size which is predicted by eqn. 3 leads to touching bands. A strong displacement effect is observed. The rear profile of the first component is convex upward whereas the rear profile of the second band is convex downward, as is conventional with Langmuir isotherms, for single components. For Fig. 4, the feed composition is such that $L_{f,1}/\alpha L_{f,2}$ is equal to 3 and the two sample sizes are equal. Note, however, that the profile predicted by the ideal model is different from the right triangle assumed by Knox and Pyper[6]. For Fig. 5, the ratio $L_{f,1}/\alpha L_{f,2}$ is larger than 3. Now the sample amount predicted by eqn. 7 is too large. The chromatogram obtained corresponds to strongly overlapping bands. To obtain touching bands, the smaller sample given by eqn. 3 should be used. It is nearly half the one predicted by eqn. 7. The column is still strongly overloaded and a marked tag-along effect is observed.

The previous discussion concerns only ideal chromatography. With real columns, the elution bands are wider and shorter than predicted by the ideal model. The concentration shock is damped by the finite rates of the axial diffusion and the

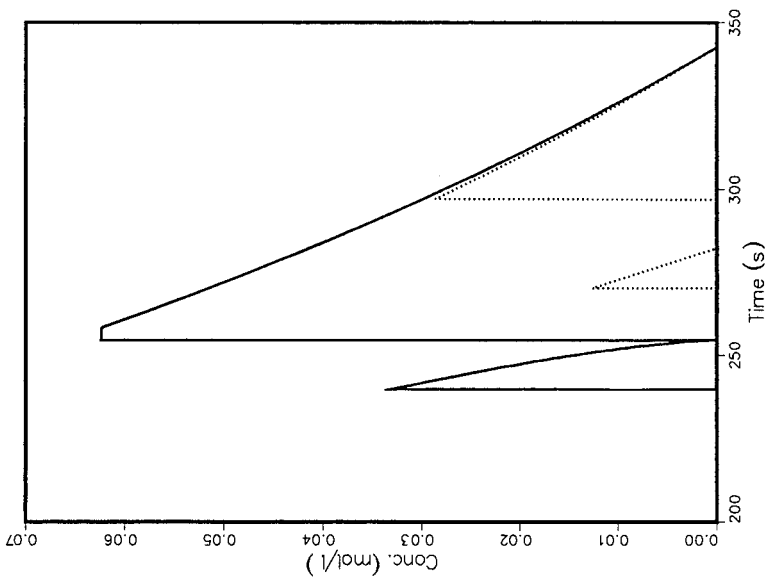

Fig. 3. Individual elution profiles of the bands of two components with Langmuir competitive adsorption isotherms. Conditions as in Fig. 1. Solid lines: elution profiles calculated with the ideal model using the sample size predicted by eqn. 3. Dotted lines: elution profiles calculated following the method of Knox and Pyper[6], with the sample size given by eqn. 7. The production rate predicted by the non-competitive model is too low.

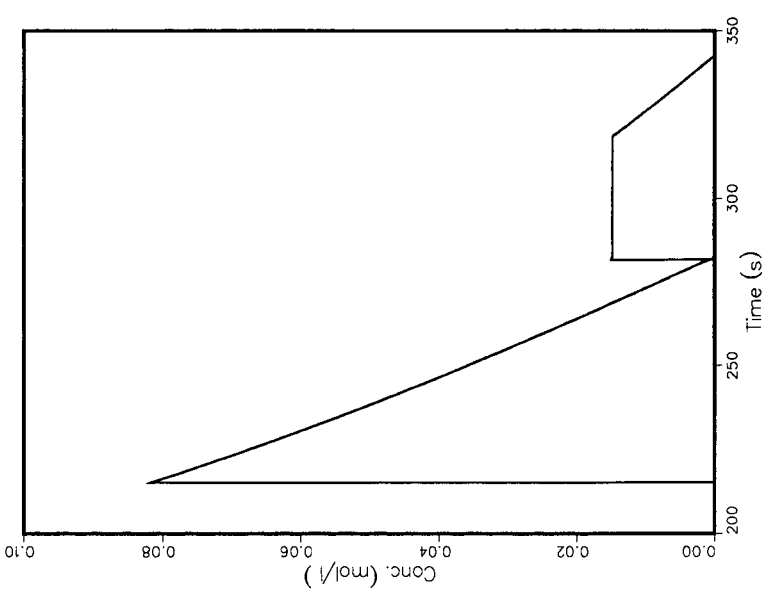

Fig. 4. Individual elution profiles of the bands of two components with Langmuir competitive adsorption isotherms. Conditions as in Fig. 3, except feed composition = 3.6:1 ($L_{f,1}/\alpha L_{f,2} = 3$). The production rates predicted by the competitive and the non-competitive models are equal.

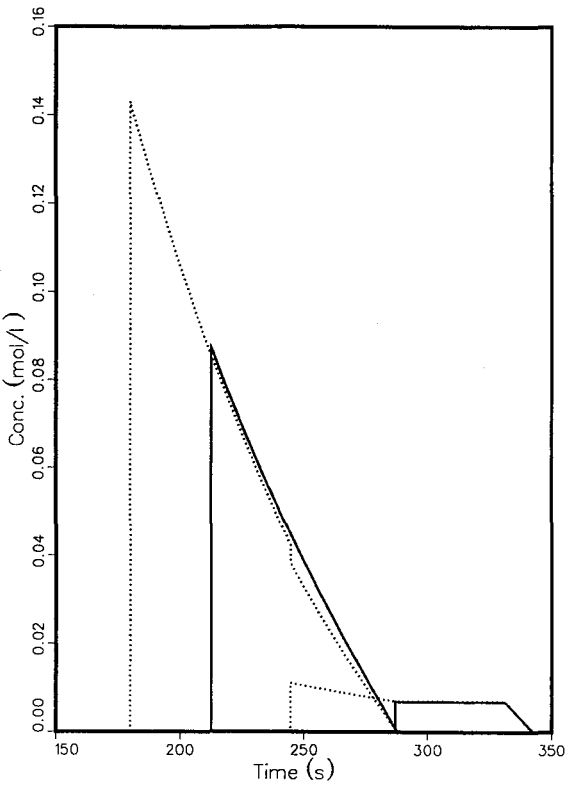

Fig. 5. Individual elution profiles of the bands of two components with Langmuir competitive adsorption isotherms. Conditions as in Fig. 3, except feed composition = 9:1. The production rate predicted by the non-competitive model is too high.

mass-transfer kinetics, so a shock layer is observed instead. In order to achieve touching bands, the sample should be smaller than predicted by eqn. 3. The calculation of the sample corresponding to touching bands for an actual column is discussed in the next section.

Touching bands in the case of a real column

In this section we derive a close-form expression of the sample size corresponding to touching bands in the case of an actual column, with a finite efficiency. This value is a function of the column efficiency and, accordingly, of the column characteristics, length, packing particle size and packing quality, and of the flow velocity. In the following section we discuss the optimization of the experimental conditions.

In a previous paper we showed that the maximum production rate is achieved when the column is operated at a high mobile phase flow velocity, so that the cycle time is short[8]. The column efficiency is then low and the relative band width is large. The effect of the band width on the degree of band interference is significant. Similarly, in the touching band case we must take into account the effect of column efficiency on the

band profile. A further difficulty is in the definition of the touching band condition. With the ideal model, the elution of a band begins and ends at well defined times. Before and after, the concentration of the compound in the mobile phase is zero. There is no such thing with real columns: the beginning and end of a band elution depend on the sensitivity of the detection. We shall neglect these effects, however, and write that the difference between the elution times of the rear of the second and first bands is equal to the total band width of the second component.

Derivation of the band width of the second component

The effect of the finite column efficiency on the band broadening during its elution can be accounted for by following the procedure first suggested by Haarhoff and Van der Linde[21] and later used by Poppe and Kraak[22] and Knox and Pyper[6]. We assume that the two contributions to the elution band width with which we are concerned, the thermodynamics (*i.e.*, the non-linear behavior of the phase equilibrium) and the kinetics (finite rates of mass transfer between phases and of axial dispersion) can be treated as two independent contributions. Therefore, their variances are additive and we have

$$\sigma_{tot}^2 = \sigma_{th}^2 + \sigma_{kin}^2 \tag{11}$$

where $\sigma_{tot}^2 = w_{tot}^2/16$ is the variance of the elution profile, $\sigma_{th}^2 = w_{th}^2/16$ the variance contribution due to the non-linear behavior of the isotherm and $\sigma_{kin}^2 = w_{kin}^2/16$ the variance contribution of the mass-transfer kinetics and of the axial dispersion, where the ws are the corresponding baseline band widths. By definition of the column height equivalent to a theoretical plate, H_{tot}, we have

$$H_{tot} = H_{th} + H_{kin} \tag{12}$$

The kinetic contribution is given by

$$w_{kin}^2 = \frac{16}{N_0}\left(\frac{k'_{0,2} + 1}{k'_{0,2}}\right)^2 (t_{R0,2} - t_0)^2 \tag{13}$$

where N_0 is the column plate number under linear conditions (in practice, for a very small size sample), $k'_{0,2}$ is the column capacity factor at infinite dilution (*i.e.*, $k'_{0,2} = a_2F$, where F is the phase ratio) and $t_{R0,2}$ and t_0 are the limiting retention time at infinite dilution of the second component and the hold-up time, respectively.

The thermodynamic contribution is calculated from the band width of the solution of the ideal model[14]. In this work we are interested in the width of the second component band. There are two cases. The ideal model solution shows that the band of the second component has completely recovered from its interaction with the first component band and achieved the same profile as if the same amount of second component was injected alone when the loading factor is equal to or smaller than $L_{f,2,p}$[14], as given by

$$L_{f,2,p} = \left(\frac{\frac{\alpha - 1}{\alpha}}{1 + \frac{b_1 r_1}{b_2}}\right)^2 = \left(\frac{\alpha - 1}{\alpha + \frac{q_{s,2}C_{0,1}}{q_{s,1}C_{0,2}}}\right)^2 = \left(\frac{\frac{\alpha - 1}{\alpha}}{1 + \frac{L_{f,1}}{\alpha L_{f,2}}}\right)^2 \tag{14}$$

When the loading factor is between the values given by eqns. 3 and 14, we still have resolved bands, but the band profile of the second component has not had time to recover from the deformation resulting from the interaction between the two component bands. Consequently, a different procedure must be used to calculate the band width of the second component, depending on whether the loading factor is smaller or larger than $L_{f,2,p}$.

Loading factor of the second component for touching band when $L_{f,2} < L_{f,2,p}$

In this case, the profile of the second component band is the same as if it is injected pure. Its width is given by the following equation[17,23]:

$$w_{th} = (2\sqrt{L_{f,2}} - L_{f,2})(t_{R0,2} - t_0) \tag{15}$$

The total band width of the second component band in the touching band case is equal to the difference between the retention times of the rear of the first band and the rear of the second band:

$$w_{tot} = t_{R0,2} + t_p - t_{e,1} \tag{16}$$

In order to calculate the loading factor corresponding to touching bands, we must know the retention time of the rear of the first component band, $t_{e,1}$. It can be derived from eqn. 63 in ref. 14 by writing that $C'_1 = 0$ in this equation. We obtain

$$t_{e,1} = t_p + t_{R0,1} - \frac{L_{f,2}}{(\alpha - 1)}(t_{R0,2} - t_0) \tag{17}$$

This equation demonstrates the consequence of band interactions in the column. Although we are looking for conditions under which the two bands are just resolved when they elute, they have interacted during their entire migration. If there were to be no interaction, the retention time of the end of the first band would be $t_e = t_p + t_{R0,1}$. Eqn. 17 shows that the band is actually eluted earlier. The decrease in the retention time is directly proportional to the loading factor for the second component.

Combining eqns. 16 and 17 gives

$$w_{tot} = (t_{R0,2} - t_0)\left(\frac{\alpha - 1}{\alpha} + \frac{L_{f,2}}{\alpha - 1}\right) \tag{18}$$

Eqn. 18 shows that the second component band width corresponding to touching bands and, accordingly, the apparent column efficiency, are a function of the sample size. This is the major difference from the simplified approach by Knox and Pyper[6], which assumed that the values of w_{tot} and N_{tot} corresponding to touching band are constant, independent of the amount of second component injected.

Combination of eqns. 11, 13, 15 and 18 gives

$$(2\sqrt{L_{f,2}} - L_{f,2})^2 + \frac{16}{N_0}\left(\frac{k'_{0,2} + 1}{k'_{0,2}}\right)^2 = \left(\frac{\alpha - 1}{\alpha} + \frac{L_{f,2}}{\alpha - 1}\right)^2 \tag{19}$$

Solving eqn. 19 for $L_{f,2}$ and putting the solution into eqn. 8 gives the production rate of the second component.

Simplified equations

Several simplifications are possible. We can assume that the loading factor is relatively small and neglect $L_{f,2}$ in comparison with $\sqrt{L_{f,2}}$ in eqn. 19. This amounts to assuming that the band profile of the second component is a right triangle, as did Knox and Pyper[6], but still conserves the competitive interaction between the two components which is introduced by the competitive Langmuir isotherms. In this case, it is easy to solve the modified eqn. 19 and to obtain

$$L_{f,2} = (\alpha - 1)^2 \left\{ 2 - \frac{1}{\alpha} - \sqrt{4\left(\frac{\alpha - 1}{\alpha}\right) + \frac{16}{N_0}\left[\frac{k'_{0,2} + 1}{k'_{0,2}(\alpha - 1)}\right]^2} \right\} \tag{20}$$

Inserting the value of $L_{f,2}$ into eqn. 8 gives the production rate:

$$\frac{Pr_2}{(1 - \varepsilon)S} = \frac{q_{s,2}u(\alpha - 1)^2}{k'_{0,2}} \left\{ 2 - \frac{1}{\alpha} - \sqrt{4\left(\frac{\alpha - 1}{\alpha}\right) + \frac{16}{N_0}\left[\frac{k'_{0,2} + 1}{k'_{0,2}(\alpha - 1)}\right]^2} \right\} \tag{21}$$

If, in addition, we assume that the competitive interaction between the two components of the mixture is negligible, we ignore the term $L_{f,2}/(\alpha - 1)$ on the right-hand side of eqn. 19 and $L_{f,2}$ compared with its square root on the left-hand side. We then obtain

$$L_{f,2} = \left[\left(\frac{\alpha - 1}{\alpha}\right)^2 - \frac{16\left(\frac{k'_{0,2} + 1}{k'_{0,2}}\right)^2}{N_0} \right] \Big/ 4 \tag{22}$$

Combination of eqns. 8 and 22 gives the production rate:

$$\frac{Pr_2}{(1 - \varepsilon)S} = \frac{q_{s,2}u}{4k'_{0,2}} \left[\left(\frac{\alpha - 1}{\alpha}\right)^2 - \frac{16\left(\frac{k'_{0,2} + 1}{k'_{0,2}}\right)^2}{N_0} \right] \tag{23}$$

This equation is the same as that given by Knox and Pyper[6] (combination of their eqns. 40, 47, 63, 67) in the case when the cycle time is equal to $t_{R0,2} - t_0$.

Loading factor of the second component for touching band when $L_{f,2} > L_{f,2,p}$

Eqn. 19 is valid only as long as the loading factor obtained is lower than the threshold value (or equal to it), $L_{f,2,p}$ derived from eqn. 14. In contrast, when $L_{f,2}$ is larger than $L_{f,2,p}$, a plateau remains on the top of the second elution band, at least within the ideal model approximation. This plateau is more or less eroded by the axial diffusion and the finite rate of the mass-transfer processes. In this instance, neither the first nor the second component band profiles are identical with the band profile obtained with a pure component sample. The first band is modified by the

displacement effect and the second has not yet recovered from the tag-along effect.

Because the concentration of the second component is constant during elution of the plateau, we can assume, as a first approximation, that the finite column efficiency does not affect the contribution of the length of this plateau to the band width[8]. Hence, the total band width in this instance should be calculated as

$$w_{tot} = w_{plateau} + \sqrt{w_{kin}^2 + (w_{th} - w_{plateau})^2} \tag{24}$$

where $w_{plateau}$ is the width of the plateau (see below). As we have shown elsewhere[8], we have

$$w_{th} - w_{plateau} = (2\sqrt{L_{f,2,p}} - L_{f,2,p})(t_{R0,2} - t_0) \tag{25}$$

where $L_{f,2,p}$ is given by eqn. 14 and w_{tot} for touching bands is given by eqn. 18.

The width of the plateau can be calculated by writing that the area of the second component band is equal to the area injected in the column, *i.e.*, that mass is conserved. Thus,

$$C_2^B w_{plateau} + \int_{t_{B'}}^{t_{R0,2}+t_p} C_2 dt = L_{f,2}(t_{R0,2} - t_0)/b_2 \tag{26}$$

where C_2^B, $t_{B'}$ and C_2 are given by eqns. 28, 48 and 47, respectively, in ref. 14. The first term on the left-hand side of eqn. 26 is the area under the plateau, the second term, the area under the continuous profile, the right-hand side of eqn. 26 is the area $C_{0,2}t_p$ of the rectangular pulse of second component injected (see eqn. 42, ref. 14). The calculation gives

$$w_{plateau} = \left(\frac{1 + \frac{\alpha b_1 r_1}{b_2}}{\alpha - 1} \right) \left[L_{f,2} - \left(\frac{\frac{\alpha - 1}{\alpha}}{1 + \frac{b_1 r_1}{b_2}} \right)^2 \right] (t_{R0,2} - t_0) \tag{27}$$

Combination of eqns. 13, 18, 24, 25 and 27 gives

$$L_{f,2} = \frac{\left(\frac{\alpha - 1}{\alpha}\right)^2}{X(1+X)^2} \left[X^2 + 3X + \frac{\alpha + 1}{\alpha} - \sqrt{\left(2X + \frac{\alpha + 1}{\alpha}\right)^2 + \frac{16\left(\frac{k'_{0,2} + 1}{k'_{0,2}}\right)^2 (1+X)^4}{N_0\left(\frac{\alpha - 1}{\alpha}\right)^2}} \right] \tag{28}$$

with

$$X = \frac{q_{s,2}C_{0,1}}{\alpha q_{s,1}C_{0,2}} = \frac{L_{f,1}}{\alpha L_{f,2}} \tag{28a}$$

Eqn. 28 gives the loading factor for touching bands for values of the loading factor between those given by eqns. 3 and 14. The production rate is then calculated using eqn. 8.

Optimization of the experimental conditions

The optimization requires the use of a plate-height equation to relate the column efficiency to the mobile phase flow velocity. There are two possibilities at this stage. We can use a very simplified equation which assumes that the column is operated at a high reduced flow velocity. We have shown previously that the optimum flow velocity for maximum production is very high[8]. In this instance, we can also solve the optimization problem in close form and give a detailed, classical analysis of the effect of each parameter. Alternatively, we can use the classical Knox equation[24] and solve the problem numerically. These two approaches are discussed below.

Optimization with a simple plate-height equation

We know that the linear mobile phase velocity, u, is related to the column design and operating parameters by the following equation:

$$u = \frac{k_0 \Delta P d_p^2}{\eta L} \tag{29}$$

where k_0 is the column specific permeability (of the order of $1 \cdot 10^{-3}$), ΔP is the pressure drop between the column inlet and outlet, d_p is the average particle size of the packing material used, η is the mobile phase viscosity and L is the column length.

As the column is operated at a high reduced mobile phase velocity, we assume that the height equivalent to a theoretical plate height (HETP) of the column, is given by the simplified equation[6]:

$$h = Cv \tag{30}$$

where h is the reduced plate height ($h = H/d_p$) and v is the reduced velocity ($v = ud_p/D_m$). The limiting column efficiency at infinite sample dilution (*i.e.*, L/H_{kin}) is therefore

$$N_0 = \frac{\eta D_m}{k_0 \Delta P C (d_p^2/L)^2} \tag{31}$$

As u and N_0 depend on the ratio d_p^2/L, not separately on the column length and the particle size, so does the production rate. As long as eqn. 30 is valid, in both the touching band and the overlapping band cases[8], long columns packed with coarse

particles may give the same production rate as short columns packed with fine particles, if they have the same value of the ratio d_p^2/L. Provided that the column length can be adjusted easily, a variety of packing materials of different sizes can be used (within reason). The existence of an optimum particle size at constant length has been demonstrated experimentally in a recent paper[5], in agreement with the results of a previous study[19].

Depending on the value of the optimum sample size, we have two different cases. When the optimum loading factor is less than $L_{f,2,p}$, we should calculate it using eqn. 19. When the optimum loading factor is greater than $L_{f,2,p}$, eqn. 19 is no longer valid, and we must use eqn. 28. This condition is awkward to use. We show later that in practice eqn. 19 must be used to calculate the optimum loading factor for touching band when $L_{f,1}/\alpha L_{f,2}$ is lower than 0.4 (and the displacement effect is dominant) whereas eqn. 28 must be used when $L_{f,1}/\alpha L_{f,2}$ is larger than 0.4 (and the tag-along effect predominates). We discuss successively the cases when $L_{f,1}/\alpha L_{f,2}$ is smaller and larger than 0.4.

Optimization with a simple plate-height equation: displacement effect dominant

Combining eqns. 8, 19, 29 and 31 gives the production rate. Differentiation with respect to d_p^2/L permits the calculation of the optimum column configuration for a certain value of the pressure drop available. The equations could not be solved in close form, but the numerical calculation is easy.

If we assume that the band profiles are right triangles, as we have shown above that this assumption is reasonable when the relative retention α is close to 1 and the loading factor is small, we perform the same calculation as above, but using eqns. 20 and 21 instead of eqn. 19. Then it is easy to solve the equation giving the optimum value of the ratio d_p^2/L. We obtain

$$\left(\frac{d_p^2}{L}\right)_{\text{opt}} = \left(\frac{\alpha - 1}{\alpha}\right) \frac{\sqrt{(\alpha - 1/2)\sqrt{\alpha^2 - \alpha + 1/36} - (\alpha^2 - \alpha - 1/12)}}{4\left(\frac{k'_{0,2} + 1}{k'_{0,2}}\right)\sqrt{\frac{2k_0 \Delta P C}{3D_m \eta}}} \tag{32}$$

Combination of eqns. 20, 31 and 32 gives the optimum value of the loading factor for touching bands:

$$L_{f,2,\text{opt}} = 3\left[\frac{(\alpha - 1)^2}{2\alpha}\right](\alpha - 1/2 - \sqrt{\alpha^2 - \alpha + 1/36}) \tag{33}$$

The value of the production rate is obtained by combining eqns. 21, 29, 32 and 33:

$$\frac{Pr_2}{(1 - \varepsilon)S} = \left[\frac{3q_{s,2}(\alpha - 1)^3}{8\alpha^2(1 + k'_{0,2})}\right]\sqrt{\frac{3k_0 \Delta P D_m}{2\eta C}}(\alpha - 1/2 - \sqrt{\alpha^2 - \alpha + 1/36}) \times$$

$$\sqrt{(\alpha - 1/2)\sqrt{\alpha^2 - \alpha + 1/36} - (\alpha^2 - \alpha - 1/12)} \tag{34}$$

Finally, if we ignore the competitive interactions between the two components of the

mixture and assume right triangle band profiles, we can use the value of the loading factor given by eqn. 22. A calculation similar to those made using eqn. 19 or 20 and described above gives in this case the following optimum value of the ratio d_p^2/L:

$$\left(\frac{d_p^2}{L}\right)_{\text{opt}} = \frac{\dfrac{\alpha - 1}{\alpha}}{4\left(\dfrac{k'_{0,2} + 1}{k'_{0,2}}\right)\sqrt{\dfrac{3k_0 \Delta PC}{D_m \eta}}} \tag{35}$$

and the optimum value of the loading factor is

$$L_{f,2,\text{opt}} = \frac{1}{6}\left(\frac{\alpha - 1}{\alpha}\right)^2 \tag{36}$$

Inserting eqn. 35 into eqn. 31 gives the optimum column efficiency:

$$N_{0,\text{opt}} = 48\left(\frac{\alpha}{\alpha - 1}\right)^2 \left(\frac{1 + k'_{0,2}}{k'_{0,2}}\right)^2 \tag{37}$$

and the maximum production rate is

$$\frac{Pr_2}{(1 - \varepsilon)S} = \frac{q_{s,2}}{24(1 + k'_{0,2})}\left(\frac{\alpha - 1}{\alpha}\right)^3 \sqrt{\frac{k_0 \Delta P D_m}{3\eta C}} \tag{38}$$

which are equivalent to the equations derived by Knox and Pyper[6].

Optimization with a simple plate-height equation: tag-along effect dominant

The optimum loading factor is now higher than the threshold ($L_{f,2,p}$) given by eqn. 14 and, as we show later, the ratio $L_{f,1}/(\alpha L_{f,2})$ is larger than 0.4. The value of the optimum loading factor for touching bands is given by eqn. 28. Eqns. 29, 30 and 31 still give the mobile phase flow velocity, the column plate height and the plate number of the column at infinite sample dilution, respectively. Combining eqns. 8, 28, 29 and 31 gives the production rate. Writing that the differential of the production rate with respect to d_p^2/L is zero gives the optimum value of this ratio:

$$\left(\frac{d_p^2}{L}\right)_{\text{opt}} = \frac{\dfrac{\alpha - 1}{\alpha}\left(X^2 + 3X + \dfrac{\alpha + 1}{\alpha}\right)}{8\left(\dfrac{k'_{0,2} + 1}{k'_{0,2}}\right)(1 + X)^2 \sqrt{\dfrac{k_0 \Delta PC}{D_m \eta}}} \times$$

$$\sqrt{\frac{1}{2} - \frac{2\left(2X + \dfrac{\alpha + 1}{\alpha}\right)^2}{\left(X^2 + 3X + \dfrac{\alpha + 1}{\alpha}\right)^2}} + \sqrt{\frac{1}{4} + \frac{2\left(2X + \dfrac{\alpha + 1}{\alpha}\right)^2}{\left(X^2 + 3X + \dfrac{\alpha + 1}{\alpha}\right)^2}} \tag{39}$$

where X is given by eqn. 28a. When X becomes large, the square-root term on the right-hand side of eqn. 39 is almost equal to unity and the equation simplifies considerably:

$$\left(\frac{d_p^2}{L}\right)_{opt} = \frac{\frac{\alpha - 1}{\alpha}}{8\left(\frac{k'_{0,2} + 1}{k'_{0,2}}\right)\sqrt{\frac{k_0 \Delta PC}{D_m \eta}}} \tag{39a}$$

This result is now independent of the feed composition.

Inserting the optimum value of d_p^2/L given by eqn. 39 into eqn. 31 gives the optimum limiting column efficiency (at negligible sample size). Combination of these equations with eqn. 28 gives the optimum sample size:

$$L_{f,2,opt} = \left(\frac{\alpha - 1}{\alpha}\right)^2 \frac{X^2 + 3X + \frac{\alpha + 1}{\alpha}}{4X(1 + X)^2} \left[3 - \sqrt{1 + 8\left(\frac{2X + \frac{\alpha + 1}{\alpha}}{X^2 + 3X + \frac{\alpha + 1}{\alpha}}\right)^2}\right] \tag{40}$$

In the case when X is large, the optimum column efficiency and loading factor are

$$N_{0,opt} = 64\left(\frac{\alpha}{\alpha - 1}\right)^2 \left(\frac{1 + k'_{0,2}}{k'_{0,2}}\right) \tag{40a}$$

$$L_{f,2,opt} = \frac{1}{2X}\left(\frac{\alpha - 1}{\alpha}\right)^2 \tag{40b}$$

This value is equal to that predicted by the non-competitive model for $X = 3$, lower when X is larger than 3 and larger when X is smaller than 3.

Finally, combination of eqns. 8, 29, 39 and 40 gives the maximum production rate which can be achieved with a certain value of the inlet pressure.

Optimization with the Knox plate-height equation

More accurate results could be obtained using the classical Knox plate-height equation[24]:

$$h = \frac{L}{d_p N_0} = \frac{B}{v} + Av^{1/3} + Cv \tag{41}$$

It is easy to calculate numerically the optimum values of the column length and particle size, flow velocity and sample size for any problem, but a close-form solution cannot be derived.

RESULTS AND DISCUSSION

We have performed a number of calculations in the two cases when either the displacement or the tag-along effect predominates, using the simplified and the more accurate plate-height equations, and we report the results in Tables I–IV, discussed in the following sections. We then compare these results with previously published data.

Optimization with a simple plate-height equation: displacement effect dominant

In this instance, the optimum sample size is given by eqn. 19. We see that, as assumed by Knox and Pyper[6], the optimum values of the sample size and of the limiting column efficiency do not depend on the composition of the feed.

Table I compares the results derived from our present approach (eqns. 8, 19, 29 and 31) and those calculated using the model derived by Knox and Pyper[6] (eqns. 35–38). The optimum values of the limiting column efficiency, of the value of the ratio d_p^2/L, of the mobile phase flow velocity and of the loading factor are given together with the maximum production rate that can be achieved. A maximum value of the inlet pressure of 200 atm has been assumed. The comparison between the two sets of results shows little difference between the optimum values of the ratio d_p^2/L, usually 10–20% larger with the Knox and Pyper assumptions than with our more exact approach. The difference in the values of the optimum limiting column efficiency is greater; our approach requires a column efficiency roughly 35% larger than that of Knox and Pyper[6]. Correspondingly, the optimum value of the mobile phase velocity is lower with

TABLE I

OPTIMUM VALUE OF THE RATIO d_p^2/L AND MAXIMUM PRODUCTION RATE UNDER TOUCHING BAND CONDITIONS

First case: $\frac{q_{s,2}C_{0,1}}{\alpha q_{s,1}C_{0,2}} = \frac{L_{f,1}}{\alpha L_{f,2}} < 0.4$. $h = Cv$.

α	N_0	d_p^2/L $\times 10^8$ (cm)	u (cm/s)	$L_{f,2}$ (%)	$Pr_2/(1-\varepsilon)S$ [μmol/(cm^2 s)]	$Pr_2{}^a/Pr_2{}^b$
1.1[a]	10500	2.2	0.44	0.41	2.72	
1.1[b]	7700	2.55	0.51	0.138	1.06	2.57
1.2[a]	3100	4.0	0.8	1.37	15.2	
1.2[b]	2260	4.7	0.94	0.46	6.1	2.51
1.3[a]	1600	5.55	1.1	2.62	37.4	
1.3[b]	1150	6.6	1.3	0.89	15.0	2.30
1.5[a]	760	8.1	1.6	5.41	97.6	
1.5[b]	550	9.55	1.9	1.88	39.8	2.45
1.7[a]	530	9.75	1.95	8.45	161.6	
1.7[b]	350	12.0	2.4	2.83	66.8	2.42

[a] Calculated with the simple HETP equation $h = Cv$, using the model described in this work. Conditions: $C = 0.1$; $k'_{0,1} = 6$, $\Delta P = 200$ atm, $D_m = 1 \cdot 10^{-5}$ cm^2/s, $\eta = 1$ cP, $q_{s,2} = 10$. The cycle time is given by $t_c = t_{R0.2} - t_0$.

[b] Calculated with the same plate-height equation, using the model of Knox and Pyper[6], which ignores the competition and assumes right triangular band profiles.

our results, by *ca.* 15–20%. However, the major difference between the two sets of results is the loading factor. Knox and Pyper neglect the band interaction. Because of the importance of the displacement effect, a nearly three times larger sample size is needed to achieve touching bands when we take into account the competitive interaction between the two components of the mixture (Table I). The end result is a production rate which is *ca.* 2.5 times larger than that predicted by the non-competitive model[6].

If we ignore the competition between the mixture components, the optimum values of d_p^2/L, N_0 and $L_{f,2,\mathrm{opt}}$ and the maximum production rate are proportional to $(\alpha - 1)/\alpha$, $[(\alpha - 1)/\alpha]^{-2}$, $[(\alpha - 1)/\alpha]^2$, and $[(\alpha - 1)/\alpha]^3$, respectively (see eqns. 35, 36, 37 and 38). When we take the competitive interaction between the two components into account, the exact dependence of these parameters on the relative retention is more complicated. The analysis of the data in Table I shows, however, that in practice the optimum sample size is given by

$$L_{f,2} = 0.5\left(\frac{\alpha - 1}{\alpha}\right)^2 \tag{42}$$

instead of $L_{f,2} = 0.166\,[(\alpha - 1)/\alpha]^2$, as predicted by the approximate eqn. 37[6]. This important increase is not surprising. The first component band is pushed forward by the second band. Eqn. 17 shows the reduction in the retention time of the rear of that band, proportional to the amount of second component injected. Accordingly, in order to reach touching band conditions, we need a wider second component band, hence a larger sample size.

Further, we see that the limiting efficiency required, N_0, is equal to four times the efficiency, N^*, necessary for the separation of the mixture with a resolution of 1 under linear (*i.e.*, analytical) conditions, instead of three times as predicted by the non-competitive model of Knox and Pyper[6]. In other words, the column should afford the separation of a very small sample with a resolution of 2.0, not 1.7.

As the optimum sample size for touching bands under a dominant displacement effect is given by eqn. 42, the threshold condition, $L_{f,2} < L_{f,2,p}$ where $L_{f,2,p}$ is given by eqn. 14, can be rewritten as

$$L_{f,2,\mathrm{opt}} \leqslant L_{f,2,p} \tag{43a}$$

or, by combining eqns. 14 and 42:

$$0.5\left(\frac{\alpha - 1}{\alpha}\right)^2 \leqslant \frac{\left(\dfrac{\alpha - 1}{\alpha}\right)^2}{\left(1 + \dfrac{L_{f,1}}{\alpha L_{f,2}}\right)^2} \tag{43b}$$

which gives

$$\frac{L_{f,1}}{\alpha L_{f,2}} \leqslant \sqrt{2} - 1 \tag{43c}$$

which is the condition mentioned above ($L_{f,1}/\alpha L_{f,2} < 0.4$). When condition 43c is not satisfied, eqn. 28 or 40 should be used instead of eqn. 19 for the optimization.

Optimization with a simple plate-height equation: tag-along effect dominant

In this case, the optimum sample size is not given by eqn. 19 but by eqn. 40. The tag-along effect dominates, so the second component band is spread over a wide range of retention times. In the ideal model approximation it exhibits a plateau whose width depends on the loading factor (see eqn. 27). The second component individual elution profile is different from the profile observed for the same amount of pure second component. Especially noteworthy is the fact that, in contrast to what happens in the previous instance, the optimum conditions depend on the feed composition.

Calculations were performed using our approach (eqns. 8, 29, 31, 39 and 40) and that of Knox and Pyper[6] for binary mixtures of different compositions and the same relative retention, $\alpha = 1.20$. The results are reported in Table II. As in the previous instance, the differences between the optimum values of the limiting column efficiency, the ratio d_p^2/L and the mobile phase flow velocity are relatively small. Compared with the optimum values predicted by Knox and Pyper, the optimum values of the column

TABLE II

OPTIMUM VALUE OF d_p^2/L AND MAXIMUM PRODUCTION RATE UNDER TOUCHING BAND CONDITIONS

Second case: $\dfrac{q_{s,2}C_{0,1}}{\alpha q_{s,1}C_{0,2}} = \dfrac{L_{f,1}}{\alpha L_{f,2}} > 0.4^a$. $h = Cv$.

Feed composition	N_0	$d_p^2/L \times 10^8$ *(cm)*	u *(cm/s)*	$L_{f,2}$ *(%)*	$Pr_2/(1-\varepsilon)S$ *[μmol/(cm² s)]*	$Pr_2{}^a/Pr_2{}^b$
1:1[a]	2100	4.9	0.98	0.98	13.2	2.17
3:1[a]	2000	5.0	1.0	0.49	6.8	1.12
9:1[a]	2470	4.5	0.9	0.189	2.36	0.39
For comparison:						
Conditions in ref. 6[b]	2260	4.7	0.94	0.46	6.08	n.a.
This work, with $L_{f,1}/\alpha L_{f,2} < 0.4$[a]	3100	4.0	0.8	1.37	15.2	2.50
Knox and Pyper column with:	2260	4.7	0.94			$Pr_2{}^a/Pr_2{}^c$
$L_{f,1}/\alpha L_{f,2} < 0.4$[c]				1.14	14.8	1.03
1:1[c]				1.0	13.2	1.0
3:1[c]				0.51	6.76	1.00
9:1[c]				0.18	2.36	1.00

[a] Values calculated with the Langmuir competitive adsorption model, using the simplified simple HETP equation $h = Cv$. Same conditions as for Table I, except $\alpha = 1.20$.

[b] Values calculated using the non-competitive model and the simplified HETP equation and assuming right triangular band profiles. The same results are obtained, regardless of the mixture composition.

[c] Values calculated for a column designed with the approach suggested by Knox and Pyper[6] ($d_p^2/L = 4.7$) and using the same velocity ($u = 0.94$) but the much larger sample size predicted by the competitive model.

efficiency range between −10 and +40%, those of the ratio d_p^2/L between −15 and +7% and those of the mobile phase velocity between −15 and +7%. On the other hand, the loading factor required to achieve touching bands decreases rapidly with decreasing concentration of the second component. The sample sizes and production rates predicted by the two methods are nearly equal for a 3:1 mixture. For mixtures richer in the second component, the sample size and the production rate are higher than those predicted by the Knox and Pyper model, because of the displacement effect, whereas for mixtures richer in the first component, the production rate is lower, because of the tag-along effect.

The optimization of the column efficiency, of its conformation and of the mobile phase velocity are not very critical and nearly identical results are obtained with the columns which have either the optimum characteristics calculated in this work or those calculated after Knox and Pyper, provided that they are both operated with the optimum sample size as calculated in this work. This is illustrated by the comparison between the data at the top and bottom of Table II.

Optimization with the Knox plate-height equation

Numerical calculations were carried out using the Knox plate-height equation with conventional values of the coefficients, $A = 1$, $B = 2$ and $C = 0.1$, which corresponds to an average quality packing material packed properly into a chromatographic column (minimum reduced plate height 2.40; optimum analytical reduced velocity 2.7). The optimization procedure is as follows. Values of the column length and particle size are selected and the mobile phase velocity is calculated (eqn. 29). The

TABLE III

OPTIMUM VALUE OF COLUMN LENGTH AND MAXIMUM PRODUCTION RATE UNDER TOUCHING BAND CONDITIONS

First case: $\frac{q_{s,2}C_{0,1}}{\alpha q_{s,1}C_{0,2}} = \frac{L_{f,1}}{\alpha L_{f,2}} < 0.4$. $h = 2/\nu + \nu^{0.33} + 0.1\nu$.

α	N_0	L (cm)	ν	$L_{f,2}$ (%)	$Pr_2/(1-\varepsilon)S$ [μmol/(cm² s)]	$Pr_2{}^a/Pr_2{}^b$
1.1[a]	8880	59.	34	0.375	1.93	
1.1[b]	6850	50.5	39.5	0.129	0.775	2.49
1.2[a]	2750	29.6	67.5	1.28	12.0	
1.2[b]	2050	25.2	79.0	0.443	4.88	2.46
1.3[a]	1480	20.9	96	2.51	30.8	
1.3[b]	1070	17.4	115	0.85	12.6	2.44
1.5[a]	700	13.8	145	51.8	83.5	
1.5[b]	500	11.5	174	1.79	34.6	2.41
1.7[a]	450	10.9	183	7.84	141.1	
1.7[b]	320	9.0	222	2.72	59.4	2.38

[a] Values calculated using the Langmuir competitive adsorption model and the general Knox HETP equation. Same parameters as for Table I except particle size $d_p = 10$ μm. The cycle time is $t_c = t_{R0.2} - t_0$.

[b] Values calculated using the non-competitive model, assuming that the band profiles are right triangles and using the general Knox HETP equation.

TABLE IV

OPTIMUM VALUE OF THE COLUMN LENGTH AND MAXIMUM PRODUCTION RATE UNDER TOUCHING BAND CONDITIONS

Second case: $\frac{q_{s,2}C_{0,1}}{\alpha q_{s,1}C_{0,2}} = \frac{L_{f,1}}{\alpha L_{f,2}} > 0.4$. $h = 2/\nu + \nu^{0.33} + 0.1\nu$.

Feed composition	N_0	L *(cm)*	ν	$L_{f,2}$ *(%)*	$Pr_2/(1-\varepsilon)S$ *[μmol/(cm² s)]*
1:1[a]	1920	24.2	82.5	0.94	10.7
3:1[a]	1810	23.4	77.0	0.46	5.5
9:1[a]	2180	26.0	85.5	0.18	1.9
For comparison:					
$L_{f,1}/\alpha L^*_{f2} < 0.4$ (this work)	2750	29.6	67.5	1.28	12.0
Knox[b]	2060	25.2	79.0	0.44	4.9

[a] Values calculated with the Langmuir competitive adsorption model, using the general Knox HETP equation ($h = 2/\nu + \nu^{0.33} + 0.1\nu$). Same conditions as for Table II, except particle size $d_p = 10\,\mu$m.

[b] Values calculated with the non-competitive model, assuming right triangle band profiles and using the general Knox HETP equation. The values are constant, regardless of the feed composition.

reduced plate height is then derived (eqn. 41) and the plate number introduced in eqn. 19 or in eqn. 28, depending on whether $L_{f,1}/\alpha L_{f,2}$ is smaller or larger than 0.4. This gives the sample size. Inserting the sample size and the velocity in eqn. 8 gives the production rate. The calculation is repeated for successive values of the column length at constant particle size to determine the optimum column length giving the maximum production rate. Alternately, the particle size could be varied at constant column length or the calculation could be made for the columns currently available in the laboratory to find which will give the highest production rate. Although this procedure of optimization is generally not correct, it gives a result which is satisfactory in practice, because particles are available in only a small number of sizes and the variation of the production rate near its optimum is fairly flat. The same procedure is followed for the calculation of the optimum conditions within the frame of the Knox and Pyper model, but eqn. 22 is used to calculate the sample size.

Tables III and IV summarize the data obtained. Optimum values of the limiting column efficiency, the column length, the reduced flow velocity and the loading factors are given in Table III for different values of the relative retention between 1.10 and 1.70 for binary mixtures having a composition such that $L_{f,1}/(\alpha L_{f,2})$ is smaller than 0.40. We have assumed the particle size to be 10 μm. Also given in Table III is the maximum production rate. Comparison between the exact values and those derived from the Knox and Pyper model again shows fairly small differences between the optimum values of the limiting column efficiency (30–40%), the column length (10–20%) and the reduced velocity (15–20%). The loading factor, on the other hand, is 2.5–3 times larger than that predicted by the Knox and Pyper model and the production rate is about 2.20 times higher. As expected, comparison between the results in Tables I and III shows general agreement for the optimum limiting column efficiency and loading factor and for the maximum production rate at high values of α when the mobile phase velocity is very high. The difference increases, however, with decreasing values of α and

TABLE V

OPTIMUM VALUE OF d_p^2/L AND MAXIMUM VALUE OF THE PRODUCTION RATE UNDER OVERLAPPING BAND CONDITIONS[a] FOR DIFFERENT FEED COMPOSITIONS

Feed composition	N_0	d_p^2/L $\times 10^8$ *(cm)*	u *(cm/s)*	$L_{f,2}$[b] *(%)*	$Pr_2/(1-\varepsilon)S$ *[μmol/(cm² s)]*
1:9	380	11.5	2.3	4.8	91.6
1:3	490	10.1	2.0	3.05	52.0
1:1	630	8.9	1.8	1.822	26.6
3:1	910	7.4	1.5	0.875	10.2
9:1	1200	6.5	1.3	0.343	3.1
Knox[c]	2260	4.7	0.94	0.46	6.1

[a] Values calculated with the competitive model and the simple HETP equation $h = Cv$, with $C = 0.1$. Same conditions as for Table II except required product purity, 99%. $\alpha = 1.2$; $q_{s,2} = q_{s,1} = 10$. In all instances the recovery yield is about 60%.

[b] Values calculated from the equation $L_{f,2} = \dfrac{1}{(1 + b_1 r_1/b_2)}\left(\dfrac{1 - 1/\alpha}{1 - x}\right)^2$, where $x = \left(\dfrac{1 - Pu_2}{Pu_2 \alpha r_1}\right)^{1/2}$, Pu_2 being the required purity of the product. This equation is derived in ref. 7.

[c] Values calculated with the non-competitive model, assuming right triangle band profiles and a simple HETP equation[6]. The results are the same, regardless of the feed composition.

for $\alpha = 1.10$, the production rate predicted is 40% less with the correct plate-height equation (eqn. 41) than with the simplified eqn. 30. A significant difference between the results obtained with the two plate height equations is expected in this case: α is low, a relatively high efficiency is needed, leading to a moderate reduced velocity (Table III). Obviously, the difference between eqns. 30 and 41 is larger at low flow velocities.

Table IV reports similar data calculated for binary mixtures of different compositions, such that $L_{f,1}/(\alpha L_{f,2})$ is larger than 0.4, for different compositions and $\alpha = 1.20$. As with the simplified plate-height equation, the production rate predicted by the Knox and Pyper model is lower than that given by the more exact approach when the relative concentration of the second component exceeds about 0.25 and is too large when the relative concentration of the second component is smaller than 0.25. The production rates are about 20% lower than those calculated with the simplified plate-height equation and reported in Table II, because of the influence of the two neglected terms of the plate-height equation.

Comparison with previous results

Depending on the required degree of purity of the prepared products and the desired recovery yield, there are two extreme strategies and a variety of possible compromises between them[25]. The first strategy is to achieve a total recovery yield (*ca.* 100%). In this instance the touching band approach as discussed in this paper must be used. The second strategy consists into looking for the maximum possible production rate without concern for the value of the recovery yield. We have previously discussed this strategy which can give recovery yields as low as 60%[8,12]. For example, data have been calculated and are reported in Table V illustrating the advantages and inconveniences of this strategy. A purity of 99% of the product was required and no condition was placed on the recovery yield.

TABLE VI

OPTIMUM VALUE OF d_p^2/L AND MAXIMUM PRODUCTION RATE UNDER OVERLAPPING BAND CONDITIONS[a] FOR DIFFERENT VALUES OF α

α	N_0	d_p^2/L $\times 10^8$ (cm)	u (cm/s)	$L_{f,2}$ (%)[b]	$Pr_2/(1-\varepsilon)S$ [μmol/(cm^2 s)]
1.1	1150	6.6	1.3	1.47	17.9
1.2	380	11.5	2.3	4.80	91.6
1.3	240	14.4	2.9	9.0	205.2
1.5	145	18.5	3.7	18.0	461.2
1.7	105	21.8	4.4	26.6	679.2

[a] Values calculated with the competitive model, using the simple HETP equation $h = Cv$, with $C = 0.1$. Same conditions as for Table I, except required product purity, 99%, relative feed composition, 1:9, $q_{s,2} = q_{s,1} = 10$. In all instances the recovery yield is about 60%.

[b] Values calculated from the equation $L_{f,2} = \dfrac{1}{(1 + b_1 r_1/b_2)}\left(\dfrac{1 - 1/\alpha}{1 - x}\right)^2$, where $x = \left(\dfrac{1 - Pu_2}{Pu_2 \alpha r_1}\right)^{1/2}$

Comparison between the results in Tables II and V shows that when the relative concentration of the first component is small, the production rate is much greater when the overlapping-band approach is used, the column is overloaded and the individual elution bands exhibit a degree of overlap than when the touching band strategy is used. As shown in Table V, for a 1:9 mixture the production rate is six times larger with overlapping bands than with touching bands (and fifteen times larger than that predicted by the model of Knox and Pyper[6]). The ratio of the production rate with overlapping bands to the production rate with touching bands decreases with decreasing relative concentration of the second component. It is still three times for a 1:3 mixture, two times for a 1:1 mixture, 1.5 times for a 3:1 mixture and only 1.3 times for a 9:1 mixture. In all instances the yield is *ca.* 60%.

The comparative advantage of using the first or the second strategy depends very much on the composition of the feed. If the second compound is in large excess, the

TABLE VII

OPTIMUM VALUE OF THE COLUMN LENGTH AND MAXIMUM PRODUCTION RATE UNDER OVERLAPPING BAND CONDITIONS[a] FOR DIFFERENT VALUES OF α

α	N_0	L (cm)	v	$L_{f,2}$ (%)[b]	$Pr_2/(1-\varepsilon)S$ [μmol/(cm^2 s)]
1.1	1000	16	120	1.47	15.0
1.2	360	9.6	210	4.80	81
1.3	220	7.3	275	9.0	186
1.5	130	5.6	357	18.0	425
1.7	95	4.7	425	26.6	630

[a] Values calculated with the competitive model, using the Knox general HETP equation, $h = 2/v + v^{0.33} + 0.1v$, and the same conditions as for Table VI, except the particle size, $d_p = 10$ μm. In all instances the recovery yield is about 60%.

[b] Values calculated from the equation $L_{f,2} = \dfrac{1}{(1 + b_1 r_1/b_2)}\left(\dfrac{1 - 1/\alpha}{1 - x}\right)^2$, where $x = \left(\dfrac{1 - Pu_2}{Pu_2 \alpha r_1}\right)^{1/2}$

overlapping band approach permits, compared with the touching band approach, a much higher production rate, for which the penalty is a decrease in yield. This advantage, however, decreases rapidly with increasing relative concentration of the first compound. Then it is reasonable to adopt an intermediate approach, where the degree of band overlapping accepted decreases with decreasing concentration of the second component, with a parallel increase in the recovery yield.

Finally, Tables VI and VII give the optimal experimental conditions in the case of overlapping band[8] for a series of 1/9 mixtures with different values of the selectivity, α, using either the simple plate height equation (eqn. 30) or the more general Knox plate height equation (eqn. 41), respectively. Comparison of these two sets of data with the data in Tables I and III show that when the ratio of the component concentrations in the feed, $C_{0,1}/C_{0,2}$, is small, the overlapping-band strategy has the following advantages over the touching-band strategy: a lower optimum column efficiency, a larger optimum ratio d_p^2/L, a larger optimum reduced velocity, and a higher production rate of the second component. The production rate increases rapidly with increasing value of the selectivity, nearly in proportion to $\left(\frac{\alpha - 1}{\alpha}\right)^3$, in both the touching-band case (Table III) and the overlapping-band case (Table VI).

CONCLUSION

As our previous discussion of the overlapping band strategy has shown, the maximum production rate with the touching band strategy increases indefinitely with increasing permissible column pressure drop, provided that the column of optimum geometry is used. For a given column, in contrast, there is an optimum pressure drop as there is an optimum flow velocity. The maximum production rate is usually achieved at very high values of the reduced flow velocity, much in excess of that which corresponds to the maximum column efficiency[8,12]. We note, however, that the optimum velocity is lower for touching bands than for overlapping bands.

For values of the ratio $L_{f,1}/(\alpha L_{f,2})$ less than 0.4, the optimum sample size is independent of the feed composition and the sample size should be such that $L_{f,2} = 0.5[(\alpha - 1)/\alpha]^2$, *i.e.*, approximately three times larger than that predicted by the simple model of Knox and Pyper[6], which neglects the interaction between the two components of the mixture during the separation. In this instance, the analytical resolution under the conditions selected for the separation should be 2, larger than the value of 1.7 suggested by Knox and Pyper. For values of the ratio $L_{f,1}/(\alpha L_{f,2})$ between 0.4 and 3, the sample size depends markedly on the feed composition but is still larger than the value predicted by the Knox and Pyper model. Finally, for values of $L_{f,1}/(\alpha L_{f,2})$ larger than 3, the sample size should be less than that predicted by Knox and Pyper. It depends strongly on the composition of the mixture and decreases rapidly with increasing concentration of the first component. In preparative chromatography a system eluting the main component first and the impurities later should be avoided as much as possible.

The use of the overlapping strategy entails a recovery yield of the order of 60% but permits a considerable increase in production rate for both components when the displacement effect predominates, a result which has already been observed experimentally and is well documented[4,19,20]. The gain in production rate decreases rapidly

with decreasing concentration of the second component in a binary mixture. The overlapping band strategy has no special advantage for the production rate of the second component when this compound is the minor one.

The quantitative accuracy of the present results depends on the extent to which the equilibrium isotherms of the components of the mixture are approximated by the competitive Langmuir model. On the other hand, the accuracy of our results is considerably better than those given by models, computerized or not, which do not take the competitive interactions of the mixture components into account properly[9]. As shown above, the production rate predicted by these models can be three times too low or too high, depending on the composition of the feed.

SYMBOLS

A	Coefficient in the Knox plate-height equation
a_i	Numerical coefficient in the competitive Langmuir isotherm
B	Coefficient in the Knox plate-height equation
b_i	Numerical coefficient in the competitive Langmuir isotherm
C	Coefficient of mass-transfer resistance in the plate-height equation
C_i	Mobile phase concentration of component i
C_{Max}	Maximum concentration of a compound in the eluent
$C_{0,i}$	Concentration of component i in the feed
C_2	Concentration of the second component during its elution. In eqn. 26, concentration of the second component in the last zone, where it is pure
C_2^{B}	Concentration of the elution plateau of the second component
D_m	Molecular diffusion coefficient of the mixture components
d_p	Average particle size of the packing material used
H_{kin}	HETP of the elution profile of a Dirac pulse under linear conditions
H_{th}	HETP of the elution profile of a Dirac pulse predicted by the ideal model under non-linear conditions
H_{tot}	HETP of the elution profile of a Dirac pulse under non-linear conditions
h	Reduced plate height ($h = H/d_p$)
k_0	Column specific permeability (of the order of $1 \cdot 10^{-3}$)
$k'_{0,i}$	Column retention factor or capacity factor of component i under linear conditions; $k'_{0,i} = (t_{R0,i} - t_0)/t_0$
L	Column length
$L_{f,i}$	Loading factor for component i
$L_{f,2,p}$	Loading factor for the second component corresponding to the elution of a band profile for which the tag-along effect has just disappeared
N_0	Column plate number under linear conditions (in practice, for a very small size sample)
opt	The subscript opt represents the optimum value of a parameter
ΔP	Pressure drop between the column inlet and outlet
Pr_i	Production rate of component i
q_i	Amount of compound i adsorbed at equilibrium with the mobile phase
$q_{s,i}$	Specific column saturation capacity for component i; $q_{s,i} = a_i/b_i$
r_1	Positive root of the characteristic equation of the problem (ref. 8, eqn. II-3). In practice, $r_1 \approx C_{0,1}/C_{0,2}$

S	Geometrical column cross-sectional area
T	Total feed throughput
$t_{B'}$	Elution time of the end of the plateau of the second component
t_c	Cycle time
$t_{e,1}$	Elution time of the rear of the first component band
t_0	Hold-up time of the column
t_p	Width of the injection pulse
$t_{R,i}$	Retention time of the front of component i
$t_{R0,i}$	Limiting retention time of component i at infinite dilution
u	Mobile phase linear velocity
w_{kin}	Baseline band width of the elution profile of a Dirac pulse under linear conditions
w_{plateau}	Width of the elution plateau of the second component; $w_{\text{plateau}} = t_{R,2} - t_{B'}$
w_{th}	Baseline band width of the elution profile of a Dirac pulse predicted by the ideal model under non-linear conditions
w_{tot}	Total baseline band width of the elution profile of a Dirac pulse under non-linear conditions
X	Dummy parameter in eqns. 28 and 39–40
α	Relative retention of the two compounds ($\alpha = a_2/a_1$)
ε	Packing porosity
η	Mobile phase viscosity
ν	Reduced velocity ($\nu = ud_p/D_m$)
σ^2_{kin}	Variance contribution of the mass-transfer kinetics and the axial dispersion
σ^2_{th}	Variance contribution due to the non-linear behavior of the isotherm (thermodynamics)
σ^2_{tot}	Variance of the elution profile

ACKNOWLEDGEMENTS

This work was supported in part by Grant CHE-8901382 of the National Science Foundation and by the cooperative agreement between the University of Tennessee and the Oak Ridge National Laboratory. We acknowledge support of our computational efforts by the University of Tennessee Computing Center.

REFERENCES

1 G. Guiochon and L. R. Snyder (Editors), *Preparative Chromatography, including the Proceedings of the 6th Symposium on Preparative Chromatography, Washington, DC, May 1989; J. Chromatogr.*, 484 (1989).
2 P. Gareil, C. Durieux and R. Rosset, *Sep. Sci. Technol.*, 18 (1983) 441.
3 L. R. Snyder, G. B. Cox and P. E. Antle, *Chromatographia*, 24 (1987) 82.
4 J. Newburger and G. Guiochon, *J. Chromatogr.*, 484 (1989) 153.
5 J. A. Perry and T. J. Szczerba, *J. Chromatogr.*, 484 (1989) 267.
6 J. H. Knox and M. Pyper, *J. Chromatogr.*, 363 (1986) 1.
7 S. Golshan-Shirazi and G. Guiochon, *Anal. Chem.*, 61 (1989) 1276.
8 S. Golshan-Shirazi and G. Guiochon, *Anal. Chem.*, 61 (1989) 1368.
9 L. R. Snyder, J. W. Dolan, D. C. Lommen and G. B. Cox, *J. Chromatogr.*, 484 (1989) 425.

10 S. Golshan-Shirazi and G. Guiochon, *Am. Biotechnol. Lab.*, 8(8) 1990) 26.
11 G. Guiochon and A. M. Katti, *Chromatographia*, 24 (1987) 165.
12 S. Ghodbane and G. Guiochon, *Chromatographia*, 26 (1989) 53.
13 L. R. Snyder and G. B. Cox, *J. Chromatogr.*, 483 (1989) 85.
14 S. Golshan-Shirazi and G. Guiochon, *J. Phys. Chem.*, 93 (1989) 4143.
15 Z. Ma, A. M. Katti and G. Guiochon, *J. Phys. Chem.*, in press.
16 S. Jacobson, S. Golshan-Shirazi and G. Guiochon, *J. Am. Chem. Soc.*, in press.
17 S. Golshan-Shirazi and G. Guiochon, *J. Phys. Chem.*, 94 (1990) 495.
18 S. Golshan-Shirazi and G. Guiochon, *J. Chromatogr.*, 506 (1990) 495.
19 J. Newburger, L. Liebes, H. Colin and G. Guiochon, *Sep. Sci. Technol.*, 22 (1987) 1933.
20 J. Newburger and G. Guiochon, *J. Chromatogr.*, in press.
21 P. C. Haarhoff and H. J. Van der Linde, *Anal. Chem.*, 38 (1966) 573.
22 H. Poppe and J. Kraak, *J. Chromatogr.*, 255 (1983) 395.
23 S. Golshan-Shirazi and G. Guiochon, *Anal. Chem.*, 60 (1988) 2364.
24 J. H. Knox, *J. Chromatogr. Sci.*, 15 (1977) 352.
25 S. Golshan-Shirazi and G. Guiochon, *J. Chromatogr.*, in press.

Journal of Chromatography, 517 (1990) 257–262
Elsevier Science Publishers B.V., Amsterdam

CHROMSYMP. 1958

Evaluation of the stability of polymer-coated silica-based packing materials for high-performance liquid chromatography

TOYOHIDE TAKEUCHI*
Research Centre for Resource and Energy Conservation, Nagoya University, Chikusa-ku, Nagoya 464 (Japan)
and
WENZHI HU, HIROKI HARAGUCHI and DAIDO ISHII
Department of Applied Chemistry, School of Engineering, Nagoya University, Chikusa-ku, Nagoya 464 (Japan)

ABSTRACT

The stability of polymer-coated silica-based packing materials for high-performance liquid chromatography was examined. Linear relationships between the pH of the eluent and the logarithm of the concentration of silicic acid dissolved in the effluent, log C_{SIL}, were observed, and the slope of the lines was dependent on the surface properties of the packing materials. A lower solubility was observed for polymer-coated silica and glass beads in comparison with common porous bare silica beads. A linear relationship between the specific surface area and log C_{SIL} was observed for porous silica beads, and the plots for polymer-coated silica and glass beads deviated from linearity.

INTRODUCTION

Silica-based packing materials are widely used in high-performance liquid chromatography (HPLC) because of the high column efficiencies and wide applicability. However, silica-based packing materials are unstable in aqueous mobile phases, especially at high pH[1,2]. This drawback is overcome by employing polymer-based materials[3,4] or coating the silica gel surface with a layer of polymer[5–9], and such stationary phases are now commercially available. Another strategy for improving the stability of silica-based materials is to use an eluent saturated with silica. Other parameters affecting the stability involve flow-rate, temperature, eluent modifier, etc.[1,2].

This paper compares the stability of polymer-coated silica-based materials with that of common silica-based materials and glass beads under various operating conditions.

0021-9673/90/$03.50

EXPERIMENTAL

Reagents

All of the reagents were of analytical-reagent grade from Wako (Osaka, Japan), unless indicated otherwise. Purified water was prepared by using a Milli-Q system (Nihon Millipore Kogyo, Tokyo, Japan). Molybdic acid and the reducing reagent solution for the detection of silicic acid were prepared as described previously[10]. The molybdic acid solution was prepared by mixing 8 ml of 10% (w/v) ammonium molybdate and 4 ml of 6 *M* hydrochloric acid, followed by dilution to 100 ml with purified water. The reducing reagent solution was prepared by mixing 8 ml of 10% (w/v) oxalic acid and 11 ml of 0.25% (w/v) 1-amino-2-naphthol-4-sulphonic acid (ANSA) solution, followed by dilution to 100 ml with purified water. The ANSA solution was prepared according to the proposed method[11] as follows: 0.5 g of 1-amino-2-naphthol-4-sulphonic acid and 2 g of sodium sulphite were dissolved in *ca.* 50 ml of purified water, mixed with 20 g of sodium sulphite dissolved in *ca.* 120 ml of purified water and diluted to 200 ml with purified water.

Silicon standard solution for atomic absorption spectrometry was obtained from Wako. Acetic acid and sodium acetate were used to adjust the pH of the eluent.

Equipment

A diagram of the detection system is shown in Fig. 1. The prepared molybdic acid and reducing reagent solutions were supplied via D and E, respectively. These reagents and the sample were supplied at 60 μl/min by using a single Minipuls 2 peristaltic pump (Gilson, Villiers le Bel, France). The sample solution was mixed with the molybdic acid solution to form yellow molybdosilicic acid during passage through the 8 m × 0.5 mm I.D. PTFE reaction tube (5 in Fig. 1) at room temperature. The yellow molybdosilicic acid was then converted into the blue molybdosilicate complex by reaction with the reducing reagent in the 5 m × 0.5 mm I.D. PTFE tube, followed by detection at 815 nm with a UVIDEC-100 III UV–visible spectrophotometer (JASCO, Tokyo, Japan). This system allows the detection of ionic monosilicate (or silicic acid).

The packing materials employed were Develosil (Nomura Chemical, Seto, Japan), Capcell C1 SG120 (Shiseido, Tokyo, Japan), non-porous glass beads

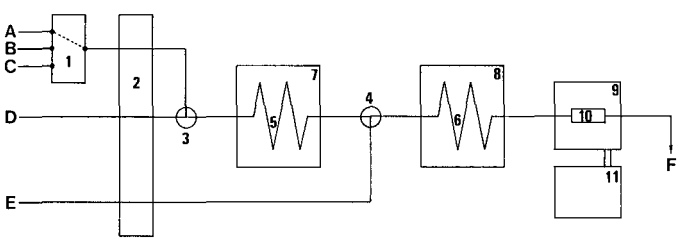

Fig. 1. Diagram of the apparatus. Equipment: 1 = sample exchange valve; 2 = peristaltic pump; 3, 4 = mixing joints; 5 = reaction tube for formation of molybdosilicic acid; 6 = reaction tube for formation of molybdenum blue; 7, 8 = aluminum block bath; 9 = spectrophotometer; 10 = flow cell (8 μl); 11 = recorder. Reagents: A = sample; B = blank; C = standard; D = molybdic acid solution; E = reducing reagent solution; F = waste.

(Whatman, Clifton, NJ, U.S.A.) and porous glass beads PSG-10μ (Fuji-Davison Chemical, Kasugai, Japan). Develosil and Capcell C1 SG120 are bare silica and polymer-coated silica beads, respectively. Develosil LOP ODS (Nomura Chemical) and Capcell C18 SG120 (Shiseido) were examined as examples of octadecyl-bonded silica gel. The base material of the latter is Capcell C1 SG120.

Table I lists the packing materials examined and their dimensional data as given by the manufacturers. The materials were packed into 50 mm × 4.6 mm I.D. columns by a dry packing method. The eluent was supplied at 0.5 ml/min by using an LC-6AD HPLC pump (Shimadzu, Kyoto, Japan), unless indicated otherwise. The effluent was sucked via A in Fig. 1.

RESULTS AND DISCUSSION

The detection system was evaluated by using the standard silicon solution and a calibration graph was prepared from steady-state signals. The steady-state signals were proportional to the concentration of silicon up to 1 ppm. The limit of detection was 1.6 ppb (10^9) at a signal-to-noise ratio of 3, and the relative standard deviation of the signal intensity was 1.0% for ten measurements of 10 ppb silicon. When the concentration of silicic acid in the effluent exceeded 1 ppm, the solution was appropriately diluted with purified water.

Fig. 2 demonstrates linear relationships between the pH of the eluent and the logarithm of the concentration of silicic acid in the effluent (log C_{SIL}) for bare silica gel, polymer-coated silica gel and glass beads. The concentration is expressed as ppm by weight of silicon (or μg/ml). The pH was adjusted with acetic acid and sodium acetate. As the dissolution behaviours of the packing materials were independent of the concentration of acetate in the eluent between 20 and 100 mM, 60 mM was adopted as the concentration of acetate throughout this work. For a series of porous bare silica beads, the slopes of the straight lines were nearly the same, and a material with a larger

TABLE I

PACKING MATERIALS EMPLOYED

Packing material	*Type*	*Particle diameter (μm)*	*Pore size (Å)*	*Specific surface area (m^2/g)*
Develosil 30-5	Silica	5	30	704
Develosil 60-5	Silica	5	60	437
Develosil 100-5	Silica	5	100	324
Develosil 300-5	Silica	5	300	152
Develosil NP silica-5	Silica	4.5	NP[a]	0.6
Capcell C1 SG120	Silica	5	120	200
PSG-10μ	Glass beads	11.5	178	157
Glass beads (Whatman)	Glass beads	40	NP	–
Develosil LOP 60	Silica	30	60	500
Develosil LOP ODS	ODS	30	100	150
Capcell C18 SG120	ODS	5	120	140

[a] NP = non-porous.

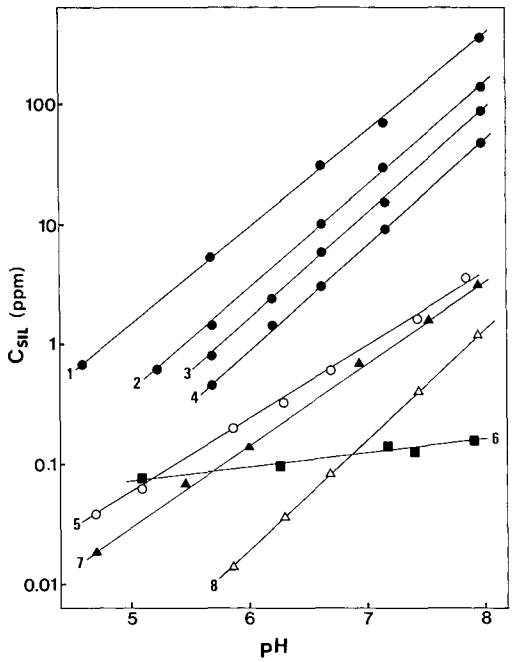

Fig. 2. Relationships between pH of the eluent and the logarithm of the concentration of silicic acid in the effluent (log C_{SIL}). Column, 50 × 4.6 mm I.D.; eluent, 60 m*M* acetate; flow-rate, 0.5 ml/min; column temperature, 20°C. Packing materials: 1 = Develosil 30-5; 2 = Develosil 60-5; 3 = Develosil 100-5; 4 = Develosil 300-5; 5 = Develosil NP silica-5; 6 = Capcell C1 SG120; 7 = PSG-10μ; 8 = non-porous glass beads (Whatman).

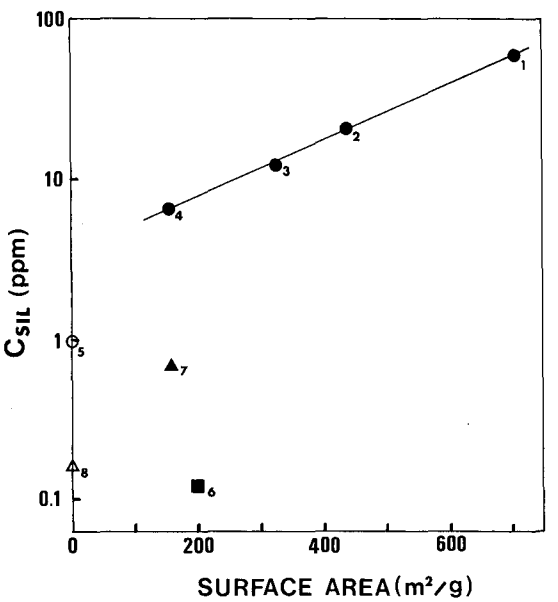

Fig. 3. Plots of log C_{SIL} as a function of specific surface area. Column, 50 × 4.6 mm I.D.; packing materials, as in Fig. 2; pH, 7.0; flow-rate, 0.5 ml/min; column temperature, 20°C.

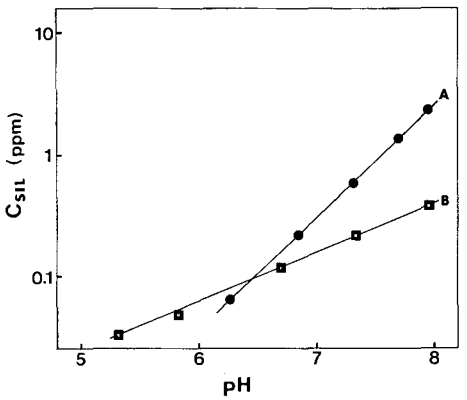

Fig. 4. Relationships between pH of the eluent and log C_{SIL} for ODS columns. Columns, 50 × 4.6 mm I.D.; (A) Develosil LOP ODS and (B) Capcell C18 SG120; eluent, 60 m*M* acetate; flow-rate, 0.5 ml/min; column temperature, 20°C.

specific surface area gave a larger log C_{SIL} value. A smaller dependence of the pH on log C_{SIL} was observed for the polymer-coated silica gel in comparison with other materials. The log C_{SIL} values for the polymer-coated silica gel were much lower than those of porous bare silica beads, especially at higher pH. Bleeding at a concentration of 10 ppm corresponds to the dissolution of 6.4 mg of silica gel for a 10-h operation.

Fig. 3 shows plots of log C_{SIL} *versus* specific surface area when the pH of the eluent was fixed at 7. The plots lie on a straight line for a series of porous silica beads. The plots for glass beads, polymer-coated silica gel and non-porous silica gel deviate from linearity. The largest deviation was observed for the polymer-coated silica gel, which may be the result of protection of the surface with a poly(dimethylsiloxane) film.

Column temperature, eluent flow-rate and eluent composition affected the dissolution behaviour. These effects were similar to those reported in the literature[1,2].

Fig. 4 illustrates linear relationships between log C_{SIL} and the pH of the eluent for ODS materials. The results shown in Figs. 2 and 4 indicate that the concentration of dissolved silicic acid is substantially decreased for Develosil LOP ODS in comparison with its original silica gel, whereas a large difference in the log C_{SIL} value is not observed between Capcell C18 SG120 and its base material, Capcell C1 SG120. The surfaces of Capcell C18 SG120 are coated with a poly(dimethylsiloxane) film, whereas Develosil LOP ODS is prepared from bare silica gel. The signal was enhanced when the effluents were treated with sodium hydrogencarbonate at elevated temperature. Such a treatment is recommended to allow the detection of soluble and/or colloidal species[11]. In addition, the signals for silica gel columns were not changed by the above treatment.

REFERENCES

1 A. Wehrli, J. C. Hildenbrand, H. P. Keller, R. Stampfli and R. W. Frei, *J. Chromatogr.*, 149 (1978) 199.
2 J. C. Atwood, G. J. Schmidt and W. Slavin, *J. Chromatogr.*, 171 (1979) 109.
3 H. W. Stuurman, J. Koehler, S. O. Jansson and A. Litzen, *Chromatographia*, 23 (1987) 341.
4 J. V. Dawkins, L. L. Lloyd and F. P. Warner, *J. Chromatogr.*, 352 (1986) 157.
5 G. Shomburg, A. Deege, J. Koehler and U. Bien-Vogelsang, *J. Chromatogr.*, 282 (1983) 27.

6 G. Shomburg, J. Koehler, H. Figge, A. Deege and U. Bien-Vogelsang, *Chromatographia*, 18 (1984) 265.
7 H. Figge, A. Deege, J. Koehler and G. Shomburg, *J. Chromatogr.*, 351 (1986) 393.
8 M. N. Schmuck, M. P. Nowlan and K. M. Gooding, *J. Chromatogr.*, 371 (1986) 55.
9 Y. Ohtsu, H. Fukui, T. Kanda, K. Nakamura, M. Nakano, O. Nakata and Y. Fujiyama, *Chromatographia*, 24 (1987) 380.
10 M. Goto, W. Hu and D. Ishii, *Bunseki Kagaku*, 38 (1989) 419.
11 Japanese Industrial Standards Committee, *Testing Methods for Industrial Water JIS K 0101-1986*, Japanese Standards Association, Tokyo, 1986, p. 172.

Journal of Chromatography, 517 (1990) 263–268
Elsevier Science Publishers B.V., Amsterdam

CHROMSYMP. 1925

Magnetic resonance imaging in reversed-phase liquid chromatography

MARTIN ILG, JÜRGEN MAIER-ROSENKRANZ, WINFRIED MÜLLER and ERNST BAYER*
Institut für Organische Chemie der Universität, Auf der Morgenstelle 18, D-7400 Tübingen (F.R.G.)

ABSTRACT

The observation of band profiles on preparative columns in liquid chromatography was hitherto not possible in real time. With the help of nuclear magnetic resonance imaging it has been possible to reveal band profiles of a reversed-phase chromatographic system completely non-invasively. The wall effect, which has been theoretically predicted, was confirmed in these proton images for the first time. Additionally, thermal effects could be revealed directly on the column. This technique is expected to have great potential for future investigations in chromatography.

INTRODUCTION

Within the last decade, nuclear magnetic resonance imaging (MRI) has become a powerful tool in medical diagnosis[1]. This imaging technique is based on the same physical properties as nuclear magnetic resonance spectroscopy, and with the help of magnetic field gradients yields an image of any desired volume element in an object[2]. At present, it is mainly limited to the visualization of protons in gel-like states. Whereas the application of MRI in the medical field has experienced rapid development, its application to non-medical problems has been less extensive and has centred largely on materials science investigations[3].

MRI, however, also offers a means of investigating elution profiles and interactions in liquid chromatography, all in real time and completely non-invasively. This is of special interest with preparative columns, where even coloured substances provide information only about the zone boundaries and afford no insight into the profile within the column. In a recent publication, we demonstrated the feasibility of using MRI for the investigation of size-exclusion and ion-exchange chromatography[4]. This paper deals with the observation of elution profiles in reversed-phase liquid chromatography (RPLC) with the help of fast proton MRI. RPLC is based on the specific and non-specific interactions between the sample, the solute and the surface of the stationary phase.

Using two-dimensional imaging, a slice is selected in the object first. The signal intensities of the picture elements ("pixels") that form the image of the slice are

0021-9673/90/$03.50

primarily dependent on the proton density and the relaxation times T_1 and T_2 in the selected volume elements of the object. Differences in these parameters lead to a high contrast image. As T_1 and T_2 are influenced differently by the interactions between eluent and mobile phase, the band profile becomes visible. As a sample we chose the diethylenetriaminepentaacetic acid–gadolinium complex, Gd(DTPA). This compound, in which seven unpaired electrons in Gd^{3+} strongly accelerate the relaxation times of the mobile phase by means of electron–nucleus interaction, resulting in high contrast images, is a widely used contrast agent in medical MRI[5]. As the mobile phase we used water–acetonitrile (80:20) because we found water to offer the best contrast for imaging the columns. With this eluent and modified silica gel, Gd(DTPA) has a capacity factor (k') of 0.05, which indicates weak interactions between the solute and the stationary phase.

EXPERIMENTAL

NMR

Experiments were performed on a 1.5-T Magnetom (Siemens, Erlangen, F.R.G.) whole-body system. The imaging technique was a 2D-FLASH pulse sequence[6]. The parameters were as follows: echo time, 10 ms; repetition time, 22 ms; flip angle, 30°; slice thickness, 5 mm; pixel matrix 256 × 256; spatial resolution, *ca.* 1 mm; and imaging time for one image, 6 s. The chromatographic column was positioned horizontally in the head coil and the images were recorded in the horizontal plane as central longitudinal slices through the column (see Fig. 1).

Chromatography

We injected 400 μl of a 10% aqueous solution of Gd(DTPA) (Magnevist; Schering, Berlin, F.R.G.) using a Merck (Darmstadt, F.R.G.) Lobar six-port valve

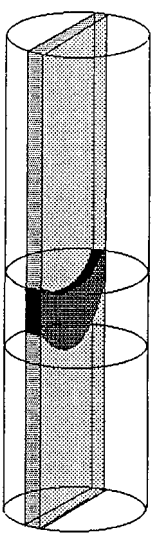

Fig. 1. Schematic diagram of the imaging slice selected in the column.

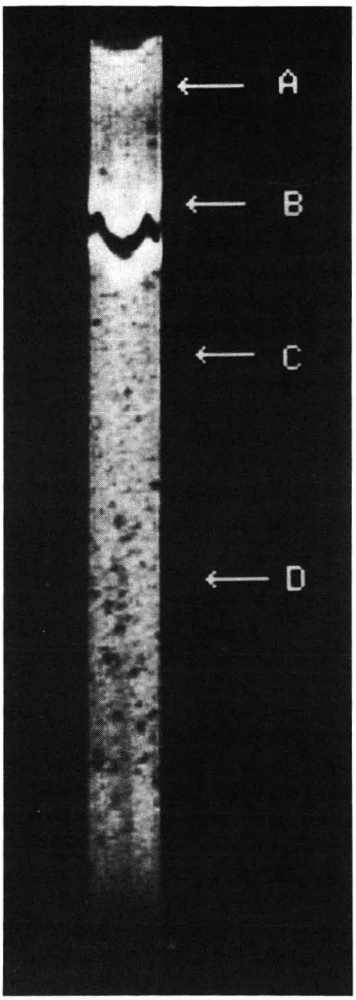

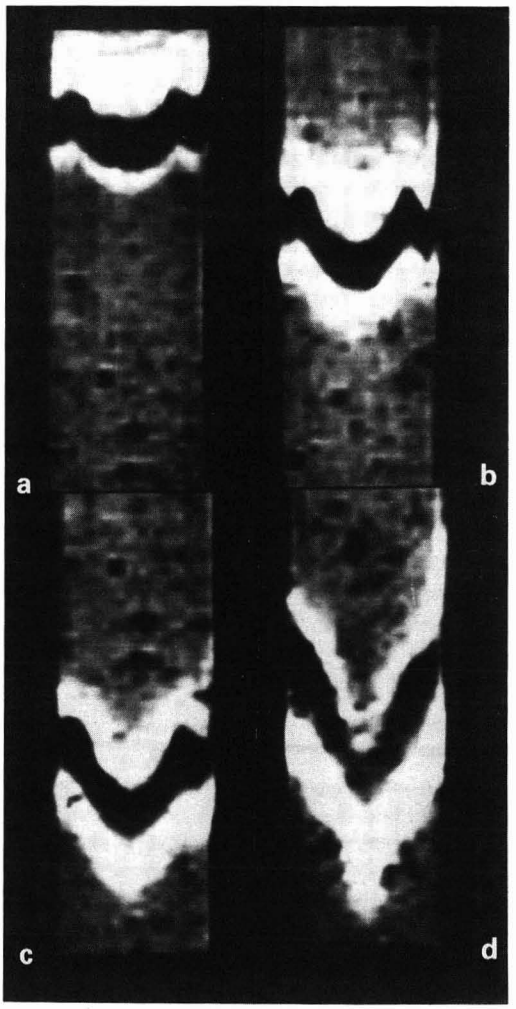

Fig. 2. MR image of the complete column.

Fig. 3. Four magnified images of the band profiles at different states of elution.

injector onto a Merck Superformance preparative glass column (300 × 26 mm I.D.) packed with reversed-phase silica gel (LiChroprep RP-8, 40–63 μm). The mobile phase was water–acetonitrile (80:20, v/v).

By means of a Bischoff (Leonberg, F.R.G.) Model 2200 HPLC pump a flow-rate of 2.0 ml/min was generated, which resulted in a pressure of 2 bar. Gd(DTPA) was detected with a Kontron (Zürich, Switzerland) Uvikon 720 LC UV–VIS detector at 215 nm. The dead volume was determined by a separate injection of uracil[7].

The elution lasted 25 min, within this time we were able to record 256 images, which were combined into a video film[8].

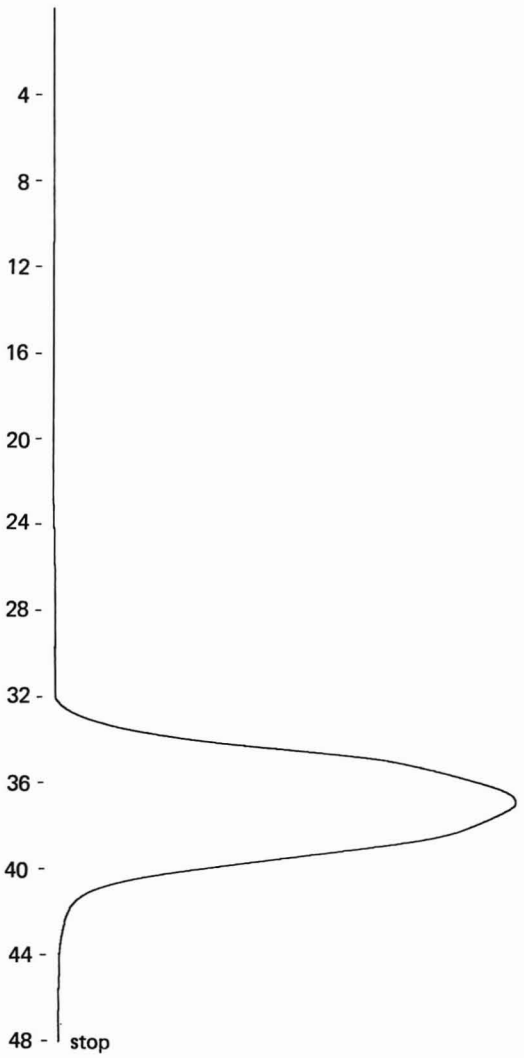

Fig. 4. Chromatogram from Gd(DTPA). Glass column (300 × 26 mm I.D.); flow-rate, 2.0 ml/min; mobile phase, acetonitrile–water (20:80); detection, 215 nm. Retention times are in min.

RESULTS

Fig. 2 shows the whole column when about one third of the elution time had elapsed. The column appears to be homogeneous, with some dark spots (diameter between 0.5 and 4 mm), which we interpret as regions that failed to be adequately wetted. The diminished contrast at the lower end of the column is due to the column exceeding the imaging range of the head coil. The chromatographic band is clearly visible. Magnified images of four selected elution profiles are shown in Fig. 3A–D. The positions of the bands on the column are indicated with the corresponding letters in Fig. 2. Fig. 4 shows the chromatogram. It is noteworthy that the band profiles were similar with flow-rates of both 0.5 and 20.0 ml/min.

DISCUSSION

The appearance of Gd(DTPA) as a black band with white edges is the result of a concentration phenomenon: phantom studies, using aqueous solutions of different Gd(DTPA) concentrations, revealed that in those regions where the concentration of Gd^{3+} is very high, the protons of surrounding liquid relax so rapidly that they are no longer detectable by MRI and the signal from this volume is eliminated. In those areas where the Gd^{3+} concentration is lower, the relaxation of these protons is slightly accelerated in comparison with uninfluenced protons. In FLASH imaging this results in a brighter signal. This effect, which is in fact the basis for the use of Gd(DTPA) as a medical contrast agent, allows an approximate estimation of the sample concentration on the column.

The interpretation of the elution profile reveals first the so-called wall effect[9,10]. This effect had been studied theoretically[11] and in practice after elution by examining the peak shapes on the chromatogram. Here it was possible for the first time to study the peak on the fly. The wall effect is mainly attributed to steel columns[12], but it also appears in glass columns. Unfortunaly, with this imaging technique we are restricted to the observation of non-metal columns and are therefore not able to compare this effect on both types of column. The wall effect is explained by a lower packing density and thus higher flow velocity in the vicinity of the walls, leading to an inverted V shaped profile. This profile, however, cannot develop completely in our system: the sample is observed to move most rapidly through the centre of the column. This effect can be ascribed to the higher temperature at the core of the column. The reason for this might be the heat of adsorption[13] of the solute on the stationary phase or the heat of friction caused by the viscosity of the solvent and pressure drop on the column[7,14,15]. The column material cannot transfer the heat rapidly enough to the walls and this thermal inertia reduces the viscosity of the mobile phase thus causing an increase in flow velocity.

Both effects counterbalance in the upper part of the column, leading to the characteristic M-shaped profile, after which the thermal effect prevails the band finally leaving the column heavily V-shaped. In addition, the band becomes broadened and more blurred on its way owing to inevitable diffusion.

Despite this band profile, the chromatogram reveals an almost symmetrical Gaussian peak. This is indicated by the calculation of the asymmetry factor:

$$T = b_{0.1}/a_{0.1} = 0.92$$

Although we have not derived any concrete figures from these first results, it is obvious that MRI offers new possibilities for basic investigations in liquid chromatography, for example to study the effects of temperature, diffusion, flow velocity and packing methods. With the help of faster imaging techniques, at present under development, we hope to be able to investigate faster elutions and systems with higher pressures in the near future.

ACKNOWLEDGEMENT

We thank B. Buszewski for fruitful discussions.

REFERENCES

1 F. W. Wehrli, D. Shaw and J. B. Kneel (Editors), *Biochemical Resonance Imaging*, VCH, New York, 1988.
2 P. C. Lauterbur, *Nature (London)*, 242 1973) 190.
3 B. Blümich, *Angew. Chem., Int. Ed. Engl.*, 27 (1988) 1406.
4 E. Bayer, W. Müller, M. Ilg and K. Albert, *Angew. Chem., Int. Ed. Engl.*, 28 (1989) 1029.
5 H. J. Weinmann, M. Laniado and W. Mutzel, *Physiol. Chem. Phys. Med. NMR*, 16 (1984) 167.
6 A. Haase, J. Frahm, D. Matthaei, K. Merboldt and W. Hänicke, *J. Magn. Reson.*, 67 (1986) 217.
7 H. Poppe and J. C. Kraak, *J. Chromatogr.*, 282 (1983) 399.
8 E. Bayer, Lecture and video presentation at the *13th Symposium on Column Liquid Chromatography, Stockholm, June 25–30, 1989.*
9 E. Bayer, *Chimia*, 17 (1963) 414.
10 W. M. Skea, in P. R. Brown and R. A. Hartwick (Editors), *High Performance Liquid Chromatography*, Wiley, New York, 1989, Ch. 12.
11 J. H. Knox, G. R. Laird and P. A. Raven, *J. Chromatogr.*, 122 (1976) 129.
12 B. Versino and H. Schlitt, *Chromatographia*, 5 (1972) 332.
13 G. Hesse and H. Engelhardt, *J. Chromatogr.*, 21 (1966) 223.
14 H.-J. Lin and Cs. Horvath, *Chem. Eng. Sci.*, 36 (1981) 47.
15 I. Halasz, R. Endele and J. Asshauer, *J. Chromatogr.*, 112 (1975) 37.

Journal of Chromatography, 517 (1990) 269–284
Elsevier Science Publishers B.V., Amsterdam

CHROMSYMP. 1965

Non-porous polybutadiene-coated silicas as stationary phases in reversed-phase chromatography

M. HANSON* and K. K. UNGER
Institut für Anorganische Chemie und Analytische Chemie, Johannes Gutenberg-Universität, J. J. Becher Weg 24, D-6500 Mainz (F.R.G.)
and
G. SCHOMBURG
Max Planck-Institut für Kohlenforschung, Kaiserplatz 1, D-4330 Mülheim (F.R.G.)

ABSTRACT

Non-porous silica of mean particle diameter 1.7 μm (Monospher) was coated with polybutadiene (PBD) following a published procedure. The silicas were prepared with graduated polymer loads up to 8% (w/w). Examination of the PBD-coated packings by means of electron spectroscopy for chemical analysis, scanning electron microscopy, diffuse reflection infrared fourier transform spectroscopy and differential thermal gravimetry indicated that the optimum polymer load was between 1 and 3% (w/w) with regard to a dense coverage corresponding to an average layer thickness of about 4 nm. No silanophilic interactions could be monitored using 1–3% (w/w) coated silicas under reversed-phase conditions. The small particle diameter combined with the chemically stable polymer coating allowed extremely fast and efficient separations of peptides and polypeptides under gradient elution conditions in less than 1 min.

INTRODUCTION

Major advances have occurred in recent years in the design and development of high-performance liquid chromatographic (HPLC) stationary phases. One focus was on the elucidation of the pore and particle structure of HPLC packings with regard to better mass transfer kinetics, higher column performance and faster analysis. This led to the family of macroporous packings of mean pore diameter of >50 nm and to non-porous packings[1,2]. Both types have been shown to generate outstanding separation capabilities for large biomolecules. The other focus was on novel concepts and improvements of the stationary phase chemistry of HPLC packings.

The objectives were to prepare stationary phases with defined and accessible functional groups, to minimize or eliminate adsorptive effects of the matrix, concur-

0021-9673/90/$03.50

rently improving the chemical stability and lifetime of the packing whilst maintaining a high mechanical stability. The most successful approach is to immobilize defined polymer layers at the surface of the rigid inorganic packing in such a way that a solute-impermeable layer results, which, *a priori*, carries functional ligands or appropriate ligands were introduced by chemical reactions. Numerous polymer-load types of HPLC packings made by different immobilization chemistries[3–8] are available.

Although the immobilization procedures have advanced, few attempts have been made to assess the properties of the immobilized polymer layers in terms of chemical structure, physical structure and morphology, and to demonstrate the way in which variation of these structural parameters affect the chromatographic properties.

This work was aimed at elucidating the structural properties of a well known polymer coating, polybutadiene (PBD), on non-porous microparticulate silicas. The lack of pores and the spherical nature of the particles provide suitable conditions for immobilizing PBD layers of different thicknesses and for studying their layer composition and morphology by surface analytical methods. Chromatographic tests with appropriate polar solutes permit residual silica adsorptivities to be monitored, thus indicating the quality of the coating. The products obtained were most suited for the rapid analysis of peptide mixtures owing to their extremely small particle size of 1.7 μm. Such packings were required for rapid peptide monitoring in process control and allow analyses to be performed in much less than 1 min.

EXPERIMENTAL

Chemicals and materials

Monospher, support (non-porous silica of mean particle diameter 1.7 μm), methanol, acetonitrile, *n*-pentane and trifluoroacetic acid were obtained from E. Merck (Darmstadt, F.R.G.). The peptides for the reversed-phase test and silanol monitoring were obtained from the Department of Biochemistry, University of Alberta, Canada. Polybutadiene and dicumyl peroxide were supplied by Aldrich Chemie (Steinheim, F.R.G.). Proteins were supplied by Boehringer (Mannheim, F.R.G.) and Serva (Heidelberg, F.R.G.). Paracelsine peptides were donated by the Institut für Lebensmitteltechnologie, Universität Hohenheim, F.R.G. ODS and TMS silanization reagents, alkylbenzenes and the polarity test mixture were donated by the Max Planck-Institut für Kohlenforschung (Mülheim, F.R.G.).

Water was deionized with a Milli-Q system (Millipore–Waters, Eschborn, F.R.G.).

Support

To clean the surface of the Monospher support from impurities caused by the manufacturing process and to remove remaining micropores, the material was calcined at 1273 K for 48 h in a shallow bed. After cooling to room temperature, 200 g of calcined Monospher were suspended in 500 ml of nitric acid (15%, v/v) and refluxed for 18 h to rehydroxylate the surface. The material was washed with deionized water until the pH of the washings was neutral. The material was then dried at 440 K under vacuum (0.1 mbar) for 30 h.

Coating of silica with polybutadiene (PBD)

The apparatus consisted of a Rotavapor, a chamfered flask and an argon purge system. Dried Monospher (15 g) was stirred in *n*-pentane (30 ml) until a homogeneous suspension was obtained. Defined amounts of polybutadiene (molecular weight 4500, 45% vinyl, 55% 1,4-*cis*/*trans*) and dicumyl peroxide (DCP) were added according to the desired loading. The batches made were as follows:

PBD batch No.	*PBD (mg)*	*DCP (mg)*
0.2	30.0	1.5
0.5	75.0	3.8
1.0	150.0	7.5
2.0	300.0	15.0
3.0	450.0	22.5
5.0	750.0	37.5
10.0	1500.0	75.5

The solvent in each batch was evaporated and the PBD was immobilized in a chamfered flask at 440 K for 4 h, the mixture being rotated at 30 rpm in a dry argon atmosphere. The loaded silicas were suspended in dioxane–toluene (1:1, v/v) and subjected to ultrasonic treatment. The suspension was then filtered through a porous PTFE membrane of 0.2 μm porosity (Cartridge system; Sartorious, Göttingen, F.R.G.), applying a pressure of 0.4–0.5 MPa. The product was washed with tetrahydroforan, methanol and diethyl ether consecutively to remove the oligomers of polybutadiene. The reaction scheme is shown in Fig. 1.

Silanization of silica

TMS presilanization. Monospher was silanized with trimethylsilyl enol ether

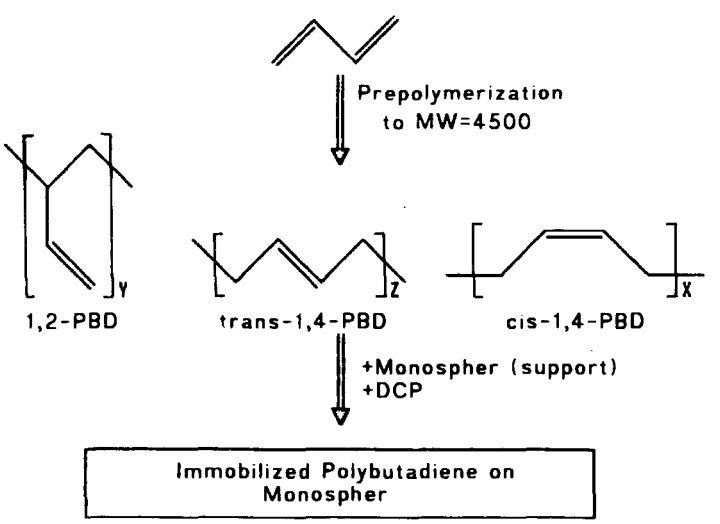

Fig. 1. Reaction scheme of the coating procedure. MW = Molecular weight.

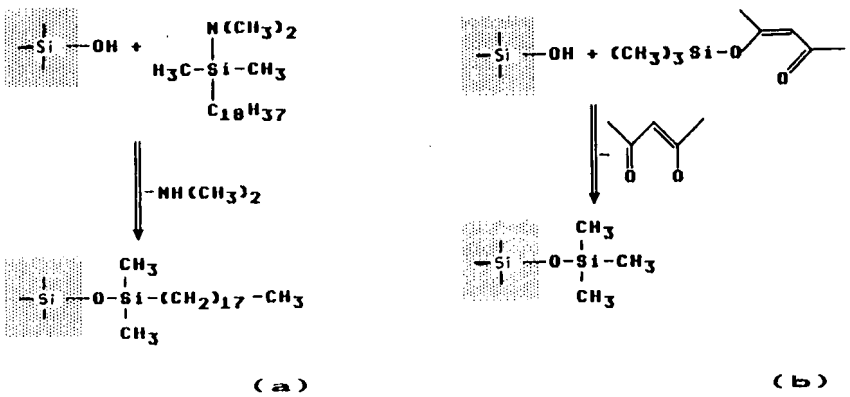

Fig. 2. Reaction scheme for the TMS and ODS modifications.

(TMS) following a procedure described by Schomburg *et al.*[9] (Fig. 2b). Silanized Monospher was also coated by the procedure described above.

ODS silanization. The same procedure was used to immobilize octadecylsilyl (ODS) residues on Monospher. Dimethyl(dimethyloctadecylsilyl)amine was used under the conditions described in ref. 9 (Fig. 2a).

Characterization of the bulk Monospher

Elemental analyses of parental and coated Monospher were obtained on a model 240 B Elemental Analyzer (Perkin-Elmer, Überlingen, F.R.G.). Duplicate analyses for carbon and hydrogen were performed. The reproducibility of the measurements was within ±0.2% (absolute standard deviation).

Thermogravimetric analysis (TGA), differential thermal analysis (DTA) and differential scanning calorimetric (DSC) measurements were conducted with a Du Pont Model 2100 TGA-Analyzer. The temperature was increased to 1120 K at 2 K/min in a dry air atmosphere. The samples were maintained in the analyser until no further weight loss was observed[10].

Diffuse reflection infrared Fourier transform (DRIFT) spectroscopy was performed on a Series 7000 FT-IR spectrometer (Nicolet, Offenbach, F.R.G.).

Electron spectroscopy for chemical analysis (ESCA) was carried out by Dr. Herzog (Hoechst Frankfurt/Main, F.R.G.) on a modified Leybold Hereaus ESCA instrument.

A Chemscan Cambridge, U.K. Series 4 scanning electron microscope was used for morphological investigations.

Chromatographic experiments

Chromatographic experiments were performed with two sets of equipment. With set 1, the screening experiments were performed with a Merck–Hitachi system equipped with a Model 655A-12 pump system, an L-5000 controller, a Model 655 A UV detector and a Rheodyne 7125 injector with a 20 μl-loop (E. Merck). The chromatograms were plotted with a C-R3A integrator (Shimadzu Europa, Duisburg, F.R.G.).

With set 2, rapid peptide separations were performed with a Bischoff (Leon-

berg, F.R.G.) LC unit consisting of an Autochrom 300 benchtop gradient controller system/terminal, two Model A2200 LC pumps and a Rheodyne 7410 injector with a 1 μl-loop. A Shimadzu SPD-6VA UV detector with a 0.6-μl cell and a time constant of < 50 ms and a Shimadzu C-R3A integrator were also used.

All eluents were degassed with a stream of helium leading through the solvent reservoirs.

Stainless steel columns of 33 × 4.6 mm I.D. (Bischoff) were used with compression fittings composed of metal screens and paper filters (Type 827; Schleicher and Schüll, Dassel, F.R.G.). The following materials were packed: (a) polybutadiene-coated Monospher (mean particle diameter 1.7 μm) with loadings of PBD between 0.2 and 8% (w/w); (b) PBD-coated Monospher presilanized with TMS; (c) ODS-bonded Monospher; (d) Monospher coated with a styrene–vinylsiloxane copolymer[11,12]. The columns were slurry packed using toluene–dioxane–cyclohexanol (1:1:1, v/v/v). The slurry, containing 1–2% (w/w) of modified Monospher, was treated ultrasonically for 4 h in a cooled bath. Columns were packed at a constant flow-rate under a constant pressure of 60 MPa.

Several test mixtures were applied in chromatographic experiments:

(a) Alkylbenzenes: ethylbenzene (C_2), propylbenzene (C_3), butylbenzene (C_4), *n*-pentylbenzene (n-C_5), isopentylbenzene (i-C_5) and *n*-hexylbenzene (C_6) were dissolved at a concentration of 1 mg/ml in methanol. The injection volume was 1–2 μl and produced satisfactory chromatographic peak sizes at a detection wavelength of 254 nm. The flow-rate was 0.5 ml/min.

(b) Polarity test: 1 mg/ml of acetophenone, benzophenone, benzyl benzoate and *n*-octylpyridine were dissolved in methanol. The chromatographic conditions were the same as in (a).

(c) Reversed-phase peptides: the following decapeptides (S1–S5), synthesized by C. T. Mant and R. S. Hodges (University of Alberta, Canada), were used in a reversed-phase test[13–15]:

S1: Arg–Gly–Ala–Gly–Gly–Leu–Gly–Leu–Gly–Lys;
S2: Arg–Gly–Gly–Gly–Gly–Leu–Gly–Leu–Gly–Lys;
S3: Arg–Gly–Ala–Gly–Gly–Leu–Gly–Leu–Gly–Lys;
S4: Arg–Gly–Val–Gly–Gly–Leu–Gly–Leu–Gly–Lys;
S5: Arg–Gly–Val–Val–Gly–Leu–Gly–Leu–Gly–Lys;

All peptides contained an N^{α}-acetylated N-terminal and a C-terminal amide, except peptide S1, which was identical with peptide S3 but had a free α-amino group. The separations were carried out in the gradient mode, using acetonitrile–water–0.1% trifluoracetic acid (TFA) as eluent. The flow-rate was 1 ml/min and the detection wavelength was 214 nm.

(d) Monitoring free silanol groups: as described in ref. 16, a method for free silanol monitoring was applied by using a mixture of undecapeptides differing in the number of lysine residues:

1: Gly–Gly–Gly–Leu–Gly–Gly–Ala–Gly–Gly–Leu–Lys;
2: Lys–Tyr–Gly–Leu–Gly–Gly–Ala–Gly–Gly–Leu–Lys;
3: Gly–Gly–Ala–Leu–Lys–Ala–Leu–Lys–Gly–Leu–Lys;
4: Lys–Tyr–Ala–Leu–Lys–Ala–Leu–Lys–Gly–Leu–Lys;

Each peptide contained an N^{α}-acetylated N-terminal and a C-terminal amide. Gradient elution was performed at pH 2, using acetonitrile–water–0.1% TFA as eluent. The chromatographic conditions were the same as in (c).

(e) Paracelsine is a membrane-active polypeptide with antibiotic activity and is secreted by the mould *Trichoderma reesi*. Its composition has a light inhomogeneity, consisting of four peptides (A–D), differing only in two positions:

A: Ac–Aib–Ala–Aib–Ala–Aib–*Ala*–Gln–Aib–*Val*–Aib–Gly–Aib–Aib–Pro–Val–Aib–Aib–Gln–Gln–Pheol

B: Ac–Aib–Ala–Aib–Ala–Aib–*Ala*–Gln–Aib–*Leu*–Aib–Gly–Aib–Aib–Pro–Val–Aib–Aib–Gln–Gln–Pheol

C: AC–Aib–Ala–Aib–Ala–Aib–*Aib*–Gln–Aib–*Val*–Aib–Gly–Aib–Aib–Pro–Val–Aib–Aib–Gln–Gln–Pheol

D: Ac–Aib–Ala–Aib–Ala–Aib–*Aib*–Gln–Aib–*Leu*–Aib–Gly–Aib–Aib–Pro–Val–Aib–Aib–Gln–Gln–Pheol

The peptides were N-terminal acetylated and C-terminated with phenylalaninol. Acetonitrile–water (36:64, v/v) containing 0.1% TFA was used as the mobile phase for the isocratic separation. The peptides were detected at a wavelength of 214 nm. The flow-rate was varied from 1 to 3 ml/min.

(f) The separation of proteins was carried out by gradient elution with acetonitrile–water–0.1% TFA using the following proteins: (1) Ribonuclease A, (2) lysozyme, (3) transferrin, (4) conalbumin, (5) β-lactoglobulin and (6) ovalbumin.

RESULTS AND DISCUSSION

Characterization of polybutadiene-coated silicas

Elemental analysis. In the immobilization procedure the load of PBD on silica was adjusted to discrete values between 0.2 and 10% (w/w). There are two additional means of assessing the load of PBD: elemental analysis of carbon and weight loss during ignition by TGA. The carbon content of the coated silica measured by elemental analysis should correspond to the load adjusted for the immobilization, assuming that no losses of PBD occurred during the procedure. Table I gives the data

TABLE I

POLYMER LOAD OF SILICA DERIVED FROM THE WEIGHT OF IMMOBILIZED PBD, CARBON ELEMENTAL ANALYSIS AND THE CALCULATED PBD CONTENT AND THERMOGRAVIMETRY

d_s = apparent layer thickness of PBD according to elemental analysis.

Sample	*PBD employed (%, w/w)*	*Carbon content (%, w/w)*	*Calculated PBD content*[a] *(%, w/w)*	*Weight loss (%, w/w)*	d_s *(nm)*
PBD 0.2	0.2	0.14	0.16	0.28	0.8
PBD 0.5	0.5	0.35	0.39	–	1.8
PBD 1.0	1.0	0.83	0.93	1.19	4.1
PBD 2.0	2.0	1.59	1.79	2.31	7.9
PBD 3.0	3.0	2.42	2.72	2.87	12.0
PBD 5.0	5.0	3.77	4.25	5.13	18.8
PBD 10.0	10.0	7.38	8.31	9.48	36.9

[a] From carbon elemental analysis.

derived from different methods. It also includes the apparent film thickness, d_s, of PBD-coated silicas calculated with the equation

$$d_s = X_{PBD}\, \rho_{PBD}/a_s$$

where X_{PBD} is the load of PBD (%, w/w) derived from carbon analysis, ρ_{PBD} is the density of PBD (g/ml) and a_s the specific surface area of the silica according to the BET method (a_s = 1.8 m^2/g). The load obtained on the basis of the carbon content is less than the amount of PBD employed in the immobilization procedure even when corrected by a factor of 1.126 to take the content of hydrogen in PBD into account. The weight loss of loaded silicas derived from TGA is seen to be slightly higher than the amount of PBD loaded, which is probably due to the removal of non-carboneous constituents from the silica during ignition. The apparent layer thickness increases proportionally with the load of PBD and ranges from about 1 nm at low loads to 40 nm at high loads.

Thermal analysis. The TGA data showed that the burning of PBD started at about 200°C and was completed at 500°C. Above 600°C no further weight loss occurred. In differential thermal analysis (DTA) of the PBD silicas three peaks appeared at 120, 300 and 500°C. DTA and differential scanning calorimetric (DSC) experiments on pure PBD as reference material gave nearly the same pattern as observed for PBD-coated silicas. Therefore, apart from the weight loss, no conclusions can be drawn from thermal analysis about the homogeneity of the PBD coating.

Diffuse reflection infrared Fourier transform spectroscopy (DRIFT). DRIFT was carried out on PBD-coated silicas in the range 1600–3200 cm^{-1} (Fig. 3). For the identification and semi-quantitative determination of PBD the C–H absorption band at 2916 cm^{-1} was employed. The intensity of this band was found to be proportional to the load of PBD. Owing to the lack of molar absorption coefficients, the quantification of PBD load from FT-IR measurements was not possible. Whereas the absorbance of the band at 2916 cm^{-1} increased with increase in the PBD load, the absorption band at 1869 cm^{-1} assigned to the silica diminished. Normally additional information would be obtained by monitoring the absorbance at 3750 cm^{-1}, assigned to the stretching vibration of free silanols. However, owing to the low surface area of

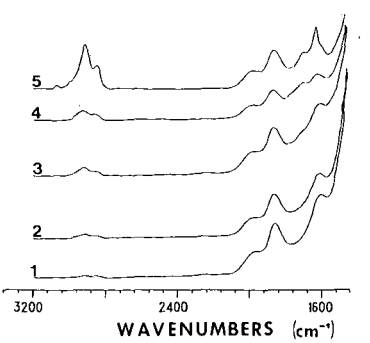

Fig. 3. DRIFT spectra of silicas with increasing PBD load in the range 1600–3200 cm^{-1}. PBD silica samples: 1, 0.5; 2, 1.0; 3, 2.0; 4, 5.0; 5, 10.0 (pure samples, no KBr).

TABLE II

DISTRIBUTION OF CARBON, SILICON AND OXYGEN IN THE LAYER OF PBD-COATED SILICAS

Sample	*Amount of PBD*[a] *(%, w/w)*	$C_{surface}$ *(atom-%)*	$Si_{surface}$ *(atom-%)*	$O_{surface}$ *(atom-%)*
Monospher	–	12.38	30.22	57.40
PBD 0.5	0.39	43.35	21.60	35.05
PBD 1.0	0.93	59.80	15.40	24.80
PBD 3.0	2.72	69.30	10.00	20.70
PBD 5.0	4.25	65.50	9.78	24.72
PBD 10.0	8.31	70.05	7.10	22.85
$RP\text{-}18_{ref.}$	–	26.97	26.88	46.15

[a] From carbon elemental analysis.

non-porous silica, the absolute concentration of free silanols is so low that they could not be detected by DRIFT.

DRIFT serves as a means of identifying the polymer used for coating and allows a crude estimate of the extent of loading, but it cannot be utilized for the assessment of the homogeneity or defects of the coating.

*Electron spectroscopy or chemical analysis (ESCA).*ESCA provides a sensitive

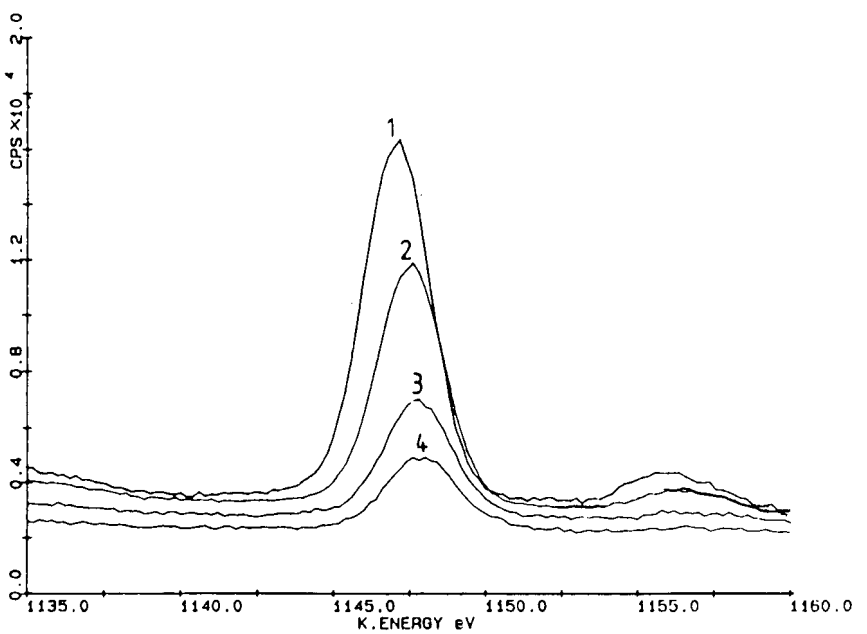

Fig. 4. Intensity of the X-ray photoelectron spectroscopic band at 1147.5 eV due to silicon at various loads: 1 = PBD 0.5; 2 = PBD 1.0; 3 = PBD 3.0; 4 = PBD 10.0.

means of characterizing the chemical composition of the surface layer by following the photoelectron bands of carbon at 966 eV, silicon at 1147.5 eV and oxygen at 718 eV[17,18]. Integration of these bands and correction of the data by equipment-specific factors (carbon 0.2, silicon 0.195, oxygen 0.61), the contents of carbon, silicon and oxygen in atom-% of the layer can be calculated (Table II) According to the penetration depth of photoelectrons, the values reflect the distribution of the surface layer at a film thickness of about 5 nm.

Inspection of the uncorrected spectra (Fig. 4) reveals that at high loadings (8% w/w) of PBD, silicon surface atoms can still be monitored. Consequently, this observation indicates that high loadings do not guarantee complete coverage of the native surface of the silica support. A loading of PBD of 8% (w/w) corresponds to an apparent layer thickness, according to elemental analysis, of about 35 nm, which should be completely impermeable to photoelectrons.

The calculated silicon content of the surface layer decreased with increasing load of PBD up to 8% (w/w) at the highest loading. The carbon content was about 43% at a 0.4% load, increasing to 60% at a 0.9% load and approaching values between 66 and 70% at higher loadings.

From the results, it can be concluded that a load of PBD above 3% does not yield a more homogeneous and denser coating than lower loadings. Assuming a dense and homogeneous layer of PBD, the layer thickness, d_s', can be calculated as

$$d_s' = \lambda \ln(100/I_s)$$

where λ is the average path length of inelastic electron diffraction and I_s the intensity of the electrons of the silica matrix in atom-%. Setting λ equal to 5 nm and using the values of I_s calculated from Table II d_s' values of 4.6, 5.9, 5.3, 6.0 and 1.6 nm are obtained for PBD samples 1.0, 3.0, 5.0 and 10.0 and RP-18_{ref}, respectively. For comparison, the layer thickness of an *n*-octadecyl-bonded silica is 1.6 nm with I_s = 73.0%. There is fairly good agreement on comparing the d_s and d_s' values for the PBD 1.0 silica.

Scanning electron microscopy (SEM). SEM provides a direct means of viewing the surface of native and coated silicas and thus allows an estimate of the morphology of the layer. Scanning electron micrographs were taken at magnifications of 30 000, 80 000 and 120 000 and Fig. 5a–d show the images of four coated silicas at the same magnification.

The images of the particle surface indicate a relatively smooth coated surface for the PBD 1.0 and 3.0 silicas. Minor imperfections are seen on the surface of PBD 5.0 silica and the particles of the PBD 10.0 sample show a flake-like surface with island structures. Beneath these clusters the surface seemed to be densely coated. As demonstrated by the ESCA measurements, the coating is not dense enough to suppress penetration by photoelectrons. The density of the coating and the morphology are reflected by the chromatographic measurements following the retention of selected compounds.

Chromatographic characterization

To establish the lipophilic and hydrophilic character of the coated silicas, several test mixtures were applied. The lipophilicity was monitored by using a mixture of

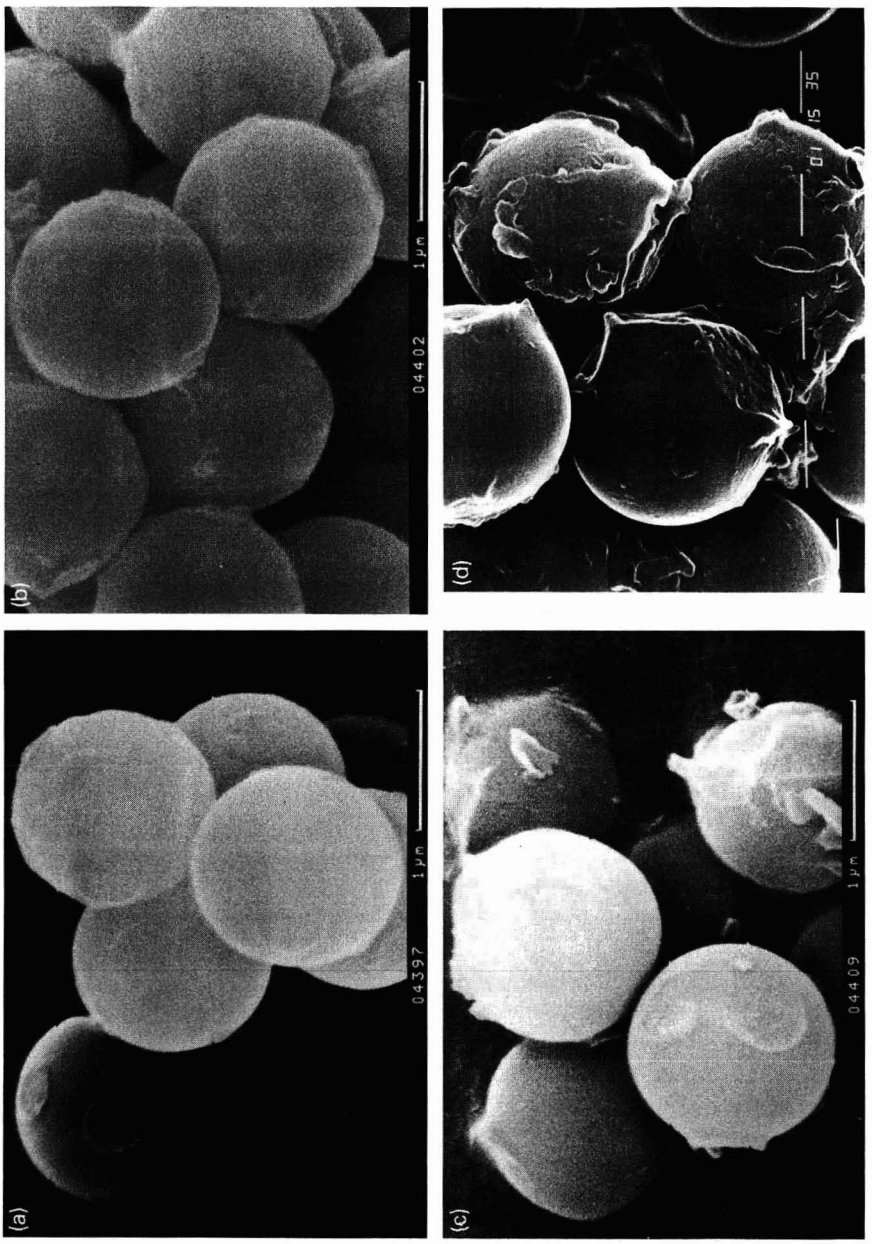

Fig. 5. Scanning electron micrographs of (a) PBD 1.0, (b) PBD 3.0, (c) PBD 5.0 and (d) PBD 10.0.

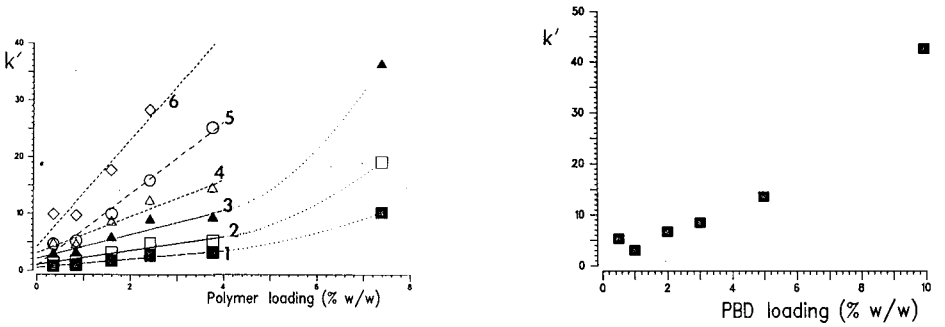

Fig. 6. Dependency of the capacity factor, k' (alkylbenzenes), as a function of the PBD loading on Monospher: 1 = ethylbenzene 2 = *n*-propylbenzene; 3 = *n*-butylbenzene; 4 = isopentylbenzene; 5 = *n*-pentylbenzene; 6 = *n*-hexylbenzene.

Fig. 7. Plot of the capacity factor, k', of *n*-octylpyridine *versus* the PBD loading on Monospher.

n-alkylbenzenes. A polarity test aiming at measuring the residual adsorptivity of the silica was carried out using acetophenone, benzophenone, benzyl benzoate and *n*-octylpyridine.

To assess the separation capabilities of the PBD-coated silicas for peptide separation, two standard peptide mixtures were chromatographed with an acidic mobile phase under gradient elution conditions with acetonitrile as the organic solvent. An isocratic separation was carried out with paracelsine peptides using a binary acidic mobile phase (water–acetonitrile). Finally, a protein mixture was separated under the same conditions as in the standard peptide test.

Test with n-alkylbenzenes. The capacity factors, k', of a homologous series of *n*-alkylbenzenes (ethyl to n-hexyl) were measured on columns packed with PBD-coated silicas with a constant mobile phase composition. For comparison the same measurements were performed on an *n*-octadecyl-bonded non-porous silica. Fig. 6 depicts the dependence of k' on the PBD loading of the stationary phase. A linear relationship is obtained for each solute up to a 4% PBD loading. Above 4% PBD each curve shows an upward swing to higher retention. This additional increase in the retention of *n*-alkylbenzenes on the PBD 10.0 silica is probably due to the fact that an additional partitioning of solute takes place with the bulky clusters of PBD attached to the underlying PBD coating.

The retention behaviour of the *n*-octadecyl-bonded silica is similar to those of the PBD 0.5 and 1.0 silicas.

Polarity test. Basic compounds such as amines are sensitive markers for monitoring the residual adsorptivity of reversed-phase materials. In this instance *n*-octylpyridine was employed. The plot of k' of *n*-octylpyridine *versus* the PBD loading of the silicas showed that the retention declines from PBD 0.5 silica to a minimum at PBD 1.0 silica and then increases proportionally at higher loadings (Fig. 7). In the first part of the curve *n*-octylpyridine is mainly retained by silanophilic interactions with the stationary phase, which reaches a minimum at the PBD 1.0 silica. On the right-hand side of the curve the lipophilic interactions dominate because the silica support is nearly completely covered by the PBD.

Further evidence of the absence of residual adsorptivity of the silica is provided

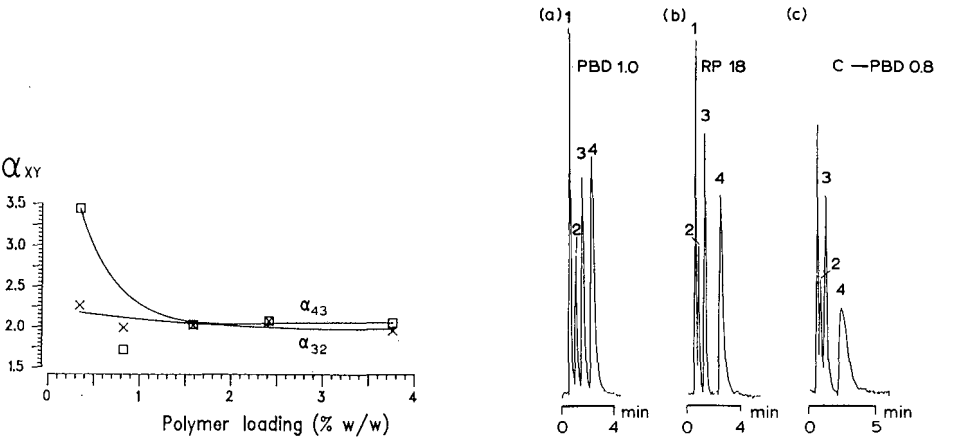

Fig. 8. Plot of the selectivity coefficients, α, of two pairs of solutes *versus* the PBD loading on Monospher.

Fig. 9. Chromatograms for the polarity test (1 = acetophenone, 2 = benzophenone, 3 = benzyl benzoate, 4 = *n*-octylpyridine) for the following columns: (a) PBD 1.0 silica, (b) RP-18 (*n*-octadecyl-bonded, not end-capped) silica and (c) presilanized PBD silica (C1-PBD 0.8). Chromatographic conditions: mobile phase, acetonitrile–water (45:55, v/v); flow-rate, 0.5 ml/min; detection wavelength, 254 nm.

by Fig. 8, where the selectivity coefficients, α, of two pairs of solutes, $\alpha_{43} = k'(n\text{-octylpyridine})/k'$ (benzyl benzoate) and $\alpha_{32} = k'$ (benzyl benzoate)/k' (benzophenone), is plotted against the PBD load of the silica. α_{43} decreases from 3.5 to about 2 from the PBD 0.5 to the PBD 2.0 silica and then remains constant.

Fig. 9 compares the chromatograms, obtained under constant conditions, for

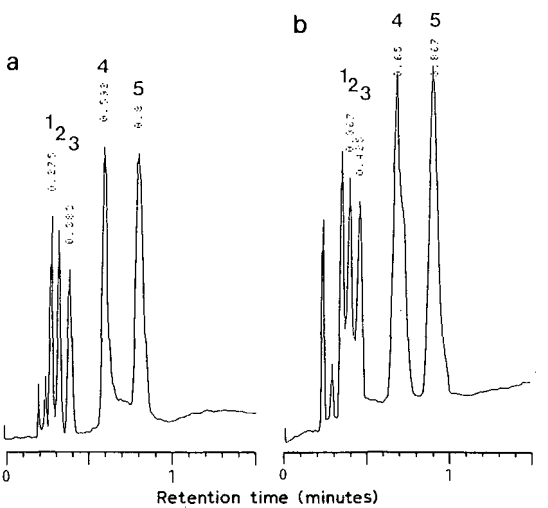

Fig. 10. Chromatograms of reversed-phase peptide standards on (a) PBD 1.0 silica and (b) PBD 3.0 silica. Chromatographic conditions: gradient from 100% A to 75% A–25% B in 1.5 min, where A = 0.1% aqueous TFA and B = acetonitrile–water (75:25, v/v) containing 0.1% TFA; flow-rate, 1.0 ml/min; detection wavelength, 214 nm (Peak numbers correspond to peptides S1–S5, p. 273).

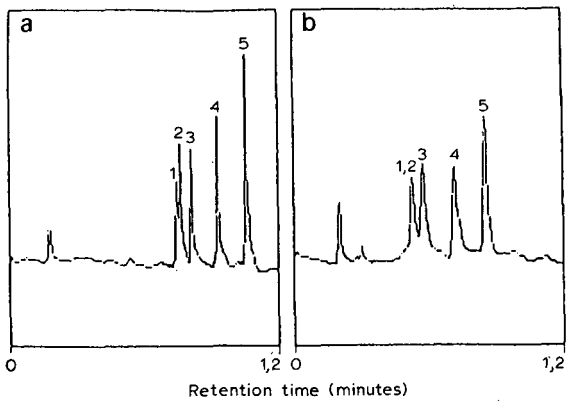

Fig. 11. Chromatograms of reversed-phase peptide standards on (a) *n*-octadecyl-bonded silica and (b) polystyrene–vinylsiloxane-coated silica. For chromatographic conditions, see Fig. 10 (Peak numbers correspond to peptides S1–S5, p. 273).

the test mixture applied to three columns: the PBD 1.0 silica, the *n*-octadecyl-bonded silica and the presilanized PBD 0.8 silica. The PBD 1.0 silica shows a baseline separation and the last eluted peak (*n*-octylpyridine) is fairly symmetrical. The resolution with the other two stationary phase is much worse.

Tests with peptide standard mixtures. The first set of five standard decapeptides enabled us to monitor the hydrophobic character of the stationary phase. Four stationary phases were selected for comparison: PBD 1.0 and PBD 3.0 silica, the *n*-octadecyl-bonded silica and the polystyrene–vinylsiloxane-coated silica. The last material was prepared following the procedure of Kurganov and co-workers[11,12]. The mobile phase was an acidic acetonitrile–water gradient. The chromatograms obtained with the PBD 1.0 and PBD 3.0 silicas are shown in Fig. 10. The first three peptides

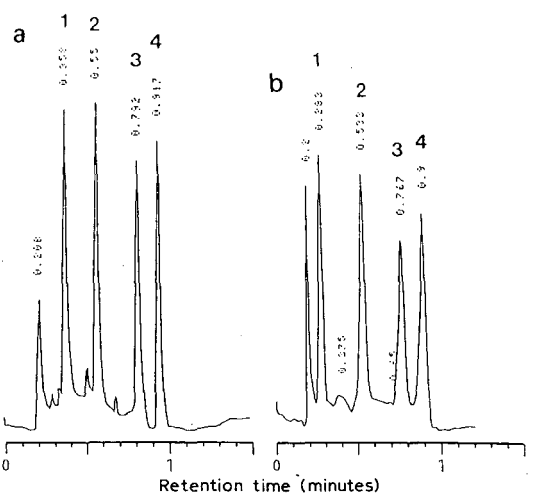

Fig. 12. Chromatograms of the "silanol monitoring" peptide test: (a) PBD 1.0 silica and (b) PBD 3.0 silica. For chromatographic conditions, see Fig. 10 (Peak numbers correspond to peptides 1–4, p. 273).

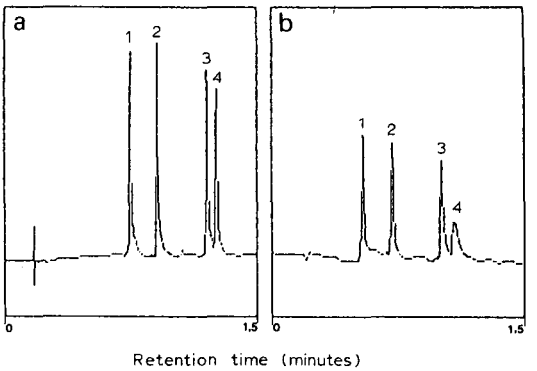

Fig. 13. Chromatograms of the "silanol monitoring" peptide test: (a) *n*-octadecyl-bonded silica and (b) polystyrene–vinylsiloxane-coated silica. For chromatographic conditions, see Fig. 10 (Peak numbers correspond to peptides 1–4, p. 273).

elute closely together as a triplet, followed by peptides 4 and 5 as a doublet. The resolution with the *n*-octadecyl-bonded silica is not as good as that with the two PBD-coated silicas. With the polystyrene–vinylsiloxane-coated silica the triplet is not resolved and the eluted peaks are broader than those in the other columns (Fig. 11).

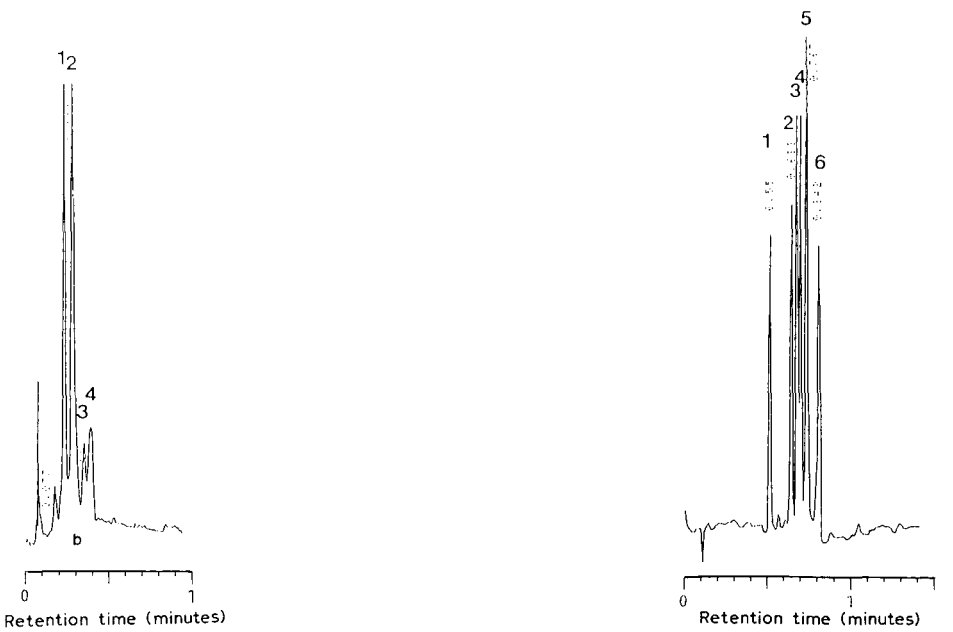

Fig. 14. Isocratic separations of paracelsine peptides on a PBD 1.0 silica column. Chromatographic conditions: Mobile phase, acetonitrile–water (36:64, v/v) containing 0.1% TFA; flow-rate, 3.0 ml/min; detection wavelength, 214 nm (Peak numbers correspond to Paracelsine peptides A–D, p. 274).

Fig. 15. Separation of proteins on a PBD 1.0 silica column. Chromatographic conditions: gradient from 100% A to 100% B in 1.0 min, where A = 0.1% aqueous TFA and B = acetonitrile–water (75:25, v/v) containing 0.1% TFA; flow-rate, 2.0 ml/min; detection wavelength, 214 nm (Peak numbers correspond to proteins, p. 274).

The second set of standard peptides serves for silanol monitoring. The basic character of the peptides increases in the sequence 1 < 2 < 3 <4 owing to the increasing content of lysine. All four peptides are baseline separated on the PBD 1.0 and PBD 3.0 silica columns (Fig. 12) with almost no tailing. The *n*-octadecyl-bonded silica exhibits slightly tailed peaks for the basic peptides. Pronounced peak tailing, particularly of the last-eluting peptide, was observed with the polystyrene–vinylsiloxane-coated silica (Fig. 13).

Paracelsine peptides. This peptide mixture consists of four peptides which differ slightly in two positions. A baseseparation of the four peptides was achieved by Lork *et al.*[19] using a ternary mobile phase and isocratic conditions. Fig. 14 shows the chromatogram of the mixture on a PBD 1.0 silica column with water–acetonitrile (64:36, v/v) as the mobile phase under isocratic conditions, obtained in less than 1 min.

Protein test mixture. A test mixture containing six proteins (1, ribonuclease A; 2, lysozyme; 3, transferrin; 4, conalbumin; 5, β-lactoglobulin; 6, ovalbumin) was chromatographed under the same conditions as applied to the peptide standards. Short gradient times of about 1 min and high flow-rates above 1 ml/min allowed very efficient, high-resolution separations, as already demonstrated by Unger and coworkers[20–23] on *n*-alkyl-bonded non-porous silica. An example is shown in Fig. 15.

CONCLUSIONS

The combination of various physico-chemical methods applied to the characterization of PBD-coated non-porous silicas provided a detailed insight into the chemical structure of the polymer layer and its morphology. For the non-porous silicas investigated, loadings of PBD between 1 and 3% (w/w) provide the most dense and homogeneous coatings.

Chromatographic measurements with various test mixtures indicate a similar lipophilic character of the PBD silica with *ca.* 1% (w/w) of PBD and the *n*-octadecyl-bonded derivative. The polymer clusters formed on the coated PBD 10.0 silica give rise to a substantially higher retention for lipophilic solutes, as expected when extrapolating from lower PBD loadings. This additional retention is probably due to partitioning of the solute between the mobile and bulk polymer phases in addition to the solute–surface interaction with the thin underlying PBD layer.

A minimum load of PBD of about 1–3% (w/w) is required to eliminate the residual adsorptivity of the silica support, as shown by the retention of *n*-octylpyridine in isocratic and basic peptides in gradient elution experiments.

The PBD silicas studied are particularly suitable for rapid chromatographic separations of peptides and proteins under gradient elution conditions in less than 1 min.

ACKNOWLEDGEMENTS

The authors express their thanks to Dr. Herzog of Hoechst (Frankfurt/Main, F.R.G.) for allowing M.H. to work with his group on ESCA measurements, Dr. Krebs of E. Merck (Darmstadt, F.R.G.) for the thermoanalytical measurements and Dr. Brückner (Institut für Lebensmitteltechnologie, Universität Hohenheim, F.R.G.) for the generous donation of the paracelsine peptides.

REFERENCES

1 H. Giesche, *Dissertation*, Johannes Gutenberg-Universität, Mainz, 1987.
2 H. Giesche, K. K. Unger, U. Esser, B. Eray, U. Trüdinger and J. N. Kinkel, *J. Chromatogr.*, 465 (1989) 39.
3 G. Schomburg, *LC·GC*, 6 (1987) 1.
4 G. Schomburg, J. Köhler and P. Kolla, *Chromatographia*, 23 (1987) 465.
5 G. Schomburg, J. Köhler and G. Heinemann, *Chromatographia*, 23 (1987) 435.
6 G. Schomburg, J. Köhler, H. Figge, A. Deege and U. Bien-Vogelsang, *Chromatographia*, 18 (1984) 265.
7 G. Schomburg, H. Figge, A. Deege and J. Köhler, *J. Chromatogr.*, 351 (1986) 393.
8 G. Schomburg, U. Bien-Vogelsang, A. Deege, H. Figge and J. Köhler, *Chromatographia*, 19 (1984) 170.
9 G. Schomburg, A. Deege, J. Köhler and U. Bien-Vogelsang, *J. Chromatogr.*, 282 (1983) 27.
10 R. C. MacKenzie, *Differential Thermal Analysis*, Academic Press, New York, 1982.
11 A. Kurganov, O. Kuzmenko, V. A. Davankov, B. Eray, K. K. Unger and U. Trüdinger, *J. Chromatogr.*, in press.
12 V. A. Davankov, A. Kurganov and K. K. Unger, *J. Chromatogr.*, in press.
13 C. T. Mant and R. S. Hodges, *LC Mag.*, 4 (1986) 250, 252 and 254.
14 J. M. R. Parker, C. T. Mant and R. S. Hodges, *Chromatographia*, 24 (1987) 832.
15 C. T. Mant, T. W. L. Burke and R. S. Hodges, *Chromatographia*, 24 (1987) 565.
16 C. T. Mant and R. S. Hodges, *Chromatographia*, 34 (1987) 805.
17 K. Siegbahn, *Nova Acta Regiae Soc. Sci. Ups., Ser. IV*, (1967) 20.
18 W. Herzog, *Farbe Lack*, 90, No. 2 (1984) 102.
19 K. D. Lork, K. K. Unger, H. Brückner and M. T. W. Hearn, *J. Chromatogr.*, 476 (1989) 135.
20 K. K. Unger, G. Jilge, R. Janzen, H. Giesche and J. N. Kinkel, *Chromatographia*, 22 (1986) 7.
21 G. Jilge, K. K. Unger, U. Esser, H. J. Schäfer, G. Rathgeber and W. Müller, *J. Chromatogr.*, 476 (1989) 37.
22 K. K. Unger, G. Jilge, J. N. Kinkel and M. T. W. Hearn, *J. Chromatogr.*, 359 (1986) 61.
23 R. Janzen, K. K. Unger, H. Giesche, J. N. Kinkel and M. T. W. Hearn, *J. Chromatogr.*, 397 (1987) 81.

Journal of Chromatography, 517 (1990) 285–295
Elsevier Science Publishers B.V., Amsterdam

CHROMSYMP. 1959

Competition between phenylalanine and acetic acid in a chromatographic column as indicated by their adsorption isotherms

SHULAMIT LEVIN* and SALEH ABU-LAFI
Pharmaceutical Chemistry Department, School of Pharmacy, The Hebrew University of Jerusalem, Jerusalem 91120 (Israel)

ABSTRACT

Competition between phenylalanine and acetic acid was investigated through their adsorption isotherms when both compounds were used as mobile phase additives. Acetic acid was the acid component of an acetate buffer of pH 3.7. The system peak corresponding to phenylalanine was used for measurement of its adsorption isotherms at four different buffer concentrations, during detection at 254 nm. The adsorption isotherms showed a considerable influence of the acetic acid on the retention of phenylalanine. Therefore, acetic acid was considered to be a mobile phase additive that modifies the stationary phase and competes with the phenylalanine. The solubility of the phenylalanine was measured at four different buffer concentrations, and appeared to be constant. Therefore, a decrease in retention due to solubility changes was ruled out. The system peak corresponding to the acetic acid was used for the determination of the adsorption isotherm of acetic acid using detection at 220 nm. Phenylalanine enabled the visualization of the same system peak at 254 nm. Comparison of the capacity factor of the acetic acid system peak, obtained in the presence of phenylalanine in the mobile phase, with that of the same peak without phenylalanine showed very small differences over a wide range of concentrations. Therefore, it was concluded that distribution of acetic acid was not much affected by the presence of the other component in the mobile phase. Phenylalanine was injected at overload concentrations into mobile phases containing the acetate buffer only. The peak shapes and retentions behaved generally as expected from the adsorption isotherms.

INTRODUCTION

The chromatographic separation of ionizable solutes such as amino acids is usually optimized by changing the buffer concentration in the mobile phase. Acetate buffer is commonly used for the separation of ionizable compounds[1]. The buffer is used to maintain a constant degree of ionization of the solute and to maintain a constant ionic strength. However, acetic acid can also modify the stationary phase

0021-9673/90/$03.50

and change the retention of solutes. In this work we studied the influence of the buffer concentration on the capacity ratio of ionizable solutes as a result of competition between them. The ionizable component chosen for this purpose was phenylalanine, an amino acid that shows absorption at 254 nm.

A mobile phase that contains buffer is multi-component. It has at least three components in addition to water, the acid or base in their molecular form and the cations and anions of the salt. In the case of the acetate buffer in our system, the pH was 3.7, and it contained acetic acid and sodium acetate in the ratio of 9:1. Molecular acetic acid is adsorbed on the stationary phase to some extent[2–4] and therefore it modifies the surface of the column. At high concentrations and a constant pH, the acetic acid can be seen as a component that plays the role of an organic solvent modifier, at least in terms of competition with the solute on the stationary phase. The interaction between acetic acid and phenylalanine was studied here by using both compounds in the mobile phase at various compositions. Competition was investigated by studying the system peaks of phenylalanine and acetic acid in the vacancy mode.

System peaks appear in the chromatograms in addition to solute peaks when a sample different from the mobile phase is injected, under the following circumstances: the mobile phase is multi-component; some or all the mobile phase components show a high detector background; and part or all of the mobile phase components are adsorbed on the stationary phase. All types of chromatographic systems display these peaks: reversed- and normal-phase[5–10], ion-pair with UV detection[1,11–27], ion-exchange[28–31] and even gel permeation[32–36] systems.

Some background on the origins, significance and behaviour of system peaks has been described previously[2–5,22–27,37–39,40–42]. When a mobile phase component is adsorbed on the stationary phase, its corresponding system peak has a capacity factor greater than zero. Identification and quantitative treatment of system peaks permitted the calculation of the capacity factors of mobile phase components[2–4]. It has also been shown that the adsorption isotherm of a particular mobile phase component can be calculated from the corresponding system peak[3].

A theoretical and experimental treatment of system peaks in non-linear chromatography was undertaken by Golshan-Shirazi and Guiochon[37–39], using conditions in which competition between the solute and mobile phase components occurs. It was shown that injection of a solute into a binary mobile phase was accompanied by two system peaks in addition to the solute peak. One of the two system peaks was eluted according to the capacity factor of the corresponding mobile phase component and the other accompanied the solute peak. Therefore, in principle, a mobile phase component can show up in more than one system peak.

System peaks were used in ion-pair chromatography with UV detection of solutes with no chromophore[21–27]. An ion-pairing UV-absorbing agent was added to the mobile phase to manipulate the selectivity and to reveal the solutes. The sample components were eluted according to their particular capacity factors, and could show up in the chromatogram owing to the presence of the detection agent in the mobile phase. Peaks of solutes with no chromophore could be revealed in this chromatographic system owing to the presence of an excess or a lack of mobile phase component in each of the solute zones. An excess or lack of a mobile phase component, exhibited as a peak, is actually a system peak. As the detector was selective only for the mobile

phase additive, the recorded chromatograms displayed only system peaks. Thus, in chromatography with UV detection, where the solute is detected via the detection agent owing to ion pairing or competition, the peak recorded in the chromatogram as the solute peak is actually a system peak.

Phenylalanine was used as the detection agent in this work; the detector, operating at 254 nm, was selctive for phenylalanine only. The strongly adsorbed additive in the mobile phase was phenylalanine and acetic acid served as the weakly adsorbed component. Various buffer and phenylalanine concentrations were used, with different degrees of interference or competition between them.

THEORY

When the mobile phase is introduced into the chromatographic column, acetic acid and phenylalanine are partitioned between the two phases according to their adsorption isotherms. Equilibrium is obtained when the ratio between the amounts of the components in the mobile and the stationary phases remains constant. At that point, the composition of the effluent is constant, the concentration of the mobile phase component is C_{eq} and the amount on the stationary phase is Q_{eq}. At low mobile phase additive concentrations, the dependence of the amounts of phenylalanine and acetic acid in the stationary phase, $Q_{eq,P}$ and $Q_{eq,A}$, respectively, on their concentrations in the mobile phase, $C_{eq,P}$ and $C_{eq,A}$, respectively, is described by the individual adsorption isotherm of each component. However, at high concentrations, $Q_{eq,P}$ may also depend on the concentration of the acetic acid, $C_{eq,A}$, and $Q_{eq,A}$ might depend also on $C_{eq,P}$. In this case a competitive adsorption isotherm can describe the mutual dependence[39].

In this work we used system peaks in the vacancy mode of chromatography to study competitive conditions. A pure solvent with no additives is injected in this mode, *i.e.*, the injection volume becomes vacant of phenylalanine and acetic acid relative to the equilibrium state. The relative vacancy induces desorption of net amounts of dQ_P and dQ_A moles from the extraction layer on the stationary phase for re-equilibration. The amount on the stationary phase within the injection volume after re-equilibration is Q_i, rather than $Q_{eq,i}$, so that

$$Q_{eq,i} - Q_i = dQ_i \qquad i = A, P \tag{1}$$

In the vacancy mode, $dQ > 0$, the amount being released from the stationary phase into the injection volume to compensate for the vacancy. The difference dC_i between the equilibrium concentration and the new concentration within the injection volume is minute when the sample volume is very small:

$$C_{eq,i} - C_{m,i} = dC_i \tag{2}$$

The small disturbance dC_i of the particular component moves down the column at a constant velocity, dictated by its adsorption properties $[u_0/(1 + dQ_i/dC_i)]$. This disturbance is called the system peak. As mentioned above, Golshan-Shirazi and Guiochon[39] showed that injection of a solute can result in more than one system peak for a mobile phase component. Nevertheless, there is always one system peak that

elutes according to a particular component's capacity factor, k'_i, which can serve for the measurement of its adsorption isotherm.

The ratio dQ_i/dC_i of each solute is actually its k'_i, which is directly proportional to the slope of its adsorption isotherm. Hence the adsorption isotherm can be measured from k'_i of the respective system peak, using the following equation:

$$Q_{eq,i} = \int_0^{C_{eq,i}} k'_i \, dC_i \tag{3}$$

This is the principle on which the minor perturbation or system peak method for adsorption isotherm measurements is based. The concentration of the particular component in the mobile phase is changed, then the respective k' of the system peak is measured experimentally according to the equation $k' = (t_R - t_0)/t_0$. The capacity factor corresponding to the particular components k'_i is multiplied by the difference in its concentration, dC_i, in each step, and summation is done over the range of concentrations from 0 to the particular point $Q_{eq,i}$.

EXPERIMENTAL

Materials

The mobile phase was prepared by dissolving the appropriate amounts of phenylalanine (Merck, Darmstadt, F.R.G.) in acetate buffer (pH 3.7). The acetate buffer consisted of analytical-reagent grade sodium acetate (Merck)–acetic acid (Frutarom, Haifa, Israel) (1:9).

Instrumentation

The high-performance liquid chromatographic (HPLC) system that was used in most of the experiments included a Model 880-UP single-line high-pressure pump (Jasco, Tokyo, Japan) with a Rheodyne injection valve using a 20-μl loop. The chromatograms were detected with a UV-1 single-path monitor (Pharmacia, Bromma, Sweden) at 254 nm in most instances and at 280 nm in some of the adsorption isotherm measurements when the background of the mobile phase was too high for the detector to balance. An SP8300 UV detector (Spectra-Physics, Santa Clara, CA, U.S.A.) operated on 254 nm was used when high concentrations of phenylalanine were injected. All the chromatograms were recorded on a single-pen Unicorder U-228 recorder (Pantos, Nippon Danshi Kagashu, Japan).

Adsorption isotherms of acetic acid were measured using another chromatographic system: the solvent delivery system was a Hitachi L-6200 (Merck) and the detector was an HP series 1050 (Hewlett Packard, Palo Alto, CA, U.S.A.) operating at 220 nm, with an HP 3396A integrator (Hewlett Packard).

The temperature was kept constant to within ± 0.5°C using a circulating water-bath.

Procedure

All the chromatographic runs were done with a LiChrosorb RP-18 cartridge (250 × 4 mm I.D.) (Merck). The temperature was kept constant at 30°C throughout

the experiments and the flow-rate was 1.5 ml/min. The system was thoroughly washed with acetonitrile–water occasionally, especially between changes in the mobile phase composition. At least 15 column volumes were eluted until a stable baseline was obtained, when phenylalanine was added to the mobile phase.

Measurements of adsorption isotherms

Adsorption isotherms of phenylalanine and sodium acetate were measured by integration of the system peak capacity factors. The concentration of phenylalanine in the mobile phase, C_{eq}, was gradually changed at each buffer concentration and the system peak capacity factors were measured. The calculation is explained in the Theory section.

Solubility of phenylalanine

An excess amount of phenylalanine (0.005 mol) was added to 25 ml of the four buffer concentrations, 0.01, 0.1, 0.5 and 1 mol/l, to obtain precipitates. The saturated solutions were stirred overnight, filtered, diluted (1:40) and re-injected into the HPLC system, with a 1 *M* buffer concentration in the mobile phase. Peaks areas were converted to concentrations by a calibration graph.

RESULTS AND DISCUSSION

Measurements of adsorption isotherms from system peaks

The chromatographic system described here consisted of a reversed-phase column and an aqueous solution of acetate buffer and phenylalanine as the mobile phase. The chromatograms obtained at four buffer concentrations are shown in Fig. 1. Detection was effected at 254 nm, so phenylalanine could serve for the detection of all three system peaks, marked A, B and C in Fig. 1. Peak A corresponds to an unretained species, whereas B and C can both be related to species adsorbed on the stationary phase. The retention times of peaks A and B can be related to acetate salt and acetic acid, respectively, in agreement with a previously described system, which included acetate buffer[3]. Peak C eluted at a capacity factor corresponding to phenylalanine. The peaks could appear negative or positive. Peaks A and B at buffer concentrations 0.5 and 1 *M* had a derive-like shape, probably due to interference from the acetate or to refractive index perturbations in the flow cell at the extremely high concentration. A peak appears negative when the detector response to the sample zone is lower than that to the mobile phase. At low acetate concentrations peaks A and B were small because the interference of phenylalanine with the other components was small.

Phenylalanine. Adsorption isotherms of phenylalanine were calculated from the capacity factors of system peak C at increasing phenylalanine concentrations in the mobile phase. Four adsorption isotherms, measured at different concentrations of the acetate buffer in the mobile phase, are shown in Fig. 2. In addition, the adsorption isotherm of the acetic acid was calculated from peak B capacity factors at increasing buffer concentrations with no other additives. The parameters a and b for phenylalanine and acetic acid, which were calculated according to the Langmuir expression:

$$Q_{eq,i} = a_i C_{eq,i}/(1 + b_i C_{eq,i}) \quad (4)$$

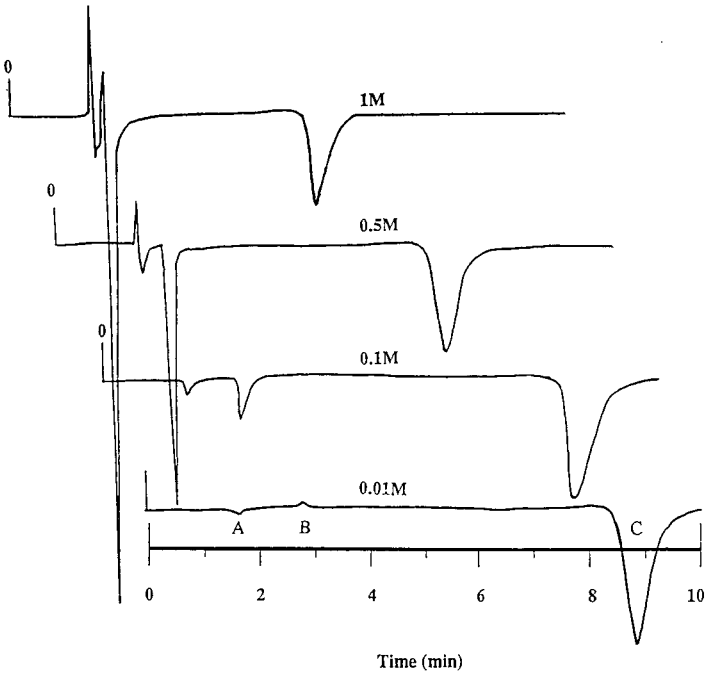

Fig. 1. Chromatograms obtained when water was injected into the mobile phase. The buffer concentrations are marked on the chromatograms. The phenylalanine concentration was 0.005 *M* and full-scale was 0.04 absorbance in all four instances.

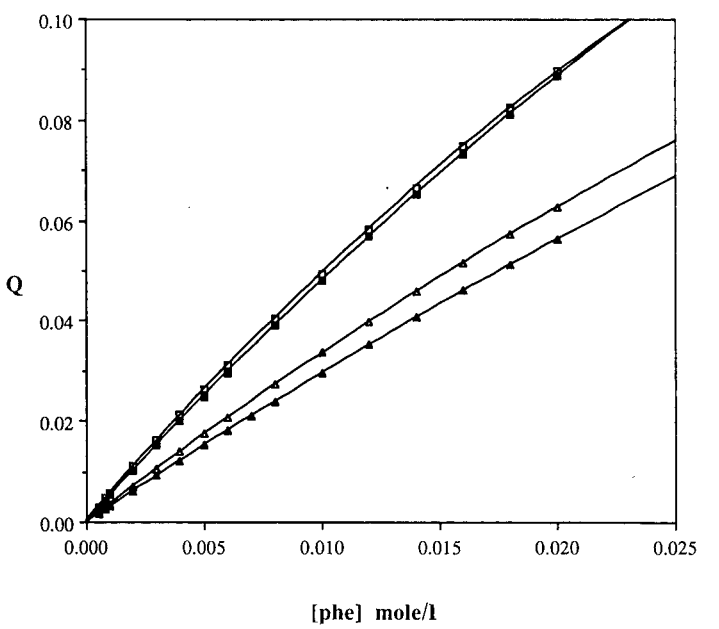

Fig. 2. Adsorption isotherms of phenylalanine at four different phenylalanine concentrations in the mobile phase. Buffer concentrations: □ = 0.01; ■ = 0.1; △ = 0.5; ▲ = 1.0 *M*.

TABLE I

ADSORPTION ISOTHERM PARAMETERS OF PHENYLALANINE AT FOUR DIFFERENT ACETATE BUFFER CONCENTRATIONS AND THE INDIVIDUAL ADSORPTION ISOTHERM OF ACETIC ACID

Compound	*Buffer concentration (mol/l)*	*a*	*b*
Phenylalanine	0.01	5.85	19.65
	0.1	5.35	13.76
	0.5	3.66	9.6
	1	3.14	6.89
Acetic acid	No phenylalanine	1.04	1.91

are given in Table I. Parameter a is actually the slope of the isotherm close to the origin, where it is linear. Parameter b is proportional to the saturation concentration in the column, namely the concentration where the isotherm levels off. It can be seen that both a and b were affected by the buffer concentration. The capacity factor of phenylalanine decreased at the origin and over the whole range of concentrations, in addition to the saturation concentration. These effects were caused by the increase in the acetic acid concentration. The acetic acid served as an organic modifier that competes with the phenylalanine on the stationary phase partition sites. In order to verify that the decrease in the retention of phenylalanine was not due to the effect of ionic strength on the solubility, a test was made. Solubility was measured by preparing saturated solutions of phenylalanine at the four buffer concentrations. The phenylalanine solubility, as shown in Table II, was not significantly changed, hence it certainly could not be responsible for the considerable change in the retention.

The isotherm parameters a_i and b_i used in eqn. 4 should actually be expressed in mathematical terms to depict the competition between the solutes over the whole range of compositions. For that purpose, there is a need for measurements of an appropriate set of adsorption isotherms at various mobile phase compositions to represent the whole range of competitive conditions. A systematic measurement of k' of the system peaks of phenylalanine and acetic acid at various concentration ratios is the key for the overall competitive isotherm. A competitive adsorption isotherm was used by Golshan-Shirazi and Guiochon[39]:

$$Q_1 = a_1 C_1/(1 + b_1 C_1 + b_2 C_2) \tag{5}$$

TABLE II

SOLUBILITY OF PHENYLALANINE IN FOUR ACETATE BUFFER CONCENTRATIONS (pH 3.7) AT ROOM TEMPERATURE

Buffer concentration (mol/l)	*Phenylalanine solubility (mol/l)*
0.01	0.158
0.1	0.135
0.5	0.141
1.0	0.153

In our system component 1 was acetic acid and 2 was phenylalanine. Here, the terms a and b from each individual adsorption isotherm, measured with no competitors, should be used. We took the parameters a and b obtained at 0.01 M buffer, *i.e.*, the conditions with the minimum competition, as the parameters of the individual isotherm of phenylalanine. Q values were calculated at buffer concentrations of 0.1, 0.5 and 1 M according to eqn. 5 using the isotherm parameters for acetic acid in Table I. Poor agreement was found between the calculated values and $Q_{eq,P}$ values measured by integration of the system peak capacity factor. The measurement of the individual isotherm of phenylalanine and the fit of eqn. 5 to the experimental isotherms obtained at various mobile phase compositions is currently under study.

Acetic acid. The capacity factor of peak B was not affected much by changes in the phenylalanine concentration in the mobile phase, as can be seen from Fig. 3. This figure shows the curves for k' of peak B as a function of acetic acid concentration with and without phenylalanine. Integration of the curve with no phenylalanine gave the individual adsorption isotherm of acetic acid from which the a and b values in Table I were calculated. The other curves show k' for peak B as function of the concentration of acetic acid at four concentrations (0.009, 0.09, 0.45 and 0.9 M). Each curve corresponds to a different phenylalanine concentration in the mobile phase as indicated.

The curves lie very close together, indicating that the presence of phenylalanine had almost no effect on the distribution of acetic acid. This observation is in agreement with a previous publication, in which the column void volume was calculated from the

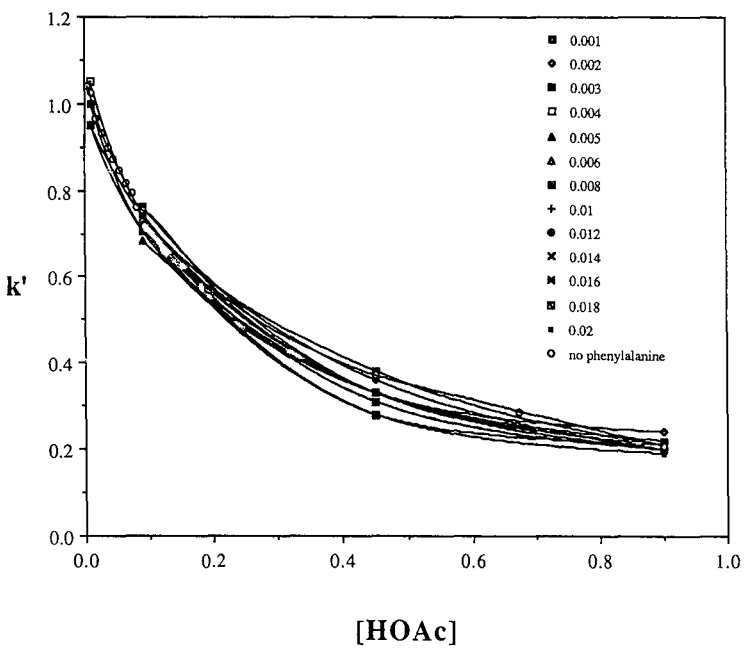

Fig. 3. Capacity factor of peak B as function of the acetic acid (HOAc) concentration in the mobile phase at various phenylalanine concentrations (as specified, in M).

acetic acid system peak[4]. In this work, the presence of various alkylsulphonates had little influence on the capacity factor of the acetic acid.

Adsorption isotherms of mixtures can also be measured by frontal analysis, provided that the inflection points in the breakthrough curves are distinguishable. Comparison of adsorption isotherms obtained by system peaks with other methods are under investigation.

Peak shape under overload conditions

The relationship between adsorption isotherms and peak shape in non-linear chromatography was intensively investigated by Guiochon[43]. The chromatograms of phenylalanine at an overloading concentration (0.1 *M*) injected into four different mobile phases are shown in Fig. 4. The concentrations of the buffer in the mobile phase are specified on the chromatograms. The most important points to note are the peaks shapes and retention. The peaks have sharp fronts and diffuse rears, as expected from their adsorption isotherms.

Retention of the phenylalanine peak in Fig. 4 decreased with increase in buffer concentration. This decrease in retention agrees with the behaviour of the adsorption isotherms due to higher concentrations of acetic acid in the mobile phase.

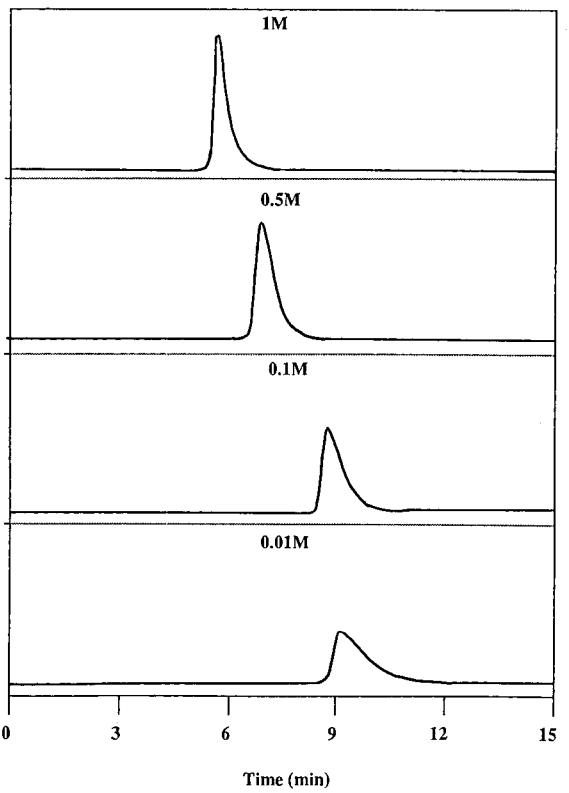

Fig. 4. Overload concentration (0.1 *M*) of phenylalanine injected into four different buffer concentrations, indicated.

CONCLUSION

When using an organic buffer in the mobile phase, it should be taken into account that the buffer can modify the stationary phase, in addition to its role in keeping the degree of ionization of the solute constant. The retention of ionizable solutes can be affected by the molecular acid or base component of the buffer, which may act like an organic modifier in the mobile phase. This point is especially important in the non-linear range of chromatography, where competition between components dictates parameters such as the separation efficiency and solute purity. Therefore, competitive adsorption isotherms are needed in order to predict the conditions and the extent of competition among the solutes, and between solutes and mobile phase components. However, the measurement of an overall competitive adsorption isotherm is not a trivial task. We suggest here that system peaks can be used for this purpose, provided that the right set of representative adsorption isotherms at various competitor compositions is chosen. The set presented in this paper is just a first example.

ACKNOWLEDGEMENTS

We are grateful to Prof. E. Breuer for allowing us to use his HPLC system to measure the adsorption isotherms of the acetic acid, and to Prof. R. Mechoulam for lending us his UV detector.

REFERENCES

1 S. Levin and E. Grushka, *Anal. Chem.*, 57 (1985) 1830–1835.
2 S. Levin and E. Grushka, *Anal. Chem.*, 58 (1986) 1602–1607.
3 S. Levin and E. Grushka, *Anal. Chem.*, 59 (1987) 1157–1164.
4 S. Levin and E. Grushka, *Anal. Chem.*, 61 (1989) 2428–2433.
5 D. J. Solms, T. W. Smuts and V. Pretorius, *J. Chromatogr. Sci.*, 9 (1971) 600–603.
6 R. M. McCormick and B. L. Karger, *J. Chromatogr.*, 199 (1980) 259–273.
7 W. R. Melander, J. F. Erard and Cs. Horváth, *J. Chromatogr.*, 282 (1983) 229–248.
8 D. Berek, T. Bleha and Z. Pevna, *J. Chromatogr. Sci.*, 14 (1976) 560.
9 D. Berek, M. Chalanyova and T. Macko, *J. Chromatogr.*, 286 (1984) 185–192.
10 R. P. W. Scott, C. G. Scott and P. Kucera, *Anal. Chem.*, 44 (1972) 100-104
11 B. A. Bidlingmeyer and F. V. Warren, Jr., *Anal. Chem.*, 54 (1982) 2351–2356
12 F. V. Warren and B. A. Bidlingmeyer, *Anal. Chem.*, 56 (1984) 487–491.
13 M. Denkert, L. Hackzell, G. Schill and E. Sjogren, *J. Chromatogr.*, 218 (1981) 31–43.
14 L. Hackzell and G. Schill, *Chromatographia*, 15 (1982) 437.
15 L. Hackzell, T. Rydberg and G. Schill, *J. Chromatogr.*, 282 (1983) 179–191.
16 P. Herne, M. Renson and J. Crommen, *Chromatographia*, 19 (1984) 274.
17 W. E. Barber and P. W. Carr, *J. Chromatogr.*, 260 (1983) 89–96.
18 W. E. Barber and P. W. Carr, *J. Chromatogr.*, 301 (1984) 25–38.
19 W. E. Barber and P. W. Carr, *J. Chromatogr.*, 316 (1984) 211–225.
20 J. J. Stranahan and S. N. Demings, *Anal. Chem.*, 54 (1982) 1540–1546.
21 B. A. Bidlingmeyer, S. N. Deming, W. P. Price, Jr., B. Sachok and M. Petrusek, *J. Chromatogr.*, 186 (1973) 419–434.
22 B. Sachok, S. N. Deming and B. A. Bidlingmeyer, *J. Liq. Chromatogr.*, 5 (1982) 389–402.
23 A. Sokolowski, T. Fornstedt and D. Westerlund, *J. Liq. Chromatogr.*, 10 (1987) 1629–1662.
24 J. Crommen, G. Schill, D. Westerlund and L. Hackzell, *Chromatographia*, 24 (1987) 252.
25 T. Takeuchi, S. Watanabe, K. Murase and D. Ishii, *Chromatographia*, 25 (1988) 107.
26 M. Johansson and D. Westerlund, *J. Chromatogr.*, 452 (1988) 241–255.

27 E. Arvidsson, J. Crommen, G. Schill and D. Westerlund, *J. Chromatogr.*, 461 (1989) 429.
28 R. M. Cassidy and M. Fraser, *Chromatographia*, 18 (1984) 369.
29 J. S. Fritz, D. T. Gjede and R. M. Becker, *Anal. Chem.*, 52 (1980) 1519–1522.
30 H. Hershcovitz, Ch. Yarnitzky and G. Schmuckler, *J. Chromatogr.*, 244 (1982) 217–224.
31 N. E. Skelly, *Anal. Chem.*, 54 (1982) 712.
32 N. Yoza, T. Ogata, Y. Ueno and S. Ohashi, *J. Chromatogr.*, 62 (1971) 295–305.
33 T. Deguchi, A. Hisanaga and H. Nagai, *J. Chromatogr.*, 133 (1977) 173–179.
34 M. Shibukawa and N. Ohta, *Anal. Chem.*, 54 (1985) 265–271.
35 I. Katime, A. Campos and J. M. T. Rivera, *Eur. Polym. J.*, 15 (1979) 291–293.
36 A. Campos, L. Borque and J. E. Fiqueruelo, *J. Chromatogr.*, 140 (1977) 219–227.
37 S. Golshan-Rhirazi and G. Guiochon, *J. Chromatogr.*, 461 (1989) 1–18.
38 S. Golshan-Shirazi and G. Guiochin, *J. Chromatogr.*, 461 (1989) 19–34.
39 S. Golshan-Shirazi and G. Guiochon, *Anal. Chem.*, 61 (1989) 2373–2380.
40 F. Riedo and E. Sz. Kovats, *J. Chromatogr.*, 239 (1982) 1–28.
41 N. Le Ha, J. Ungvaral and E. Sz. Kovats, *Anal. Chem.*, 54 (1982) 2410–2421.
42 W. R. Melander, J. F. Erard and Cs. Horvath, *J. Chromatogr.*, 282 (1983) 211.
43 G. Guiochon and A. Katti, *Chromatographia*, 24 (1987) 165–189.

Journal of Chromatography, 517 (1990) 297–304
Elsevier Science Publishers B.V., Amsterdam

CHROMSYMP. 1972

Design of liquid chromatography capillary columns

RAYMOND P. W. SCOTT
Chemistry Department, Georgetown University, Washington, DC 2001 (U.S.A.)

ABSTRACT

The theory of open tubular columns is extended to liquid chromatography without regard to the limitations of the associated chromatographic equipment. Methods are given to permit the optimum column length, radius and film thickness to be calculated to provide the minimum analysis time for any given separation. The basic data required are the separation ratio of the critical pair, the distribution coefficient between the stationary and mobile phase of the first eluted solute of the critical pair, its diffusion coefficient in the mobile phase, the separation ratio of the last eluted peak to the first eluted solute of the critical pair, the viscosity of the mobile phase and the maximum available inlet pressure. It is shown that, with the phase system considered, if the separation is to be achieved in the minimum time then the first solute of the critical pair should be eluted at a capacity factor (k') of 2.7 irrespective of the separation ratio of the critical pair. Consequently the optimum film thickness depends solely on the optimum radius and the distribution coefficient of the solute between the two phases. Due to an optimum value for k' being identified the equations for analysis time and column length are greatly simplified.

INTRODUCTION

Liquid chromatography (LC) column theory is now well established and equations have been developed for packed columns that allow the column length, radius and particle diameter to be calculated, that provides the minimum analysis time for any given separation[1]. These equations were derived employing the Van Deemter equation[2] to describe the dispersion taking place in a packed column. The Van Deemter equation has been shown to accurately predict the plate height at, and around, the optimum mobile phase velocity from basic chromatographic and physical data of the solute–solvent system employed[3]. The equations necessary to design capillary columns have not, so far, been developed to the same extent for LC and it is the purpose of this paper to examine capillary column design and to develop procedures to calculate the column length, radius and stationary phase film thickness that will achieve a specific separation in the minimum time.

To develop these procedures, the reduced chromatogram will be employed that contains the closest eluted pair of solutes (the critical pair) and the last eluted solute of

0021-9673/90/$03.50

any given complex mixture. If the closest eluted solute pair is separated and the last peak of the mixture eluted then it is assumed that the mixture has been completely resolved. There may be rare exceptions where this may not be the case, possibly if the two solutes of the closest eluted pair differ widely in molecular weight[4], but in the vast majority of separations the assumption will be correct. The basic data that will be employed will be the separation ratio of the critical pair, the distribution coefficient of the first solute of the critical pair between the stationary phase and the mobile phase, its diffusion coefficient in the mobile phase, the separation ratio of the last eluted peak to that of the first solute of the critical pair, the viscosity of the mobile phase and the maximum inlet pressure.

Although capillary, or open tubular columns are the most efficient for chromatographic separations, the demands they make on the associated chromatographic equipment are so stringent that, at this time, their effective use is largely confined to *gas* chromatographic separations. Although much research is being carried out in this area, at this time, there are few, if any, LC capillary column chromatographs commercially available. Small volume sample valves have been developed and the detector cell volumes have been much reduced, but despite this, the column diameters must be made much above the optimum size for effective LC separations to be successfully carried out. In due course, instrumentation will no doubt meet the demands of the optimized, very small diameter, LC capillary columns. As a result, in this paper the shortcomings of contemporary apparatus are largely ignored and thus, by developing LC capillary column design, very fast and highly efficient columns will be ready and available when the appropriate instrumentation is developed.

THEORY

The basic equation describing the dispersion that takes place in an open tubular column was developed by Golay[5,6] and takes the following form:

$$H = 2D_M/u + (1 + 6k' + 11k'^2)r^2u/24(1 + k')^2D_M + k'^3r^2u/6(1 + k')^2K^2D_S \quad (1)$$

where H is the variance per unit length of the column for the given solute, k' is the capacity factor of the eluted solute, K is the distribution coefficient of the solute between the two phases, D_M is the diffusivity of the solute in the mobile phase, D_S is the diffusivity of the solute in the stationary phase, r is the radius of the column, and u is the linear velocity of the mobile phase. The Golay equation can be put in the reduced form:

$$H = B/u + Cu \quad (2)$$

where $B = 2D_M/u$ and $C = (1 + 6k' + 11k'^2)r^2/24(1 + k')^2D_M + k'^3r^2/6(1 + k')^2K^2D_S$. Differentiating eqn. 2 with respect to u:

$$dH/du = -B/u^2 + C$$

Thus, when $H = H_{min}$:

$$-B/u^2 + C = 0$$

and

$$u_{opt} = (B/C)^{0.5} \tag{3}$$

Furthermore,

$$H_{min} = B/u_{opt} + Cu_{opt}$$

$$= B/(B/C)^{0.5} + C(B/C)^{0.5}$$

or

$$H_{min} = 2(BC)^{0.5} \tag{4}$$

Eqns. 1, 3 and 4 are all well established and important in column design.

The equation that allows the number of theoretical plates required to effect a given separation was derived from the plate theory by Purnell[7] and is as follows:

$$n = [4(1 + k')/k'(\alpha - 1)]^2 \tag{5}$$

where α is the separation factor of the critical pair, n is the number of theoretical plates, and k' is as previously defined. It should be noted that k' refers to the *first* eluted solute not the second which is also often used and results in a slightly different equation for n.

Now the time required to elute the first of the critical pair, which will be simply related to the total analysis time, is given by:

$$t = l(1 + k')/u_{opt} \tag{6}$$

where t, is the elution time for the first solute of the critical pair and l, is the length of the column. Now, $l = nH_{min}$, thus,

$$t = nH_{min}(1 + k')/u_{opt} \tag{7}$$

$$= n2(BC)^{0.5}(1 + k')/(B/C)^{0.5}$$

$$= 2nC(1 + k') \tag{8}$$

Substituting for C and n from eqns. 1 and 5,

$$t = [32(1 + k')^3/k'^2(\alpha - 1)^2][(1 + 6k' + 11k'^2)r^2/24(1 + k')^2D_M + k'^3r^2/6(1 + k')^2K^2D_s]$$

which can be simplified to,

$$t = 4(r^2/k'^2 + 7r^2/k' + 17r^2 + 11k'r^2 + 4k'r^2/\beta K^2 + 4k'^2r^2/\beta K^2)/3D_M(\alpha - 1)^2 \tag{9}$$

where $\beta = D_s/D_M$. Now it would appear at first sight, that by differentiating eqn. 9 with respect to r and equating to zero, an expression would be obtained that would give an optimum value r for minimum analysis time. However k' is a function of both d_f, the film thickness of stationary phase *and* r.

It is, therefore, necessary to obtain an expression for t that does not include either k' or d_f. Now $k' = K/a$, where a is the phase ratio of the column. Furthermore, the volume of mobile phase in the column is $\pi r^2 l$ and the volume of stationary phase is $2\pi r l d_f$. Consequently a is given by, $\pi r^2 l/2\pi r l d_f = r/2d_f$ and

$$k' = 2Kd_f/r \tag{10a}$$

Substituting for k' in eqn. 9 from eqn. 10a and simplifying,

$$t = [4/3D_M(\alpha - 1)^2][r^4/(2K^2d_f^2) + 7r^3/(2Kd_f) + 17r^2 + (11 + 4/\beta K^2)2Krd_f + 16d_f^2/\beta] \tag{10b}$$

Now in order to solve for r or d_f for a minimum value of the analysis time (t) then a further relationship must be obtained between r and d_f. From Poiseuille's equation $l = Pr^2/(8\eta u_{opt})$, thus $l = nH_{min} = 2n(BC)^{0.5} = Pr^2/[8\eta(B/C)^{0.5}]$; thus, $2nB = Pr^2/(8\eta)$, where P is the inlet pressure and η is the solvent viscosity.

Now from the Golay equation $B = 2D_M$, thus,

$$n = Pr^2/(32\eta D_M) \tag{11}$$

It is interesting to note from eqn. 11 that when a column is run at its optimum velocity, the efficiency attainable from a capillary column is directly proportional to the inlet pressure and the square of the radius and inversely proportional to the solvent viscosity and *the diffusivity of the solute* in the mobile phase.

Substituting for n in eqn. 11 from eqn. 5,

$$[4(1 + k')/k'(\alpha - 1)]^2 = Pr^2/(32\eta D_M)$$

Substituting $2Kd_f/r$ for k' and simplifying,

$$d_f = r/(2K(r\psi - 1) \tag{12}$$

where,

$$\psi = [(\alpha - 1)^2 P/512\eta D_M]^{0.5} \tag{13}$$

Eqn. 12 gives the required independent relationship between r and d_f. Thus, substituting in eqn. 10 for d_f from eqn. 12,

$$t = [4/3D_M(\alpha - 1)^2]\{r^4\psi^2 + 5r^3\psi + 11r^2 + (11 + 4/\beta K^2)r^2/(r\psi - 1) + \\ + 4r^2/[\beta K^2(r\psi - 1)^2]\} \tag{14}$$

In order to determine the optimum value of the column radius r for the minimum value of analysis time t eqn. 14 should be differentiated and equated to zero and solved for r. However, the algebra becomes extremely clumsy and the solution difficult if not impossible to identify. A simple and practical alternative is to employ a computer with an iterative program that will calculate t for a range of values of r and identify that value of r that gives the minimum value of t. Thus, by employing the appropriate equations the optimum values of d_f *and* k' can also be calculated.

After identifying the optimum values of r, d_f and consequently k' the column length can be determined as follows:

$$l = nH_{min}$$

Substituting for n and H_{min} from eqns. 5 and 4,

$$l = \{[4(1 + k')/k'(\alpha - 1)]^2\}2(BC)^{0.5}$$

$$= \{[4(1 + k')/k'(\alpha - 1)]^2\}2\{(2D_M)[(1 + 6k' + 11k'^2)r^2/24(1 + k')^2D_M + k'^3r^2/6(1 + k')^2K^2D_S]\}^{0.5} \quad (15)$$

DISCUSSION OF THEORY

Eqns. 1–8 are well established and although essential for the subsequent development of the equations necessary to calculate optimum column parameters, do not in themselves deserve comment. Eqns. 9 and 10 are similar to those developed by Scott and Hazeldine[8] for gas chromatographic separations on nylon capillary columns. The treatment given here, however, avoids the assumption of a given column radius and then the optimum film thickness calculated. In this case the optimum radius is *directly determined.* Consequently, the optimum film thickness *appropriate for the optimum column radius* can be calculated. In effect, both column radius and stationary phase film thickness are considered variables.

Eqn. 11 demonstrates that the number of theoretical plates available from a capillary column depends on its radius, inlet pressure, viscosity of the mobile phase and, perhaps a little surprisingly, the diffusivity of the solute in the stationary phase. Taking a viscosity value of 0.003967 P (the viscosity of *n*-heptane at 25°C), a diffusivity value of $2.5 \cdot 10^{-5}$ (the diffusivity of benzyl acetate in *n*-heptane) the efficiency obtainable from columns of different diameter can be calculated for an inlet pressure of 1000 p.s.i. The results are shown in Table I.

It is seen that changing the radius of the column from 1 to 100 μm results in an efficiency change from about two hundred thousand theoretical plates to two thousand million plates. It is also seen that *the smaller the column radius the lower the maximum number of theoretical plates* obtainable from the column. This is contrary to the general impression of many workers in the field who consider that the maximum efficiency is always obtained using columns with the smallest radius. A similar situation has been shown to be true for a packed column where it has been demonstrated[1] that the smaller the particle diameter of the packing the less the maximum number of theoretical plates obtainable for a given inlet pressure. This is

TABLE I

MAXIMUM EFFICIENCIES ATTAINABLE FROM COLUMNS OF DIFFERENT RADIUS

Column radius (μm)	*Column efficiency (theoretical plates)*
1	$2.17 \cdot 10^5$
10	$2.17 \cdot 10^7$
100	$2.17 \cdot 10^9$
Inlet pressure	1000 p.s.i.
Viscosity of mobile phase	0.00397 P
Diffusivity of solute in the mobile phase	$2.5 \cdot 10^{-5}$ cm^2/s

a result of a limited pressure being available and if the fastest separation is obtained by operating at the optimum velocity on a particular column, then to increase the number of theoretical plates the column must be made longer. It follows, that a longer column will have too high an impedance to permit the optimum velocity to be achieved and thus the radius must be increased. In summary, narrow capillary columns should be used for simple separations (large α) and wide columns for difficult separations (small α).

Employing eqn. 14 the analysis time was calculated using a simple iterative computer program that identified both the optimum radius and the optimum film thickness that provided the minimum analysis time. The physical values of the system stated previously were employed with an inlet pressure of 1000 p.s.i. Calculations were carried out for a range of separation ratios for the critical pair extending from 1.01 (a difficult separation) to 1.1 (a moderately simple separation). Three different values 50, 250 and 500 were taken for the distribution coefficient of the first solute of the eluted pair. The value of the capacity factor (k') was also calculated for each separation. The results obtained are shown in Table II.

It is seen that the optimum column radius depends only on the *separation ratio* of the critical pair and is independent of the distribution coefficient. It is also seen that the optimum separation ratio is constant at 2.7 and is independent of both the separation ratio of the critical pair and the distribution coefficient of the first eluted solute. As a consequence the optimum film thickness is defined by the optimum radius and the distribution coefficient.

The value of 2.7 agrees well with the values for the optimum mobile phase velocity predicted by Grushka and Cooke[9]. In the hypothetical design of a capillary column there would be two approaches that would provide the optimum film thickness. One alternative could be to adjust the phase system until the first solute of the critical pair was eluted at a k' of 2.7 and then calculate the optimum radius that would provide the minimum analysis time by the iterative procedure. A second alternative, could be to measure or estimate the magnitude of the distribution coefficient of the first solute and calculate the optimum film thickness after determining the optimum radius. The former method appears more practical, as it employs the column with whatever film thickness it happens to have, and adjusts the phase system to ensure that, that particular film thickness, is optimum for the separation.

TABLE II

OPTIMUM RADIUS AND FILM THICKNESS FOR CAPILLARY COLUMNS CHROMATOGRAPHING SOLUTES OF DIFFERENT SEPARATION RATIOS AND DIFFERENT DISTRIBUTION COEFFICIENTS

Inlet pressure 1000 p.s.i. Viscosity of mobile phase 0.003967 P. Diffusivity of solute in mobile phase $2.5 \cdot 10^{-5}$ cm^2/s. K is the distribution coefficient of the first solute of the critical pair between the mobile and stationary phase.

Separation ratios	*Optimum radius (μm)*	*Optimum k'*	*Optimum film thickness (10^{-6} cm)*		
			K = 50	*K = 250*	*K = 500*
1.01	1.175	2.7	3.175	0.635	0.318
1.02	0.588	2.7	1.588	0.318	0.159
1.03	0.392	2.7	1.058	0.217	0.106
1.04	0.294	2.7	0.794	0.159	0.079
1.05	0.235	2.7	0.635	0.126	0.064
1.06	0.196	2.7	0.529	0.106	0.053
1.07	0.167	2.7	0.454	0.091	0.045
1.08	0.147	2.7	0.397	0.079	0.040
1.09	0.131	2.7	0.353	0.071	0.035
1.10	0.118	2.7	0.318	0.064	0.032

It also follows, that as k' is a constant, with an optimum value of 2.7 for the physical conditions assumed, then the equations for the analysis time and the column length for those conditions can be greatly simplified. Now,

$$t = [32(1 + k')^3/k'^2(\alpha - 1)]2[(1 + 6k' + 11k'^2)r^2/24(1 + k')^2 D_M + k'^3 r^2/6(1 + k')^2 K^2 D_S]$$

Substituting 2.7 for k' in the equation for t, then t_{min} is given by:

$$t_{min} = 222(0.296 r_{opt}^2/D_M + 0.239 r_{opt}^2/K^2 D_S)/(\alpha - 1)^2 \quad (16)$$

where r_{opt}^2 is determined by the iterative program described above.

Now as stated before, $l = nH_{min}$. Thus substituting for n and H_{min} from eqns. 4 and 5,

$$l = 85[(0.296 r_{opt}^2 + 0.239 r_{opt}^2/\beta K^2)^{0.5}/(\alpha - 1)]^2$$

where, again, r_{opt}^2 is determined by the iterative program described above.

It is clear that the column properties determined in this report, depend on the physical constants associated with the phases employed. The effect of solvents of different viscosities, solutes of different diffusivities and columns with different inlet pressures on the optimum column and chromatographic parameters must, in due course, also be identified. It may then be possible, to completely define the fully optimized capillary column and, perhaps, to identify those types of separation that may be amenable to analysis by capillary column LC, employing equipment that is presently available.

REFERENCES

1 E. Katz, K. L. Ogan and R. P. W. Scott, *J. Chromatogr.*, 289 (1984) 65.
2 J. J. Van Deemter, F. J. Zuiderweg and A. Klinkenberg, *Chem. Eng. Sci.*, 5 (1956) 24.
3 E. Katz, K. L. Ogan and R. P. W. Scott, *J. Chromatogr.*, 270 (1983) 51.
4 E. D. Katz and R. P. W. Scott, *J. Chromatogr.*, 270 (1983) 29.
5 M. J. E. Golay, in H. J. Nobels and I. S. Fagerson (Editors), *Gas Chromatography*, Academic Press, New York, 1958, p. 1.
6 M. J. E. Golay, in D. H. Desty (Editor), *Gas Chromatography 1958*, Butterworths, London, 1958, p. 36.
7 J. H. Purnell, *Nature (London)*, 184 (1959) 2009.
8 R. P. W. Scott and G. S. F. Hazeldine, in R. P. W. Scott (Editor), *Gas Chromatography 1960*, Butterworths, London, 1960, p. 4.
9 E. Grushka and W. D. Cooke, *J. Chromatogr. Sci.*, 9 (1971) 310.

Journal of Chromatography, 517 (1990) 305–315
Elsevier Science Publishers B.V., Amsterdam

CHROMSYMP. 1937

Reversed-phase ion-pair chromatography with indirect photometric detection of inorganic anions from residues of low explosives[a]

D. WOOLFSON-BARTFELD and ELI GRUSHKA*
Department of Inorganic and Analytical Chemistry, The Hebrew University, Jerusalem (Israel)
and
SARA ABRAMOVICH-BAR, SHLOMO LEVY and YAIR BAMBERGER
Division of Criminal Identification, National Police Headquarters, Jerusalem (Israel)

ABSTRACT

The analysis of inorganic anions found in residues of low explosives present a difficult forensic problem. Current methods are neither quantitative nor sensitive. While the liquid chromatographic separation of these anions is relatively easy, their detection is difficult since they cannot be detected by conventional high-performance liquid chromatography detectors. We report a method that can detect inorganic anions, which are commonly found in combustion residues of low explosives, by reversed-phase ion-pair liquid chromatography, using indirect UV detection. The ion-pair reagent is benzyltributylammonium chloride. In addition, the phosphate buffer mobile phase contains hexane sulfonate. There is little sample preparation since no interferences were encountered while testing real samples from explosive residues. Detection limits are low and selectivity is high compared with existing techniques. Analysis time is short and the separation can be repeated immediately.

INTRODUCTION

Low explosive residues are difficult to analyze since they contain inorganic salts which originate from the oxidizers. For example, the most popular oxidizers are usually nitrate and chlorate salts with potassium or ammonium as the co-ion[1,2]. Since these explosives are frequently improvised (home made), and since there is no way to predict the ingredients and their amounts in the bomb, they present a complex analytical problem. Additional difficulties in the analysis involve (a) handling the traces which are left for analysis after an explosion, and (b) interferences that result from

[a] This paper was delivered in parts at the *3rd Symposium on Analysis and Detection of Explosives, Mannheim-Neuostheim, F.R.G., July 10–13, 1989.*

0021-9673/90/$03.50

debris and other impurities that are collected together with the sample at the scene of the explosion[2].

The analysis of post explosion samples involves techniques such as extraction with water (for inorganic compounds) or acetone (for organic compounds), spot tests, Fourier-transform infrared spectroscopy, mass spectrometry and ion-exchange chromatography. Other methods are microscopic analysis and X-ray diffraction[3–5]. These methods, while useful, are frequently not specific or sensitive enough for the analysis of inorganic anions. There is a need to develop an analytical method that will be able to detect inorganic anions of explosives and explosive residues.

The method which is described here can separate and detect inorganic anions, which are commonly found in combustion residues of low explosives, by reversed-phase ion-pair liquid chromatography, using indirect UV detection. Inorganic anions are difficult to detect by conventional UV detectors because they are UV transparent. The problem is solved in the present work by using a mobile phase containing a UV-absorbing ion-pair reagent (IPR). Due to adsorption of the IPR on the stationary phase, the reversed-phase column becomes a dynamically coated anion exchanger. The solutes interact with the IPR and, as a result, zones of IPR deficiencies are formed in the column[6]. The inorganic anions are detected indirectly as a result of the detector response to this deficiency of IPR in the mobile phase. The continuous flow of the IPR ensures the stability of the column and of the separation. Indirect detection in high-performance liquid chromatography (HPLC) has been used previously in the forensic laboratory for the analysis of many anions; see for the example the work of Wheals[7].

Reversed-phase columns are commonly used in modern chromatography and are available at a reasonable cost. The instrumentation needed for this method consists of an HLPC system, which is very common in many forensic laboratories. Thus, this new method can be used in many laboratories immediately and without any major expenses which are associated with new instrumentation or columns.

EXPERIMENTAL

Materials

The mobile phase was prepared using deionized water which was filtered through a 0.45-μm Schleicher & Schull membrane filter membrane. Benzyltributylammonium chloride (BTA) and hexane sulfonate were obtained from Sigma Israel (Tel-Aviv, Israel). All chemicals were of analytical-reagent grade.

The column (50 mm × 4.5 mm I.D.) and the guard colum (25 mm × 4.5 mm I.D.) were LiChrospher RP-18 cartridges (Merck, Darmstadt, F.R.G.).

The mobile phase consisted of 4 m*M* BTA, 0.14 m*M* hexane sulfonate and 7 m*M* phosphate buffer (pH 5).

Instrumentation

The chromatographic system consisted of a SP 8000 HPLC system (Spectra-Physics) with a Rheodyne injector (10-μl loop). The detector was a Perkin-Elmer 85B UV–VIS variable-wavelength detector. The recorder and integrator were part of the HPLC system. The column was thermostated at 35 ± 0.1°C.

The spectrum of BTA was obtained with a Perkin-Elmer Lambda 5 UV–VIS spectrophotometer.

Sample preparation

Samples containing post-explosive residues were extracted with water and then filtered and concentrated over a water bath. The solids which remained in the flask were weighed (between 15–30 mg) and diluted to 5–10 ml. Samples were filtered and injected immediately.

RESULTS AND DISCUSSION

In this study we have examined the behavior of nitrite, nitrate, chlorate, sulfate (as sodium salts), thiocyanate and perchlorate (as potassium salts) ions as the inorganic anions. The chromatographic method is a modification of the system described by Barber and Carr[6]. The modifications were made to fit the needs of a forensic laboratory.

Characterization of the ion-pair reagent

The UV spectrum of BTA is shown in Fig. 1. BTA has three absorption maxima: at 269, 262 and 257 nm. We chose 262 nm as the working wavelength of detection since at this wavelength BTA absorbs the most and it should provide the most sensitive detection. Another wavelength, 222 nm, was investigated to detect nitrite and nitrate. The high native absorbance of these anions at this wavelength ensures high sensitivities.

To maintain short analysis times, we used a 5-cm column. This short column did not affect the selectivity but shortened the retention times of most anions and gave sharper peaks. Phosphate buffer was used in order to further ensure sharp chromatographic peaks. The buffer was kept at pH 5 due to the better buffering capacity at that pH. To better control the analysis time and the selectivity of the column, hexane sulfonate was added to the mobile phase. Fig. 2 shows a typical chromatogram of this system with a standard mixture of anions.

Before describing the actual separations, we will examine the effects of some of the experimental parameters. Many parameters influence the retention and selectivity

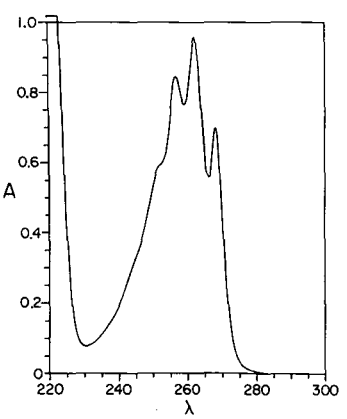

Fig. 1. The UV spectrum of BTA. The solvent is water. λ = Wavelength in nm.

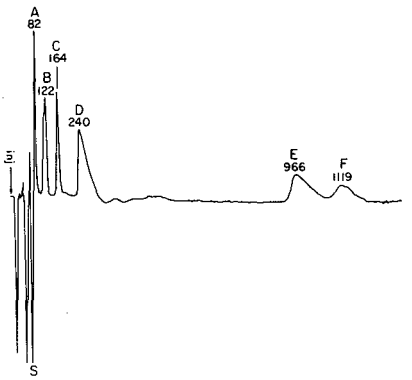

Fig. 2. Chromatogram showing the separation of all six anions studied. Chromatographic conditions are given in the heading of Table I. Peaks: S = system peak; A = nitrite; B = nitrate, C = chlorate; D = sulfate; E = thiocyanate; F = perchlorate. Numbers at peaks are retention times in s.

of the chromatographic system. To optimize the chromatographic system, these experimental parameters must be studied and understood.

Temperature effects

The effect of the temperature on the retention is shown in Fig. 3 which plots ln k' (k' = capacity factor) of five anions as a function of the reciprocal of the temperature (T). The nitrate, chlorate, perchlorate and thiocyanate behave in the 'normal fashion'; namely, the retention times of these solutes decrease as the temperature increases. The retention of sulfate, on the other hand, *increase* with increasing temperatures. As will be shown throughout this paper, the sulfate ion behaves in a different fashion than the rest of the anions. It is thought that in the present chromatographic system the adsorption isotherm of the sulfate ion is not linear.

The slopes of the perchlorate and thiocyanate lines are close in value (2140 as

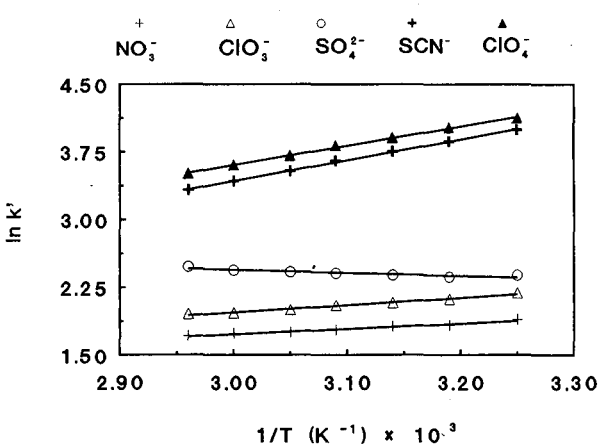

Fig. 3. Dependence of ln k' on $1/T$. The mobile phase contained 4 mM BTA, 5 mM phosphate buffer pH 4.6 and 0.25 mM hexane sulfonate. The flow-rate was 2 ml/min. Detection at 262 nm.

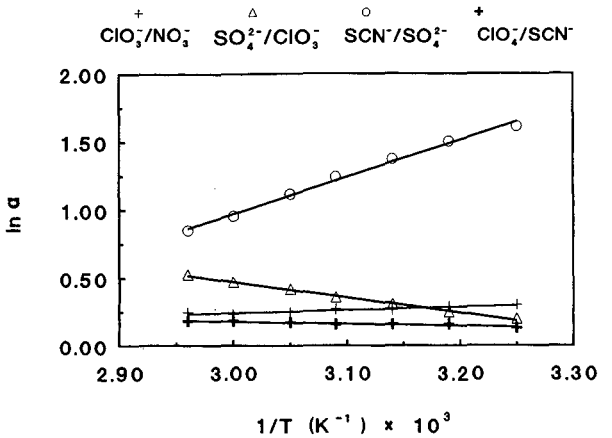

Fig. 4. Dependence of ln α on $1/T$. Chromatographic conditions as in Fig. 3.

compared to 2307). Thus, the selectivity of the system toward these two ions should be, to a large extent, temperature independent. Similarly, the slopes of the nitrate and chlorate lines are fairly similar (590 as compared to 800). The temperature dependence of the selectivity between these two ions should be small. Fig. 4, which gives the dependence of the selectivity, α, on the temperature, shows the temperature independence of α in the case of SCN^- and ClO_4^- and the small temperature dependence of α in the case of nitrate and chlorate. Because of the temperature dependence of the sulfate retention, the selectivity between the sulfate and the chlorate increases with increasing temperatures, while the selectivity between thiocyanate and sulfate decreases sharply as the temperature increases.

Effect of buffer concentration

Fig. 5 shows the dependence of the k' values of nitrite, nitrate, chlorate and

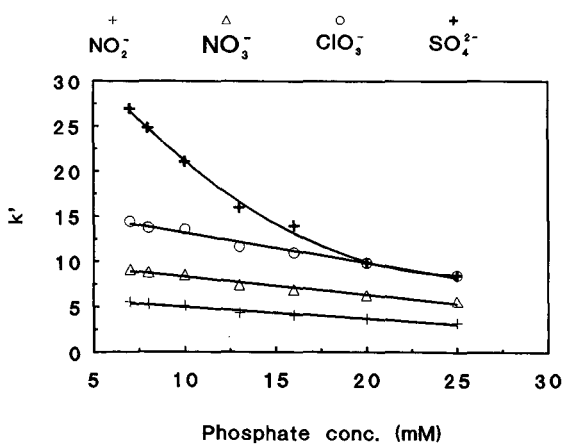

Fig. 5. Dependence of k' on the phosphate concentration. Chromatographic conditions as in Fig. 3, with the exception that the phosphate concentration varied.

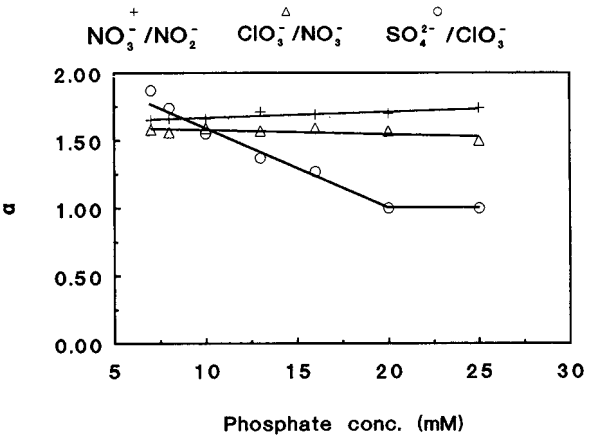

Fig. 6. Selectivity, α, as a function of phosphate concentration. Chromatographic conditions as in Fig. 3, with the exception that the phosphate concentration varied.

sulfate on the buffer concentration. As expected, the k' values of the solutes decrease as the phosphate concentration increases. The greatest change occurs in the case of the sulfate ions. This great change in the retention of sulfate ions with buffer concentration is in agreement with the non-linearity of its adsorption isotherm.

Fig. 6 shows the dependence of the selectivity on the buffer concentration. The selectivity between nitrate and nitrite increases a little with increasing buffer concentrations. The selectivity between chlorate and nitrate decrease a little with increasing phosphate concentrations. However, the selectivity between sulfate and chlorate decreases drastically with buffer concentrations. In fact, at high amounts of phosphate, the resolution between these two solutes disappears completely. Similar behavior of the retention of sulfate was observed by Barber and Carr[8]. Clearly, for the chromatographic system at hand, running at low buffer concentration is advantageous.

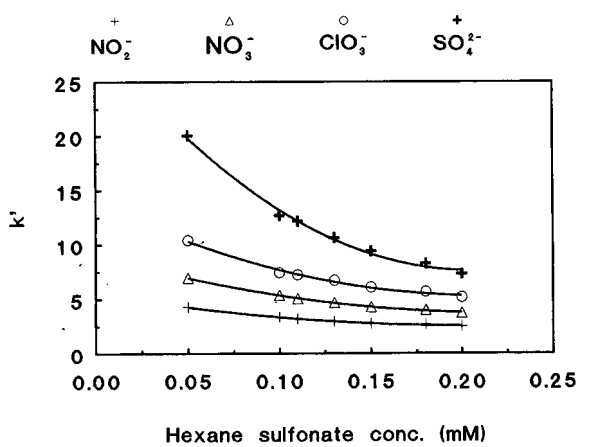

Fig. 7. Dependence of k' on the hexane sulfonate concentration. Chromatographic conditions as in Fig. 3, with the exception that the hexane sulfonate concentration varied.

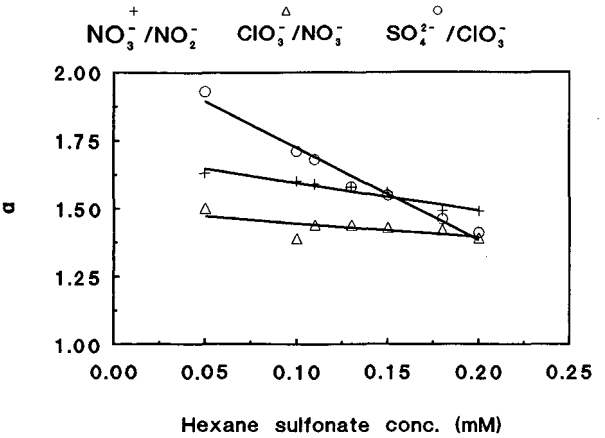

Fig. 8. Dependence of α on the hexane sulfonate concentration. Chromatographic conditions as in Fig. 3, with the exception that the hexane sulfonate concentration varied.

Effect of hexane sulfonate concentration.

The effect of increasing the concentration of the hexane sulfonate in the mobile phase is similar to the effect of changing the buffer concentration. As the hexane sulfonate concentration increases, the retention of the solutes decrease. Fig. 7 shows the k' values of four anions as a function of the sulfonate concentration. Again, the sulfate ions show the greatest dependence on the concentration of the sulfonate.

The selectivity dependence on hexane sulfonate is given in Fig. 8. In all cases, the selectivity decreases with increasing sulfonate in the mobile phase. However, in cases where sulfate ions are not involved, the decrease in the selectivity is small. Figs. 7 and 8 indicate that is is more advantageous to achieve the separation at low concentration of the sulfonate.

Based on the above studies, the chromatographic system which we chose for the separation of nitrite, nitrate, chlorate and sulfate ions, found in post-explosive residues, consisted of an RP-18 column, 4 m*M* BTA, 7 m*M* phosphate buffer at pH 5, 0.14 m*M* hexane sulfonate and temperature of 35°C.

Detection linearity and detection limits

The linearity and the detection limit of the present chromatographic system was examined by preparing calibration curves for all anions at both 262 and at 222 nm. In the concentration range between 0.05 to 10 m*M*, the response was linear for all anions. However, there was a difference in detection limits between the two wavelengths. Table I gives the regression parameters obtained from correlating the peak areas to the concentrations of nitrite, nitrate, chlorate and sulfate. Also given in the table are the detection limits of these four solutes in both wavelengths. The better detection limit toward nitrite and nitrate at 222 nm is due to the strong UV absorption by these two anions. Chlorate and sulfate, on the other hand, show better detection limits at 262 nm. It is felt that the high background absorption of BTA at 222 nm hinders in the detection of low amounts of chlorate and sulfate ions.

TABLE I

REGRESSION PARAMETERS OF PEAK AREAS *VS.* CONCENTRATION (m*M*)

Mobile phase contained 4 m*M* benzyltributylammonium chloride, 7 m*M* phosphate buffer (pH 5), and 0.14 m*M* hexane sulfonate in water. Flow-rate was 2 ml/min. Detection wavelengths were 222 and 262 nm. Temperature was 35 ± 0.1°C. All anions were determined in the present of the other three. a = Slope (divided by 10^4); b = intercept (divided by 10^3); R = correlation coefficients; n = number of different concentrations used to calibrate; DL = detection limits.

Anion	*a*	*b*	*R*	*n*	*DL (ppm)*
Wavelength 222 nm					
Nitrite	17.2	−3.87	0.9997	10	2.8
Nitrate	12.4	−4.07	0.9985	10	0.8
Chlorate	0.85	−3.48	0.9906	6	21.3
Sulfate	1.15	−4.80	0.9930	5	28.4
Wavelength 262 nm					
Nitrite	1.03	−1.11	0.9996	5	48.3
Nitrate	1.16	−2.01	0.9974	7	8.5
Chlorate	1.05	−2.59	0.9976	7	10.7
Sulfate	1.59	−3.23	0.9973	7	14.2

Concentration effects of the solutes

It has been reported[6,9] that the retention times of the solutes can be a function of their injected concentration. In general, as the concentration of the solute increased the retention time decreased. This effect was observed in our system for the sulfate anion and it caused a problem in the identification and quantification of sulfate ions in samples where its concentration was not known (as is the case in explosive residues). To overcome this problem, we have used the sulfate calibration curve and another curve which is obtained by plotting the retention time of sulfate as a function of the injected concentration. Fig. 9 shows the dependence of the area and of the retention time of sulfate on the concentration of that anion. The two curves are used as follows: The concentration of a suspected sulfate peak is ascertained by extrapolation from the retention time. This concentration is correlated to the peak area from

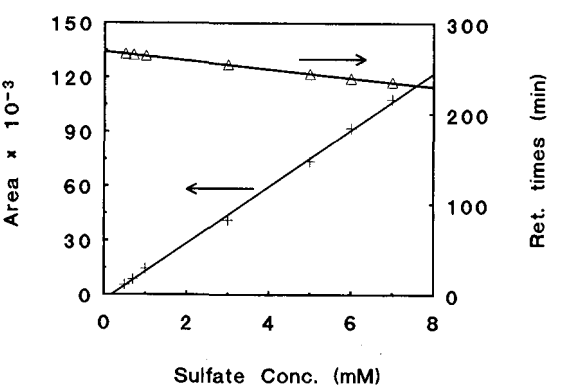

Fig. 9. Dependence of sulfate peak area (+) and retention time (△) on that anion concentration.

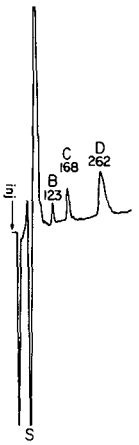

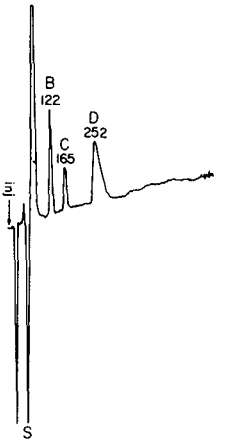

Fig. 10. Chromatogram of water extract from sample 1. The chromatographic conditions are given in Table I. Peaks: S = system peak; B = nitrate; C = chlorate; D = sulfate.

Fig. 11. Chromatogram of water extract from sample 2. Conditions as in Fig. 3. Peaks: S = system peak; B = nitrate; C = chlorate; D = sulfate.

the calibration curve. The calculated peak area is then compared with the experimental value. Agreement between the two values established the concentration and identification of the sulfate anion. In the present work it was found that, at 222 nm, the line correlating the retention to the concentration is described by the equation:

$$t_R = 267 - 5.24C$$

and at 262 nm:

$$t_R = 269 - 4.84C$$

In these two expressions, the retention time t_R is given in s and the concentration C in mM. The correlation coefficients are 0.995 and 0.979, respectively.

Applications of the method

The utility of the chromatographic method for identification and quantitation of post-explosive residues was examined by analyzing several explosive residues from actual cases. Fig. 10 shows the chromatogram obtained from the remains of an explosive charge which was found and detonated by the police. The remains from the explosion were sent for an analysis. Spot test identified potassium chlorate and sulfur. The chromatogram confirmed the presence of these anions. In addition, the presence of nitrate was found as well.

Fig. 11 shows the chromatogram of another sample which was obtained from the remains of a bomb, again, discovered and detonated by the police. The sample was extracted from parts of a pipe which made up the bomb. Conventional analysis found only traces of $KClO_3$. The chromatogram confirmed the presence of chlorate

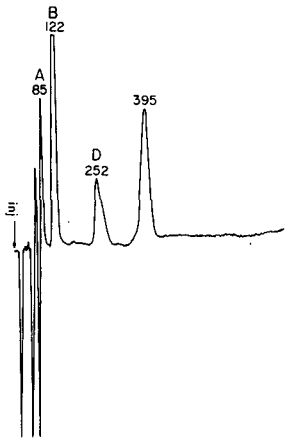

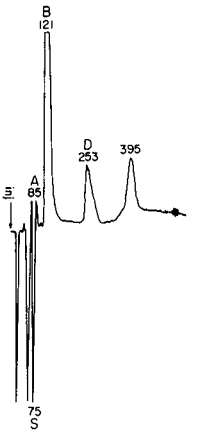

Fig. 12. Chromatogram of water extract from sample 3. Conditions as in Fig. 3. Peaks: S = system peak; A = nitrite, B = nitrate; D = sulfate.

Fig. 13. Chromatogram of water extract from sample 4. Conditions as in Fig. 3. Peaks: S = system peak; A = nitrite; B = nitrate; D = sulfate.

ion. The chromatography was also able to detect the presence of nitrate and sulfate ions.

Fig. 12 shows a chromatogram of a third example. It was obtained from the center of an explosion. Spot test analysis indicated the presence of minute amounts of KNO_2 and sulfur. the chromatographic analysis confirmed the presence of these two ions as well as of nitrate ion. Spot tests and IR techniques cannot differentiate easily between nitrate and nitrite. No such difficulty exists in the method described here. The presence of sulfate, nitrate and nitrite may be indicative of black gunpowder.

Fig. 13 shows a chromatogram of a fourth example. The sample collected from

TABLE II

QUANTITATIVE ANALYSIS OF EXPLOSIVE RESIDUES

See Table I for conditions. Results are in % of the total sample weight.

No. of sample	*Nitrite*	*Nitrate*	*Chlorate*	*Sulfate*
Wavelength 222 nm				
1 (Fig. 10) –	0.11	1.70	5.27	
2 (Fig. 11) –	0.27	3.15	11.07	
3 (Fig. 12)	0.53	6.61	–	18.85
4 (Fig. 13)	0.12	3.27	–	23.27
Wavelength 262 nm				
1 (Fig. 10) –	–	1.68	4.82	
2 (Fig. 11) –	0.69	3.73	12.22	
3 (Fig. 12) –	22.54	–	22.13	
4 (Fig. 13)	0.63	29.89	–	20.63

the site of an explosion. Spot test analysis found traces of potassium nitrite and sulfur. the chromatogram shows nitrite, nitrate and sulfate ions. In Figs. 12 and 13 chlorate ion is missing. However, in both figures there is an unidentified peak which elutes at 395 s.

A comparison between Figs. 10 and 11 and Figs. 12 and 13 shows that different explosives were used in the two groups of explosions. In all chromatograms there is a clear indication of the various anions, and identification is immediate and without interferences. The sulfate anion was identified and quantified according to the method described above.

Table II shows the results of the quantitative analysis of the samples. The analysis was based on the calibration curves that were described in Table I. The quantitation was done both at 262 and 222 nm. It is of interest to note that the quantitative results for chlorate and sulfate agree quite well at both wavelengths. The agreement in the results of nitrite and nitrate is less satisfactory. The reasons for the disagreement in the quantitation of nitrite and nitrate at the two wavelengths is not clear to us.

CONCLUSIONS

The new chromatographic method for the analysis of nitrite, nitrate, chlorate and sulfate ions in explosive residues is fast, selective and sensitive. The system has a linear response for all these anions. It shows selectivity toward nitrate and chlorate, which presents a problem in conventional ion chromatography. There is no need for elaborate sample preparation and the sample can be injected into the chromatograph immediately after water extraction from the bulk sample. Samples from explosive residues yield clean chromatogram with no interferences. A chromatographic system that will identify and quantify thiocyanate and perchlorate is now under development.

ACKNOWLEDGEMENT

This research would not have been possible without the help and the support of the Israeli Police Force Forensic Laboratory and its team of analytical chemists.

REFERENCES

1 J. G. Grasselli, *Anal. Chem.*, 55 (1983) 1468A
2 D. J. Reutter and R. C. Buechele, *Proceedings of the International Symposium on the Analysis and Detection of Explosives, Quantico, VA, 1983*, U.S. Government, 1983, p. 199.
3 J. Yinon and S. Zitrin, *The Analysis of Explosives* (*Pergamon Series in Analytical Chemistry*, Vol. 3), Pergamon Press, Oxford, 1981.
4 T. L. Rudolph, *Proceedings of the International Symposium on Analysis and Detection of Explosives, Quantico, VA, 1983*, U.S. Government, 1983, p. 213.
5 D. D. Garner, M. L. Fultz and E. B. Byall, *J. Energ. Mater.*, 4, (1986) 133.
6 W. E. Barber and P. W. Carr, *J. Chromatogr.*, 260 (1983) 89.
7 B. B. Wheals, *J. Chromatogr.*, 262 (1983) 61.
8 W. E. Barber and P. W. Carr, *J. Chromatogr.*, 301 (1984) 25.
9 B. Sachok, S. N. Deming and B. A. Bidlingmeyer, *J. Liq. Chromatogr.*, 5 (1982) 389.

Journal of Chromatography, 517 (1990) 317–331
Elsevier Science Publishers B.V., Amsterdam

CHROM. 22 552

High-performance liquid chromatography of amino acids, peptides and proteins

C.[a] Characterisation of coulombic interactive regions on hen lysozyme by high-performance liquid anion-exchange chromatography and computer graphic analysis[b]

A. N. HODDER
Department of Biochemistry and Centre for Bioprocess Technology, Monash University, Clayton, Victoria 3168 (Australia)
K. J. MACHIN
St. Vincent's Institute of Medical Research, Princess Street, Fitzroy, Victoria 3065 (Australia)
and
M. I. AGUILAR and M. T. W. HEARN*
Department of Biochemistry and Centre for Bioprocess Technology, Monash University, Clayton, Victoria 3168 (Australia)

ABSTRACT

The molecular characteristics of the dominant anion-exchange binding site of hen egg white lysozyme (HEWL) has been investigated using a combination of high-performance liquid chromatographic techniques and computer graphic analysis of the X-ray crystallographic structure. These studies have indicated that the site of highest electrostatic potential, in terms of the density of negatively charged amino acid side chains, is located around the catalytic cleft area. The four residues tentatively identified to be involved in the electrostatic binding domain were aspartic acid 48, 52, 101 and glutamic acid 35. The number of these charged groups correlated with the maximum value of the chromatographically determined retention parameter (Z_c value). Variations in the range of experimental Z_c values obtained under different elution conditions have been interpreted in terms of conformational flexibility of the structural domains of HEWL which result in the opening or closure of the catalytic cleft during the retention process.

[a] For Part XCIX, see ref. 47.

[b] It is with great pleasure that the authors submit this manuscript to the Honour Volume for Professor J. Calvin Giddings as a token of their good wishes on his 60th birthday. As an outstanding scientist and inspired wilderness traveller, he has provided a great stimulus to the field of separation sciences on an international front. Acknowledging the intellectual innovation which he has represented for over three decades, this manuscript is dedicated to the scientific objectives which he has so incisively championed.

0021-9673/90/$03.50

INTRODUCTION

Protein retention in high-performance ion-exchange chromatography (HPIEC) arises from electrostatic interactions between the solute and the stationary phase surface. In analytical chromatography the retention behaviour of protein solutes is commonly characterised by the dependence of the capacity factor, k', on the concentration, c, of the displacer salt. Over a limited range of the salt concentration the dependence of log k' on log $(1/c)$ can be approximated by a linear relationship in the form

$$\log k' = \log K + Z_c \log (1/c) \quad (1)$$

where K is the ion-exchange distribution coefficient obtained by extrapolation of plots of log k' *versus* log $(1/c)$. While the precise physicochemical significance of the Z_c term remains to be determined, this parameter has frequently been taken to represent the number of charged interactive binding sites established between unique ionic patches on the protein surface, called *ionotopes*[1], and the stationary phase support.

In anion-exchange systems the magnitude of Z_c has been found to be influenced by a number of mobile phase components, such as buffer pH[2,3], the salt concentration[4,5], the type of displacer salt[4–6], the buffer concentration and the elution mode[3,5]. Variation in the magnitude of Z_c is associated with subtle changes in the interactive surface structure or ionotope of the protein. The non-uniform distribution of charged groups arising from the unique primary structure of the protein results in patches of high electrostatic potential, which participate in binding to the support surface. These areas of localised charge can occur as a result of either sequentially linked amino acids or via topographic arrangements involving through space alignment of amino acid side chains. Under a particular set of chromatographic conditions the distribution, charge density and surface accessibility of these groups generate a specific charge vector which controls the orientation, the contact area A_{cont}, and the approach distance a, of the ionotope in the interaction established between the protein and the stationary phase[1,8]. Furthermore, the molecular composition of these interactive segments, which present themselves at the chromatographic surface, ultimately determines the thermodynamic properties of the solute binding at the solid–liquid interface. The ability to locate these interactive sites on the surface of a protein solute under a defined set of experimental parameters would therefore provide significant insight and predictive power into the chromatographic behaviour of a particular protein.

In the present study the X-ray crystallographic structures determined for lysozyme variants[9,10] have been analysed to locate potential anion-exchange binding sites on the surface of hen egg white lysozyme (HEWL). The three-dimensional structure of this protein was visualised by computer simulated graphics of the X-ray structural atomic coordinates. Patches or clusters of glutamic acid and aspartic acid residues, which are negatively charged under the chromatographic elution conditions, were located and assessed on the basis of their surface accessibility, charge density and steric interference. This information was then utilised in the development of an anion-exchange binding model for HEWL.

MATERIALS AND METHODS

All chromatographic experiments were performed with a Pharmacia (Uppsala, Sweden) fast protein liquid chromatography (FPLC) system as previously described[7].

Computer assisted molecular modelling

A Silicon Graphics (Mountain View, CA, U.S.A.) Iris 3120 computer system combined with a University of California, San Diego, U.S.A. (UCSD) Molecular Modelling System (version 1.3) was used to visualise the three-dimensional structure of various proteins. X-ray crystallographic coordinates for HEWL were obtained from the Brookhaven protein database. Photographs of these computer simulated molecular models were taken directly from the monitor using a Nikon F3 SLR 35 mm camera with a 55 mm lens. The camera aperture was set at f 2.8 and shutter speeds of 1/4 or 1/8 s were used.

RESULTS AND DISCUSSION

HEWL is a small enzyme made up of a single polypeptide chain of 129 amino acids, the primary structure of which is shown in Fig. 1. X-ray crystallography studies[9] have revealed that the HEWL molecule is approximately ellipsoidal with dimensions 45 × 30 × 30 Å. A deep cleft located on one side divides the molecule into two domains. The smaller domain is sheet-like with the thickness of only one chain and is comprised mainly of hydrophilic residues which are exposed to the outside solvent or the cleft of the molecule. Hydrophobic residues are found mainly in the larger domain where they form a central core. HEWL is involved in the destruction of gram-negative bacteria by cleaving the polysaccharide component of their cell walls. X-ray crystallographic[12] and solution[13,14] studies on enzyme-substrate and enzyme-inhibitor complexes have identified the cleft as the active site for the degradation of particular gram-negative bacterial cell wall polysaccharides, where negatively charged residues located in the cleft play a major role in the degradation process. In particular, Asp 52 and Glu 35 are thought to contribute directly to the cleavage of the glucosidic bond via an acid–base catalysis mechanism. Furthermore, Asp 101, Trp 62 and Trp 63 are believed to support the polysaccharide substrate in the cleft through hydrogen-bonding interactions.

HEWL is a basic protein with an isoelectric point (pI_{HEWL}) of 11.0. In anion-exchange chromatographic systems where the buffer pH is less than pI_{HEWL},

```
        *         *         *         *         *         *
KVFGRCELAAAMKRHGLDNYRGYSLGNWVCAAKFESNFNTQATNRNTDGSTDYGILQINS
        *         *         *         *         *         *
RWWCNDGRTPGSRNLCNIPCSALLSSDITASVNCAKKIVSDGNGMNAWVAWRNRCKGTDV
        *
QAWIRGCRL
```

Fig. 1. Primary structure of hen egg white lysozyme.

HEWL will have an overall net positive charge and on the basis of the net charge hypothesis is not expected to be retained. However, as shown in our earlier studies[6,7] on the HPIEC of proteins, HEWL is retained on high-performance anion-exchange supports at high pH, through interaction of localised areas of negative charge. These localized areas of negative-charge groups will be manifested as coulombic patches —or ionotopes— accessible to the chemical moeities of complementary charge present on the sorbent surface. These quaternary ammonium ligands, in the case of strong anion-exchange systems, thus function as molecular probes for the region(s) of highest electron density. The interaction will be characterised, in part, by the parameter Z_c, which will vary according to the extent of ionisation and the extent of ion-interaction of the dominant ionotope. As such, the value of Z_c is anticipated to correlate with the numbers of charge groups on the ionotope and its accessibility to the chromatographic ligand. Table I shows Z_c values, representing the number of charged interactions between HEWL and the positively charged Mono-Q column, derived with elution systems of pH 9.60 and a variety of neutral salts. Values of Z_c were found to vary between *ca.* 0.5 and 4.5 over these elution conditions. While it is known that the magnitude of the Z_c value may also be influenced by hydrophobic interaction effects[2,3,6], experimental conditions can be chosen (*e.g.* as used in the present study) to maximise the electrostatic effects and thereby minimising the contribution of hydrophobic effects to Z_c. Under such conditions, a high correlation in the linearity of the log k' *versus* log $(1/c)$ plots is predicted from thermodynamic, near equilibrium and stoichiometric models for electrostatic retention behaviour of proteins in HPIEC. The correlation coefficient for the derivation of Z_c values in Table I was $R^2 \geqslant 0.90$ which is in accord with the concept that electrostatic effects dominate the retention behaviour.

TABLE I

Z_c VALUES FOR LYSOZYME AT pH 9.60

Salt	*Elution mode*		
	Varied t_G[a]	*Varied flow*[b]	*Isocratic*[c]
LiCl	2.50 ± 0.26	4.46 ± 0.25	0.80 ± 0.20
LiBr	4.21 ± 0.66	3.96 ± 0.77	–[d]
		1.96 ± 0.09[f]	
NaF	2.99 ± 0.31	2.91 ± 0.12	0.74 ± 0.31
NaCl	1.48 ± 0.17	1.88 ± 0.23	–[e]
NaBr	2.41 ± 0.44	3.30 ± 0.33	1.59 ± 0.21
		0.56 ± 0.00[f]	
KF	3.58 ± 0.14	3.23 ± 0.50	–[d]
KCl	1.16 ± 0.15	1.73 ± 0.11	–[e]
KBr	3.28 ± 0.24	4.52 ± 0.75	–[d]
	0.98 ± 0.14[f]	2.53 ± 0.28[f]	

[a] Varied gradient time, constant flow elution conditions.
[b] Varied flow-rate, constant gradient time elution conditions.
[c] Constant flow-rate isocratic elution conditions.
[d] Not eluted with this salt.
[e] Mixed modal retention.
[f] A non-linear dependency of log k' on log $(1/c)$ resulted in more than one Z_c value.

The origins of the differences between Z_c values obtained by isocratic and gradient elution have been discussed in detail elsewhere[4,7].

Several studies[14–16] have shown good correlation between the number of charged groups on highly charged biomolecules, such as oligonucleotides, and the resultant chromatographically derived Z_c values. However, when solute molecules are sufficiently large that they can adopt some degree of tertiary structure, lower correlation between Z_c and the total number of charges on the molecule has been reported[17]. In terms of average charge interactions, one positive charge at the surface of the quaternary ammonium sorbent will be required for full electrostatic interaction and the establishment of charge electroneutrality with a unitary negative charge associated with an ionised amino acid side chain at the surface of the protein. Experimentally observed non-integer values could conceivably arise from (1) system effects such as the precision of instrumental measurement, (2) solute effects such as the distribution, orientation and solvation of charged or polarised groups in the micro-environment of the contact regions, (3) changes in the hydrogen bonding structure associated with salt bridges and (4) restricted accessibility and clustering of the positively charged ligands on the sorbent. In the current study, the distribution of negatively charged Glu and Asp residues at the surface of the net positively charged HEWL molecule, allows a unique opportunity to examine the relationship of the chromatographically derived Z_c values with the number of potential interacting residues on the protein surface. This correlation also gives valuable insight into the anion-exchange retention mechanisms for proteins.

Fig. 2 shows the computer simulated structure of HEWL and the location of all glutamic acid (yellow) and aspartic acid (orange) residues which may be involved in the retention process. Noticeably, the acidic side chain groups are sparsely located over the surface of the molecule except for Asp 101, Glu 35, Asp 52 and Asp 48. All of these latter group of amino acid residues lie in close proximity to each other and are positioned in, or adjacent to, the active site cleft area. If it is assumed that stoichiometric interactions occur between HEWL and the chemical ligands on the stationary phase surface, *i.e.* one quarternary ammonium group is required to bind to each acidic amino acid side chain, then the number of charged groups in this cleft area accessible to the ligands would be between one and four depending on the salt or pH condition. These values correlate well with the range of Z_c values shown in Table I. From spatial considerations, the remaining amino acid side chains are sufficiently distant or on opposite faces of the protein to preclude simultaneous interaction as would be required for a Z_c value of 4. Fig. 3 shows the distribution of positively charged arginine (blue) and lysine (pink) groups in HEWL. X-ray crystallographic[9] and enzyme-activity[18] studies have determined that the six lysyl amino groups are on the surface of the molecule and not in the active-site cleft. Fig. 4 also shows that access to the cleft is not obstructed to any great extent by arginine residues wich project away from the plane of the four acidic amino acids. Furthermore, Blake *et al.*[9] noted that intermolecular contacts observed in the protein crystal may also represent the attachment sites during the dimerisation and polymerisation of HEWL reported to occur in solution at high pH[19]. Again these intermolecular contacts would not obstruct access to the cleft.

In Figs. 5 and 6 the topography of the cleft is further examined. It can be seen in Fig. 4 that a number of additional amino acid residues may enhance or interfere with

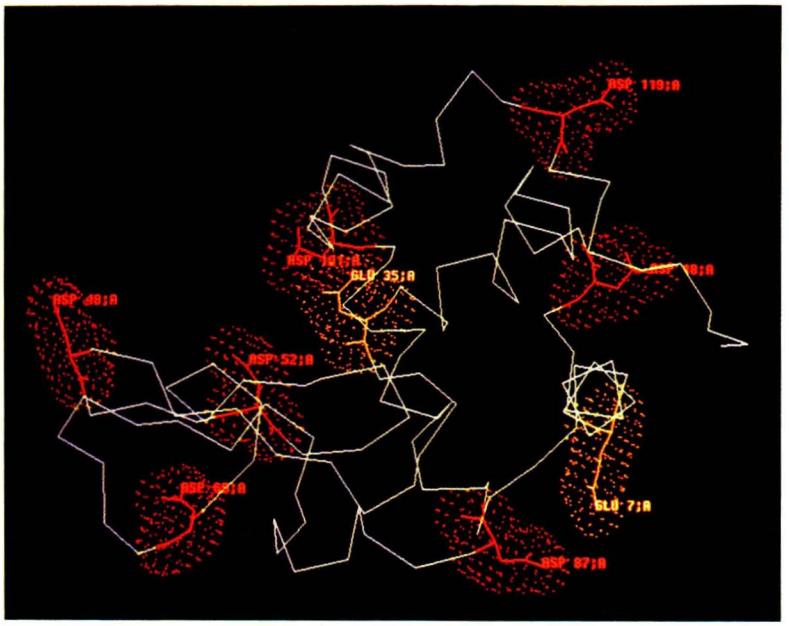

Fig. 2. Computer graphic simulation of the X-ray crystal structure of HEWL indicating the location of all glutamic acid (yellow) and aspartic acid (orange) residues. Residues Asp 101, Glu 35, Asp 52 and Asp 48 were identified as the dominant anion-exchange binding domain. Picture produced by a computer program written by Lesk and Hardman[46].

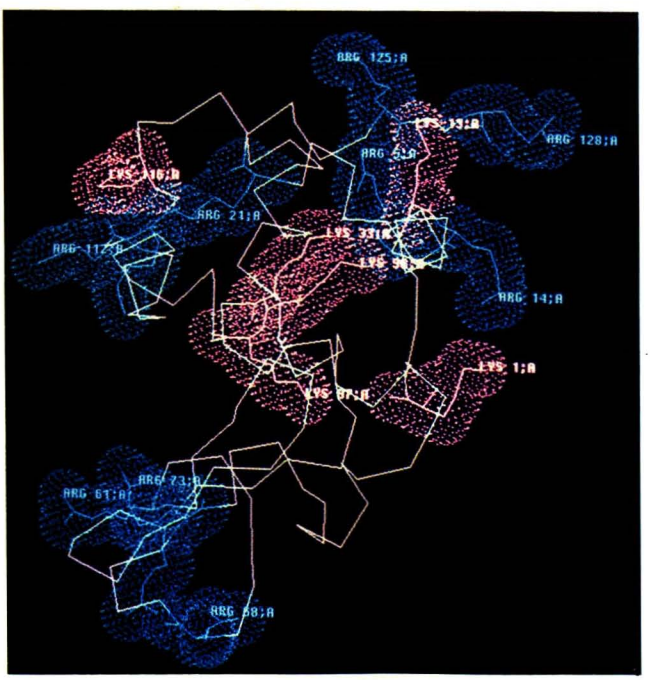

Fig. 3. Computer graphic simulation of the HEWL crystal structure showing the distribution of positively charged lysine (pink) and arginine (blue) residues. Picture produced by a computer program written by Lesk and Hardman[46].

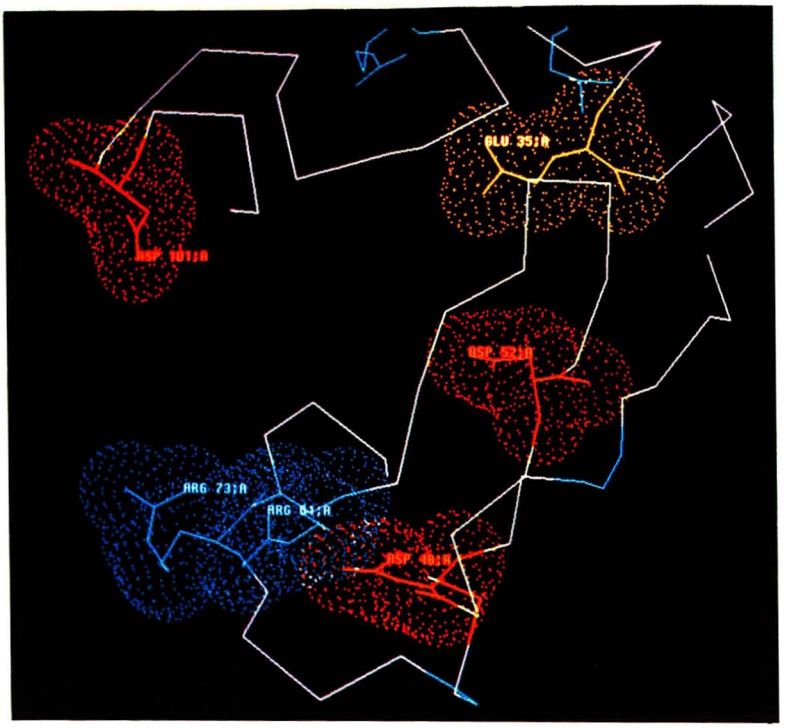

Fig. 4. Computer graphic representation of the spatial proximity of Arg 61 and Arg 73 (blue) around the negatively charged groups in the active site. Picture produced by a computer program written by Lesk and Hardman[46].

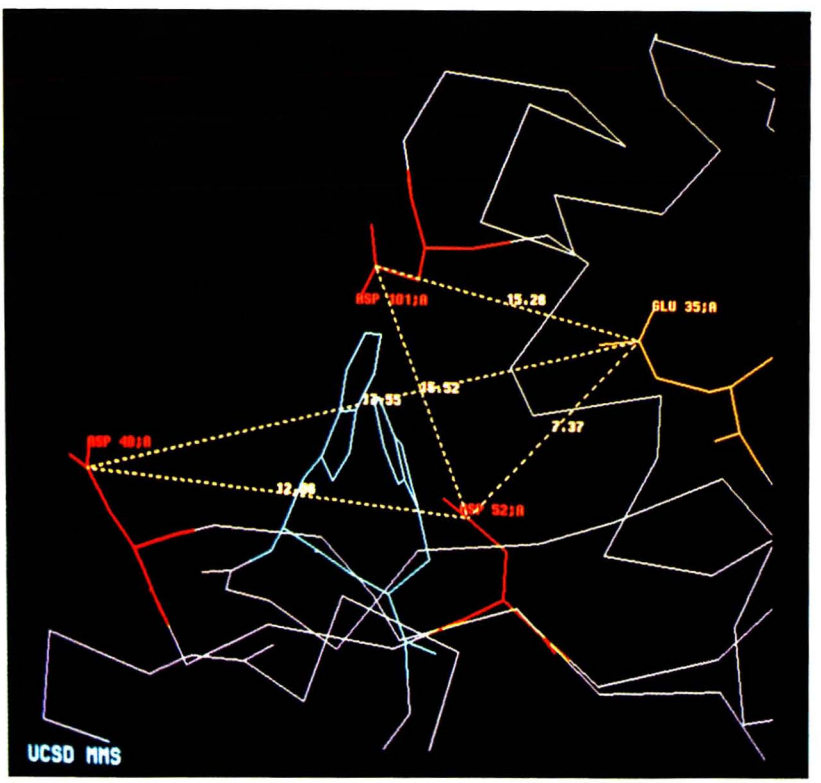

Fig. 5. Computer simulation demonstrating the spatial topography of Trp 62, 63 and 108 (light blue) around the active cleft. Contour lines have been drawn to measure the distances between Asp 101, Glu 35 and Asp 52. The area of the dotted triangle was used to calculate the charge density of 0.55 charge per 10 Å^2. Similarly, the charge density of the binding domain encompassing Glu 35, Asp 52 and Asp 48 was calculated to be 0.85 charge per 10 Å^2. Picture produced by computer program written by Lesk and Hardman[46].

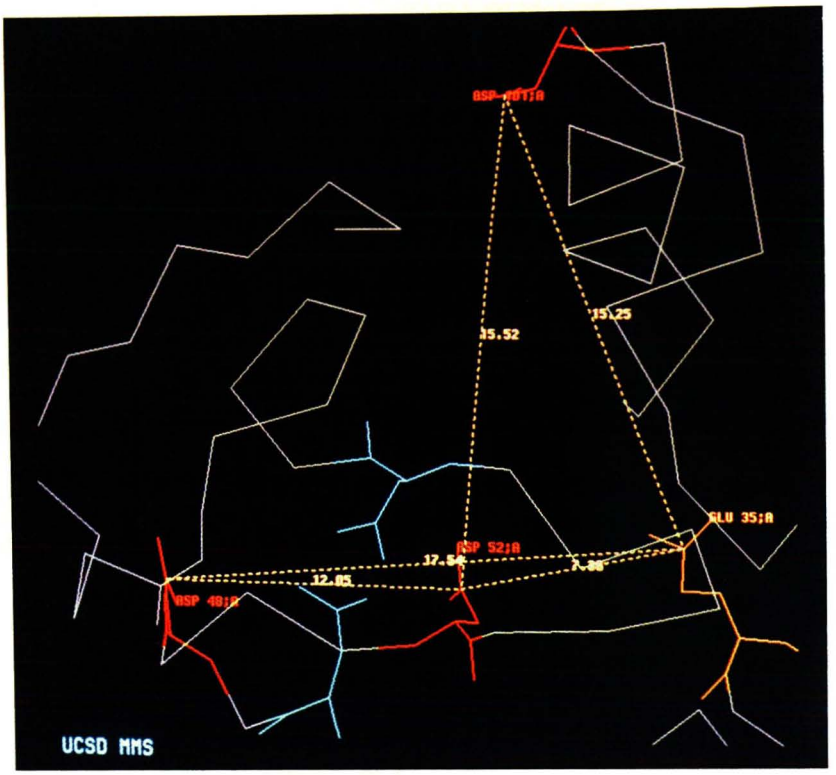

Fig. 6. Computer graphic representation of the spatial proximity of Asn 46 and Asn 59 (blue) around the active cleft of HEWL.

the electrostatic interactions at the protein–stationary phase interface. Three of the six tryptophan residues of HEWL (that is, Trp 62, 63 and 108) are located in the active site[11]. Trp 62 has been identified as the most surface accessible of these three residues via X-ray crystallographic methods and its reactivity in solution with N-bromosuccinomide[20]. Fig. 5 shows the spatial arrangement of Trp 62 and Trp 63 (light blue) which are the closest to the four negatively charged amino acid residues in the cleft. Both tryptophan residues occupy a substantial volume and would be expected to sterically interfere with the ion-exchange binding process. However, binding studies involving HEWL and polysaccharide inhibitors have found that the alicyclic rings in sugars and the tryptophan rings in the enzyme rotate to accomodate each other when the cleft is occupied[21]. Rotation of these tryptophans induced by specific salt interactions could also occur during HPIEC to facilitate the binding of the negatively charged residues in the cleft to the support surface. Studies with lysozyme[21,22] and other proteins[23], in salt solutions using intrinsic fluorescence quenching techniques have demonstrated this behavioural characteristic of tryptophan residues. Furthermore, as aromatic residues can potentially act as electron donors, the tryptophan residues may also enhance the binding process through ion-induced dipole interactions.

The amino acid residue Asp 48 has been shown not to be involved with

enzyme–substrate binding due to its location outside the bottom of the cleft. If Z_c does reflect the total number of electrostatic interactions occurring between the solute and stationary phase, then the chromatographic data in Table I indicate that up to four negatively charged groups are involved in the electrostatic binding. Since Asp 48 is located in close proximity to the cleft and is spatially aligned with the other side-chain carboxyl groups this amino acid residue has been assigned to be the fourth negatively charged group participating in the HPIEC retention process. However, several neighbouring (but not charge interacting) residues may hinder its participation in the binding process. From Fig. 6, which illustrates views taken from above and opposite the cleft, it can be concluded that Asp 48, Asp 52 and Glu 35 have an essentially linear topographic arrangement. However, the side chains of Asn 59 and Asn 46 (light blue) are both located close to the space occupied by Asp 48 and Asp 52. If a rigid structure is assumed, according to the known atomic coordinates of lysozyme[9], then the side chains of these two amino acid residues could sterically interfere with a linear electrostatic binding site incorporating Asp 48, Asp 52 and Glu 35. As evident from Fig. 4 the interactive capability of Asp 48 may be further diminished by the close proximity of the positively charged Arg 61 and Arg 73 residues. If Asp 48 does participate in the binding process (*i.e.*, when $Z_c \approx 4$) these positively charged arginine residues may be instrumental in determining the orientation of the cleft at the stationary phase surface.

During ion-exchange chromatography, localised areas of high electrostatic potential on the protein surface will generate an overall charge vector, which will control the approach and the orientation of the protein solute to the stationary phase surface. The identification of these areas of high electrostatic potential will assist in determining the chromatographic retention mechanisms of protein solutes. In Figs. 5 and 6 dotted three-dimensional contours have been drawn between the negatively charged residues in and around the cleft. The areas of these three-dimensional contours were then calculated and used to estimate the charge density in these two regions. For the area incorporating Asp 101, Glu 35 and Asp 52 a charge density of 0.55 negative charge per 10 Å^2 was determined. The area encompassed by Glu 35, Asp 52 and Asp 48 was estimated to have a higher charge density of 0.85 negative charge per 10 Å^2 and hence should play a more dominant role in steering lysozyme toward the stationary phase surface from the bulk solvent. The concept that high electrostatic charge density, arising from the sequential or spatial clustering of charged groups, can direct the site of electrostatic interaction has been used to design specific protein purification protocols. For example, a recombinant protein, β-urogastrone has been produced with a C-terminal polyarginine (polyArg) tail which enhanced its purification on a cation exchanger[24]. This polyArg tail functions to define a unique region within the total three-dimensional structure which directs and orientates the recombinant β-urogastrone to the cationic surface of the sorbent. In terms of the total number of amino acids in the folded protein, the polyArg region was small, *i.e.* only 6 amino acids out of a total 59 residues. Nevertheless, binding still occurs mainly through the alignment of the arginine residues with the cationic ligands, whilst the other side-chain groups on the polypeptide surface create secondary interactive preferences. In the case of HEWL, once the molecule is in the vicinity of the double layers of the solvated ligand and during the final stage of adsorption, other amino acid groups on the protein surrounding the active site cleft, such as Arg 61 and Arg 73, can

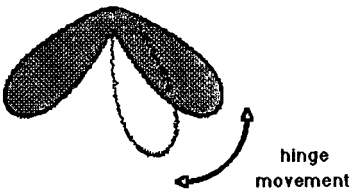

Fig. 7. Diagramatic representation of the hinge-bending mechanism for HEWL.

be anticipated to influence in an analogous manner the orientation and magnitude of the interactive ionotope on the protein surface.

The adsorption of proteins onto the stationary phase surface involves dynamic processes which may also induce conformational changes in the protein solute. These processes could involve the motion of only a few atoms or could result in movements of entire structural subunits or domains. If the negatively charged residues in the cleft participate in the ion-exchange binding process, then the fluctuation in Z_c values, between *ca.* 1 and 4, with various elution conditions suggests that there is a change in accessibility to these residues. More specifically, the degree of structural fluctuations arising from conformational changes in the interactive ionotope, and induced by the elution conditions, can be assessed through changes observed in protein Z_c values. It is well known that portions of polypeptide chains frequently fold into compact, local semi-independent units or domains. There are numerous examples of proteins, including HEWL, that have elongate double-lobed structures comprising two domains separated by an active cleft[25–27]. X-ray crystallographic studies have shown, for some double-lobed enzymes, that these domains can move relative to each other through a hinge-bending mode of vibration as shown in Fig. 7. This hinge-bending mode also plays an important role in their catalytic function[28,31]. For example, when glucose binds to yeast hexokinase the small lobe of the enzyme molecule rotates by 12° relative to the large lobe, moving the polypeptide backbone as much as 8 Å (ref. 30). These conformational rearrangements result in the closure of the cleft and a reduction in the radius of gyration for hexokinase[31]. There is substantial experimental evidence that the two structural domains in HEWL can also move relative to each other via a hinge-bending mode of vibration[32–34]. In the absence of solvent molecules and with an unoccupied cleft, the hinge-bending mode for HEWL has been calculated[33] to have a vibrational frequency of $1.3 \cdot 10^{11}$ Hz. Furthermore, energy calculations indicate that hinge-bending rotations of several degrees are permissible in the HEWL molecule. In solution the lobe vibration is reported to be dampened by the hydrodynamic friction of the lobe motion and the two domains move relative to each other in a diffusive manner.

As regions of highest charge density and electrostatic potential represent the possible site of electrostatic interaction, the range of Z_c values suggests that the interaction of HEWL with the charged anion-exchange sorbent may also be mediated by a similar hinge-bending mechanism associated with the catalytic cleft as shown diagrammatically in Fig. 7. The number of negatively charged residues in the cleft area that interact with the stationary phase surface will then be determined by the extent of domain motion. The Z_c value will, therefore, reflect the degree of opening or closure of the cleft on HEWL. A similar retention mechanism has also been proposed by Chicz

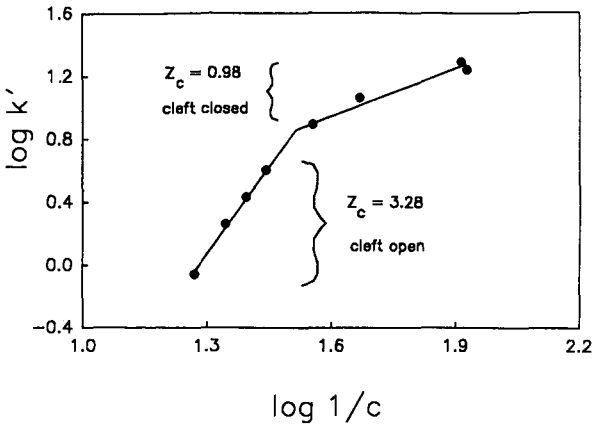

Fig. 8. Plots of log k' *versus* log $(1/c)$ for lysozyme separated on a Mono-Q anion exchanger by gradient elution at pH 9.6 with KBr as displacer salt, with gradient times between 8.6 and 171 min and a flow-rate of 1 ml/min. The Z_c values corresponding to the open cleft and closed cleft were 3.28 $\pm$ 0.24 and 0.98 $\pm$ 0.14 respectively.

and Regnier[35] for subtilisins chromatographed on a cation exchanger where the structural state of an ion bridge on the surfac of subtilisin was observed to be dependent on the ionic strength of the displacer salt.

Various studies[36–38] have shown that neutral salts influence the stability, solubility and biological activity of macromolecules in solution. Neutral salts can also interfere with the intermolecular forces involved in the association/dissociation of proteins and their subunits[39,40]. The resulting changes in the structure of the macromolecule arise as a consequence of complex processes which regulate the layer of hydration and electrostatic potential about the surface of the molecule. In addition to responding to these subtle changes in structure, HEWL is also known to polymerise at high pH. Hence, the choice of neutral salt will regulate the approach to, and orientation of, HEWL at the stationary phase surface through manipulation of the size and shape of the monomer and also of the degree of polymerisation.

As is evident from Table I, Z_c values of HEWL were found to vary as a result of a number of systematic changes to the mobile phase composition. As discussed elsewhere[4], the type of displacer salt and the elution mode can have a profound influence on the magnitude of Z_c. This behaviour is particularly evident with HEWL. For example, as demonstrated in Fig. 8, the magnitude of Z_c for HEWL was observed to be dependent on the concentration of bromide salts under varied flow or varied gradient time elution conditions. Similarly, a non-linear dependence of log k' on log $(1/c)$ has been reported for subtilisins eluted with sodium chloride[35]. In these instances, retention plots of log k' *versus* log $(1/c)$ can be divided into two linear regions (*i.e.*, with different slopes) with a distinct inflexion point. The dependence of the Z_c value of HEWL on the bromide salt concentration is consistent with the chaotropic or water-structure-breaking properties of bromide ions. Unlike heavily hydrated anions such as fluoride, bromide ions are relatively less hydrated. In aqueous-based chromatographic systems bromide ions can reduce the surface area of the solute exposed to water molecules by preferentially binding to the stationary phase or protein

surfaces. Therefore, at higher bromide concentrations, it is possible that the cleft of HEWL is forced open by a large number of bromide ions condensing onto the surface of the cleft which results in the larger Z_c values observed in Table I. At a critical concentration, differing for each bromide salt, the number of bromide ions in the cleft is sufficiently reduced to allow hinge movement and the relative closure of the cleft. This behaviour will result in a decrease for Z_c observed for the lower bromide concentrations. The observation that ion-exchange-adsorbed HEWL and other enzymes show decreased catalytic activity which is restored on elution with salts and that substrate-specific elution can be achieved for enzyme adsorbed to ion-exchange or biomimetic-affinity sorbents[41,42] provides further support to the concept that, in the

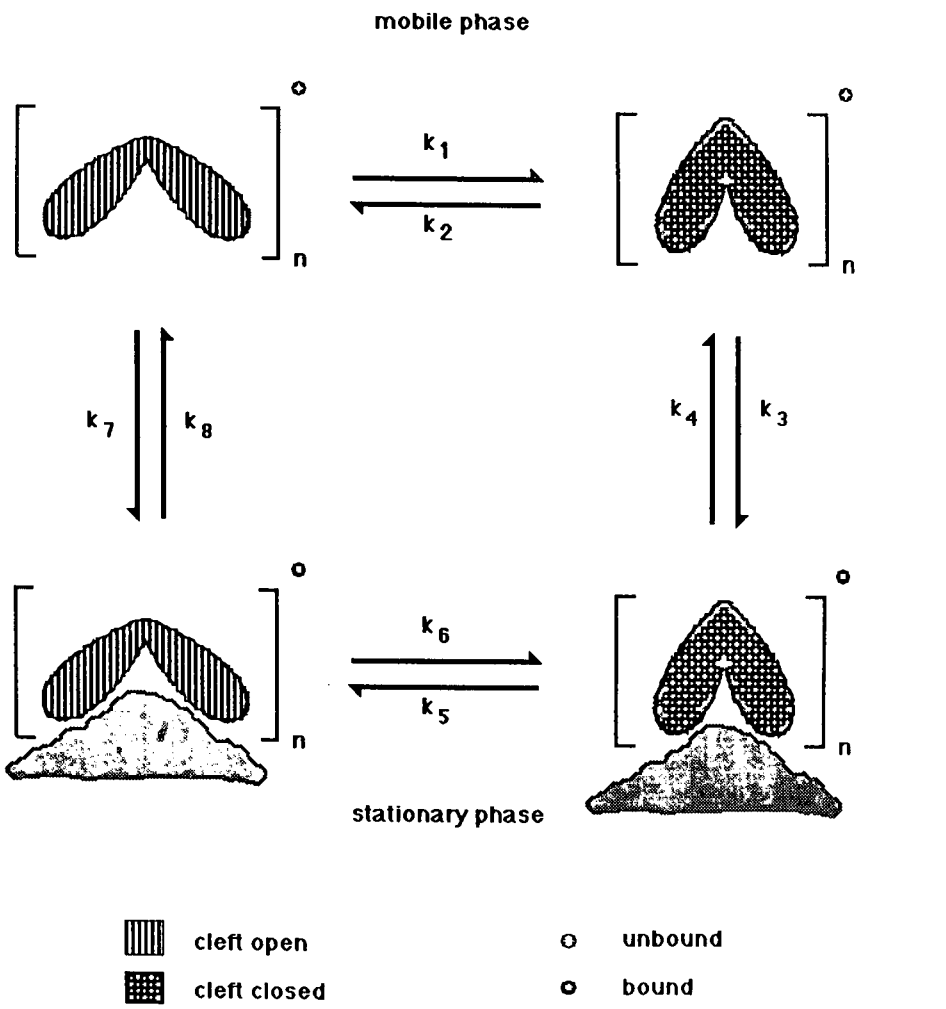

Fig. 9. Schematic representation of the structural equilibria associated with the binding of lysozyme to the anion-exchange surface, involving the opening and closure of the active cleft as a result of a hinge-bending mechanism.

case of HEWL, the cleft region is involved with coulombic recognition with the cationic ligand.

Inspection of the data in Table I also reveals that the choice of elution mode, *i.e.* either varied gradient time, varied flow-rate or isocratic elution, can influence the binding process and the hinge-bending movement of HEWL. For example, as shown in Table I, the elution of HEWL with LiCl results in significantly different Z_c values for these two different elution modes. Hence, the length of exposure to the stationary phase surface which is controlled by the rate of change in the displacer-salt concentration also determines the extent of opening or closure of the lysozyme cleft.

In this study, changes in Z_c value have been quantitatively related to the movement of the catalytic cleft of HEWL. Fig. 9 schematically depicts the structural equilibria associated with the binding of HEWL to the anion-exchange surface. Assuming HEWL is a monomer, *i.e.* when $n = 1$, the binding process which occurs at the cleft–stationary phase interface can be characterised in terms of the degree of opening or closing of the cleft and will be governed in part by the nature of the displacer-salt. The variation in entropy resulting from these salt-induced structural changes will contribute toward the free energy required for hinge-movement in HEWL. The hinge-bending process will be governed by the rate constants k_1 to k_8. When the cleft is closed, *i.e.* when $Z_c = 1$ only the surface residue will be accessible whilst the negatively charged groups located inside the cleft are sterically prevented from direct electrostatic interaction with the support surface (*i.e.* the structure on the right-hand side of Fig. 9). In contrast, larger Z_c values, *i.e.* $Z_c = 3$–4 correspond to the opened cleft which results in maximal electrostatic interactions (the left-hand side of Fig. 9). The thermodynamics and kinetics of adsorption will be further complicated under conditions where the polymerisation of HEWL can be induced, *i.e.* when $n > 1$. The dependence of the hinge-movement equilibria on the bromide concentration, which is reflected by non-continuous retention plots such as the data shown in Fig. 8, can also be accomodated by this model where the interconversion process will be controlled by the rate constants k_3, k_4, k_5 and k_6.

CONCLUSIONS

The present study introduces an approach to the correlation of anion-exchange chromatographic data with protein three-dimensional structures in order to allow the identification and characterisation of the molecular identity of the electrostatic interactive binding site on proteins. In the case of HEWLs, the mechanism by which HEWL approaches and orientates itself at the stationary phase surface can be determined through the analysis of the spatial disposition of neighbouring positively charged and hydrophobic residues. The existence of conformationally flexible structures and analysis of the influence of elution conditions on the underlying equilibrium processes also provide significant insight on the experimental factors which can be used to control the interaction between proteins and chromatographic surfaces. The interactive behaviour of lysozyme variants on both a cation-exchange resin and a hydrophobic interaction stationary phase has been recently investigated[43,44] and partly correlated with amino acid sequence differences. The potential therefore now exists to chromatographically map the surface topography of proteins through the correlation of retention properties in different interactive modes with the three-dimensional structure of a protein.

The identification, analysis and prediction of the surface-accessible interactive regions of biomacromolecules is also central to a wide range of biological systems which are controlled by biorecognition, interfacial phenomena or surface–surface interactions. For example, the residues Asp 48 and 52 of HEWL, which are located in the anion-exchange binding site, have also been implicated as forming part of the antigenic determinants recognised by specific T-cell hybridomas[45]. While the intrinsic chemical and stereospecific features which immunologically distinguish the most reactive and the least reactive sites of a protein are not fully understood, the most frequently recognised antigenic and immunogenic sites form three-dimensional superassemblies characterised by high local mobility, convex surface shape and negative electrostatic potential. Furthermore, the prevalence of complementary hydrophobic and aromatic residues in the binding sites of antibodies[40] also suggests an important binding role for buried hydrophobic side chains. Clearly, high-performance liquid chromatographic techniques have the potential to characterise the relative spatial disposition of amino acid residues within the three-dimensional structure of *e.g.*, a protein. Definition of the molecular basis of the interactions between the biomacromolecule and a biological or synthetic surface has not only significant implications for the optimisation of separation performance *per se* but also would impact on the design and development of synthetic peptidic vaccines and new peptidic analogues for use in therapy.

ACKNOWLEDGEMENTS

Research grants to M.T.W.H. from the National Health and Medical Council of Australia, the Australian Research Council and the Monash University Research Fund Committee are gratefully acknowledged.

REFERENCES

1 M. T. W. Hearn, A. N. Hodder and M. I. Aguilar, *J. Chromatogr.*, 458 (1988) 45.
2 M. T. W. Hearn, A. N. Hodder, P. G. Stanton and M. I. Aguilar, *Chromatographia*, 24 (1987) 769.
3 W. Kopaciewicz, M. A. Rounds, J. Fausnaugh and F. E. Regnier, *J. Chromatogr.*, 266 (1983) 3.
4 A. N. Hodder, M. I. Aguilar and M. T. W. Hearn, *J. Chromatogr.*, 512 (1990) 41.
5 W. Kopaciewicz and F. E. Regnier, *Anal. Biochem.*, 133 (1983) 251.
6 A. N. Hodder, M. I. Aguilar and M. T. W. Hearn, *J. Chromatogr.*, 443 (1988) 97.
7 A. N. Hodder, M. T. W. Hearn and M. I. Aguilar, *J. Chromatogr.*, 458 (1988) 27.
8 A. N. Hodder, M. I. Aguilar and M. T. W. Hearn, *J. Chromatogr.*, 476 (1989) 391.
9 C. C. F. Blake, G. A. Mair, A. C. T. North, D. C. Philips and V. R. Sarma, *Proc. Roy. Soc.*, B167 (1967) 365.
10 D. C. Philips, *Proc. Natl. Acad. Sci. U.S.A.*, 57 (1967) 484.
11 C. C. F. Blake, L. N. Johnson, G. A. Mair, A. C. T. North, D. C. Philips and V. R. Sarma, *Proc. Roy. Soc.*, B167 (1967) 378.
12 N. Sharon, *Proc. Roy. Soc.*, B167 (1967) 402.
13 J. A. Rupley, *Proc. Roy. Soc.*, B167 (1967) 416.
14 R. R. Drager and F. E. Regnier, *J. Chromatogr.*, 359 (1986) 147.
15 E. D. Green and J. V. Baenziger, *Anal. Biochem.*, 158 (1986) 42.
16 T. Tsuji and T. Osawa, *J. Biochem.*, 101 (1987) 241.
17 W. Kopaciewicz, M. A. Rounds, J. Fausnaugh and F. E Regnier, *J. Chromatogr.*, 266 (1983) 3.
18 I. I. Geschwind and C. H. Li, *Biochim. Biophys. Acta*, 25 (1957) 171.
19 A. J. Sophianopoulos, C. K. Rhodes, D. N. Holcomb and K. E. Van Holde, *J. Biol. Chem.*, 237 (1962) 1107.

20 K. Hayashi, T. Imoto and M. Funatsu, *J. Biol. Chem. (Japan)*, 54 (1963) 381.
21 R. E. Bruccoleri, M. Karplus and J. A. McCammon, *Biopolymers*, 25 (1986) 1767.
22 C. Formoso and L. S. Forster, *J. Biol. Chem.*, 250 (1975) 3738.
23 N. K. Vyas, M. N. Vyas and F. A. Quiocho, *Science (Washington, D.C.)*, 242 (1988) 1290.
24 H. M. Sassenfeld and S. J. Brewer, *Biotechnology*, 2 (1984) 76.
25 R. D. Banks, C. C. F. Blake, P. R. Evans, R. Haser, D. W. Rice, G. W. Hardy, M. Merrett and A. W. Philips, *Nature (London)*, 279 (1979) 773.
26 G. L. Gilliland and F. A. Quiocho, *J. Mol. Biol.*, 146 (1981) 341.
27 S. C. Harrison, A. J. Olson, C. E. Schutt, F. K. Winkler and G. Bricogne, *Nature (London)*, 276 (1978) 368.
28 S. Remington, G. Wiegand and R. Huber, *J. Mol. Biol.*, 158 (1982) 111.
29 W. S. Bennet and T. A. Steitz, *J. Mol. Biol.*, 140 (1980) 211.
30 W. S. Bennet and T. A. Steitz, *Proc. Natl. Acad. Sci. U.S.A.*, 75 (1978) 4848.
31 R. C. McDonald, T. A. Steitz and D. M. Engelman, *Biochemistry*, 18 (1978) 338.
32 M. J. E. Sternberg, D. E. P. Grace and D. C. Philips, *J. Mol. Biol.*, 130 (1979) 231.
33 J. A. McCammon, B. R. Gelin, M. Karplus and P. G. Wolynes, *Nature (London)*, 262 (1976) 325.
34 J. Janin and S. J. Woodak, *Prog. Biophys. Molec. Biol.*, 42 (1983) 21.
35 R. M. Chicz and F. E. Regnier, *J. Chromatogr.*, 443 (1988) 193.
36 P. H. Von Hippel and T. Schleich, in S. N. Timasheff and G. D. Fasman (Editors), *Structure and Stability of Macromolecules*, Vol. II, Marcel Dekker, New York, 1969, p. 417.
37 F. A. Long and W. F. McDevit, *Chem. Rev.*, 51 (1952) 119.
38 W. A. P. Luck, in A. Pullman, V. Vasileui and L. Packer (Editors), *Water and Ions in Biological Systems*, Plenum Press, New York, 1985, p. 95.
39 T. T. Herskovits and M. G. Hamilton, *Biochim. Biophys. Acta*, 915 (1987) 157.
40 T. T. Herskovits and G. B. Villanueva, *Biochemistry*, 25 (1986) 931.
41 R. K. Scopes, *Protein Purification: Principles and Practice*, Springer, Berlin, Heidelberg, New York, 2nd ed., 1987.
42 B. Anspach, A. Johnston, H.-J. Wirth, K. K. Unger and M. T. W. Hearn, *J. Chromatogr.*, 476 (1989) 205.
43 J. L. Fausnaugh and F. E. Regnier, *J. Chromatogr.*, 359 (1986) 131.
44 J. L. Fausnaugh-Pollit, G. Therenon, L. Janis and F. E. Regnier, *J. Chromatogr.*, 443 (1988) 221.
45 E. D. Getzoff, H. M. Geyson, S. J. Rodda, H. Alexander, J. A. Tainer and R. A. Lerner, *Science (Washington, D.C.)*, 235 (1987) 1191.
46 A. M. Lesk and K. D. Hardman, *Science (Washington, D.C.)*, 216 (1982) 539.
47 M. Fridman, M. I. Aguilar and M. T. W. Hearn, *J. Chromatogr.*, 512 (1990) 57.

Journal of Chromatography, 517 (1990) 333–344
Elsevier Science Publishers B.V., Amsterdam

CHROMSYMP. 1945

Optimization study of octane-in-water emulsions by sedimentation field-flow fractionation

MARCIA E. HANSEN*,[a] and DAVID C. SHORT
The Procter & Gamble Company, Packaged Soap and Detergent Division, 5299 Spring Grove Avenue, Cincinnati, OH 45217 (U.S.A.)

ABSTRACT

The droplet size distributions of octane-in-water emulsions have been studied by sedimentation field-flow fractionation (SdFFF). Initially, the experimental parameters of the SdFFF experiment were examined to optimize these conditions for an octane emulsion stabilized by sodium dodecyl sulfate (SDS). The carrier flow-rate had a large impact on sample recovery. Resolution of the various size species was optimized by using the appropriate field strength and relaxation parameters. Comparison of the SDS emulsion to a similar SDS emulsion with added sodium chloride and to an non-ionic system, Brij 35, confirmed the sensitivity of the SdFFF method to differences in size distribution. Examination of the droplet size distribution over a 70-h period provided insights into the stability of these systems.

INTRODUCTION

In order to characterize the efficiency of surfactants in stabilizing oil droplets in solution, we developed a method for monitoring oil droplet size distributions. We expected that information about the initial droplet size and the demulsification kinetics of oil-in-water emulsions would provide insights into the structure of the surfactant–oil interface as well as the overall performance of each individual surfactant system in suspending oil droplets in aqueous solutions. As a first approach, we chose *n*-octane as a model oil and studied *n*-octane emulsions as prepared by ultrasonic dispersion of octane in the presence of simple surfactant systems. These surfactant systems included anionic and non-ionic surfactants. Specifically, sodium dodecyl sulfate (SDS) and Brij-35 (a polyethylene glycol ether of lauryl alcohol) systems at concentrations slightly above their critical micelle concentrations (CMC) were studied. The effect of salt in the anionic surfactant system was also investigated. The sonication of octane in the presence of surfactant was expected to generate a system of large oil

[a] Present address: FFFractionation, Inc., P.O. Box 58718, Salt Lake City, UT 84158-0718, U.S.A.

0021-9673/90/$03.50

droplets, formally termed a macro-emulsion. Differences in the packing of surfactant molecules at the surfactant–octane interface should lead to differences in the droplet size resulting from sonication. Also, the physical structure of the surfactant–octane interface should be reflected by the stability of the system of oil droplets against demulsification into larger droplets.

For the analysis of the oil droplet size distributions, a sedimentation field-flow fractionation (SdFFF) technique was optimized. This technique has been extensively used for the determination of particle size distributions of latex particles[1,2]. Since oil droplets are more delicate than typical particle samples, we could not assume that this sample would behave as a "hard sphere". Therefore, in this study, we report the optimization of the experimental parameters of the SdFFF technique, such as the field strength, the carrier flow-rate, relaxation time, and injection method.

SdFFF is a high-resolution particle sizing technique, which separates sample species according to their buoyant mass. This technique has been described in great detail elsewhere[1]. Basically, in SdFFF a centrifugal field is imposed perpendicularly across a thin, open flow channel. SdFFF channels are typically 80 cm × 2.0 cm × 0.025 cm. Sample species are deposited in zones of a characteristic thickness according to their interaction with the field. The buoyant mass of the sample species and the centrifuge rpm and rotor radius determine the sample–field interaction. The laminar flow profile across the thin dimension of the channel allows sample species to be differentially eluted due to their varying zone thicknesses. In the case of emulsions, the larger, more buoyant oil droplets form a more compressed sample zone near the upper channel wall. This sample zone is eluted after the less dense sample zones of smaller droplets.

SdFFF is potentially superior to competing particle sizing methods for the analysis of emulsions. This technique was applied to commercial emulsions of safflower and soybean oils by Yant *et al.*[3]. The buoyancy of the sample causes no problem, as in other methods; oil droplets are deposited at the top channel wall, but are fractionated just like the particles with negative buoyancy which are deposited at the bottom wall. Light-scattering and centrifugal techniques[4,5] have been most commonly applied to the study of emulsion droplet size. However, as samples must not be stirred for light-scattering measurements, results are possibly biased due to the differential float-rate of the droplets of varying diameter. Also, analysis of emulsions with general centrifugal techniques is difficult as these systems are designed for particles heavier than the suspension media. Alternatively, application of microscopic techniques to the sizing of emulsion droplets is cumbersome and droplets below 0.5 μm are not readily detected. With SdFFF it is additionally possible to obtain true distribution data, as opposed to the mean diameter and polydispersity data provided by light-scattering techniques. Sample species are separated into mass-based fractions in SdFFF. Following separation, the turbidimetric response of a UV detector individually quantifies each fraction.

Another advantage of the SdFFF separation scheme is the inherent flexibility of the system. Retention of a sample may be fine-tuned by adjusting the centrifuge speed. Increased retention yields greater resolution between particles of similar diameter, although experiment run time is concomitantly increased. Offset of the time factor may be accomplished by increasing carrier flow-rate.

The trends described above hold only for the idealized "hard-sphere" particle

sample. For the delicate type of sample studied in this report, increases in field strength and flow-rate may adversely affect the integrity of the droplets. At higher field strengths the zone thickness of the sample is decreased. The zone is concentrated and compressed towards the channel wall so that there is a danger of oil droplets coalescing or sticking irreversibly to the channel wall. At increasing flow-rates, shearing the oil droplets is risked. Alternatively, higher flow-rates may encourage total recovery of sample as the droplets attached to the channel wall are dislodged. The present study examines these trade-offs between field strength and flow-rate conditions with the ultimate goal of producing optimal size distribution data in the shortest time under conditions that maintain the integrity of the oil droplets.

EXPERIMENTAL

Instrumentation

The SdFFF unit used was a DuPont SF^3 2000 which is similar to the systems described previously[2,6], except for the data station. For this upgraded model an IBM computer and software are used. Otherwise, the instrumental components are the same as in other sedimentation field-flow fractionators[3]. Typically, the instrument consists of the SdFFF channel which fits inside a centrifuge, a high-performance liquid chromatography-type pump, and a UV detector set at 254 nm. The channel length and width were 56 and 2.5 cm, respectively. The channel volume, 2.92 ml, was measured using the retention time of a non-retained marker eluted at low flow-rate. The channel thickness, 0.021 cm, was calculated using the channel volume, length, and width measurements.

Methods

The carrier composition used for the elution of the emulsion sample was identical to the surfactant system used in generating the emulsion, unless otherwise noted. Doubly distilled water was equilibrated with octane prior to the addition of the appropriate surfactant and salt. After the surfactant was thoroughly dissolved, the carrier solution was vacuum-filtered through a 0.22-μm filter. The carrier was sparged with helium.

The octane emulsions were prepared using the method described by Avranas *et al.*[7]. A 5-ml portion of octane was added to 25 ml of the surfactant system prepared as described above. Emulsions were generated with a sonic probe (Branson Model 184V ultrasonic power supply with a Branson Model A410 watt meter), operating at 1000 W and 20 000 KHz under an atmosphere of nitrogen.

THEORY AND CALCULATIONS

Retention equations

As the theoretical aspects of retention in SdFFF have been adequately explored and reported earlier[1], we will only briefly discuss those aspects of SdFFF pertinent to this study. In normal SdFFF, sample particles interact with the externally imposed sedimentation field so as to form zones with an exponential profile according to the following equation

$$c = c_0 \exp(-x/l) \tag{1}$$

where c is the concentration of particles at a distance x from the channel wall, c_0 is the concentration at the wall, and l is the mean zone thickness. The critical retention parameter, λ, is the ratio of l to the full channel thickness, w, and is related to the thermal energy, kT, and the force, F, exerted on a particle

$$\lambda = l/w = kT/Fw \tag{2}$$

The experimentally observed retention ratio (R) is related to λ as follows

$$R = 6\lambda[\coth(1/2\lambda) - 2\lambda] \tag{3}$$

Eqn. 3 is commonly simplified[3] to

$$R = 6\lambda - 12\lambda^2 \tag{4}$$

We further define λ in eqn. 5 so that the particle diameter, d, may be calculated from the observed retention ratio from the field strength, G, as determined by using the angular speed, ω, and rotor radius, r_r, of the centrifuge, and with $\Delta\rho$, the absolute difference between carrier and particle density. Particles are assumed to be spherical.

$$\lambda = 6kT/(d^3\pi\Delta\rho\omega^2 r_r w) \tag{5}$$

The retention equation, eqn. 3, assumes particles to be point spheres with no hydrodynamic interaction due to physical size. When this consideration is added, the retention equation becomes more complicated. The sterically corrected retention equation has been expressed[8] as follows

$$R = 6\gamma(\alpha - \alpha^2) + 6\lambda(1 - 2\alpha)\{\coth[(1 - 2\alpha)/2\lambda] - 2\lambda/(1 - 2\alpha)\} \tag{6}$$

where $\alpha = d/2w$ and γ is a dimensionless factor with dependence on flow-rate, field strength, and particle diameter[9].

In sterically corrected SdFFF theory, the retention volume increases with particle diameter until the steric effect dominates. At this steric inversion point, there is a foldback in elution order. Particles larger than those eluted at the inversion point are eluted earlier under the dominating steric influences.

Relaxation calculation

Relaxation time, t_r, is the time required for each sample species to come to equilibrium in its respective zone. The velocity with which a sample particle travels from the far channel wall to the accumulation wall may be calculated by means of the classical Svedberg equation

$$\text{velocity} = (1 - v_1\rho)mG/f = (4/3)\pi\Delta\rho r_p^3 G/f \tag{7}$$

in which v_1 is the partial molar volume of the sample particle, m is the particle mass, r_p is the particle radius, and f is the frictional coefficient. Since the particle must travel the

distance of the channel thickness, w, we calculate the relaxation time, t_r, by using the Stoke's approximation for the friction coefficient.

$$t_r = 18\eta w/(\Delta\rho d^2 G) \tag{8}$$

The viscosity of the carrier solution is represented by η.

Peak dispersion calculations

Peak dispersion in SdFFF has been characterized in terms similar to that of liquid chromatography[1]. Plate height, H, which is variance, σ^2, per channel length, L, is expressed by

$$H = 2D/R[v] + \chi w^2[v]/D + \Sigma H_i \tag{9}$$

where D is the diffusion coefficient of the sample particles, $[v]$ is the average carrier linear flow velocity, χ is a non-equilibrium term as described below, and H_i includes all other miscellaneous contribution to peak dispersion, such as sample injection effects, channel irregularities, and dead volume effects. χ is a complicated term, but in the limit of high retention, this factor is reduced to a simple function of

$$\chi = 24\lambda^3 \tag{10}$$

RESULTS AND DISCUSSION

Optimization of experimental parameters

In general, we found that the octane emulsions, as generated by sonic dispersion, had bimodal particle size populations. These emulsions were unstable in that the size distribution changed with time. Initially, the emulsions had a single mode of smaller droplets which grew into larger droplets. In order to track this aging process, we optimized the SdFFF method so that the broad size range of droplets could be monitored under a single set of conditions, *i.e.* field strength, flow-rate, and relaxation time. At the lower end of the distribution, sufficient relaxation time and field strength were required to allow resolution of the small particles from the void. Optimization for the larger particles present in the distribution required a minimization of field strength or retention so that sample recovery was acceptable and analysis time was not excessive. A retention range of $R = 0.15$–0.05 has been recommended for optimum recovery and accuracy in the analysis of polystyrene lattices[10]. We used these limits as a guideline for our optimization study.

Optimization of field strength

As relaxation time is strongly dependent on field strength, we first scanned a range of centrifuge speeds to determine the optimum for the expected oil droplet size range. Assuming the density of the oil droplets at 0.7, the density of *n*-octane, we approximated an initial rpm for beginning the scan. Using a limiting upper diameter of 1 μm and a minimum retention ratio of 0.05, we calculated from eqns. 4 and 5 a field strength of 2.39 g, which requires a centrifuge speed of 150 rpm.

In Fig. 1 we compare the resolution and retention obtained by scanning from 150

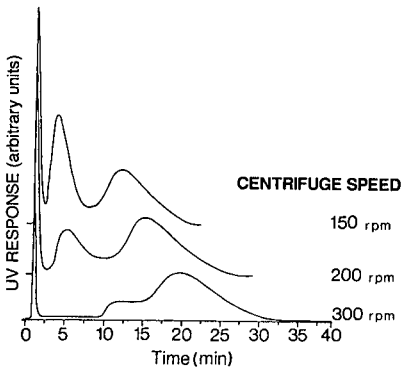

Fig. 1. Fractograms illustrating the effect of varying field strengths. Surfactant system, 0.3% SDS; emulsion age, 20 h; carrier flow-rate, 3.0 ml/min.

to 300 rpm at 3.0 ml/min using a 20-h-old octane-in-0.3% SDS emulsion. At this age, the emulsion has an intermediate range of particle size as will be discussed in the last section. At 300 rpm, the retention of the larger mode of particles is excessive at $R = 0.040$. At 150 rpm, the resolution between the void and first peak is just sufficient, but for younger emulsions with smaller particles, this level of resolution would not be acceptable. We continued the remainder of our optimization study at a centrifuge speed of 200 rpm. At this field strength (4.25 *g*), the retention ratios of the first and second modes of the bimodal size distribution are 0.15 and 0.060, indicating droplet diameters of 0.503 and 0.699 μm, respectively.

The possibility of sample degradation due to the concentrating effects of the centrifugal field could not be entirely eliminated. As a partial check, a 20-h-old emulsion was split into two portions and one of the portions was exposed to a centrifugal field of approximately 5 *g* for a period of 1 h. The resulting fractograms for analysis of these two sampels at 4.25 *g*, 3.0 ml/min, were compared and no significant differences were noted.

Optimization of relaxation time

Resolution of the smallest mode of particles from the void peak is dependent on a sufficient relaxation time. The void peak in SdFFF contains non-retained molecular components as well as very large particles which are eluted quickly due to steric effects and small particles not completely at equilibrium in their characteristic sample zone. The smallest droplet diameter of the 20-h sample mentioned above was 0.45 μm so that a 25-min relaxation time is required at a centrifuge speed of 200 rpm. However, we stressed the optimization of relaxation time by examining a fresh 1-h-old emulsion. Hypothetically, this sample had the smallest droplet. The droplet growth processes of the emulsion were presumably quenched by dilution at injection. Scanning from a relaxation time of 5 to 60 min, the dramatic effects of relaxation are evident (Fig. 2). Resolution between the void and the first size modes of droplets increases as the relaxation time is increased from 5 up to 45 min. In our opinion, the slight gain in resolution obtained by increasing the relaxation time from 45 to 60 min is not worth the extra analysis time. No loss in recovery, as determined by measuring the peak area, was observed by increasing the relaxation time.

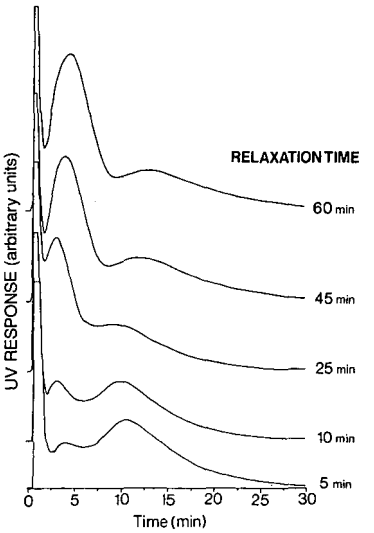

Fig. 2. Fractograms resulting from use of varying relaxation times. Surfactant system, 0.3% SDS; emulsion age, 1.0 h; field strength, 4.25 *g*; carrier flow-rate, 3.0 ml/min.

Injection flow-rate optimization

In the DuPont SF^3 2000 system the sample is introduced via an injection valve, connected to the head of the SdFFF channel with approximately 80 cm of polystyrene tubing, at a volume of 0.55 ml. The flow-rate for the injection process is an optional parameter. It is automatically continued so until a total of 1.1 ml is washed through the injection valve and connecting tubing. The centrifuge field is on during sample injection so that sample begins relaxation as it enters the channel and theoretically does not travel an appreciable distance down the channel during the injection period. The default injection flow-rate in the SF^3 2000 is 0.1 ml/min. This low flow-rate should minimize the migration of sample down the channel, but allow for band broadening in the 0.55 ml of tubing.

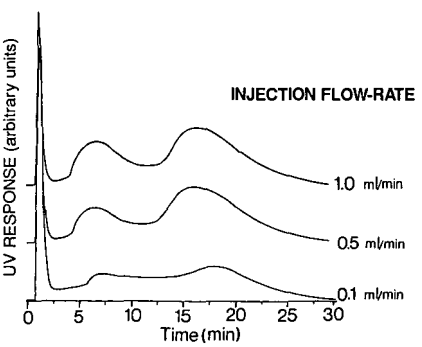

Fig. 3. Fractograms resulting from the use of varying injection flow-rates. Surfactant system, 0.3% SDS; emulsion age, 20 h; field strength, 4.25 *g*; carrier flow-rate, 3.0 ml/min.

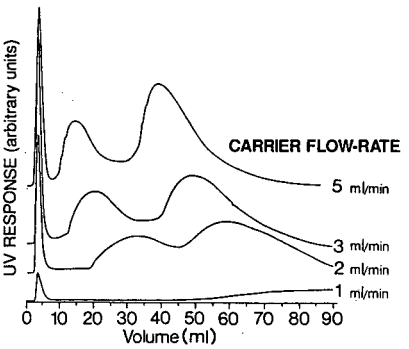

Fig. 4. Fractograms illustrating effect of varying carrier flow-rate on retention, resolution, and sample recovery. Emulsion age, 20 h; field strength, 4.25 *g*; relaxation time, 25 min.

When the injection flow-rate was varied, only a slight decrease in peak broadening with increasing flow-rate was observed (Fig. 3). The peak position did not shift appreciably with increasing flow-rate, indicating that sample migration down the channel during the injection process is not significant. The overall effect observed for increased flow injection velocities was increased recovery, implying that the sample sticks to the polystyrene tubing when the injection is slower. To minimize analysis time and maximize recovery we used an injection flow-rate of 1.0 ml/min.

Carrier flow-rate optimization

The final experimental parameter studied was carrier flow-rate. Obviously, analysis time is decreased with higher flow-rates. Potentially, sample recovery increases with flow-rate. However, from the plate-height equation, we calculated an increase in peak broadening and, thus, a decrease in resolution with increasing carrier velocities. Also, shearing of sample droplets may be induced at higher flow-rates. More importantly, the steric transition point is approached more rapidly with faster flow-rates. As these hydrodynamic steric effects are not sufficiently characterized at this time, the accuracy of the particle diameter calculation suffers. In the extreme case in which the particle diameter exceeds the diameter at the steric transition point, the foldback of retention leads to total confusion in the calculation of the size distribution[9].

In Fig. 4 the fractograms for various carrier flow-rates are compared on the basis of volume rather than time. This allows direct comparison and makes the effect on retention, peak broadening, and sample recovery obvious. A decrease in retention was noted as the carrier velocity was increased. This is explained by steric effects. The hydrodynamic lift forces that oppose normal retention mechanisms accelerate sample elution. The observed trend in peak width opposed the effect predicted by the plate height equation (eqn. 9). Plate heights measured from the two peaks of the bimodal population decreased with carrier velocity. Presumably, steric effects interfere with the normal peak broadening effect. Also, at larger carrier velocities the chromatographic effect of sample reversibly adhering to the channel wall is reduced. In the absence of this process, peak broadening is minimized.

An increase in recovery with flow-rate was also noted. The poor recovery and

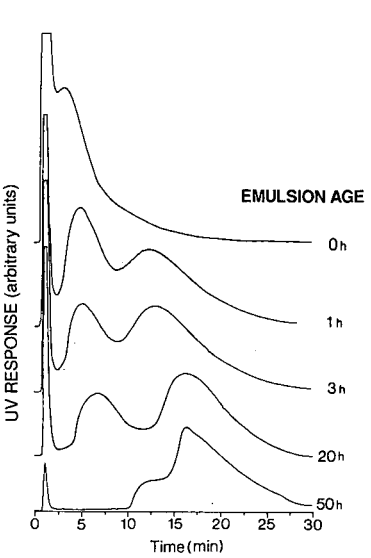

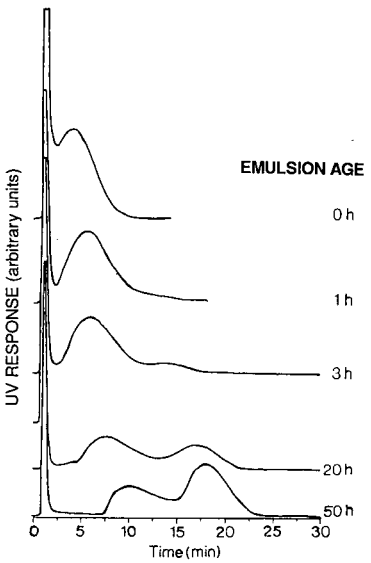

Fig. 5. Fractograms for emulsions of octane in 0.3% SDS at varying ages. Field strength, 4.25 *g*; carrier flow-rate, 3.0 ml/min; relaxation time, 45 min; injection flow-rate, 1.0 ml/min.

Fig. 6. Fractograms for emulsions of octane in 0.3% SDS with 0.2% sodium chloride at varying ages. Field strength, 4.25 *g*; carrier flow-rate, 3.0 ml/min; relaxation time, 45 min; injection flow-rate, 1.0 ml/min.

excessive retention at a flow-rate of 1.0 ml/min illustrates the definite advantage of using higher flow-rates to dislodge the sample. The previous set of experiments for optimizing the injection flow-rate further validate this effect. As a compromise between the advantages of higher flow-rates and the problems of steric effects induced at elevated flow-rates, an intermediate flow-rate, 3.0 ml/min, was chosen for the study of the dynamics of the octane emulsions.

Effect of surfactant system on the size distribution of octane-in-water emulsions

The sensitivity of the SdFFF method, as optimized above, was tested by examining the droplet size distribution of octane emulsions prepared in three different surfactant sytems. Two anionic systems at 0.3% SDS and 0.3% SDS with 0.2% sodium chloride, and a non-ionic system, 0.10% Brij 35, the polyethylene glycol ether of lauryl alcohol, $CH_3(CH_2)_{10}CH_2(OCH_2CH_2)_{23}OH$, were studied. These surfactant concentrations are slightly above the CMC of each system. The fractograms so obtained were reproducible for emulsions of similar age and composition. Carrier composition was found to affect the analysis. Emulsions generated in the presence of 0.3% SDS with 0.2% sodium chloride, but analyzed in a saltless carrier behaved similar to the emulsions generated and analyzed in solutions without sodium chloride. Possibly, the effects noted with salt are reversible.

The surfactant systems aged similarly, with a few notable differences (*cf.* Figs. 5–7). In all cases, the emulsions appeared to be dynamic: droplet diameter distributions changed with sample age. The most dramatic effects were noted in the first several hours. Immediately following sonication, the emulsions showed a monomodal size

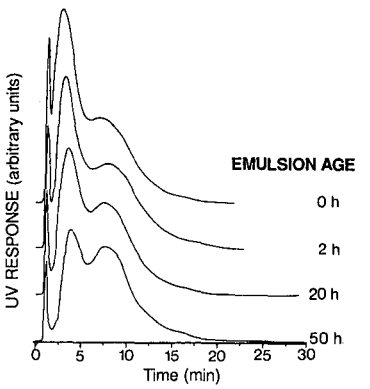

Fig. 7. Fractograms for emulsion of octane in 0.1% Brij 35 at varying ages. Field strength, 4.25 *g*; carrier flow-rate, 3.0 ml/min; relaxation time, 45 min; injection flow-rate, 1.0 ml/min.

population. A second mode of oil droplet diameters generally developed within the 3 h.

For the surfactant system with 0.3% SDS plus 0.2% sodium chloride, only a small amount of the second population developed in 3 h. The 0.1% Brij 35 system, on the other hand, showed a bimodal population immediately, but thereafter changed less rapidly with time than the other surfactant systems. Superior performance of the Brij system in stabilizing oil droplet is implied by the slower kinetics of droplet growth. According to a similar line of reasoning, the addition of sodium chloride to the 0.3% SDS solution increases the stability of the emulsion system: the small mode of droplet diameters is apparently more resistant to droplet growth. The current models for emulsion instability due to droplet growth are coalescence and molecular diffusion of the oil through the surfactant barrier[4]. At this point, we cannot distinguish between these models.

Table I shows the droplet diameters calculated for a larger range of emulsion age using the sterically corrected retention equation with a constant γ of 1. Again, the

TABLE I

COMPARISON OF DROPLET DIAMETERS (μm) FOR VARIOUS OCTANE EMULSIONS *VERSUS* EMULSION AGE

Field strength, 4.25 *g*; carrier flow-rate, 3.0 ml/min; relaxation time, 45 min; injection flow-rate, 1.0 ml/min.

Emulsion age (h)	*0.3% SDS*		*0.3% SDS + 0.2% NaCl*		*0.1% Brij 35*	
	1st Mode	*2nd Mode*	*1st Mode*	*2nd Mode*	*1st Mode*	*2nd Mode*
0	0.376	–	0.408	–	0.344	0.500
1	0.438	0.631	0.464	–		
2			0.471	–	0.365	0.524
3	0.448	0.643	0.474	0.661		
6	0.445	0.666	0.480	0.679		
20	0.503	0.699	0.522	0.716	0.379	0.516
50	0.627	0.709	0.580	0.738	0.396	0.522
70	0.641	0.721	0.580	0.740	0.404	0.522

results for the non-ionic Brij system are notably different from those of the anionic systems. Droplet diameters are smaller and more stable over the 70-h time span tested. Presumably, differences in the structure of the non-ionic micelle *versus* an anionic micelle generate these effects. The packing of non-ionic surfactant molecules around the octane droplet is possibly tighter than the packing of anionic surfactant molecules, and this may protect the droplets from coalescence. Alternatively, a thicker coat of surfactant may be a less penetrable barrier to molecular diffusion. The presence of salt in the SDS system initially led to larger droplets. We suggest that sodium chloride also changes the structure of surfactant packing in the micelle. The increase in ionic strength allows the surfactant to pack more closely, decreasing the curvature at the octane–SDS interface[5]. Thus the resulting droplet assumes a larger diameter.

CONCLUSIONS

In this optimization study the experimental parameters used in analyzing the droplet size distribution of octane emulsions were found to impact the results significantly. Additionally, the calculations and considerations needed to search for the optimum conditions were expressed. The major effect noted involved the flow-rates used and the implication on sample recovery.

Both carrier and injection flow-rate had to be optimized. Apparently, the octane emulsions tested adhere extensively to the surfaces of the channel wall and polystyrene tubing. Relaxation time of sample in the system was also crucial for the resolution of the lower end of the particle size distribution.

The surfactant systems tested with the optimized experimental parameters illustrated the sensitivity of this method to changes in the size distribution. Bimodal populations were prevalent. These types of distributions are difficult to characterize by light-scattering techniques. The non-ionic surfactant system studied, Brij 35, showed differences in droplet diameter as well as droplet growth dynamics. As opposed to the anionic SDS system, the diameter of droplets in the non-ionic system were smaller and changed less with emulsion age. A comparison of anionic surfactant systems with and without sodium chloride showed the theoretically expected differences in the micelle structure. The droplets were initially larger in the system with salt due to the closer surfactant packing possible in the presence of salt and the resulting decrease in curvature at the octane–surfactant interface. The emulsions generated with salt were also more resistant to particle growth. This substantiates the hypothesized thicker packing of surfactant molecules.

Overall, the study confirmed the feasibility of using SdFFF for the study of emulsion dynamics. Sensitivity to the two populations of droplet diameters was demonstrated. Analysis time was not so excessive that the dynamics of the changing system could not be observed.

ACKNOWLEDGEMENTS

The authors wish to thank the Procter & Gamble Company for financial support and for allowing them to publish this material. Also, thanks are due to the Fabricated Products Department of E. I. du Pont de Nemours & Company for use of the SF^3 2000 sedimentation field-flow fractionator.

REFERENCES

1 J. C. Giddings, F. J. F. Yang and M. N. Myers, *Anal. Chem.*, 47 (1975) 126.
2 J. J. Kirkland, W. W. Yau and W. A. Dorner, *Anal. Chem.*, 50 (1980) 1944.
3 F. S. Yang, K. D. Caldwell, M. N. Myers and J. C. Giddings, *J. Colloid Interface Sci.*, 93 (1982) 115.
4 H. M. Cheung, *Langmuir*, 3 (1987) 744.
5 M. L. Robbins, J. Bock and J. S. Huang, *J. Colloid Interface Sci.*, 126 (1988) 114.
6 J. J. Kirkland, S. W. Rementer and W. W. Yau, *Anal. Chem.*, 51 (1981) 1730.
7 A. Avranas, G. Stalidis and G. Ritzoulis, *Colloid Polym. Sci.*, 266 (1988) 937.
8 M. N. Myers and J. C. Giddings, *Anal. Chem.*, 54 (1982) 2284.
9 S. Lee and J. C. Giddings, *Anal. Chem.*, 60 (1988) 2328.
10 K. D. Caldwell and J. Lee, presented at the *First International FFF Symposium, Park City, UT, June 1988.*

Journal of Chromatography, 517 (1990) 345–359
Elsevier Science Publishers B.V., Amsterdam

CHROMSYMP. 1944

Potential-barrier field-flow fractionation, a versatile new separation method

A. KOLIADIMA and G. KARAISKAKIS*
Department of Chemistry, University of Patras, GR-26110 Patras (Greece)

ABSTRACT

A new method called potential-barrier field-flow fractionation, which is a combination of potential-barrier chromatography and sedimentation field-flow fractionation (SdFFF), is presented for the separation and characterization of colloidal materials. The separation is based either on particle size differences or on Hamaker constant, surface potential and Debye–Hückel reciprocal distance differences. In its simplest form the technique consists in changing the ionic strength of the carrier solution from a high value, where only one of the colloidal materials of the binary mixture subjected to separation is totally adsorbed at the beginning of the SdFFF channel wall, to a lower value, where the total number of adhered particles is released. The method was applied to the separation of haematite and titanium dioxide spherical colloidal particles and to the separation of haematite spherical particles with different sizes. At the same time as separation was occurring, the particle sizes of the colloidal materials of the mixture were determined. The experimental values of particle diameters were in good agreement with those obtained by transmission electron microscopy or determined by normal SdFFF. Finally, the retention perturbations due to particle (α-Fe_2O_3 and TiO_2)–wall interactions in SdFFF were investigated.

INTRODUCTION

During the last few years, interest has arisen in methods for the separation of suspended particles, in analogy with techniques used for matter in solution. Hydrodynamic chromatography[1], gel chromatography[2], potential-barrier chromatography[3] and field-flow fractionation (FFF)[4–8] have already been studied, and potential-barrier FFF (PBFFF) has recently been suggested[9,10]. The latter is a combination of FFF and potential-barrier chromatography.

Basically, FFF is a one phase-chromatographic system in which an external field or gradient replaces the stationary phase. The applied field can be of any type that interacts with the sample components and causes them to move perpendicular to the flow direction in the open channel. The most highly developed of the various FFF modes is sedimentation FFF (SdFFF), in which the separations of suspended parti-

0021-9673/90/$03.50

cles are performed with a single, continuously flowing mobile phase in a very thin, open channel under the influence of an external centrifugal force field[4].

SdFFF yields experimental data in the form of a fractogram, which is a plot of the detector response of the emerging sample *versus* the time or volume of its emergence. For constant field conditions, the retention volume (or time) in SdFFF is immediately related to the particle mass. Thus, in normal SdFFF, where the particle–wall interactions are negligible, the separation is based on particle size differences.

Potential-barrier chromatography (PBC) can be applied to separate particles based on differences in size or in any of the physico-chemical parameters involved in the potential energy of interaction between the particles and the packing of the column. This method, which is based on the existence of a surmountable potential barrier between particles and deposition surface, is classified as an FFF method rather than a chromatographic method, because the selective interaction is experienced in one phase. Thus, by combining PBC with normal SdFFF one could separate according to two mechanisms, one governed by the depth of the potential energy well for the different particles and the other determined by the interactive force between the particles and the external field.

The purpose of this work was to study the interactions between the particle and the channel wall in SdFFF and to show the applicability of PBFFF in the separation of colloidal particles.

THEORY

In normal SdFFF, where the particle–wall interactions are absent, the potential energy of a spherical particle is given by the relation[10]

$$V(x) = \frac{\pi d^3}{6}(\rho_s - \rho)Gx = \frac{\pi d^3}{6} \cdot \Delta\rho Gx \tag{1}$$

where d is the diameter and ρ_s the density of the spherical particle, ρ is the carrier density, G is the sedimentation field strength expressed as acceleration and x is the coordinate position of the centre of particle mass.

The retention ratio, R, in SdFFF is given by the ratio of the column void volume, V_0, to the component retention volume, V_R. For highly retained peaks and spherical particles, R can be expressed as

$$R = \frac{V_0}{V_R} \approx 6\lambda = \frac{6l}{w} = \frac{36kT}{\pi d^3 Gw\Delta\rho} \tag{2}$$

where l is the characteristic mean layer thickness of the solute, w is the channel thickness, $\lambda\ (= l/w)$ is a dimensionless retention parameter, k is Boltzmann's constant and T is the absolute temperature.

When the colloidal particles interact with the SdFFF channel wall, the potential energy given by eqn. 1 must be corrected by considering the potential energy of

interaction $V(h)$. The latter can be estimated by the sum of the contributions of the Van der Waals, $V_6(h)$, and double-layer, $V_{DL}(h)$, forces:

$$V(h) = V_6(h) + V_{DL}(h) \tag{3}$$

where h is the separation distance between the sphere and the channel wall.

The Van der Waals interaction energy is approximated by[3]

$$V_6(h) = \frac{A_{132}}{6}\left[\ln\left(\frac{h + 2\alpha}{h}\right) - \frac{2\alpha(h + \alpha)}{h(h + 2\alpha)}\right] \tag{4}$$

where α is the particle radius and A_{132} is the effective Hamaker constant for media 1 and 2 interacting across medium 3. Combining laws are frequently used for obtaining approximate values for unknown Hamaker constants in terms of known values. The constant A_{132} can be approximately related to A_{131} and A_{232} via[11]

$$A_{132} \approx \sqrt{A_{131}A_{232}} \tag{5}$$

where A_{131} represents the interaction of two nearby bodies of material 1, separated by medium 3. A corresponding meaning applies to A_{232}. Two other useful relationships developed by Israelachvili[11] are the following:

$$A_{131} \approx \left(\sqrt{A_{11}} - \sqrt{A_{33}}\right)^2 \tag{6}$$

$$A_{232} \approx \left(\sqrt{A_{22}} - \sqrt{A_{33}}\right)^2 \tag{7}$$

which when combined with eqn. 5 give

$$A_{132} \approx \left(\sqrt{A_{11}} - \sqrt{A_{33}}\right)\left(\sqrt{A_{22}} - \sqrt{A_{33}}\right) \tag{8}$$

The Hamaker constants can be calculated on the basis of the Lifshitz theory from the relationship[11]

$$A_{132} \approx \frac{3h\nu_e}{8\sqrt{2}} \cdot \frac{(n_1^2 - n_3^2)(n_2^2 - n_3^2)}{(n_1^2 + n_3^2)^{\frac{1}{2}}(n_2^2 + n_3^2)^{\frac{1}{2}}[(n_1^2 + n_3^2)^{\frac{1}{2}} + (n_2^2 + n_3^2)^{\frac{1}{2}}]} + \\ + \frac{3}{4}kT\left(\frac{\varepsilon_1 - \varepsilon_3}{\varepsilon_1 + \varepsilon_3}\right)\left(\frac{\varepsilon_2 - \varepsilon_3}{\varepsilon_2 + \varepsilon_3}\right) \tag{9}$$

where n_1, n_2 and n_3 are the refractive indices of the three media, ε_1, ε_2 and ε_3 are the corresponding static dielectric constants and ν_e is the mean value of the absorption frequency of the three media.

The Hamaker constants A_{ii} can also be determined experimentally by measuring the corresponding surface tensions, since[11]

$$A_{ii} \approx 2.1 \cdot 10^{-21} \gamma_{ii} \tag{10}$$

where γ_{ii} is in mJ m^{-2} and A in J.

Eqn. 4 shows that the energy $V_6(h)$ depends on the Hamaker constant and on the particle radius, α.

The double-layer interaction potential, resulting from the development of electrical double layers at the solid–liquid interfaces is given by[3]

$$V_{DL}(h) = 16\varepsilon\alpha\left(\frac{kT}{e}\right)^2 \tanh\left(\frac{e\psi_1}{4kT}\right)\tanh\left(\frac{e\psi_2}{4kT}\right)e^{-\kappa h} \tag{11}$$

where ε is the dielectric constant of the liquid phase, e is the electronic charge, ψ_1 and ψ_2 are the surface potentials of the solid surfaces and κ is the reciprocal Debye length.

For oxides in water, as is the case here, the surface potential, ψ, is determined by the pH of the solution, as H^+ and OH^- are potential-determining ions. The potential is given by[12]

$$\psi = \frac{kT}{2.303e}(pH_{zpc} - pH) \tag{12}$$

where pH_{zpc} is the pH at which the net charge on the surface is zero.

For comparison purposes, apart from the surface potential, one could use the ζ potential calculated from the electrophoretic mobility, u, via the equations[13]

$$\zeta = \frac{6\pi n u}{\varepsilon} \qquad (\kappa\alpha \ll 1) \tag{13}$$

$$\zeta = \frac{4\pi n u}{\varepsilon} \qquad (\kappa\alpha \gg 1) \tag{14}$$

where n is the viscosity and ε is the dielectric constant of the suspending medium.

The reciprocal double-layer thickness is given by the expression

$$\kappa^{-1} = BI^{-\frac{1}{2}} \tag{15}$$

where B is a constant and I is the ionic strength of the suspending medium.

Eqns. 11 and 15 show that the energy $V_{DL}(h)$ is influenced from the surface potentials, ψ_1 and ψ_2, the ionic strength, I, and the particle radius, α.

The total potential energy, V_{tot}, of a spherical particle in PBFFF will equal the sum of the expressions in eqns. 1, 4 and 11:

$$V_{tot} = \frac{4}{3}\pi\alpha^3 \Delta\rho G x + \frac{A_{132}}{6}\left[\ln\left(\frac{h+2\alpha}{h}\right) - \frac{2\alpha(h+\alpha)}{h(h+2\alpha)}\right] + \\ + 16\varepsilon\alpha\left(\frac{kT}{e}\right)^2 \tanh\left(\frac{e\psi_1}{4kT}\right)\tanh\left(\frac{e\psi_2}{4kT}\right)e^{-\kappa h} \qquad (16)$$

The last equation shows that the energy V_{tot} in PBFFF (at a given SdFFF system, where the surface potential of the wall ψ_2 is constant) is a function of the size and of the surface potential of the particle, of the Hamaker constant and of the ionic strength of the carrier solution.

EXPERIMENTAL

The experimental procedure has been described in detail elsewhere[6,8,14]. The two SdFFF systems used in this work had the following dimensions: system I, 38.4 × 2.05 × 0.0262 cm^3 with a channel void volume of 2.06 cm^3, measured by the elution of the non-retained peak of sodium benzoate; system II, 38.5 × 2.3 × 0.0181 cm^3 with a channel void volume of 1.60 cm^3. In both systems the column was 6.85 cm from the centre of rotation. A Gilson Holochrome UV detector was used for detection at 254 nm and a Gilson Minipuls 2 peristaltic pump was used to pump the carrier solution and the sample to the channel.

The electrophoretic mobilities of α-Fe_2O_3 and TiO_2 particles were measured in a microelectrophoresis apparatus (Rank, Mark II) by using a four-electrode capillary cell. The velocities of at least twenty particles in each direction of the electric field were measured at the two stationary layers with an accuracy of ± 10%. The pH of the colloidal suspensions was measured by using a combination glass–saturated calomel electrode (Metrohm).

For the identification of the type of modification of TiO_2, a Philips Model PW 1130/00 X-ray diffractometer was used. The form of TiO_2 was found to be anatase. The transmission electron microscopic (TEM) pictures for the α-Fe_2O_3 and TiO_2 particles, some examples of which are shown in Fig. 1, were taken with a JEOL Model JSM-2 transmission electron microscope.

The surface tensions of the titanium dioxide and haematite colloidal particles were measured with a torsion balance from White Electrical Instruments.

Titanium dioxide monodisperse colloidal particles from PolySciences with an average diameter (obtained by TEM) of 0.388 μm, and haematite nearly monodisperse colloidal particles of two sizes (α-Fe_2O_3(I) with d = 0.148 μm and α-Fe_2O_3(II) with d = 0.248 μm, supplied by Prof. J. Lyklema (Agricultural University, Wageningen, The Netherlands) were used as samples.

The carrier was triply distilled water containing 0.5% (v/v) of detergent FL-70 and 0.02% (w/w) sodium azide as bacteriocide. The electrolyte added to this carrier solution in order to adjust its ionic strength was potassium nitrate from Riedel-de Haën. The ionic strength of FL-70 alone was taken to be 10^{-3} M from conductivity measurements.

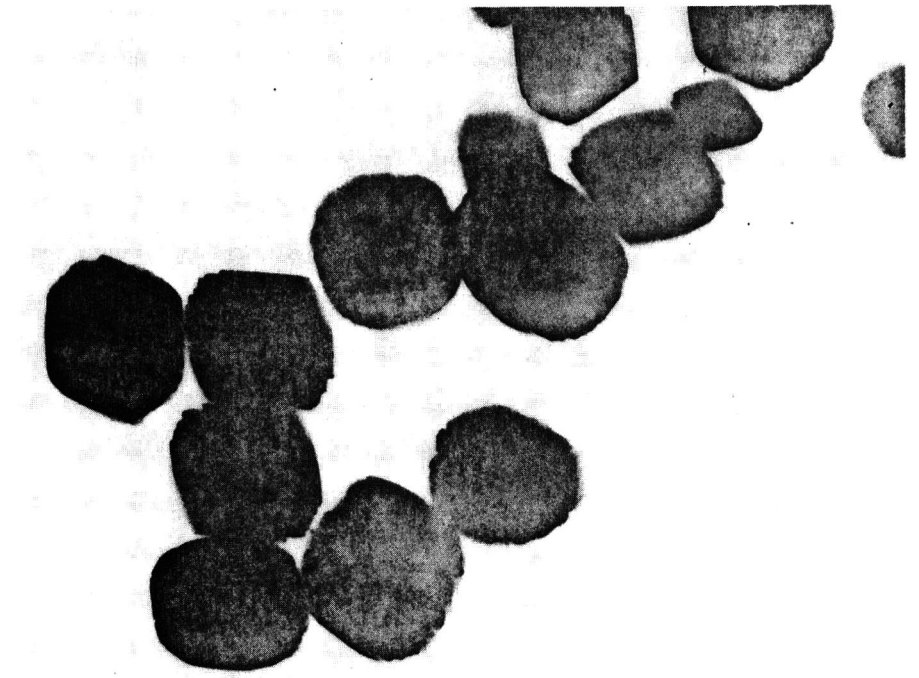

(b)

(a)

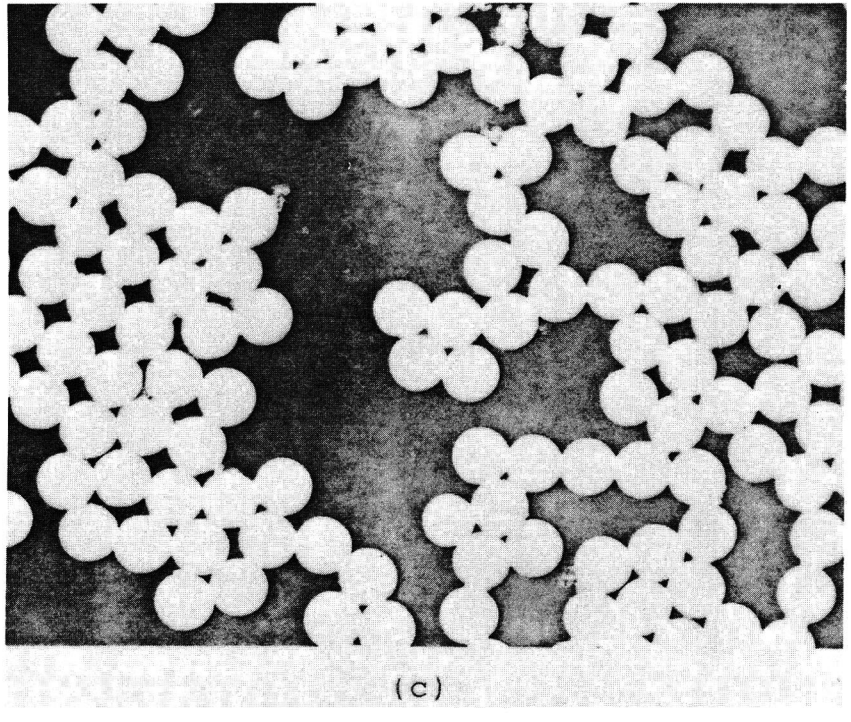

Fig. 1. Transmission electron micrographs: (a) haematite-I (80 000 ×); (b) haematite-II (80 000 ×); (c) TiO_2 (20 000 ×).

RESULTS AND DISCUSSION

Interactions between haematite and the SdFFF channel wall

Haematite-I (H-I, d_{TEM} = 0.148 μm). In order to select the optimum experimental conditions for minimizing the interactions between H-I and the SdFFF channel wall, the retention ratios or the particle diameters of the H-I particles were measured at various field strengths and at a constant flow-rate, and also at various flow-rates and at a constant field strength.

Fig. 2a, in which the variation of the experimental diameter, $d^{exp.}$, with the field strength and the constant theoretical diameter, d^{TEM} (determined by TEM) are presented, shows that the optimum field strength for H-I is $G = 15\,212$ cm s^{-2} (450 rpm). The optimum flowrate found from Fig. 2b, which shows the variation of $d^{exp.}$ with the carrier flow-rate at a constant field strength and constant d^{TEM} value, is *ca.* 150 cm^3 h^{-1}. Ideally, no differences should be observed with varying field and flow conditions. However, with increasing field strength the interaction between the particles and the SdFFF channel wall is intensified. Further, the increase in flow-rate offsets the interaction, as the hydrodynamic lift forces accelerate elution. Of course, more experimental work is necessary in order to investigate these variations.

Using the optimum experimental conditions found ($G = 15\,212$ cm s^{-2}, $\dot{V}$ = 150 cm^3 h^{-1}) the variation of the retention ratio or of the particle diameter with the ionic strength of the carrier solution was investigated. Fig. 3 illustrates the results of a series of retention measurements at different ionic strengths for the heamatite sample H-I with a nominal diameter of 0.148 μm in the stainless-steel channel wall and with two carrier flow-rates. At both carrier flow-rates for the more concentrated solutions (*ca.* $3 \cdot 10^{-2}$ *M* KNO_3), the retention ratio decreased and the particle diameter was higher than the theoretical value, although the data points in Fig. 3a have a relatively large random error.

The above observations are in accord with the analysis of particle–wall interactions presented under Theory. It was predicted there that at higher ionic strengths the

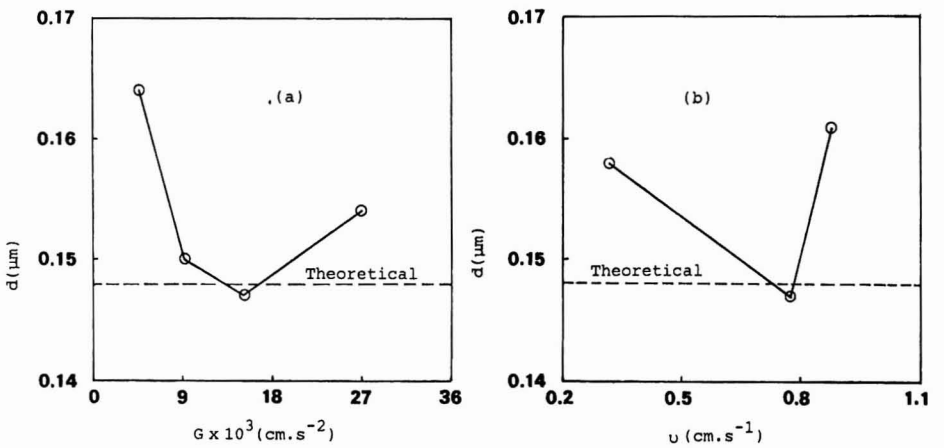

Fig. 2. Variation of particle diameter for the haematite-I sample (a) with the field strength at a constant flow-rate and (b) with the carrier flow-rate at a constant field strength. In both instances the SdFFF system I was used.

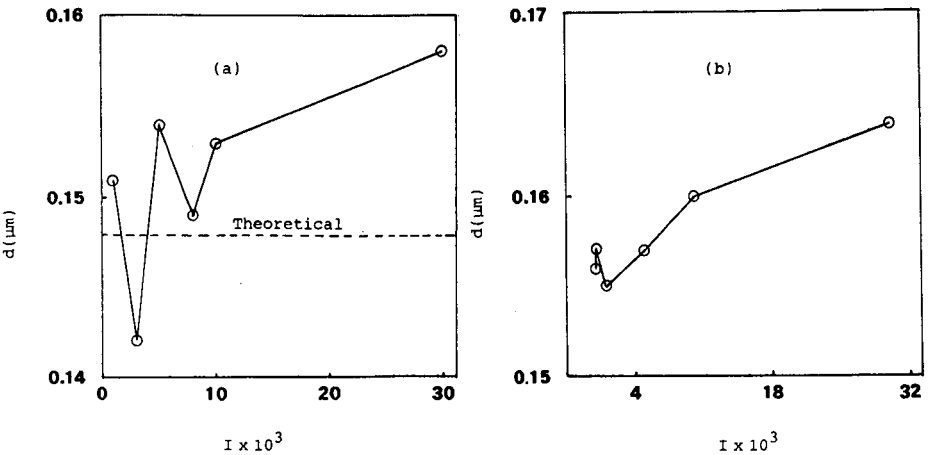

Fig. 3. Variation of the particle diameter for the haematite-I sample with the ionic strength of the carrier solution at 450 rpm. Flow-rate: (a) 150 and (b) 60 $cm^3\ h^{-1}$. In both instances the SdFFF system I was used.

attractive forces play an increasing role, eventually leading to a decrease in the R value and subsequently to an increase in the d value. Changing the carrier solution to one containing a higher concentration of KNO_3 (*ca.* $5 \cdot 10^{-2}$ M) led to the adsorption of all of the H-I particles on the stainless-steel channel wall, as no elution curve was obtained. In the system under investigation, in which the α-Fe_2O_3 particles and the collector (stainless-steel channel wall) carry charges of the same sign (both are negative), the deposition of the particles on the SdFFF channell wall at high electrolyte concentrations is due to the compression of the double layer. When the carrier solution was changed to one containing a lower ionic strength (*ca.* 10^{-3} M KNO_3), a sample peak appeared as a consequence of the desorption of the H-I particles. The mean diameter of the H-I particles (0.148 μm) is identical with that (0.148 μm) obtained by TEM or found (0.148 μm) by the direct injection of the H-I particles into the channel using the carrier in which no adsorption occurs.

These data show that the adsorption of the H-I particles on the channel wall took place at the beginning of the column, thus making possible the use of the real value of V_0 for the calculation of d. Another important point to examine is whether the deposition of the particles of H-I is fully reversible because, if some particles are still deposited on the channell wall after the change of carrier solution, then the channel wall will gradually be fouled. A strong indication for the desorption of all of the material was the fact that no elution peak was obtained, even when the field strength was reduced to zero.

Haematite-II (H-II, $d^{TEM} = 0.248$ *μm).* Fig. 4 illustrates the variation of the retention ratio or of the calculated particle diameter for the H-II particles with the field strength at a constant flow-rate, and with the carrier flow-rate at a constant field strength. Using the optimum experimental conditions found (G = 9202 cm s^{-2}, $\dot{V}$ = 171 $cm^3\ h^{-1}$), the variation of the retention ratio or of the particle diameter for the H-II sample with the ionic strength of the carrier solution was investigated. Whereas at low ionic strengths the H-II–wall interactions are negligible, at higher electrolyte concentrations there is a limiting critical concentration (*ca.* $3 \cdot 10^{-2}$ M KNO_3) at

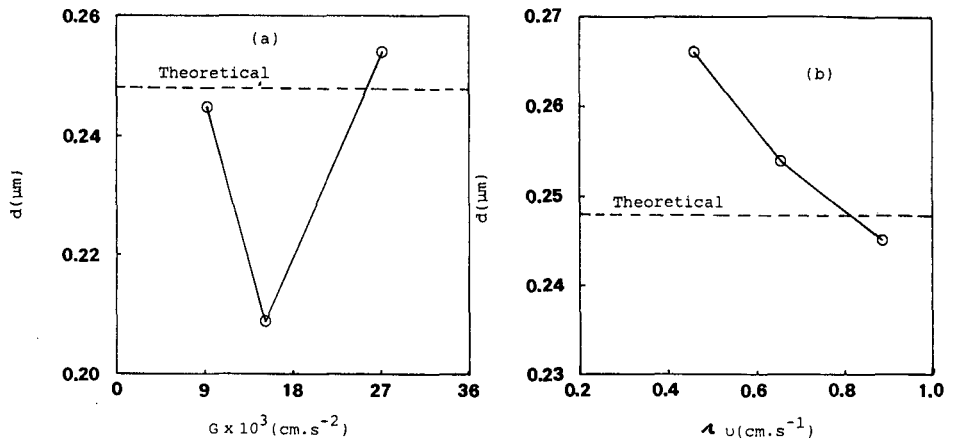

Fig. 4. Particle diameter for the haematite-II sample *versus* (a) field strength and (b) flow-rate. In both instances the SdFFF system II was used.

which adsorption of all of the H-II colloidal particles occurs at the beginning of the column. Variation of the carrier solution to one containing a lower electrolyte concentration (*ca.* 10^{-3} *M* KNO_3) released the total number of adherent H-II particles and gave a particle size (0.245 μm) in good agreement with that obtained by TEM (0.248 μm) or found (0.245 μm) when the colloidal particles were injected into the channel with the carrier solution in which no adsorption occurs.

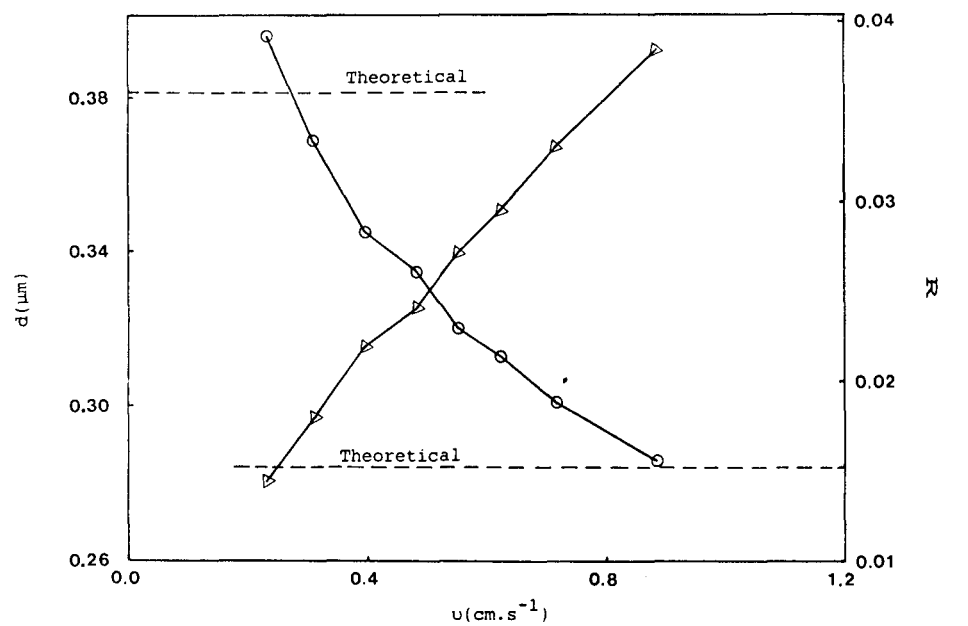

Fig. 5. Particle diameter (○) and retention ratio (△) *versus* carrier flow-rate for the TiO_2 colloidal sample in the SdFFF system II.

Interactions between titanium dioxide and the SdFFF channel wall

Fig. 5 shows the variation of the retention ratio and of the particle diameter for the TiO_2 particles with the carrier flow-rate at constant field strength (G = 9202 cm s^{-2}). Although the optimum flow-rate from Fig. 5 was found to be *ca.* 45 cm^3 h^{-1}, the investigation of the variation of the retention ratio or of the particle diameter for the TiO_2 sample with the ionic strength of the carrier solution was carried out at *ca.* 170 cm^3 h^{-1} in order to avoid long analysis times and broad peaks (Fig. 6).

The latter investigation showed that the critical electrolyte concentration for the total adsorption of the TiO_2 particles on the stainless-steel channel wall was that containing $3 \cdot 10^{-2}$ M KNO_3. Variation of the carrier solution to one containing a lower electrolyte concentration (*ca.* 10^{-3} M KNO_3) released all of the adherent TiO_2 particles and gave a particle size (0.302 μm) in good agreement with that (0.298 μm) obtained when the colloidal TiO_2 particles were injected into the channel with the carrier solution in which no adsorption occurs.

Fractionation of titanium dioxide and haematite-I by PBFFF

Fig. 7a shows the fractionation of the TiO_2 and H-I particles by the normal SdFFF procedure, which is based on the particle size difference, and Fig. 7b shows the fractionation of the same particles by the PBFFF technique, which is based on the total potential energy, V_{tot} (given by eqn. 16), difference. In the PBFFF technique the mixture was injected in the carrier solution containing $3 \cdot 10^{-2}$ M KNO_3. At this high electrolyte concentration all of the TiO_2 colloidal particles adhered at the beginning of the SdFFF stainless-steel channel wall, whereas all of the TiO_2 colloidal particles

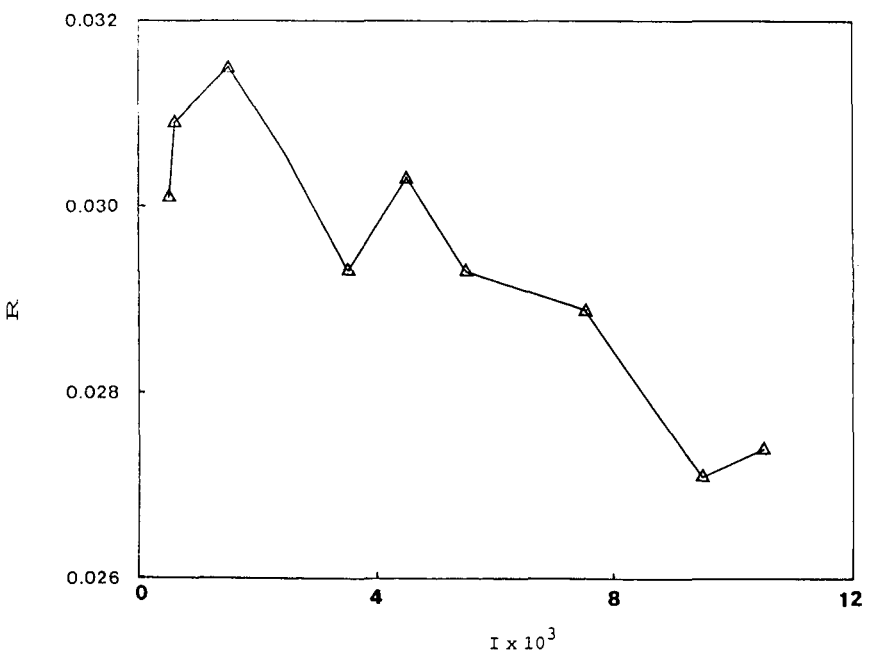

Fig. 6. Variation of the retention ratio for the TiO_2 sample with the ionic strength of the carrier solution. The SdFFF system II was used.

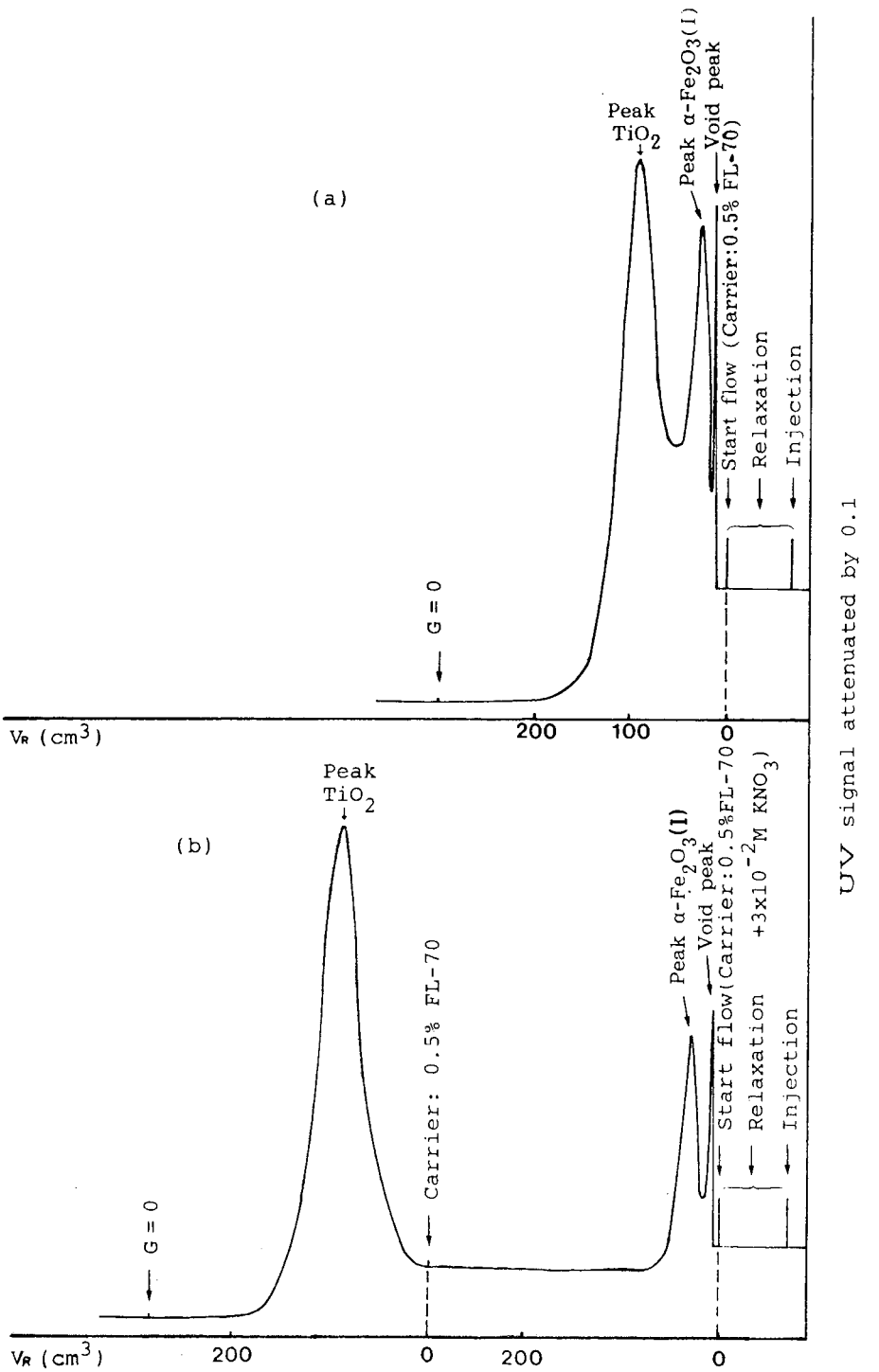

Fig. 7. Fractionation of haematite-I and TiO_2 colloidal particles by (a) the normal SdFFF and (b) the PBFFF technique.

adhered at the beginning of the H-I particles were eluted from the channel. The average diameter of the eluted H-I particles was found (by the PBFFF technique) to be 0.143 μm, in good agreement with that obtained by TEM (0.148 μm) or determined by normal SdFFF (0.150 μm) during the fractionation of TiO_2 and H-I particles. It must be pointed out that the particle diameter was obtained from eqn. 2 when the particles were run in the normal SdFFF mode, after the total adsorption following the PBFFF mode.

Changing the carrier solution to one containing only 0.5% detergent FL-70 released all of the adherent TiO_2 particles and gave a particle diameter (0.302 μm) in good agreement with that (0.298 μm) obtained during the fractionation of TiO_2 and H-I particles by the normal SdFFF technique.

The desorption of all of two colloids during the PBFFF procedure was verified by the fact that no elution peak was obtained even when the field strength was reduced to zero. A second indication for the desorption all of the material was the fact that the peaks of α-Fe_2O_3 and TiO_2 after adsorption and desorption of the particles (*cf.*, Fig. 7b) emerge without degradation, in contrast to the peaks in Fig. 7a. The different limiting electrolyte concentrations for the total adsorption of the TiO_2 and H-I colloidal particles on the SdFFF stainless-steel channel wall and hence the separation of the above particles by the PBFFF technique are due to the different total potential energies, V_{tot}, given by eqn. 16. Therefore, the separation of TiO_2 and H-I colloidal particles by the PBFFF technique is based on the particle size difference and/or on the Hamaker constant and the surface potential difference of the particles. The difference in diameters for the TiO_2 and H-I particles is known from the TEM pictures. Let us examine now whether or not the two samples have different Hamaker constants and surface potentials.

The Hamaker constant A_{132} ($= 1.02 \cdot 10^{-20}$ J) for the system steel–water–iron (III) oxide was calculated from eqn. 8, by taking $2.2 \cdot 10^{-19}$ J (A_{11}) for steel, which is the Hamaker constant for iron[15], $4.4 \cdot 10^{-20}$ J (A_{33}) for water, as calculated from the Lifshitz theory[11] (*cf.*, eqn. 9), and $6.2 \cdot 10^{-20}$ J (A_{22}) for haematite[15]. The Hamaker constant for haematite was also determined from eqn. 10 by surface tension measurements. This value ($7.0 \cdot 10^{-20}$ J), which was found to be equal to the value for TiO_2, appears to be much too high. As pointed out by Hogg *et al.*[12], it seems reasonable to assume that the Hamaker constant is approximately the same for inorganic oxides dispersed in an aqueous medium, as the surface are essentially similar, being composed primarily of oxygen anions. Thus, the Hamaker constant for the system steel–water–titanium dioxide approaches that for the system steel–water–iron (III) oxide and the separation of TiO_2 and H-I colloidal particles is not based on the Hamaker constant difference.

The surface potentials of haematite and TiO_2 were calculated from eqn. 12 by using for pH_{zpc} the values given by Hunter[16]: pH_{zpc}(α-Fe_2O_3) = 8.5 and pH_{zpc}(TiO_2, rutile) = 5.8. Therefore ψ(α-Fe_2O_3) = -15.6 mV and ψ(TiO_2) = -45.7 mV. The latter values show that the total potential energy, V_{tot}, at a given Hamaker constant, particle size and Debye–Hückel parameter, is less for the haematite sample than for TiO_2, contrary to our experimental results, according to which the heamatite sample is more stable than TiO_2 at an electrolyte concentration of $3 \cdot 10^{-2}$ *M* KNO_3. This is probably due to the fact that the value of pH_{zpc} used is referred to the rutile modification of TiO_2 and not to the anatase form. For this reason, the electrophoretic

mobilities of the TiO_2 and α-Fe_2O_3 particles were measured at various ionic strengths of the carrier solution.

From the latter, the ζ potentials were determined by using eqns. 13 and 14. At the critical electrolyte concentration $3 \cdot 10^{-2}$ M KNO_3, where the TiO_2 colloidal particles adhered to the SdFFF channel wall, whereas the α-Fe_2O_3 particles were

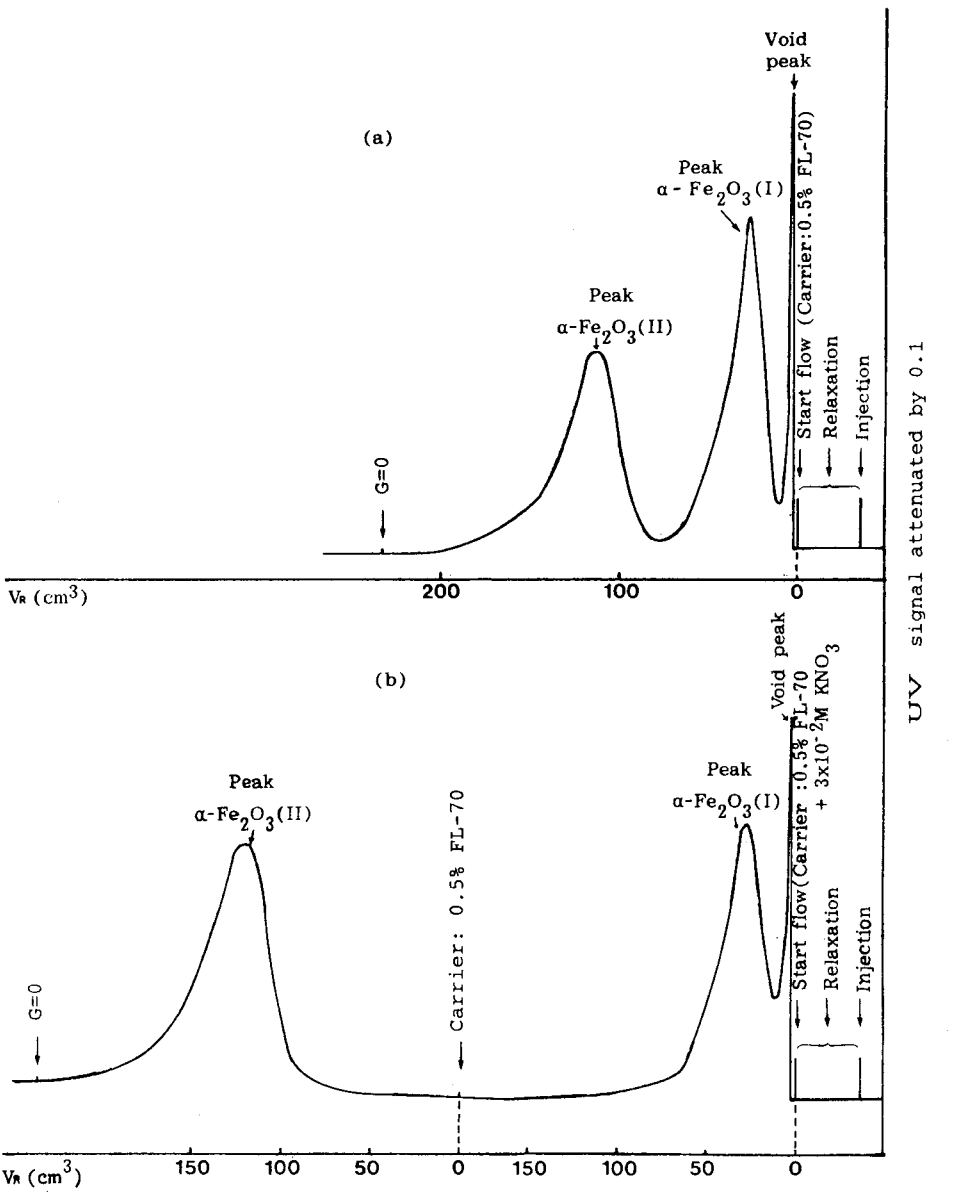

Fig. 8. Fractionation of haematite-I and haematite-II coloidal particles by (a) the normal SdFFF and (b) the PBFFF technique.

eluted from the channel, the ζ potentials were found to be $\zeta(\alpha\text{-}Fe_2O_3) = -20.4$ mV and $\zeta(TiO_2) = -19.1$ mV. These values are consistent with the experimental results showing that the fractionation of TiO_2 and H-I particles by the PBFFF technique is based on the particle size and the surface potential differences.

In the second example of fractionation by the PBFFF technique we used two samples of haematite with different particle diameters (Fig. 8). Here the separation is based only on the particle size difference, as the Hamaker constants and the surface potentials of the two samples are identical. Fig. 8a shows the fractionation of the haematite samples with different particle diameters by the normal SdFFF technique, and Fig. 8b that of the same samples by the PBFFF technique. The particle diameters obtained from eqn. 2 in the latter instance (0.151 μm for H-I and 0.244 μm for H-II) are in good agreement with those found by normal SdFFF (0.145 μm for H-I and 0.237 μm for H-II) or determined by TEM (0.148 μm for H-I and 0.248 μm for H-II).

ACKNOWLEDGEMENTS

We are grateful to Professor J. Calvin Giddings (University of Utah, U.S.A.), who supplied the SdFFF system, to Professor J. Lyklema (University of Wageningen, The Netherlands), who supplied the haematite samples, and to M. Barkoula for her kind assistance.

REFERENCES

1 H. Small, *J. Colloid Interface Sci.*, 48 (1974) 147.
2 V. K. F. Krebs and W. Wunderlich, *Angew. Makromol. Chem.*, 20 (1971) 203.
3 E. Ruckenstein, A. Marmur and W. N. Gill, *J. Colloid Interface Sci.*, 61 (1977) 183.
4 J. C. Giddings, F. J. F. Yang and M. N. Myers, *Anal. Chem.*, 46 (1974) 1917.
5 J. C. Giddings, G. Karaiskakis, K. D. Caldwell and M. N. Myers, *J. Colloid Interface Sci.*, 92 (1983) 66.
6 E. Dalas and G. Karaiskakis, *Colloids Surf.*, 28 (1987) 169.
7 G. Karaiskakis and E. Dalas, *J. Chromatogr. Sci.*, 26 (1988) 29.
8 A. Koliadima and G. Karaiskakis, *J. Liq. Chromatogr.*, 11 (1988) 2863.
9 G. Karaiskakis and A. Koliadima, *Chromatographia*, 28 (1989) 31.
10 M. E. Hansen and J. C. Giddings, *Anal. Chem.*, 61 (1989) 811.
11 J. N. Israelachvili, *Intermolecular and Surface Forces*, Academic Press, London, 1987, pp. 144–158.
12 R. Hogg, T. W. Healy and D. W. Fuerstenau, *Trans. Faraday Soc.*, 62 (1966) 1638.
13 P. C. Hiemenz, *Principles of Colloid and Surface Chemistry*, Marcel Dekker, New York, 1977, pp. 457–467.
14 E. Dalas, P. Koutsoukos and G. Karaiskakis, *Colloid. Polym. Sci.*, 268 (1990) 155.
15 R. J. Kuo and E. Matijevic, *J. Colloid Interface Sci.*, 78 (1980) 407.
16 R. J. Hunter, *Zeta Potential in Colloid Science*, Academic Press, London, 1981, p. 279.

Journal of Chromatography, 517 (1990) 361–376
Elsevier Science Publishers B.V., Amsterdam

CHROMSYMP. 1940

Particle characterization in centrifugal fields

Comparison between ultracentrifugation and sedimentation field-flow fractionation

JIANMIN LI and KARIN D. CALDWELL*
Department of Bioengineering, University of Utah, Salt Lake City, UT 84112 (U.S.A.)
and
WALTER MÄCHTLE
Kunststofflaboratorium, BASF AG, D-6700 Ludwigshafen (F.R.G.)

ABSTRACT

A ten-component mixture of polystyrene latex particles in the 67–1220 nm size range was subjected to analysis by analytical ultracentrifugation (AUC) and sedimentation field-flow fractionation (SdFFF) using programmed and constant fields. The AUC analysis of the mixture yielded diameter values in good agreement with data determined on the separate components; the relative amounts of each component in the mixutre were likewise closely reproducing the sample's known composition. Diameters determined by SdFFF, either in a constant- or programmed-field mode, were in good agreement with the AUC for particles smaller than about 500 nm. For the sample's larger components, however, particularly the programmed mode showed diameter values smaller than expected. In addition, field programming resulted in incomplete recoveries of the larger particles, leading to more or less distorted mass distributions for the complex sample.

The observed discrepancies, which are thought to result from events at the analytical wall in the FFF channel, suggested a protocol for accurate sizing, as opposed to fingerprinting, of samples with broad size distribution. By tracking sizes and amounts of the different components at different but constant field strengths, and retaining as analytically valid only those data recorded in a retention range from five to about thirty column volumes, it was possible to determine sizes and amounts in good agreement with known parameters for the sample.

Unlike the AUC procedure, SdFFF produces fractions of a high degree of uniformity, which lend themselves to a secondary analysis, *e.g.* by electron microscopy, as shown in the study.

0021-9673/90/$03.50

INTRODUCTION

Since the days of Svedberg, centrifugal fields have been used routinely to determine sizes and size distributions for particulate samples in the diameter range 10–5000 nm[1]. Traditionally, such measurements are performed on dilute particle suspensions using the analytical ultracentrifuge, the optically transparent sample cell of which allows the operator to follow the unobstructed radial migration of a sample's components under the influence of the field. The rate of sedimentation at a given field strength is a measure of a spherical component's buoyant mass, which is convertible into an actual size if the densities of particle and suspension medium are known. Since amplitudes of the optical signals associated with each sedimenting species are measures of their relative amounts, the analytical ultracentrifugation (AUC) study leads to a determination of the sample's size distribution. Through the use of sensitive detection techniques[2–4] it is possible to perform the analysis at low sample concentration to avoid particle interactions and other non-ideal behavior. The technique is non-intrusive, and at the end of an analysis the sample can be retrieved for subsequent evaluation by other analytical methods. However, removing the field causes the components to remix, and any information relating size to, *e.g.*, composition or biological function, is not normally available by this route.

An alternate way of utilizing the field was proposed by Giddings, who in 1965 introduced the concept of field-flow fractionation (FFF)[5]. In the FFF mode of operation, the centrifugal field is applied perpendicularly to a laminar flow of suspension medium through a thin, flat channel. As in the ultracentrifugation experiment, particles injected into the FFF channel will migrate under the influence of the sedimentation field. However, their migration across the thin (typically 250 μm) channel is stopped by its outer wall where the particles are forced to accumulate and rapidly equilibrate. The field affects each particle in proportion to its mass, so that the more massive particles will form distributions that are more compact than those of lesser mass. Thus, a fully equilibrated polydisperse sample will consist of several exponentially distributed particle clouds superimposed on one another, each characterized by a thickness which relates to the mass of its constituents and to the strength of the applied field. This equilibration is normally allowed to occur with the liquid at rest, and as flow is resumed at the end of the relaxation period, the various particle zones are carried downstream with minimal disturbance of their equilibrium distributions. In the parabolic velocity profile maintained by the thin channel, zones of different degree of compression will move at different rates, so that the downstream transport results in a mass-based separation. At the end of the channel, the effluent is routed through one or more detectors, and the separated components may subsequently be collected for further analysis or evaluation.

The ability to fractionate polydisperse samples into cuts of a uniform and quantifyable particle size makes the FFF a powerful tool for particle characterization[6,7]. Ideally, the technique is applicable to samples ranging in size from a few tens of nanometers to well over a micrometer. An accurate sizing based on existing theory for so called "normal" FFF[8,9] requires that the particles behave as point masses, free from interactions with neighboring particles or with the accumulation wall. In practice, this condition may be difficult to meet for all components of a highly polydisperse sample. Often, the strong fields necessary to retain a distribution's finer particles to such

a degree that they can be accurately sized will force its large particles into extremely compact zones where steric effects[9] and overloading[10] lead to highly non-ideal behavior.

In the present study we make use of a ten-component mixture of nearly monodisperse polystyrene latex particles to compare performances of AUC and sedimentation FFF (SdFFF) in terms of accuracy in their diameter assignment as well as in their ability to determine relative amounts of each component. This comparison will demonstrate the overall good agreement between the two approaches for small particles. It will also pin-point some systematic errors encountered in the FFF analysis of particles larger than about 500 nm, and suggest operational procedures to reduce, or correct for, such errors, so that the positive features of the elution technique may be enjoyed even for samples of broad size distribution.

THEORY

Fig. 1 outlines the principal differences between AUC and SdFFF in terms of

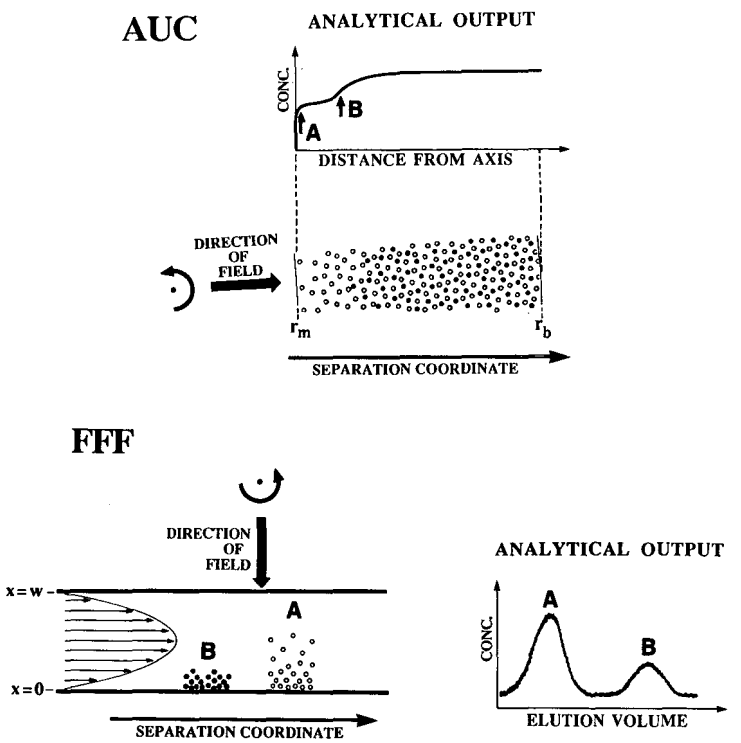

Fig. 1. Principles of AUC and FFF. The AUC analysis is based on the observation of rates of radial migration of the various depletion boundaries formed in the optically transparent analytical cell. Distances between the axis of rotation, the meniscus (r_m), and the outer wall (r_b) are not drawn to scale. The FFF analysis is based on the equilibrium distribution of sample in the thin (dimension w) separation chamber. Migration of the equilibrated sample constituents in a direction perpendicular to the field takes place at rates determined by the thickness of each sample zone. In both cases, solid black dots represent a more massive component than the open circles.

their use of the centrifugal field. In both applications, a particle of mass m and density ρ_s, which is suspended in a medium of density ρ, will experience a force F in the direction of the field. Under a gravitational acceleration G, the force is expressed by:

$$F = m(\Delta\rho/\rho_s)G \tag{1}$$

where $\Delta\rho$ is the density difference between particle and suspension medium. For spherical particles of diameter d, the mass m can be replaced by the product of volume and density:

$$F = (\pi d^3/6)\Delta\rho G \tag{2}$$

Stokes' law specifies the relationship between the particle's friction coefficient f, its diameter d, and the viscosity η of the medium:

$$f = 3\pi\eta d \tag{3}$$

which implies that the field induces the particle to move with a steady state velocity U, equal to:

$$U = F/f = d^2\Delta\rho G/18\eta \tag{4}$$

In AUC, this motion is quantified from observations of the movement of the various depletion boundaries which are created at the meniscus and transported outward towards the bottom of the cell. In evaluating d from the observed U, it is necessary to account for the fact that the boundary moves a significant fraction of the distance between the axis of rotation and the bottom of the cell[4], and that G therefore will vary with position r as measured from the axis:

$$G = \omega^2 r \tag{5}$$

Here, ω is the angular velocity of the rotor.

In FFF, the thin channel is positioned far enough from the axis of rotation that its thickness dimension w becomes a negligible fraction of r, and G therefore remains constant across the channel. Under the influence of the field, particles in the FFF channel will move radially, as in AUC. Due to the small gap width, their transport across the channel is rapid, and for particles denser than the medium accumulation takes place at the outer wall. After a brief relaxation period, the field induced concentration at the wall is exactly balanced by dispersion due to Brownian motion, and the particle zone is at equilibrium with a concentration distribution $c(x)$ in the direction of the field (x-axis), which is described by[8,11]:

$$c(x) = c(0)\exp(-x/\lambda w) \tag{6}$$

In this equation, λ is a dimensionless layer thickness related to the particles' drift velocity U and diffusivity D:

$$\lambda = D/Uw = kT/Fw \tag{7}$$

where k and T have the usual meaning of Boltzmann constant and temperature.

The concentration at the accumulation wall, expressed as $c(0)$ in eqn. 6, is rapidly increasing with decreasing λ; even for weakly retained samples, characterized by moderately large values of this parameter, $c(0)$ is well approximated by[10]:

$$c(0) = <c>/\lambda \tag{8}$$

where $<c>$ is the average sample concentration across the channel in the field direction.

Initiation of a laminar flow of liquid along the length dimension of the channel, *i.e.* in a direction perpendicular to the field, will transport the equilibrated particle zones downstream at rates determined by their respective λ values. Due to differences in zonal compression, resulting from differences in size and/or density, a mixture of particles will separate into its components during migration through the channel. The separated zones will emerge from the channel at different elution volumes V_e, which each bears a direct relationship to the characteristic layer thickness λ, and thus to the particle's diameter d (ref. 12) via eqns. 2 and 7:

$$V_0/V_e = R = 6\lambda[\coth(1/2\lambda) - 2\lambda] \tag{9}$$

The retention ratio R, defined as the ratio of average carrier velocity to sample velocity, is determined experimentally as the ratio of the channel's void volume V_0 to the elution volume V_e.

Eqn. 9 presumes the particles to be point masses, moving independently of one another without interactions with the wall. Larger particles become sterically excluded from the wall region, and corrections for this effect lead to a modified retention equation[13,14]:

$$R = 6\gamma(\alpha - \alpha^2) + 6\lambda(1 - 2\alpha)\{\coth[(1 - 2\alpha)/2\lambda] - 2\lambda/(1 - 2\alpha)\} \tag{10}$$

Here, α symbolizes $d/2w$, and γ is a factor the value of which appears close to unity. As will be discussed below, eqn. 10 fails to fully describe the retention of large particles, and attempts are presently under way to further modify the retention equation to correct for velocity and size dependent lift forces induced by the presence of the channel wall.

EXPERIMENTAL

Samples

The major focus of this study is a ten-component mixture of nearly monodisperse polystyrene (PS) latex spheres, prepared by BASF in the form of two nearly identical samples, referred to as "5" and "5R". The two mixtures are made up from the same close to monodisperse components, with the exception of the smallest particles which derive from different batches. The relative concentration of each component in these mixtures is 10% (w/w), and the density of the particles is reported to be 1.057 g/ml. In addition, the study uses monodisperse PS latex standards from Seragen.

Suspension medium (carrier)

For the AUC procedure, the medium is a 0.05% (w/v) solution of the ionic surfactant K30 (sodium salt of a [^{14}C]alkyl sulfonate from Bayer) in deionized water. In the case of SdFFF, the carrier is a 0.1% (v/v) solution in deionized water of the surfactant FL-70 from Fisher Scientific.

Equipment

The analytical ultracentrifuge at the Kunststofflaboratorium of BASF is an in-house modified version of a preparative ultracentrifuge (Model Omega 2) equipped with an analytical 8-cell rotor, both from Hereaus-Christ, which has been described in detail elsewhere[3]. Each 3-mm wide sector cell has a volume of 0.25 ml; the contents of all eight cells are monitored pseudo-continuously with a detection system based on the response by a photomultiplier to light traversing the cell, in a direction parallel to the axis of rotation, from a source emitting at 546 nm. An apertured mask with a 0.2-mm slit is positioned in the middle of each cell. The AUC detector response is corrected for Mie scattering, as described elsewhere[3,4], using $n(25°C, 546\ nm) = 1.59$ for polystyrene.

As the meniscus region becomes depleted with respect to particles of a given size, a concentration boundary is established the migration of which in the radial direction (across the perpendicular slit) can be followed as a function of time. The distance between meniscus and outer wall in these cells is kept constant at 1.30 cm, so that the distances between the axis of rotation and the meniscus, slit and outer wall are fixed at 5.85, 6.50 and 7.15 cm, respectively. Each cell is loaded with 0.25 ml of a 0.1% (w/v) sample suspension.

The SdFFF system was built at the University of Utah, essentially according to the description in ref. 15, although the rotor radius r in the present system is 15.5 cm, permitting the accommodation of a longer separation chamber; the dimensions of the present channel are 94 cm × 2.0 cm × 0.0254 cm for a measured void volume of 4.78 ml. The effluent from this system is monitored by a Linear Model 106 UV detector with a 254-nm light source, the output of which is fed to the system's IBM compatible AT personal computer. Elution volumes are based on weight, as described elsewhere[16], and are continuously input to the computer's RS232 port by the system's Ohaus Model C501 electronic balance. The field strength, relaxation time, and rate of carrier flow from the system's Minipuls 3 peristaltic pump Model 312, are all controlled by the computer. In the present study, sample volumes were 5 μl (1% solids), unless otherwise specified; the samples were manually injected at the head of the channel and allowed to relax for periods of 20 to 30 min. Absence of any effects of the length of the relaxation period on the level of retention was assured through multiple runs under different conditions. At the end of each run, diameters were evaluated from the elution position at peak maximum in accordance with eqns. 9 or 10, as specified by the operator. When needed, the detector response was corrected for Mie scattering as described in ref. 17, using 1.7685 (ref. 17) and 0.012 (ref. 18) as values for the real and imaginary parts of the refractive index for polystyrene, and 1.3702 as the real part of the refractive index for the carrier at 254 nm (the imaginary part being zero). The extinction cross sections calculated as described in ref. 17 were verified experimentally using polystyrene latex standards of accurately known concentrations. The area under each scattering corrected peak in the recorded fractogram was then found by integration after baseline

adjustment, and was considered proportional to the number of particles of the size determined from the peak elution volume; multiplication by the particle volume computed for this size gave the mass-based relative amount of the component.

The studies of recovery involved the observation fixed loads (4 μl of a sample suspension containing 1% solids) of standard polystyrene latices from Seragen. The areas under the elution peaks, recorded at different field strenths, were normalized by division with the area under a peak at no field. The small size of the void peak in fractograms collected at high particle retention obviated any correction for the presence of low-molecular-weight contaminants. As these studies involved comparisons of the behavior of one particle type at the time, there was no need to correct the detector response for Mie scattering.

Analysis of collected fractions

A BI-90 fixed-angle (90°) photon correlation spectrometry (PCS) system from Brookhaven Instruments was used routinely (in cases where the concentration of

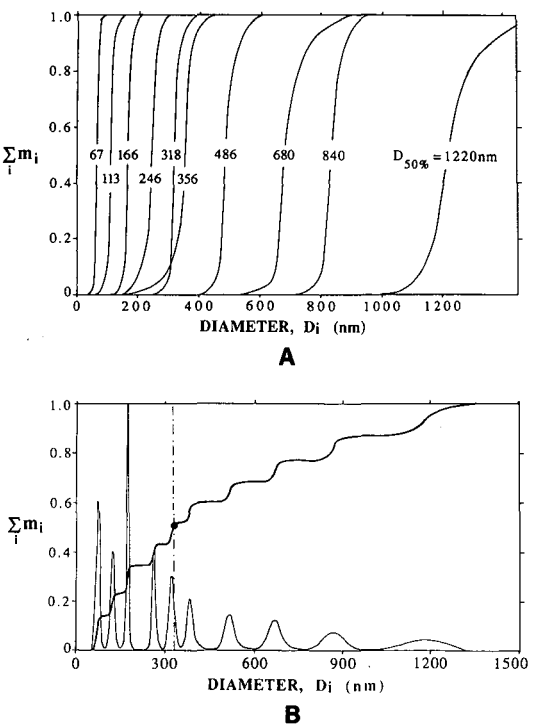

Fig. 2. (A) Size distribution curves for ten different polystyrene latex samples (density 1.057 g/ml) determined separately by AUC. The ordinate reflects the cumulative mass of particles below a given size D_i, indicated on the abscissa. (B) Size distribution curve for a mixture of the ten polystyrene latex samples analyzed separately in (A) (upper curve). Also shown (lower curve) is the derivative of the distribution function, the peak values of which indicate the average diameter for each component. The upper profile is a composite of two analyses run simultaneously in different cells, one at a sample concentration of 0.35 g/l (for the heavier components), and the other at 3.5 g/l. The heavy dot in the diagram represents the "coupling point"[4], indicating that data for larger diameters, D_i, derive from the lower concentration cell and smaller diameters from the higher.

TABLE I

PARTICLE DIAMETERS AND RELATIVE AMOUNTS DETERMINED FOR THE 10-COMPONENT MIXTURE OF PS LATEX PARTICLES USING DIFFERENT TECHNIQUES

Component No.	*Sample 5*		*Sample 5R*		*AUC-5*		*AUC-5R*		*DuPont*[a]		*SdFFF-C*[b]		*PCS*[d]*/SEM*[e]
	d(nm)	*%*	*d(nm)*	*%*	*d(nm)*	*%*	*d(nm)*	*%*	*d(nm)*	*%*	*d(nm)*	*%*	
1	67	10	85	10	85	12	72	14	70	26	96	–[c]	
2	113	10	116	10	116	10	121	9	119	16	113	8	
3	166	10	163	10	163	12	172	11	175	15	162	9	
4	246	10	257	10	257	11	259	8	261	13	259	16	252[d]/
5	318	10	306	10	306	10	320	10	319	11	320	18	307[d]/
6	356	10	365	10	365	11	379	8	374	9	376	17	381[d]/
7	486	10	504	10	504	9	515	9	479	7	524	10	/530[e]
8	680	10	650	10	650	6	665	8	588	3	716	9	/680[e]
9	840	10	834	10	834	9	870	10	695	0.5	917	7	/896[e]
10	1220	10	1142	10	1142	8	1180	13	805	0.5	1221	6	/1216[e]

[a] Data obtained from Dr. Roger Blaine of DuPont (published with permission). Analysis made in blind, using field programming in the time-delayed exponential mode.

[b] For an explanation of "SdFFF-C", see Results and Discussion section.

[c] The low resolution of this component from the void peak prohibits quantification.

[d] Diameters obtained by PCS.

[e] The magnification used in the SEM analysis of the FFF fractions does not allow accurate sizing of the smaller components. Relative amounts not obtained by this technique.

eluting particles was sufficient to permit a PCS analysis) to verify the diameters calculated from SdFFF.

Electron microscopy was performed on collected samples using a JEOL JFM 35 scanning electron microscopy (SEM) system. Prior to analysis, the collected fractions were concentrated on Nucleopore filters with pore sizes of 0.1 or 0.2 μm. The filtered samples were mounted on copper stubs and gold coated prior to imaging.

RESULTS AND DISCUSSION

AUC of each of the ten polystyrene latices prepared by BASF yields the size distributions shown in Fig. 2A; particle diameters reported in Table I as "Sample 5", and "Sample 5R", respectively, are determined from the midpoints of such distribution curves. Fig. 2B shows the result of an AUC analysis of that mixture of the ten components, referred to as "Sample 5". In order to produce this distribution curve, the rotor was ramped up during the 1.5-h run in an essentially exponential fashion[4], from 0 rpm via weak fields suitable for generating readily measurable sedimentation velocities for the largest particles in the mixture, to a final spin rate of 40 000 rpm. The sizes determined for each constituent in the AUC analysis of the two sample mixtures are listed as AUC 5 and AUC 5R in Table I. The duration of these runs ranged from 1 to 2 h. As is seen from this table, the AUC is faithfully reproducing both the number of components in the mixture as well as their sizes and relative amounts.

In contrast to the AUC analysis just described, field-programmed SdFFF begins at a high spin rate, which produces retention even of small particles, and progresses to weaker fields where, ideally, the more massive particles are being transported through the channel at measurable rates[19]. Fig. 3 represents a 4-h SdFFF run of the sample using the time-delayed exponential program introduced by Yau and Kirkland[20]. The experimental parameters chosen to produce Fig. 3 were not optimized for high resolution; yet, the run is clearly informative as to the complexity of the sample. The presence of at least nine components is indicated, and the tenth could presumably have been resolved, had we been able to spin our system at a higher speed than the 2000 rpm (692 *g*) which is our current upper limit.

The ten-component sample (Sample 5) was also submitted for a routine analysis (analytical conditions not optimized) to DuPont, whose SF[3] Particle Fractionator was

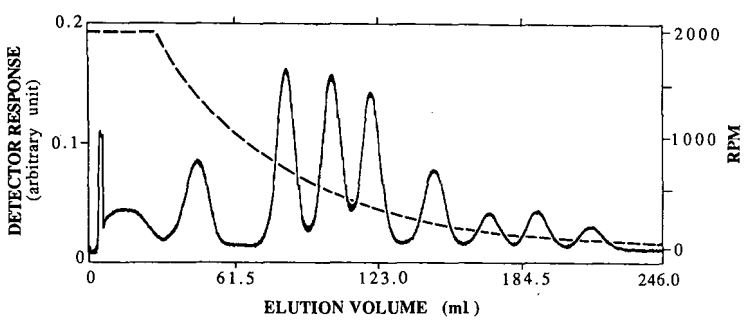

Fig. 3. Screening of the ten-component polystyrene latex sample, using field-programmed SdFFF. The form of the program was a time-delayed exponential, with an initial field of 2000 rpm and a time constant of 20 min; the flow-rate was 1.0 ml/min.

the first SdFFF instrument to be produced commercially. In contrast to the Utah system, DuPont's SF[3] is capable of handling spin rates of 18 000 rpm (35 000 *g*), and could therefore resolve and quantify even the smallest particles of the mixture, as seen in Table I; the duration of this analysis was around an hour. Although diameter assignments for the smaller particles (less than 500 nm) were in good agreement with the AUC data, the table shows an increasing departure from the nominal diameter values with an increase in size. From Table I it is also clear that quantification of the larger components is less accurate, as recoveries appear to decrease with increasing particle size.

As seen from eqn. 8 above, the exponential distribution of sample in the field direction implies a concentration at the accumulation wall which is inversely related to λ. Since λ, in turn, is an inverse function of the product d^3G, it follows that an increase in G has a strongly compressing effect, particularly on zones containing large particles; hence, any tendency of the particles to adsorb at the solid–liquid interface will be promoted by increased wall concentrations, *i.e.* by increasing the strength of the settling field. It is therefore easily seen that the strong fields needed to resolve the fines

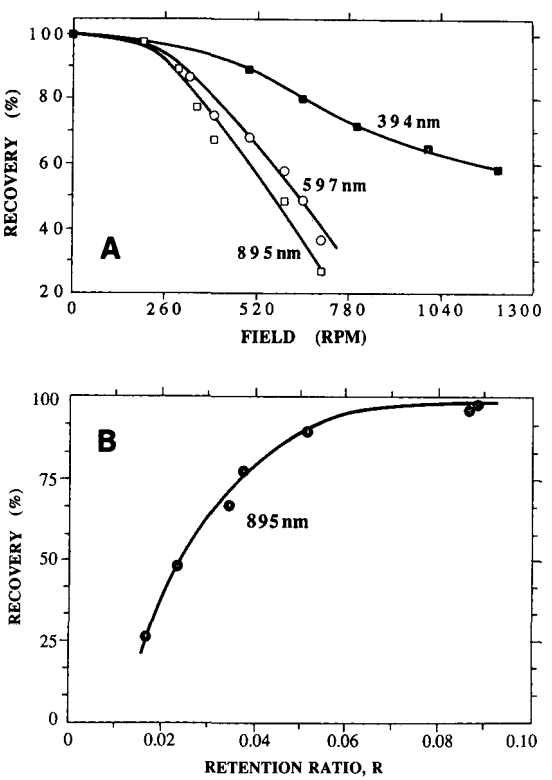

Fig. 4. (A) Sample recovery in SdFFF as function of field strength and particle size. All data represent injections of 4 μl of suspensions containing 1% solids; the flow-rate is constant at 1.0 ml/min. Diameters of the three polystyrene standard particles (Seragen) are indicated in the figure. (B) Sample recovery plotted *vs.* retention ratio, R for the 895-nm standard particle. Experimental conditions are the same as in (A). Significant losses are seen to occur at retentions larger than 25–30 column volumes, corresponding to R values of 0.03–0.04.

in a broadly distributed sample may severely hamper recovery and distort quantification at the high end of the distribution. This effect is clearly illustrated in Fig. 4A, where relative recovery is plotted as a function of field strength for three monodisperse PS latex standards analyzed at different spin rates. The trend of increased sample loss with increasing retention is further demonstrated in Fig. 4B, using the data collected for the largest of the three particles in Fig. 4A. It should be noted that both the metal wall of the channel and the PS beads carry negative charges[21] at neutral pH, which would make this sample less prone to adhesive particle–wall interactions than many other colloidal systems in which the two interact by Van der Waals forces alone or in addition to attractive Coulombic forces. Operation at strong fields must therefore be used judiciously, if quantification of large diameter components is the desired outcome of an FFF analysis.

An alternative way, although more cumbersome than the one presented in Fig. 3, to approach the analysis of broadly distributed samples is to make several consecutive runs at different fields, and only determine size/quantity data for particles of moderate zonal compression; for this purpose, analytically useful retentions appear to range from 5 to *ca.* 30 column volumes. The lower end of this "accuracy window" marks the position in the fractogram where, on the average, transients due to sluggish diffusion seize to play a major role[22] and retentions therefore fairly reflect the diameter of the particle, while the upper end, which is strongly size dependent, is defined by the onset of sample losses of the type shown in Fig. 4B, as well as by other non-ideal behavior discussed below. An example of this strategy, applied to the ten-component sample focused on in the present study, is seen in Fig. 5. Here, three fractograms were collected at constant fields in the "weak", "intermediate", and "strong" range for the

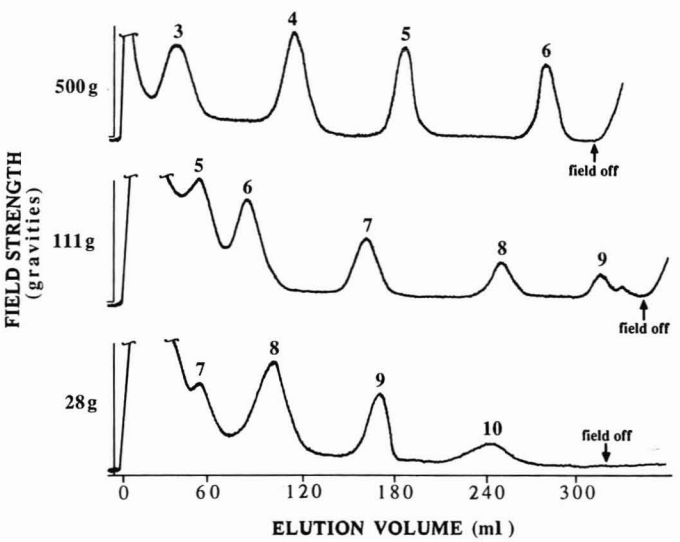

Fig. 5. Sequential SdFFF analyses of the ten-component polystyrene latex sample at constant fields of different strength. The numbers in the fractograms refer to specific components, as defined in Table I. The weak (28 *g*) field analysis was able to visualize component 10, but provided poor resolution of the smaller components. By contrast, the strong (500 *g*) field resolved several of the smaller components, but failed to demonstrate the presence of component 10. The flow-rate was maintained at 2.8 ml/min.

instrument at hand; the flow-rate was kept constant throughout. Each component in the figure is numbered from 1 to 10 in accordance with Table I. The weak field (28 *g*) permitted detection and quantification of component 10, which was otherwise

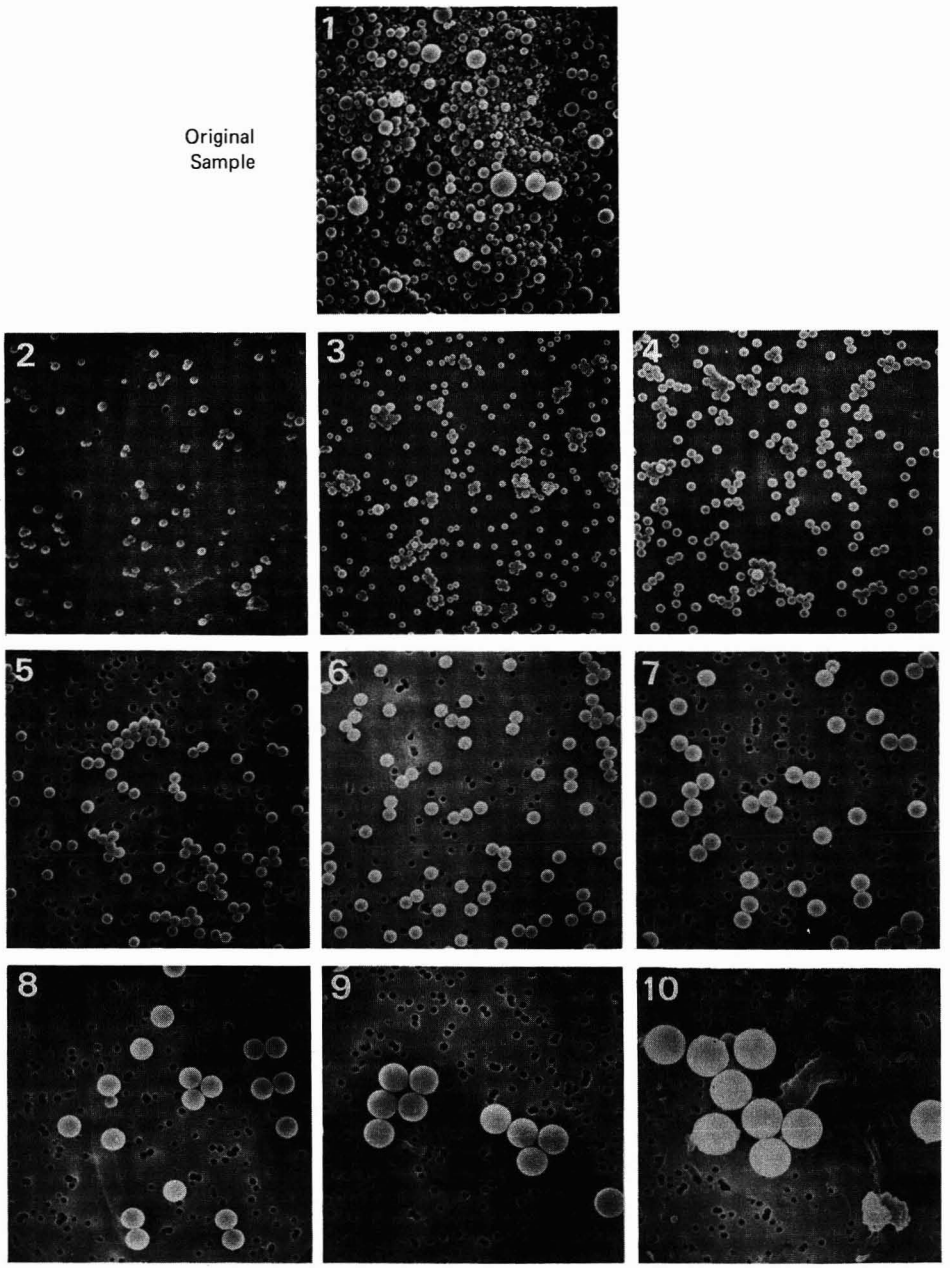

Fig. 6. SEM record of the starting material (top), as well as of the resolved fractions 2 through 10. Sizes measured for the four largest particle types from these micrographs are included in Table I.

undetectable, while this field strength clearly was inadequate for resolution of the finer particles resolved by the stronger fields. During the process, fractions were collected within the "window" for further analysis by SEM (see Table I) and PCS, where the concentration reached above the detection limit for our BI-90 instrument. The SEM images compiled in Fig. 6 give a clear indication that the fractionation is efficient, and produces highly monodisperse cuts without any evidence of contamination from other components in the sample. While the magnification is insufficient to permit accurate sizing of the smaller components, Table I contains SEM size assignments for the four largest particle types separated by SdFFF. These sizes are in good agreement with those determined by AUC.

In addition to affecting sample recovery, as discussed above, the presence of the analytical wall in FFF results in steric exclusion from the interfacial region, as well as in the establishment of a velocity and size dependent lift force directed towards the center of the channel. While the former effect was recognized and modelled by Giddings[13] over a decade ago, the latter is just recently gaining attention, as efforts are under way to expand the range of particle sizes which can be profitably handled by the high resolution SdFFF technique. The present ten-component mixture of monodisper se particles proved to be an ideal sample for demonstrating the existence of such wall effects, as illustrated by Fig. 7. In carrying out the procedure of size analysis at different field strengths described above, it became evident that diameters determined for the larger particles were strongly dependent on the chosen gravitational acceleration G. This obvious anomaly, which was not present for small particles, is an indication that eqn. 9 does not adequately describe the retention of all particles in what is often referred to[9] as the "normal" (as opposed to "steric") mode of FFF operation.

The need for a steric correction to eqn. 9 was realized early on by Giddings and co-workers[13,14], who proposed the modified form of the retention equation listed above as eqn. 10. Further studies by Lee and Giddings[23] supported the notion that parameter γ in this equation had the magnitude of unity, although its actual value was shown to vary with particle size and the chosen experimental conditions. An attempt at re-processing the data in Fig. 7, using eqn. 10 together with values for γ in the range

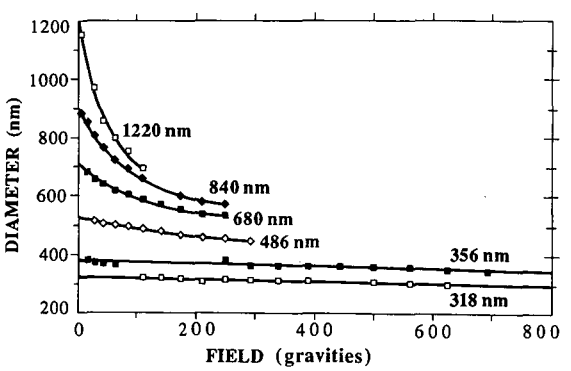

Fig. 7. Effect of field strength on diameters determined by SdFFF using eqn. 9. The small particles behave ideally, and show no effect of G, while a progressively non-ideal behavior is seen for the larger particles. For the four largest particles the diameters listed in Table I were determined by extrapolation to zero field using a fourth order polynomial fit of the data; linear extrapolations were used for the smaller particles. The flow-rate was held constant at 2.8 ml/min.

0.5–2.0, was not successful in removing the influence of field strength on the calculated diameters.

The lack of success in a direct evaluation of particle diameter from retention forced a more detailed analysis of the field effect than first envisioned. Thus, the data set in Fig. 7 is reflecting the sample's behavior under a large number of different field strengths, chosen to allow an extrapolation of diameter data for each particle to a value at zero field, presumably free from wall effects. For the four largest particles, a fourth degree polynomial fit was shown to represent the data with a 99% confidence level, while sizes of the smaller particles were determined by linear extrapolation to zero field. Extrapolated diameters obtained in this way are listed in Table I under the heading "SdFFF-C", and are seen to compare well with those from the AUC over the entire size range. The smallest particle was barely retained even at our maximum field strength of 2000 rpm (692 *g*), and was therefore excluded from this extrapolation procedure.

Also listed in Table I are relative amounts of nine out of the sample's ten components, calculated from areas under the scattering-corrected peaks in the different fractograms. Only baseline resolved peaks with retentions ranging from 5 to 30 column volumes were considered suitable for this analysis, in keeping with the notion of an "accuracy window" mentioned above. Due to its weak retention and poor resolution from the void peak, the smallest particle was not included in this quantification.

Although the relative amounts determined by this approach of multiple runs at different, but constant, field strengths are closer to the true values than those determined by the faster exponential decay method used in the DuPont analysis, they fall short of indicating the actual 10% in relative weight of each component. This is probably due both to difficulties in correctly assessing the position of the baseline when determining the area under a given peak, as well as to the incomplete recovery at high retention illustrated by Fig. 4.

CONCLUSION

One run in the AUC is shown to accurately determine both sizes and relative amounts for complex spherical samples of known density, as in the case of the present ten-component mixture of polystyrene latex particles. Concentration non-idealities are absent in this type of analysis, which involves the observation of freely moving particles, far from any interface and unperturbed by fluid flow. In SdFFF the analysis is complicated by the sample's compression into thin layers at the solid/liquid interface. For small particles at modest retention, the complications are minimal, and good agreement is seen between diameters determined by the SdFFF and AUC techniques. By contrast, particles with diameters above about 500 nm show increasingly severe departures from ideal FFF behavior with increasing field.

For multi-modal samples, such as the one focused on in the present study, diameters can be correctly determined by a systematic observation of values determined at different field strengths, followed by an extrapolation to zero field. This approach is clearly not available for more realistic samples which are often monomodal and highly polydisperse, so that tracking of the field-dependent migration of a particular component becomes impossible. In order to correctly analyze such

samples, it is necessary to develop a modified retention equation which accounts for both the lift forces and steric exclusion effects known to influence the behavior of large particles. Efforts in this regard are currently under way in several laboratories.

The times required for the different approaches were comparable in the cases of AUC and the DuPont SF[3] analysis using an exponentially decaying field. However, unlike in SF[3], the AUC rotor simultaneously accommodates up to seven different samples, which significantly reduces the time per sample. The constant-field approach to SdFFF proposed here is by its very nature time consuming, as it involves multiple runs with relaxation periods of tens of minutes and run times of 1–2 h. It does, however, provide good recoveries of particles in a broad size range, and should be used whenever fractions of exactly sized particles are required.

Despite the wall-related complications discussed above, SdFFF has a clear advantage over AUC in the analysis of samples which require correlations between size and some other sample property, *e.g.* chemical composition or biological activity. Here, one relies on the SdFFF system's proven ability to separate a sample into fractions of uniform size, which can be subjected to one or several secondary analysis steps. To this end, viral infectivity has been associated with fractions representing a given molecular weight[24], X-ray fluorescence in conjunction with SEM has been used to correlate chemical composition with size in an analysis of particulates in stream water[25], and PCS has been used to determine the size associated with particular fractions of samples with unknown density[7]. Although both AUC and SdFFF have been successfully used to analyze samples of unknown density by systematic variations in the density of the carrier or suspension medium[26,27], this approach is only applicable to stable samples that remain unperturbed by changes in the environment. For emulsions and other fragile systems of unknown density it is often appropriate to let SdFFF produce fractions using a highly sample compatible medium, and subsequently size these fractions by an independent method such as PCS or SEM.

ACKNOWLEDGEMENTS

K.D.C. wishes to express her gratitude to Dr. J. Calvin Giddings for many years of educational collaboration. Support for this work via grant number GM 38008-02 from the National Institutes of Health is gratefully acknowledged.

REFERENCES

1 T. Svedberg and H. Rinde, *J. Am. Chem. Soc.*, 46 (1924) 2677.
2 W. Scholten and H. Lange, *Kolloid-Z. Z. Polym.*, 250 (1972) 782.
3 W. Mächtle, *Makromol. Chem.*, 185 (1984) 1025.
4 W. Mächtle, *Angew. Makromol. Chem.*, 162 (1988) 35.
5 J. C. Giddings, *Sep. Sci.*, 1 (1966) 123.
6 F.-S. Yang, K. D. Caldwell, M. N. Myers and J. C. Giddings, *J. Colloid Interface Sci.*, 92 (1983) 81.
7 K. D. Caldwell and J.-M. Li, *J. Colloid Interface Sci.*, 132 (1989) 256.
8 J. C. Giddings, *J. Chem. Ed.*, 50 (1973) 667.
9 M. N. Myers and J. C. Giddings, *Anal. Chem.*, 54 (1982) 2284.
10 K. D. Caldwell, S. L. Brimhall, Y.-S. Gao and J. C. Giddings, *J. Appl. Polymer Sci.*, 36 (1988) 703.
11 J. C. Giddings and K. D. Caldwell, in B. W. Rossiter and J. F. Hamilton (Editors), *Methods in Physical Chemistry*, Vol. 3B, Wiley, 1989, p. 867.
12 J. C. Giddings, F. J. F. Yang and M. N. Myers, *Anal. Chem.*, 46 (1974) 1924.
13 J. C. Giddings, *Sep. Sci. Technol.*, 13 (1978) 241.

14 K. D. Caldwell, T. T. Nguyen, M. N. Myers and J. C. Giddings, *Sep. Sci. Technol.*, 14 (1979) 935.
15 J. C. Giddings, M. N. Myers, K. D. Caldwell and S. R. Fisher, in D. Glick (Editor), *Methods of Biochemical Analysis*, Vol. 26, Wiley, 1980, p. 79.
16 J.-M. Li and K. D. Caldwell, *J. Chromatogr.*, submitted for publication.
17 M. R. Schure, *Anal. Chem.*, 61 (1989) 2735.
18 T. Depireux, F. Dumont and A. Watillon, *J. Colloid Interface Sci.*, 118 (1987) 314.
19 J. C. Giddings and K. D. Calwell, *Anal Chem.*, 56 (1984) 2093.
20 W. W. Yau and J. J. Kirkland, *Sep. Sci. Technol.*, 16 (1981) 577.
21 M. E. Hansen and J. C. Giddings, *Anal. Chem.*, 61 (1989) 811.
22 M. R. Schure, *Anal. Chem.*, 61 (1989) 2735.
23 S. Lee and J. C. Giddings, *Anal. Chem.*, 60 (1988) 2328.
24 K. D. Caldwell, G. Karaiskakis and J. C. Giddings, *J. Chromatogr.*, 215 (1981) 323.
25 G. Karaiskäkis, K. A. Graff, K. D. Caldwell and J. C. Giddings, *Int. J. Environ. Anal. Chem.*, 12 (1982) 1.
26 W. Mächtle, *Colloid Polymer Sci.*, 262 (1984) 270.
27 J. C. Giddings, G. Karaiskakis and K. D. Caldwell, *Sep. Sci. Technol.*, 16 (1981) 607.

Journal of Chromatography, 517 (1990) 377–393
Elsevier Science Publishers B.V., Amsterdam

CHROM. 22 327

Retention effects in thermal field-flow fractionation[a]

J. J. KIRKLAND*, L. S. BOONE[b] and W. W. YAU
E. I. Du Pont de Nemours & Co., Inc., Central Research and Development Department, Experimental Station, B-228 Wilmington, DE 19880-0228 (U.S.A.)

ABSTRACT

While the basis of the thermal field-flow fractionation (TFFF) method presumably is thermal diffusion, predicting retention for different polymer types in different solvents is generally not possible. To clarify the TFFF retention mechanism, we developed a data base for a range of experimental conditions. Retention is strongly a function of polymer and carrier solvent types, and is proportional to solvent viscosity. Studies suggest that polymer retention significantly increases when using a mixed carrier solvent that has a higher concentration of "poor" solvent relative to "good" solvent. Although no apparent correlation was found between retention and various physical properties of the system, more effective practical TFFF experiments can be done because of these studies.

INTRODUCTION

Quantitative molecular-weight distributions (MWD) of a wide range of organic-soluble[1–6] and certain water-soluble[7] polymers are possible with the high-resolution separation method called thermal field-flow fractionation (TFFF). Because of higher resolution, TFFF generally has higher molecular-weight accuracy than the widely used size-exclusion (or gel permeation) method[6]. Especially attractive is the ability of TFFF to characterize fragile polymers of very high molecular weight[4,8].

TFFF separations typically use a single carrier liquid by applying a large thermal gradient across a very thin channel formed from two highly polished, parallel plates. Because of this temperature difference, sample components are pushed against one wall (the accumulation wall). Higher-molecular-weight (MW) materials are forced closer to the wall compared to lower-MW components. The essentially laminar flow profile created within the thin channel creates a very steep velocity profile near the walls. Higher-MW components that are closer to the accumulation wall are swept

[a] Presented in part at the *First International Symposium on Field Flow Fractionation, Park City, UT, U.S.A., June 14–16, 1989.*

[b] Present address: Chemistry Department, University of Chicago, Chicago, IL, U.S.A.

down the channel by slower flow streams near the wall. They lag behind and elute after lower-MW components. Thus, retention differences result from the different redistribution of solutes from fast- to slow-moving flow streams within the laminar flow profile.

Previous studies have shown that TFFF retention is dependent on the chemical composition and molecular size of the polymer investigated[1,2,6,9]. TFFF retention allows the determination of thermal diffusion coefficients in different solvents[10]. Also reported is the effect of temperature on thermal diffusion, to provide a better basis for choosing optimum conditions for TFFF experiments[11]. Still, even with these studies, the *a priori* prediction of TFFF retention characteristics of new or previously uncharacterized polymers is not possible.

The purpose of this study was to develop data for a range of polymer types and solvents. The expectation was that this information might lead to a better fundamental understanding of thermal diffusion and the TFFF retention process. Retention relationships were determined with the time-delay, exponential-decay programming method. After an initial period of constant temperature difference between the two channel faces, the temperature difference decreases exponentially during the separation. With this method, TFFF retention follows a simple log MW *vs.* solute retention time relationship that provides a convenient way to organize and analyze data.

The results of this study still do not allow quantitative predictability of polymer retention. Nevertheless, improved techniques for carrying out TFFF experiments resulted, with a clearer definition of some strengths and limits of TFFF.

EXPERIMENTAL

Equipment

The apparatus was essentially the same as that previously described[5], with one exception. A Model 150 computer equipped with Model 5088-2057 and Model 61012A interface components (Hewlett-Packard, Palo Alto, CA, U.S.A.) remotely controlled the setpoint of the temperature controllers during programming. Instrument control was by in-house-developed Basic software. A Hewlett-Packard Model 18652A analog-to-digital converter digitized the outputs from a UV absorption detector (Model 783, Kratos Analytical Instruments, Ramsey, NJ, U.S.A.) and a refractive index detector (Optilab Model 5902, Tecator Instruments, Herndon, VA, U.S.A.). Signals were processed with a Hewlett-Packard Model 3357 LAS system equipped with in-house-developed software[6]. Time-delayed exponential-decay (TDE)-TFFF calibration data were log–linear regressed and plotted with a Vectra Model 45 personal computer (Hewlett-Packard), using Graphwriter II software (Lotus Development Corporation, Cambridge, MA, U.S.A.) and a Model 7475 plotter (Hewlett-Packard).

Reagents

HPLC-grade solvents were from Fisher Scientific (Fair Lawn, NJ, U.S.A.) or American Burdick and Jackson (Muskegon, MI, U.S.A.). Polymer MW standards were from Polymer Labs. (Amherst, MA, U.S.A.). All other materials were from DuPont.

THEORY OF RETENTION IN TIME-DELAYED EXPONENTIAL-DECAY TFFF

TDE-TFFF permits the separation of a wide range of polymer molecular weights with a single experiment in a convenient time. With this approach, the temperature difference between the plates decreases exponentially during the run[5]. Temperature programming speeds up the elution of higher MW components, reduces analysis time, and improves the detection of later-eluting species[12]. Previous studies have shown some advantages of using time-delayed exponential-decay temperature programming in thermal field flow fractionation[5–7]. With this approach, uniform resolution and MW accuracy occurs over a wide dynamic MW range in a practical analysis time. A similar form of force field programming is used in sedimentation FFF[13,14].

In the TDE-TFFF experiment, the separation begins with an initial temperature difference between the two plates, $(\Delta T)_0$, that is held constant for a time τ. Then, ΔT decreases exponentially also with a time-constant τ. With this approach, retention times of well-retained solutes can be described by[5,6]

$$t_R = \alpha\tau(\ln M) + \tau \ln[eV_0(\Delta T)_0/6F\beta\tau] \quad (1)$$

When $\beta = b/D_T$, where b is a constant and D_T is the thermal diffusion coefficient, then

$$t_R = \alpha\tau(\ln M) + \tau \ln\{[D_T/b][eV_0(\Delta T)_0/6F\tau]\} \quad (2)$$

where, t_R is the retention time of the eluted component; $\alpha \approx 0.6$ for random-coil polymer conformations; τ is the time-delay, exponential-decay time constant; M is the molecular weight; F is the flow-rate; V_0 is the volume of the separating channel; and $(\Delta T)_0$ is the initial temperature difference between the hot and cold blocks. Eqns. 1 and 2 suggest that a plot of retention time t_R *vs.* ln M is a straight-line relationship with a slope set by the time-delay/decay constant τ. Other operating parameters such as the flow-rate F and the initial temperature difference $(\Delta T)_0$ determines the intercept of this plot. The value of τ primarily controls the elution of sample components, with smaller influence by the other operating parameters.

The relationship in eqn. 2 provides a convenient and accurate method for calibrating and measuring the MWD of polymers over a wide MW range. The TDE-TFFF method permits convenient data handling for quantitative MWD analyses[6]. Accurate peak-position calibrations follow from the simple log MW *vs.* retention time relationship. Also, the valuable single- or two-broad-standard calibration procedures[15] are readily used. Further, eqn. 2 predicts exact changes in the elution of components with variations in the various operating parameters such as τ, F and $(\Delta T)_0$. Nomographs simplify this calculation[16].

The relationships in eqn. 2 are convenient to obtain certain physical data on polymers of interest. For example, eqn. 1 suggests that the slope of the log–linear TDE-TFFF calibration curve can be used to find the α value for a polymer in a particular solvent system. Since the slope $= 1/\alpha\tau$, the α value is easily calculated, as indicated later in this paper. This α value is related to the well-known Mark–Houwink a constant. This constant is, in turn, related to polymer intrinsic viscosity by the expression[15]

$$[\eta] = KM^a \quad (3)$$

where $[\eta]$ is the polymer intrinsic viscosity in a particular solvent, K is a constant for the system, M is the polymer molecular weight, and a is the Mark–Houwink constant describing polymer conformation[15]. Now,

$$R_g \approx ([\eta]M)^{1/3} \tag{4}$$

and

$$R_g \approx M^{[(1+a)/3]} \tag{5}$$

where, R_g is the radius of gyration of the polymer molecule in the solvent. Because of these correlations,

$$D \approx 1/R_g \approx M^{-[(1+a)/3]} \tag{6}$$

and

$$D = bM^{-\alpha} \tag{7}$$

It can be calculated that

$$\alpha = [(1 + a)/3] \tag{8a}$$

and

$$a = (3\alpha - 1) \tag{8b}$$

where, D is the familiar solute–solvent diffusion coefficient, and the constant b is proportional to $1/\eta_{\text{solvent}}$. Therefore, the well-recognized Mark–Houwink a constant directly relates to the α value of eqns. 1 and 2. The α value also can be used to describe the conformational characteristics of a polymer molecule in a particular solvent.

RESULTS AND DISCUSSION

Effect of polymer type

Previous studies show that retention in TFFF varies with both polymer type and the solvent used in the separation[1,2,6,16]. With TDE-TFFF this effect is shown by the somewhat constant slopes of the log–linear calibration plots for different random-coil polymers and for different organic solvents. However, the intercept of the calibration plots can vary[5,6,16]. Fig. 1 illustrates these effects for four different sets of polymer standards fractionated with toluene as the mobile phase. All calibration curves were linear with essentially the same slopes. The same general effect occurs for the same polymer fractionated in different solvents, as discussed below.

Effect of carrier solvent type

We initially proposed that solvent effects on polymer solubility might be

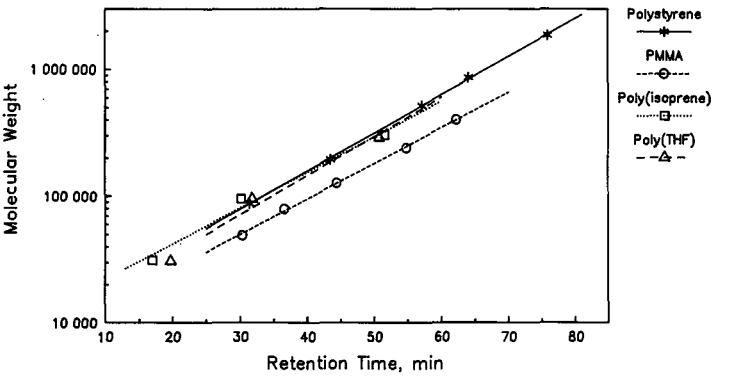

Fig. 1. TDE-TFFF calibration plots for several polymers. Carrier, toluene; flow-rate, 0.15 ml/min; channel, 132 μm; Initial hot block temperature, 90°C; cold block temperature, 20°C; exponential time delay/constant, τ = 25.0 min; sample, 50 or 100 μl of 1 mg/ml in carrier solvent; PMMA = poly(methyl methacrylate); poly(THF) = poly(tetrahydrofuran).

a central feature of TFFF retention phenomena. Our approach in defining this supposition was to develop a data base for polymer–solvent systems, in the hope that key elements regarding TFFF retention and thermal diffusion coefficients might be revealed. Fig. 2 illustrates the effect of solvent type on retention for polystyrene standards fractionated with a variety of solvents. Again, the slopes of the TDE-TFFF calibration plots are similar, suggesting approximate constancy of polymer conformation in these solvents. The greatest difference in retention was between toluene and chloroform, with the former showing the highest retention of these solvents. Fig. 3 shows similar data developed for the more polar polymer, poly(methyl methacrylate) (PMMA). For this system, greatest retention was in toluene, least in N,N′-dimethylformamide (DMF). The slope of the TDE-TFFF calibration plot appears somewhat dependent on the type of polymer and solvent. The slope also is characterized by the value of α from eqn. 1, as discussed later.

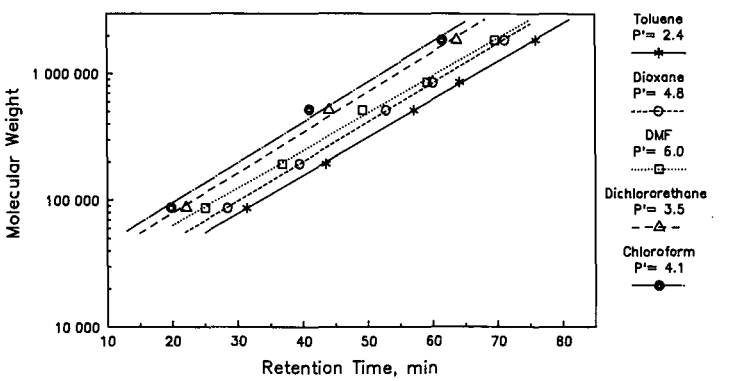

Fig. 2. Effect of carrier solvent on polystyrene calibration plots, Solute, polystyrene; other conditions as in Fig. 1; DMF = N,N′-dimethylformamide.

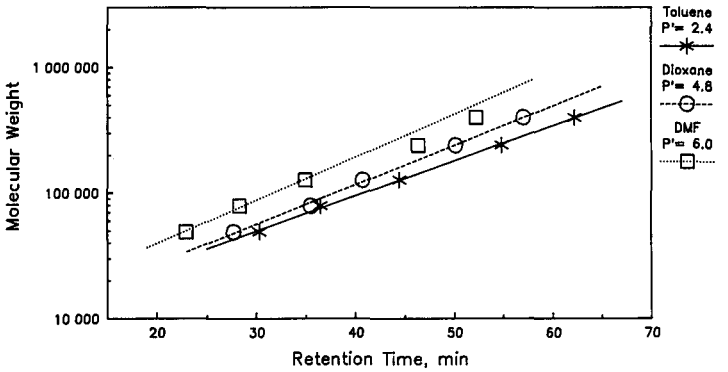

Fig. 3. Effect of carrier solvent on poly(methyl methacrylate) calibration plots. Solute, poly(methyl methacrylate standards); other conditions as in Fig. 1.

What is the retention change that occurs when a polymer is dissolved in solvents of highly different characteristics? The answer to this question depends on the particular solvent and the polymer of interest. Still, insight can be gained by observing the retention characteristics of a polymer that is soluble in both organic and aqueous systems. We have previously shown that retention occurs for certain water-soluble polymers, permitting their characterization by TFFF[7]. For example, poly(ethyleneoxide) shows TFFF retention in both organic and aqueous media. This polymer provides an interesting test case for studying retention changes as a function of mobile phase effects. Fig. 4 shows the TDE-TFFF calibration plots for poly(ethyleneoxide) standards in water and chloroform. In this instance, similar calibration plots occur in

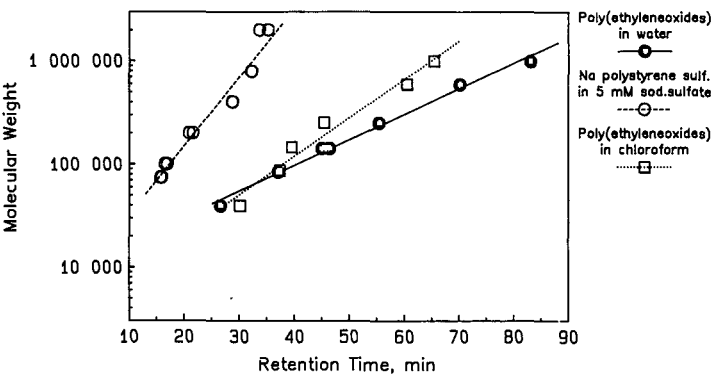

Fig. 4. Comparison of calibration plots for aqueous- and organic-soluble polymers. Poly(ethyleneoxide) standards: in water: 254 μm channel; flow-rate, 0.30 ml/min; 25 μl, 2 mg/ml each; in chloroform; 136 μm channel; flow-rate, 0.15 ml/min; 50 μl, 1 mg/ml each; sodium polystyrene sulfonate standards: 254 μm channel; flow-rate, 0.30 ml/min; 25 μl, 1 mg/ml each in 5 m*M* Tris–sodium sulfate, pH 7.5. Other conditions as in Fig. 1.

both solvents; retention also is similar in the very different solvents, water and chloroform.

However, strikingly different polymer retention differences occur for other water-soluble polymers. For example, sodium polystyrene sulfonate exhibits unusual retention characteristics in a very dilute salt solution[7]. The steep calibration curve found for this ionic polymer (Fig. 4), whose conformation should be rodlike in low ionic-strength media[17], is decidedly uncharacteristic, as discussed below.

Data in this report and elsewhere[9,18] support the contention that the mass of the solute and its normal diffusion characteristics primarily govern the MW dependency of TFFF retention. An MW increase decreases the diffusion coefficient and increases retention because normal diffusion cannot overcome the force pushing molecules to the accumulation wall. The result is that larger molecules remain in slower flow streams near the wall and elute later. One can speculate that, for this effect to occur, the force created by thermal diffusion to push components to the accumulation wall must be largely independent of solute mass (see also refs. 9, 10 and 18).

On the other hand, the data for sodium polystyrene sulfonate in Fig. 4 suggest that this picture is not so simple for some systems. At the ionic strength used, this compound extends to a rod-like conformation, with a resulting smaller diffusion coefficient than for non-ionic, random-coil polymers (*e.g.*, poly(ethyleneoxide) of the same MW in organic solvents. Based on this, one would expect that the poorer diffusion of the extended polymer would result in greater retention, not less retention, as in Fig. 4 (also, see discussion below). Clearly, the mechanism of TFFF retention is complex for some systems and not satisfactorily understood.

Effect of solvent strength

The variability of polymer TFFF retention in different solvents previously has been documented[1,2,6,9]. Yet, explanations for the physical reasons for this variability are lacking, other than a change in solvent causes a change in thermal diffusion coefficients[1,10,19]. Unfortunately, the molecular basis for thermal diffusion still is unknown. We need the means to calculate thermal diffusion coefficients in order to predict TFFF retention for new systems.

Data in Fig. 2 strongly suggest that solvent strength is not the main feature that controls solute retention in TFFF. Solvent strength P' values calculated according to Snyder[20] and shown on Fig. 2 show no relationship to retention characteristics. The weakest solvent, toluene, with a P' value of 2.4 shows highest retention. But, the strongest solvent, DMF, with a P' value of 6.0, causes intermediate retention. Dichloroethane and chloroform with intermediate P' values of 3.5 and 4.1, respectively, produce similar weaker retention.

The strength (P' values) of mixed "good" and "poor" solvents for the polymer also do not correlate with TDE-TFFF retention, as illustrated by the data in Fig. 5. Here, plots obtained for three "good" solvents diluted with an equal volume of heptane, a "poor" solvent, still show the general relationship of Fig. 2 for undiluted solvents. Mixed dioxane still shows the highest retention, and mixed chloroform the lowest retention, as in Fig. 2.

It appears, therefore, that solvent strength *per se* does not directly correlate with TFFF retention.

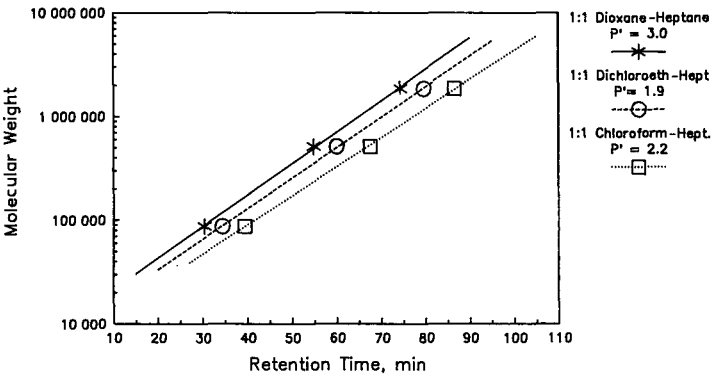

Fig. 5. Effect of carrier solvent strength on retention (different solvent types). Dioxane, dichloroethane, chloroform carrier solvents diluted with heptane. Conditions as in Fig. 1, except: polystyrene standards, 25 μl, 1 mg/ml; initial hot block temperature, 90°C; initial cold block temperature, 20°C; final temperature of both blocks after programming, 35°C. Solvent strength P' values calculated according to Snyder[20].

Effect of solvent viscosity

Carrier solvent viscosity has a significant effect on TDE-TFFF retention. Fig. 6 illustrates this for two polystyrene MW standards fractionated in four pure solvents, dioxane (η = 1.2), cyclohexane (η = 0.90), dichloroethane (η = 0.78), and chloroform (η = 0.53). A straightline relationship appears for these systems, with a smaller slope for the plot of the higher-MW polymer. TFFF theory anticipates this trend, since retention is dependent on the relative strength of the interaction between the applied thermal force field and the opposing diffusion of the solute[1]. As suggested by eqns. 2 and 7, retention time, t_R, in TDE-TFFF is proportional to ln $(1/D)$. Therefore, as carrier solvent viscosity increases, the diffusion coefficient decreases for the polymer. Molecules with poorer diffusion cannot overcome the thermal force field. Retention then increases because polymer molecules are forced closer to the accumulation wall. Slower flow streams intercept molecules close to the accumulation wall so that they

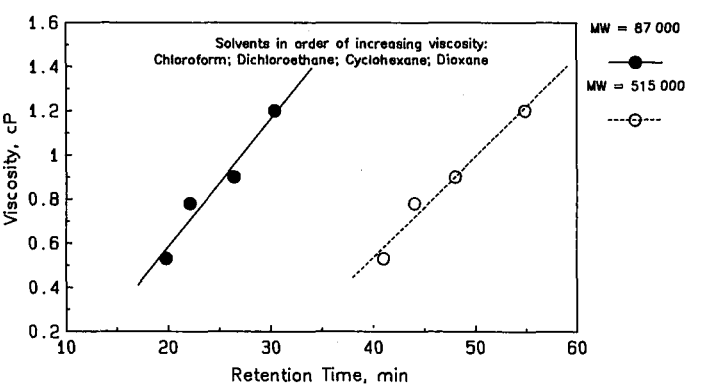

Fig. 6. Effect of carrier solvent viscosity on polystyrene retention (different solvent types). Conditions as in Fig. 5, with different dilutions with hexane; solutes, 87 000 and 515 000 MW polystyrene standards.

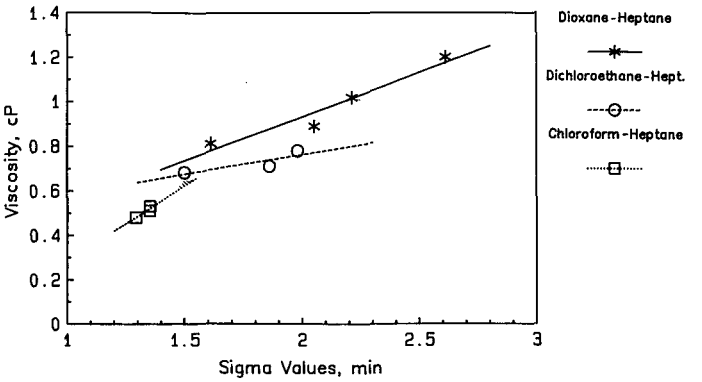

Fig. 7. Effect of solvent viscosity on band width. Solute, 87 000 MW polystyrene standard; sigma values = band standard deviation; conditions as in Fig. 5.

elute later. These results strongly suggest that thermal diffusion is not viscosity dependent, and that viscosity only affects conventional diffusion, which, in turn, strongly influences TFFF retention.

Note for the data in Fig. 5 that we used a "dual-mode" form of exponential temperature programming which was slightly different from previous experiments. To obtain these data the initial ΔT was 70°C, as usual, with the initial hot and cold block temperatures of 90 and 20°C, respectively. However, the cold block temperature was *not* held constant during the experiments. Using appropriate computer software, the temperature of *both* the hot and cold blocks was programmed to a final temperature of 35°C (hot block temperature decreased, cold block temperature increased). In this manner, the ΔT again was exponentially decreased with the desired τ value.

The results obtained with "dual-mode" exponential time delay/decay programming are similar to those of the traditional mode of holding the cold block temperature constant. But, sometimes there may be a practical advantage in dual-mode programming, since demands on precise temperature control are relaxed somewhat in experiments with small τ values (fast temperature decrease).

The viscosity of the carrier solvent also affects the standard deviation (width) of the solute peak, as might be predicted[21]. Fig. 7 shows that the peak width (in sigma values, min, where sigma is the standard deviation of the TDE-TFFF band) increases with increasing viscosity. This effect is because of poorer diffusion and increased resistance to mass transfer. Least change in sigma values occurs with the chloroform–heptane mixtures, since the viscosities of these two solvents are similar.

Effect of polymer solubility

All the solvents used to obtain the data in Fig. 2 are "good" solvents for polystyrene[22]. This leads to the question: Does the level of polymer solubility in the carrier solvent influence thermal diffusion and resultant TFFF retention? In an attempt to answer this question, we measured TDE-TFFF retention for polystyrene with "good" carrier solvents mixed with varying amounts of heptane, a "poor" solvent (actually, a non-solvent for polystyrene). Fig. 8 shows retention results from mixing heptane separately with dioxane. Increasing the concentration of the heptane diluent

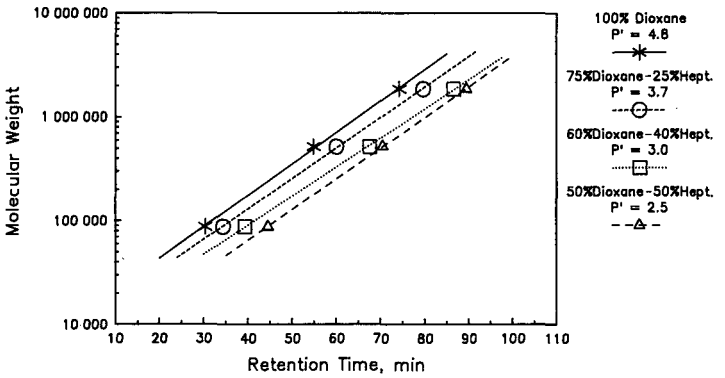

Fig. 8. Effect of solvent composition on retention. Solutes, polystyrene standards; dioxane diluted with heptane; conditions as in Fig. 1.

significantly increased retention. But, the slopes of the calibration curves remained essentially constant with increasing heptane content (potential decrease in polymer solubility).

Fig. 9 illustrates the increase in retention by diluting several "good" solvents with a "poor" solvent. Significant increases in polymer retention time occur as the volume fraction of heptane increases. Solubility of the polymer in the mixed solvent ultimately limits this effect. In the systems of Fig. 9, volume fractions of heptane exceeding about 0.5 precipitated the polymer and prevented TFFF characterization.

We believe that the results in Figs. 8 and 9 might be explained by changes in the thermal diffusion of the polymer, rather than by solvent power effects on molecular size and the normal diffusion coefficient. The reasoning is that the level of retention changes seen in Figs. 8 and 9 are much more than could be anticipated by changes in polymer diffusion due to solvation conformational changes. Increased diffusion is predicted for a decrease in polymer hydrodynamic radius due to less solvation

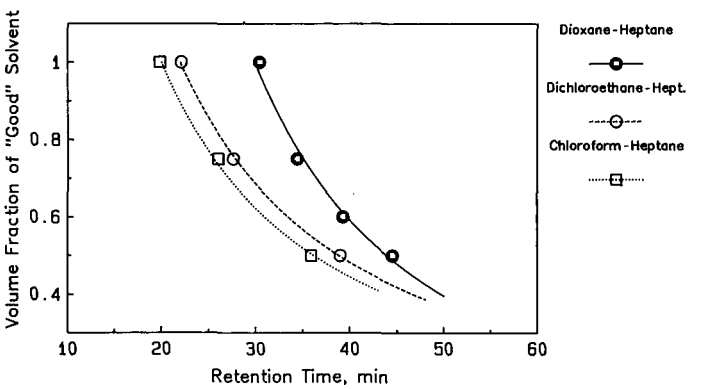

Fig. 9. Increased retention with higher "poor" solvent concentrations. Dioxane, dichloroethane and chloroform carrier solvents diluted with heptane; solute, 87 000 MW polystyrene standard; conditions as in Fig. 1.

resulting from diluting "good" solvents with a "poor" solvent. Such an increase in diffusion would reduce retention and, therefore, would not account for the retention increases observed in experiments with higher "poor" solvent concentrations.

The results from above study may not significantly contribute to our quantitative understanding of thermal diffusion. However, they do furnish useful guidelines for increasing the scope of TFFF applicability for solving real problems in determining the molecular weight distribution of polymers. For example, the data of Figs. 8 and 9 suggest that a significant increase in polymer retention occurs by using mobile phases that result in very high thermal diffusion, here, by diluting "good" solvents with "poor" solvents for the polymer. This is a practical approach when additional retention is needed, especially if the V_0 channel "dead" volume peak interferes with low-MW components. Fig. 10 shows the significantly increased retention afforded by this technique for a mixture of polystyrene standards. Note the significant increase in resolution between the channel dead volume V_0 peak and the first-eluting 87 000 MW polystyrene standard peak, as heptane dilutes the carrier.

Effect of temperature difference, ΔT

Maintaining a constant temperature difference ΔT between the channel walls by varying the temperature level affects TFFF retention, as previously noted[11]. Fig. 11 demonstrates this effect for an 87 000 MW polystyrene standard fractionated in cyclohexane with a ΔT of 30 and 40°C. Here, the polymer is more strongly retained at the lowest temperature range with the hot block at 50 and 60°C, respectively, and the cold block at 20°C (Fig. 11a and e). At the highest temperature levels (Fig. 11d and h), retention slightly decreases. The tailing, broad bands seen in Fig. 11a and e apparently are associated with poor solubility of polystyrene in cyclohexane at lower temperatures.

Correlation of retention with certain physical properties

Limited attempts to correlate TDE-TFFF retention with four pure carrier solvents (toluene, dichloroethane, dioxane and cyclohexane) with other physical properties produce no meaningful results. Fig. 12 shows that TDE-TFFF retention failed to correlate with carrier solvent thermal conductivity, heat capacity, surface

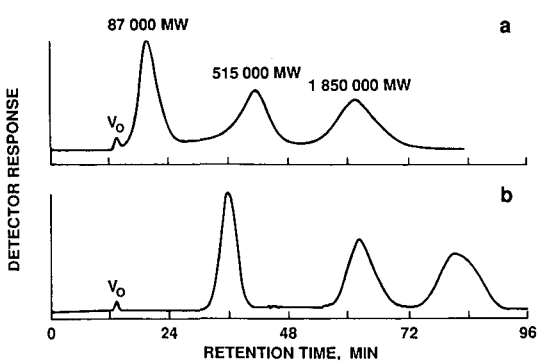

Fig. 10. Retention increase by diluting "good" carrier solvent with "poor" solvent. (a) 100% chloroform carrier; (b) chloroform–heptane (50:50) carrier; polystyrene standards; conditions as in Fig. 1.

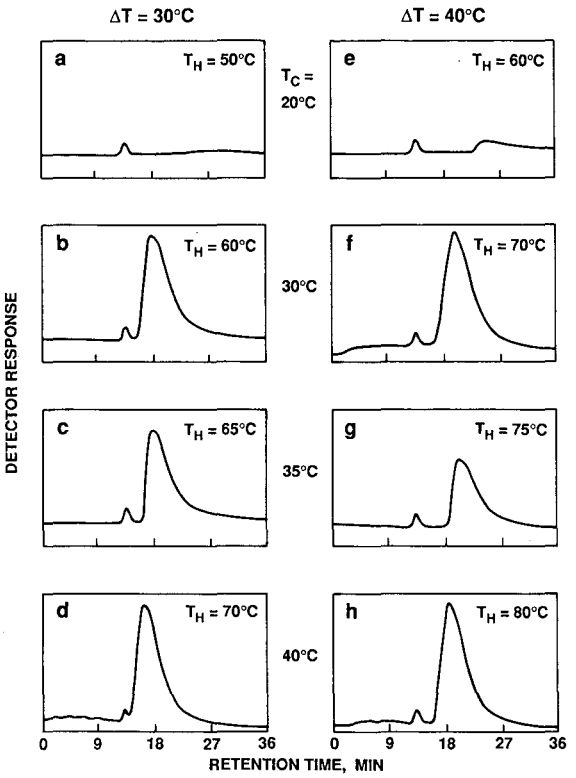

Fig. 11. Effect of level of ΔT on retention. Solute, 87 000 MW polystyrene; constant ΔT = 30 and 40°C; other conditions as in Fig. 1. T_H = Hot block temperature; T_C = cold block temperature.

tension, heat of formation, or solvent entropy data. While these results suggested no significant correlation with certain physical properties, only a limited data base was used. More complete documentation requires further studies. Another limitation is that the Fig. 12 data on the various physical parameters came from widespread reference sources that may be variable, incorrect or incomplete. It should be stressed, however, that TFFF is a superior method for measuring certain physical constants. Normal solute–solvent diffusion coefficients and thermal diffusion coefficients are readily determined, as described by Giddings and co-workers[9,10].

As described above, TDE-TFFF is a convenient method for measuring α values. This value relates to the Mark–Houwink a constant widely used in preparing universal calibrations in size-exclusion chromatography (SEC), as predicted by eqn. 8b. Table I summarizes the α values calculated from the slope of the calibration curves obtained during this study and from calibration curves given in a previous publication[15]. These α values also are compared with Mark–Houwink a values from the literature[23] for some polymer–solvent systems. In general, the correlation between a values from these two sources is reasonable, considering that literature a values themselves are quite variable.

Because of experimental limitations, we estimate that the α values reported in

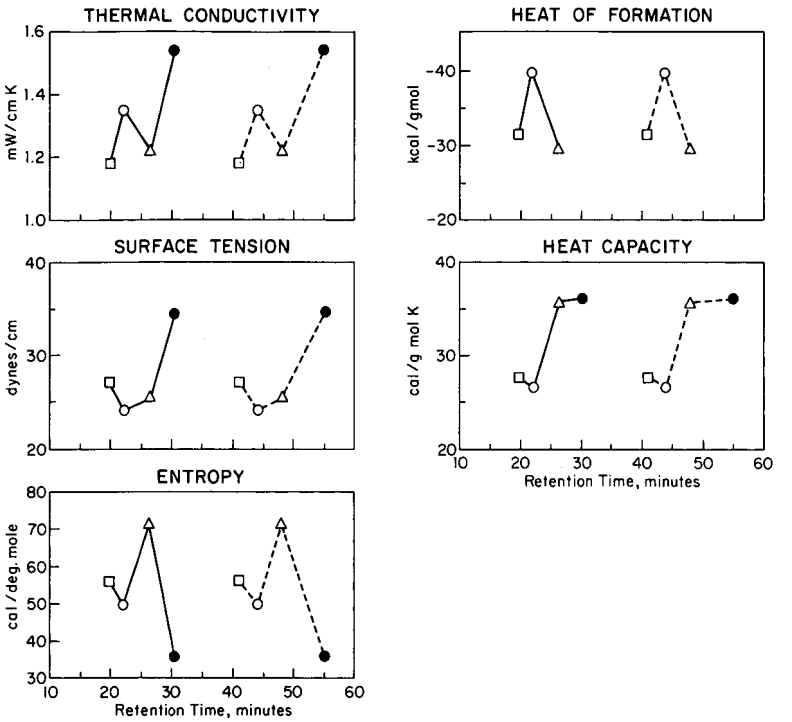

Fig. 12. Effect of physical parameters of carrier solvents on retention. Conditions as in Fig. 5; □ = chloroform; ○ = dichloroethane; △ = cyclohexane; ● = dioxane; physical data obtained from literature sources, based on 20°C, where appropriate.

Table I probably have a precision of about 0.08 (2σ) for all the polymers studied. (Variations are significantly less for some polymers, particularly those with narrow molecular weight distributions.) Therefore, the precision for calculated a values by this approach is three-fold poorer, or no better than about 0.24, since a is proportional to 3α (eqn. 8b). This level of experimental error makes it difficult to recognize slight changes in the slope of Fig. 8 plots that may result from polymer conformational changes by diluting a "good" solvent with a "poor" solvent.

The exception to correlation of the a values are data for sodium polystyrene sulfonate at the bottom of Table I. The near zero value calculated by TDE-TFFF for a is completely erroneous. This peculiar result is in keeping with the curious, very steep calibration curve for this polymer in Fig. 4. The rod-like structure for this polymer in low ionic-strength aqueous solution would be expected to produce a plot with a slope less than for poly(ethyleneoxide) (Fig. 4) in an aqueous solvent. Rod-like molecules should have a less-steep calibration plot because of the expected strong dependence of the diffusion coefficient on molecular weight. The data in Fig. 4 show just the opposite effect. The sodium polystyrene sulfonate plot is steeper, rather than less steep, than the calibration plot for a random coil molecule. Clearly, TFFF retention in aqueous media sometimes does not follow the same pattern as in organic solvents. This result suggests

TABLE I

COMPARISON OF TDE-TFFF α VALUES WITH MARK–HOUWINK CONSTANT a VALUES

Polymer	*Solvent*	*Measured* α	*Calculated a value*[a]	*Literature a value*[b]
Polystyrene	Toluene	0.58	0.73	0.79
	DMF	0.59	0.76	–
	Dioxane	0.56, 0.57	0.67, 0.72	0.69
	Dioxane–heptane (75:25)	0.59	0.77	–
	Dioxane–heptane (60:40)	0.62	0.86	–
	Dioxane–heptane (50:50)	0.59	0.76	–
	Dichloroethane	0.54	0.63	0.66
	Dichloroethane–heptane (75:25)	0.59	0.76	–
	Dichloroethane–heptane (50:50)	0.60	0.80	–
	Chloroform	0.55	0.64	0.76
	Chloroform–heptane (75:25)	0.62	0.86	–
	Chloroform–heptane (50:50)	0.60	0.80	–
Poly(methyl methacrylate)	Toluene	0.62, 0.62	0.86, 0.86	0.73
	Dioxane	0.55	0.66	–
	DMF	0.58	0.75	–
Polyisoprene	Toluene	0.62, 0.54	0.85, 0.61	0.77
	Cyclohexane	0.61	0.82	0.70
Poly(tetrahydrofuran)	Toluene	0.54	0.63	0.78
Poly(ethyleneoxide)	Chloroform	0.58	0.74	0.50
	Water	0.70	1.10	0.78
Sodium polystyrene sulfonate	5 m*M* Na_2SO_4	0.33	0(?)	0.93

[a] From eqn. 8.
[b] From ref. 19.

that a different retention TFFF mechanism may dominate for particular polymers in aqueous systems.

Universal calibration curve for TFFF

The plots of Figs. 1–3 conclusively show that the intercept of TDE-TFFF log MW *vs.* retention time calibration plots vary with polymer and with solvent. This effect is also characteristic of SEC plots of log MW *vs.* retention volume, when polymer type or solvent varies. Similarly, different plots occur with log $[\eta]$ (intrinsic viscosity) *vs.* retention volume or retention time plots, respectively, for SEC and TDE-TFFF, as illustrated for the latter in Fig. 13. However, it is well-known in SEC that a plot of log $([\eta] \cdot M)$ *vs.* retention volume produces a universal calibration plot that is the same for all polymers and solvents[16]. This is not so in TDE-TFFF, as illustrated by the data in Fig. 14. Changes in polymer type and solvent produce significant changes in the intercepts of the calibration plots. This effect largely shows the change in polymer thermal diffusion coefficients. Therefore, the consequences of thermal diffusion are not normalized for the polymer hydrodynamic volume by using $([\eta] \cdot M)$ as a plotting parameter.

One means of obtaining an equivalent universal calibration in TDE-TFFF is to include the normal polymer diffusion coefficient and the polymer thermal diffusion

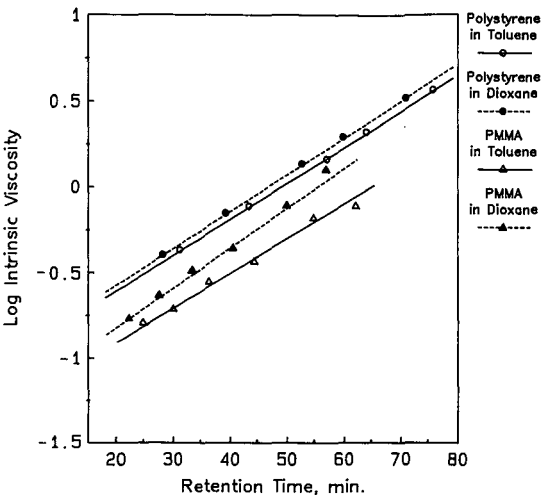

Fig. 13. Log intrinsic viscosity *vs.* retention time calibration plots. Solutes, narrow polystyrene and poly(methyl methacrylate) standards; conditions as in Fig. 1.

coefficient in the calibration relationship. Fig. 15 shows that this can be done by plotting polymer retention time *vs.* log ($S_0 \cdot M$), where the Soret coefficient[22] S_0 is D_T/D (ref. 24). Ref. 10 supplied data for calculating the Soret coefficients in Fig. 15. Unfortunately, such data for polymers are not generally available, so that the approach of Fig. 15 now has limited practical utility.

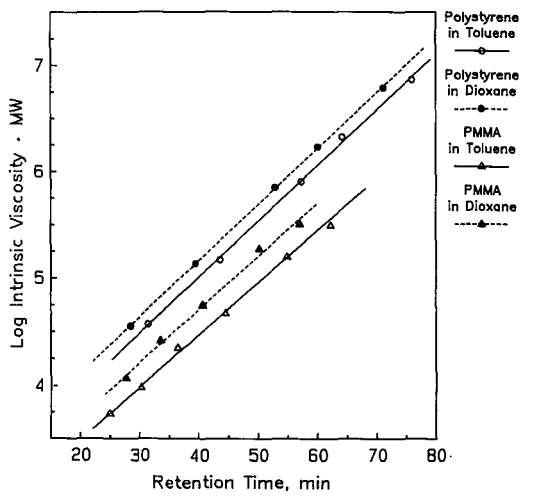

Fig. 14. Log ($[\eta] \cdot M$) *vs.* retention time calibration plots. Conditions as in Fig. 13.

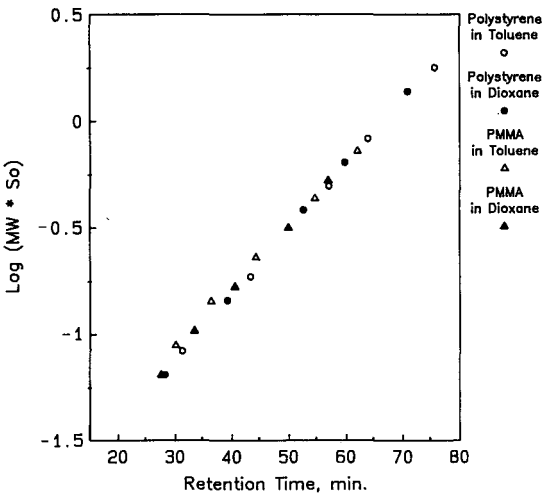

Fig. 15. Universal calibration plot for TDE-TFFF. Conditions as in Fig. 13; S_0 = Soret coefficient, D/D_T.

CONCLUSIONS

While thermal diffusion significantly influences TFFF retention, the mechanism for this effect is not well understood. Predicting TFFF retention is generally not possible for different polymer types in various solvents. We have studied TFFF retention over a range of experimental conditions, using the time-delay exponential-decay operating mode. Here, after an initial period of constant temperature difference between the two faces of the channel, the temperature decreases exponentially during the separation. A plot of log molecular weight *vs.* polymer retention time shows a linear relationship that provides a convenient way to organize and interpret TFFF retention data. Polymer and carrier solvent types strongly influence TFFF retention. Retention also appears directly proportional to solvent viscosity. Diluting "good" polymer solvents with certain "poor" solvents significantly increases polymer retention, presumably because of large changes in polymer thermal diffusion coefficients. No obvious correlation exists between TFFF retention and carrier solvent thermal conductivity, heat capacity, heat of formation, surface tension and solvent entropy. These studies still do not allow a quantitative prediction of TFFF retention for unknown systems, but they do provide a basis for conducting more effective TFFF experiments. For example, diluting a "good" solvent with a "poor" solvent provides a convenient way of increasing the retention of low molecular weight components. This is especially useful in resolving lightly-retained components from the channel dead volume V_0 peak.

ACKNOWLEDGEMENTS

We thank V. E. Burton and C. H. Dilks, Jr. for their skillful assistance in this study.

REFERENCES

1 M. N. Myers, K. D. Caldwell and J. C. Giddings, *Sep. Sci.*, 9 (1974) 47.
2 J. C. Giddings, M. N. Myers and J. Janca, *J. Chromatogr.*, 186 (1979) 37.
3 S. L. Brimhall, M. N. Myers, K. D. Caldwell and J. C. Giddings, *Sep. Sci. Technol.*, 16 (1981) 671.
4 Y. S. Gao, K. D. Caldwell, M. N. Myers and J. C. Giddings, *Macromolecules*, 18 (1985) 1272.
5 J. J. Kirkland and W. W. Yau, *Macromolecules*, 18 (1985) 2305.
6 J. J. Kirkland, S. W. Rementer and W. W. Yau, *Anal. Chem.*, 60 (1988) 610.
7 J. J. Kirkland and W. W. Yau, *J. Chromatogr.*, 353 (1986) 95.
8 J. J. Kirkland and R. M. McCormick, *Chromatographia*, 24 (1987) 58.
9 M. E. Schimpf and J. C. Giddings, *Macromolecules*, 20 (1987) 1561.
10 J. C. Giddings, K. D. Caldwell and M. N. Myers, *Macromolecules*, 9 (1976) 106.
11 S. T. Brimhall, M. N. Myers, C. D. Caldwell and J. C. Giddings, *J. Polym. Sci., Polym. Phys. Ed.*, 23 (1985) 2443.
12 J. C. Giddings, L. K. Smith and M. N. Myers, *Anal. Chem.*, 48 (1976) 1587.
13 W. W. Yau and J. J. Kirkland, *Sep. Sci. Technol.*, 16 (1981) 577.
14 J. J. Kirkland and W. W. Yau, *U.S. Pat.*, 4 285 810 (Aug. 25, 1981).
15 W. W. Yau, J. J. Kirkland and D. D. Bly, *Modern Size-Exclusion Liquid Chromatography*, Wiley, New York, 1979, Ch. 9.
16 J. J. Kirkland and W. W. Yau, *J. Chromatogr.*, 499 (1990) 655.
17 H. Morawetz, *Macromolecules in Solution*, Wiley, New York, 2nd ed., 1975, p. 358.
18 J. J. Gunderson and J. C. Giddings, *Macromolecules*, 19 (1986) 2618.
19 J. C. Giddings, M. E. Hovingh and G. Thompson, *J. Phys. Chem.*, 74 (1970) 4291.
20 L. R. Snyder, *J. Chromatogr. Sci.*, 16 (1978) 223.
21 L. K. Smith, M. N. Myers and J. C. Giddings, *Anal. Chem.*, 49 (1977) 1750.
22 J. Brandrup and E. H. Immergut (Editors), *Polymer Handbook*, Wiley, New York, 2nd ed., 1975, p. IV-6.
23 A. H. Emery, in M. J. R. Cantow (Editor), *Polymer Fractionation*, Academic Press, New York, 1967.
24 J. J. Kirkland and W. W. Yau, *9th International Symposium on Column Liquid Chromatography, Edinburgh, U.K., July 1–5, 1985*, poster.

Journal of Chromatography, 517 (1990) 395–403
Elsevier Science Publishers B.V., Amsterdam

CHROMSYMP. 1969

Sedimentation field-flow fractionation for pigment quality assessment

L. KOCH*, T. KOCH[a] and H. M. WIDMER
Central Analytical Department, CIBA-GEIGY Ltd., CH-4002 Basle (Switzerland)

ABSTRACT

Sedimentation field-flow fractionation is presented as an alternative method for pigment particle size characterization for the purpose of industrial quality control. The technique is demonstrated for three pigments of variously broad particle size distributions having average particle diameters ranging from *ca.* 0.1 to 0.6 μm. The analysis times compared favourably with those of disc centrifugation, and the reproducibility of the shape and mean particle size distributions were sufficient to obtain a reliable quality standard "fingerprint" with which samples of unknown quality could be compared.

INTRODUCTION

Pigments are always virtually insoluble materials that exist in the form of very small crystals that are incorporated into a colourless binding agent in the solid state. Whereas the properties of dyestuffs (soluble colorants) are determined by their molecular structure and by their interaction with the substrate, the properties of pigments are determined to a large extent by their physical characteristics. Through controlled changes in these physical characteristics, especially the particle size distribution, the properties of pigments can be optimized for certain applications or shifted in a desired direction. In certain instances, these physical properties can have such a significant impact on the final properties of the pigment that a certain pigment must be preferentially selected for use in an application where the chemically identical pigment in another physical form led to problems in processing or other unsatisfactory application results in the coloured medium.

As pigments are not soluble compounds but rather dispersed, microscopically small crystals, the particle size influences all application properties, albeit to various extents. Hue and strength, important properties of both pigments and dyestuffs, are primarily a function of the absorption wavelength region and the molar absorption coefficient. With pigments, however, the particle size also plays a significant role. After

[a] Present address: Heinz Schlegel Ltd., CH-4313 Möhlin, Switzerland.

0021-9673/90/$03.50

synthesis, the pigment aggregate must be reduced in size through milling. Down to a certain level, the smaller are the pigment particles, the stronger is the colour of the pigment. In addition, the particulate structure of the pigment gives rise to light scattering which is responsible for the extremely important application property of hiding power, *i.e.*, the ability to obliterate from view a background substrate. In many instances, unattractive substrates are covered through painting or lacquering, which also acts to provide protection against corrosion or degradation. The more strongly the non-absorbed light is scattered, the better is the covering power of the pigment. There is a need for pigments possessing either high or low hiding power, depending on their intended use. For example, pigment systems with high hiding power are required for heavy-duty industrial paints for machinery, whereas a transparent packaging film necessitates a low hiding power. The hiding power can be influenced through the choice of the pigment, the particle size distribution and additives.

Unfortunately, physical or physico-chemical measurements on dry pigment powder usually provide no real relevant conclusions on the final application properties of the pigment system. Untreated pigment powder is always in an aggregated state, and these aggregates and agglomerates must undergo a multi-step process of dispersion, through which they are wetted, reduced in size, dispersed and stabilized, in order to attain and maintain a sufficiently fine distribution. Almost all important properties of pigments or pigmented systems are, in fact dependent on how successful this dispersing process is. The optimum dispersed state of a pigment distribution is obtained when all primary particles, *i.e.*, either pigment aggregates or crystals as colloidal stabilized single particles, are homogeneously distributed. A series of different methods are suitable for the determination of the dispersibility as a function of various parameters, and most of these methods accomplish this through evaluation of the particle size distribution. These methods commonly include electron microscopy, various light-scattering techniques rheological measurements, Joyce–Loebl photosedimentometry, sedigraphic methods and Coulter Counter measurements. Our aim is to develop and utilize field-flow fractionation (FFF) methods and related techniques, *i.e.*, split-flow lateral transport thin (SPLITT)[1] separation cells, to help solve industrial particle sizing problems in situations where more conventional techniques have not yielded satisfactory results. When the pigment is most effectively analysed in a specific medium, or when the particle size distribution is characterized by multi-modality or shows non-Gaussian behaviour, FFF is likely to be the analytical method of choice. In this paper we propose and, using several examples from practice, demonstrate the use of sedimentation field-flow fractionation for the determination of particle size distributions for the purpose of pigment quality assessment in industry.

Sedimentation field-flow fractionation (SdFFF) has emerged as a versatile technique for the characterization of both simple and complex particle populations[2–5]. A particulate sample is entrained in a stream of liquid within the flat, circular channel of a specially designed, flow-through centrifuge rotor. The spinning of the centrifuge produces a field, oriented perpendicular to the direction of longitudinal channel flow, which causes sample particles denser than the mobile carrier to sediment radially outward towards the outer channel wall. Larger, or denser, particles interact more strongly with this applied field than the smaller, or less dense, particles in the sample mixture. Opposing this accumulation at the outer wall is the diffusion of the particles towards the centre of the flow channel. The combination of these two phenomena

culminates in the formation of thin steady-state concentration layers, or particle "clouds", which lie parallel to the accumulation wall, and which exhibit a characteristic degree of compression known as the steady-state layer thickness. The extent to which this layer protrudes into the parabolic flow streamlines on initiation of flow down the channel determines the average downstream particle velocity and thus the resulting elution sequence. The elution times can therefore be related by exact theory to particle size, mass and density[6].

However, although this separation principle has been used successfully to analyse a variety of submicron-sized particles relatively very few of the numerous FFF publications have dealt with its use in industrial applications. Our aim is to make use of FFF or related methods where other, more conventional techniques do not yield satisfactory results, *e.g.*, for multi-modal particle size distributions or in cases where a particular dispersing agent is required to ensure retention of certain particle properties.

Although Joyce–Loebl photosedimentometry (disc centrifugation), Coulter Counter and light-scattering methods are frequently used for pigment characterization, they all exibit certain intrinsic limitations which restrict their applicability. By requiring the use of density modifiers in the spin fluids, disc centrifugation cannot provide an analysis of the particles in their "as marketed" state. In contrast, by allowing an almost unrestricted choice of carrier, field-flow fractionation techniques are able to maintain the most meaningful environment for the pigment in terms of application properties. In addition, the use of the optimum carrier type greatly reduces the possibility of inducing additional aggregation and flocculation of the sample. The Coulter Counter has the disadvantage of not providing a particle size continuum. This limits the use of the instrument for quality assurance purposes, for which an accurate "fingerprint" of the sample, *i.e.*, a continuous particle size distribution curve, would be desirable for comparison with a standard "fingerprint" already on file. Light scattering is not an elution technique, *i.e.*, it does not separate as it analyses, and hence it cannot provide samples for further analysis by microscopy. This latter possibility can be extremely useful when, for example, it is necessary to determine whether anomalies in the particle size distribution are due purely to multi-modalities in size or if the particle shape is a contributory factor.

EXPERIMENTAL

Instrumentation

All measurements were performed on a DuPont SF[3] Model 1000 sedimentation field-flow fractionator (DuPont Instrument Systems) with a Hewlett Packard 9000/217 data-processing system. The initial temperature of the SdFFF system was 23°C (room temperature) in all instances. A temperature probe inserted in the centrifuge served to monitor the temperature of the air around the channel throughout the runs.

The various mobile phases were prepared with either Tween 20 (Fluka) or Teepol (Fluka) and doubly distilled water to the specifications given in Table I; 0.01% sodium azide (Merck) was added to retard bacterial growth. Samples were prepared by dilution in the mobile phase to *ca.* 1% by weight. Immediately before injection into the SdFFF channel, all samples were sonicated for precisely 1 min using a Branson Model

250 Sonifier, on high power, fitted with a micro-tip for use directly within the sample tubes.

For the evaluation of the fractogram in terms of actual particle diameters it is essential to know the density of both the sample and the carrier very accurately. Mobile phase densities were determined on a Paar Model DMA-60/602 densitometer, and found to be 1.00 g/ml in all instances. The densities of solid samples were precisely measured in the Physics Department at CIBA-GEIGY. Pigment A, an organic DPP (diketopyrrolopyrrole) colorant, was thereby found to possess a density of 1.55 g/ml. Pigments B and C, both azo colorants, each possessed a density of 1.3 g/ml. When analysing pigments, it is particularly important that the solid density be determined on the same crystal modification as that to be analysed by FFF. As the purpose of this study was to demonstrate "fingerprinting" of the particle size distribution of a particular pigment type by SdFFF, exact values for the particle and carrier densities are not required. They were necessary later, however, to evaluate the instrument performance when retention times were in question.

The injection volumes were 50 μl, and injection was carried out automatically with two Rheodyne pneumatically activated injection valves that had been fixed inside the system to minimize the prechannel dead volume. These valves were connected to a Gilson Model 221 sample changer which controlled the injection procedure, and a Gilson Model 401 diluter, which served to pump the sample very accurately onto the channel for the relaxation process. The eluate was detected at 254 nm with a Spectroflow Model 783 programmable absorbance detector (Applied Biosystems).

As most of the sample preparation was not performed within our laboratory, *e.g.*, the dispersion step was done in the plant, the concentrations varied slightly from sample to sample. However, the detector response is dependent on both particle concentration and size (as a consequence of their light scattering), which necessitates a correction of the response if a true concentration distribution is to be obtained from the fractogram[7]. Through moment analysis one may calculate the area under the retained peak, which reflects the total amount of retained particles, and the centre of the peak, reflecting the average diameter of retained particles. Future implementation of this in our data collection system will permit accurate computer comparison of fractograms.

Fractions for subsequent electron microscopy were collected with a Gilson Model 203 fraction collector.

Operating conditions

Time-delayed, field-decay programming was used in all instances. The proper functioning of the SdFFF equipment was routinely checked by injection of a mixture of Seragen Diagnostics standard polystyrene latex sphere particles of known density and diameter [0.460 $\pm$ 0.0048 μm, 0.318 μm (standard deviation unknown) and 0.204 $\pm$ 0.0020 μm]. The resulting fractograms were evaluated in terms of consistency in position of the void peak and the particle peak and shape of the particle peak.

All runs for a given pigment type were performed under identical FFF operating conditions. These conditions are given in Table I.

The fractogram obtained from all three pigment systems were repeatable and showed no undue noise or apparent distortion other than that which could be attributed to the properties of the particle populations themselves. The raw data

TABLE I

FFF OPERATING CONDITIONS

Pigment code	*Initial rpm*	*Relaxation time (min)*	*Time constant (= delay time) (min)*	*Carrier*	*Flow-rate (ml/min)*
A	600	10	8	0.01% Tween 20	3.0
B	2000	10	3	0.01% Teepol	2.0
C	3000	10	5	0.01% Teepol	2.0

(fractograms) were examined to identify and evaluate the void peak, which contains all particles and macromolecules small enough to be unaffected by the centrifugal field as they pass through the channel and the particle peak.

RESULTS AND DISCUSSION

The average particle diameters of the three pigments ranged from *ca.* 0.1 to 0.6 μm. The shape of the particle size distributions, as previously determined by either Coulter Counter or disc centrifugation measurements, also varied. The samples were crystalline and, while primary particles of pigment A were small, stable aggregates, B and C consisted of single crystals. Thus, any measurement of pigment A was actually a measurement of aggregate size. This made the decision to sonicate these samples before running them in the FFF particularly difficult, as it was not our intention to disrupt the particles from their natural states. In fact, SdFFF experiments on pigment A showed significant reductions in the mean particle size with increasing sonication time, leading us to believe that, with extended sonication time, aggregates had been reduced to an artificially high degree of fineness.

Electron micrographs of the three original samples (after 1 min of sonication) are shown in Fig. 1. Micrographs of samples B and C showed that they contained particles from the submicron range up to more than 100 μm in diameter, and thus spanned the ranges of both normal and steric FFF. For these cases, a more meaningful particle size determination would include either an off-line preseparation step (filtration), or an on-line preseparation realized by performing two subsequent runs at different conditions. The latter strategy permits the analyis of the submicron particles separately from the particles larger than 1 μm. This can be very useful for complex mixtures, and ensures that a steric foldback[8], which distorts the fractograms and limits their information content, is avoided.

By adhering to a fixed set of experimental conditions for each of the three pigments A, B and C, the fractograms become directly comparable for a rapid evaluation of similarities or differences in the particle size distributions. Our approach was thus to obtain a reproducible fractogram in which sample components were well retained, and for which the total run time had been reasonably well optimized, and to use this as a standard fractogram with which others could be compared. These standard fractograms are shown as solid lines in Fig. 2a, b and c. The traces denoted by dashed lines in Fig. 2a represent additional samples of pigment A which were drawn from the same production line at periodic intervals. Even small differences in mean particle diameter could be seen by comparing fractograms. Concentration differences,

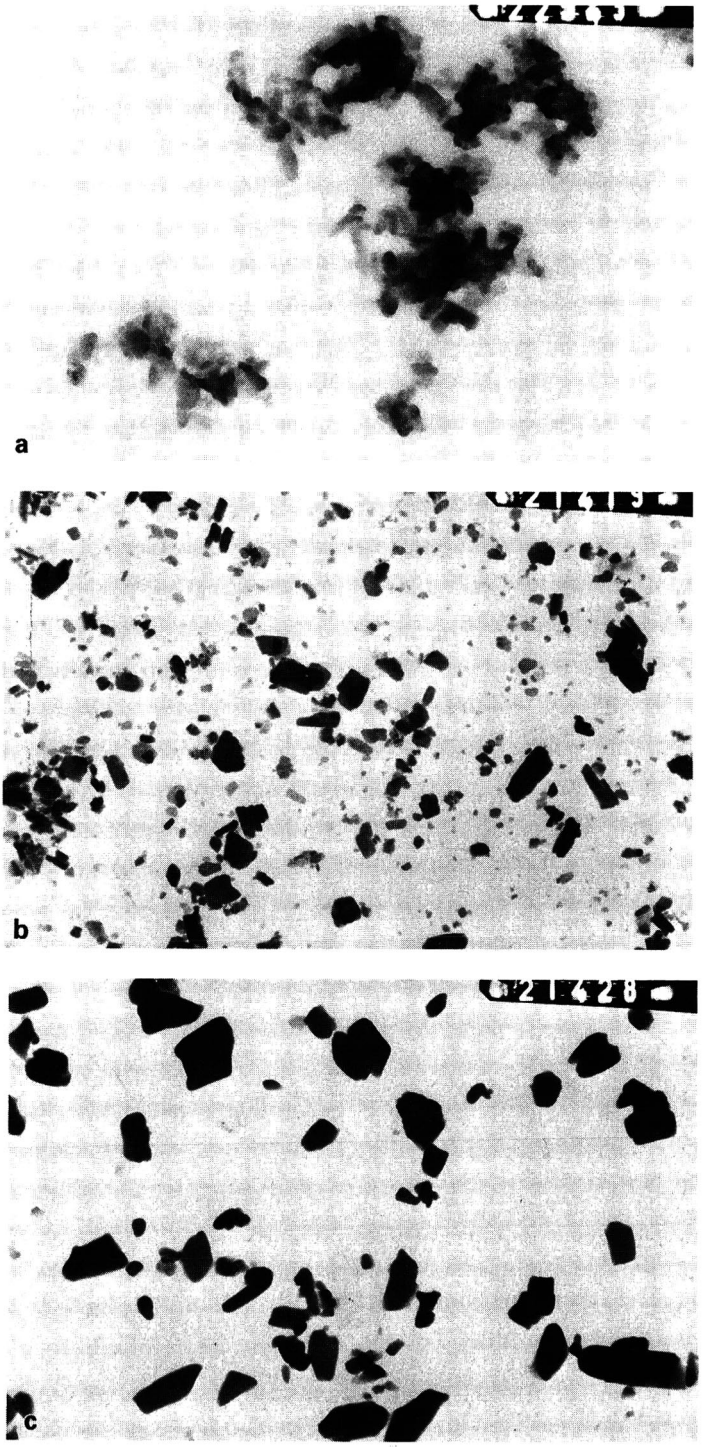

Fig. 1. Electron micrographs of the original pigment samples: (a) A; (b) B; (c) C. The magnification of A is twice that of B and C.

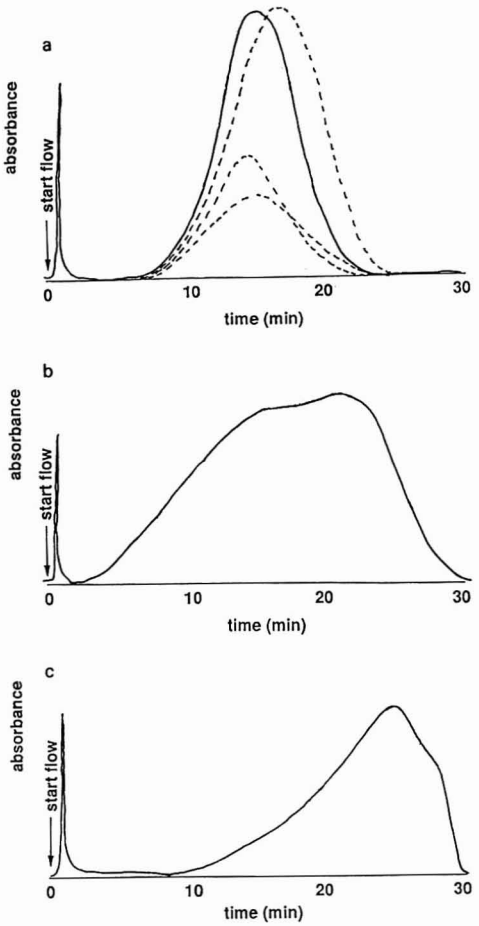

Fig. 2. Standard fractograms of (a) pigment A (solid line), (b) pigment B and (c) pigment C. The dashed lines in (a) correspond to fractograms of samples subsequently drawn from production.

visible as differences in peak amplitude, can be traced to the sample preparation step (dilution). The standard analysis procedure for these pigments within our company is disc centrifugation, and the total SdFFF run times, of the order of 30 min, were comparable to the times required for a disc centrifugation analysis.

As for any analytical technique, method development in FFF can be very time consuming. This learning process is considerably accelerated when the approximate particle diameter and densities, and a suitable dispersing agent, are known in advance. Fortunately, this information is generally readily available or obtainable for pigment particles. However, even when this basic knowledge exists, the varying complexity of samples can lead to great differences in the time needed for method development, as was the case for the three pigments examined in this study. Pigment A, which exhibited monomodal Gaussian distributions in the SdFFF, and indicated no significant interaction with the accumulation wall, required only an extremely short method development (two or three preliminary runs) and could have actually been analysed

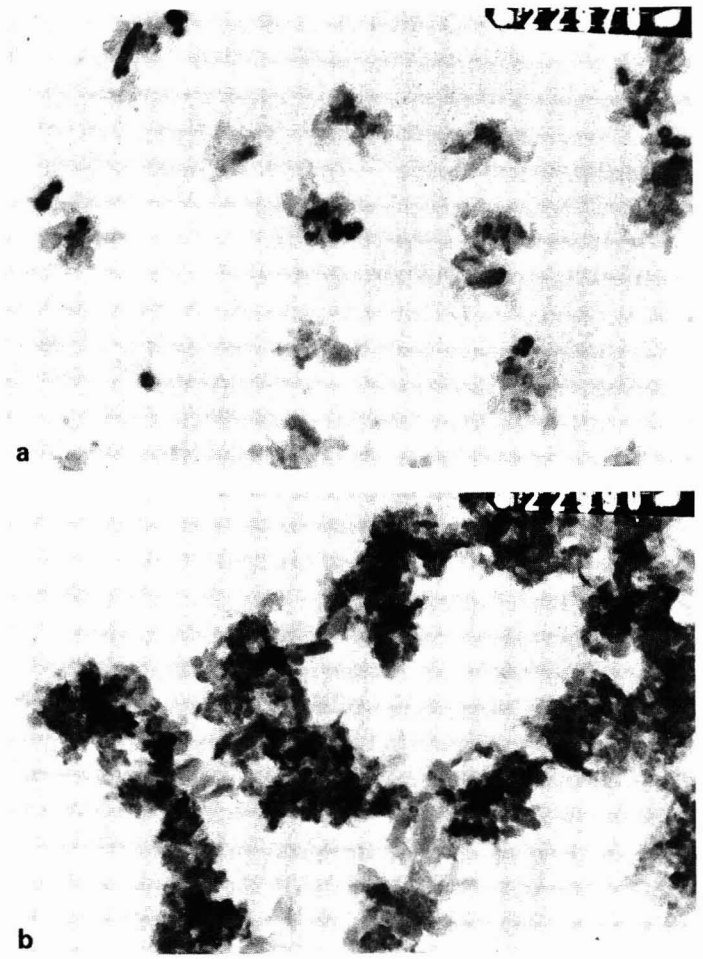

Fig. 3. Electron micrographs of fractions collected during a SdFFF run of pigment A, (a) at $t = 20$ min and (b) at $t = 30$ min.

after the first run. In contrast, samples B and C, with very broad, complex distributions, required several days of method development before a satisfactory, reproducible fractogram could be obtained. It should be noted that the system parameters for the last two pigments were not necessarily optimized, but rather a stable, reproducible fractogram was produced which could serve for comparison with latter fractograms. Whether the phenomenon leading to the non-Gaussian particle size distributions is adsorption, steric foldback or multi-modality in particle sizes remains unknown and is not of significant importance to this study. In fact, the shapes of the particle size distributions were in good agreement with those obtained by light scattering and disc centrifugation. There was, however, some discrepancy in the mean particle diameter.

In all instances the particles were considerably under-retained in SFFF. This may be a consequence of an incorrect value for the channel void volume. The effect

became more pronounced with increasing diameter, culminating in a size discrepancy of up to 30% for particles eluting at the peak maximum. In order to gain an insight into this discrepancy, we collected fractions of the continuously eluting sample for further analysis by electron microscopy. Fig. 3a shows a fraction collected from sample A at $t = 20$ min and Fig. 3b a fraction collected at $t = 30$ min. While the microscopy clearly served to verify the separation, the mean diameters of the particle population were difficult to assess with microscopy because of the non-spherical nature of the particles. However, careful evaluation of the microscopy data supported the disc centrifugation particle size data. The cause of the observed under-retention is still being investigated.

The results obtained show that SdFFF, when used as part of a "fingerprinting" strategy, is suitable for the quality assessment of pigments within the particle diameter range studied. Further developments are necessary to ensure that the excellent reproducibility of the distributions is coupled with reliable particle size data. Careful study is required to locate the cause of the discrepancies between actual and experimental particle size, likewise exhibited in runs with polystyrene standards.

Because the analysis times were comparable to those for disc centrifugation analyses, and because field-flow fractionation systems lend themselves to fully automated operation with an autoinjector (difficult to implement in a disc centrifugation system), SdFFF shows great promise for unattended, constant use for quality control purposes in the production plant itself. The realization of this goal would be facilitated by the development of simple, inexpensive FFF analysers which monitor the industrial pigment milling process through periodic, automated analyses and actually serve to determine the end-point of the milling process. This would provide a considerable advantage over the present method of allowing the milling process to proceed for an extended time to ensure that the particles have definitely reached the desired size. In addition, the high densities of pigment particles could ideally be exploited with the development of a simple SdFFF system which utilizes only gravitational force as the applied field. With such a simple system it would be feasible to couple an analyser to each mill in production.

REFERENCES

1 J. C. Giddings, *Sep. Sci. Technol.*, 23 (1987) 119.
2 S. M. Mozersky, K. D. Caldwell, S. B. Jones, B. E. Maleeff and R. A. Barford, *Anal. Biochem.*, 172 (1988) 113.
3 L. E. Schallinger, E. C. Arner and J. J. Kirkland, *Biochim. Biophys. Acta*, 966 (1988) 231.
4 H. K. Jones, B. N. Barman and J. C. Giddings, *J. Chromatogr.*, 455 (1988) 1.
5 L. E. Oppenheimer and G. A. Smith, *Langmuir*, 4 (1988) 144.
6 J. C. Giddings, G. Karaiskakis, K. D. Caldwell and M. N. Myers, *J. Colloid Interface Sci.*, 92 (1983) 66.
7 F. S. Yang, K. D. Caldwell and J. C. Giddings, *J. Colloid Interface Sci.*, 92 (1983) 81.
8 S. Lee and J. C. Giddings, *Anal. Chem.*, 60 (1988) 2328.

Journal of Chromatography, 517 (1990) 405–421
Elsevier Science Publishers B.V., Amsterdam

CHROMSYMP. 1988

Characterization of polymers by thermal field-flow fractionation

MARTIN E. SCHIMPF
Department of Chemistry, Boise State University, Boise, ID 83725 (U.S.A.)

ABSTRACT

Thermal field-flow fractionation (ThFFF) is a useful technique for separating complex polymer mixtures. The unique features of ThFFF make it applicable to many polymers that are difficult to characterize by conventional methods. Advances in channel design, spearheaded by work at the University of Utah's Field-Flow Fractionation Research Center, have recently culminated in the introduction of a commercially available instrument. Motivated by this progress, ThFFF is reviewed in this paper with an emphasis on implementation. Theories governing retention, zone dispersion and optimization are summarized. Procedures for obtaining accurate molecular-weight distributions on polymers are reviewed along with sample handling techniques. Also discussed is the application of ThFFF to studies of thermal diffusion in polymer solutions. The paper concludes with a discussion of current trends in the field.

INTRODUCTION

Great strides have been made in the understanding, implementation, and optimization of thermal field-flow fractionation (ThFFF) since its introduction over 20 years ago[1]. In characterizing polymeric materials, ThFFF benefits from the open well-defined geometry of the separation channel. Polymer scientists have become increasingly aware of the advantages of ThFFF, catalyzing the recent introduction of a commercial instrument (FFFractionation, Salt Lake City, UT, U.S.A.).

In ThFFF, a temperature gradient is used to drive polymer components into slower flow regions near the cold wall (Fig. 1). This process, termed thermal diffusion, is opposed by ordinary (Fickian) diffusion. The resulting distribution of polymer concentration across the bullet-shaped velocity profile is governed by the balance of the two diffusional processes. Like all FFF subtechniques, movement of components down the channel toward the detector is determined by their mean steady-state position in the velocity profile.

The unique features of ThFFF give it several advantages over size-exclusion chromatography (SEC). The ThFFF channel is open and lacks a stationary phase.

0021-9673/90/$03.50

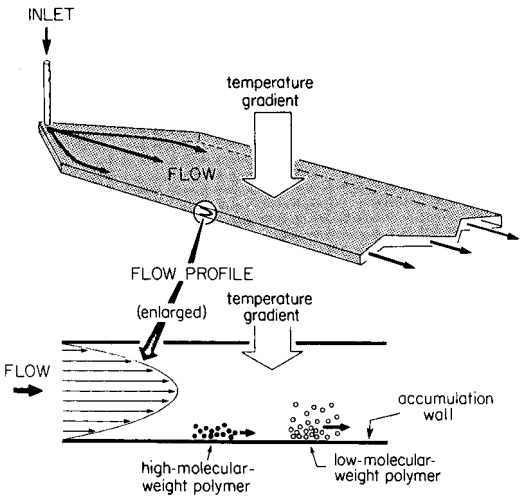

Fig. 1. Illustration of the principles of polymer separation by ThFFF (reprinted from ref. 44 courtesy of ACS Publications).

Thus, the flow profile of the carrier liquid and the dispersion of the sample zone are well characterized. Known equations relate zone retention and dispersion to transport coefficients of the polymer–carrier liquid system and to experimental parameters. These equations are used to compensate for zone dispersion in obtaining highly accurate information on molecular weight distributions (MWDs). The equations are also used to obtain values of the transport coefficients from retention data. Furthermore, they designate the experimental conditions that optimize individual separation problems. The unique channel features also provide excellent separation reproducibility; in the separation of >90 polymers in 7 solvents using the same instrument, both retention and zone broadening were highly consistent[2–4]. Finally, retention volume, limited to one column volume in SEC, is theoretically unlimited in ThFFF (for practical reasons, however, retention volume is limited to approximately 20 channel volumes). This feature offers the ability to separate significantly more components in a single mixture (large peak capacity).

Among the factors that influence retention in ThFFF is the magnitude of the externally applied temperature gradient. This can be varied rapidly and precisely to accommodate molecular weights from 1000 (ref. 5) to $>20 \cdot 10^6$ (ref. 6). By changing the temperature gradient continuously (programming), polymer mixtures containing components with a wide range in molecular weight can be handled in a single run[7]. While retention is also governed by the molecular weight of the polymer, the additional influence of chemical composition gives ThFFF an added dimension not present in SEC. This is illustrated in Fig. 2, which compares the resolving power of ThFFF and SEC on two polymers of similar molecular weight but varying chemical composition. The polymers coelute with SEC but are resolved by ThFFF because of differences in chemical composition.

Finally, separation in ThFFF is gentle; there is no interfacial transport or strong shear gradients. Thus, ThFFF is an ideal tool for characterizing fragile molecules such as high-molecular-weight polymers.

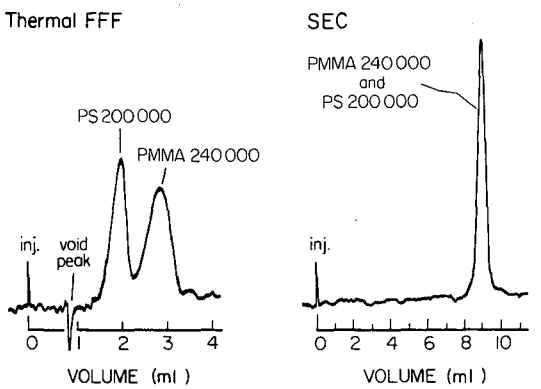

Fig. 2. Elution profiles of $2.0 \cdot 10^5$ MW polystyrene (PS) and $2.4 \cdot 10^5$ MW poly(methyl methacrylate) (PMMA) by ThFFF and SEC (reprinted from ref. 20 courtesy of Pergamon Press).

This paper reviews the application of ThFFF for characterizing polymers. Additional discussions on the conceptual basis and implementation of FFF and ThFFF are contained elsewhere[8–21].

THEORY

ThFFF theory is well-developed and has been described in a number of papers[22–32]. Summarized below are theories relevant to the understanding and implementation of ThFFF.

Retention

The opposing forces of thermal and ordinary diffusion result in an exponential profile in polymer concentration, with decreasing concentration away from the cold wall (coordinate x). The center of mass of the concentration profile is defined by its distance l from the cold wall. For mathematical convenience, parameter l is expressed in the dimensionless form $\lambda = l/w$, where w is the channel thickness. Retention parameter λ is related to the transport coefficients by

$$\lambda = \frac{D}{wD_T(dT/dx)} \tag{1}$$

where dT/dx is the temperature gradient across the channel, and D and D_T are the ordinary and thermal diffusion coefficients, respectively, of the polymer–carrier liquid system.

As in chromatography, the extent to which an analyte component is retained in FFF can be specified by the "retention ratio" R, defined as

$$R = \frac{V^0}{V_r} \tag{2}$$

where V^0 is the volume of the channel and V_r is the volume of carrier liquid required to elute the component. By considering the profiles across the channel of both analyte component and carrier-liquid velocity, R can be related to retention parameter λ. Values of λ, computed from experimental R values, are used to calculate transport coefficients from eqn. 1. Accurate values of λ are also crucial in establishing the column dispersion function, as discussed below.

For most FFF subtechniques the shape of the velocity profile is parabolic, and the dependence of R on λ is

$$R = 6\lambda(\coth \frac{1}{2\lambda} - 2\lambda) \tag{3}$$

In ThFFF the temperature gradient and attendant carrier-liquid viscosity changes in the channel result in a velocity profile that is skewed, with maximum flow shifted toward the hot wall. Motivated by the need for accurate λ values the following relation between R and λ was derived[28], accounting for the skewed velocity profile:

$$R = \frac{1}{\sum_{i=1}^{5} \frac{h_i}{(i+1)}} \left\{ \frac{1}{(1 - e^{-1/\lambda})} \left[\sum_{i=1}^{5} h_i \sum_{j=0}^{i-1} \frac{i!}{(i-j)} \lambda^j \right] + \sum_{i=1}^{5} i!\, h_i\, \lambda^i \right\} \tag{4}$$

Parameters h_i are defined as

$$h_1 = \theta b_0 \tag{5a}$$

$$h_2 = (b_0 + \theta b_1)/2 \tag{5b}$$

$$h_3 = (b_1 + \theta b_2)/3 \tag{5c}$$

$$h_4 = (b_2 + \theta b_3)/4 \tag{5d}$$

$$h_5 = b_3/5 \tag{5e}$$

where

$$\theta = \left(\frac{b_0}{2} + \frac{b_1}{3} + \frac{b_2}{4} + \frac{b_3}{5}\right) \Big/ \left(b_0 + \frac{b_1}{2} + \frac{b_2}{3} + \frac{b_3}{4}\right) \tag{6}$$

and parameters b_i are defined as

$$b_0 = a_0 + a_1 T_C \tag{7a}$$

$$b_1 = a_1 S \tag{7b}$$

$$b_2 = -\frac{1}{2K_C} (dK/dT) a_1 S^2 \tag{7c}$$

$$b_3 = \frac{1}{2}\left(\frac{1}{K_C}\frac{dK}{dT}\right)^2 a_1 S^3 \tag{7d}$$

Here T_C is the cold wall temperature, K_C is the thermal conductivity of the carrier liquid at the cold wall, dK/dT is the rate of change in thermal conductivity with temperature, and

$$S = \Delta T + \frac{1}{K_C}\frac{dK}{dT}\frac{(\Delta T)^2}{2} \tag{8}$$

where ΔT is the temperature difference between the hot and cold walls. Parameters a_0 and a_1 are the linear least-squares-fit parameters that describe the dependence of carrier-liquid fluidity, $1/\eta$, on temperature according to

$$\frac{1}{\eta} = a_0 + a_1 T \tag{9}$$

The relationship between R and λ can be significantly altered in accounting for the temperature dependence of viscosity. Fig. 3 compares the dependence of R on λ according to eqn. 4 (for a specific case) with the isoviscous dependence (eqn. 3).

Zone broadening

Dispersion of a solute band in FFF and chromatography is characterizd by plate height H, the variance of the band relative to the distance traveled. The major contributions to plate height in ThFFF have been studied in detail[29–34]. The dispersion of a monodisperse sample is represented by the channel or column contribution to plate height H_C. For a polydisperse polymer, there is in addition to column dispersion, a selective dispersion arising from the tendency of the higher-molecular-weight species to migrate behind the lower-molecular-weight species. This polydispersity contribution is represented by H_P. Thus, the observed plate height is the sum of the two terms

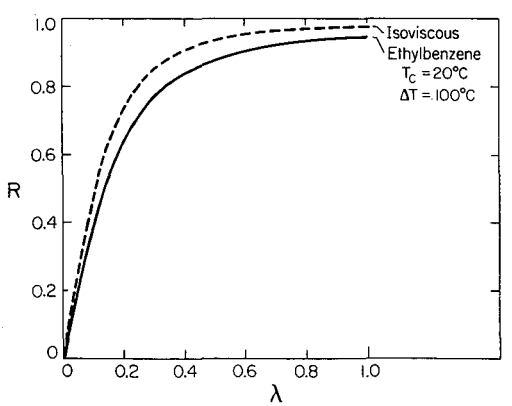

Fig. 3. Retention ratio R as a function of λ for the isoviscous system (eqn. 3) and ethylbenzene at T_C = 20°C and ΔT = 100°C, according to eqn. 4.

$$H = H_P + H_C \tag{10}$$

For narrow MWDs, the polydispersity contribution is approximated by[29]

$$H_P = LS_M^2(\mu - 1) \tag{11}$$

where L is the channel length, μ is the polydispersity, and S_M is the mass-based selectivity, defined as the dependence of retention volume V_r on molecular weight M according to

$$S_M = \frac{\mathrm{d}\ \log V_r}{\mathrm{d}\ \log M} \tag{12}$$

Zone dispersion in ThFFF is usually dominated by polydispersity ($H_P \gg H_C$) because of the open channel geometry and high resolving power inherent to ThFFF. However, column dispersion is significant when characterizing ultra-narrow polymer standards. Column dispersion is also significant for broad MWDs when high carrier-liquid flows are used to shorten analysis time. For ThFFF, H_C is described by

$$H_C = H_D + H_N + H_R + H_{EC} \tag{13}$$

The first term on the right side of eqn. 13 accounts for broadening due to longitudinal diffusion. This term generally is negligible because of the slow diffusion of macromolecules. The second term on the right is the non-equilibrium (mass transfer) term. This term arises because sublayers of the sample zone are displaced unequally by the non-uniform velocity profile. Under appropriate conditions, the non-equilibrium term dominates column dispersion in ThFFF. The third term on the right accounts for dispersion that occurs while the sample zone is "relaxing" to its steady state profile at the accumulation wall after injection. During relaxation, the zone is briefly subjected to a greater than normal range of longitudinal flow velocities. While this term is usually negligible, it can be significant at high carrier-liquid velocities. Relaxation effects can be avoided by using a stop–flow procedure in which flow is halted during relaxation[29]. The last term in eqn. 13 accounts for the influence of extra-channel volume on plate height. This unwanted effect can be kept negligible by using minimum lengths of narrow-bore tubing between the sample valve and channel head, and between the channel outlet and detector cell. Large-volume detector cells must also be avoided.

The non-equilibrium contribution to plate height H_N is expressed as[22]

$$H_N = \frac{\chi w^2 \langle v \rangle}{D} \tag{14}$$

where $\langle v \rangle$ is the average carrier-liquid velocity and χ is a complicated function of λ and R[34]. Martin and Giddings[23] developed an approximation for χ based on a third-degree polynomial expression for the velocity profile with one adjustable parameter υ. The resulting equation for χ is

$$\chi = \frac{2\lambda^2 F}{R(1 - \mathrm{e}^{-1/\lambda})} \tag{15}$$

Here

$$F = 2A[6(1+\upsilon) - (1/\lambda) - (A/\lambda) + 36\upsilon\lambda^2 - 6\lambda(1+6\upsilon) + 18\lambda e^{-1/\lambda}(1+10\upsilon\lambda)] + 72\lambda^2[(1+\upsilon)^2 - 10\lambda(1+4\upsilon+3\upsilon^2) + 4\lambda^2(7+69\upsilon+90\upsilon^2) - 672\upsilon\lambda^3(1+3\upsilon) + 4464\upsilon^2\lambda^4] - 72\lambda^2 e^{-1/\lambda}[7 - 2\upsilon + \upsilon^2 + 2\lambda(5-68\upsilon+15\upsilon^2) + 4\lambda^2(7-69\upsilon+180\upsilon^2) - 672\upsilon\lambda^3(1-3\upsilon) + 4464\upsilon^2\lambda^4] \quad (16)$$

and

$$A = 12\lambda e^{-1/\lambda}(6\upsilon\lambda - 1)/(1 - e^{-1/\lambda}) \quad (17)$$

The value of υ corresponding to the skewed velocity profile present in ThFFF can be approximated by[32]

$$\upsilon = \frac{h_1}{6\sum_{i=1}^{5}\frac{h_i}{(i+1)}} - 1 \quad (18)$$

Substitution of eqn. 15 into eqn. 14 yields

$$H_N = \frac{2F\lambda^2 w^2 \langle v \rangle}{RD(1 - e^{-1/\lambda})} \quad (19)$$

Previous studies[29,32] confirm that column dispersion in ThFFF is dominated by non-equilibrium dispersion which is accurately defined by eqns. 14–19. When characterizing narrow polymer samples, H_N can be simply subtracted from the overall plate height, and polydispersity information calculated from eqn. 11. In the separation of polydisperse samples, however, column dispersion cannot be accounted for by a single value of H_C because H_C varies with retention volume. To account for column dispersion in the separation of polydisperse samples, the following column dispersion function was derived[32]:

$$G(V,V_r) = \frac{V^0}{2wV_r}\left(\frac{D_T(1 - e^{-1/\lambda})\Delta T}{\lambda\pi F V_r \langle v \rangle B w}\right)^{\frac{1}{2}} \times \exp\left[\frac{-(V - V_r)^2 D_T (V^0)^2 (1 - e^{-1/\lambda})\Delta T}{4\lambda F V_r^3 \langle v \rangle B w^3}\right] \quad (20)$$

Here B is the channel breadth and V is the volume of carrier liquid eluting through the channel. Eqn. 20 defines the volume-based response of non-equilibrium dispersion as a function of retention volume V_r. By deconvoluting this function from a ThFFF fractogram[32], the "ideal" elution profile is obtained. Here "ideal" refers to the elution profile that would be obtained if all dispersion in the channel were molecular-weight selective, directly reflecting the MWD.

Most polymer samples have relatively broad MWDs. The development of deconvolution methods for removing column dispersion was motivated by the goal of shortening the time required to analyze broad polymers without losing accuracy in the resulting MWD. Temperature programming, discussed in detail below, is another way to achieve this goal. By decreasing the temperature throughout the run, analysis time is

reduced without introducing column dispersion associated with increasing the carrier-liquid flow-rate.

METHODOLOGY

Instrumentation

The experimental apparatus for ThFFF is similar to that for high-performance liquid chromatography (HPLC) except for the channel itself. Equipment consists of a pump to drive the carrier liquid, the separation channel, and a detector and chart recorder to monitor the column eluent. Samples are injected with a microsyringe or injection valve. A computer can be used for data analysis and to control operating conditions, such as the temperature gradient across the channel.

The basic design of the ThFFF channel is illustrated in Fig. 4. It consists of two copper or copper alloy bars with highly polished chrome-plated faces. The bars are clamped together over a Mylar® spacer that has been cut out to form the channel. The thickness of the channel is typically 2–10 mils (51–127 μm). Thinner channels result in less column dispersion and higher speeds of analysis, while thicker channels can accommodate greater sample loads. Holes are drilled in each bar, at opposite ends, to from the inlet and outlet for the channel. The bars are sandwiched between boards of insulating material and the whole assembly is clamped together between aluminum plates.

The top bar is heated with electrical cartridge heaters; heat is removed from the bottom bar by circulating coolant through holes that run the length of the bar. Crude temperature control ($\pm$ 2°C) of the hot bar can be achieved by controlling the power to the heaters with a voltage control device. More precise control ($\pm$0.1°C) is possible by cycling the heaters on and off using computer-controlled relay switches. The cold-wall temperature is controlled by adjusting the flow of coolant through the bottom bar. The temperature difference established between the bars is generally from 5 to 80°C, with higher values applicable to lower molecular weight polymers.

Like HPLC, ThFFF is commonly used in connection with a concentration-sensitive detector, such as a refractometer or UV photometer. These can be paired with other detectors to provide additional information on polymers. For example, a continuous viscosity detector and refractometer have been coupled to provide information on the inherent viscosity distribution of polymers[35]. This characterization

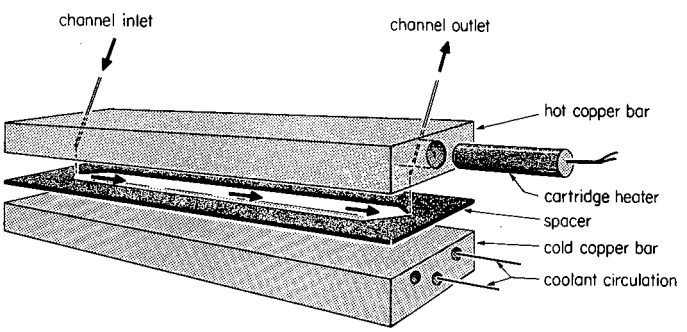

Fig. 4. Basic design of ThFFF channel.

property is often more directly relevant to end use than are MWD data. The use of a light-scattering photometer as a ThFFF detector has also been studied[36].

Sample loading

Transport coefficients vary with polymer concentration. Since these changes affect the retention ratio, it is important to use a range of polymer concentrations when measuring retention-derived parameters (such as D). Values are then extrapolated to zero concentration for accurate definition. The effect of polymer concentration on transport coefficients is particularly strong near the critical concentration, where polymer solutions undergo an abrupt transition from "dilute" to "semidilute" behavior[37]. When the polymer zone in the ThFFF channel is near the critical concentration, overloading effects are observed[38]. Sample overloading in ThFFF generally is accompanied by peak "fronting" and a shift toward higher retention volumes. Excessive overloading gives rise to additional peaks at higher retention volumes, probably due to polymer aggregation. Whenever overloading is suspected the sample should be run at more than one concentration, and the individual fractograms should be examined for consistency in retention volume and peak shape.

The mass of polymer that can be injected without overloading increases with the solvating power of the carrier liquid and with the thickness of the channel; the maximum amount is also inversely proportional to the molecular weight and sample concentration. Thus when overloading is a concern, it is better to inject a large volume at low concentration than to inject a small volume at high concentration[38].

Signal enhancement using splitters

The analysis of high-molecular-weight polymers ($> 1 \cdot 10^6$), requires the use of dilute solutions (< 1 mg/ml) to prevent overloading. If the MWD is broad, the required concentration may be too dilute to be detected because the eluting zone is spread over a wide range in retention volume. To overcome this problem, the concentration of the sample in the detector can be increased with the use of a stream splitter[39]. A stream splitter divides the carrier flowstream at the outlet end of the channel such that the concentrated sample layer near the accumulation wall is split away from the bulk of the carrier stream. The concentrated sample stream is routed to the detector for a greatly enhanced signal.

Temperature programming

Selectivity S_M is relatively constant for $R > 0.3$, but decreases rapidly[40] as R approaches 1. To optimize the resolution of all components in a polymer sample, the field strength must be sufficient to retain each component for at least three channel volumes. When separating polymer samples that span a broad molecular weight range, the field strength required to sufficiently retain the lowest-molecular-weight component may lead to excessive retention times of higher-molecular-weight species. Therefore, it is prudent to program the temperature gradient, beginning at a high value and decreasing continuously during the run. The initial high-temperature gradient optimally resolves the low-molecular-weight components; as the gradient drops to lower values the high-molecular-weight components are resolved.

A variety of mathematical functions have been used to program a decreasing temperature gradient. In the first report of temperature programming[41], Giddings *et*

al. used a time-delay parabolic decay function to separate nine polymers ranging in molecular weight from 4000 to $7.1 \cdot 10^6$. The use of a linear function was also reported in this work. An exponential decay function developed by Kirkland and co-workers[42,43] produces a linear calibration plot of log M *vs.* retention time. More recently, Giddings *et al.*[44] have reported the development of a power function for programming temperature gradients in ThFFF.

In power programming the field strength S_T is changed with time t according to the function

$$S_T = S_T^0 \left(\frac{t_1 - t_a}{t - t_a} \right)^p \tag{21}$$

where S_T^0 is the initial field strength, t_a is an arbitrary time constant, t_1 is the predecay time between the start of the run and the beginning of decay, and p is the decay power. These parameters are subject to the constraints $t \geqslant t_1 > t_a$ and $p > 0$. When $p = 2$ and $t_a = -2t_1$, the fractionating power (defined as the resolution of two components divided by their relative difference in molecular weight) is nearly independent of molecular weight. A constant fractionating power is desirable when highly polydisperse samples are characterized. Fig. 5 illustrates the use of power programming to separate 7 polymers ranging in molecular weight from 9000 to $5.5 \cdot 10^6$.

OPTIMIZATION

The greatest accuracy in measurements of MWDs can be obtained by maximizing the ratio P of the polydispersity plate-height contribution to the non-equilibrium contribution. Parameter P is equivalent to the square of the resolution between molecular-weight components located at $\pm$ 2 standard deviations from the mean of the MWD. Using eqns. 11 and 14, P can be written in the following form

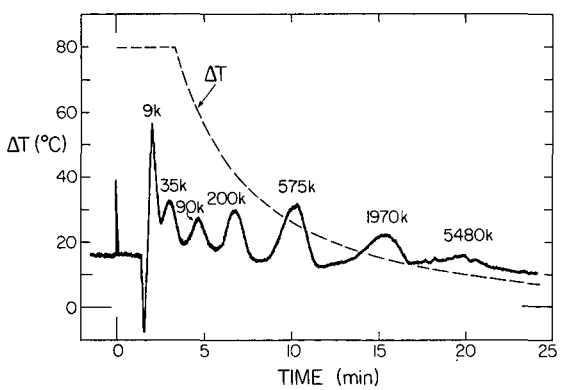

Fig. 5. Separation of 7 polymers of indicated molecular weights (in thousands, k) by power-programmed ThFFF (reprinted from ref. 44 courtesy of ACS Publications).

$$P = \frac{H_P}{H_N} = \frac{LS_M^2 (\mu - 1)}{\chi w^2 \langle v \rangle / D} \tag{22}$$

If χ is approximated[34] as $24\lambda^3$, and λ by $R/6$ (ref. 45), then

$$P = \frac{9LS_M^2 (\mu - 1)D}{w^2 R^3 \langle v \rangle} \tag{23}$$

Parameter P increases with the ratio $L/\langle v \rangle$. Although channel length L (typically about 50 cm) is fixed, flow-rates can be reduced to increase the accuracy of MWDs or the resolution between components. However, this has the simultaneous effect of increasing run time. Thus, a trade-off exists between accuracy or resolution, and speed. This situation is illustrated in Fig. 6, where the resolution between two components from five- and one-minute separations (in the same channel) is compared[46]. The former shows superior resolution but takes longer. The reduced resolution of the latter results from the proportionality of H_N to the mean carrier-liquid velocity $\langle v \rangle$.

Eqn. 23 shows that retention ratio R and channel thickness w are the most effective optimization parameters. For highest resolution, channel thickness should be minimized while the temperature gradient is maximized to reduce R. The cost of using thinner channels is reduced sample capacity. Lower R values increase run time, and temperature programming is used to optimize this trade-off. In characterizing industrial polymers, temperature programming is often essential to achieving accurate MWDs in a reasonable time.

APPLICATIONS

ThFFF has been applied to a wide variety of lipophilic polymers, including polystyrene[1–7,29,32–35,41–46], poly(methyl methacrylate)[3,47,48], polyisoprene[3,47,48], poly(tetrahydrofuran)[47], polypropylene[49], polyethylene[49] and nitrocellulose[50]. Al-

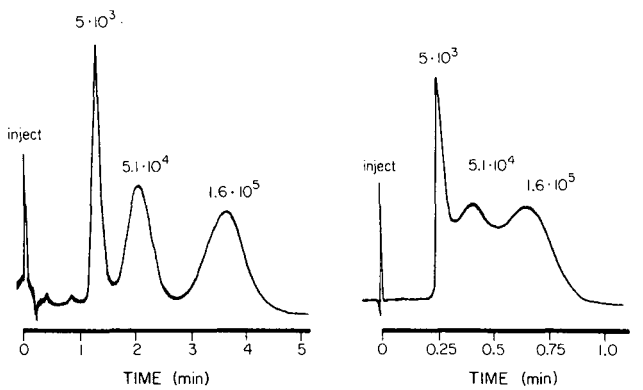

Fig. 6. Illustration of trade-off between resolution and speed in the separation of a three-component mixture of polystyrenes by ThFFF. Experimental conditions: $\Delta T = 60°C$, $w = 51$ μm, and $\langle v \rangle = 0.56$ cm/s (left) or 3.05 cm/s (right) (reprinted from ref. 20 courtesy of Pergamon Press).

though thermal diffusion is generally weak in aqueous systems[33,45,51], some non-ionic materials such as poly(ethylene oxide), poly(vinyl pyrrolidone) and poly(ethylene glycol) are sufficiently retained in water to permit characterization[52]. The advantages of ThFFF are particularly suited to the analysis of very-high-molecular-weight polymers, copolymers and polymers that interact with surfaces. Polymers needing corrosive solvents or high temperatures for solvation, and narrow-MWD polymers that require an accurate determination of polydispersity are also well handled by ThFFF. With the introduction of an instrument into the commercial marketplace, ThFFF is now being used for routine polymer analysis in several laboratories.

Polymer characterizations

ThFFF currently relies on a calibration curve to relate molecular weight to retention volume. When the temperature gradient is held constant, calibration curves take the following form

$$\log V_r = S_M \log M \tag{24}$$

where S_M is the selectivity defined by eqn. 12. ThFFF is more accurate than SEC for measuring MWDs because selectivity in ThFFF is higher (typical S_M values are in the range 0.5–0.6) and column dispersion is well-defined. The high degree of accuracy of ThFFF has been clearly demonstrated in its application to polymer standards[29,32].

When characterizing narrow polymer fractions, polydispersity is obtained from H_P using eqn. 11. Accurate values of H_P are obtained by subtracting H_N from the plate height of the elution profile, provided H_r is negligible. To obtain H_N from eqn. 19, the diffusion coefficient of the polymer fraction and several carrier-liquid parameters are required. If these values are unavailable, H_P can be determined by plotting plate height *versus* flow velocity. If H_r is negligible, a linear plot will be obtained with H_P as the intercept. Fig. 7 shows such a plot for a narrow polystyrene standard[29]. On the right-hand side of this plot, the ordinate is expressed in terms of $\mu - 1$, illustrating that any μ value significantly above 1.01 can be unambiguously ruled out. This is much smaller than the ceiling value of 1.06 determined by the supplier using SEC. The plot in Fig. 7 has a high degree of linearity and the slope is within 3% of its theoretical value, suggesting that the value $\mu = 1.003$ is reasonably accurate.

With broad MWDs, column dispersion is negligible when low flow-rates are used. If column dispersion is significant, it can be removed by deconvolution to obtain the "ideal" elution profile. To obtain the MWD $m(M)$, the fractogram or "ideal" elution profile is transformed using the following equation[53]

$$m(M) = c(V_r) \frac{dV_r(M)}{dM} \tag{25}$$

where $c(V_r)$ is the detector trace of the mass-based concentration c (if a mass-sensitive detector is used); the scale factor $[dV_r(M)/dM]$ is related to the selectivity by

$$\frac{dV_r}{dM} = \frac{V_r}{M} S_M \tag{26}$$

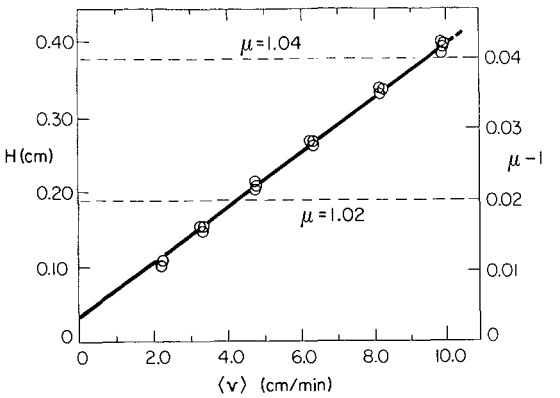

Fig. 7. Plot of plate height *vs.* flow velocity for a $1.7 \cdot 10^5$ MW polystyrene sample illustrating polydispersity value $\mu = 1.003$ (reprinted from ref. 20 courtesy of Pergamon Press).

Thermal diffusion studies

Separation in ThFFF is governed by differences in the ordinary and thermal diffusion coefficients of polymer components. Although the underlying physicochemical parameters important to ordinary diffusion are well understood, those governing the thermal diffusion of polymers in solution are less clear. By increasing our understanding of thermal diffusion, and its dependence on polymer properties, we gain access to more information on polymers through ThFFF. Theories on the thermal diffusion of polymers in solution vary widely in conceptual basis and often predict contradictory results; experimental data lack consistency and wide applicability, partly due to the difficulty of conventional methodology. Fortunately, ThFFF is capable of producing accurate values of thermal diffusion parameters in polymer solutions, making it the best technique for the systematic study of thermal diffusion and thus of its own foundations.

In the first of a three-part study of thermal diffusion in polymer solutions, the ThFFF retention of a variety of linear and branched polystyrenes was examined with ethylbenzene as the carrier liquid[2]. A linear dependence of retention parameter λ on diffusion coefficient D was found, as illustrated in Fig. 8. According to eqn. 1, the slope of this plot is $(wD_T\ dT/dx)^{-1}$. Since w and dT/dx were identical for all runs, the constant slope demonstrates that D_T is independent of both polymer size and branching configuration.

Next, D_T values were obtaned for 17 polymer–solvent systems[3,54]. The results were used to search for correlations between D_T and physiochemical parameters of the polymer and carrier liquid. D_T was found to be inversely proportional to the viscosity and solvating power of the carrier liquid. These correlations have been supported in similar studies by Kirkland *et al.*[55]. D_T was also found to increase with polymer density and with the thermal conductivity difference of the polymer and carrier liquid. D_T also correlates inversely with the activation energy of the solvent viscous flow[3].

In the third part of the study[4], the thermal diffusion of several copolymers in toluene was characterized. For random copolymers, D_T values apparently assume the weighted average of the corresponding homopolymer values, where the weighting

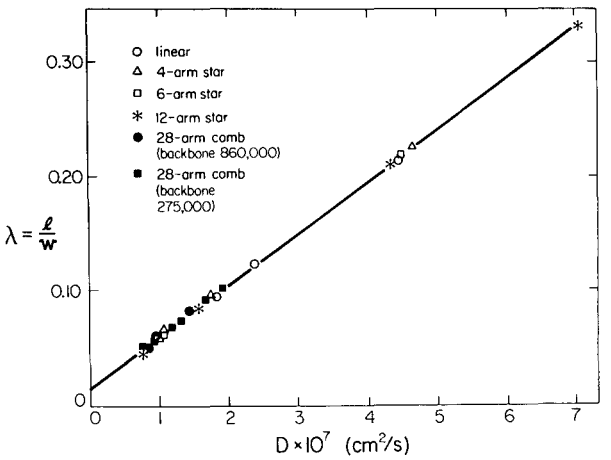

Fig. 8. Illustration of linear dependence of λ on diffusion coefficient D (reprinted from ref. 2 courtesy of ACS Publications).

factors are the mole-fractions of each monomer type in the copolymer. For block copolymers subject to radial segregation of their monomers, thermal diffusion appears to be dominated by monomers located in the outer (free-draining) regions of the solvated polymer molecule.

TRENDS

Interest in ThFFF has surged in recent years with the need for new techniques to better characterize an expanding variety of polymeric materials. Since the introduction of a commercial instrument, the application of ThFFF to routine polymer analysis is growing. As awareness of its unique features continue to increase, ThFFF will be applied with increasing frequency to polymers that are difficult to characterize accurately by traditional methods.

More work is needed to clarify the utility of ThFFF in characterizing copolymers. The studies referenced above suggest that the analysis of random copolymers is straightforward. However, additional work must be done to confirm these indications. The retention of block copolymers in ThFFF appears more complex; fundamental studies of copolymer retention continue.

The time required to resolve two polymer components by ThFFF continues to decrease. This is primarily the result of using thinner channels, although for broad MWDs, temperature programming has also contributed significantly to this trend. According to eqn. 23, for each two-fold reduction in channel thickness, the carrier velocity can be increased by a factor of four without losing resolution. Channels designed for high flow velocity are currently made with a thickness of 76 μm, but thinner channels will become routine as channel surfaces are made smoother by improved techniques[56]. Channel thickness will ultimately be limited by detector sensitivity since thinner channels require lower sample concentrations to avoid overloading.

SYMBOLS

a	coefficient of fluidity dependence on temperature
A	term defined by eqn. 17
b	term defined by eqn. 7
B	channel breadth
c	concentration
D	diffusion coefficient
D_T	thermal diffusion coefficient
F	term defined by eqn. 16
G	non-equilibrium dispersion function
h	term defined by eqn. 5
H	plate height
H_C	column dispersion contribution to plate height
H_D	longitudinal diffusion contribution to plate height
H_{EC}	extra-column volume contribution to plate height
H_N	non-equilibrium contribution to plate height
H_P	polydispersity contribution to plate height
H_R	relaxation contribution to plate height
K	carrier-liquid thermal conductivity
K_C	carrier-liquid thermal conductivity at the cold-wall temperature
l	altitude of the center of gravity of the analyte zone above the accumulation wall
L	channel length
$m(M)$	molecular weight distribution
M	molecular weight
p	power programming decay power
P	optimization ratio H_P/H_N
R	retention ratio V^0/V_r
S	term defined by eqn. 8
S_M	mass-based selectivity
S_T	field strength
S_T^0	initial field strength in temperature programming
t	time
t_1	predecay-time constant in power programming
t_a	decay-time constant in power programming
T	temperature
T_C	cold-wall temperature
v	velocity profile term defined by eqn. 18
$\langle v \rangle$	average velocity of the carrier liquid in the channel
V	elution volume
V^0	void volume of the channel
V_r	retention volume
w	channel thickness
x	altitude above the accumulation (cold) wall
ΔT	temperature drop across the channel
η	viscosity

θ term defined by eqn. 6
λ retention parameter l/w
μ polydispersity
χ non-equilibrium coefficient

REFERENCES

1 G. H. Thompson, M. N. Myers and J. C. Giddings, *Sep. Sci. Technol.*, 2 (1967) 797–800.
2 M. E. Schimpf and J. C. Giddings, *Macromolecules*, 20 (1987) 1561–1563.
3 M. E. Schimpf and J. C. Giddings, *J. Polym. Sci., Polym. Phys. Ed.*, 27 (1989) 1317–1332.
4 M. E. Schimpf and J. C. Giddings, *J. Polymer Sci., Polym. Phys. Ed.*, in press.
5 J. C. Giddings, L. K. Smith and M. N. Myers, *Anal. Chem.*, 47 (1975) 2389–2394.
6 Y. S. Gao, K. D. Caldwell, M. N. Myers and J. C. Giddings, *Macromolecules*, 18 (1985) 1272–1277.
7 J. C. Giddings, L. K. Smith and M. N. Myers, *Anal. Chem.*, 48 (1976) 1587–1592.
8 J. C. Giddings, S. R. Fisher and M. N. Myers, *Am. Lab. (Fairfield, Conn.)*, 10 (1978) 15–31.
9 J. C. Giddings, M. N. Myers, K. D. Caldwell and S. R. Fisher, in D. Glick (Editor) *Methods of Biochemical Analysis*, Vol. 26, Wiley, New York, 1980, pp. 79–136.
10 E. N. Lightfoot, A. S. Chiang and P. T. Noble, *Annu. Rev. Fluid Mech.*, 13 (1981) 351.
11 J. C. Giddings, *Anal. Chem.*, 53 (1981) 1170A–1175A.
12 J. C. Giddings, M. N. Myers and K. D. Caldwell, *Sep. Sci. Technol.*, 16 (1981) 549–575.
13 J. C. Giddings, K. A. Graff, K. D. Caldwell and M. N. Myers, in C. D. Craver (Editor), *Advances in Chemistry Series*, No. 203, American Chemical Society, Washington, DC, 1983, Ch. 14, pp. 257–269.
14 T. Hoshino, *Bunseki*, 12 (1985) 856–864.
15 J. Janca, *Chem. Listy*, 81 (1987) 1034–1057.
16 J. C. Giddings, *Chem. Eng. News*, 66 (1988) 34–48.
17 K.-G. Wahlund, *Eur. Chrom. News*, 2 (1988) 12–15.
18 K. D. Caldwell, *Anal. Chem.*, 60 (1988) 959A–971A.
19 J. C. Giddings, *J. Chromatogr.*, 470 (1989) 327–335.
20 J. J. Gunderson and J. C. Giddings, in C. Booth and C. Price (Editors), *Comprehensive Polymer Science, Vol. I, Polymer Characterization*, Pergamon, Oxford, 1989, pp. 279–291.
21 M. Martin and P. Reynaud, *Anal. Chem.*, 52 (1980) 2293.
22 J. C. Giddings, *J. Chem. Phys.*, 49 (1968) 81–85.
23 M. Martin and J. C. Giddings, *J. Phys. Chem.*, 85 (1981) 727–733.
24 J. C. Giddings, M. R. Schure, M. N. Myers and G. R. Velez, *Anal. Chem.*, 56 (1984) 2099–2104.
25 J. M. Davis and J. Calvin Giddings, *Sep. Sci. Technol.*, 20 (1985) 699–724.
26 J. C. Giddngs, *Anal. Chem.*, 58 (1986) 735–740.
27 M. Martin and A. Jaulmes, *Sep. Sci. Technol.*, 16 (1981) 691.
28 J. J. Gunderson, K. D. Caldwell and J. C. Giddings, *Sep. Sci. Technol.*, 19 (1984) 667–683.
29 M. E. Schimpf, M. N. Myers and J. C. Giddings, *J. Appl. Polym. Sci.*, 33 (1987) 117–135.
30 L. K. Smith, M. N. Myers and J. C. Giddings, *Anal. Chem.*, 49 (1977) 1750–1756.
31 M. Martin, M. N. Myers and J. C. Giddings, *J. Liq. Chromatogr.*, 2 (1979) 147–164.
32 M. E. Schimpf, P. S. Williams and J. C. Giddings, *J. Appl. Polym. Sci.*, 37 (1989) 2059–2076.
33 M. E. Hovingh, G. E. Thompson and J. C. Giddings, *Anal. Chem.*, 42 (1970) 195–203.
34 J. C. Giddings, Y. H. Yoon, K. D. Caldwell, M. N. Myers and M. E. Hovingh, *Sep. Sci. Technol.*, 10 (1975) 447–460.
35 J. J. Kirkland, S. W. Rementer and W. W. Yau, *J. Appl. Polym. Sci.*, 38 (1989) 1383–1395.
36 M. Martin, *Chromatographia*, 15 (1982) 426–432.
37 P. G. DeGennes, *Macromolecules*, 9 (1976) 594.
38 K. D. Caldwell, S. L. Brimhall, Y. Gao and J. C. Giddings, *J. Appl. Polym. Sci.*, 36 (1988) 703–719.
39 J. C. Giddings, H. C. Lin, K. D. Caldwell and M. N. Myers, *Sep. Sci. Technol.*, 18 (1983) 293–306.
40 J. J. Gunderson and J. C. Giddings, *Anal. Chim. Acta*, 189 (1986) 1–15.
41 J. C. Giddings, L. K. Smith and M. N. Myers, *Anal. Chem.*, 48 (1976) 1587–1592.
42 J. J. Kirkland and W. W. Yau, *Macromolecules*, 18 (1985) 2305–2311.
43 J. J. Kirkland, S. W. Rementer and W. W. Yau, *Anal. Chem.*, 60 (1988) 610–616.
44 J. C. Giddings, V. Kumar, P. S. Williams and M. N. Myers, in C. D. Craver and T. Provder (Editors), *Polymer Characterization by Interdisciplinary Methods*, American Chemical Society, Washington, DC, in press.

45 M. N. Myers, K. D. Caldwell and J. C. Giddings, *Sep. Sci. Technol.*, 9 (1974) 47–70.
46 J. C. Giddings, M. Martin and M. N. Myers, *J. Chromatogr.*, 158 (1978) 419–435.
47 J. C. Giddings, M. N. Myers and J. Janca *J. Chromatogr.*, 186 (1979) 37–44.
48 J. J. Gunderson and J. C. Giddings, *Macromolecules*, 19 (1986) 2618–2621.
49 S. L. Brimhall, M. N. Myers, K. D. Caldwell and J. C. Giddings, *Sep. Sci. Technol.*, 16 (1981) 671–689.
50 M. E. Schimpf, S. L. Brimhall and J. C. Giddings, *Thermal Field-Flow Fractionation of Nitrocellulose*, Report to USAAMCCOM - LCWSL, University of Utah, Salt Lake City, UT, October 25, 1985.
51 F. J. Bonner, *Chem. Scr.*, 3 (1973) 149.
52 J. J. Kirkland and W. W. Yau, *J. Chromatogr.*, 353 (1986) 95–107.
53 J. C. Giddings, M. N. Myers, F. J. F. Yang and L. K. Smith, in M. Kerker (Editor), *Mass Analysis of Particles and Macromolecules by Field-Flow Fractionation, Colloid and Interface Science*, Vol. IV, Academic Press, New York, 1976, pp. 381–398.
54 M. E. Schimpf and J. C. Giddings, presented at the *192nd National ACS Meeting, Anaheim, CA, September 1986.*
55 J. J. Kirkland, L. S. Boone and W. W. Yau, presented at *1st International Symposium on Field-Flow Fractionation, Park City, UT, June 15, 1989.*
56 J. C. Giddings, K. D. Caldwell and L. F. Kesner, in A. R. Cooper (Editor), *Molecular Weight Determination (Chemical Analysis Series,* Vol. 103), Wiley-Interscience, New York, 1989, Ch. 12.

Journal of Chromatography, 517 (1990) 423–433
Elsevier Science Publishers B.V., Amsterdam

CHROMSYMP. 1949

Evaluation of pinched inlet channel for stopless flow injection in steric field-flow fractionation

MYEONG HEE MOON, MARCUS N. MYERS* and J. CALVIN GIDDINGS
Field-Flow Fractionation Research Center, Department of Chemistry, University of Utah, Salt Lake City, UT 84112 (U.S.A.)

ABSTRACT

In this article the concept of utilizing a pinched inlet channel for field-flow fractionation (FFF), in which the channel thickness is reduced over a substantial inlet segment to reduce relaxation effects and avoid stopflow, is evaluated for steric FFF using one conventional channel and two pinched inlet channels. It is shown that with the proper adjustment of flow-rate, the stopflow process in FFF can be completely avoided, thus bypassing the flow interruption associated with stopflow and reducing separation time. The maximum flow-rate that can be used for stopless flow operation without incurring zone distortion is shown to agree reasonably well with simple theory; slight departures from theory are attributed to the existence of reduced transport rates of large particles through thin channel structures.

INTRODUCTION

In a previous paper it was suggested that the relaxation process in field-flow fractionation (FFF) can be hastened by reducing the thickness of the FFF channel at the inlet end[1]. The use of such a modified channel structure, designated by the term "pinched inlet channel", has the potential of reducing separation time in FFF, reducing the adhesion of sample material to the channel walls and, in some instances, simplifying the FFF procedure. The object of this work is to achieve the first implementation of pinched inlet FFF. The system chosen for this study is a steric FFF channel utilizing a gravitational driving force.

FFF is generally carried out by using a stopflow procedure[2]. Here, following sample introduction, the channel flow is stopped for a time of sufficient duration to permit the sample material, under the influence of the driving force, to accumulate in the vicinity of one of the channel walls. After accumulation, the flow is restarted and the separation process is carried out. The purpose of the stopflow procedure is to reduce the band broadening associated with the accumulation or "relaxation" process[2]. However, the stopflow procedure has two or three negative side-effects. First, stopflow lengthens the time required for completion of the run, sometimes by

0021-9673/90/$03.50

a substantial amount[3]. Second, stopflow requires the interruption of flow, which is not only experimentally awkward but is capable of causing baseline perturbations due to the pressure transients associated with the flow changes. Third, the static conditions encountered in stopflow are conducive to the adhesion of sample particles to the channel wall, which may cause sample loss. For all these reasons it would be desirable to eliminate the stopflow procedure providing excessive band broadening could somehow be avoided.

By reducing the channel thickness at the inlet end, the relaxation time, equal to the time required for a given component to be transported across the thickness of the channel, is reduced. Therefore the stopflow time t_{sf} can be correspondingly decreased. Even if the channel flow is maintained and stopflow avoided, the incremental band broadening associated with relaxation in such a system is greatly reduced relative to its magnitude in conventional FFF channels of uniform thickness. Specifically, theory indicates that the increment in the variance in elution time of a component carried at a given flow-rate in an FFF channel increases with the fourth power of channel thickness w providing the relaxation process is confined to a segment of constant thickness[1]. In order to take full advantage of this strong dependence on w, it is necessary to reduce the channel thickness at the inlet end. Moreover, in order to realize full relaxation within the confines of this pinched inlet or relaxation segment without stopping the flow, the pinched segment must extend a substantial distance into the channel. It is very likely that pinched inlet segments that occupy approximately 50% of the channel length will prove highly practical in the implementation of the pinched inlet concept. In the present study, 40% of the channel length is utilized for the relaxation segment.

While the pinched inlet concept will be most ideally realized by using a constant and uninterrupted flow throughout the FFF process, there will be occasions in which the relaxation time is so large that full relaxation cannot be achieved in the pinched inlet section at normal channel flow-rates. In that instance, the channel flow-rate can be reduced to a value that will allow for the full relaxation of the slowest component in the pinched sector. Following the relaxation of all components, normal flow is resumed. With this *slow flow injection* procedure, there is still an abrupt flow change (although the magnitude of the change is reduced), but one would still have the advantage of a reduced analysis time associated with the reduced relaxation time. Alternatively, one could revert to the normal stopflow procedure while using a pinched inlet, again realizing the advantage of a reduced relaxation time and faster analysis.

The pinched inlet concept appears to be applicable to all of the normal operating modes of FFF, including sedimentation FFF, thermal FFF, flow FFF, and electrical FFF[1]. It would appear to be particularly advantageous for programmed field operation. It should also be applicable to the characterization of larger particles ($\geqslant 1$ μm diameter) by steric FFF. The simplicity of a steric FFF channel system designed to utilize the earth's gravity as a driving force is an important factor in choosing steric FFF for the initial evaluation of the pinched inlet concept.

THEORETICAL

The essential equations governing the behavior of a pinched inlet system used in the steric FFF mode are summarized below. We start with the central parameter, the relaxation time τ, given by the following expression

$$\tau = \frac{w}{U} \tag{1}$$

where w is the channel thickness and U is the field-induced velocity of the particle driven across the channel. Because of the finite relaxation time, the particle band broadens out into a bimodal distribution along the flow coordinate[4]. The distance h_0 between band extremities is given by

$$h_0 = \frac{\dot{V}}{bU} \tag{2}$$

where $\dot{V}$ is the volumetric flow-rate through the channel and b is the channel breadth. We note that this expression for band width is independent of channel thickness w.

Because of relaxational band broadening represented by h_0, the peak emerging from the FFF system is incrementally broadened in time units. The time-based variance of the peak induced by relaxation is given by[1]

$$\sigma_t^2 = \frac{17}{140}\frac{\tau^2}{R^2} \tag{3}$$

where R is the retention ratio of the particle band in the pinched segment of the channel. With the help of eqn. 1 this expression assumes the form

$$\sigma_t^2 = \frac{17}{140}\frac{w^2}{U^2R^2} \tag{4}$$

This equation is generally valid for most operating forms of FFF. For steric FFF, we substitute the applicable expression for R (ref. 5)

$$R = \frac{3\gamma d}{w} \tag{5}$$

which converts eqn. 4 into the previously derived expression for steric FFF[1]

$$\sigma_t^2 = 0.0135\frac{w^4}{\gamma^2 d^2 U^2} \tag{6}$$

Under the influence of a sedimentation field of acceleration G, the settling velocity for a particle obeying Stokes equation is given by[6]

$$U = \frac{d^2 \Delta\rho G}{18\eta} \tag{7}$$

where $\Delta\rho$ is the density difference between the particle and the liquid carrier and η is the viscosity. With the help of this expression, eqns. 1, 2 and 6 become

$$\tau = \frac{18\eta w}{d^2 \Delta\rho G} \tag{8}$$

$$h_0 = \frac{18\eta \dot{V}}{d^2 \Delta\rho G b} \tag{9}$$

$$\sigma_t^2 = \frac{4.37\, w^4 \eta^2}{\gamma^2 d^6 \Delta\rho^2 G^2} \tag{10}$$

The last equation shows that the time-based variance originating in relaxation is proportional to the fourth power of channel thickness w and inversely proportional to the sixth power of particle diameter d. We note that these dependencies are slightly modified by the correction term γ, which will exhibit a slight dependence on both w and d (ref. 5).

Plate height

The apparent (or measured) plate height in a chromatographic or FFF elution system is given by

$$\hat{H} = L\frac{\sigma_t^2}{t_R^2} \tag{11}$$

where σ_t^2 is the observed variance in time units, t_R is the retention time, and L is the length of the column or channel.

For a segmented system such as the pinched inlet channel, the apparent plate height is related to the plate heights (H_1 and H_2) of the two segments by[7]

$$\hat{H} = \frac{\dfrac{H_1 L_1}{R_1^2 < v_1 >^2 L} + \dfrac{H_2 L_2}{R_2^2 < v_2 >^2 L}}{\left[\dfrac{L_1}{R_1 < v_1 > L} + \dfrac{L_2}{R_2 < v_2 > L}\right]^2} \tag{12}$$

where the lengths, retention ratios, and mean cross-sectional velocities in the two successive segments are L_1 and L_2, R_1 and R_2, and $< v_1 >$ and $< v_2 >$, respectively. If the mean velocity ($R_1 < v_1 >$) of the particle band in segment 1 (the pinched segment) is M times larger than its velocity ($R_2 < v_2 >$) in segment 2, eqn. 12 becomes[7]

$$\hat{H} = \frac{H_1 \dfrac{L_1}{L} + M^2 H_2 \dfrac{L_2}{L}}{\left(\dfrac{L_1}{L} + M\dfrac{L_2}{L}\right)^2} \tag{13}$$

For both channels used here, $L_1/L = 0.4$ and $L_2/L = 0.6$. With these values $\hat{H}$ reduces to

$$\hat{H} = \frac{0.4H_1 + 0.6M^2H_2}{(0.4 + 0.6M)^2} \tag{14}$$

Because $<v>$ and R (see eqn. 5) are both inversely proportional to channel thickness w (a conclusion valid for normal as well as steric FFF), M can be written as

$$M = \frac{R_1\langle v_1\rangle}{R_2\langle v_2\rangle} = \left(\frac{w_2}{w_1}\right)^2 \tag{15}$$

Thus for channel I, for which $M = 4$, $\hat{H}$ is

$$\hat{H} = 0.0510H_1 + 1.2245H_2 \tag{16}$$

For channel II, for which $M = 100/9$, we get

$$\hat{H} = 0.0080H_1 + 1.4833H_2 \tag{17}$$

These equations show (by way of specific examples) that excessive band broadening (large H_1) due to relaxation effects is largely cancelled out by the small weighting factors associated with the rapid transit through the constricted relaxation segment. Furthermore, it can be shown that H_1 due to relaxation approaches a maximum of 0.1214 L_1 for particles whose relaxation distance $h_0 \rightarrow L_1$. (The justification for the weighting factor for H_2 exceeding unity can be found in ref. 7.)

Plate height H_1 consists of contributions both from relaxation (which becomes the dominant term when h_0 is a significant fraction of L_1) and from normal band broadening processes. To a first approximation, H_1 can be expressed as the sum of the two contributions

$$H_1 = H_1(\text{relaxation}) + H_1(\text{stop flow}) \tag{18}$$

where H_1(relaxation) is based on the variance obtained from eqns. 3, 4, 6, or 10 and H_1(stop flow) is the plate height observed under stopflow conditions in which band broadening due to relaxation is eliminated.

EXPERIMENTAL

For the purposes of comparison two channel geometries were used, one with and one without the pinched inlet configuration. The channel volumes were cut out of thin plastic spacers and sandwiched between glass plates, then clamped together between Lucite bars. This general structure, described in an earlier publication[8], has been found suitable for steric FFF using gravity as the driving force.

A Teflon spacer of 254 μm thickness was used for the uniform channel (lacking a pinched inlet). The channel, cut from the spacer, has a tip-to-tip length L of 38.4 cm and a breadth b of 2 cm. The void volume, measured as the elution volume of an unretained sodium benzoate peak, is 1.84 ml.

Two pinched inlet channels were constructed. Both utilized two sheets of Mylar

in their construction, one with the full channel length removed and the other cut in such a way that a "blocking element" was left in place. The blocking element is a strip of material that occupies the inlet end of the channel in order to reduce its thickness and thus realize the pinched inlet geometry[1]. The construction of the systems is illustrated in Fig. 1. The combined thickness of the two films is 254 μm in both cases, the same as the thickness of the uniform channel. For pinched inlet channel I, the two thicknesses are both 127 μm. For channel II, the film with the blocking element is 178 μm thick and the film from which the pinched inlet is cut is 76 μm thick. The length (38.4 cm) and breadth (2 cm) of the pinched inlet channel systems are identical to those used for the uniform channel. The length L_1 of the blocking element, measured from the channel tip to the blocking edge, is 15.4 cm in both cases, 40% of the total length. The void volumes, also measured with a non-retained peak, are 1.52 ml for channel I and 1.41 ml for channel II.

The samples used in this study were polystyrene latex beads (Duke Scientific, Palo Alto, CA, U.S.A.) with mean diameters of 15 and 20 μm. The carrier liquid was doubly distilled water with 0.01% FL-70 detergent (Fisher Scientific, Fairlawn, NJ, U.S.A.) and 0.02% sodium azide used as a bacteriocide. All runs were carried out at room temperature, 293 $\pm$ 1 K. From 15 to 20 μl of the sample suspension (containing $2 \cdot 10^4$–$3 \cdot 10^4$ particles) was injected into the channel through a septum by means of a microsyringe.

For the stopflow method the sample was slowly carried to the head of the channel with a Gilson (Madison, WI, U.S.A.) Minipuls 2 pump. The flow was then completely stopped for a period adequate to allow the particles to relax to the accumulation wall. The relaxation time was calculated from the Stokes–Einstein equation. Following relaxation, flow was resumed.

In the case of stopless flow injection, the sample was introduced by syringe directly into the carrier stream. The flow of the latter was held constant, without change or interruption.

The eluted sample was monitored by a Model 106 UV detector, from Linear

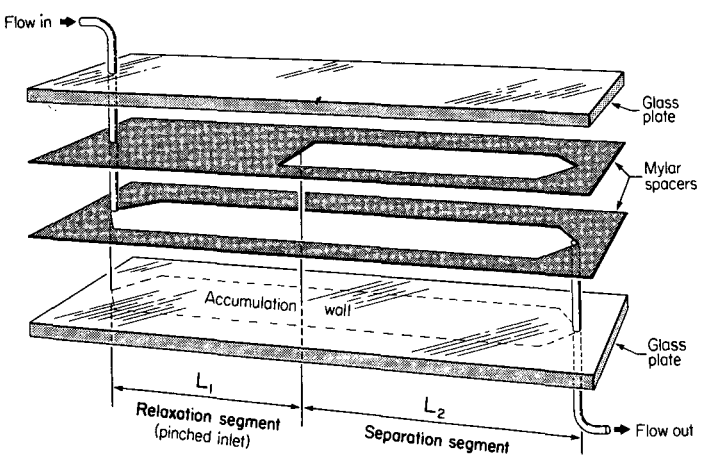

Fig. 1. Layers assembled to form pinched channel system.

Instrument (Reno, NV, U.S.A.) at a wavelength of 229 nm. A strip chart recorder from Houston Instrument (Austin, TX, U.S.A.) was used to record the emerging peaks.

RESULTS AND DISCUSSION

Fig. 2 shows three different elution profiles for the 15-μm polystyrene latex spheres run at the same flow-rate, 0.73 ml/min, equivalent to a linear flow velocity of 0.24 cm/s in the separation segment of the channel where the channel thickness (254 μm) is greatest. Fig. 2a shows the concentration profile of the particles emerging from the reference (uniform or non-pinched) channel after application of the stopflow procedure. For this case the stopflow time was 42 s, equal to the calculated relaxation time of the particles across the full channel thickness (254 μm). Fig. 2b shows the results of a run identical in all respects to that of Fig. 2a except that the stopless flow procedure was used to bypass the flow interruption of stopflow. The emerging peak in this case shows a substantial loss of sharpness as expected for stopless flow operation. (For smaller particles with longer relaxation times than that of the 15-μm particle, the stopless flow profile would be much broader and would have a bimodal shape.) We also observe that the trailing edge of the peaks in Fig. 2a and b nearly coincide in their positions; the leading edge of the Fig. 2b profile, however, appears considerably earlier than that for the Fig. 2a peak as a consequence of the accelerated elution of those particles starting the run near the top wall of the channel where relaxation effects are maximal.

Fig. 2c shows the profile of the 15-μm beads emerging from pinched inlet channel system I after stopless flow injection. We observe that the excessive band broadening illustrated by Fig. 2b has been eliminated through the use of the pinched inlet channel. The band width is comparable to that in Fig. 2a for normal stopflow operation. More

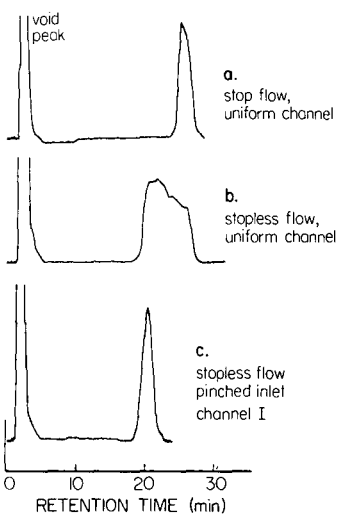

Fig. 2. Elution profiles for 15-μm latex particles at a flow-rate of 0.73 ml/min. Runs a and b are made in the conventional channel of uniform thickness with and without stopflow, respectively. Run c was also executed without stopflow, but in this case with pinched inlet channel system I.

specifically, the standard deviation σ_t in time units for the three profiles are 52, 141, and 46 s for Fig. 2a, b and c, respectively. The corresponding plate heights are 0.43, 3.7, and 0.52 mm, respectively.

We note that to fully utilize the capabilities of the pinched inlet channel system, the flow-rate must be matched to the dimensions of the pinched inlet segment in order to assure complete relaxation of all components before they enter the second stage, the separation segment. The flow-rate used in conjunction with Fig. 2 accordingly yields an h_0/L value of 0.26, well below the maximum allowable value of 0.4, equal to the ratio of the length of the pinched segment to the total channel length.

Figs. 3 and 4 further illustrate the need to match the operating flow-rate to the dimensions of the pinched (relaxation) segment and the consequences of failing to adhere to the required relationship. These figures show the elution profiles of the two particle diameters in systems I and II expressed along the elution volume axis. In "normal" (non-steric) FFF operation, the peaks observed at different flow-rates would be expected to center about the same mean elution volume position, differing only in peak width. The figures show that other factors are involved in the present study.

Fig. 3a shows the elution profiles of a 15-μm latex particle eluted from system I under different flow conditions. The different flow velocities lead to different values of the ratio h_0/L; values of the latter are shown in the figure. The peak furthest right, for which $h_0/L = 0.21$, has been eluted with the lowest flow-rate, 0.58 ml/min. The peaks are displaced to the left as the flow-rate increases in the sequence 1.12, 1.34, and 1.79 ml/min, respectively. The two peaks with the greatest displacement to the left are

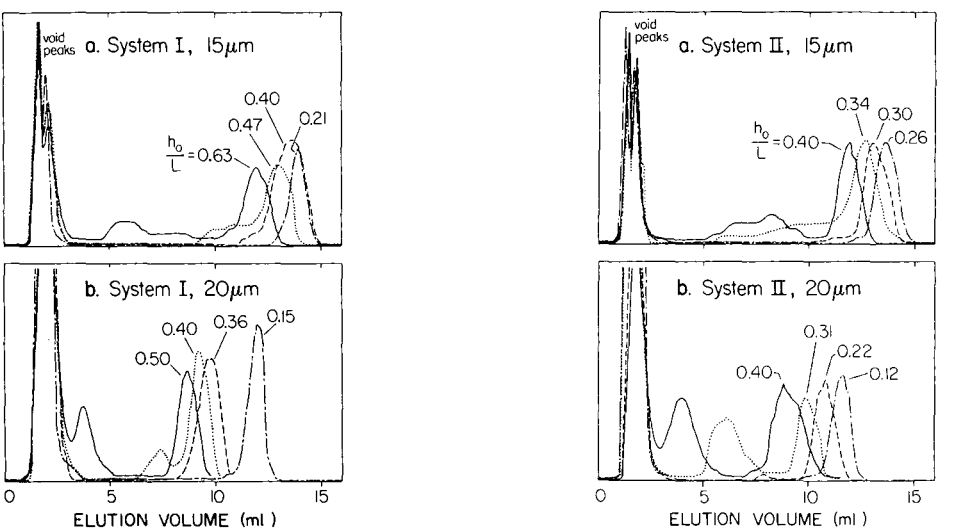

Fig. 3. Comparison of elution profiles at different flow-rates for 15-μm and 20-μm microspheres in pinched inlet system I. Values of the ratio h_0/L are shown. The flow-rates from left to right are 1.79, 1.34, 1.12, and 0.58 ml/min for panel a and 2.50, 1.98, 1.79, and 0.76 ml/min for panel b.

Fig. 4. Elution profiles of 15-μm and 20-μm latex particles at different flow-rates in system II. The flow-rates from left to right are 1.12, 0.94, 0.85, and 0.73 ml/min for panel a and 2.01, 1.55, 1.10, and 0.91 for panel b.

further distorted by satellite peaks or bumps preceding the main peak. These spurious peaks represent the early elution of a portion of the injected sample that has not been fully relaxed. Such distortions are expected when h_0/L exceeds the critical value 0.4. As seen in the figure, the critical h_0/L ratio is greater than 0.4 for both of the distorted peaks; in the worst case this ratio is 0.63 and the corresponding peak is associated with a prominent early satellite peak.

While the appearance of satellite peaks is associated with the failure to achieve complete relaxation, some other mechanism must be sought to explain the shift in the position of the main peak with changes in flow-rate. While not expected in the normal operating mode of FFF, such shifts are common in steric FFF[9] and reflect the increasing influence of lift forces with increasing flow-rate.

Fig. 3b, involving 20-μm particles in system I, shows much the same effect. In this case, too, the leading satellite peaks are associated with the larger h_0/L values. However, we note that a small satellite peak is still found when h_0/L reaches its threshold value of 0.40. This may be due to the fact that the actual relaxation of particles in a confined channel, particularly when they are very near the channel walls, is somewhat slower than that calculated from the Stokes equation which serves as the basis for eqn. 7. Thus relaxation times, particularly for larger particles, may be somewhat longer than calculated, giving h_0/L values somewhat greater than the ideally calculated values shown in the figure. In accordance with this hypothesis, the satellite peak has disappeared by the time h_0/L has dropped only slightly to 0.36.

Similar results are shown in Fig. 4 for system II, in which the relaxation segment is even thinner, 76 μm in place of 127 μm. While the same overall effects are apparent in the two figures, the satellite peaks have become more prominent in Fig. 4. Thus in Fig. 4a, a significant satellite bump is still present for the case in which h_0/L has dropped to 0.34, well below the threshold. Only when this ratio drops to 0.30 does the satellite profile become largely eliminated. This heightened departure from ideal relaxation in Fig. 4 is again consistent with the hypothesis that an anomaly arises due to the decreased transport rate and increased relaxation time expected for large particles in thin channels. Since the thickness of the relaxation segment has dropped from 127 to 76 μm in going from Fig. 3 to Fig. 4, the increasing departure from ideal relaxation is expected. This conclusion is further reinforced by Fig. 4b, showing runs with 20-μm instead of 15-μm particles. Here, a major satellite is still found with $h_0/L = 0.31$, but has disappeared by the time this ratio reaches 0.22.

In general, the departure from the ideally calculated h_0/L value will increase with the ratio of the particle diameter to the thickness of the relaxation segment. Fig. 4b has the largest ratio and, correspondingly, the largest departure. For particles of submicron size separated by the normal operating mode of FFF, the departure should be negligible for almost any practical thickness of the relaxation segment. We note that the anomaly unique to the relatively large particles subject to analysis by steric FFF can be neutralized by dropping to slightly lower flow-rates than those calculated on the basis of eqn. 9 subject to the condition $h_0 \leqslant L_1$.

We note that lift forces, as such, should not lead to anomalous satellite peaks. With strong lift forces, the particles will not settle to a position where they make contact with the accumulation wall. Instead, the particles will be pushed by lift forces away from the wall, where they will form a thin band or hyperlayer. Upon passage from the relaxation to the separation segment, the equilibrium hyperlayer position

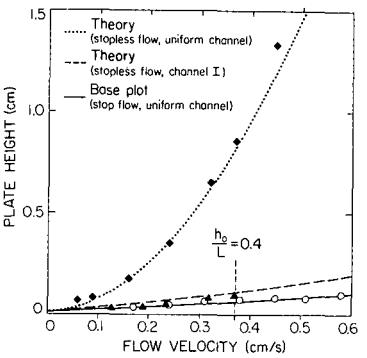

Fig. 5. Observed plate height *versus* mean flow velocity plots contrasting performance of pinched inlet channel I and uniform channel under stopless flow conditions. Experimental data: (◆) stopless flow, uniform channel; (▲) stopless flow, channel I; (○) stopflow, uniform channel.

may change significantly relative to the various streamplanes in the channel. However, as long as all particles emerge from the relaxation segment in a thin band, the transition should lead to little additional dispersion no matter what the relative positions of the bands in the two segments are. Thus, in general, the object of the relaxation segment is to rapidly gather component particles into a thin lamina whose position can lie anywhere between the channel walls.

The efficacy of the pinched inlet structure is further illustrated in the plate height *versus* velocity plots of Fig. 5, obtained for the 15-μm latex. The lower plot is based on measured values (open circles) of plate height ($\hat{H}$ based on eqn. 11) obtained for the uniform (non-pinched) channel structure under the stopflow conditions. The plot immediately above applies to pinched inlet channel I operated under stopless flow conditions. The experimental points (solid triangles) do not lie significantly higher than those of the lower plot, despite the stopless flow operation. The dashed line, calculated from eqn. 18 [where the lower plot is taken as the base plot corresponding to H_1 (stopflow)], verifies that there is little increase in the plate height when the pinched inlet configuration is used for stopless flow. However, stopless flow operation with the uniform channel displays a dramatic rise in plate height as illustrated by the experimental points (solid diamonds) and theoretical curve (dotted line) of the upper plot. These plots clearly illustrate the potential usefulness of the pinched inlet configuration for a stopless flow operation in FFF.

ACKNOWLEDGEMENT

This work was supported by Grant GM10851-33 from the National Institutes of Health.

REFERENCES

1 J. C. Giddings, *Sep. Sci. Technol.*, 24 (1989) 755.
2 F. J. Yang, M. N. Myers and J. C. Giddings, *Anal. Chem.*, 49 (1977) 659.
3 J. C. Giddings, *Anal. Chem.*, 57 (1985) 945.
4 M. E. Hovingh, G. H. Thompson and J. C. Giddings, *Anal. Chem.*, 42 (1970) 195.

5 R. E. Peterson II, M. N. Myers and J. C. Giddings, *Sep. Sci. Technol.*, 19 (1984) 307.
6 C. A. Price, *Centrifugation in Density Gradient*, Academic Press, New York, 1982.
7 J. C. Giddings, *Anal. Chem.*, 35 (1963) 353.
8 J. C. Giddings, M. N. Myers, K. D. Caldwell and S. R. Fisher, in D. Glick (Editor), *Methods of Biochemical Analysis*, Vol. 26, Wiley, New York, 1980, p. 79.
9 T. Koch and J. C. Giddings, *Anal. Chem.*, 58 (1986) 994.

Journal of Chromatography, 517 (1990) 435–447
Elsevier Science Publishers B.V., Amsterdam

CHROMSYMP. 1979

Use of field-flow fractionation to study pollutant–colloid interactions

RONALD BECKETT*, DEIRDRE M. HOTCHIN and BARRY T. HART
Water Studies Centre, Monash University, Caulfield East, Victoria (Australia)

ABSTRACT

A new approach has been developed utilizing field-flow fractionation (FFF) methods to determine adsorption density distributions across the size spectrum of a particulate sample. The approach has been tested using sedimentation FFF to separate colloidal matter, concentrated from river water, to which radiolabelled pollutants (orthophosphate, glyphosate, atrazine) have been adsorbed. It is expected that the methodology will be expanded to cover the broad size range from 1 nm to 100 μm by using a number of FFF subtechniques (including sedimentation FFF): the use of various sensitive analytical methods will extend the range of adsorbates that can be studied. This provides a powerful new method for studying the pollutant–particle interactions occurring in environmental samples, as well as other similar systems.

INTRODUCTION

The association of pollutants and other trace elements and compounds with particle surfaces plays a dominant role in determining their transport, fate, biogeochemistry, bioavailability and toxicity in natural waters, sediments and soils[1,2]. An example that has received much attention over a number of years is the adsorption of various pollutants (*e.g.* trace metals, nutrients and toxic organics) to suspended particulate matter in river water[3]; such interactions affect the transportation and eventual deposition of these pollutants in bottom sediments. The pollutants may then concentrate at certain locations, such as in reservoirs and estuaries, with important ecological and even human health implications. Another example, is the role of soil and rock in adsorbing materials such as fertilizers, pesticides and radionuclides, which influences their bioavailability to plants and pests and their transport through soils and groundwater aquifers[4].

Despite the general awareness of the importance of both particulate[5] and colloidal[6] matter in pollutant transport, most work has been confined to the study of particulate matter–pollutant interactions. Even this work is dominated by the study of model surfaces such as clays and iron, aluminium and manganese oxides rather than the more complex natural samples. This lack of study of the interactions between

0021-9673/90/$03.50

pollutants with natural colloidal matter is understandable given the difficulties in separating colloidal matter from the aqueous solution. Here we use a fairly general, but somewhat arbitrary, definition for particulate matter as material greater than 1 μm in size and colloidal matter as material in the range 0.001–1 μm. The colloidal fraction will therefore include very small particles and macromolecules, and in most studies will be included as part of the "filterable" or "dissolved" fraction[7].

Thus, in the many studies undertaken to measure the uptake of a pollutant by natural waters where the solid phase is separated from the liquid phase by either filtration or centrifugation, the interactions between colloidal matter and the pollutant will not have been measured accurately. In particular, those cases where significant colloidal matter–pollutant interaction occurs, the proportion of the pollutant associated with surfaces will be seriously underestimated. This may have significant implications regarding predictions of the toxicity, since surface-bound pollutants are generally found to be less toxic than uncomplexed pollutants.

It is well known that particle size has a major influence on the properties of sedimentary material and their associated pollutants[8]. It directly affects the specific surface area, settling rates, resuspension and the mechanism and extent of aggregation in natural water, as well as the ability of colloidal matter to permeate through soils and rock.

The adsorption of pollutants to sediments depends on the specific surface area and the nature of the particle surface. Although the sediment mineralogy is of some importance, particularly in the case of clay minerals and Fe and Mn oxides, we contend that the ubiquitous coatings of these oxides and organic matter, which is invariably present on the surface of natural particles[9], may well be the dominant factor in determining the surface adsorption density (*i.e.* amount adsorbed per unit area). Evidence exists suggesting that in a given sediment sample different mineral and organic phases may be concentrated in different size ranges[10].

Although there are many useful techniques available for particle size determination and fractionation all suffer from quite serious limitations making this a difficult area of scientific endeavour. The limitations include; the limited size range covered, inaccuracies in the theory, lack of resolution, and inability to fractionate as well as size the sample. These deficiencies in the commonly used separation methods have hindered attempts to gather information on the distribution of mineral phases and pollutant species within a sediment sample.

The development of a range of field-flow fractionation (FFF) techniques[11] over recent years now provides new experimental methods for separating particulate, colloidal and macromolecular (*e.g.* humic matter) materials from natural waters. These techniques show much promise in eliminating or at least reducing most of the short comings noted above[12]. Sedimentation FFF has been successfully applied to the separation and characterisation of colloidal matter from natural waters[13]. Additionally, flow FFF has been utilised for the characterisation of macromolecules[14], humic matter[15,16] and smaller colloidal particles[17].

With the advent of these new FFF techniques, there now exists the possibility that uptake studies can be undertaken using real water samples, with the final mixture separated using the appropriate FFF technique. One problem that still exists is that, with a few exceptions, the FFF techniques available can only process very small quantities of sample. Thus extremely sensitive analytical methods are required to

detect the often small amounts of pollutant associated with the colloidal or macromolecular matter. One such technique involves the use of radiolabelled pollutants.

In this paper we report some preliminary results of work undertaken to study the interaction of the nutrient orthophosphate (^{32}P labelled) and the herbicides glyphosate and atrazine (both ^{14}C labelled) with natural colloidal matter, in which sedimentation FFF was used as the separation technique. This work illustrates a very promising approach that will make it possible to obtain detailed information on the distribution of pollutants in natural sediment and soil samples.

THEORY

Sedimentation FFF

The mechanism and theory of FFF has been detailed fully elsewhere[11,18–20]. The general retention equation relates the conventional retention ratio R, defined by

$$R = \frac{V^0}{V_r} = \frac{t^0}{t_r} \tag{1}$$

to a retention parameter λ as follows[21]

$$R = 6\lambda\left(\coth\frac{1}{2\lambda} - 2\lambda\right) \tag{2}$$

where V^0 and V_r are the carrier volumes required to elute unretained or retained samples respectively through the FFF channel; t^0 and t_r are the corresponding void time and retained sample elution time, assuming the carrier flow-rate is constant.

In this work a simplified approximate expression was usually used for the retention ratio[22]

$$R = 6\lambda(1 - 2\lambda) \tag{3}$$

In the case of sedimentation FFF the retention parameter for sample particles of equivalent spherical diameter d and density ρ is given by[23]

$$\lambda = \frac{6kT}{\pi\omega^2 rw(\rho - \rho_s)d^3} \tag{4}$$

where k = Boltzmann's constant
T = absolute temperature
ω = centrifuge angular velocity
r = centrifuge radius
w = channel thickness
ρ_s = carrier density

Thus for constant field sedimentation FFF experiments, the diameter of particles eluting at a given V_r can be calculated by combining eqn. 2 or 3 with eqn. 4.

For samples with a broad size distribution such as the suspended particulate matter used in this study it is almost mandatory to use some form of field decay during the run[24]. Since in programmed field runs a given sample component will experience a decreasing field strength during its elution, the value of λ will also decrease. This is accounted for by applying the general expression in eqn. 5 (assuming the carrier flow-rate is constant)[25] to obtain specific equations for a given program form.

$$t^0 = \int_0^{t_r} R \, dt \tag{5}$$

In previous work on river-borne colloids we used a time delayed exponential decay field program[13]. However, in the work presented here a time delayed power program[26] was used, where the centrifugal field [$G_{(t)} = \omega^2 r$] takes the form

$$G_{(t)} = G_0 \left(\frac{t_1 - t_a}{t - t_a} \right)^8 \tag{6}$$

where G_0 = the initial field, t_1 = the constant field period before decay begins, t_a = a constant with the restriction that $t \geqslant t_1 > t_a$.

The advantage of this field program is that by choosing suitable parameters for G_0, t_1, and t_a, it can be made to yield a fairly constant resolving power or fractionating power[27] over the size range of interest[26].

The elution time (or volume) for a particular component can be used to calculate the particle diameter as follows: (1) for $t \leqslant t_1$: the eqns. 1, 3 and 4, which are applicable for constant field conditions, were used; (2) for $t_r > t_1$: in all runs t_a was set to $-8t_1$, hence the simplified equation

$$\lambda_r = \frac{3t^0}{2(t_r - t_a)} \tag{7}$$

can be used to calculate the retention parameter of the particles, λ_r, at their time of elution (see eqn. 41 of ref. 26). Application of eqn. 6 above to evaluate the field strength at elution and then eqn. 4 yields the value of d.

Fractograms

The fractogram is a plot of the particular detector response *versus* volume or time. The ordinate should be a measure of the amount of sample (or sample component) per unit volume, *i.e.* dm/dV. The most common method for monitoring the concentration of particles eluting from a sedimentation FFF channel is a conventional liquid chromatography UV light detector most often operated at a wavelength of 254 nm. This measures the attenuation of light in a small cell volume which, for particle sizes the same order of magnitude as the wavelength of the light, will be primarily caused by a scattering mechanism rather than absorption. As dictated by the quite complex Mie theory[37] of light scattering, the relationship between solution turbidity and particle mass concentration will be size dependent, with a sample of

larger particles expected to yield a higher absorbance than the same mass concentration of smaller particles. We have not attempted to correct for this complication in the work reported here, but have simply assumed that absorbance is proportional to the mass concentration. Some evidence that this assumption may not cause excessive errors was obtained in previous work[13] in which a fractogram of a river water sample obtained using an evaporative light scattering mass detector was quite similar to that obtained with a UV detector at 254 nm.

The other approach used was to collect fractions of the eluent and chemically analyse for specific elements or compounds in the separated fractions. Very sensitive analytical techniques are required as the particle concentration in the eluent is very low. As we were interested in looking at pollutant adsorption characteristics of natural aquatic colloids, the most convenient method was to utilize radioisotope labelled compounds in the uptake experiments. Since unadsorbed material will elute with the void peak, any measured radioactivity in the post void volume carrier will represent material associated with particles. Thus the fractogram for monitoring the adsorbed component is simply a plot of the measured counts per minute (cpm) in a ml of eluent solution plotted against the elution volume.

Particle size distributions

The particle size distribution should represent the amount of material in different size ranges and is usually in the form of a plot of dm/dd against d; where m is the mass of particles and d is the particle diameter. It is a relatively easy matter to convert the fractogram abcissa into a particle diameter scale using the equations above.

In order to obtain the correct ordinate for the size distribution $dm_{(i)}/dd_{(i)}$, we divide the volume-axis of the fractogram into a large number of increments of width $\delta V_{(i)}$ and use the expression

$$\frac{dm_{(i)}}{dd_{(i)}} \approx \frac{dm_{(i)}}{dV_{(i)}} \cdot \frac{\delta V_{(i)}}{\delta d_{(i)}} \tag{8}$$

where $dm_{(i)}/dV_{(i)}$ is the value of the fractogram ordinate at the midpoint of a given volume increment and $\delta d_{(i)}$ is the diameter increment corresponding to that same increment in V. In this way the corresponding fractogram can be converted into either a particle mass $[dm_{(i)}/dd_{(i)}]$ or adsorbate amount $[dm_{\mathrm{ads}(i)}/dd_{(i)}]$ based particle size distribution. Here $m_{(i)}$ is used to indicate the mass of sample particles eluted up to fraction i and $m_{\mathrm{ads}(i)}$ represents the mass of adsorbed material.

Adsorption density distribution

In the adsorbate based particle size distributions generated by the above method, the area under the curve between given values of d will represent the amount of pollutant adsorbed in that particular size range. This will depend on the surface area of particles in the size range as well as the relative adsorption intensity of the solid.

Since the mass of sample is represented by the UV detector response ordinate $[dm_{(i)}/dd_{(i)}]$ of the particle size distribution, dividing this into the adsorbate activity ordinate $[dm_{\mathrm{ads}(i)}/dd_{(i)}]$ yields a relative measure of the amount of adsorbate per mass of solid adsorbent. The same quantity is more directly obtained using the two fractogram ordinates; *i.e.*

$$\frac{dm_{ads(i)}}{dm_{(i)}} = \frac{dm_{ads(i)}/dV_{(i)}}{dm_{(i)}/dV_{(i)}} \tag{9}$$

Furthermore, if spherical particles are assumed the particle area $A_{(i)}$ is given by $6\delta m_{(i)}/d_{(i)}\rho$. Thus, by affecting a change of variable to eqn. 9 and assuming a sample with constant density, we can compute the adsorption density [amount adsorbed per unit particle surface area (A)] for each increment by

$$\frac{dm_{ads(i)}}{dA_{(i)}} = \frac{dm_{ads(i)}/dV_{(i)}}{dm_{(i)}/dV_{(i)}} \cdot d_{(i)} \tag{10}$$

Note that $dm_{ads(i)}/dA_{(i)}$ is expressed in arbitrary units as the absolute value of $dm_{(i)}/dV_{(i)}$ is not known with the UV detector response being used as a measure of this quantity and the term $\rho/6$ is assumed to be constant across the size distribution and is thus omitted from eqn. 10. The adsorption density distribution is a plot of $dm_{ads(i)}/dA_{(i)}$ *versus* $d_{(i)}$.

EXPERIMENTAL

Sample collection

Suspended particulate matter from two Australian rivers was studied. Water from the Darling River was sampled near its confluence with the Murray River in NSW, and the Yarra River was sampled at Dights Falls in Melbourne. These river systems were chosen because of their high suspended solids load (Darling River: 254 mg/l; Yarra River: *ca.* 70 mg/l) at the time of sampling[28].

Darling River water was fractionated and concentrated about one hundred-fold using a continuous flow centrifuge and tangential flow filtration. A nominal particle size cutoff of approximately 1 μm is expected for the continuous flow centrifuge[5] (centrifuge speed: 8200 rpm giving 5260 g; assumed particle density: 2.5 g/ml). With the tangential flow filtration apparatus, a nominal particle size cutoff of 0.2 μm was obtained using Millipore polysulphone membrane filters[28,29].

The water from the Yarra River was concentrated about one hundred-fold by a coagulation and settling procedure[13]. The raw sample was initially passed through a Whatman GF/C glass fibre filter to remove particles of size greater than about 1 μm. $CaCl_2$ solution was added to the water sample in sufficient quantity to give a final concentration of 0.03 M. The mixture was stirred for 1 h and allowed to settle for 24 h. The supernatant was removed and the aggregate added to a small amount of deionized water. This mixture was aggitated and allowed to settle. The clarified water was drawn off, and once again deionized water introduced. This washing procedure was repeated three times to remove excess $CaCl_2$.

River water concentrates were stored at 4°C and prior to use were subject to ultrasound to break up any aggregates present.

Adsorption procedure

^{32}P in its orthophosphate form was obtained from Australian Nuclear Science and Technology Organization (ANSTO). An aliquot of 0.3 ml of stock solution

containing 0.02 mg/ml H_3PO_4 was added to 1 ml of Darling or Yarra River colloid concentrate. The resultant activity was approximately 0.06 MBq.

^{14}C labelled glyphosate and atrazine were obtained from Amersham Australia. A small volume (0.01 ml) of the radiolabelled glyphosate solution (7.4 MBq/ml or 0.661 mg/ml) was added to 1 ml of Darling River colloid concentrate. Similarly, 0.02 ml of atrazine solution (3.7 MBq/ml or 0.862 mg/ml) was added to another 1 ml of Darling River colloid concentrate.

In each case an adsorption equilibration time of several hours was allowed before separation by sedimentation FFF was commenced.

Sedimentation FFF apparatus

The sedimentation FFF apparatus was essentially the same as described previously[13,18]. The FFF channel was made by clamping two concentric nickel-chromium rich alloy (Hastalloy C) rings with a 0.0254-cm thick mylar spacer (which had the channel shape cut out) sandwiched between them. The channel was 93.1 cm long (inlet to outlet) and 2.1 cm in breath. The channel void volume was 5.30 ml and detector dead volume was 0.54 ml. From these measurements, the channel thickness was calculated to be 0.0266 cm.

The channel was fitted inside a centrifuge basket so that its radius was 15.5 cm. O-ring seals at the ends of the axle allowed liquid to flow through the channel while the centrifuge rotated. The rotor was powered by a DC motor and speed controller, type DPM-613OE from the Bodine Electric Company. Rotation speed was computer controlled using hardware and software from FFFractionation, UT. The speed was measured by a photocell whose light path was interrupted as the rotor spun by a notched disc attached to the end of the centrifuge axle. This enabled the centrifuge speed to be kept constant or in the case of field programming, to be decayed during the run.

The carrier solution was pumped by a Gilson Minipuls 2 peristaltic pump and the outlet stream from the channel was passed through a Waters 441 UV detector operating at 254 nm. The detector signal was monitored on an Omniscribe chart recorder (Houston Instruments). A Gilson Microcol TDC80 fraction collector was used throughout these experiments.

FFF run parameters

An injection volume of 10 μl was introduced onto the channel through a septum. To relax the sample, an initial field of 1000 rpm was maintained for 20 min under stop-flow conditions. The channel flow was then started and the field decay program commenced according to the power program outlined in the theory section above, using the following parameters. The initial field of 1000 rpm was held for a time lag t_1 of 10 min. A decay parameter t_a of -80 min reduced the field to a hold value of 10 rpm at 205 min. It should be noted that the time required to reach the hold rpm was far in excess of that needed for the completion of these experiments.

An aqueous solution of 0.1% sodium dodecylsulphate and 0.02% sodium azide at a flow-rate of 2 ml/min was used as the carrier. Detector sensitivity ranged between 0.02 to 0.05 a.u.f.s. The chart recorder was maintained at 10 cm/h. Fractions were collected over 4 min intervals for the phosphate experiments and over 2.5 min intervals for the herbicide experiments.

Analysis of activity

Fractions collected during these experiments were further analyzed for β radiation activity using a scintillation counter (Packard tri-carb 300 CD). An aliquot of one ml of the fractions collected during the sedimentation FFF experiment was placed in a scintillation vial. Toluene based PPO–POPOP–teric X10 scintillation fluid (5 ml) was then added (PPO = 2,5-diphenyloxazole, POPOP = phenyloxazolylphenyloxazolylphenyl, teric X10 = a non-ionic surfactant from ICI, Australia). After aggitation each sample was measured for 10 min in the scintillation counter. The data collected was uncorrected for quenching.

RESULTS AND DISCUSSION

Fig. 1 shows the raw fractograms for the adsorption experiments performed in this work. The solid lines show the UV detector response, which were used as a measure of the mass concentration of particles being eluted, and the points show the concentration of adsorbed material as measured by the radioactivity (cpm/ml) of the suspension at various elution volumes. It should be noted that the elution time is proportional to the elution volume for constant flow-rate runs. The error bars on the points indicate the calculated counting statistic errors. Fig. 2 depicts the corresponding

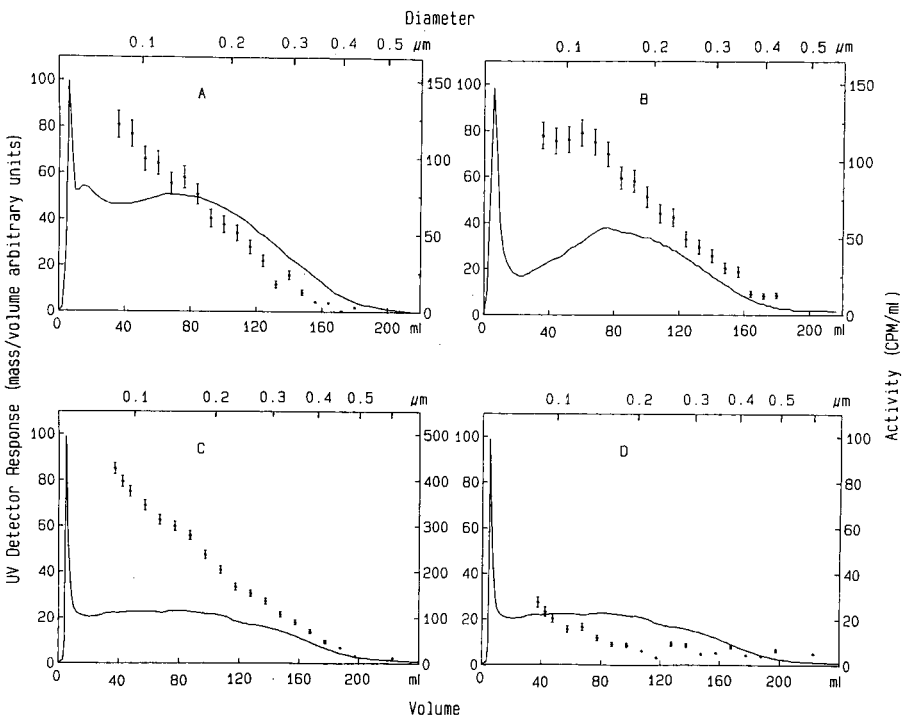

Fig. 1. Fractograms showing the sedimentation FFF separation of natural colloid samples with adsorbed radiolabelled pollutant: (A) orthophosphate onto Darling River colloid concentrate; (B) orthophosphate onto Yarra River colloid concentrate; (C) glyphosate onto Darling River colloid concentrate; (D) atrazine onto Darling River colloid concentrate. Solid lines give the UV detection response and points give the radioactivity (cpm/ml) in the effluent.

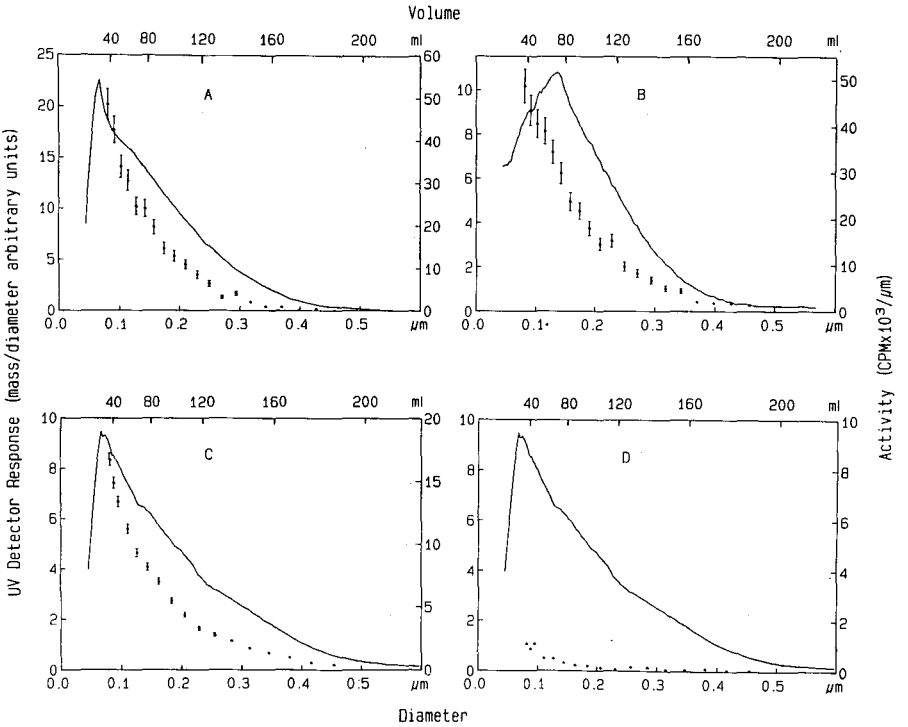

Fig. 2. Particle mass based and adsorbate based size distributions for the corresponding colloid samples and adsorbed radiolabelled pollutants given in Fig. 1A–D. Solid lines give the particle size distributions and points give the amount of pollutant adsorbed per unit mass of adsorbent (arbitrary units).

mass based (solid lines) and adsorbate based (points) particle size distributions calculated from the fractograms in Fig. 1 as outlined in the theory section. The mass based particle size distribution for the two samples (Darling and Yarra Rivers) show a broad size distribution between 0.05 and 0.5 μm. The upper limit is controlled by the continuous flow centrifuge conditions used to concentrate the samples from river water. The fact that particles less than the 0.2-μm filter cutoff are present is most likely due to partial blockage of the pores during filtration or perhaps variations in the particle density, from the value of 2.5 g/ml assumed, which would affect the calculated particle size. The data show that the Darling River sample contains a higher proportion of smaller particles than the Yarra River sample as evidenced by the maxima in the particle size distributions of approximately 0.08 μm and 0.14 μm, respectively. The Darling River samples are from the same stock except that the sample used in Fig. 1C and D are more dilute than for Fig. 1A.

Both the fractograms and adsorption distributions (points in Figs. 1 and 2) show that significant amounts of phosphate and glyphosate adsorbs to the particles, but very little of the less polar herbicide atrazine is adsorbed. This is consistent with the results from conventional adsorption isotherm experiments that have recently been conducted in our laboratory[30].

The adsorption distributions given in Fig. 2 show clearly the general trend often

observed for sediment samples, with the smaller particles containing the highest pollutant content. This is an important point for pollutant transport in aquatic systems, since these particles will usually remain in suspension until an aggregation process occurs to induce settling and deposition. The two reasons often advanced to explain this trend in pollutant sorption are the increase in specific surface area as particle size decreases and changes in the geochemistry of the particles with size. Organic matter and reactive hydrous iron and manganese oxides would be the most significant phases influencing pollutant sorption, since both are known to be strong scavengers of many pollutants.

The surface adsorption density distributions calculated for these experiments are given in Fig. 3. These plots show the amount of adsorbate per unit area of particle surface (arbitrary units) as a function of particle size, calculated as outlined in the theory section.

A model that explains many of the properties of natural particles is one in which all particles irrespective of their core mineralogy are assumed to be coated with a common layer of organic matter and perhaps iron and manganese hydrous oxides[8]. For example, this model explains the observation that (with few exceptions) all natural aquatic particles are negatively charged, and that within a given sample they have a very narrow range of electrophoretic mobilities[9]. Of relevance to the studies reported here, this model would predict that the adsorption density for a given pollutant–colloid system would be constant across the size range investigated. This was found to be the case for the adsorption of orthophosphate onto Darling River suspended particulate matter (Fig. 3A).

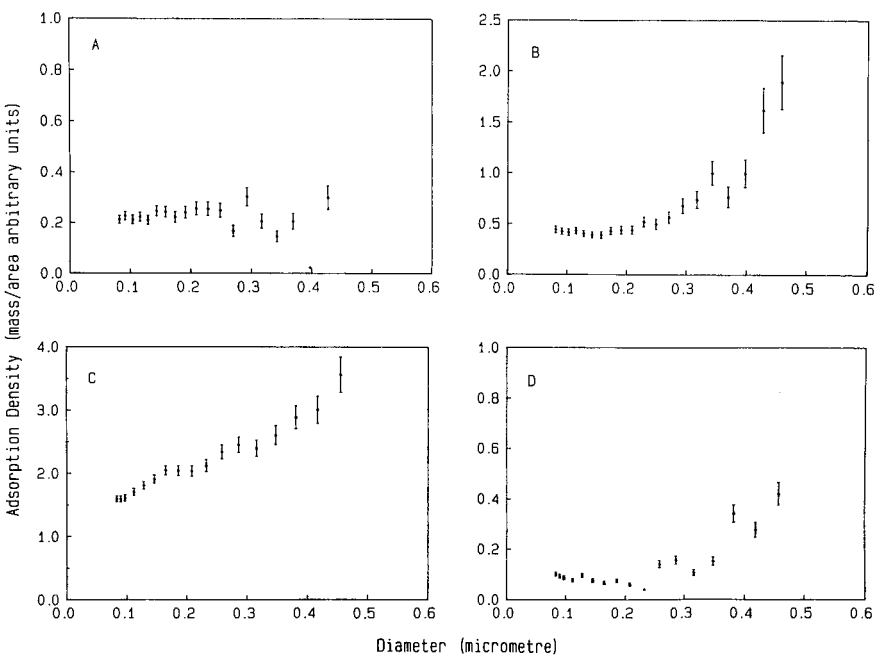

Fig. 3. Adsorption density distributions (amount adsorbed per unit area *versus* particle diameter) calculated using the data shown in Fig. 1.

However, in contrast to the orthophosphate Darling River experiment, the adsorption density distributions for the other systems showed a distinct increase towards the larger diameter end of the range (Fig. 3B–D). This is not an anomoly introduced by the use of the UV detector to monitor particle mass, since light scattering effects would in fact tend to down weight the large diameter end of the distribution. However, it is feasible that changes in shape factor could cause the specific surface area to be greater than expected for the larger particles as the calculations here are based on a constant spherical shape. Scanning electron micrographs of a limited number of Yarra River suspended particulate matter samples separated by sedimentation FFF did show higher proportions of clay-like plates in the 0.3–0.4 μm fraction[31]. However, the samples used in this series of experiments have not been examined by electron microscopy.

Perhaps the most likely explanation for the upwards trend in the adsorption density distributions is a change in mineralogy or coating density across the size range. We do not have information on this at present although two current collaborative projects, one with Dr. H. Taylor (US Geological Survey, Denver) using inductively coupled plasma–mass spectroscopy (ICP–MS) and the other with Dr. D. Chittleborough (Waite Agricultural Research Institute, University of Adelaide) using transmission electron microscopy and diffraction techniques, should provide some insights into this question.

One further point that should be noted is that the experiments performed in this study will only monitor adsorbate species which are strongly bound to the adsorbent surface. During the FFF separation processes, the colloid sample is continually washed with fresh carrier giving ample opportunity for desorption to occur. However, it is possible that equilibrium experiments could be performed by including a fixed concentration of the adsorbate in the carrier liquid. This approach would be feasible provided the experimental conditions are such that significant adsorption to the particles occurs causing the adsorbate concentration in the eluent to be elevated above the background carrier solution level, so that the changes can be detected.

The size range that can be conveniently covered using the sedimentation FFF instrument we are using (FFFractionation) is approximately 0.05–1 μm in diameter. Higher speed centrifuges (*e.g.* Dupont SF^3) may reduce the lower size limit to perhaps 0.01 μm. The methodology developed here could equally be applied to data produced from other high resolution separation techniques. For example, we have used flow FFF to determine molecular weight distributions of humic substances[15,16]. Considering the recent interest in the association of trace metals and toxic organic compounds with humic substances in natural waters[32,33] this should be a valuable tool for investigating the molecular size dependence of such association.

Although sedimentation FFF is capable of separating particles of diameter greater than 1 μm using the steric mode[34], this has lower resolution and theoretical exactness than the normal mode generally used for particles less than 1 μm in size. However, recent work reported from Giddings' laboratory in Utah[35,36] has shown excellent resolution and reproducibility for the larger particles (1–100 μm) using a new hyperlayer mode of FFF.

Thus, it is conceivable that a combination of these FFF techniques [hyperlayer FFF (1–100 μm); sedimentation FFF (0.05–1 μm); Flow FFF (0.001–0.05 μm)] could allow particles in the ranges between 1 μm to 100 μm to be separated, permitting the

complex relationship between size, geochemistry and pollutant binding in natural aquatic systems to be unravelled.

CONCLUSIONS

Previous work[13] has demonstrated that aquatic colloids can be separated with high resolution and sized using sedimentation FFF. In this study we have shown how adsorption experiments using radiolabelled compounds can be used to compute surface adsorption density distributions to yield hitherto unobtainable information about the adsorption of various pollutants to natural particles. The use of other sensitive analytical techniques such as ICP–mass spectrometry or electrochemical detectors should extend the range of adsorbates that can be studied. In this preliminary study we have demonstrated the general methodology using sedimentation FFF, however, the size range that can be covered should be able to be extended by the use of different FFF subtechniques or other high resolution separation methods.

ACKNOWLEDGEMENTS

This research was supported by a grant from the Australian Research Council. We wish to thank Professor Giddings for his continued help and encouragement in our efforts to establish an FFF research program.

REFERENCES

1 W. Stumm, *Water Sci. Technol.*, 14 (1982) 481.
2 B. T. Hart (Editor), *The Role of Particulate Matter in the Transport and Fate of Pollutants*, Water Studies Centre, Chisholm Institute of Technology, Melbourne, 1986.
3 B. T. Hart, *Hydrobiologia*, 91 (1982) 299.
4 R. P. Schwarzenbach and J. Westall, *Environ. Sci. Technol.*, 15 (1981) 1360.
5 P. Sinclair, R. Beckett and B. T. Hart, *Hydrobiologia*, 176/177 (1989) 239.
6 J. C. Means and R. Wijaratne, *Science (Washington, D.C.)*, 215 (1982) 968.
7 W. Salomons and U. Forstner, *Metals in the Hydrocycle*, Springer-Verlag, Berlin, 1984, p. 10.
8 R. Beckett, B. T. Hart (Editor), *The Role of Particulate Matter in the Transport and Fate of Pollutants*, Water Studies Centre, Chisholm Institute of Technology, Melbourne, 1986, p. 113.
9 R. Beckett and N. P. Le, *Colloids Surf.*, 44 (1990) 35.
10 R. J. Gibbs, *J. Sed. Petrology*, 47 (1977) 237.
11 J. C. Giddings, *Chem. Eng. News*, 66 (1988) 34.
12 R. Beckett, *Environ. Technol. Lett.*, 8 (1987) 339.
13 R. Beckett, G. Nicholson, B. T. Hart, M. Hansen and J. C. Giddings, *Water Res.*, 22 (1988) 1535.
14 K. G. Wahlund, H. S. Winegarner, K. D. Caldwell and J. C. Giddings, *Anal. Chem.*, 58 (1986) 735.
15 R. Beckett, Z. Jue and J. C. Giddings, *Environ. Sci. Technol.*, 21 (1987) 289.
16 R. Beckett, J. C. Bigelow, Z. Jue and J. C. Giddings, in I. H. Suffet and P. MacCarthy (Editors), *Aquatic Humic Substances (Advances in Chemistry Series*, Vol. 219) American Chemical Society, Washington, DC, 1989, p. 65.
17 J. C. Giddings, G. C. Lin and M. N. Myers, *J. Colloid Interface Sci.*, 65 (1978) 67.
18 J. C. Giddings, M. N. Myers, K. D. Caldwell and S. R. Fisher, in D. Glick (Editor), *Methods of Biochemical Analysis*, Vol. 26, Wiley, New York, 1980, p. 79.
19 J. C. Giddings, *Sep. Sci. Technol.*, 19 (1984) 831.
20 J. Janca, *Field-Flow Fractionation Analysis of Macromolecules and Particles (Chromatographic Science Series*, Vol. 39), Marcel Dekker, New York, 1988.
21 M. E. Hovingh, G. H. Thompson and J. C. Giddings, *Anal. Chem.*, 42 (1970) 195.
22 J. C. Giddings, *J. Chem. Educ.*, 50 (1973) 667.

23 J. C. Giddings, G. Karaiskakis, K. D. Caldwell and M. N. Myers, *J. Colloid Interface Sci.*, 92 (1983) 66.
24 J. C. Giddings and K. D. Caldwell, *Anal. Chem.*, 56 (1984) 2093.
25 F. J. Yang, M. N. Myers and J. C. Giddings, *Anal. Chem.*, 46 (1974) 1924.
26 P. S. Williams and J. C. Giddings, *Anal. Chem.*, 59 (1987) 2038.
27 J. C. Giddings, P. S. Williams and R. Beckett, *Anal. Chem.*, 59 (1987) 28.
28 G. B. Douglas, R. Beckett and B. T. Hart, *Hydrological Processes*, (1990) submitted.
29 A. J. Horowitz, *Environ. Sci. Technol.*, 20 (1986) 155.
30 G. M. Day, *M. App. Sci. Thesis*, Chisholm Institute of Technology, Melbourne, 1990.
31 G. J. Nicholson, *M. App. Sci. Thesis*, Chisholm Institute of Technology, Melbourne, 1987.
32 B. T. Hart, *Environ. Technol. Lett.*, 2 (1981) 95.
33 J. Buffle, *Complexation Reactions in Aquatic Systems*, Ellis Horwood, Chichester, 1988.
34 T. Koch and J. C. Giddings, *Anal. Chem.*, 58 (1986) 994.
35 S. K. Ratanathanawongs and J. C. Giddings, *J. Chromatogr.*, 467 (1989) 341.
36 B. N. Barman, M. N. Myers and J. C. Giddings, *Powder Technol.*, 59 (1989) 53.
37 M. Kerker, *The Scattering of Light and Other Electromagnetic Radiation*, Academic Press, New York, 1969.

Journal of Chromatography, 517 (1990) 449–458
Elsevier Science Publishers B.V., Amsterdam

CHROMSYMP. 1924

Quantitative correlations between solute molecular structure and solubility in supercritical fluids

JERRY W. KING* and JOHN P. FRIEDRICH
Northern Regional Research Center, Agricultural Research Service, United States Department of Agriculture, 1815 North University Street, Peoria, IL 61604 (U.S.A.)

ABSTRACT

There is a current need in the fields of supercritical fluid extraction and supercritical fluid chromatography (SFC) for rapid and simple methods of estimating a solute's solubility level in the dense gaseous solvent. Utilizing the solubility parameter theory developed by Giddings, we have developed a method which permits the quantitative estimation of solute solubility levels in dense and liquefied gas media over a range of pressure and temperatures. The described method incorporates the ratio of the solubility parameter of the extraction gas to that of the dissolved solute, thereby permitting correlations to be made for a number of solute–gas combinations. Techniques are also presented that permit solute solubilities to be estimated from a knowledge of the solute's molecular structure. The above methods have been applied to such applications as the extraction of organic solutes from aqueous media with liquefied carbon dioxide and supercritical fluid chromatography.

INTRODUCTION

The modern era of supercritical fluid extraction (SFE) has spawned a wide number of diverse applications in the areas of natural product extraction and food processing. As in many fields of technological endeavor, theoretical developments in supercritical fluid technology have trailed experimental and application studies. This trend is most unfortunate since there is a critical need for basic thermodynamic and kinetic models upon which to optimize extraction and separation conditions. Current theoretical developments in this field have included the application of statistical mechanical models[1,2], equation of state methods[3,4] and a diverse array of solution thermodynamic concepts[5–7] to explain and correlate phase equilibria and solubility phenomena in supercritical fluids. In general, the above approaches require extensive physicochemical data to characterize solute–solvent (gas) interactions and they have been applied mostly to a limited number of structurally-simple solutes dissolved in supercritical carbon dioxide. Such theoretical methods currently find limited use in practical applixcations, in part due to the molecular complexity of the solutes that are

being extracted and the lack of physical property data on these moieties.

Over the past seven years, we have applied solubility parameter theory[8], interaction parameters[9] and corresponding states methods to explain the salient features of SFE. One advantage of the above approach is the availability of required data for both the solvent gas and extracted solutes that are required by the regular solution or corresponding states theory. Utilizing critical property data and solute–solvent solubility parameters, one can estimate the required gas pressures (or density) to affect maximum solute solubility in the dense gas phase. Prediction of this solubility maximum can be determined by[10]

$$\chi = \bar{V}_1(\delta_1 - \delta_2)^2/RT + \chi_s \tag{1}$$

where χ is the total interaction parameter, χ_s is the entropic interaction parameter, δ_1 is the solubility parameter of the gas as a f(T, P), δ_2 is the solubility parameter of the solute as a f(T, P), and $\bar{V}_1$ is the molar volume of the gas as a f(T, P), R is the molar gas constant, T is the absolute temperature and P is the pressure.

Similarly, miscibility of the solute in the supercritical fluid can be predicted to occur at a discrete pressure, which can be ascertained by solving for the intersection of χ and χ_c as a function of pressure, where the Flory critical interaction parameter, χ_c, is given by

$$\chi_c = (1 + x^{\frac{1}{2}})^2/2x \tag{2}$$

and $x = \bar{V}_2/\bar{V}_1$, where $\bar{V}_2$ is the molar volume of the solute.

The above equations have been tested in a number of cases involving supercritical fluid equilibria and have been found to predict results that agree with experimental data, provided that the temperature and pressure dependence of solubility parameters and molar volumes are utilized in the calculations. Pertinent applications have included vegetable oil extraction[11] polymer solution thermodynamics[12] and supercritical fluid chromatography (SFC)[10,13].

HISTORICAL BACKGROUND

Correlation of a solute's molecular structure with its solubility in a supercritical fluid has been qualitatively attempted by several investigators. Stahl *et al.*[14], utilizing the results from his extensive micro-extraction studies, formulated several extraction rules based on changes in a solute's molecular structure to qualitatively predict the extent of a solute's dissolution in supercritical carbon dioxide. Qualitative trends in solute solubilities have also been summarized by Hyatt[15] and by Dandge *et al.*[16] who supplemented the extensive liquid carbon dioxide data of Francis[17] with additional data from their experimental studies. A concise summary of solubility in liquid carbon dioxide has also been reported by Sims[18]. In a recent extensive review Rizvi *et al.*[19] have discussed the current state of knowledge regarding solute solubilities in supercritical fluid media.

There is currently a need for methods that allow the rapid quantitative assessment of a solute's solubility in a supercritical fluid. Such information is critical for rendering decisions regarding the feasibility of applying supercritical fluid

extraction to an array of engineering and analytical problems. As noted by McHugh and Krukonis[20], there have been several bizarre attempts to apply SFE to the extraction of compounds exhibiting limited solubility in supercritical fluid media. Such questionable applications could be avoided if correlations existed between a solute's molecular structure and its recorded solubility in a particular supercritical fluid. The development of simple predictive methods to address the above problem is difficult due to the limited solubility data bases available and the diversity of units in which solute solubility data are frequently reported.

THE REDUCED SOLUBILITY PARAMETER CONCEPT

In this study, we have utilized the concept of the reduced solubility parameter, Δ, to correlate solubilities and their distribution coefficients in supercritical and near-critical fluids under a variety of extraction conditions. The reduced solubility parameter is defined as[21]

$$\Delta = \delta_1/\delta_2 \tag{3}$$

where δ_1 can be calculated by methods described below and δ_2 is determined from standard sources[22]. It should be noted that this definition of "reduced solubility parameter" differs from that utilized by Prausnitz[23] and Allada[24] who defined the term as the solubility parameter of the gas divided by the square root of the gas critical pressure. The ratio of the solubility parameter of the solvent (gas) to that of the solute acutely reflects the strength of the solute–solvent interactions under a variety of pressure and temperature conditions and was first suggested by Giddings *et al.*[21] in 1969. As an aid in our correlations we have employed the group contribution method of Fedors[25] to compute the solubility parameters for many structurally complex solutes such as carotenoids, alkaloids, pesticides, sterols and antibiotics. By incorporating this latter concept into our method, we have made δ_2 a function of molecular structure and therefore Δ sensitive to changes in solute structure relative to the solvent gas.

To describe the solvent power of the dense gas, we have used the equation proposed by Giddings *et al.*[26] in which the solubility parameter of the gas is given by

$$\delta_1 = 1.25\, P_c^{\frac{1}{2}}(\rho_{r,\,SF})/(\rho_{r,\,liquid}) \tag{4}$$

where P_c is the fluid critical pressure, $\rho_{r,\,SF}$ the reduced density of the critical fluid, and $\rho_{r,\,liquid}$ is the reduced density of the fluid in the liquid state. This equation has been shown to reflect the variance in solvent power of the gas as a function of pressure and temperature and is dependent on the chemical nature of the extraction fluid through P_c. Reduced densities for a variety of fluids can be determined by using gas densities and the appropriate critical constant, or in the absence of actual gas density data, through corresponding states relationships. Reduced densities of fluids in their liquid state are computed at infinite pressure and the proper reduced temperature from corresponding states tables.

RESULTS AND DISCUSSION

Solute solubilities in supercritical fluids depend not only on a variance in the molecular structure, between solutes, but also on the pressure and temperature at which the extraction is performed. Such factors can make a solute's solubility in the dense gas phase vary over many orders of magnitude. However, in general, solubilities recorded in supercritical fluids are less than those recorded in liquid solvents. An example of this solubility trend is shown in Fig. 1 where weight fraction solubilities for various solutes dissolved in supercritical fluid ethylene are plotted against the reduced solubility parameters Δ. The solubility data were obtained from the "classical Zosel" patent issued to SGK[27] and encompass a variety of solutes of varying polarity the solubility parameters of which are known. The reported solubility data in ethylene for these compounds encompassed a wide range of reduced pressures (1.19–3.96) and essentially isothermal conditions (20–25°C). The wide variation in reported solubilities is conveniently handled by using a logarithmic concentration scale for the ordinate while the variation in solute solubility parameters (7.77–14.4 $cal^{1/2}/cm^{3/2}$) and gas solubility parameters (3.84–6.4 $cal^{1/2}/cm^{3/2}$) is encompassed in the reduced solubility parameter scale on the abscissa. Note that as the ratio of the solubility parameter of the gas to that of solute increases, there is a substantial increase in the recorded solubility up to a reduced solubility parameter of 0.5. To a large extent, the recorded trend in the solubility data is reflective of the changing chemical nature of the solute molecule with maximum solubilities being recorded as the reduced solubility parameter tends to unity. The data shown in Fig. 1 appear to obey a functional form that can be conveniently fitted by a polynomial equation over the entire range of experimental data.

As indicated in Fig. 1, solute solubilities recorded at reduced solubility parameter values of less than 0.5 are extremely sensitive to changes in solute molecular structure. The results presented in Fig. 2 for supercritical carbon dioxide–solute systems further corroborate this trend, even among polar solutes of varying molecular

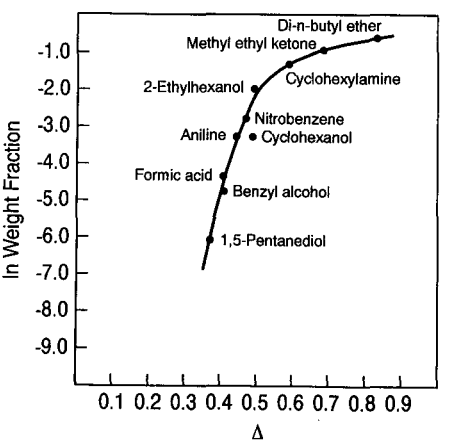

Fig. 1. Natural logarithm of solute weight fraction solubility in ethylene *vs.* reduced solubility parameter (based on experimental solubility data by Zosel[27]).

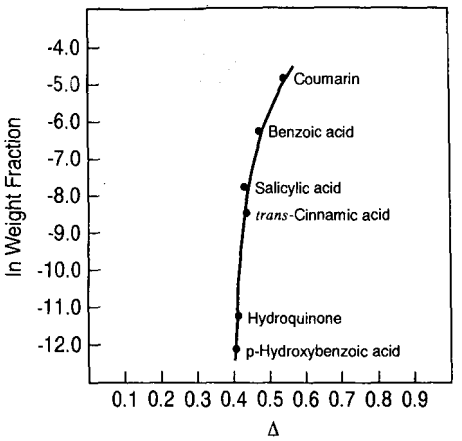

Fig. 2. Natural logarithm of solute weight fraction solubility in carbon dioxide (100 atm, 40°C) *vs.* reduced solubility parameter.

structure. The recorded weight fractions for the compounds (taken at 100 atm and 40°C), in Fig. 2 were interpolated from the studies of Schilz[28], while the solute solubility parameters were computed by the Fedors method. Fig. 2 shows the relationship between the natural logarithm of the weight fraction solubility and the corresponding reduced solubility parameter Δ for the designated solutes in carbon dioxide at 100 atm and 40°C. The data presented range in magnitude from a weight fraction of $7.7 \cdot 10^{-3}$ for coumarin ($\delta_2 = 10.5$ cal$^{1/2}$/cm$^{3/2}$) to a value of $5.5 \cdot 10^{-6}$ for polar *p*-hydroxybenzoic acid ($\delta_2 = 13.94$ cal$^{1/2}$/cm$^{3/2}$). A similar correlation has also been found to hold for phenolic solutes dissolved in supercritical carbon dioxide in which the solubility parameters of the solutes ranged from 13.96 to 21.4 cal$^{1/2}$/cm$^{3/2}$. Such correlations are valuable for they permit the rapid estimation of solute solubilities under similar extraction conditions when knowledge of the solute's solubility parameter and molecular structure are available.

TABLE I

CALCULATION OF THE SOLUBILITY PARAMETER FOR CAFFEINE

	Group	$\Delta\varepsilon_i$ *(cal/cm^3)*	Δv_i *(cm^3/mol)*
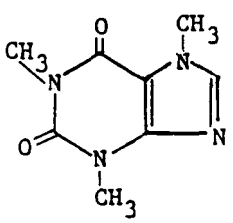	3 CH_3	3375	100.5
	2 C=	2060	−11.0
	1 CH=	1030	13.5
	3 N	3000	−27.0
	1 –N=	2800	5.0
	2 C=O	8300	21.6
	2 5–6-member rings	500	32.0
	2 conjugated double bonds	800	−4.4
$\delta_2 = 12.96$		21 865	130.2

An example of the above approach using the group contribution method of Fedors is given in Table I. Here the solubility parameter for caffeine has been computed by summing the individual group contributions for the energy of vaporization $\Delta\varepsilon_i$ and molar volume Δv_i to the overall structure of the solute molecule. The solute's solubility parameter is calculated by taking the square root of the ratio of the sum of the energy contributions over the sum of respective group molar volumes[24], $\delta_2 = (\Sigma\Delta\varepsilon_i/\Sigma\Delta v_i)^{1/2}$. For caffeine, which has been extracted industrially with supercritical carbon dioxide, the solubility parameter value is 12.96 $cal^{1/2}/cm^{3/2}$. Interpolating in Fig. 2 using a reduced solubility parameter of 0.44 yields a value of $4.0 \cdot 10^{-4}$ for the weight fraction solubility of caffeine under the same extraction conditions. This value compares favorably with the experimentally determined value of $3.3 \cdot 10^{-4}$ determined by Schilz[28].

Fedors' method is extremely valuable in ascertaining the cohesional energy density of complex molecules. With this method one does not even have to depend on the type of relationships noted above to reach seminal conclusions regarding the potential for extracting a compound under SFE conditions. Applications of this group contribution method to bioactive molecules, such as imipenum and efrotomycin which have been extracted by Larson and King[29] with supercritical carbon dioxide at 40°C and 5000 p.s.i.g. ($\delta_1 = 8.2$ $cal^{1/2}/cm^{3/2}$), supports the correspondence between solute solubility parameter and solute solubility levels in supercritical fluids. For example, efrotomycin, a large molecule exhibiting antibiotic activity, has a solubility parameter of 12.1 $cal^{1/2}/cm^{3/2}$ and a weight fraction solubility in the dense gas phase of $3.0 \cdot 10^{-4}$. By comparison, imipenum, whose molar volume is 6.5 times smaller then efrotomycin's has a solubility parameter of 16.4 $cal^{1/2}/cm^{3/2}$ and exhibits no recorded solubility in carbon dioxide under the above-cited conditions. Good agreement is also recorded when one compares solubility parameters computed from Fedors' method with those obtained from other sources. As shown in Table II, the solubility parameters determined by Fedors' method for sterols agree well with the values given by Wong and Johnston[30].

Reduced solubility parameter correlations can provide a better understanding of the solubility trends in liquefied gases. Fig. 3 shows the correlation between Δ and the molar distribution coefficients, K (m), of various solutes partitioning between water and liquefied carbon dioxide held at 16°C ($\delta_1 = 7.15$ $cal^{1/2}/cm^{3/2}$). The distribution coefficient data presented in Fig. 3 were taken from the studies of Schultz and Randall[31], in which odoriferous alcohols and esters were recovered from aqueous

TABLE II

COMPARISON OF SOLUBILITY PARAMETERS CALCULATED BY TWO DIFFERENT METHODS FOR STEROLS

Sterol	*Solubility parameter* ($cal^{1/2}/cm^{3/2}$)	
	Wong and Johnston[30]	*Fedors*[25]
Cholesterol	9.2	9.6
Stigmasterol	8.8	9.5
Ergosterol	9.1	9.4

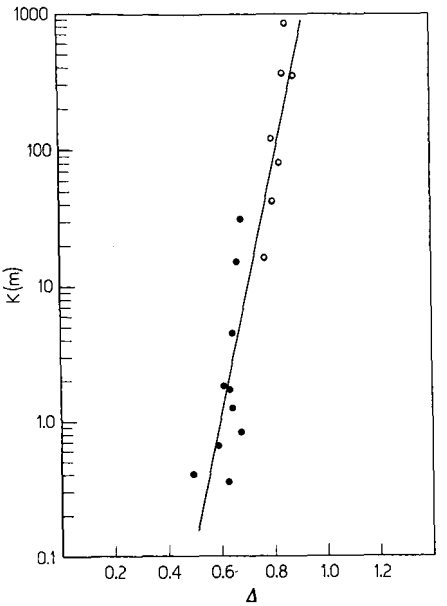

Fig. 3. Molar distribution coefficient *vs.* reduced solubility parameter for solutes partitioning between water and liquid carbon dioxide (16°C). Symbols: ● = alcohols; ○ = esters.

media by partitioning into liquid carbon dioxide. The semilogarithmic relationship between distribution coefficients and Δ is exemplified by the fit of a linear regression line to the data in Fig. 3. The value of such a correlation becomes apparent when one is considering the recovery of other candidate solutes from aqueous media. For example, the small distribution coefficients (0.002–0.010) found for polar solutes such as acetic acid, dimethylformamide and ethylene glycol are predicted by use of the reduced solubility parameter scale. Extraction of these solutes into liquefied carbon dioxide is somewhat impractical, in part due to the high solvent-to-feed ratio requirements. Nevertheless, their removal by critical fluid extraction has been proposed and cited in the literature[32,33].

The comprehensive solubility studies performed in liquefied carbon dioxide by Francis[17] over three decades ago have been cited by numerous investigators as a qualitative guideline for predicting solute solubilities in supercritical carbon dioxide. Such a data base, consisting of over 260 binary systems, is potentially correlatable by using the reduced solubility parameter concept. Unfortunately, much of the solubility data consisted of visual observations concerning total or complete immiscibility, determined in an era when appropriate quantitative analytical methods were limited. However, for certain cited systems, compositions were determined for both the liquefied carbon dioxide and second component layers. By using the weight fraction compositions for each of the respective phases, we have been able to define a distribution coefficient $K(\mathrm{w})$ as:

$$K(\mathrm{w}) = \frac{\text{weight fraction of solute in the liquefied carbon dioxide phase}}{\text{weight fraction of solute in the second phase}} \qquad (5)$$

which is a measure of solute (second component) partition into the liquid carbon dioxide phase. Thirty-four of these solute distribution coefficients for an array of solutes partitioning into liquefied carbon dioxide have been plotted *versus* Δ on a semi-logarithmic graph in Fig. 4. Upon initial examination of Fig. 4, the data appear to yield no recognizable trend. However, classification of the individual systems by type of compound and their respective solubility parameters allows some conclusions to be drawn. The filled circle symbols represent very polar solutes, such as glycols, amides and amines, the solubility parameter values of which fall between 13 and 18 $cal^{1/2}/cm^{3/2}$ and which have a Δ of 0.2–0.5. Distribution coefficients for these compounds appear generally to lie below 0.01, consistent with their low solubility in liquefied carbon dioxide. Solutes of intermediate polarity (open circles), appear to have a Δ that falls between 0.5 and 0.7. Compounds in this group include substituted aromatic moieties, halogenated solutes and alcohols. Finally, solutes having solubility parameters less than 9.0 $cal^{1/2}/cm^{3/2}$ (half-filled circles) tend to exhibit distribution coefficients greater than 0.1. These include hydrocarbons, which partition partially into liquefied carbon dioxide or exhibit total miscibility with the liquefied gas. When the results of Fig. 4 are viewed in the above context, one has only to obtain a solute's solubility parameter to ascertain that solute's propensity for partitioning into the liquefied carbon dioxide phase.

Currently, the field of SFC is undergoing a renaissance due largely to improvements in instrumentation that can conviently handle highly compressed supercritical fluid eluents. Here, as in the above cases, a knowledge of the relative solubilities or partitioning behavior of the injected solutes in the column is critical to maximizing component resolution in the minimum amount of analysis time. The

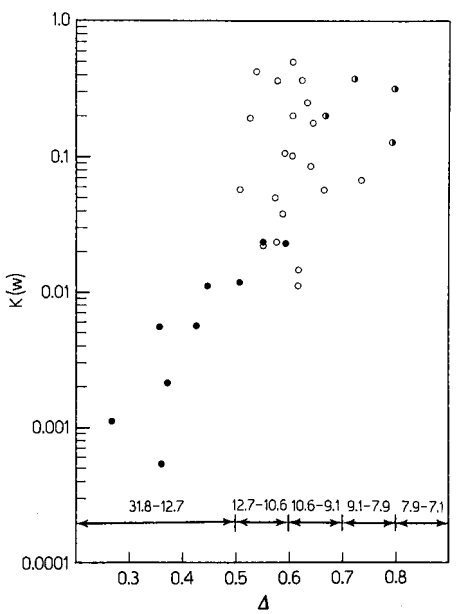

Fig. 4. Distribution coefficient *vs.* reduced solubility parameter for solutes partitioning into the liquid carbon dioxide phase (25°C).

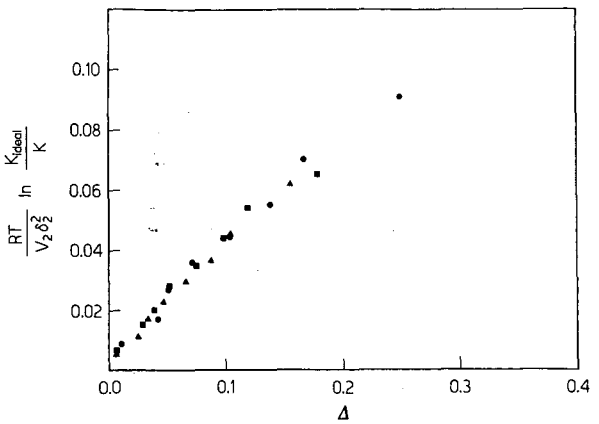

Fig. 5. $RT/\bar{V}_2\delta_2^2$ $\ln(K_{ideal}/K)$ *vs.* the reduced solubility parameter for solutes partitioning between supercritical carbon dioxide and squalane (40°C). Symbols: ● = benzene; ▲ = methanol; ■ = ethanol.

relative partitioning behavior of solutes with respect to each other and a low-pressure reference state (K_{ideal}) was formalized by Giddings *et al.*[21]

$$RT/\bar{V}_2\delta_2^2 \ln(K_{ideal}/K) = (2 - \Delta)\Delta \tag{6}$$

where K is the chromatographic partition coefficient. Eqn. 6 is expressed in reduced coordinates and predicts a general parabolic dependence of the solute's partition coefficient ratio on Δ. To illustrate the usefulness of the above concept, data interpolated from the studies of Sie *et al.*[34] have been used (Fig. 5) to construct a graph from Eqn. 6 for three solutes partitioning between squalane and carbon dioxide held at 40°C over the pressure range of 1–70 atm. By using the reduced solubility parameter as the ordinate of this figure, all of the data points for the solutes having significantly different solubility parameters can be made to conform to the same equation over the entire experimental pressure range. This conformity suggests that the partition coefficients could be predicted for additional solutes chromatographed under similar conditions if their reduced solubility parameters were computed. The above relationship has been shown to apply to other solute–column combinations, and its general applicability shows that pressure-induced changes in solute distribution coefficients are primarily independent of the chromatographic stationary phase. A similar method has been used by Ziger and Eckert[35] to describe solubility enhancement of solutes in supercritical fluids.

CONCLUSION

The cited examples show that it is possible to correlate a large body of supercritical fluid extraction data in a quantitative manner by relating the data to chnges in the molecular structure of the extracted solute. This can be accomplished readily by using the reduced solubility parameter concept as a measure of the solute–solvent interaction in the supercritical state. The advocated method is relatively

simple, requiring a minimum of experimental and physical data for the rapid estimation of solute solubilities in supercritical fluids. Such a concept is a valuable technical aid to the chromatographer faced with the need to make rapid decisions in utilizing SFE or SFC and for understanding the general solubility characteristics of these unique solvents.

REFERENCES

1 D. J. Vezzetti, *J. Chem. Phys.*, 77 (1982) 1512.
2 S. K. Kumar, R. C. Reid and V. W. Suter, in T. G. Squires and M. E. Paulaitis (Editors), *Supercritical Fluids: Chemical Engineering Principles and Applications*, American Chemical Society, Washington, DC, 1987, p. 88.
3 U. Deiters and G. M. Schneider, *Ber. Bunsen-Ges. Phys. Chem.*, 80 (1976) 276.
4 W. B. Whitting and J. M. Prausnitz, *Fluid Phase Equilib.*, 9 (1982) 119.
5 J. Chrastil, *J. Phys. Chem.*, 86 (1982) 3016.
6 R. T. Kurnik and R. C. Reid, *Fluid Phase Equilib.*, 8 (1982) 93.
7 G. A. Mansoori and J. F. Ely, *J. Chem. Phys.*, 82 (1985) 406.
8 J. W. King, *16th ACS Annual Great Lakes Regional Meeting, Normal, IL, June 9, 1982*, Abstract No. 245.
9 J. W. King and J. F. Friedrich, *20th ACS Annual Great Lakes Regional Meeting, Milwaukee, WI, June 2, 1986*, Abstract No. 170.
10 J. W. King, *J. Chromatogr. Sci.*, 17 (1989) 355.
11 J. W. King, *J. Am. Oil Chem. Soc.*, 60 (1983) 711.
12 J. W. King, *Polymeric Materials Sci. Eng. Preprints*, 51 (1984) 707.
13 J. W. King and J. F. Friedrich, *13th Annual Meeting of the Federation of Analytical Chemistry and Spectroscopy Societies, St. Louis, MO, Sept. 29, 1986*, Abstract No. 32.
14 E. Stahl, W. Schilz, E. Schultz and E. Willing, *Angew. Chem., Int. Ed. Engl.*, 17 (1978) 731.
15 J. A. Hyatt, *J. Org. Chem.*, 49 (1984) 5097.
16 D. K. Dandge, J. P. Heller and K. V. Wilson, *Ind. Eng. Chem. Prod. Des. Dev.*, 24 (1985) 162.
17 A. W. Francis, *J. Phys. Chem.*, 58 (1954) 1099.
18 M. Sims, *Chem. Eng.*, 89 (1982) 50.
19 S. S. H. Rizvi, J. A. Daniels, A. L. Benado and J. A. Zollweg, *Food Technol. (Chicago)*, 40, No. 7 (1986) 57.
20 M. A. McHugh and V. J. Krukonis, *Supercritical Fluid Extraction*, Butterworths, Boston, MA, 1986.
21 J. C. Giddings, M. N. Myers and J. W. King, *J. Chromatogr. Sci.*, 7 (1969) 276.
22 A. F. M. Barton, *Handbook of Solubility and Other Cohesional Parameters*, CRC Press, Boca Raton, FL, 1983.
23 J. M. Prausnitz, in T. S. Storvick and S. I. Sandler (Editors), *Phase Equilibria and Fluid Properties in the Chemical Industry*, American Chemical Society, Washington, DC, 1977, p. 11.
24 S. R. Alada, *Ind. Eng. Chem. Process Des. Dev.*, 23 (1984) 344.
25 R. F. Fedors, *Polym. Eng. Sci.*, 14 (1974) 147.
26 J. C. Giddings, M. N. Myers, L. McLaren and R. A. Keller, *Science (Washington, D.C.)*, 162 (1968) 67.
27 K. Zosel, *U.S. Pat.*, 3 969 196 (1976).
28 W. Schilz, *Ph.D. Thesis*, University of Saarland, Saarbrücken, 1978.
29 K. A. Larson and M. L. King, *Biotechnol. Prog.*, 2 (1986) 73.
30 J. M. Wong and K. P. Johnston, *Biotechnol. Prog.*, 2 (1986) 29.
31 W. G. Schultz and J. M. Randall, *Food Technol. (Chicago)*, 24, No. 11 (1970) 94.
32 R. P. DeFilippi and J. M. Moses, in C. D. Scott (Editor), *Fourth Symposium on Biotechnology on Energy Production and Conservation*, Interscience, New York, 1982, p. 205.
33 E. J. Shimshick, *Chem. Tech.*, 13 (1983) 374.
34 S. T. Sie, W. van Beersum and G. W. A. Rijnders, *Sep. Sci.*, 1 (1966) 459.
35 D. E. Ziger and C. A. Eckert, *Ind. Eng. Chem. Process. Des. Dev.*, 22 (1983) 582.

Journal of Chromatography, 517 (1990) 459–476
Elsevier Science Publishers B.V., Amsterdam

CHROMSYMP. 1961

Use of chromatographic retention measurements to obtain solubilities in a liquid or supercritical fluid mobile phase

KEITH D. BARTLE, ANTHONY A. CLIFFORD*, SAAD A. JAFAR, JACOB P. KITHINJI and GAVIN F. SHILSTONE
School of Chemistry, University of Leeds, Leeds LS2 9JT (U.K.)

ABSTRACT

A thermodynamic analysis is given of the relationship between the capacity factor in high-performance liquid chromatography (HPLC) and supercritical fluid chromatography (SFC) and the solubility of the solute in the mobile phase. The analysis shows that in certain circumstances, where particular assumptions are valid, there is a simple inverse relationship between the two quantities. In these circumstances the proportionality constant has a fixed value for a particular column, temperature and solute, and is independent of the mobile phase. Furthermore, the logarithm of the constant is approximately linearly related to the inverse of the absolute temperature over a limited temperature range. Some experimental studies are then described which show that practical conditions exist where these relationships are valid. It is shown that the same equation-of-state, with the same parameters, can be used to predict quantitatively both supercritical fluid solubilities and the temperature dependence of retention in SFC. Experimental results illustrate the inverse relationship between solubility and retention where the same column was used in both SFC and HPLC. Results are also given for the variation of the proportionality constant with temperature. The various ways in which these relationships could be used to measure solubilities are discussed and examples of experimental measurements are given for some methods.

INTRODUCTION

The degree of retention of a solute in supercritical fluid chromatography (SFC), as measured by the capacity factor, k', is at least qualitatively inversely related to the solvating power of the mobile phase for that solute: the more soluble it is in the mobile phase, the less it will be retained. The relationship has been used qualitatively and also to obtain quantitative information related to solubilities for both liquids and supercritical fluids. In one study chromatographic retention has been used to obtain pressure thresholds for the solubilities of various compounds at different temperatures[1]. In another, the relative solvating power of supercritical CO_2 compared with that of hexane has been discussed in terms of the differences in retention when the two

0021-9673/90/$03.50

fluids were used as mobile phases[2]. A preliminary study has been carried out of solute fugacities in a stationary phase in SFC, with a view to obtaining by chromatography solute fugacities or enhancement factors (relating to solubilities) in a supercritical fluid[3]. High-performance liquid chromatography (HPLC) is used to obtain hydrophobicity constants, and also solubilities of organic electrolytes have been estimated using HPLC retention data to obtain parameters in the modified Hildebrand–Scott equation[4]. Normal-phase HPLC has been used to obtain oil–water partition coefficients, and "ideal solubilities" have been calculated from the ratios[5].

In this paper it will be argued that in some situations at constant temperature, solubility of solid solutes in the mobile phase can be inversely proportional to k'. When this is the case, chromatographic retention can be used to measure solubilities relatively rapidly in both liquids and supercritical fluids. The relationship between the two quantities is investigated theoretically and experimentally, before discussing the various routes for obtaining solubilities from chromatographic retention measurements. These measurements could provide an important source of solubility data, particularly for supercritical fluids, and the studies are very much in the tradition of the use of chromatography for obtaining physical and chemical data, in which Professor Giddings has been a pioneer.

THERMODYNAMIC ANALYSIS

Thermodynamic analyses of the type given below have appeared previously in a number of publications. However, it is necessary to detail a treatment of this type, which is directly relevant to the present situation, in order to identify the assumptions which must be made to arrive at the eventual simple equation. In general we must allow for the fact that the solubility and chromatographic experiments will be carried out at different pressures, p_s and p_c, respectively. This will not be the case for supercritical fluid experiments, where solubilities refer to a particular pressure, and the corresponding retention measurements must be made at the same pressure. But it will be the case for liquids, where pressures of the order of 100 bar are needed to pass the mobile phase through the column in HPLC, whereas solubilities are usually and most easily done at low (atmospheric) pressure. For both types of mobile phase, pressure is decreasing along the column though much less so for SFC. For HPLC the arguments below refer to one point in the column, but for SFC pressure is assumed to be constant along the column, and this subject is discussed later as an experimental problem.

We begin by discussing the situation for chromatography. At equilibrium at constant pressure and temperature, equating the chemical potentials of the solute in both phases gives

$$\mu_m^\ominus + \int_0^{p_c} V_m dp + RT \ln a_m = \mu_{st}^\ominus + \int_0^{p_c} V_{st} dp + RT \ln a_{st} \qquad (1)$$

where $\mu_m^\ominus$ and $\mu_{st}^\ominus$ are the standard chemical potentials of the solute in the mobile and stationary phases, respectively, and refer to infinite dilution and standard pressure. In all cases, but importantly in the case of a supercritical fluid, the state at the standard

pressure of 1 atm is a hypothetical and ideal one, where the activity coefficient, defined as being unity in the limit of zero pressure, is also unity in the standard state. V_m and V_{st} are the partial molar volumes at infinite dilution of the solute, a_m and a_{st} are the activities of the solute in the corresponding phases, R is the molar gas constant and T is the temperature. Rearrangement of eqn. 1 gives

$$\mu_m^\ominus - \mu_{st}^\ominus + \int_0^{p_c} (V_m - V_{st})dp = RT \ln (a_{st}/a_m) \tag{2}$$

If we assume that chromatography is carried out under conditions which approximate to infinite dilution, the activities can be replaced in eqn. 2 by the concentrations divided by standard concentrations, $c_m/c_m^\ominus$ and $c_{st}/c_{st}^\ominus$. The standard concentrations are shown as different, in general, for the two phases, as will necessarily be the case for adsorption chromatography, where $c_{st}^\ominus$ will be a surface concentration. For partition chromatography the standard concentrations will usually be identical amounts of solute per unit volume. Analytical chromatography is normally carried out at very low dilution and, if it is not the case, is observable as a distortion of the chromatographic peak shape and a variation of the degree of retention with the amount of solute injected. The ratio of these concentrations is related to k' by

$$k' = rc_{st}/c_m \tag{3}$$

where r is the stationary to mobile phase ratio, which in the simplest case of partition chromatography, when the standard concentrations in the two phases are identical, will be the ratio of the volumes of the two phases. For adsorption chromatography or a bonded stationary phase r will involve an area-to-volume ratio. r will be a constant for a particular chromatographic column. Substitution of eqn. 3 into eqn. 2, with the activities replaced by concentration ratios, gives the following expression:

$$\mu_m^\ominus - \mu_{st}^\ominus + \int_0^{p_c} (V_m - V_{st})dp = RT \ln (k'c_m^\ominus/rc_{st}^\ominus) \tag{4}$$

We now consider solubility and a saturated solution of the solute in the mobile phase. Discussion is restricted to conditions where the solid solutes remain as solids in the presence of the mobile phase, *i.e.* do not form a solute-rich liquid phase, and the solids are assumed not to absorb the mobile phase, and thus the chemical potential of the solute can be considered to be a constant at constant pressure and temperature. After equating chemical potentials in both phases, we obtain

$$\mu_s^\ominus - \mu_m^\ominus + \int_0^{p_c} (V_s - V_m)dp = RT \ln a_m^{sat} \tag{5}$$

where $\mu_s^\ominus$ and V_s are, respectively, the chemical potential and molar volume of the solid, and a_m^{sat} the activity of the solute at saturation in the solvent or mobile phase. (In situations where different allotropic forms of the solid can exist, there will be no difficulty at the transition temperature, where the chemical potentials and solubilities of the two forms will be identical. At other temperatures one form will be the stable allotrope and have the lower chemical potential, and this is the form to which this thermodynamic analysis strictly applies. However, it may be possible to study solubilities of metastable allotropes by the methods described in this paper, by determining the constant, C, defined below, from solubilities of the metastable allotrope.) Eqns. 4 and 5 are then added to obtain:

$$\mu_s^\ominus - \mu_{st}^\ominus + \int_0^{p_s} (V_s - V_m)dp + \int_0^{p_c} (V_m - V_{st})dp = RT \ln (a_m^{sat} k' c_m^\ominus / r c_{st}^\ominus) \quad (6)$$

In the case of a supercritical fluid $p_c = p_s$, and the integral terms cancel, if it is assumed that the partial molar volume of the solute in the stationary phase, V_{st}, is equal to its molar volume, V_s, and eqn. 6 becomes:

$$\mu_s^\ominus - \mu_{st}^\ominus = RT \ln (a_m^{sat} k' c_m^\ominus / r c_{st}^\ominus) \quad (7)$$

For the case of a liquid, where p_c and p_s are different, eqn. 7 may also be obtained, but in this case it must be assumed that the partial molar volumes of the solute in both the stationary and mobile phases are equal to the molar volume (and that this is the case at all points in the column). The assumptions that must be made about partial molar volumes are not unreasonable in many cases, where the interaction between the solute and the phases are not strong as is often the case.

Eqn. 7 may be rearranged to give the following expression for the activity of the solute at saturation:

$$a_m^{sat} c_m^\ominus = (r c_{st}^\ominus \exp [(\mu_s^\ominus - \mu_{st}^\ominus)/RT](1/k') \quad (8)$$

The quantity $\mu_{st}^\ominus$, which is the chemical potential of the solute in the stationary phase at infinite dilution and standard pressure and at a particular temperature, will be a constant for a given solute and chromatographic column, provided that the interaction of the solute and stationary phase is not affected by the nature of the mobile phase. This will often not be the case, for example with cross-linked polymer phases used in SFC, which absorb the mobile phase and swell to an extent dependent upon pressure and change their solvating properties[6,7]. However, it is likely to be true for octadecylsilyl (ODS) bonded phases and CO_2, as it will be shown below that it is not necessary to take into account effects of the mobile phase on the stationary phase to quantitatively account for the dependence of retention on temperature. Adsorption of carbon dioxide on an ODS phase has been observed and this is maximised in the region of the critical point[8]. However, it does not follow that this affects the adsorption of solutes, and the effect is such that the environment of the ODS phase does not change as much with a drop in pressure as it would if this adsorption did not occur. In cases

where the above assumption can be made, the right-hand side of eqn. 8, apart from the factor $(1/k')$ is therefore a constant for a particular system and temperature. Eqn. 8 can therefore be written as

$$a_m^{sat} c_m^{\ominus} = C/k' \tag{9}$$

where C is a constant for a particular solute, column and temperature.

If the assumption is now made that the activity coefficient of the solute in the mobile phase is constant (*i.e.* unity) from infinite dilution up to the solubility limit, the activity can be replaced by concentration (which for the saturated solution will be the solubility, S) divided by the standard concentration, and eqn. 9 can be rewritten as

$$S = C/k' \tag{10}$$

This assumption will not always be valid in liquids, as will be seen from the experimental results below. For supercritical fluids, such as carbon dioxide, where interactions are not strong or specific, the activity coefficient can be calculated from equations of state with reasonable confidence and here it is known that the assumption is a good approximation, especially as supercritical solubilities are usually low.

Returning to the problem of pressure drop in SFC, equations have been obtained for the average capacity factor in a column with pressure drop[9,10], and calculations have been carried out for a model system of the percentage difference of the true average and the value at the average of the inlet and outlet pressures[10]. These show that differences of up to a factor of two are obtained for a 30-bar drop 1 K above the critical temperature and near the critical pressures. The effect decreases with rise in temperature, with the peak effect rising to higher pressures. For the quantitative measurements described in the last section a short column and low flow-rates were used to reduce the pressure drop to around 2 bar and the critical region avoided.

The constant C, introduced in eqn. 9, is given by

$$C = r c_{st}^{\ominus} \exp\left[(\mu_s^{\ominus} - \mu_{st}^{\ominus})/RT\right] \tag{11}$$

The difference in standard chemical potentials in eqn. 11 corresponds to the standard Gibbs function change for the precipitation of the solid solute from solution at infinite dilution in the stationary phase. In common with other types of equilibria, it may be assumed, therefore, that the constant C is given approximately by

$$C = A \exp(B/T) \tag{12}$$

where A and B are constants over a limited temperature range for a particular column and solute. This equation allows the possibility of limited interpolation or extrapolation to obtain values of C, by plotting ln C *versus* $1/T$.

PREDICTON OF SOLUBILITY AND RETENTION BASED ON THE SAME EQUATION OF STATE FOR A SUPERCRITICAL FLUID

Prediction of solubilities

Prediction of solubilities may be made on the basis of eqn. 5. This can be modified by assuming, firstly, that the solid molar volume does not change with pressure and, secondly, that as before, as the saturated solutions are dilute, a_m^{sat} can be replaced by the mole fraction y^{sat}. The choice of mole fraction, rather than the concentrations used earlier, is correct if it is consistent wihtin the present calculation and implies different numerical values of the chemical potentials. Eqn. 5 becomes

$$\mu_s^{\ominus} - \mu_m^{\ominus} + p_s V_s = \int_0^{p_s} V_m dp + RT \ln y^{sat} \tag{13}$$

V_m is a quantity which varies greatly from the solute molar volume (becoming large and negative in the critical region), but can be calculated from an appropriate equation of state. Expressions are given usually in published equations of state for the fugacity coefficient, ϕ (in this case the fugacity coefficient at infinite dilution), which is related to the integral on the left side of eqn. 13. This equation can now be expressed as

$$\mu_s^{\ominus} - \mu_m^{\ominus} + p_s V_s = RT \ln (p_s \phi / p^{\ominus}) + RT \ln y^{sat} \tag{14}$$

In the absence of any supercritical fluid, $p_s = p_v$, the vapour pressure of the solute, y^{sat} is unity and as the pressure is low and ϕ is also approximately unity, eqn. 14 becomes approximately

$$\mu_s^{\ominus} - \mu_m^{\ominus} = RT \ln (p_v / p^{\ominus}) \tag{15}$$

The solubility, S, in concentration terms, is related to y^{sat} by $SV = y^{sat}$, where V is the molar volume, approximately the molar volume of the pure supercritical fluid. Substitution of this relationship and eqn. 15 into eqn. 14 gives

$$\ln S = \ln (p_v / p_s) - \ln \phi - \ln V + pV_s / RT \tag{16}$$

This equation can then be used to calculate supercritical solubilities, provided the vapour pressure is known, using a suitable equation-of-state for predicting the fugacity coefficient. In the studies described here the Peng–Robinson equation-of-state is used[11], which, in common with other possibilities, requires knowledge of an interaction parameter for each pair of components. These interaction parameters are empirical fine-tuning parameters for the bimolecular interactions to which predicted solubilities are very sensitive. Fig. 1 shows solubilities predicted for naphthalene based on a range of the interaction parameter, d, for naphthalene and CO_2 at two temperatures, which illustrate this sensitivity along with the published experimental results[12,13]. In principle, the parameter d is a constant independent of temperature. In a comprehensive study, Haselow *et al.*[14] have shown that the use of temperature-

independent parameters often give poor predictions of solubility, and Fig. 1 also illustrates this. However, Yamato *et al.*[15] have shown that the use of a temperature-dependent parameter can fit some of the experimental data more accurately. The approach used here is therefore to obtain temperature-dependent interaction parameters, d, from published experimental solubility data where available and interpolate these graphically. All published solubility data have been treated by us in this way, where vapour pressures and parameters for the equation of state were available and some of the results have already been published[16]. Fig. 2 shows smoothed plots of the interaction parameters obtained from published solubilities[12,13,17–20] for four polynuclear aromatic compounds, which will be of use in the next section. For the two compounds fluorene and pyrene, the variation of d with temperature is inside the experimental error and constant values are shown.

Using values of d obtained in this way, good predictions of solubility can be made, which fit the experimental data well. In the interest of minimising the number of figures given, this can be appreciated from Fig. 1B, where it can be seen that using a value for d of about 0.09 will give good agreement.

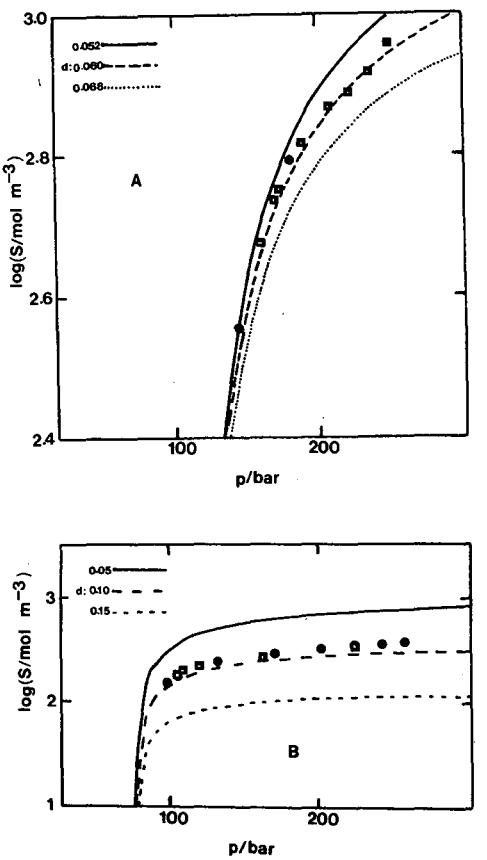

Fig. 1. Dependence of predicted values of the solubility, S, of naphthalene in CO_2 as a function of pressure, p, on the Peng–Robinson interaction parameter, d. A is at 55°C and B at 35°C. Experimental results: ◻ = McHugh and Paulaitis[12]; ○ = Tsekhanskaya[13].

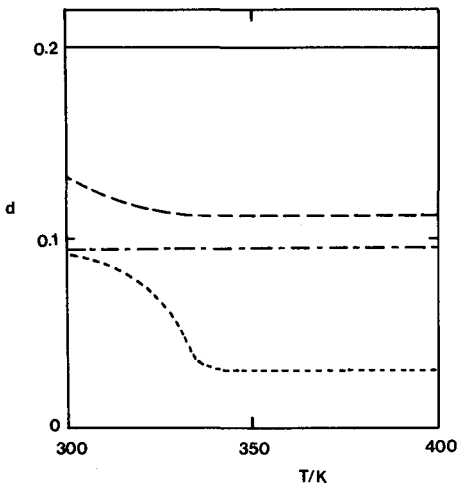

Fig. 2. Smoothed values of the Peng–Robinson parameter, d, obtained from experimental solubilities plotted as a function of temperature. ——— = Pyrene; – – – = phenanthrene; - - - - - - - - - = fluorene; ------- = naphthalene.

Prediction of the temperature dependence of retention in SFC

At constant pressure, k' is observed to pass through a maximum with increasing temperature[21]. The qualitative explanation of this phenomenon is as follows. The rising portion of the curve is due to the decreasing density of the supercritical fluid, decreasing its solvating effect. The rising portion of the curve occurs when the increasing volatility of the solute outweighs this earlier effect. Quantitative analyses of this effect have been made[22,23]. The purpose here is to show that the same equation of state used to predict solublities, described above can also give a good quantitative explanation of such results. Fig. 3 shows some experimental results obtained in our laboratory for the retention of four polynuclear hydrocarbons as a function of temperature[24]. A 25-cm ODS column was used with pure CO_2 as the mobile phase at an average pressure of 130 bar and a pressure drop along the column of 36 bar. Under the conditions used, the error caused by the pressure drop is not too important, although having studied the effect of pressure drop[10], shorter columns and much lower pressure drops were used in subsequent experiments.

The equation used for the analysis of the experimental results can be obtained from eqn. 2. To obtain the appropriate chemical potentials, which will give the Gibbs function change for vaporisation from solution in the stationary phase, the activities are replaced, assuming dilute conditions, by $c_{st}/c_{st}^{\ominus}$ and $y = c_m V$, respectively. The ratio a_{st}/a_m is therefore equal to (using eqn. 3) $k'/c_{st}^{\ominus}V$. Making also the assumptions, described earlier, that V_{st} is independent of pressure and equal to the molar volume, V_s, and that the integral involving V_m can be replaced by $RT \ln (p_c\phi/p^{\ominus})$, eqn. 2 can be rewritten as

$$\mu_m^{\ominus} - \mu_{st}^{\ominus} - V_s p_c = RT \ln (p_c \phi k'/p^{\ominus} c_{st}^{\ominus} V) \qquad (17)$$

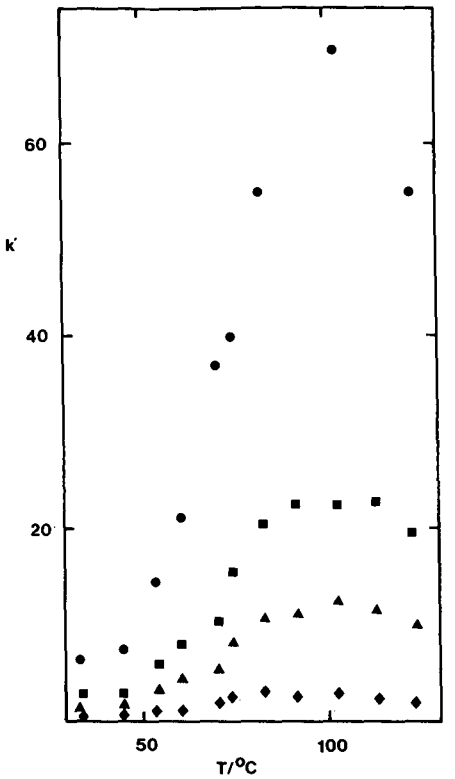

Fig. 3. Dependence of the capacity factor, k', on temperature for an ODS column and CO_2 as the mobile phase. ● = Pyrene; ■ = phenanthrene; ▲ = fluorene; ◆ = naphthalene.

Eqn. 17 can be rearranged to

$$\ln k' - \ln \phi - \ln V\mathcal{C}_{st}^{\ominus} = D - (p_c V_s + \mu_{st}^{\ominus} - \mu_m^{\ominus})/RT \tag{18}$$

where

$$D = \ln r + \ln (p_c/p^{\ominus}) \tag{19}$$

is a constant at constant pressure. The terms $\mu_{st}^{\ominus} - \mu_m^{\ominus}$ are equal to the standard Gibbs function change for solution of the solute from the vapour to the stationary phase, which can be expressed in terms of the entropy, $\Delta S_s^{\ominus}$, and enthalpy, $\Delta H_s^{\ominus}$ components. Eqn. 18 becomes

$$\ln k' - \ln \phi - \ln V\mathcal{C}_{st}^{\ominus} = D + \Delta S_s^{\ominus}/R - (p_c V_s + \Delta H_s^{\ominus})/RT \tag{20}$$

If it can be assumed that the enthalpy and entropy changes are not very sensitive to temperature, a graph of the left side of eqn. 20 against $1/T$ should give an approximately straight line.

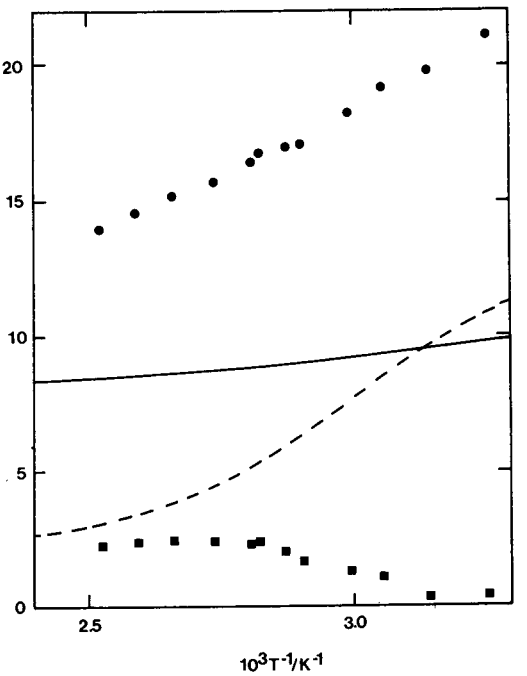

Fig. 4. Contributions to ($\ln k' - \ln Vc_{st}^{\ominus} - \ln \phi$) for fluorene as a function of reciprocal temperature. ■ = $\ln k'$; ——— = $-\ln Vc_{st}^{\ominus}$; - - - - = $-\ln \phi$; ● = ($\ln k' - \ln Vc_{st}^{\ominus} - \ln \phi$).

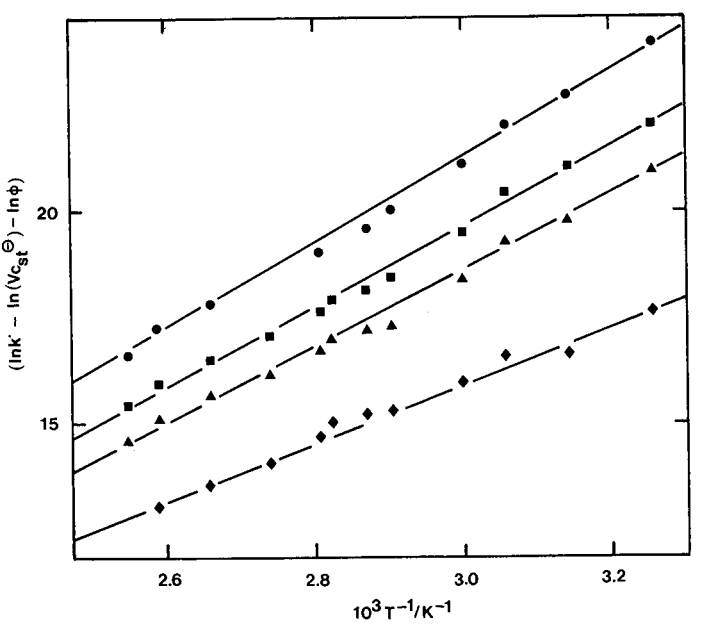

Fig. 5. Plots of ($\ln k' - \ln Vc_{st}^{\ominus} - \ln \phi$) *versus* reciprocal temperature. ● = Pyrene; ■ = phenanthrene; ▲ = fluorene; ◆ = naphthalene.

Fig. 4 shows the calculation of the left side of eqn. 20 for fluorene, with the curve in the experimental points becoming an approximately straight line as the terms in V and especially ϕ are added. Fig. 5 shows the final curves for the four polynuclear hydrocarbons, from the slopes of which values for $\Delta H_s^{\ominus}$ are obtained and given in Table I. These are compared in the table with enthalpies of vaporisation of the solid solutes[25], and there is agreement within experimental error, indicating that the enthalpies of solution of the solid solutes in the stationary phase are small.

The success of this analysis, with data obtained from solubilities, indicates the validity of the assumptions made in the thermodynamic derivations for these particular systems and confirms the strong relationship between retention and solubility. In particular, it shows that for an ODS column the stationary phase does not appreciably change its solvation properties towards these solutes, either with temperature or with supercritical fluid density.

TABLE I

VALUES OF $\Delta H_s^{\ominus}$, THE ENTHALPIES OF SOLUTION FROM THE VAPOUR INTO THE ODS PHASE, OBTAINED FROM FIG. 5, COMPARED WITH THE ENTHALPIES OF VAPOURISATION OF THE SOLID, $\Delta H_v^{\ominus}$ (REF. 25)

	$-\Delta H_s^{\ominus}/kJ\ mol^{-1}$	$\Delta H_v^{\ominus}/kJ\ mol^{-1}$
Naphthalene	70 ± 3	70
Fluorene	82 ± 3	83
Phenanthrene	87 ± 2	87
Pyrene	95 ± 3	94

DIRECT INVESTIGATION OF THE RELATIONSHIPS $S = 1/k'$ AND $C = A \exp(B/T)$ FOR SOME SYSTEMS

The relationship $S = 1/k'$

In this section direct experimental tests of the inverse relationship between the solubility and capacity factor for both SFC and HPLC are described. These results are representative of a more extensive study[26], in which the same type of ODS column was used as before, but of shorter length (10 cm) to reduce the pressure drop. The polyaromatic hydrocarbons, naphthalene, fluorene, anthracene, pyrene and chrysene, were used as the solutes with the same column throughout for both types of mobile phase. CO_2 was used as the mobile phase in the SFC measurements at pressures for which published solubility data for the solutes in CO_2 are available. For the HPLC measurements mixtures of methanol and water were used as the mobile phase and solubilities of the solutes in the same methanol–water mixtures were also measured by UV absorption. The systems chosen constitute a severe test of the inverse relationship. Polyaromatic hydrocarbons tend to associate in a hostile polar environment, which could have a large effect on their activity coefficients, even at low concentrations. At the same time, the environment of the stationary phase covers a wide range from the non-polar pressurised CO_2 fluid to a polar liquid the dielectric constant of which will vary markedly with composition.

As k' is related to retention volumes for the solute and mobile phase, V_R and V_M, respectively, by $k' = (V_R - V_M)/V_M$, a test of the relationship $k' = C/S$ is therefore the linearity of plots of $1/S$ against $(V_R - V_M)$. It is better to use these plots rather than plots of S *versus* $1/(V_R - V_M)$, because the estimated errors in $(V_R - V_M)$ contain a constant element and their percentage errors increase as the values fall.

Some results for naphthalene are shown in Fig. 6. Because of the wide range of values, two plots are given with different scales to show the low and high values. (The alternative of a log–log plot is a less obvious test of linearity.) The lines drawn on both parts of the figure have the same slope and correspond to a value for $S(V_R - V_M)/mg$ of 35. In spite of deviations due in part to experimental error, the figure is a remarkable display of linearity, in view of the fact that the data cover a range of 2.5 orders of magnitude, two different types of mobile phase or solvent, and a wide range of solvent polarity. The major deviations from the straight line may be explained as follows. The highest point arises from a very low supercritical fluid solubility which may be less

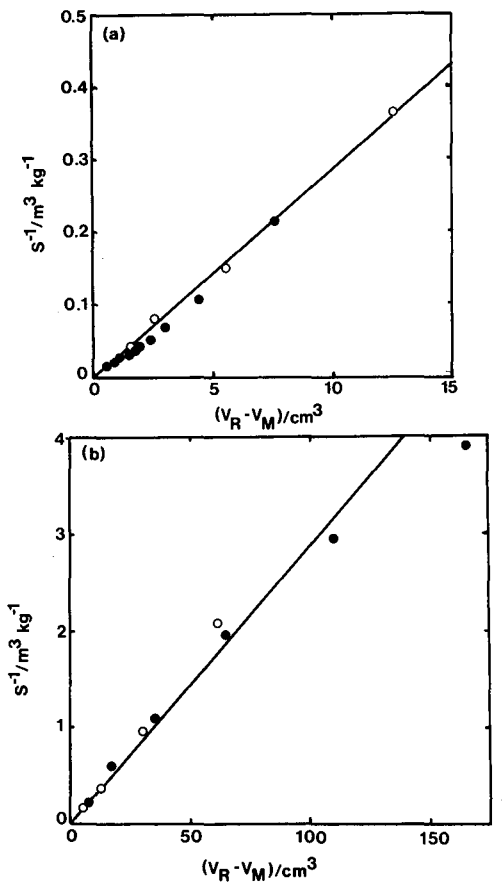

Fig. 6. The reciprocal solubility, $1/S$, plotted against $V_R - V_M$ for naphthalene at 318.2 K. ○ = Liquid; ● = supercritical fluid. Lower and higher values are shown in (a) and (b), respectively and the lines drawn in the two parts are of the same slope equal to 1/35.

accurate in percentage terms than the other values. The SFC points which lie below the curve in Fig. 6a are from low retention volumes which will be more erroneous. Thus, the assumptions listed in the introduction appear to be valid for these systems and, in particular, the assumption that the solvating effect of the stationary phase does not seem to be greatly affected by the nature of the mobile phase in the case of naphthalene and therefore probably in the case of the other solutes. Results at 308.2 K show similar linearity, although measurements at lower pressures were not made because of the errors introduced by the proximity of the critical point.

For the other solutes studied, the linear relationship was found to hold well for supercritical CO_2, but the plots for the methanol–water mixtures, which were sometimes curved, did not coincide with the supercritical fluid curves. An example is given for phenanthrene in Fig. 7. This can be explained as follows. In supercritical fluids, because calculations based on equations of state indicate that activity coefficients in supercritical fluids do not change markedly with concentration over the range up to the solubility limit, the inverse relationship of solubility and capacity factor holds well for all solutes. The deviations for the methanol–water mixtures are caused by molecular association (which sometimes increases with water content) reducing the activity coefficients. In conclusion, it appears that the relationship of eqn. 10 is valid in some situations, but not in others. It holds fairly well for naphthalene in both HPLC and SFC, but for the other solutes for SFC only.

The relationship $C = A \exp(B/T)$

The validity of eqn. 12 is tested in Fig. 8 for phenanthrene by plotting the natural logarithm of the mean values of the product $S(V_R - V_M) = CV_M$ at each temperature against $1/T$. The values deviate from the straight line by less than 5% of $S(V_R - V_M)$.

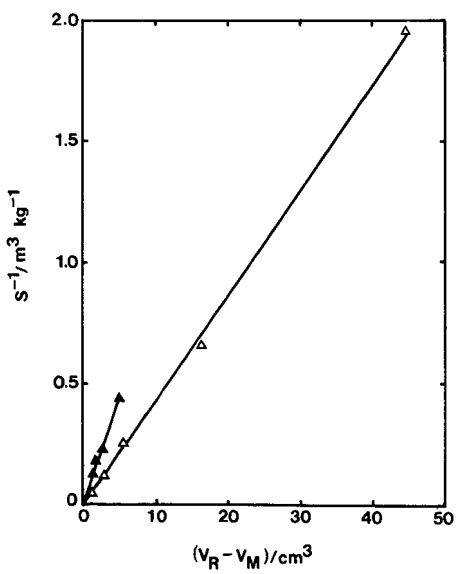

Fig. 7. The reciprocal solubility, $1/S$, plotted against $V_R - V_M$ for phenanthrene at 318.2 K. △ = Liquid; ▲ = supercritical fluid.

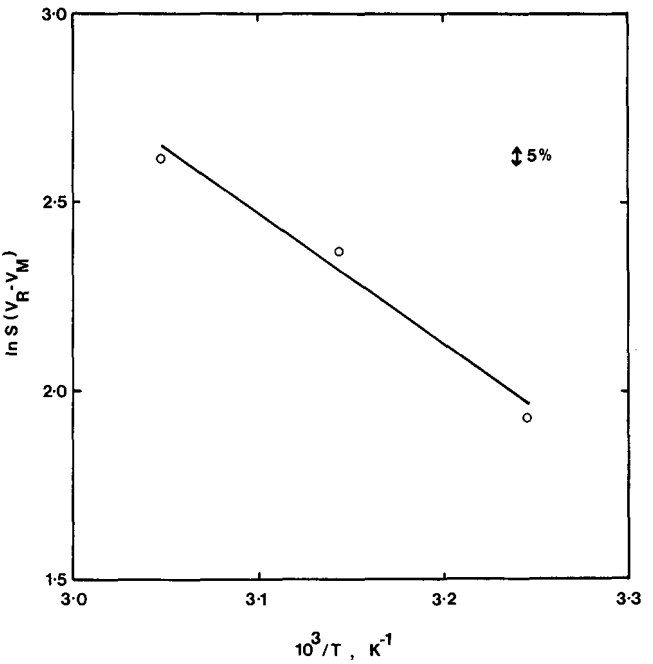

Fig. 8. Plot of ln $S(V_R - V_M)$ *versus* reciprocal temperature for phenanthrene.

The slope of the line corresponds to a standard enthalpy of solution (absorption) into the ODS stationary phase of 23 kJ mol^{-1}. This compares with enthalpy of fusion for phenanthrene of 19 kJ mol^{-1}. Although further tests of this relationship would be desirable, consistency with eqn. 12 is observed.

METHODS OF MEASURING SOLUBILITIES FROM RETENTION VALUES

Solubilities in liquids especially liquid mixtures using HPLC

The systems with liquid solvents, studied above, do not obey the inverse relationship well in all cases for perhaps predicable reasons. For this reason, solubilities in water, calculated from retention data, are described as ideal solubilities[5]. However, given the success with the unpromising naphthalene–water–methanol system, it is likely that there will be many systems of solutes and (particularly non-polar) solvents where it will be obeyed quite accurately. The relationship could therefore in many cases provide a method for generating rapidly a large body of solubility data, particularly for multicomponent solvent mixtures. The procedure would be to make by a relatively small number of direct solubility measurements with corresponding retention measurements at certain temperatures to establish linearity and obtain the constants C or A and B. A large number of retention measurements could then be made to generate solubility data.

Solubilities in supercritical fluids at low pressures using SFC and vapour pressures

If retention measurements are made in SFC which extend down to lower (subcritical) pressures, it may be possible to extrapolate k' to obtain a value, k'_0, corresponding to zero mobile phase pressure. The corresponding "solubility", S_0, will arise from the vapour pressure and will be equal to p_v/RT. Thus the constant C can be obtained from

$$C = k'_0 \, p_v/RT \tag{21}$$

The method of extrapolating k' is obtained by first writing eqn. 18 for the condition of zero mobile phase pressure, where since ϕ and p_c are essentially unity and zero, respectively, and $V = RT/p_v$, it becomes

$$\ln k'_0 - \ln (RTc^{\ominus}_{st}/p_v) = \ln r + \ln (p_v/p^{\ominus}) - (\mu^{\ominus}_{st} - \mu^{\ominus}_{m})/RT \tag{22}$$

Subtraction of eqn. 22 from eqn. 18 and rearranging gives

$$\ln k' + p_c V_s/RT = \ln k'_0 + \ln \phi + \ln (p_c V/RT) \tag{23}$$

For extrapolation to low pressures the virial equation of state may be used to give an expression for ϕ, which is

$$\ln \phi = \ln (RT/p_c V) + (2/V)B_{12} + (2/3V^2)C_{112} + \ldots \tag{24}$$

where B_{12} and C_{112} are virial coefficients. At pressures below 5 MPa, the second virial coefficient alone is sufficient[27], and after substituting a simplified eqn. 24 into eqn. 23 we obtain

$$\ln k' + p_c V_s/RT = \ln k'_0 + (2/V)B_{12} \tag{25}$$

This equation shows that k'_0 can be obtained by extrapolating the left-hand side of eqn. 25 against $1/V$, from which the second mixed virial coefficient can also incidentally be obtained.

Retention measurements have been made to show the feasibility of the method, and results for 1-methylnaphthalene in CO_2 are reported here. The column used was an open stainless-steel tube, 0.5 m × 0.5 mm I.D. Solubility results are shown in Fig. 9 and compared to results obtained by freezing a known volume of saturated solution in liquid nitrogen, allowing the CO_2 to evaporate and measuring the amount of solute by gas chromatography. The solubilities, measured directly at the lowest pressures, where little solute was recovered, are accurate to only around 50% and the values obtained from retention appear to be superior.

Generation of a larger body of supercritical solubility data from a small number of data at the same temperature

If, in principle one solubility, or better a few solubililty results, obtained by conventional methods, are available at one temperature, a value for the constant C can be obtained at that temperature by making retention measurements under corre-

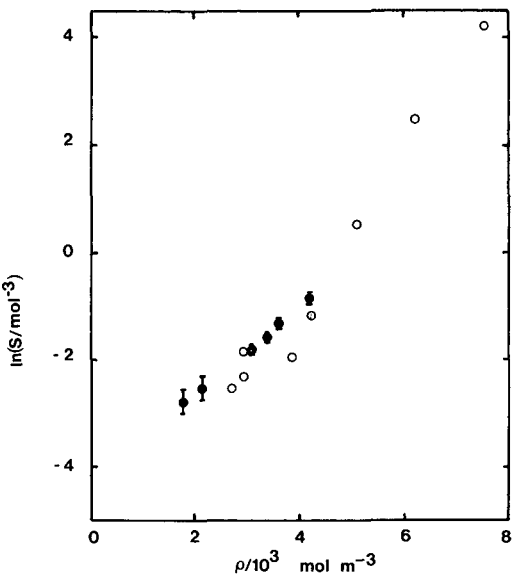

Fig. 9. Solubility, S, of 1-methylnaphthalene in CO_2 *versus* density, $\rho = 1/V$. ● = Retention results; ○ = trapping results.

sponding conditions. This value can then be used to generate a larger body of data relatively rapidly, by making a large number of retention measurements. The supercritical data shown in Fig. 7 were used to determine C for phenanthrene in an ODS column at 318 K. In fact the second lowest point was not used as this gave a constant out of line from those obtained from the other three points. From the average value of C from the other three points and further retention measurements a large number of solubilities were obtained and shown in Fig. 10 in terms of mole fraction (the square solid points). Also shown are the conventionally measured values as open squares, which naturally fall on the same line except for the point which was not used in the calculation of C. (This is an indication that this published datum point could be in error.) The procedure described was also carried out at 308 and 328 K, in these cases by using all the published solubilities, and the results are also shown in Fig. 10.

Measurement of supercritical solubilities at a temperature close to other temperatures where solubility data are available

If conventially measured solubility data are not available at the temperature of interest, but are at two or more close temperatures, interpolation of ln C *versus* $1/T$ may be used to obtain C at the required temperature. An example is given here, where the proportionality constant has been obtained for phenanthrene in CO_2 at 323 K from the plot shown in Fig. 8. The results obtained by this method are given as the solid triangles in Fig. 10.

Measurement of solubilities in modified supercritical fluids

The use of modified supercritical fluids, such as by the addition of some

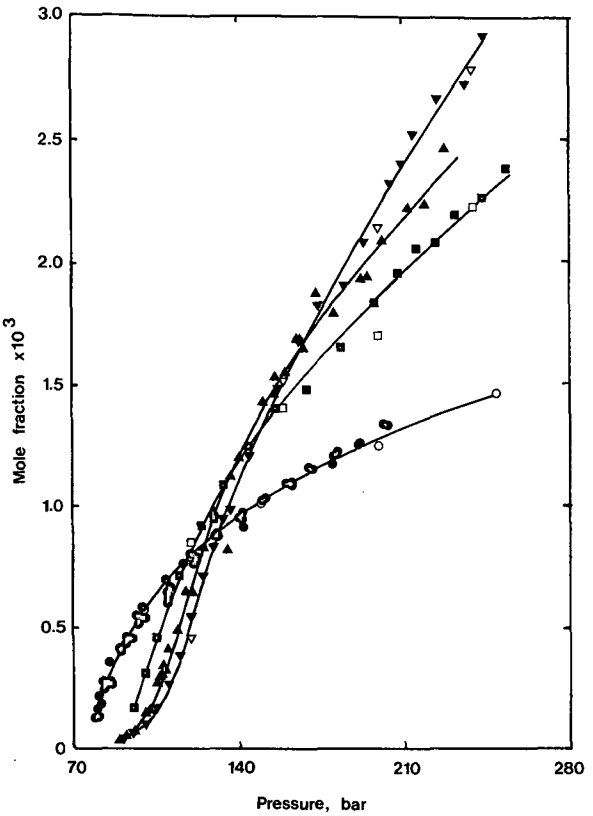

Fig. 10. Solubility of phenanthrene in supercritical carbon dioxide. Present work: ● = 308.2 K; ■ = 318.2 K; ▲ = 323.2 K; ▼ = 328.2 K. Dobbs *et al.*[18]: ○ = 308.2 K. Kurnik *et al.*[19]: □ = 318.2 K; ▽ = 328.2 K.

methanol to CO_2, adds another dimension to the range of conditions to be covered, and relatively little published data are available. The use of chromatography could be of great advantage here as in many systems values of C obtained for the pure fluids would be applicable to the modified fluids. Of course, this would have to be tested for representative systems, including the effect of the modifier on the solvating properties of the stationary phase.

Measurement of supercritical fluid solubilities from SFC, HPLC and liquid solubility measurements

The most promising use of the relationship is perhaps the fact that supercritical fluid solubilities could in the right circumstances be obtained from SFC and HPLC retention measurements and the more easily measured liquid solubilities. No results are published for this method, although in principle the results obtained for naphthalene and given in Fig. 6 could be used to obtain supercritical solubilities. However, as so many data are available for the naphthalene–carbon dioxide system, this would not be worthwhile. It seems likely, though, that the method would work for

many systems, even for the polynuclear hydrocarbons, if the chromatography were carried out in normal- rather than reversed-phase mode (*e.g.* with an amino-bonded column and a non-polar solvent, such as hexane). It is possible, perhaps likely, that the relationship given in eqn. 10 would hold for both SFC and HPLC. Where the method could be used, it would be considerably easier and quicker than the convential methods for supercritical fluid solubilities.

ACKNOWLEDGEMENTS

The authors would like to thank the Science and Engineering Research Council, British Gas and the Royal Society of Chemistry for financial support and Dr. T. Boddington for discussions.

REFERENCES

1 R. D. Smith, H. R. Usdeth, B. W. Wright and C. R. Yonker, *Sep. Sci. Tech.*, 22 (1987) 1065.
2 J. H. Phillips and R. J. Robey, *J. Chromatogr.*, 465 (1989) 177.
3 B. O. Brown, A. J. Kishbaugh and M. E. Pautaitis, *Fluid Phase Equilibria*, 36 (1987) 247.
4 T. L. Hafkenscheid and E. Tomlinson, *J. Chromatogr.*, 218 (1981) 409.
5 S. H. Yalkowsky and S. C. Valvani, *J. Pharm. Sci.*, 69 (1980) 912.
6 M. Novotny and P. David, *J. High Resolut. Chromatogr. Chromatogr. Commun.*, 9 (1986) 647.
7 J. Shim and K. P. Johnston, *AIChE J.*, 35 (1989) 1097.
8 J. R. Strubinger and J. F. Parcher, *Anal. Chem.*, 61 (1989) 951.
9 D. E. Martire, *J. Chromatogr.*, 461 (1989) 165.
10 K. D. Bartle, T. Boddington, A. A. Clifford and G. F. Shilstone, *J. Chromatogr.*, 471 (1989) 347.
11 D. Y. Peng and D. B. Robinson, *Ind. Eng. Chem. Fundam.*, 15 (1976) 59.
12 M. McHugh and M. E. Paulaitis, *J. Chem. Eng. Data*, 25 (1980) 326.
13 Yu. V. Tsekhanskaya, M. B. Iomtev and E. V. Mushkina, *Russian J. Phys. Chem. (Engl. Transl.)*, 38 (1964) 1173.
14 J. S. Haselow, S. J. Han, R. A. Greenkorn and K. C. Chao, in K. C. Chao and R. Robinson (Editors), *Equations of State Theories and Applications* (*ACS Symposium Series*, No. 300), American Chemical Society, Washington, DC, 1986, Ch. 7.
15 H. Yamato, F. Kanegae, K. Mishima, Y. Iwai and Y. Arai, *Mem. Fac. Eng., Kyushi Univ.*, 47 (1987) 95.
16 K. D. Bartle, A. A. Clifford and G. F. Shilstone, *J. Supercritical Fluids*, 2 (1989) 30.
17 K. P. Johnston, D. H. Ziger and C. A. Eckert, *Ind. Eng. Chem. Fundam.*, 21 (1982) 191.
18 J. M. Dobbs, J. M. Wong and K. P. Johnston, *J. Chem. Eng. Data*, 31 (1986) 303.
19 R. T. Kurnik, S. J. Holla and R. C. Reid, *J. Chem. Eng. Data*, 26 (1981) 47.
20 J. Kwiatkowski, Z. Lisicki and W. Majewski, *Ber. Bunsenges. Phys. Chem.*, 88 (1984) 865.
21 E. Klesper and D. Leyendecker, *Int. Lab.*, 17 (1985) 18.
22 T. L. Chester and D. P. Innis, *J. High Resolut. Chromatogr. Chromatogr. Commun.*, 8 (1985) 561.
23 C. R. Yonker, R. W. Gale and R. D. Smith, *J. Phys. Chem.*, 91 (1987) 3333.
24 K. D. Bartle, A. A. Clifford, J. P. Kithinji and G. F. Shilstone, *J. Chem. Soc., Faraday Trans. 1*, 84 (1988) 4487.
25 R. C. Weast (Editor), *CRC Handbook of Chemistry and Physics*, CRC Press, Boca Raton, FL, 62nd ed., 1981, p. C690.
26 K. D. Bartle, A. A. Clifford and S. A. Jafar, *J. Chem. Soc., Faraday Trans.*, 86 (1990) 855.
27 I. K. Barker, K. D. Bartle and A. A. Clifford, *Chem. Eng. Commun.*, 84 (1988) 4487.

Journal of Chromatography, 517 (1990) 477–489
Elsevier Science Publishers B.V., Amsterdam

CHROMSYMP. 1939

Element-selective detection after supercritical fluid chromatography by means of a Surfatron plasma in the near-infrared spectral region

DEBRA R. LUFFER and MILOS NOVOTNY*
Department of Chemistry, Indiana University, Bloomington, IN 47405 (U.S.A.)

ABSTRACT

A microwave-induced plasma, known as the Surfatron, is evaluated as a detector for supercritical fluid chromatography. The spectral range that is investigated is the near-infrared region because of its relative freedom from many spectral interferences, compared to the UV and visible regions. A novel method of heating the column restrictor is described, which is compatible with the very limited space and inaccessibility of the discharge tube configuration in the Surfatron cavity. Sensitivities and selectivities are determined for sulfur, chlorine, and bromine, using both a carbon dioxide and a nitrous oxide mobile phase. The detector is also evaluated in the "universal detection" mode by monitoring the carbon line when a nitrous oxide mobile phase is used. An application is demonstrated through the analysis of a mixture of sulfur-containing pesticides.

INTRODUCTION

During the 1980s, supercritical fluid chromatography (SFC) has gradually realized its potential, as predicted by the pioneering studies of Klesper *et al.*[1], Sie and Rijnders[2,3], and Giddings and co-workers[4–6]. The detection scope of this method had been significantly expanded by the adaptation of "gas chromatography (GC)-like" detectors, primarily because of the advantages inherent in small-bore SFC, both in capillary and packed column systems[7,8]. The flame-based detectors have proven to be a key to both the universal detection (*i.e.*, flame ionization detection, FID), and element-selective measurements, such as the flame photometric detection (FPD)[9–11] and thermionic detection (TID)[12–15] principles. A major drawback of both of these detectors is that they are limited to certain specific elements, and therefore lack versatility. For example, an unsuccessful attempt was made[16] to modify TID for selective detection of elements, such as B, Cl, and S. However, electron-capture detection (ECD) was recently successfully coupled with capillary SFC for the detection of halogenated and nitro compounds[17].

0021-9673/90/$03.50

Alternatively, consideration of plasma-based devices appears logical due to their increasing technological availability. In principle, the selectivity of plasma detectors should be adjustable to various elements simply by "dialing in" the wavelength by either scanning a monochromator, or selecting an appropriate filter. In addition, these detectors are believed to be less prone to concomitant spectral interferences than the flame-based detectors. For this reason, plasma detection has been investigated in our laboratory[18,19], and, more recently by Skelton *et al.*[20]. Both of these systems exploited the near-infrared spectral region because it is especially suitable for non-metal detection, due to a limited number of molecular bands such as CO and C_2 acting as spectral interferences[21].

Skelton *et al.*[20] adapted radio-frequency plasma detection (RPD) for the detection of sulfur and chlorine, with both CO_2 and N_2O mobile phases; detection limits ranged from 50 to 300 pg/s. Luffer *et al.*[18] evaluated the Surfatron microwave plasma detector for sulfur and a CO_2 mobile phase. The Surfatron had been developed and investigated by others for GC[22–24], and recently, a thorough spectroscopic investigation was performed on a He–CO_2 Surfatron plasma; detection limits of 6.3 ng were found for sulfur in the visible region [S(II), 545.3 nm][25].

Based on these results, it seemed promising to evaluate the Surfatron further in the near-infrared region, with respect to the detection of non-metals other than sulfur, such as Cl and Br. In addition, it was suggested[19] that N_2O might be a better choice than CO_2 because it was thought to produce fewer troublesome molecular bands than CO_2, and universal detection possibilities were available through the use of a carbon wavelength channel. The present work summarizes the results of these continued studies, and reports sensitivities and selectivities for S, Cl, and Br. In addition, a pesticide mixture is separated and compared to a similar analysis by SFC–TID[12].

EXPERIMENTAL

Chromatographic equipment

Most of the system has been described previously[18,19]. The changes that have been made will be noted below.

In addition to the SE-30 stationary phase, a different column was used in the analysis of the pesticide mixture (SB-Cyanopropyl-50, Lee Scientific, Salt Lake City, UT, U.S.A.); this 10 m × 50 μm I.D. column contained a 0.15-μm film of a 50%-substituted cyanopropyl methylpolysiloxane. The restrictors were of the frit type, obtained from Lee Scientific.

The circulating bath (Haake Buchler, Saddle Brook, NJ, U.S.A.) that replaces the column oven was filled with Therminol 6, a heat-exchange fluid (Monsanto, St. Louis, MO, U.S.A.). All unions were purchased from Scientific Glass Engineering (SGE, Austin, TX, U.S.A.). The gases were CO_2 and N_2O of supercritical fluid grade from Scott Specialty Gases (Plumsteadville, PA, U.S.A.).

The injection volume was 60 nl (without split), which ensured improved quantitation. A 60 cm × 50 μm I.D. fused-silica capillary was used as a retention gap; the capillary was positioned as close to the injection rotor as possible at one end, and connected to the column at the other end. With this configuration, no overloading of the column was noted and the solvent peak did not exhibit significant tailing.

Spectroscopic system

The Surfatron was constructed by our departmental machine shop according to the design of Abdallah *et al.*[26]. The microwave generator was a Microtron 200 operating at 2450 MHz (Electro-Medical Supplies, Wantage, U.K.). Typical powers used ranged from 110 to 120 W. Since the spectroscopic system was designed for the near-infrared region, a glass lens of 50 mm diameter and 180 mm focal length was used to focus the axial (end-on) image of the plasma with a magnification of 1.2 on the variable entrance slit of the HR-320 monochromator (Instruments, SA, Metuchen, NJ, U.S.A.). The height of the slit was adjusted to match the diameter of the plasma image. The holographic grating was blazed 1 μm and had 1200 grooves/mm. The R632 photomultiplier tube (PMT) from Hamamatsu (Middlesex, NJ, U.S.A.) was biased at -1400 V by a power supply (Products for Research, Danvers, MA, U.S.A.) and mounted in a thermoelectrically-cooled housing (Products for Research). The output from the PMT was converted by a picoammeter (Keithley Instruments, Cleveland, OH, U.S.A.). A 4-pole filter, constructed in-house, was used to filter high-frequency noise by setting the cut-off to 0.5 or 1 Hz. Data were collected on a strip chart recorder.

The helium gas was high-purity (Air Products, Tamaqua, PA, U.S.A.). The model compounds used to evaluate the system (Fig. 1) were obtained from Aldrich (Milwaukee, WI, U.S.A.).

The apex of each emission line was found by scanning the wavelength region with a stepper motor controller (Instruments, SA). A volatile compound containing the element of interest was bled into the plasma by way of a headspace sampling device[27]. In order to simulate the operating conditions of the system, the appropriate mobile phase gas was doped into the headspace vapor mixture during the scans. The color of the plasma was indicative of the content of the mixture; *i.e.*, a helium-only plasma was pink-orange, a helium–carbon dioxide plasma was blue-green, and a helium–nitrous oxide plasma was purple-pink. These colors agree with those noted for a He-RPD[20].

Development of a heated interface

The original interface between SFC and microwave-induced plasma consisted of pre-heating the helium and passing the effluent plus support gas through the aperture of a small nozzle inserted in the discharge tube[18]. However, it was determined that, due to the low heat capacity of helium and the low flow-rate of gas, the helium was losing most of the heat by the time it arrived at the tip of the restrictor. The direct consequences of insufficient heating of the restrictor are condensation of the mobile phase and detector "spiking", caused by condensed effluent erratically spurting into the plasma. Work with other SFC detectors has indicated that a restrictor temperature

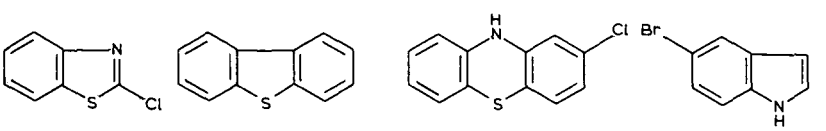

1 2 3 4

Fig. 1. Model solutes used, and their respective molecular weights. 1 = 2-Chlorobenzothiazole, 170 g/mol; 2 = dibenzothiophene, 184 g/mol; 3 = 2-chlorophenothiazine, 234 g/mol; 4 = 5-bromoindole, 196 g/mol.

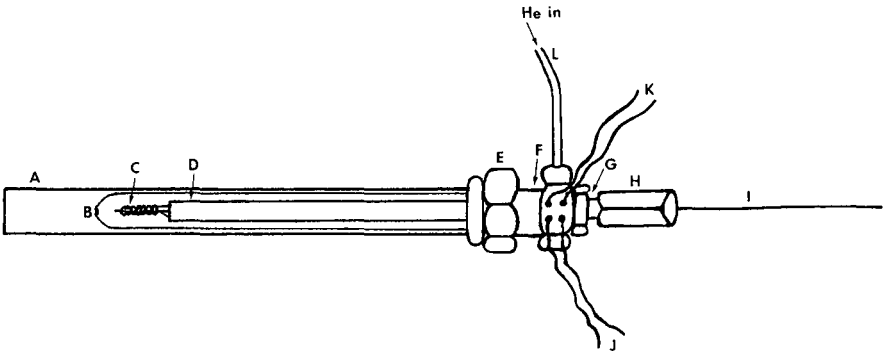

Fig. 2. Schematic diagram of the restrictor heating device (not to scale). A = Quartz discharge tube, 4 mm I.D.; B = quartz nozzle insert, 3 mm I.D.; C = heating coil, 1 cm long, and coated with high-temperature cement; D = ceramic insulating tube with 4 holes; E = Swagelok 1/4-in. nut wit PTFE ferrule; F = Swagelok 1/4-in. reducing union; G = SGE 1/16-in. male nut silver-soldered to union F; H = SGE 1/16-in. female nut with Vespel ferrule; I = frit restrictor sleeved through and terminating at C; J = fine gage thermocouple wires exiting F; K = heater wires exiting F; L = 1/16-in. stainless-steel tubing silver-soldered into F.

of at least 300°C is warranted. This minimum operating temperature is also required for the elution of high-molecular-weight analytes. A suggested means of overcoming the heating problem was to increase the mass flow-rate of helium as it passes through an intensely heated length of stainless-steel tubing situated right at the tip of the restrictor. Unfortunately, this attempt was unsuccessful because the plasma does not operate optimally at very high helium flow-rates, and the maximum temperature that could be reached was still only 175°C.

A different approach that was taken involved the coating of the restrictors with a solution of gold in an organic matrix (Liquid Bright Gold), in a manner described elsewhere[28]. The goal was to attach electrical leads of small dimensions directly to this gold coating, however, the connection proved to be too difficult due to the fragility of the restrictor configuration.

The successful design is based upon the construction of a very small wire coil that is resistively heated, in a manner very similar to that utilized by Reinhold *et al.*[29] for direct chemical ionization in SFC–mass spectrometry. The entire assembly is shown schematically in Fig. 2. The coil was prepared by wrapping a length of No. 34 copper–nickel wire (Wilbur Driver, Newark, NJ, U.S.A.) around a post of slightly larger diameter. The strand of wire was doubled, wrapped in one direction for about 1 cm, and then wrapped in the opposite direction until returning to the point of origin. The wire assembly is then removed from the post on which it was wound, producing a coil consisting of two very closely wound layers that becomes a region of very high current density when heated. The wire also possesses a high temperature (260°C maximum) enamel coating, which allows the tightly wound coil to be resistively heated without shorting out; however, the temperature range of the heating coil assembly was targeted to be greater than 300°C. This problem was surmounted by conditioning the coil with slow increments to the applied voltage, which allows the gradual formation of a protective oxide layer capable of sustaining the higher temperatures.

The wire leads of the coil were subsequently threaded through 2 of the 4 holes (1/64 in. diameter) of a ceramic rod (1/16 in. O.D.) made of Omegatite 200 (Omega Engineering, Stamford, CT, U.S.A.) (D in Fig. 2). The leads of an unsheathed fine gauge (0.005 in. diameter) Chromel-Alumel thermocouple (Type K, Omega Engineering) are threaded through the other two holes of the rod. The exit holes for the four wires were drilled through a nut in the assembly (F in Fig. 2), so that the connections can be made far from the area of intense heating. The restrictor is sleeved through one of the four holes and exists just past the end of the coil. It is held firmly in place by an SGE nut and ferrule at the back of the assembly (H in Fig. 2). The ceramic rod is sleeved through a small plug of PTFE (not shown in schematic) that has a hole (1/16 in. diameter) drilled through its side. The PTFE plug (1/8 in. diameter) is placed sideways in the nut and wedged firmly in place, which centers the ceramic rod in the quartz tube (William A. Sales, Wheeling, IL, U.S.A.) while allowing the passage of helium gas around it. A quartz nozzle insert surrounds the coil and rod, as shown in Fig. 2.

Temperature stability of the coil was improved by coating it and the junction of the thermocouple with a high temperature cement (Omega Engineering) and letting it cure for 24 h. A typical coil that is being swept by 300 ml/min of helium easily attains 320°C, requiring only 1.0 A and 13 V from a d.c. power supply. The high flow of mobile phase through the restrictor does not lower the temperature of the coil device, although the helium support gas flow exterts a dramatic effect. Monitoring the temperature at the tip of the coil was accomplished by connecting the leads from the thermocouple to a digital volt meter, which typically reads 12 mV for a temperature of 320°C.

A coil assembly, once conditioned, can last indefinitely, unless a high-voltage spark from a Tesla coil causes it to short out. For this reason, the plasma was ignited by inserting a length of copper wire a short distance into the discharge tube in order to seed the plasma with electrons. This method is superior to the tungsten wire method previously used[18,19] because the latter leaves a substantial oxide film on the walls of the discharge tube, whereas copper does not.

It may seem surprising that a resistively heated wire coil placed approximately 2 cm from the plasma discharge does not disrupt or degrade the performance of the plasma. However, the additional insulating effects of the quartz inner nozzle and the high-temperature cement coating appear to be sufficient to prevent any problems. The main consequence of including the heating device is a stabilization of the plasma discharge because of the elimination of condensation of mobile phase at the tip of the restrictor, and therefore, a less "noisy" introduction of the heated effluent into the plasma.

It should be noted that this heating device is superior to simply inserting the restrictor into the plasma, as seen in other studies[20], because the temperature at the tip of the restrictor is known, stable, and damage to the frit material is virtually impossible. In addition, the very small size of the assembly (< 3 mm O.D.) makes it useful in any type of application where space and accessibility are limiting factors.

RESULTS AND DISCUSSION

It was ascertained in our earlier work[18] that the quartz nozzle inserted into the discharge tube was essential for high-sensitivity detection of sulfur due to the

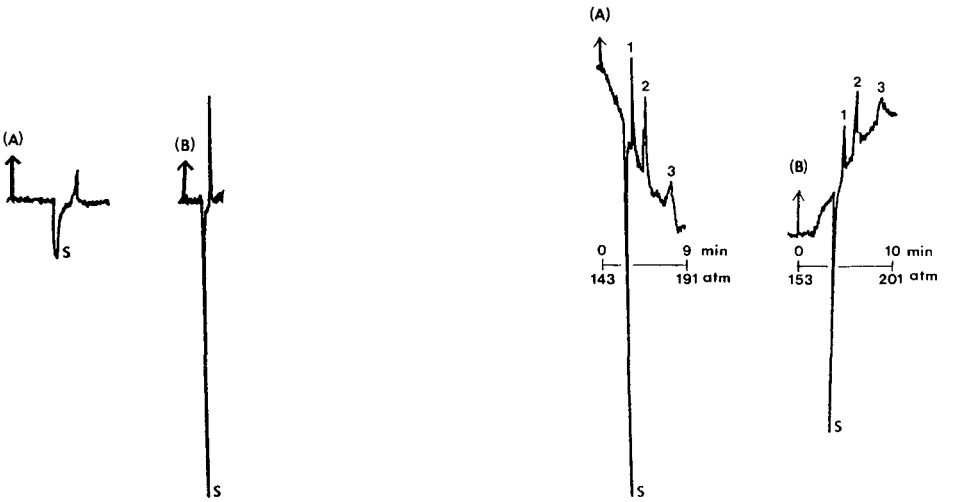

Fig. 3. Sulfur-selective detection of 2-chlorobenzothiazole and methanol solvent (denoted by S). (A) Without nozzle; (B) with nozzle.

Fig. 4. Variation of baseline as a function of helium support gas flow for the separation of compounds 1, 2, and 3 (Fig. 1) using S(I) line and CO_2 mobile phase at 130°C. Helium flow-rate: (A) 100 ml/min; (B) 300 ml/min.

"focusing" of effluent into the plasma. In the present study, however, the use of the heating element directly on the frit restrictor was thought to produce a similar effect, which would preclude the use of a nozzle. In order to test this hypothesis, two injections of a sulfur-containing compound in methanol were performed under identical conditions, except that in one case the nozzle was present and in the other case it was absent. Fig. 3A illustrates the effect of removing the nozzle; both the solvent and solute peaks are severely reduced in intensity, compared to those in Fig. 3B. Hence, in all subsequent work, the nozzle insert was present, as shown in the schematic in Fig. 2.

A major impediment to the acceptance of the Surfatron as a detector for SFC applications was the sloping baseline occurring during density-programmed runs[18]. While methods of background correction were originally proposed and attempted, a simpler and more efficient manner of eliminating this effect was discovered and is illustrated by Fig. 4. A separation of model compounds was performed at a low (100 ml/min) and high (300 ml/min) flow-rate of helium. Fig. 4A exhibits the decreasing baseline that we have noted previously[18], while Fig. 4B exemplifies the opposite trend. From this information it seemed likely that an intermediate flow of helium would produce stable baseline during a density-programmed separation. A similar finding has been noted recently for RPD for SFC[20]. Once the optimum helium flow had been determined, separations were performed to illustrate the sensitivity and selectivity of different lines, initially with a carbon dioxide mobile phase. Fig. 5A illustrates such a separation using the sulfur line (921.3 nm). However, when the same separation was performed using the chlorine line at 837.6 nm, the baseline exhibited a serious decline at this helium flow-rate. Therefore, it was determined that there exists an optimum flow of helium for each line, which probably depends on the background near that line.

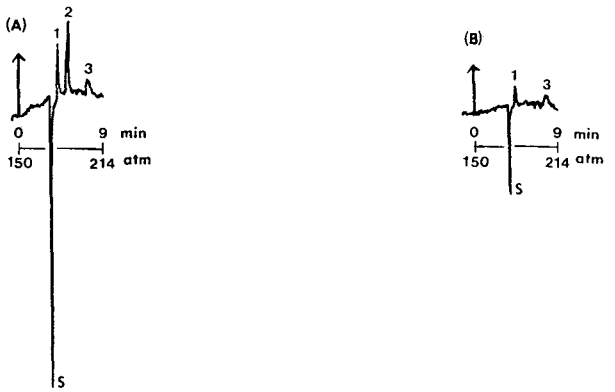

Fig. 5. Selective detection of compounds 1,2, and 3 (Fig. 1) with CO_2 at 130°C. (A) S(I) line (921.3 nm), 125-μm slits, 180 ml/min He; (B) Cl(I) line (837.6 nm), 125-μm slits, 280 ml/min He.

In addition, this optimum flow is completely different when nitrous oxide is substituted for carbon dioxide, which is further proof that the background determines the ideal support gas flow. For example, the maintenance of the level baseline shown in Fig. 5B required a much higher (280 ml/min) flow of helium than that in Fig. 5A (180 ml/min). The other point to note concerning this separation is the absence of peak 2 in Fig. 5B, which illustrates the good selectivity of this line since this compound contains no chlorine atoms. No comparisons were made with the other strong chlorine line in the near-infrared (912.1 nm) because the signal-to-background and signal-to-noise ratios were rather poor.

Evaluation of the system was repeated using a nitrous oxide mobile phase. A comparison of the sensitivity and selectivity of different lines in the near-infrared region is shown in Fig. 6. The first point of note is the positive solvent peak for methanol on all four lines. This is entirely logical in the case of the C(I) line depicted in Fig. 6A, however, it portends poor selectivity for the other lines. The existence of a large, positive solvent signal can be attributed to the intense CN-band emission throughout the near-infrared region; evidently, the carbon from methanol is combining with the abundant nitogen from N_2O to produce a large signal. The separation shown in Fig. 6D illustrates high-sensitivity sulfur detection, whereas the separations on the two chlorine lines in Fig. 6A and 6B are discouraging because of the noticeable peak in both cases for dibenzothiophene, which contains no chlorine atoms. Apparently, the CN-band emission is a significant problem when a nitrous oxide mobile phase is used because it is not possible to know how much of the signal is due to analyte emission, and how much is from carbon. This problem was found for all lines examined, except for one; Fig. 7B illustrates the elution of 5-bromoindole using the 889.8 nm line and the corresponding negative solvent peak, in contrast with the same injection using the 827.2 nm Br(I) line, with a corresponding positive solvent peak (Fig. 7A).

Sensitivities and selectivities for all these lines, in conjunction with both mobile phases, are summarized in Table I. The molar selectivities listed in Table I were calculated using naphthalene, unlike some other studies that used an alkane, such as

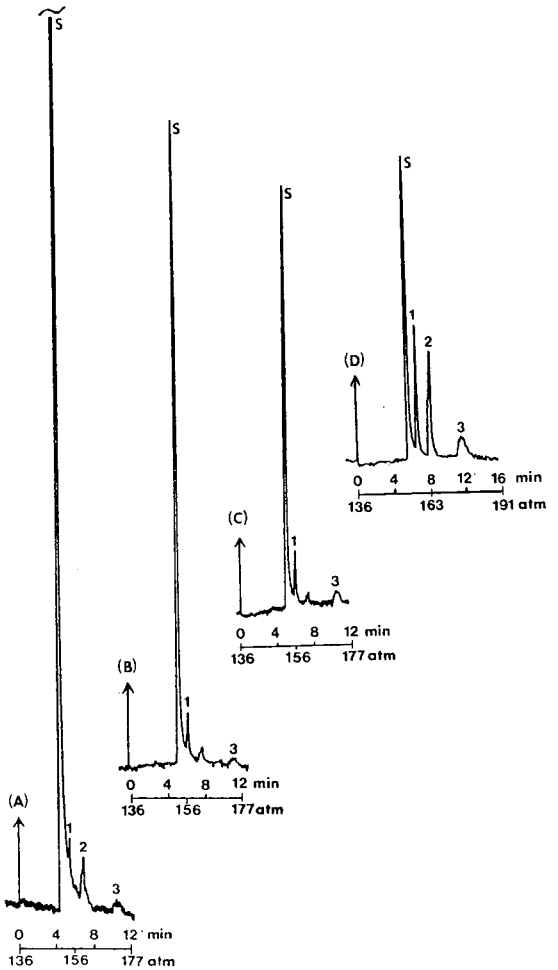

Fig. 6. Selective detection of compounds 1, 2, and 3 (Fig. 1) with N_2O at 130°C. (A) C(I) line (909.5 nm), 130-μm slits, 100 ml/min He; (B) Cl(I) line (912.1 nm), 150-μm slits, 100 ml/min He; (C) Cl(I) line (837.6 nm), 100-μm slits, 80 ml/min He; (D) S(I) line (921.3 nm), 150-μm slits, 100 ml/min He.

decane, to determine the carbon signal. This is because naphthalene should more closely approximate the shape, and therefore, the excitation and atomization of the model compounds in the plasma. In all cases, except for Br(I) at 889.8 nm and N_2O, the selectivities for N_2O were significantly poorer than for CO_2, and therefore, the detection limits determined for the former are somewhat uncertain.

As expected, the detection limits for the N_2O mobile phase were superior to the corresponding results for CO_2. The detection limits listed for sulfur and chlorine were determined using compounds 1 and 3 (Fig. 1). These results give an idea of the dependence of sensitivity on molecular weight, which seems to be consistent with the results found previously[18]. It is likely that this effect is a result of an increased amount of mobile phase entering the plasma[18,20].

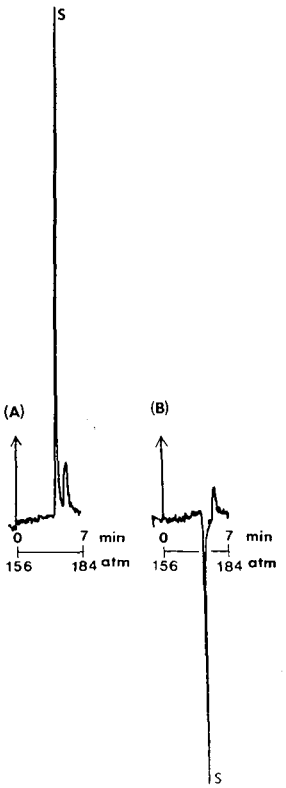

Fig. 7. Injection of 5-bromoindole in methanol, with N_2O at 130°C. (A) Br(I) line (827.2 nm), 100-μm slits, 100 ml/min He; (B) Br(I) line (889.8 nm), 125-μm slits, 80 ml/min He.

TABLE I

SENSITIVITIES AND SELECTIVITIES OF VARIOUS ELEMENTS AS A FUNCTION OF MOBILE PHASE

Mobile phase	*Element*	*Line (nm)*	*Sensitivity[a] (pg/s)*		*Molar selectivity[b]*
CO_2	S(I)	921.3	73	140	325
	Cl(I)	837.6	210	250	100
	Br(I)	827.2	780		110
	Br(I)	889.8	780		165
N_2O	S(I)	921.3	26	85	185
	Cl(I)	837.6	110	400	50
	Cl(I)	912.1	97	550	45
	Br(I)	827.2	300		20
	Br(I)	889.8	520		>500
	C(I)	909.5	550	2600	–

[a] The values listed on the left were obtained from either 2-chlorobenzothiazole or 5-bromoindole; the values on the right were obtained from 2-chlorophenothiazine.

[b] Molar selectivities were all calculated from the response of either 2-chlorobenzothiazole or 5-bromoindole over naphthalene.

In general, detection in the near-infrared region does not seem as promising as it was initially for non-metal selective detection with the Surfatron, as evidenced by the results for sulfur[18]. In addition, the potential for universal detection with the carbon line and N_2O is limited because of the high detection limits found for the strongest line in this spectral region (909.5 nm), and the decrease in sensitivity as molecular weight of the solute increases (Table I).

As an example of an application, the separation of four pesticides (Fig. 8) is illustrated. Since they contain both phosphorus and sulfur atoms, this permits a comparison with the results obtained with a thermionic detector, in the P-mode, for SFC[12]. It was determined in that study that these compounds exhibited only limited solubility in CO_2, so that only a nitrous oxide mobile phase was used. For the sake of comparison, this mixture was separated in N_2O and detected using the sulfur channel. The resultant separation is shown in Fig. 9, where the stationary phase utilized was a 50% cyanopropyl-substituted methylpolysiloxane. As expected, the sensitivity of each compound is dependent on the number of sulfur atoms in each molecule.

A point that has not yet been mentioned explicitly is that the condition of the discharge tube affects the detection limit for each element. This is because the background increases and the baseline becomes much noisier as the discharge tube ages. For this reason, a new length of tubing was used each day. The effect is exemplified by Fig. 10, where Fig. 10A shows the separation of the pesticide mixture at the end of one day, where the discharge tube is quite old and devitrified; Fig. 10B is the same separation performed the next day under identical chromatographic conditions, using a new discharge tube.

By means of comparison, the results recently reported for SFC–TID, SFC–FPD, and SFC–ECD will be briefly described here, and evaluated with respect to the SFC–Surfatron results reported in the present study.

The thermionic detector has been shown to possess very high selectivities for nitrogen and phosphorus, in conjunction with very low detection limits, *i.e.* < 2 pg/s and < 1 pg/s, respectively[12]. In addition, this detector was shown to be extremely useful for detection of biological compounds and their metabolites in physiological fluids, using CO_2 and N_2O (refs. 13–15). FPD has been characterized in the dual-flame mode[9] as well as in the single-flame mode[10,11] for a wide variety of organosulfur compounds, with corresponding high selectivity and low detection limits (8 pg/s)

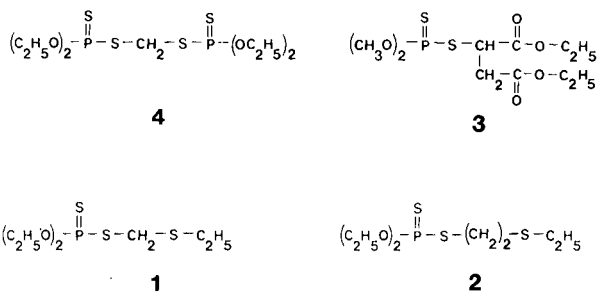

Fig. 8. Pesticides used, and their respective molecular weights. 1 = Phorate, 260 g/mol; 2 = di-syston, 274 g/mol; 3 = malathion, 330 g/mol; 4 = ethion, 384 g/mol.

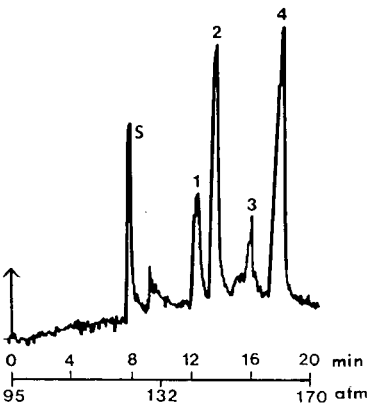

Fig. 9. Detection of four pesticides (Fig. 8) using the S(I) line and N_2O at 110°C and a cyanopropyl-substituted stationary phase.

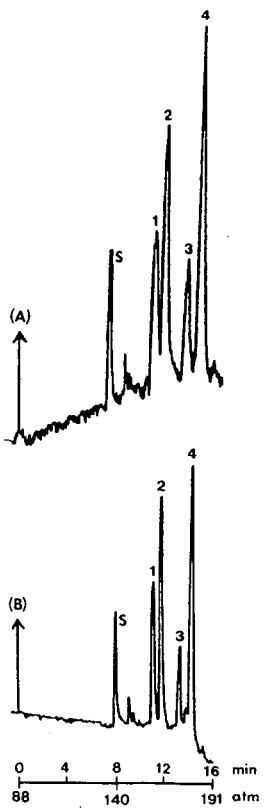

Fig. 10. Separation of four pesticides (Fig. 8) under identical conditions using N_2O at 105°C and the S(I) line. (A) Old discharge tube; (B) new discharge tube.

utilizing an improved design[11]. ECD yields detection limits of high femtograms for halogenated compounds containing chlorine and bromine[17].

The combination of SFC with the Surfatron, in the near-infrared region, demonstrates more versatility than the previous three detection methods because of a theoretically limitless selection of elements. Plasma detection is superior to FPD for the determination of sulfur because the latter suffers from a non-linear response, whereas the former is linear for all elements studied over 2–3 orders of magnitude, and the effective linear concentration range is 10^{-4}–10^{-2} M, corresponding to an unsplit 60-nl injection volume. More concentrated samples can be detected with larger injection volumes, but the calibration curve would no longer be linear in this range. However, the drawbacks of the Surfatron detector are that sensitivity suffers from a dependence on solute molecular weight, and that selectivity suffers from a dependence on the chosen mobile phase.

The cost of assembling this detection system was approximately US$ 20 000, which is not as expensive as some laser-based detectors used for LC, especially considering that the plasma detector is capable of simultaneous multielement selective detection, if equipped with a photodiode array. In addition, the detector appears useful for the detection of low nanogram quantities of compounds containing various non-metals, with simultaneous universal detection by FID, if necessary. Further investigation of other plasma sources and spectral regions appears worthwhile.

ACKNOWLEDGEMENTS

This research was supported by the National Science Foundation through Grant CHE 86-05935. The authors would like to acknowledge Robert Ensman (Electronic Instrument Services, Indiana University) and Douglas M. Sheeley (Department of Nutrition, Harvard School of Public Health, Boston, MA, U.S.A.) for invaluable suggestions in the construction of the heating device. We would also like to thank Larry Sexton in our machine shop for the construction of the Surfatron cavity, Steven R. Springston (Brookhaven National Laboratory, Upton, NY, U.S.A.) for his help in the gold-coating of restrictors, and members of Professor G. M. Hieftje's research group for helpful suggestions. D. R. L. would like to acknowledge financial support through a Doctoral Research Fellowship from the Indiana University Graduate School, and an American Chemical Society Analytical Division Full-Year Fellowship, sponsored by the DuPont Company.

REFERENCES

1 E. Klesper, A. H. Corwin and D. A. Turner, *J. Org. Chem.*, 27 (1962) 700.
2 S. T. Sie and G. W. A. Rijnders, *Sep. Sci.*, 2 (1967) 729.
3 S. T. Sie and G. W. A. Rijnders, *Sep. Sci.*, 2 (1967) 755.
4 M. N. Myers and J. C. Giddings, *Sep. Sci.*, 1 (1966) 761.
5 L. McLaren, M. N. Myers and J. C. Giddings, *Science (Washington, D.C.)*, 159 (1968) 197.
6 J. C. Giddings, M. N. Myers, L. McLaren and R. A. Keller, *Science (Washington, D.C.)*, 162 (1968) 67.
7 M. Novotny, S. R. Springton, P. A. Peaden, J. C. Fjeldsted and M. L. Lee, *Anal. Chem.*, 53 (1981) 407A.
8 Y. Hirata, *J. Chromatogr.*, 315 (1984) 39.
9 K. E. Markides, E. D. Lee, R. Bolick and M. L. Lee, *Anal. Chem.*, 58 (1986) 740.
10 L. A. Pekay and S. V. Olesik, *Anal. Chem.*, 61 (1989) 2616.
11 S. V. Olesik, L. A. Pekay and E. A. Paliwoda, *Anal. Chem.*, 61 (1989) 58.

12 P. A. David and M. Novotny, *Anal. Chem.*, 61 (1989) 2082.
13 P. A. David and M. Novotny, *J. Chromatogr.*, 452 (1988) 623.
14 P. A. David and M. Novotny, *J. Chromatogr.*, 461 (1989) 111.
15 P. A. David and M. Novotny, *Anal. Chem.*, in press.
16 P. A. David, *Ph. D. Dissertation*, Indiana University, Bloomington, IN, 1989.
17 H.-C. K. Chang and L. T. Taylor, *J. Chromatogr. Sci.*, 28 (1990) 29.
18 D. R. Luffer, L. J. Galate, P. A. David, M. Novotny and G. M. Hieftje, *Anal. Chem.*, 60 (1988) 1365.
19 L. J. Galante, M. Selby, D. R. Luffer, G. M. Hieftje and M. Novotny, *Anal. Chem.*, 60 (1988) 1370.
20 R. J. Skelton, Jr., P. B. Farnsworth, K. E. Markides and M. L. Lee, *Anal. Chem.*, 61 (1989) 1815.
21 J. E. Freeman and G. M. Hieftje, *Spectrochim. Acta*, 40B (1985) 475.
22 G. Chevrier, T. Hanai, K. C. Tran and J. Hubert, *Can. J. Chem.*, 60 (1982) 898.
23 T. Hanai, S. Coulombe, M. Moisan and J. Hubert, in R. M. Barnes (Editor), *Developments in Atomic Plasma Spectrochemical Analysis*, Heyden, London, 1981, p. 337.
24 Y. Takigawa, T. Hanai and J. Hubert, *J. High Resolut. Chromatogr. Chromatogr. Commun.*, 9 (1986) 698.
25 B. Riviere, J.-M. Mermet and D. Deruaz, *J. Anal. At. Spectrom.*, 3 (1988) 551.
26 M. H. Abdallah, S. Coulombe, J.-M. Mermet and J. Hubert, *Spectrochim. Acta*, 37B (1982) 583.
27 J. E. Freeman and G. M. Hieftje, *Spectrochim. Acta*, 40B (1985) 653.
28 S. R. Springston, *J. Chromatogr.*, 517 (1990) 67.
29 V. N. Reinhold, D. M. Sheeley, J. Kuei and G.-R. Her, *Anal. Chem.*, 60 (1988) 2719.

Journal of Chromatography, 517 (1990) 491–501
Elsevier Science Publishers B.V., Amsterdam

CHROMSYMP. 1989

Use of sulfur chemiluminescence detection after supercritical fluid chromatography

H.-C. KAREN CHANG and LARRY T. TAYLOR*
Department of Chemistry, Virginia Polytechnic Institute and State University, Blacksburg, VA 24061 (U.S.A.)

ABSTRACT

A newly developed sulfur chemiluminescence detector is evaluated for supercritical fluid chromatography (SFC). The detection chemistry for sulfur chemiluminescence detection (SCD) is based on the chemiluminescent reaction between sulfur monoxide, which is produced from the decomposition of sulfur-containing analytes in a H_2/O_2-reducing flame and ozone. Detection limits are determined to be 12 pg sulfur via capillary-column SFC–SCD. Detector linearity is three orders of magnitude, and a selectivity of at least 10^7 was obtained. Quenching of SCD signals resulting from both the supercritical-fluid mobile phase and co-eluting hydrocarbons is discussed. Separation of thermally labile pesticides, and the determination of the ethylene oxide distribution for a thioethoxylate surfactant are demonstrated.

INTRODUCTION

Specific detection of sulfur-containing compounds, such as polycyclic aromatic compounds and pesticides, is important because of their natural toxicity or mutagenicity. The separation and detection of sulfur-containing compounds has been most often accomplished with gas chromatography (GC) coupled with different sulfur-selective detectors[1,2]. In these studies, excellent separation and detection of sulfur compounds was achieved. However, many sulfur-containing compounds are difficult to analyze by GC due to either their thermal instability or their non-volatility.

Supercritical fluid chromatography (SFC) offers some advantages over GC for analytical problem solving. For example, analysis of thermally unstable and relatively non-volatile compounds which cannot be achieved in GC has been performed by SFC[3–5]. Furthermore, because SFC employs supercritical mobile phases like CO_2, which is a gas under ambient conditions, it is relatively easy to interface SFC to GC-like detectors[6]. A variety of sulfur-selective detections have been coupled to SFC, such as flame photometric detection (FPD)[7–9], surface-wave-sustained microwave-induced plasma detection (surfatron MIP)[10], radio-frequency plasma detection (RPD)[11] and fluorine-induced sulfur chemiluminescence detection (SCD)[12,13]. Good

0021-9673/90/$03.50

performance with certain limitations has been shown from each coupling.

In spite of its non-linear response to sulfur compounds, FPD is the most popular sulfur-selective detector used in GC. Detailed characterization and optimization of FPD for use after capillary SFC has been recently studied[8]. A detectivity of 8.2 pg S/s for dibenzothiophene was reported. In another study, analysis of thermally labile and relatively high-molecular-weight compounds was demonstrated using capillary SFC–FPD[9]. A detection limit of 150 pg/s (or 26 pg S/s) of dibenzothiophene was reported via a capillary SFC–surfatron MIP system[10]. Detector linearity was reported to be only two orders of magnitude and signal quenching from CO_2 was severe. However, it was reported that improved performance could be obtained if the SFC–surfatron MIP system was optimized. The element-selective RPD when operated in the sulfur mode provided detection limits ranging from 50 to 300 pg S/s depending on the mass flow of CO_2 into the detector[11]. The advantage for the surfatron MIP and RPD is that both can provide selective detection to other elements, such as chlorine, bromine and nitrogen.

Fluorine-induced SCD in which the detection chemistry is based on the gas-phase reaction of F_2 with organic sulfur compounds is probably the most sensitive sulfur-selective detector that has been reported for SFC[12,13]. A 0.72 pg S/s detection limit for dodecanethiol[13] was obtained, and a selectivity of 10^4 was observed. The fluorine-induced SCD is, however, somewhat limited in that it shows strong response only for those organic sulfur compounds that have certain structural configurations[12]. For example, a sulfur compound whose structure is represented as R_1–S–R_2, yields a very strong response if the R-groups bonded to the sulfur are hydrogen or have an alkyl group which contains hydrogen.

Recently, a new sulfur chemiluminescence detector was developed for analyzing sulfur-containing compounds[14]. Its detection principle is based on the chemiluminescence reaction of ozone gas with sulfur monoxide (SO) which is produced in a H_2/O_2-reducing flame that contains the sulfur-containing analyte. This reaction mechanism can be summarized as follows:

$$\text{S-compounds} + H_2/O_2 \rightarrow SO + \text{other products} \quad (1)$$

$$SO + O_3 \rightarrow SO_2^* + O_2 \quad (2)$$

$$SO_2^* \rightarrow SO_2 + h\nu \quad (3)$$

Reaction (2) is highly exothermic, and the energy produced is large enough to excite SO_2 at the same time. The wavelength of the emitted light ranges from 260 to 480 nm with a peak maximum at 350 nm. Unlike the fluorine-induced SCD, this ozone-induced SCD responds to all sulfur-containing compounds. Nearly equimolar response to various sulfur compounds and a selectivity (g S/g C) greater than 10^7 was observed from the GC–SCD studies[14–16]. A detection limit of 400 fg/s of sulfur was reported by Shearer *et al.*[15] In addition, it was found that the SCD sensitivity was not affected significantly by environmental CO_2 and water vapor, which are the two major interferences in FPD.

This report describes the direct interfacing of this newly developed SCD to open tubular and packed capillary column SFC employing both CO_2 and 2% (w/w) meth-

anol-modified CO_2 as the mobile phase. Signal quenching from the mobile phase is addressed. Applications of the SFC–SCD to the analyses of thermally labile pesticides and a sulfur-containing surfactant are given.

EXPERIMENTAL

Chromatography

The flame sampling probe of the sulfur chemiluminescence detector (SCD 350, Sievers Research, Boulder, CO, U.S.A.) was mounted directly on top of the flame ionization detector of the Lee Scientific 501 supercritical-fluid chromatograph [Lee Scientific (LSI), Salt Lake City, UT, U.S.A.]. The FID temperature was maintained at 375°C. Grade 4.3 oxygen (Airco, Murray Hill, NJ, U.S.A.) was used as the ozone-generator gas. SFC-grade CO_2 and 2% (w/w) methanol-modified CO_2 were obtained from Scott Specialty Gases (Plumsteadville, PA, U.S.A.).

Both 50-μm and 100-μm I.D. frit restrictors (LSI) were used to control the capillary column and packed-capillary-column flow, respectively. Direct injection with a helium actuated Valco (Houston, TX, U.S.A.) injector (60-nl rotor) was employed as the sample introduction method[17]. Exact chromatographic conditions are cited in the figure legends. All data were recorded by a Spectra-Physics 4290 integrator.

Columns

Both capillary columns (50 μm I.D. coated with a 0.25-μm film thickness; LSI) and packed-capillary columns (250 μm I.D. packed with 5 μm Deltabond-CN; Keystone, Bellefonte, PA, U.S.A.) were used to achieve chromatographic separations. The packed-capillary columns were slurry-packed in-house. A 3–5% (w/w) slurry of stationary phase in methanol was used as the packing medium. A Haskel air pump was used to deliver the methanol. A pressure of 6000 p.s.i. was employed for packing the column. The pressure was increased to 7000 p.s.i. for 4–5 h after packing in order to condition the column.

Reagents

Dimethyl sulfide (49.9 ppm in nitrogen; Scott Specialty Gases) was used for the signal-quenching study. Sulfur-containing pesticides were purchased from Chemical Service (West Chester, PA, U.S.A.). Benzo[*b*]thiophene and dibenzothiophene were obtained from Aldrich (Milwaukee, WI, U.S.A.). These pesticides and chemicals were used as-received without further purification. The surfactant (ethoxylated thiols) was obtained from Shell (Houston, TX, U.S.A.). Garlic oil (Nature Made Nutritional Product, Los Angeles, CA, U.S.A.) was purchased from a local store. HPLC-grade solvents (Fisher, Raleigh, NC, U.S.A.) were used for preparing standard solutions.

RESULTS AND DISCUSSION

Without any modification, the SCD system was used after capillary SFC employing CO_2 or 2% (w/w) methanol-modified CO_2 as the mobile phase. A schematic diagram of this SFC–SCD is given in Fig. 1. All the flame-decomposed products were drawn from FID to SCD via a ceramic sampling probe and a transfer line by a

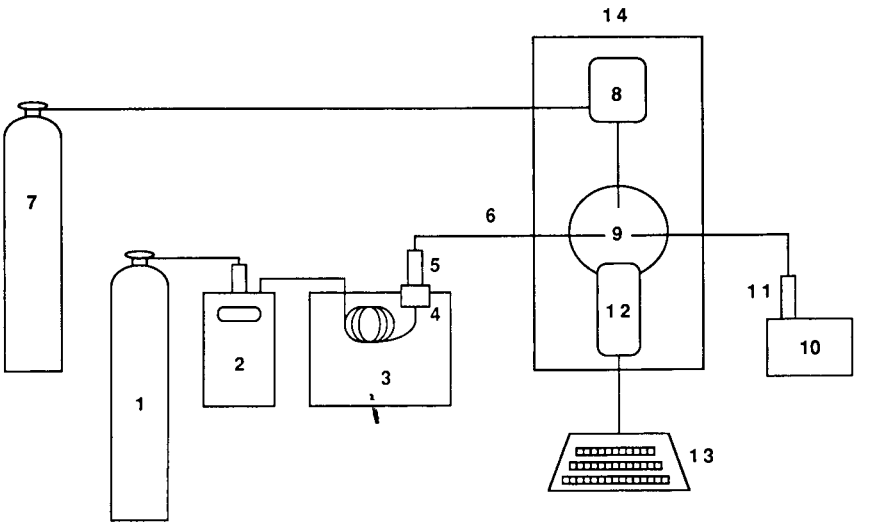

Fig. 1. Schematic diagram of SFC–sulfur chemiluminescence detector. Key: 1 = SFC grade CO_2 or 2% (w/w) methanol-modified CO_2; 2 = syring pump; 3 = chromatographic oven; 14 = flame ionization detector; 5 = flame sampling probe; 6 = transfer line; 7 = oxygen; 8 = ozone generator; 9 = reaction cell; 10 = vacuum pump; 11 = chemical trap; 12 = photomultiplier tube; 13 = integrator; 14 = SCD 350 main body.

vacuum pump. In order to efficiently transfer the short-lived sulfur monoxide to the reaction cell, pressure inside the SCD system was maintained at 15 Torr. This low-pressure system also prevented water condensation from occurring inside the transfer line and reaction chamber and reduced the collisions of other molecular species with sulfur monoxide.

The flame chemistry involved in SCD is expected to be as complex as that in FPD. It has been reported[18] that the major combustion products from sulfur analytes are SO, SH, SO_2, S_2, H_2S and some non-sulfur-containing products when a hydrogen-rich reducing flame is employed. The relative abundances of these species are strongly dependent on the flame gas composition (ratio of the H_2/O_2) and the position in the flame. It was also reported[13] that in a hydrogen-rich flame, SO_2, was the dominant sulfur species and SO accounted for at least 20% of the total products while the amount of S_2, was less than 1%.

The suggested hydrogen and air flows for obtaining maximum selectivity in GC–SCD are arround 200 and 380 ml min^{-1}, respectively[15]. It was found that SCD sensitivity was more dependent on the air flow-rate than the hydrogen flow-rate. While decreasing air flows increased sensitivity, it was accompanied by a loss of selectivity. This phenomenon was also observed in the SFC–SCD system. At a fixed hydrogen flow (205 ml min^{-1}), the optimum air flow was found to be lower in SFC–SCD than that in GC–SCD. An air flow of 330 ml min^{-1} and a hydrogen flow of 205 ml min^{-1} were used throughout this SFC–SCD study. Further investigation of the optimized flame gas composition for SCF–SCD may be necessary.

Signal quenching

It is believed that quenching resulting from collisions between the primary monitored species, S_2^*, and other molecular species produced in the flame are the main factors that cause signal quenching in FPD[16]. Quenching of SO_2^* emission is probably a considerable problem in SCD because the reaction mechanism can be considered similar for both FPD and SCD. However, it is important to note that the chemiluminescence is occurring in the hot flame at atmospheric pressure in FPD, and it occurs downstream at reduced pressure and room temperature in SCD. Consequently, collisional quenching in SCD would be expected to be less than in FPD. Indeed, this reaction in SCD quenching has been observed[14,15].

A significant signal quenching in FPD results from co-eluting hydrocarbons. Co-eluting hydrocarbons can serve as fuel gas in the flame, hence, they change the flame temperature which consequently perturbs the flame chemistry and therefore, changes the distribution of sulfur species. In addition, if the amount of hydrocarbons is large enough, the probability of collisions between the monitored sulfur species, *e.g.* S_2^* in FPD and SO_2^* in SCD, and the flame-decomposed products (such as CH_4, CO_2 or H_2O) is increased. In order to examine the quenching from co-eluting hydrocarbons in SFC–SCD, an experiment was designed such that benzol[*b*]thiophene (1 ng injected) co-eluted with 20 nl of either *n*-hexane, methanol, or toluene ($\approx$ 20 μg) using a capillary column (1 m $\times$ 50 μm I.D.; SB-Methyl-100). A decompressed CO_2 gas flow of less than 1 ml min^{-1} was controlled by frit restrictor. It was found that quenching resulting from co-elution of the sulfur-containing analytes with *n*-hexane or methanol was not significant. However a 15% decrease in signal was observed if the component co-eluted with toluene. This quenching from toluene has also been observed with SFC–FPD[8].

Another quencher which is thought to be important in SFC–SCD is the mobile phase employed in SFC. Most of the mobile phases used in SFC are polyatomic, *e.g.* CO_2, N_2O or modified CO_2. These mobile phases are more effective quenchers than most of the mobile phases used in GC such as monoatomic He or diatomic H_2. Furthermore, the decompressed mobile phase gas flow-rates (at their high densities) at the outlet of the column are usually higher in SFC than those from GC using a column with the same dimensions. It has been reported[19] that a 15% signal decrease was observed from a redox chemiluminescence detector by comparing the signal generated from decompressed CO_2 at a flow-rate of 0.75 ml min^{-1} with that from helium.

Quenching of the SCD signal resulting from the SFC mobile phase was examined for CO_2, which is the most widely used mobile phase. Curve a in Fig. 2 is the SCD background signal at different decompressed CO_2 gas flow-rates. The reason why the SCD signal increases with increasing CO_2 flows is not clear. It may be due to the CH* emission (at 390 nm) resulting from hydrocarbon contaminants (less than 5 ppm) in CO_2 (ref. 18). Curve c in Fig. 2 is the hypothetical SCD response for low nanogram level (49.9 ppm) of dimethyl sulfide. This curve is plotted under the assumption that no quenching was obtained from CO_2. However, the experimental SCD response of the dimethyl sulfide (49.9 ppm) is shown in curve b which indicates that CO_2 does quench the signal at a decompressed flow-rate above 5 ml min^{-1}. From the difference between curves b and c, this quenching becomes more and more severe with increasing CO_2 gas flow above 15 ml min^{-1}. About 70% of the signal is

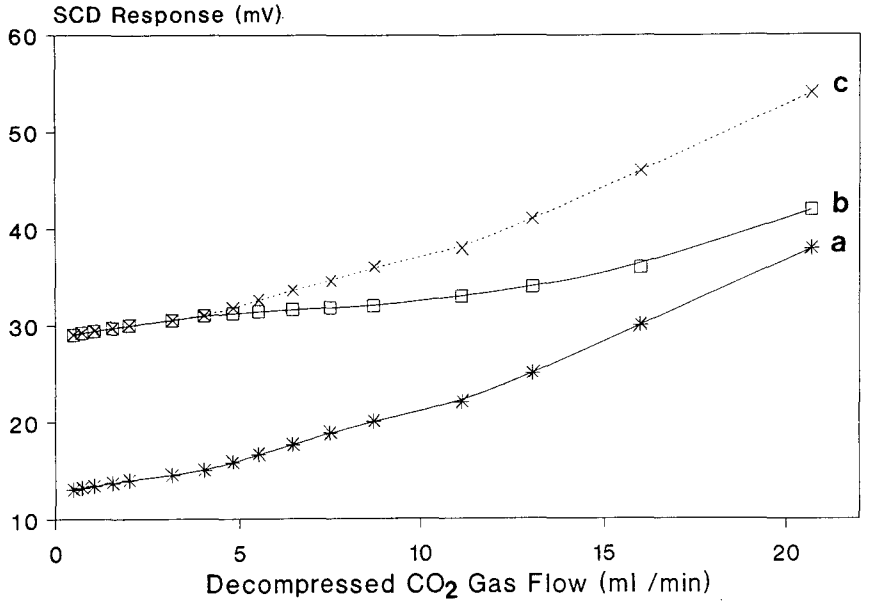

Fig. 2. Quenching of SCD signals resulting from different decompressed CO_2 gas flow-rates. a = CO_2; b = dimethyl sulfide (49.9 ppm) in CO_2 (experimental data); c = dimethyl sulfide (49.9 ppm) in CO_2 (hypothetical data obtained by adding 15 mV, SCD response of 49.9 ppm dimethyl sulfide, to curve a.

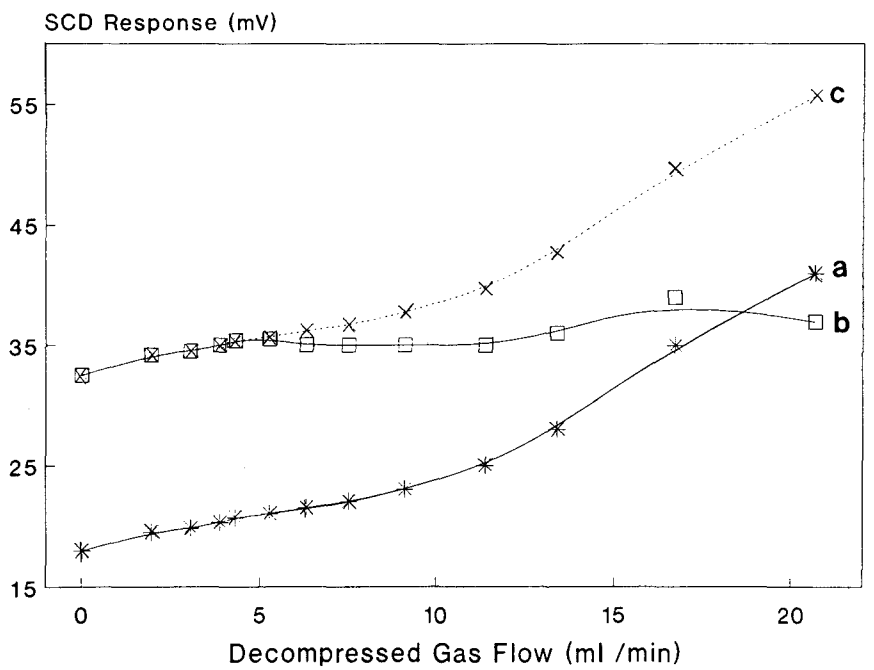

Fig. 3. Quenching of SCD signals resulting from different decompressed 2% (w/w) methanol-modified CO_2 gas flow-rates. (a) 2% (w/w) methanol-modified CO_2; (b) dimethyl sulfide (49.9 ppm) in 2% (w/w) methanol-modified CO_2 (experimental data); (c) dimethyl sulfide (49.9 ppm) in 2% (w/w) methanol-modified CO_2 (hypothetical data obtained by adding 15 mV, SCD response of 49.9 ppm dimethyl sulfide, to curve a.

lost at a CO_2 gas flow of 20 ml min^{-1}. This suggests that a packed column (I.D. $\geqslant$ 1 mm), which produces gas flow higher than 20 ml min^{-1}, is not compatible with the current SFC–SCD configuration.

In contrast to the high gas flow, the quenching in SCD is not significant when the gas flow is less than 5 ml min^{-1}. For typical capillary column (*i.e.* 50 μm I.D.) SFC operating conditions, the measured decompressed CO_2 gas flow was less than 3 ml min^{-1} (which corresponds to 390 atm CO_2 pressure). Hence, the signal quenching due to the presence of CO_2 should not be a significant problem when a capillary column is employed for SCF–SCD analysis.

The quenching phenomenon resulting from the SFC mobile phase was also studied for 2% methanol-modified CO_2. The flame gas composition and chromatographic conditions were the same as those used in the study of quenching from 100% CO_2. The results are shown in Fig. 3. For low decompressed flow-rates (<4 ml min^{-1}), quenching does not appear to be a problem. However, the rate of SCD signal decrease was faster in this case than that observed with 100% CO_2 at flow-rates higher than 10 ml min^{-1}. It was also noticed that quenching from either CO_2 or 2% methanol-modified CO_2 was even more severe when a higher concentration of dimethyl sulfide was used.

Although quenching is significant at high gas flows for both CO_2 and modified CO_2, a packed capillary column (250 μm I.D.) can be used in SFC–SCD because its highest decompressed CO_2 flow is typically less than 10 ml min^{-1}. One advantage of using a packed capillary column is that a higher sample capacity can be obtained than with an open tubular capillary column, although some loss of the SCD sensitivity and detector linearity are observed.

Detector performance

A detection limit was found to be 12 pg S (signal-to-noise ratio 3) or 2 pg S/s with dibenzothiophene in capillary SFC–SCD. Detector linearity was at least three orders of magnitude (0.07–70 ng of dibenzothiophene) using a packed capillary column. Almost equimolar response was observed when injecting benzo[*b*thiophene, dibenzothiophene, and tri-allate (a thiocarbamate) using identical chromatographic conditions. Selectivity of seven orders of magnitude was determined by comparing methanol response and benzo[*b*thiophene response. It is interesting to note that hexane did not give a response, and toluene gave a negative response under these conditions.

Fig. 4 demonstrates the superior selectivity afforded by SCD. It is known that garlic oil contains many sulfur-containing compounds, many of which are thermally labile. The garlic oil analyzed here was sealed in a gel tablet in which the garlic oil had been premixed with vegetable oil. The garlic oil was then dissolved in *n*-hexane after being removed from the tablet. One advantage of using this SCD system is that the signals from both FID and SCD could be obtained simultaneously when employing 100% CO_2 as the SFC mobile phase. The FID and SCD chromatograms are shown in Fig. 4. These volatile sulfur compounds were detected by SCD (Fig. 4a). However, they were not detected using FID either because they had low response in FID or co-eluted with solvent (Fig. 4b). Non-sulfur triglycerides (micrograms were injected) contained in the vegetable oil were detected by FID; however, they were not detected by SCD.

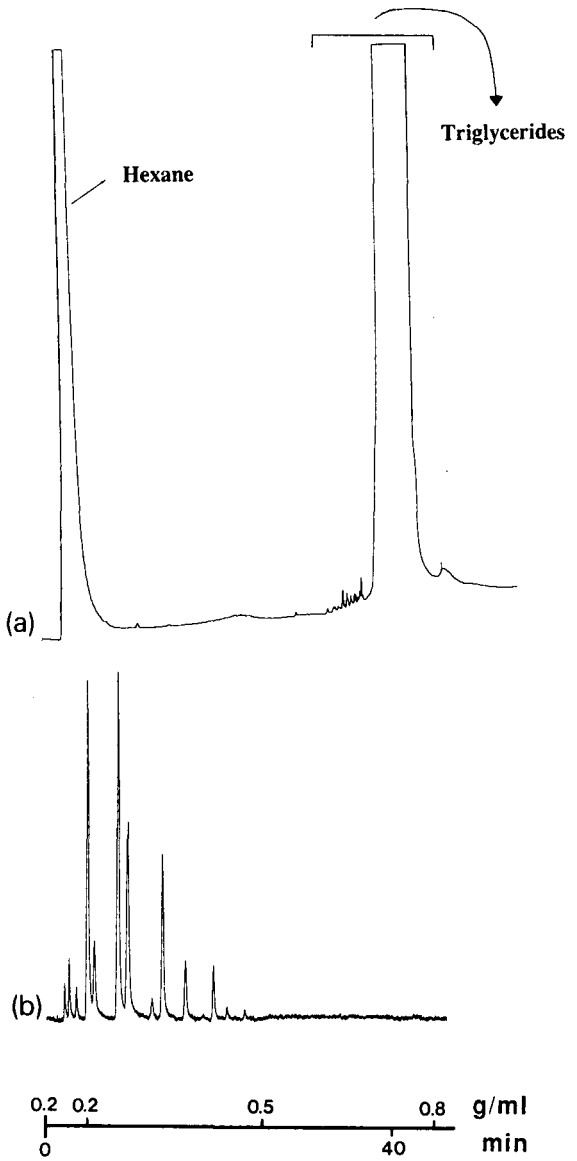

Fig. 4. Detection of sulfur-compounds from garlic oil by (a) FID and (b) SCD. Chromatographic conditions: CO_2 density programmed from 0.20 to 0.8 g ml^{-1} at 0.015 g ml^{-1} min^{-1} after a 3-min isoconfertic period; oven temperature at 80°C; packed capillary column was used.

Applications

The separation of C_{12}-ethoxylated thiols by capillary SFC–SCD is demonstrated in Fig. 5. Ethoxylated alcohols or thiols are widely used as non-ionic surfactants. Determination of the distribution of oligomers and average number of ethylene

$$C_{12}—S—(-CH_2CH_2O-)_n-H$$

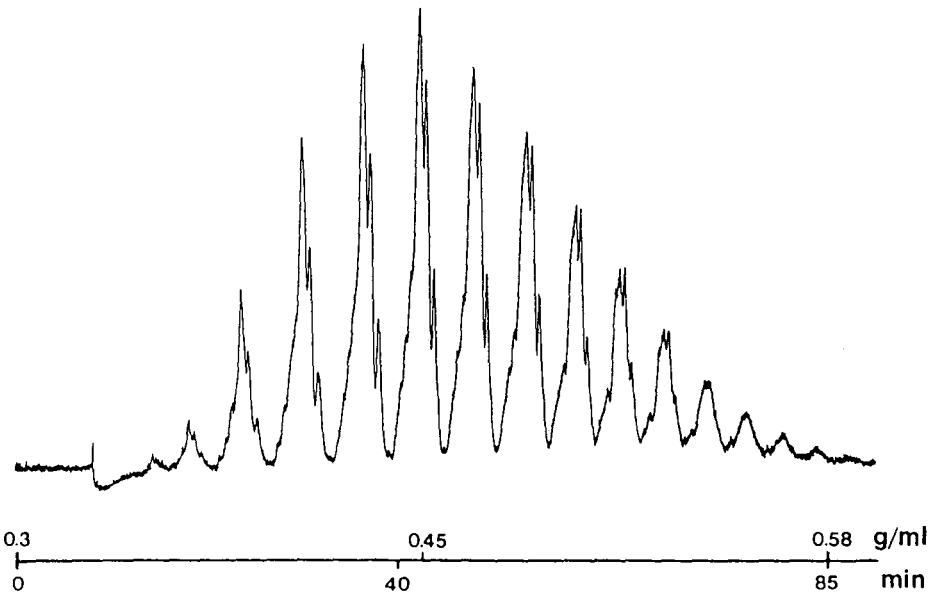

Fig. 5. Capillary supercritical fluid chromatogram of C_{12}-ethoxylated thiols. Chromatographic conditions: CO_2 density programmed from 0.30 to 0.45 g ml^{-1} at 0.004 g ml^{-1} min^- after a 5-min isoconfertic period, then to 0.58 g ml^{-1} at 0.003 g ml^{-1} min^-; oven temperature held at 100°C; column was SB-Phenyl-5.

oxide (EO) units is important because they affect the chemical properties and performance of the surfactant. SFC has been shown to be an effective method for separating the oligomers in ethoxylated alcohols using FID[20]. Because SCD responds only to the amount of the sulfur contained in each oligomer (*i.e.* one sulfur atom per molecule), the average number of EO units per mole of ethoxylate can be determined directly employing SCD. Since the response factors vary in the separated oligomers such a direct analysis via FID is not possible. By integrating each broad peak (each peak was comprised of many branched isomers) which represents one oligomer (Fig. 5), the calculated average EO unit was 6.8, which was in good agreement with the number provided by a combination of other techniques.

Analysis of thermally labile and polar sulfur-containing pesticides with 2% methanol-modified CO_2 is demonstrated in Fig. 6. A low nanogram amount of each pesticide was injected. It was found that these pesticides started to decompose when the analysis temperature was increased above 70°C; therefore, their separation and detection using GC was precluded. It was also difficult to chromatograph these compounds from the same column using 100% CO_2 because of the irreversible adsorption between these polar pesticides and the stationary phase[21]. Methanol, however, changes the surface activity of the packing material, thus enabling the polar compounds to be eluted.

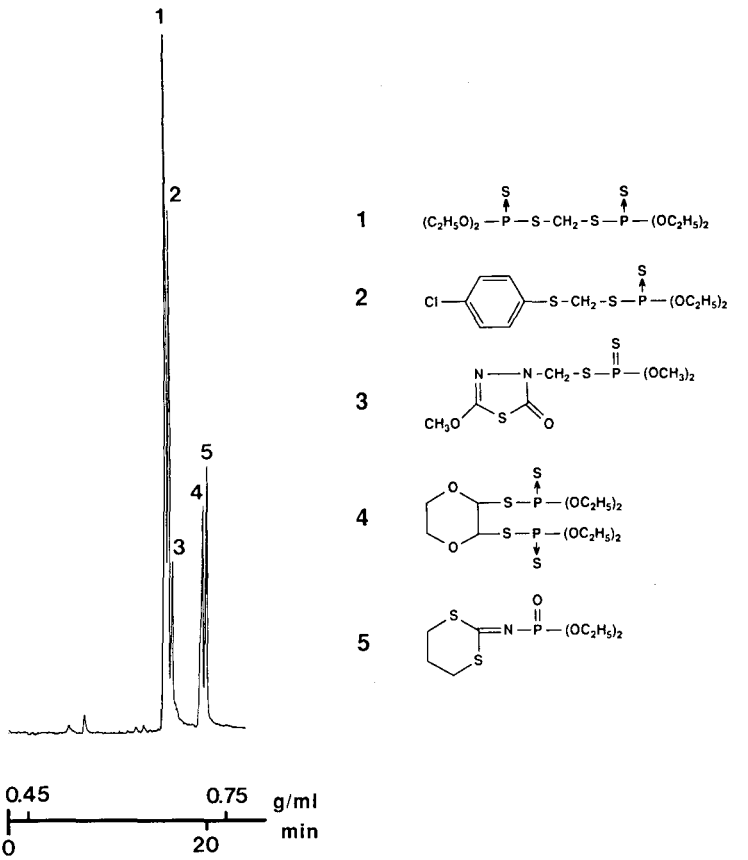

Fig. 6. Separation of five thermally labile sulfur-containing pesticides. Chromatographic conditions: density programmed from 0.45 to 0.75 g ml^{-1} at 0.015 g ml^{-1} min^{-1} after a 3-min isoconfertic period; oven temperature at 50°C; 2% (w/w) methanol-modified CO_2 was the mobile phase; packed capillary column was used. Peaks: 1 = ethion; 2 = carbophenothion; 3 = methidathion; 4 = dioxathion; 5 = phosfolan.

CONCLUSIONS

The ozone-based sulfur chemiluminescence detector, which was originally designed for GC, has been found to be suitable for use in capillary SFC without any modification. It affords the most selective detection for sulfur that has been reported for capillary SFC. In addition, this detector has been demonstrated to be useful for SFC employing 2% methanol-modified CO_2 as the mobile phase, thus increasing the SFC–SCD capability for analyzing polar compounds and relatively non-volatile compounds. Although suffering some loss of sensitivity, SCD also has been shown to be compatible for use after packed-capillary-column (250 μm I.D.) SFC. A study of the complex flame chemistry involved in this ozone-based SCD is necessary in order to more efficiently utilize this detector in SFC employing modified CO_2 as the mobile phase.

ACKNOWLEDGEMENTS

Financial support from the United States Environmental Protection Agency is gratefully appreciated. Special thanks go to Shell Development Company for promoting this study.

REFERENCES

1 M. Dressler, *Selective Gas Chromatographic Detectors*, Elsevier, Amsterdam, 1986, Ch. 7–9.
2 R. J. Skelton, Jr., H.-C. K. Chang, P. B. Farnsworth, K. E. Markides and M. L. Lee, *Anal. Chem.*, 61 (1989) 2292.
3 M. Novotny, S. R. Springston, P. A. Peaden, J. C. Fjeldsted and M. L. Lee, *Anal. Chem.*, 53 (1981) 407A.
4 K. D. Bartle, in R. M. Smith (Editor), *Supercritical Fluid Chromatography*, St. Edmundsbury Press, England, 1988, pp. 1–28.
5 R. D. Smith, B. W. Wright and C. R. Younker, *Anal. Chem.*, 60 (1988) 1323A.
6 B. E. Richter, D. J. Bornhop, J. T. Swanson, J. G. Wangsgard and M. A. Andersen, *J. Chromatogr. Sci.*, 27 (1989) 303.
7 K. E. Markides, E. D. Lee, R. Bolick and M. L. Lee, *Anal. Chem.*, 58 (1986) 740.
8 S. V. Olesik, L. A. Pekay and E. A. Paliwoda, *Anal. Chem.*, 61 (1989) 58.
9 L. A. Pekay and S. V. Olesik, *Anal. Chem.*, 61 (1989) 2616.
10 D. R. Luffer, L. J. Galante, P. A. David, M. Novotny and G. M. Hieftje, *Anal. Chem.*, 60 (1988) 1365.
11 R. J. Skelton, Jr., P. B. Farnsworth, K. E. Markides and M. L. Lee, *Anal. Chem.*, 61 (1989) 1815.
12 W. T. Foreman, C. L. Shellum, J. W. Birks and R. E. Sievers, *J. Chromatogr.*, 465 (1989) 23.
13 D. J. Bornhop, B. J. Murphy and L. Krieger-Jones, *Anal. Chem.*, 61 (1989) 797.
14 R. L. Benner aznd D. H. Stedman, *Anal. Chem.*, 61 (1989) 1268.
15 R. L. Shearer, D. L. O'Neal, R. Rios and M. D. Baker, *J. Chromatogr. Sci.*, 28 (1990) 24.
16 M. Legier, Sievers Research, Inc., personal communication.
17 M. L. Lee, B. Xu, E. C. Huang, N. M. Djordjevic, H-C. K. Chang and K. E. Markides, *J. Microcol. Sep.*, 1 (1989) 7.
18 S. O. Farwell and C. J. Barinaga, *J. Chromatogr. Sci.*, 24 (1986) 483.
19 W. T. Foreman, R. E. Sievers and B. W. Wenclawiak, *Fresenius Z. Anal. Chem.*, 330 (1988) 231.
20 P. R. Geissler, *J. Am. Oil Chem. Soc.*, 66 (1989) 685.
21 M. Ashraf-Khorassani and L. T. Taylor, in C. M. White (Editor), *Modern Supercritical Fluid Chromatography*, Hüthig, Heidelberg, 1988, pp. 115.

Journal of Chromatography, 517 (1990) 503–519
Elsevier Science Publishers B.V., Amsterdam

CHROMSYMP. 1975

Static coating of 5 to 50 μm I.D. capillary columns for open tubular column chromatography

S. R. SUMPTER, C. L. WOOLLEY[a], E. C. HUANG[b], K. E. MARKIDES and M. L. LEE*
Department of Chemistry, Brigham Young University, Provo, UT 84602 (U.S.A.)

ABSTRACT

Dichlorofluoromethane, trichlorofluoromethane and tetramethylsilane were used in the static coating of small diameter capillary columns (5 to 50 μm I.D.) in order to obtain highly efficient columns for gas and supercritical fluid chromatography. Capillary columns of 5-, 10-, 25-, and 50-μm I.D. were coated with stationary phase films of SE-33, SE-54, OV-215, 50% *n*-octyl, 45% phenoxypolyethyl ether, 50% liquid crystal, 25% biphenyl, 50% pentafluorophenyl and 50% cyanopropyl polysiloxane stationary phases. Resultant evaluations of these columns in gas chromatography gave approximately 9000, 66 000, 45 000, and 19 000 plates m^{-1}, respectively, for the different internal diameters. Important parameters which affect coating efficiency are identified and discussed in detail.

INTRODUCTION

Several advantages are realized from the use of small diameter ($\leqslant 100$ μm I.D.) open tubular columns in gas chromatography (GC) and supercritical fluid chromatography (SFC). The Golay equation indicates that small internal diameter columns should yield higher numbers of theoretical plates than larger I.D. columns. Fields *et al.*[1] showed that experimental height equivalent to a theoretical plate (HETP) data for a 50 μm I.D. column closely matched the theoretical values, and that the experimental HETP data for a 25 μm I.D. column were about 1.5 times higher than the theoretical values in SFC. These authors also showed experimental and theoretical plots of plates m^{-1} *vs.* the capacity ratio, k, for 25 to 100 μm I.D. columns. Results revealed that the practical efficiencies for the 25 μm I.D. columns were significantly better than those for the larger diameter columns.

In SFC, open tubular columns can be operated with relatively small pressure

[a] Present address: Supelco Inc., Supelco Park, Bellefonte, PA 16823-0048, U.S.A.
[b] Present address: Equine Drug Testing and Toxicology, New York State College of Veterinary Medicine, Cornell University, 925 Warren Drive, Ithaca, NY 14850, U.S.A.

0021-9673/90/$03.50

drops along the length of the column. Pressure drop is important in SFC because a change in pressure not only changes the mobile phase density and solvating power, but also the selectivity and resolution in a separation. Roth and Ansorgova[2] calculated pressure drops with a CO_2 mobile phase at 107°C for 10, 25, and 50 μm I.D. columns in SFC. Using inlet pressures of 74 and 148 atm, and linear velocities of 2 and 5 cm s^{-1}, the greatest pressure drop was 16.2 atm for a 10 m × 25 μm I.D. column.

The use of small diameter capillary columns in GC is restricted by the low sample capacities of these columns. In addition, conventional GC inlet systems are not designed for the high pressures required for small I.D. columns (up to 27 atm for 25 μm I.D. columns). SFC, on the other hand, is performed under high-pressure conditions (from 60–400 atm) and requires the use of 100 μm I.D. and smaller columns[3,4]. Extremely small diameter columns must be used in open tubular column liquid chromatography (LC) because of the slow diffusion rates of solutes in the mobile phase. Such columns must have internal diameters in the range of 2–15 μm[5–7]. The preparation of efficient columns with such small internal diameters is extremely difficult.

Several methods have been used to prepare small I.D. columns for open tubular column chromatography. First, the dynamic coating method[8] is the oldest coating method, and was originally used to coat 200 μm to 1 mm I.D. columns. Desty *et al.*[9] and Gaspar *et al.*[10] used this method to coat 35 and 67 μm I.D. columns, respectively. The problem associated with the dynamic coating of small I.D. tubing is that the solutions required for reasonably thick films (>0.25 μm) are extremely viscous and require high filling pressures.

Second, the chemical bonding method of coating involves the bonding of monomeric reagents to the column wall. Alkyl groups are covalently bonded by reacting alkylchlorosilanes with surface silanol groups. The problem associated with this method is that the column sample capacity is low, and the tubing must first be etched to produce a greater surface area for the stationary phase films. Currently, fused-silica etching processes are not well developed, and there are an insufficient number of silanol groups on the column wall for the bonding of alkyl groups. Therefore, borosilicate or soda-lime glass columns are more often used. St. Claire and Jorgenson[11] have prepared a 126 cm long, 8 μm I.D. borosilicate glass column yielding 175 000 theoretical plates in LC using this method.

Third, a precipitation coating method developed by Dluzneski and Jorgenson[12] is based on the variable solubilities of the stationary phase polymer in selected solvent systems at various temperatures. Using this method, OV-17 was dissolved in heptane–cyclohexane (70:30) at 70°C. Then the fused-silica tubing was filled with this solution. After the column was filled, the temperature was reduced to room temperature, and the polymer was precipitated onto the column wall. Finally, the solvent was purged out of the column, and the stationary phase was dried and cross-linked. The process was reportedly quite simple and was used to coat columns down to 5 μm I.D. and 4 m long. This coating procedure was reported for LC, but it could be easily applied in the preparation of SFC and GC capillary columns. The main disadvantage is that there is presently no satisfactory method to control the film thickness in this coating process. The stationary phase film thickness is adjusted by changing the temperature used during the precipitation process.

Fourth, the static coating process[13] also requires viscous stationary phase

solutions for coating adequate film thicknesses on the inner walls of small diameter columns. These solutions require high pressures to fill the tubing, and once the tubing is filled, evacuation of the solvent is troublesome. Even with these problems, the static coating process is widely used because the method generally produces the most efficient capillary columns, and film thicknesses are easy to control. Rutten and Luyten[14] compared the static and dynamic coating methods. They found that the static coating method consistently produced higher efficiencies. Later, Alexander *et al.*[15] confirmed these results.

Various techniques have been applied to improve the static coating procedure for small diameter columns. Coating at temperatures much higher than the normal boiling point of the solvent, and under vacuum conditions, often produces sudden expansion in the stationary phase solution in the column. This expansion leaves sections of solution and vapor in the column, which destroys the process. Xu and Vermeulen[16] developed a free release static coating procedure which is done at high temperature (75–85°C), at relatively high pressure (atmospheric), and with a buffer column at the free end of the column (the end not sealed during the evaporation process). They reported that "bumping" was subdued, and that coating speeds were faster than conventional coating speeds.

EXPERIMENTAL

Column material

Fused-silica capillary tubing (5, 10, 25, 50 and 200 μm I.D.) was obtained from Polymicro Technologies (Phoenix, AZ, U.S.A.).

Polysiloxane stationary phases

All stationary phases used in this study have previously been reported. The 25% biphenyl (poly-25-biphenyl)[17], 50% liquid crystal (poly-50-LC)[18], 50% *n*-octyl (poly-50-C_8)[19], 50% pentafluorophenyl (poly-50-F_5)[20], 45% phenoxypolyethyl ether (poly-45-PPEE)[21] and 50% cyanopropyl (poly-50-cyano)[22] stationary phases were synthesized as reported. Commercially available OV-215 (50% trifluoropropyl, SE-33 (1% vinyl, 99% methyl), and SE-54 (1% vinyl, 5% phenyl) were obtained from Alltech (Deerfield, IL, U.S.A.).

Coating solvents

The following coating solvents were used: dichlorofluoromethane ($CHCl_2F$, Freon 21®), 99.9% pure, Alphagaz (Denver, CO, U.S.A.); trichlorofluoromethane (CCl_3F, Freon 11®), 99.9% pure, MG Industries (Valley Forge, PA, U.S.A.); and tetramethylsilane (TMS), 99.9% pure, Petrarch Systems, (Bristol, PA, U.S.A.). The dichlorofluoromethane and trichlorofluoromethane were both filtered into 1 dram vials with PTFE seals in the caps before use. The $CHCl_2F$ was maintained at −15°C before use due to its low boiling point.

Preparation of stationary phase solutions

The concentration of polymer needed for a desired film thickness was calculated from the following equations[23]:

$$C = 1000\,[(\rho r^2)/(r-d_f)^2 - \rho] \quad (1)$$

where C is the concentration (mg ml^{-1}) and ρ is the specific density (g ml^{-1}) of the stationary phase, r is the column internal radius (μm), and d_f is the desired film thickness (μm). When the desired film thickness was insignificant compared to the column internal diameter (200 μm I.D. columns with 0.25-μm films), the following equation was used to calculate the concentration of the coating solutions:

$$C = 2000\ (\rho d_f)/r \tag{2}$$

The stationary phase solutions were prepared by weighing out an appropriate amount of polymer into a crimp-seal vial (Supelco, Bellefonte, PA, U.S.A.). An aliquot of 1 ml of solvent was added, and the vial was sealed. The solutions were sonicated for about 10 min to dissolve the polymers.

Column pretreatment and deactivation

Before deactivation, the fused-silica tubing required a hydrothermal treatment followed by dehydration. However, several of the columns ($\leqslant 25$ μm I.D.) were not pretreated, but were coated as received. Distilled water was passed through the tubing, and the tubing was flame sealed at both ends before being heated to 250°C for 4 h. Dehydration at 250°C for 2 h was performed by purging a stream of dry nitrogen through the tubing after removing the seals. Deactivation of the pretreated tubing with 50% phenyl polyhydrosiloxane at 350°C for 10 h[24] or 50% cyanopropyl polymethylhydrosiloxane at 250°C for 10 h[25] was performed as decribed in the literature. The polymers were dissolved in dichloromethane in concentrations of about 1% (w/v) prior to being coated by the dynamic method.

Filling and coating of columns

Fused-silica tubing that was to be filled with a stationary phase solution was wrapped on a column basket, so that one end could unwind freely, after the tubing was on the basket. This end is herein defined as the front of the tubing (or column). The tubing to be filled was placed in a constant temperature bath filled with propylene glycol (for coating temperatures greater than 40°C) or water (when coating temperatures were close to room temperature). The coating bath temperature was maintained using a thermoregulating pump. The front end of the tubing was pushed into the crimp-seal vial containing the coating solution, which was then placed in a stainless steel filling device. Pressure to the filling apparatus was controlled by a high-pressure regulator on a nitrogen gas tank. Pressures ranging from 10–51 atm were used to push the coating solution into the fused-silica tubing. When the solution emerged from the end of the tubing, the end of the tubing was sealed by pushing it into a septum, or forceps were used to push the end into a tube of Apiezon (M or N) grease which was kept cold in a Dewar flask filled with water and ice.

After the tubing was filled with the coating solution, the front end was pulled out of the filling apparatus and connected to a vacuum apparatus equipped with a vacuum meter and gauge tube (DV-6M type; Teledyne Hastings-Raydist, Hampton, VA, U.S.A.), which were used to monitor the vacuum pressure. The minimum observable pressure was 8 μm Hg. As the solvent evaporated, the illuminated tubing changed from the dark, dull color to a shiny, light color. The column baskets had a circumference of 50 cm and nine equally spaced posts, 5.6 cm apart. One post was designated as the

observation point, and each time the solvent front reached it, the time and pressure were recorded. When the entire column was coated, the front was pulled free of the vacuum, and the end was pulled out of the septum or Apiezon grease. After a column was coated, the front was connected to a nitrogen line and the column was purged for 1 to 2 h at about 10–20 atm to ensure that the solvent was removed.

Stationary phase immobilization

Stationary phases were cross-linked using an azo-*tert.*-butane–argon purge[26] for 1 to 4 h. The purging pressures ranged from 2 atm for 50 μm I.D. columns to 4 atm for 10 and 25 μm I.D. columns. Both ends of the column were flame sealed, and the column was heated from 40 to 220°C at 4°C min^{-1}, and held at 220°C for 1 h. Then, the columns to be used in SFC were rinsed overnight with 3 ml of dichloromethane or *n*-pentane.

Column evaluation

A Carlo Erba Fractovap 4160 gas chromatograph was modified by replacing the split valve with a high-pressure regulating valve. The helium head pressure was adjusted using a high-pressure regulator at the helium tank to accommodate high split flows (500–600 ml min^{-1}) and high head pressure (up to 100 atm). Before evaluation, the columns were purged with helium at about 7 atm during a temperature program from 40 to 225°C at 4°C min^{-1}. The evaluation was started after a stable baseline was obtained at 200°C. Carrier flow was adjusted to 24 cm s^{-1}, and 1 μl of an *n*-alkane test mixture (about 10 mg ml^{-1} each of C_{15}–C_{24}) was injected (split injection) with a 10 μl gas-tight syringe. The flame ionization detector sensitivity was 1 to $2 \cdot 10^{-11}$ A full scale. Injector and detector temperatures were 275 and 300°C, respectively. Peak widths at half height and retention times were recorded using a Hewlett-Packard 3388A integrator.

Two 50 μm I.D. columns were cut into short pieces (1.5-m segments) to evaluate the efficiencies and retention characteristics of the various sections of the column. The front and the end of the columns (1.5 meters each) were evaluated using a Hewlett-Packard 5890 GC (flame ionization detector) equipped with a Hewlett-Packard 3392A integrator which was used to record peak widths, heights, areas and retention times. Helium carrier gas linear velocities were between 23.1 and 24.6 cm s^{-1} with split flows of 245 to 351 ml min^{-1}. The temperatures of the oven, injector and detector were 200, 275 and 300°C, respectively. Efficiencies were calculated from the following equation:

$$n = 5.545\ (t_r/W_{1/2})^2 \tag{3}$$

where n is the total number of theoretical plates, t_r is the retention time of the test solute and $W_{1/2}$ is the peak width at half height. Theoretical plate heights, h_{theor}, were calculated using the simplified Golay–Giddings equation[27]:

$$h_{theor} = r[(11k^2+6k+1)/3(1+k)^2]^{1/2} \tag{4}$$

where r is the column radius, and k is the capacity ratio.

A Lee Scientific (Salt Lake City, UT, U.S.A.) Model 501 supercritical fluid chromatograph equipped with a flame ionization detector was used in this study for

SFC measurements. The injection port consisted of a Valco C14W (Valco, Houston, TX, U.S.A.) high-pressure 4-port injector with a 0.2-μl sample loop rotor and a standard SGE (Austin, TX, U.S.A.) stainless steel splitter. Split ratios were adjusted to about 30:1 by varying the length of either a 25 μm I.D. or a 50 μm I.D. fused-silica tube connected to the split line after an on/off valve. The SFC operating conditions are cited in the text.

Samples were obtained from the following: alcohol ethoxylate was obtained from Shell Development (Houston, TX, U.S.A.); tricaproin, tricaprylin, tricaprin, trilaurin, trimyristin, tripalmitin, tristearin, triarachidin, tribehenin and *n*-alkanes were obtained from Sigma (St. Louis, MO, U.S.A.). All samples were used as received.

RESULTS AND DISCUSSION

There are several problems, both theoretically and practically, with the preparation of small-diameter open tubular columns. Bartle *et al.*[28] described a phenomenon called Rayleigh instability as one of the driving forces behind stationary phase rearrangement and loss of efficiency. This rearrangement results from infinitesimal perturbations in the stationary phase. Ultimately, stationary phase droplets can be formed in the column from the growth in amplitude of a standing wave in the stationary phase. The rate of growth of this standing wave is given by the following equation:

$$\ln(b/b_0) = (\gamma d_f^3 t)/(12\eta r^4) \quad (5)$$

where b_0 and b are the wave amplitudes at times zero and t, respectively, r is the radius of the column (cm), and γ, d_f and η are the surface tension (mN m^{-1}), film thickness (cm) and viscosity (P) of the stationary phase, respectively. Typical values for η range from 1–10^7 P; values for r, for small I.D. columns, range from 1.5–50 μm; values for γ range from 20–50 mN m^{-1}; and values for d_f range from 0.05–1 μm.

During evacuation of the solvent, in the column coating process, the stationary phase begins to rearrange, and efficiency decreases. Efficiency half-life is defined as the point when one half of the original column efficiency is lost; at this point, $t = t_{1/2}$. Woolley[23] studied the change in efficiency with time at 100°C for a 200 μm I.D. column coated with OV-17. The efficiency decreased by one half after 2.7 h, indicating that a 7% increase in the standing wave amplitude in the stationary phase had occurred. Rearranging eqn. 5 and solving for t at $t_{1/2}$ with a 7% amplitude increase gives:

$$t_{1/2} = 12\ (\ln 1.07)(\eta a^4/\gamma d_f^3) \quad (6)$$

Efficiency half-life values for 5 to 50 μm I.D. columns are found in Table I. These values indicate that the stationary phase films in small internal diameter open tubular columns are very susceptible to Rayleigh instability. Theoretically, rearrangement occurs so quickly that these columns are impractical, unless a highly viscous stationary phase is coated and immobilized (cross-linked) in a short period of time. Eqn. 5 shows that there are several parameters which can be adjusted (some easier than others) to produce a more stable stationary phase on a column of given radius: the surface tension of the stationary phase, the viscosity of the stationary phase, the time required to coat a column, and the film thickness of the stationary phase.

TABLE I

THEORETICAL EFFICIENCY HALF-LIVES OF SMALL DIAMETER COLUMNS COATED WITH OV-17 STATIONARY PHASE AT 22°C

The $t_{1/2}$ values were calculated using eqn. 6. Values for η and γ were 12.20 P and 33 mN m^{-1}, respectively. These values for η and γ were determined experimentally[23].

Column I.D. (μm)	$t_{1/2}$ *(s)*
5	0.07
10	1
25	50
50	700

The critical surface tension, γ_c, of the surface to be coated, must be greater than or equal to the surface tension of the stationary phase, γ, or the surface is not wetted. There are no wettability problems associated with untreated fused silica due to its high γ_c of 50–70 mN m^{-1}, and the stationary phases used in this study all had surface tensions less than the critical surface tensions of the deactivated surfaces. Therefore, poor wettability could not be blamed for any lower than theoretical coating efficiencies that were achieved.

Increased coating bath temperatures enhance the movement of solvent molecules toward the vacuum region, thereby increasing coating velocities and reducing the tendency for column plugging. The utilization of higher temperatures in the static coating of small-diameter tubing was pioneered by Kong and Lee[29]. The static coating of SE-54 in a 50 μm I.D. column, using *n*-pentane as the coating solvent at 50°C, provided high efficiency (16 700 plates m^{-1}) in GC. However, lower column efficiencies (1000–6000 plates m^{-1}) were reported for 50% phenyl[30], 25% biphenyl[31] and 50% polymethylsiloxanes under the same high temperature static coating conditions. Woolley *et al.*[31] proposed that the major factor leading to such poor column efficiencies was linked to the drastically low viscosities of these stationary phases and their solutions at the higher coating temperatures. They suggested that the viscosities of alkylsubstituted (methyl and *n*-octyl) polysiloxanes are only marginally reduced with increasing temperature, while phenyl and biphenyl polymethylsiloxanes undergo dramatic viscosity losses (from about 10^9 to 10^3 cP for a temperature change of 20 to 50°C, respectively). In spite of the improved coating velocities at high temperatures, the increase in Rayleigh instability more than offsets this advantage.

Woolley *et al.*[31] found that the solution to this coating efficiency problem was solved by addressing the variable $(1/\eta)$ in eqn. 5. A highly volatile coating solvent (trichlorofluoromethane, b.p. = 23.7°C), capable of dissolving the polarizable phenyl or biphenyl polysiloxanes, could be used at low coating temperatures. Utilizing highly viscous polysiloxane gums and higher polysiloxane solution viscosities at lower coating temperatures proved to increase the stability of the stationary phase film during coating. The static coating of 50 μm I.D. columns at 22–38°C[31] with 50% phenyl or 25% biphenyl polysiloxanes yielded higher numbers of theoretical plates (12 000–15 000 plates m^{-1} in GC) than those coated at higher temperatures. These results provided evidence that appropriate conditions for the static coating of

TABLE II

PROPERTIES OF COATING SOLVENTS

Data taken from ref. 40.

Coating solvent	*Chemical formula*	ΔH_{vap} *(cal mol^{-1})*	*B.p. (°C at 1 atm)*	*Dipole moment (debye)*	*Density at 25°C (g ml^{-1})*
Dichlorofluoromethane (Freon 21)	$CHCl_2F$	6,287	8.9	1.29	1.366
Trichlorofluoromethane (Freon 11)	CCl_3F	6,424	23.8	0.46	1.467
Tetramethylsilane (TMS)	SiC_4H_{12}	6,439	26.5	0.00	0.648
n-Pentane	C_5H_{12}	6,595	36.1	≤ 0.05	0.626[a]
Dichloromethane	CH_2Cl_2	7,572	40.0	1.60	1.327

[a] Density at 20°C.

small-diameter columns with selective stationary phases include low bath temperatures, highly volatile solvents and highly viscous polysiloxanes.

Thus, a most important parameter in the static coating process is the type of solvent used during the coating process. In the coating solution, the solvent facilitates the dispersion of the highly interwoven polymer strands and decreases the viscosity of the solution. The higher the solvent to polymer ratio, the less viscous is the solution, and the easier is the filling and coating of a capillary tube. A good universal coating solvent is one which would dissolve a wide range of polymers to give a non-viscous solution. Many studies have been done to find polymer–solvent systems that will both make a less viscous coating solution, and facilitate the evacuation of the solvent. Several authors[29,32–37] have used single solvents that are volatile and that yield efficient coatings. Janák *et al.*[36] reported that the use of volatile coating solvents increased the coating speed of a column and decreased the viscosity of the coating solution. The tubing is filled easier with a less viscous coating solution and the solvent is easier to evacuate. Other authors[38,39] have tried using mixed solvents with varying degrees of success.

Table II lists some of the physical properties of two commonly used coating solvents, *n*-pentane and dichloromethane, as well as the physical properties of the three volatile coating solvents used in this study. The most notable difference is in the boiling points of the solvents. Dichlorofluoromethane has the lowest boiling point (8.9°C) of all of the solvents listed. The dipole moment of the solvent also has an effect on the viscosity of the coating solution. Table II lists the dipole moments of the solvents used in this study. Dichlorofluoromethane clearly has the highest dipole moment, 1.29 debye, of the three solvents examined in this study, while TMS has the lowest, 0.00 debye, due to its symmetry. All of the polymeric stationary phases used in this study dissolved readily into $CHCl_2F$, fewer dissolved into CCl_3F, and only the non-polar phases dissolved into TMS, and then only slowly. The use of $CHCl_2F$ and TMS in the coating of open tubular columns has not been reported before in the literature.

As shown previously in eqn. 1, decreasing the column radius, *r*, increases the

TABLE III

COATING VELOCITIES FOR 50 μm I.D. COLUMNS

Stationary phase	*Solvent*	*Coating temperature (°C)*	*Coating velocities (cm min^{-1})*				*Coating pressure (mmHg)*			*Length (m)*	*Film thickness (μm)*
			Start	*Middle*	*End*	*Avg.*[a]	*Start*	*Middle*	*End*		
Poly-50-LC	$CHCl_2F$	35.6	22.2	24.6	61.2	29.8	30	15	10	12	0.10
SE-33	CCl_3F	54.0	22.2	6.8	17.1	9.5	35	14	12	10	0.10
SE-33	$CHCl_2F$	22.6	12.9	12.1	46.3	13.5	19	12	10	7	0.10
Poly-45-PPEE	$CHCl_2F$	38.4	30.7	17.7	136	27.0	28	14	12	15	0.11
Poly-50-C_8	TMS	38.2	27.3	5.7	52.6	9.9	32	16	12	13	0.25
Poly-25-biphenyl	CCl_3F	60.0	31.2	23.6	292	28.6	28	13	10	20	0.25

[a] Avg. = Average coating velocity. This is the observed length of tubing (in cm) that is coated, divided by the time required for it to coat (in min).

required polymer concentration in the coating solution . For example, a 0.15 μm film thickness in a 25 μm I.D. column required a 29 mg ml^{-1} solution for the poly-5-LC stationary phase. The solution was viscous and cloudy at 30.2°C, while it was less viscous and clear at 70°C. A 10 μm I.D. column with a 0.1 μm film thickness required 83 mg ml^{-1} of an SE-54 coating solution. This solution was extremely viscous. Clearly, as the diameter decreases, and even when using a thinner stationary phase film, the coating solution concentration must increase. At film thicknesses greater than 0.25 μm, the poly-25-biphenyl stationary phase formed polymer aggregates at the required concentration.

From eqn. 5, the relationship of coating speed to stationary phase stability is readily observed. Since coating speed is one of the parameters that can be manipulated to minimize Rayleigh instability, coating solvents that provide fast coating speeds should be used. The three solvents used in this study had relatively fast average coating velocities in 50 μm I.D. columns (10–30 cm min^{-1}). This led to the following observation: the coating velocity decreased from the starting rate, and then increased dramatically in the last few meters of the column. Table III lists coating speed data for 50 μm I.D. columns and several selective stationary phases. The starting, middle and ending coating velocities are reported. These range from 12.9 to 30.7 cm min^{-1} at the start, 5.7 to 24.6 cm min^{-1} in the middle and 17.1 to 292 cm min^{-1} at the end of the column. Coating pressures in the vacuum line between the vacuum pump and column are also listed for the start, middle and end sections of the columns. This same change in coating velocity was observed for 25 μm I.D. columns. However, a dramatic change in coating velocity was not observed in the coating of 200 μm I.D. columns. Table IV shows the observed starting, middle and ending coating velocities for several 200 μm I.D. columns. Not only are the average coating velocities slower for the 200 μm I.D. columns (5 to 12 times slower), but the coating velocity steadily decreases to the end of the column. The average coating velocities of 200 μm I.D. columns with *n*-pentane and dichloromethane are 2.5 to 5 times slower than the average coating velocity of the column coated with the more volatile TMS.

To understand why coating velocities changed for these 50 μm I.D. columns, a 14 m × 50 μm I.D. column coated with a 0.25 μm film thickness of poly (50% *n*-octyl) methyl siloxane stationary phase was cut into 1.5-m sections and then evaluated in GC.

TABLE IV

COATING VELOCITIES FOR 200 μm I.D. COLUMNS

Stationary phase	*Solvent*	*Coating temperature (°C)*	*Coating velocities (cm min^{-1})*				*Length (m)*	*Film thickness (μm)*
			Start	*Middle*	*End*	*Avg.*[a]		
Poly-50-cyano	CH_2Cl_2	22.3	4.3	2.6	1.9	2.5	7	0.25
OV-17v	CH_2Cl_2	24.1	4.8	2.2	1.6	2.3	10	0.25
Poly-50-LC	CH_2Cl_2	23.5	3.3	2.8	1.2	1.3	9	0.25
OV-17v	*n*-Pentane	21.8	4.7	3.4	1.5	2.1	8	0.10
SE-33	TMS	21.9	9.4	8.6	5.4	6.4	11	0.25

[a] Avg. = Average coating velocity. This is the observed length of tubing (in cm) that is coated, divided by the time required for it to coat (in min).

TABLE V

MEASURED k VALUES FOR SEGMENTS OF 50 μm I.D. COLUMNS

Segment location (in m)[a]	*Measured k*
Column 1[b]	
0.0–1.5	23.9
3.0–4.5	20.4
6.0–7.5	15.0
9.0–10.5	7.3
12.5–14.0	2.6
Column 2[c]	
0.0–1.5	21.7
10.5–12.0	2.4

[a] The 1.5-m column segments are reported by their location in the original column before being cut out, with 0.0 m being the front of the original column.

[b] Column 1 was a 14.0 m × 50 μm I.D. column coated with poly-50-C_8 stationary phase (d_f = 0.25 μm).

[c] Column 2 was a 12.0 m × 50 μm I.D. column coated with poly-25-biphenyl stationary phase (d_f = 0.25 μm).

Table V shows that the values of k were found to fall between 23.9 at the front of the column to 2.6 at the end of the column. Table V also gives the k values for two, 1.5 m sections cut from a 12.0 m × 50 μm I.D. column coated with poly-25-biphenyl (d_f = 0.25 μm) as evaluated by GC. Again, the same decrease in k values was observed; the k values at the front and end of the column were 21.7 and 2.4, respectively. Both columns produced k values at the front of the column which were 9 times higher than k values at the end of the column. These results indicate that the static coating of 50 μm I.D. columns does not yield a uniform film, but rather, a decreasing film thickness with length.

One explanation for the formation of this phase ratio gradient is that as the polymer solution is pushed through the front of the column when it is being filled, the solution becomes less and less concentrated as it nears the end of the column because the polymer precipitates onto the tubing surface. Fresh solution entering the front of the column continues to deposit stationary phase, becoming less concentrated, as it progresses toward the end of the column. Thus, a phase ratio gradient is developed. A less concentrated solution at the end of the column would also lead to faster coating velocities, since solution viscosity is decreased, and there is less resistance to the escaping solvent. The surface area to volume ratio is four times higher for a 50 μm I.D. column than for a 200 μm I.D. column, so there is less relative polymer-surface contact in 200 μm I.D. tubing. Thus, phase ratio gradients in 200 μm I.D. columns are not expected to be as significant. The consistently decreasing coating velocities in 200 μm I.D. columns tend to support this explanation.

The presence of phase ratio gradients in small I.D. capillary columns present two important, practical considerations. First, if two or more 50 μm I.D. columns are to be made from one long column after it is coated, the front piece of the column will always produce higher k values than the next piece of column, and the end of the column will

TABLE VI

CALCULATED RATIOS OF STATIONARY PHASE FILM THICKNESS RESULTING FROM SLIGHT VARIATIONS IN COLUMN DIAMETER

Column I.D. (μm)	d_f/d'_f
5	6.8
10	5.4
25	4.0
50	3.2
100	2.6

give the lowest k values of all. Second, phase ratio focusing of solutes may be accomplished by putting the lowest k value end of a column at the injector and the highest k value end at the detector. If the column is connected opposite to this, band broadening will take place over the length of the column.

Other influences on coating of capillaries, described by Giddings[41], are capillary forces. These forces are one of the principal means of retaining the stationary phase on the column surface. Giddings explained that stationary phase accumulates in the column where slight negative deviations in the radius of curvature occur. In a capillary column that has a fractional difference in radius of curvature r' and r, where $r' > r$, and assuming $r \gg d_f$, the stationary phase film thickness, the following equation was derived:

$$d_f^3/d_f'^3 = 1 + (d_f^3\ \Delta r/J^3 r^2) \tag{7}$$

where J was approximated by Giddings to be nearly the same value for all liquids and to be in the order of 10^{-5}; $\Delta r/r$ is the fractional variation in tube size; and r is the column radius (cm). Differences in starting and ending diameters on rolls of fused-silica tubing are commonly 1 μm, so $\Delta r/r$ ranges from 0.20 to 0.02 for 5 to 50 μm I.D. columns, respectively. Choosing $\Delta r/r$ as 0.01 and $d_f = 2.5 \cdot 10^{-5}$ cm, calculated values for the ratio of stationary phase film thicknesses at the two sites (d_f/d'_f) are found in Table VI. Clearly, column diameter plays a significant role in the calculated ratios. The smaller the column internal diameter, the higher the ratio. Just a slight variation in the radius of curvature is enough to cause stationary phase voids on some parts of the surface and thick films of phase on other parts of the surface, especially when 5 to 25 μm I.D. columns are considered. Rayleigh instability would have a more pronounced effect on the thick film areas in the column, and column efficiency would be diminished. These thick film areas, combined with Rayleigh instability in these regions, partially explain the low efficiency observed for the 5 μm I.D. column in Table IX. Giddings predicted that $\Delta r/r$ must be kept to within several parts in 10^5 to have a film thickness within a 10% tolerance. Thus column efficiency and coating capacity are directly related to the inner surface of the tubing.

Although there are several problems associated with the successful preparation of highly efficient small I.D. columns, optimization of the coating parameters has led to some successful results. Tables VII, VIII and IX show coating data and GC

TABLE VII

GC EFFICIENCIES FOR 50 μm I.D. FUSED-SILICA COLUMNS COATED WITH POLYSILOXANE STATIONARY PHASES (0.25 μm FILM THICKNESS)

Stationary phase	*Coating temperature (°C)*	*Coating solvent*	*Column length (m)*	*Capacity factor (k)*	*Efficiency[a] (plates m^{-1}) ($\times 10^3$)*
SE-33	56.7	TMS	1.5	33.9	19.2 ± 5.6
SE-33	54.0	CCl_3F	10.0	9.2	13.6 ± 3.2
SE-33	67.7	CCl_3F	2.0	34.8	10.8 ± 1.5
Poly-50-C_8	38.3	TMS	12.5	20.0	14.7 ± 0.5
Poly-50-C_8	37.7	CCl_3F	14.0	15.2	12.6 ± 0.6
Poly-50-C_8	37.0	TMS	12.0	7.6	12.5 ± 0.2
OV-215	24.4	$CHCl_2F$	17.0	9.6	15.8 ± 3.6
OV-215	23.5	$CHCl_2F$	10.4	3.7	10.0 ± 3.5
OV-215	23.0	$CHCl_2F$	10.0	4.5	8.9 ± 1.1
				4.2	10.2 ± 3.8[b]
Poly-45-PPEE	37.5	$CHCl_2F$	15.0	5.2	12.2 ± 2.7
Poly-45-PPEE	38.4	$CHCl_2F$	15.0	3.8	11.5 ± 0.3
Poly-45-PPEE	24.5	$CHCl_2F$	10.0	7.3	10.3 ± 1.6
Poly-50-LC	38.1	$CHCl_2F$	19.5	10.5	16.7 ± 3.5
Poly-50-LC	35.6	$CHCl_2F$	15.5	4.9	13.3 ± 2.7
Poly-50-LC	38.5	$CHCl_2F$	17.0	9.3	11.8 ± 1.6
			11.5	13.1	12.8 ± 2.2[c]

[a] Column efficiencies are an average of three values. The standard deviation is also shown.
[b] After 5 days of use in SFC-CO_2, uncross-linked.
[c] After 18 days of use in SFC-CO_2, uncross-linked; the end 5.50 m was cut off.

TABLE VIII

GC EFFICIENCIES FOR 25 μm I.D. FUSED-SILICA COLUMNS COATED WITH POLYSILOXANE STATIONARY PHASES

Stationary phase	*Film thickness (μm)*	*Coating solvent*	*Coating temperature (°C)*	*Column length (m)*	*Efficiency[a] (plates m^{-1}) ($\times 10^3$)*
SE-33	0.25	CCl_3F	78	4.0	25.8 ± 5.1
SE-33	0.25	CCl_3F	56	1.8	19.7 ± 2.4
SE-33	0.25	TMS	56	1.8	18.2 ± 1.7
SE-33	0.50	$CHCl_2F$	28	3.5	28.4 ± 3.1
SE-54	0.50	$CHCl_2F$	25	4.0	45.2 ± 0.1
Poly-50-C_8	0.50	$CHCl_2F$	25	4.0	26.1 ± 0.8
Poly-25-biphenyl	0.12	CCl_3F	38	6.5	19.0 ± 4.1
Poly-50-LC	0.20	$CHCl_2F$	19	8.0	11.9 ± 0.3
Poly-50-LC	0.15	$CHCl_2F$	25	4.0	21.2 ± 0.6

[a] The k values ranged between 12 and 20 for the above columns. The only exception was the column coated with poly-50-C_8 which had a k of 33.0 using *n*-hexadecane as the test solute. Normal alkane test solutes (C_{14}–C_{21}) were used to determine k and efficiency data for all of the columns except the liquid crystal columns where phenanthrene was used. These reported values are the average and standard deviation of two to three values.

TABLE IX

GC EFFICIENCIES FOR 5 AND 10 μm I.D. FUSED-SILICA COLUMNS COATED WITH POLYSILOXANE STATIONARY PHASES

Stationary phase	*Film thickness (μm)*	*Coating solvent*	*Coating temperature (°C)*	*Column length (m)*	*Capacity factor (k)*	*Efficiency[a] (plates m^{-1}) ($\times 10^3$)*
10 μm I.D. columns						
Poly-25-biphenyl	0.05	$CHCl_2F$	26.6	2.0	3.7	13.3 ± 1.3
Poly-50-F_5	0.05	$CHCl_2F$	26.4	2.0	14.2	62.9 ± 7.5
Poly-50-F_5	0.05	$CHCl_2F$	27.2	2.1	17.3	53.0 ± 9.4
5 μm I.D. column						
Poly-50-F_5	0.15	$CHCl_2F$	27.8	0.9	3.3	9.2 ± 6.4

[a] Columns were evaluated at 175°C or 200°C. The average and standard deviation of three measurements are shown.

efficiencies of 50 , 25, 10 and 5 μm I.D. columns, respectively. The static coating of 50 μm I.D. columns with solute-selective stationary phases at lower temperatures with any of the three selected volatile coating solvents (TMS, CCl_3F or $CHCl_2F$) yielded highly efficient columns. Stationary phases, such as poly-25-biphenyl or poly-50-LC polymethylsiloxanes, that have been traditionally difficult to coat on small-diameter capillaries with dichloromethane as the coating solvent, presented no problems when coated at low-to-moderate temperatures with CCl_3F or $CHCl_2F$ (13 000–16 000 and 12 000–17 000 plates m^{-1}, respectively, which is up to 75% of the theoretical efficiency). The poly-45-PPEE polysiloxane stationary phase that contains polar polyethyl ether side groups dissolved well in $CHCl_2F$ and coated almost as well (10 000–12 000 plates m^{-1}) as the more easily-coated poly-50-C_8 (13 000–15 000 plates m^{-1}), or SE-33 (19 000 plates m^{-1}, up to 90% of the theoretical efficiency) stationary phases. In addition, OV-215, a commercially available stationary phase that is generally quite difficult to coat with more conventional solvents (ethyl acetate, b.p. = 77.2°C, and acetone, b.p. = 56.2°C), was readily dissolved in $CHCl_2F$ and uniformly coated on 50 μm I.D. columns to yield high numbers of theoretical plates (9000–16 000 plates m^{-1} in GC, up to 75% of the theoretical efficiency). By coating these solute-selective polysiloxanes at low bath temperatures and at rapid coating speeds, highly efficient 50 μm I.D. capillary columns were prepared for GC and SFC.

Several 25 μm I.D. columns were successfully coated using the low boiling solvents. Film thicknesses, coating temperatures, column lengths, *k* values, and GC efficiencies are listed in Table VIII. The column coated with SE-33 using TMS had about the same efficiency as the column coated using CCl_3F at the same temperature and with the same film thickness. The 56–78°C coating temperatures for three of the SE-33 columns appeared to have little effect on coating efficiency. The high efficiencies of these columns (18 000–25 000 plates m^{-1}) can be attributed to the high viscosity of this stationary phase, even at the higher temperatures. Fig. 1 is a chromatogram of an ethoxylated alcohol sample (ethoxylated C_{12} and C_{13} alcohols) which shows the high efficiency separation possible on a 25 μm I.D. column. The number of ethylene oxide groups in the starting alcohols ranged from 0 to 27. This chromatogram shows that the

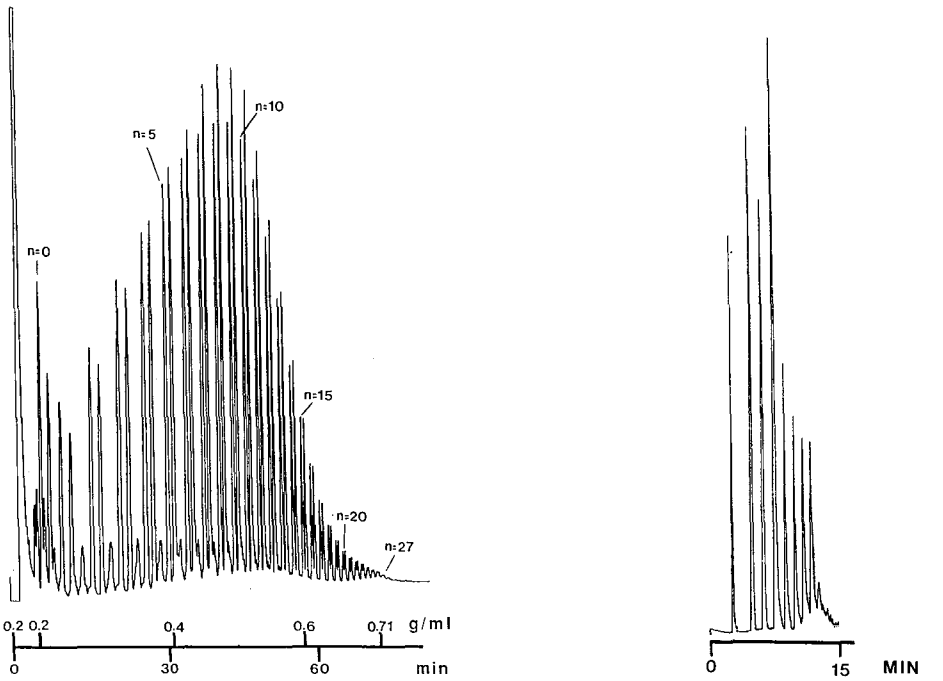

Fig. 1. SFC chromatogram of ethoxylated C_{12} and C_{13} alcohols. Column: 5 m × 25 μm I.D. fused-silica column coated with a poly-25-biphenyl stationary phase (d_f = 0.25 μm). Conditions: CO_2 at 120°C; and linear density program from 0.2 g ml^{-1} to 0.71 g ml^{-1} at 0.0075 g ml^{-1} min^{-1} after an initial 5-min isopycnic period.

Fig. 2. SFC chromatogram of triglycerides (T_{18-60}). Column: 0.7 m × 10 μm I.D. fused-silica column coated with a poly-50-cyano stationary phase (d_f = 0.1 μm). Conditions: solvent backflush injection; inject at 0.3 g ml^{-1}, ramp down to 0.1 g ml^{-1} at 0.096 g ml^{-1} min^{-1}, then, ramp from 0.1 g ml^{-1} to 0.3 g ml^{-1} at 0.068 g ml^{-1} min^{-1}; the chromatographic analysis was started at 0.3 g ml^{-1} and ramped at 0.01 g ml^{-1} min^{-1} to 0.7 g ml^{-1}.

25 μm I.D. column has adequate sample capacity for this sample when coated with a 0.25 μm film thickness.

An important parameter in Rayleigh instability and column efficiency is the film thickness of the stationary phase. Although the coating of thick films in 25 μm I.D. tubing is difficult, a film thickness of 0.5 μm was coated on short pieces of 25 μm I.D. tubing. Table IX shows that three columns were successfully coated with thick films of non-polar stationary phases, and yielded high efficiencies (up to 103% of the theoretical efficiency). Columns longer than 4 m were difficult to coat with a film thickness of 0.5 μm because the coating velocity decreased to zero. Often, only 2 m lengths coated successfully. The effects of increased polymer concentration and column length on coating efficiency is seen in the two columns coated with the liquid crystal stationary phase. Increasing the film thickness (from 0.15 to 0.20 μm) and column length (4 to 8 m) resulted in decreased coating efficiency.

The 10 μm I.D. columns were coated with poly-50-C_8, poly-25-biphenyl, poly-50-cyano, poly-50-F_5, and SE-54 stationary phases. Table IX lists the coating

data for the 10 μm I.D. columns that were evaluated by GC. The poly-50-F_5 columns coated well and resulted in efficiencies up to 59% of the theoretical efficiency. The 10 μm I.D. columns coated with poly-50-cyano and SE-54 were not successfully evaluated by GC. For 10 and 5 μm I.D. columns that were 1 to 2 m long, the problem was not in coating the columns, but in evaluating these columns. Extremely high pressures were required for the GC carrier gas (100 atm), and the GC injector proved to be totally inadequate; the carrier gas leaked around the septum and a seal on the split valve failed. The poly-50-F_5 polysiloxane statically coated on a 5 μm I.D. column quite easily. The chromatogram in Fig. 2 shows a separation of a triglyceride mixture in SFC on a 0.7 m × 10 μm I.D. column. The solvent backflush injection method described by Lee *et al.*[42] was used to inject the sample onto the column. Although the injection volume diminished the resolution of this separation, the analysis time was less than 15 min, and 6 of the 9 components had baseline resolution. Injection and detection methods presently limit what can be done with these small I.D. columns in GC and SFC and must be improved before use of these columns becomes practical.

ACKNOWLEDGEMENTS

This work was supported by the Gas Research Institute (Contract No. 5088-260-1640).

REFERENCES

1 S. M. Fields, R. C. Kong, J. C. Fjeldsted, M. L. Lee and P. A. Peaden, *J. High Resolut. Chromatogr. Chromatogr. Commun.*, 7 (1984) 312.
2 M. Roth and A. Ansorgova, *J. Chromatogr.*, 465 (1989) 176.
3 C. P. M. Schutjes, E. A. Vermeer, J. A. Rijks and C. A. Cramers, *J. Chromatogr.*, 253 (1982) 1.
4 P. A. Peaden and M. L. Lee, *J. Chromatogr.*, 259 (1983) 1.
5 F. J. Yang, *J. Chromatogr. Sci.*, 20 (1982) 241.
6 J. H. Knox and M. T. Gilbert, *J. Chromatogr.*, 186 (1979) 405.
7 G. Guiochon, *Anal. Chem.*, 53 (1981) 1318.
8 G. Dijkstra and J. de Goey, in D. H. Desty (Editor), *Gas Chromatography*, Academic Press, New York, 1958, p. 56.
9 D. H. Desty, A. Goldup and W. T. Swanton, in N. Brenner, J. E. Callen and M. D. Weiss (Editors), *Gas Chromatography*, Academic Press, New York, 1962, p. 105.
10 G. Gaspar, P. Arpino and G. Guiochon, *J. Chromatogr.*, 15 (1977) 256.
11 R. L. St. Claire and J. W. Jorgenson, *J. Chromatogr. Sci.*, 23 (1985) 186.
12 P. R. Dluzneski and J. W. Jorgenson, *J. High Resolut. Chromatogr. Chromatogr. Commun.*, 11 (1988) 332.
13 J. Bouche and M. Verzele, *J. Gas Chromatogr.*, 6 (1968) 501.
14 G. A. F. M. Rutten and J. A. Luyten, *J. Chromatogr.*, 74 (1972) 177.
15 G. Alexander, G. Garzo and G. Palyi, *J. Chromatogr.*, 91 (1974) 25.
16 B. Xu and N. P. E. Vermeulen, *Chromatographia*, 18 (1984) 520.
17 J. C. Kuei, J. I. Shelton, L. W. Castle, R. C. Kong, B. E. Richter, J. S. Bradshaw and M. L. Lee, *J. High Resolut. Chromatogr. Chromatogr. Commun.*, 7 (1984) 13.
18 J. S. Bradshaw, L. Schregenberger, H-C. K. Chang, K. E. Markides and M. L. Lee, *J. Chromatogr.*, 358 (1986) 95.
19 J. C. Kuei, B. J. Tarbet, W. P. Jackson, J. S. Bradshaw, K. E. Markides and M. L. Lee, *Chromatographia*, 20 (1985) 25.
20 J. S. Bradshaw, R. S. Johnson, N. W. Adams, M. A. Pulsipher, K. E. Markides and M. L. Lee, *J. Chromatogr.*, 357 (1986) 69.
21 C. A. Rouse, A. C. Finlinson, B. J. Tarbet, J. C. Pixton, N. M. Djordjevic, K. E. Markides, J. S. Bradshaw and M. L. Lee, *Anal. Chem.*, 60 (1988) 901.

22 B. E. Richter, J. C. Kuei, L. W. Castle, B. A. Jones, J. S. Bradshaw and M. L. Lee, *Chromatographia*, 17 (1983) 570.
23 C. L. Woolley, *Ph. D. Dissertation*, Brigham Young University, Provo, UT, 1987.
24 K. E. Markides, B. J. Tarbet, C. L. Woolley, C. M. Schregenberger, J. S. Bradshaw and M. L. Lee, *J. High Resolut. Chromatogr. Chromatogr. Commun.*, 8 (1985) 378.
25 K. E. Markides, B. J. Tarbet, C. M. Schregenberger, J. S. Bradshaw, M. L. Lee and K. D. Bartle, *J. High Resolut. Chromatogr. Chromatogr. Commun.*, 8 (1985) 741.
26 R. C. Kong, S. M. Fields, W. P. Jackson and M. L. Lee, *J. Chromatogr.*, 289 (1984) 105.
27 J. C. Giddings, *Anal. Chem.*, 36 (1964) 741.
28 K. D. Bartle, C. L. Woolley, K. E. Markides, M. L. Lee and R. S. Hansen, *J. High Resolut. Chromatogr. Chromatogr. Commun.*, 10 (1987) 128.
29 R. C. Kong and M. L. Lee, *J. High Resolut. Chromatogr. Chromatogr. Commun.*, 6 (1983) 319.
30 C. L. Woolley, K. E. Markides, M. L. Lee and K. D. Bartle, *J. High Resolut. Chromatogr. Chromatogr. Commun.*, 9 (1986) 506.
31 C. L. Woolley, B. J. Tarbet, K. E. Markides, J. S. Bradshaw, M. L. Lee and K. D. Bartle, *J. High Resolut. Chromatogr. Chromatogr. Commun.*, 11 (1988) 113.
32 K. Grob and B. Grob, *J. High Resolut. Chromatogr. Chromatogr. Commun.*, 8 (1985) 856.
33 K. Grob, *J. High Resolut. Chromatogr. Chromatogr. Commun.*, 1 (1978) 93.
34 T. Wännman, L. Blomberg and S. Schmidt, *J. High Resolut. Chromatogr. Chromatogr. Commun.*, 8 (1985) 32.
35 B. L. Goodwin, *J. Chromatogr.*, 172 (1979) 31.
36 K. Janák, V. Kahle, K. Tesarik and M. Horká, *J. High Resolut. Chromatogr. Chromatogr. Commun.*, 8 (1985) 843.
37 B. Xu and N. P. E. Vermeulen, *J. High Resolut. Chromatogr. Chromatogr. Commun.*, 8 (1985) 181.
38 R. Kong and M. L. Lee, *Chromatographia*, 17 (1983) 451.
39 B. Xu and N. P. E. Vermeulen, *J. High Resolut. Chromatogr. Chromatogr. Commun.*, 11 (1988) 713.
40 R. L. Weast (Editor), *Handbook of Chemistry and Physics*, CRC Press, Boca Raton, FL, 67th ed., 1986.
41 J. C. Giddings, *Anal. Chem.*, 4 (1962) 458.
42 M. L. Lee, B. Xu, E. C. Huang, N. M. Djordjevic, H-C. K. Chang and K. E. Markides, *J. Microcolumn Sep.*, 1 (1989) 7.

Journal of Chromatography, 517 (1990) 521–547
Elsevier Science Publishers B.V., Amsterdam

CHROMSYMP. 1938

Influence of thermal variation of diffusion coefficient on non-equilibrium plate height in capillary zone electrophoresis

JOE M. DAVIS
Department of Chemistry and Biochemistry, Southern Illinois University at Carbondale, Carbondale, IL 62901 (U.S.A.)

ABSTRACT

A numerical algorithm is developed by which the radial profiles of temperature and mobility in an electrophoretic capillary can be computed from the steady-state equation of heat conduction. To determine these profiles accurately, the viscosity at any temperature is calculated to four significant figures from an expression different from the commonly used Andrade equation. The profiles so computed are used in a theory derived here, which addresses the impact of the thermal variation of diffusion coefficient on the axial dispersion of analyte ions in capillary zone electrophoresis. The magnitude of this dispersion is expressed as the non-equilibrium plate height. The numerical computation of this plate height indicates that this variation becomes significant only when the difference in temperature between the capillary center and wall exceeds *ca.* 5°C. The plate heights computed here can differ by more than a factor of two from those based on the Andrade equation, even when the variation of the diffusion coefficient is ignored. These differences originate from the relative inaccuracy of this equation.

INTRODUCTION

This paper addresses the influence of the thermal variation of diffusion coefficient on the non-equilibrium plate height of analyte ions in capillary zone electrophoresis (CZE). The origin of non-equilibrium dispersion in CZE is the gradient in temperature caused by the Joule heating of the capillary contents. Because electrophoretic mobilities increase with temperature, analyte ions migrate faster near the capillary center, where the temperature is higher, than near the capillary wall, where the temperature is lower. The resultant dispersion is mitigated by the radial diffusion of analyte ions, which averages out these differences in velocity to some degree.

Other theories for the non-equilibrium plate height or the effective diffusion coefficient, which is proportional to this plate height, in CZE have been derived. (As shown below, the effective diffusion coefficient is a calculated measure of the axial dispersion caused by the radial variation of analyte velocity.) Many of these theories

0021-9673/90/$03.50

differ only slightly from one another. By representing the Poiseuille flow in an open tube by three discrete components, Konstantinov and Oshurkova[1] derived an approximate effective diffusion coefficient analogous to that of Taylor[2,3]. Martin and Everaerts[4] suggested an analogy between the effective diffusion coefficient for chromatography, as derived by Golay[5], and that for CZE. Cox *et al.*[6] approximated the radial variation of analyte velocity by an equation derived by Hjertén[7]; he then solved the equation of continuity, from which the plate height was calculated, by making an analogy with the work of Aris[8]. In a work closely related to that of Konstantinov and Oshurkova[1], Virtanen[9] calculated an effective diffusion coefficient for CZE by modifying Taylor's effective diffusion coefficient for dispersion in open tubes. Similarly, Knox and Grant[10] modified Taylor's theory of dispersion to calculate the non-equilibrium plate height. Most recently, Grushka *et al.*[11] adapted the theory of Reejhsinghani *et al.*[12] to calculate from the equation of continuity an effective diffusion coefficient, from which the non-equilibrium plate height was evaluated.

A common attribute among these theories is the calculation (by a variety of means) of the mean square axial displacement of the analyte from the mean analyte position. The random-walk theory of dispersion shows that this result is proportional to the time required for ions to diffuse between two characteristic positions in the capillary, at which their velocities significantly differ[13]. In all of the above theories, this time is approximated as a constant. Because the diffusion coefficient of analyte ions increases with temperature, however, the time required for ions to diffuse from one position to another is reduced near the capillary center, where the temperature is higher, relative to that near the capillary wall, where the temperature is lower. In other words, this time is not constant but varies with the radial position in the capillary. No attempt has been made to determine under what conditions this approximation breaks down and the radial variation of the diffusion coefficient becomes important. This paper does so.

In some of the theories referenced above, detailed equations for plate height were evaluated with analytical expressions for the temperature and electrophoretic mobility of analyte ions in the capillary. In general, these expressions apply when the difference in temperature between the capillary wall and center is vanishingly small. They are only approximately correct, however, when this temperature difference is large, *i.e.*, when non-equilibrium dispersion is large. Because the temperature difference, above which the variation of diffusion coefficient is important, is unknown (indeed, its determination is the goal of the paper), one does not know *a priori* if these expressions are appropriate for this study. To obtain a fairly rigorous solution, these expressions are not used here except in limiting cases. Instead, expressions for the temperature and electrophoretic mobility are computed numerically from the steady-state equation of heat conduction. These expressions are free of all but the most fundamental assumptions and are, in principle, applicable over a wide range of temperatures.

THEORY

The theory of this paper is composed of two parts. In Part I, the profiles of temperature and electrophoretic mobility are computed from the steady-state equation of heat conduction. In Part II, an expression for the non-equilibrium plate height is derived, in which the radial variation of the diffusion coefficient is addressed.

Numerical values of this expression are then evaluated with the temperature and mobility profiles computed in Part I.

Part I: Determination of radial temperature and electrophoretic-mobility profiles

Here, one will assume that thermal convection, thermal diffusion, and heat transfer from electroosmotically induced forced convection are negligible. One will also assume the analyte concentration is vanishingly small, such that the electrical and thermal properties of the capillary contents are determined by the buffer only, and the analyte does not alter the electric field strength. Finally, one will assume that the equilibrium constants governing the dissociation of the buffer and analyte do not vary over the range of temperatures experienced by the buffer. (These assumptions will be critiqued later.) The radial temperature profile in the capillary is then governed by the steady-state equation of heat conduction[14,15]

$$-\frac{1}{r}\frac{\mathrm{d}}{\mathrm{d}r}\left[rk_t(r)\frac{\mathrm{d}T(r)}{\mathrm{d}r}\right] = k_e(r)E^2 \tag{1}$$

where r is the radial coordinate, $T(r)$ is temperature, $k_t(r)$ and $k_e(r)$ are the thermal and electrical conductivities of the buffer, and E is the electric field strength. Although one should strictly interpret the conductivities $k_e(r)$ and $k_t(r)$ as functions of radial coordinate r[14,15], one alternatively can (as commonly does) interpret them as functions of temperature $T(r)$ (ref. 15). By introducing the variables

$$y = \frac{r}{a};\ \theta(y) = \frac{T(y) - T_o}{T_o} \tag{2}$$

one can reexpress eqn. 1 in the dimensionless form[14]

$$-\frac{1}{y}\frac{\mathrm{d}}{\mathrm{d}y}\left[y\frac{k_t(y)}{k_{to}}\frac{\mathrm{d}\theta(y)}{\mathrm{d}y}\right] = \frac{k_e(y)}{k_{eo}}B \tag{3}$$

where a is the capillary radius, T_o is the temperature at the (inner) capillary wall, k_{to} and k_{eo} are the thermal and electrical conductivities of the buffer at this wall, and B is

$$B = \frac{k_{eo}a^2E^2}{k_{to}T_o} \tag{4}$$

Several solutions to eqn. 3 have been developed, which differ in the approximations chosen for the reduced conductivities $k_e(y)/k_{eo}$ and $k_t(y)/k_{to}$. When these approximations equal the constant, one (*i.e.*, when the conductivities are independent of temperature); the solution to eqn. 3 is simply

$$\lim_{B\to 0}\theta(y) = \frac{B}{4}(1 - y^2) \tag{5}$$

Others have solved eqn. 3 more rigorously to address the dependences of $k_e(y)/k_{eo}$ and

$k_t(y)/k_{to}$ on temperature. Broer[14] expressed these functions as two-term expansions in $\theta(y)$ and so accounted for the linear variations with temperature of the electrical and thermal conductivities. By equating $k_t(y)/k_{to}$ to one and $k_e(y)/k_{eo}$ to a two-term expansion in $\theta(y)$, Coxon and Binder[16], Brown and Hinckley[17], and Jones and Grushka[18] obtained Bessel functions as solutions to eqn. 3. These functions account for only the linear variation with temperature of the electrical conductivity.

The most general solution to eqn. 3, subject to the boundary conditions $d\theta(y)/dy = 0|_{y=0}$ (because of radial symmetry) and $\theta(y) = 0|_{y=1}$ (because $T = T_o$ at the wall), is

$$\theta(y) = B\int_0^1 \frac{1}{\left[\frac{k_t(y)}{k_{to}}\right]y}\left[\int_0^y \frac{k_e(y)}{k_{eo}} y\,dy\right]dy = B\int_0^1 \frac{1}{h(y)y}\left[\int_0^y f(y)y\,dy\right]dy \tag{6a}$$

$$f(y) = k_e(y)/k_{eo};\ h(y) = k_t(y)/k_{to} \tag{6b}$$

where the ratios, $k_e(y)/k_{eo}$ and $k_t(y)/k_{to}$, are now represented by the functions $f(y)$ and $h(y)$, respectively. These functions vary with the radial coordinate y because the conductivities vary with temperature. In other words, $h(y)$ and $f(y)$ vary with $T(y) = T_o[1 + \theta(y)]$. But $\theta(y)$ is unknown; it is the function one seeks. In solving eqn. 6a, one is saddled with the circular task of determining $\theta(y)$ from two functions which themselves depend on $\theta(y)$.

A general solution to eqn. 6a is developed here, but not because the solutions to $\theta(y)$ referenced above are inadequate. Rather, as will be shown below, the non-equilibrium plate height depends on the function $f(y)$, which describes the radial variation of the electrophoretic mobility. By judiciously developing the solution to eqn. 6a, one can determine $f(y)$ without any assumptions beyond those outlined at the beginning of this section. To achieve this objective, one must sacrifice analytical rigor for numerical methods. As compensation, however, one circumvents the shortcomings that others have encountered in the derivation of approximations to $f(y)$, especially for large values of B.

An iterative numerical algorithm by which $f(y)$ can be computed is now outlined. For any value of B, one can solve eqn. 6a numerically by initially equating $f(y)$ and $h(y)$ to one. In this case, the solution to $\theta(y)$ is eqn. 5, within numerical error. For any value of T_o, this solution to $\theta(y)$ defines the temperature T at all values of y (in this case, $T = T_o[1 + B(1 - y^2)/4]$, from which new approximations to $f(y)$ and $h(y)$ can then be calculated from empirical functions of temperature for the electrical and thermal conductivities. In other words, the temperature at any coordinate y defines the values of the electrical and thermal conductivities at that coordinate; the ratios of that electrical conductivity to k_{eo}, and that thermal conductivity to k_{to}, define the values of the functions $f(y)$ and $h(y)$, respectively, at that coordinate. One can then substitute these new approximations to $f(y)$ and $h(y)$ into eqn. 6a, numerically integrate with respect to y, and compute a new solution to $\theta(y)$. This solution will differ from the previous one, because the functions $f(y)$ and $h(y)$ now differ from one. From this new solution to $\theta(y)$, one can again calculate the temperature at all values of y and new approximations to $f(y)$ and $h(y)$, as before. One can iteratively repeat this algorithm,

until f(y), h(y), and $\theta(y)$ converge to constant values. When this convergence is reached, then one has an excellent approximation to the function f(y) that one needs to describe the radial variation of electrophoretic mobility.

To implement this algorithm, one must have accurate functions for h(y) and f(y) at different temperatures. These functions will be represented by $h[T(y)] = h[T_o, \theta(y)]$ and $f[T(y)] = f[T_o,\theta(y)]$, respectively. Over the temperature range, 7–97°C, the function $h[T_o,\theta(y)]$ for water can be described with an accuracy of one part per thousand [at least, for the values 280, 290, 300, ..., 370 K (ref. 19)] by the quadratic

$$h[T_o,\theta(y)] = 1 + \alpha_1\theta(y) + \alpha_2\theta(y)^2 \tag{7}$$

where

$$\alpha_1 = (6.090 \cdot 10^{-3}\, T_o - 1.511 \cdot 10^{-5} T_o^2)/\Delta \tag{7a}$$

$$\alpha_2 = -7.555 \cdot 10^{-6}\, T_o^2/\Delta \tag{7b}$$

$$\Delta = -0.5390 + 6.090 \cdot 10^{-3}\, T_o - 7.555 \cdot 10^{-6}\, T_o^2 \tag{7c}$$

and where T_o is expressed in degrees Kelvin. These equations were determined by fitting a quadratic function of T to tabulated values of the thermal conductivity of water[19] and then by reexpressing $T = T(y)$ in terms of $\theta(y)$, eqn. 2. The function Δ (eqn. 7c) is the quadratic approximation to the thermal conductivity of water at the temperature T_o, in W/(mK). Lest any ambiguity exist in the use of eqn. 7, one should perhaps again state that the value of $h[T_o,\theta(y)]$ at coordinate y in a given iteration is determined from T_o and the value of $\theta(y)$ computed at that coordinate in the previous iteration. Eqn. 7, although determined for water, is also adequate for electrolytic buffers, because salts contribute to the thermal conductivity by an amount less than $2 \cdot 10^{-5}$ W/(mK) or so per ion, as long as their molar concentration is less than 0.1 (ref. 20), a concentration which is rarely exceeded in CZE.

The function $f[T_o,\theta(y)]$ is developed from the electrical conductivity $k_e(T)$, which is[21]

$$k_e(T) = F\sum_i z_i(T)|\mu_i(T)|C_i(T) = eF\sum_i \frac{z_i^2(T)}{f_{ri}(T)}C_i(T) \tag{8}$$

where F is the Faraday constant; e is the fundamental electrical charge; and z_i μ_i, C_i, and f_{ri} are the unsigned number of charges, the electrophoretic mobility, the concentration, and the friction coefficient of the ith ion, respectively. If one neglects the variation of z_i and C_i with temperature (the former, from changes in screening by the electrical double layer, extent of ionization, etc.; the latter, from volume expansion), then eqn. 8 may be expressed as

$$k_e(T) = \frac{eF}{\eta(T)}\sum_i \frac{A_i^*}{A_i(T)} \tag{9}$$

where A_i^* equals the constant $z_i^2 C_i$ and the explicit dependence of friction coefficient f_r on viscosity η has been expressed as $f_{ri}(T) = A_i(T)\eta(T)$. If one now assumes that the plane of hydrodynamic shear (and hence the effective ionic radius) is independent of temperature, then A_i is also independent of temperature. Consequently, as first shown by Hjertén[7], f$[T_o,\theta(y)]$ can be approximated as

$$\mathrm{f}[T_o, \theta(y)] = \frac{\eta_o}{\eta[T_o, \theta(y)]} \tag{10}$$

where η_o is the viscosity at the inner capillary wall.

Many empirical equations have been proposed to describe the dependence of viscosity on temperature[20]. Here, two such functions for the viscosity η of water are critiqued. Over the temperature range, 15–100°C, η can be described to four significant figures by[22]

$$\eta = \eta_{293} 10^{\frac{1.3272(293-T) - 1.053\cdot 10^{-3}(293-T)^2}{T-168}} \tag{11}$$

where T is expressed in degrees Kelvin and η_{293} is the viscosity of water at 293 K. This empirical equation accurately predicts to four significant figures values of viscosity measured to five significant figures[23]. By combining eqns. 10 and 11, one can express f$[T_o,\theta(y)]$ as

$$\mathrm{f}[T_o,\theta(y)] = 10^{T_o[\beta_1\theta(y) + \beta_2\theta(y)^2]/\beta_3} \tag{12a}$$

where

$$\beta_1 = 165.9 + (1.053 \cdot 10^{-3})(293 - T_o)(43 - T_o) \tag{12b}$$

$$\beta_2 = (1.053 \cdot 10^{-3})T_o(T_o - 168) \tag{12c}$$

$$\beta_3 = (T_o - 168)\{T_o[\theta(y) + 1] - 168\} \tag{12d}$$

For small values of B, eqn. 12 can be linearized by expanding eqn. 12a as a two-term Taylor series, neglecting the quadratic power of $\theta(y)$ in this expansion, and neglecting $\theta(y)$ in coefficient β_3. The result is

$$\lim_{B\to 0} \mathrm{f}(y) \approx 1 + \alpha\theta(y) = 1 + \alpha B\frac{(1 - y^2)}{4} \tag{13a}$$

$$\alpha = \frac{\ln(10)\beta_1 T_o}{(T_o - 168)^2} \tag{13b}$$

where $\theta(y)$ has been approximated by eqn. 5.

In other studies[7,11], η alternatively was represented by the Andrade equation[20]

$$\eta = \eta^* e^{B_A/T} \tag{14}$$

for which

$$f[T_o, \theta(y)] = e^{B_A\theta(y)/\{T_o[1+\theta(y)]\}} \tag{15}$$

where B_A is an empirical temperature commonly equated to 2400 K. By representing this equation by a two-term Taylor-series expansion and expressing $\theta(y)$ in this expansion by eqn. 5, others showed[7,11]

$$\lim_{B\to 0} f(y) \approx 1 + \frac{B_A}{T_o} B \frac{(1-y^2)}{4} \tag{16}$$

The expansions, eqns. 13 and 16, are clearly different; they are equal only when T_o satisfies the equation

$$B_A = \frac{\ln(10)\beta_1 T_o^2}{(T_o - 168)^2} \tag{17}$$

or when $T_o \approx 4°C(B_A = 2400$ K). At all other temperatures, eqns. 13 and 16 will predict different values for the variation of electrophoretic mobility with temperature and consequently the non-equilibrium plate height.

In spite of its common use, eqn. 14 describes the variation of η with temperature somewhat poorly. In support of this assertion, Table I reports estimates of η calculated from eqns. 11 and 14 for selected temperatures grouped in intervals of two degrees. This two-degree interval was chosen as an arbitrary upper limit to the temperature difference between the capillary center and wall that one might encounter in CZE, under experimental conditions where Joule heating is marginal. For each group, the parameter η^* was computed by fitting to eqn. 14 ($B_A = 2400$ K) with least-squares methods the three values of η computed from eqn. 11. The η values so calculated agree with those calculated from eqn. 11 only to within two significant figures. Also, the variation of η^* from group to group is substantial, which indicates that a larger temperature range could not be spanned by eqn. 14 with any accuracy. These equations predict different values of η at different temperatures, principally because they have different values of $d\eta/dT$.

The differences between these values raise some doubts about the accuracy of electrophoretic mobilities calculated from the Andrade equation. In this paper, eqn. 11 will be used for this task, unless otherwise stated. As will be shown below, these differences are so substantial that eqn. 16 predicts non-equilibrium plate heights that can be 150% larger than those predicted by eqn. 13, other factors being equal.

Part II: Derivation of non-equilibrium plate height for radially dependent diffusion coefficient

Here, the dispersion theory of Reejhsinghani *et al.*[12] is used to address the influence of the radial variation of the analyte diffusion coefficient on the non-equilibrium plate height in CZE. This theory draws heavily on Taylor's studies of dispersion[2,3] and was also used by Grushka *et al.*[11] in a recent calculation of plate height, in which this variation was ignored. In essence, this theory simplifies the

TABLE I

COMPARISON OF VISCOSITIES η CALCULATED FROM EQNS. 11 AND 14

Parameter η^* was determined by least-squares regression.

T (°C)	*Eqn. 11*	*Eqn. 14*	$\eta^* \cdot 10^4$ *(cP)*
25	0.8905	0.8942	
26	0.8705	0.8704	2.843
27	0.8513	0.8475	
35	0.7194	0.7231	
36	0.7053	0.7051	2.986
37	0.6916	0.6877	
45	0.5960	0.5995	
46	0.5856	0.5855	3.163
47	0.5755	0.5719	
55	0.5041	0.5074	
56	0.4962	0.4962	3.369
57	0.4885	0.4854	
65	0.4335	0.4365	
66	0.4274	0.4275	3.600
67	0.4214	0.4187	
75	0.3781	0.3805	
76	0.3732	0.3731	3.848
77	0.3685	0.3658	
85	0.3337	0.3359	
86	0.3298	0.3297	4.119
87	0.3259	0.3236	

equation of continuity to an ordinary differential equation, whose solution determines an effective diffusion coefficient from which the plate height is calculated. The theory developed below may be construed as an extension of these more fundamental works.

One develops this ordinary differential equation from the equation of continuity in radial coordinates, which is[14]

$$\frac{\partial c}{\partial t} + \frac{1}{r}\frac{\partial}{\partial r}(rN_r) + \frac{\partial N_z}{\partial z} = 0 \tag{18}$$

where N_r and N_z are respectively the one-dimensional radial and axial fluxes

$$N_r = v_r c - D_r \frac{\partial c}{\partial r} \tag{19}$$

$$N_z = v_z c - D_z \frac{\partial c}{\partial z} \tag{20}$$

and where z is the axial coordinate, t is time, $c = c(r,z,t)$ is the analyte concentration, and v_r and v_z (D_r and D_z) are the analyte velocities (diffusion coefficients) in the radial and axial directions. No angular flux appears, because of radial symmetry. If one again assumes that thermal convection and thermal diffusion are negligible, then $v_z = v_z(r)$ is

$$v_z(r) = [\mu(r) + \mu_{eo}]E \tag{21}$$

where $\mu(r)$ is the electrophoretic mobility at coordinate r and μ_{eo} is the electroosmotic flow coefficient (both μ and μ_{eo} are signed quantities). Here, one has assumed that capillary diameters are sufficiently large that one can neglect the variation of electroosmotic flow in the electrical double layer at the capillary–buffer interface. Hence, the electroosmotic flow equals $\mu_{eo}E$. One has also assumed that the steady-state equation of heat conduction applies and that v_z does not vary with t, as it does during a brief initial transient[16].

The mobility can be expressed as $\mu(r) = -\varepsilon\zeta/\eta(r)$ (ref. 24), where ε and ζ are the electrical permittivity of the buffer and the zeta potential of the analyte. If one neglects the variation of these parameters with temperature, eqn. 21 may be expressed as[7,11]

$$v_z(r) = \left\{ -\frac{\varepsilon\zeta}{\eta_o}\left[\frac{\varepsilon\zeta/\eta(r)}{\varepsilon\zeta/\eta_o}\right] + \mu_{eo}\right\}E = [\mu_o f(r) + \mu_{eo}]E \tag{22}$$

where $\mu_o = -\varepsilon\zeta/\eta_o$ is the electrophoretic mobility of the analyte at the capillary wall and $f(r)$ is the equivalent of $f(y)$, but now expressed in terms of the dimensioned coordinate, r, instead of the dimensionless coordinate, $y = r/a$. (For the moment, equations in r are more convenient than equations in y; the final results will be expressed in terms of y.) Eqn. 22 marks the first appearance of the function $f(r)$ [or $f(y)$], which is determined numerically as described in Part I.

If one now assumes that D_z is independent of z and that thermal diffusion is negligible (*i.e.*, that $v_r = 0$), then the substitution of eqns. 19 and 20 into eqn. 18 yields

$$\frac{\partial c}{\partial t} + v_z(r)\frac{\partial c}{\partial z} = \frac{1}{r}\frac{\partial}{\partial r}\left[rD_r(r)\frac{\partial c}{\partial r}\right] + D_z\frac{\partial^2 c}{\partial z^2} \tag{23}$$

where the dependence of $D_r = D_r(r)$ on radial coordinate r is expressed explicitly.

By defining the coordinate $z_1 = z - \bar{v}t$, where $\bar{v}$ is the average analyte velocity in the axial direction, one can implement the standard coordinate transformation

$$\left(\frac{\partial c}{\partial t}\right)_z = \left(\frac{\partial c}{\partial t}\right)_{z_1} - \bar{v}\left(\frac{\partial c}{\partial z_1}\right)_t \tag{24}$$

with which eqn. 23 can be expressed as

$$\frac{\partial c}{\partial t} + [v_z(r) - \bar{v}]\frac{\partial c}{\partial z_1} = \frac{1}{r}\frac{\partial}{\partial r}\left[rD_r(r)\frac{\partial c}{\partial r}\right] + D_z\frac{\partial^2 c}{\partial z_1^2} \tag{25}$$

The theory of Reejhsinghani *et al.*[12] is now used to simplify eqn. 25. First, the concentration c is approximated by the two-term expansion

$$c = c_m(z_1) + \frac{\partial c_m(z_1)}{\partial z_1} g(r) \tag{26}$$

where $c_m(z_1)$ is the cross sectional average concentration (2)

$$c_m(z_1) = \frac{2}{a^2}\int_0^a rc\,dr \tag{27}$$

and $g(r)$ is a function to be determined. By combining eqns. 26 and 27, one can show[12]

$$\int_0^a rg(r)dr = 0 \tag{28}$$

which will prove useful later.

Because $c_m(z_1)$ is independent of r, and derivatives of $c_m(z_1)$ with respect to z_1 of order two or greater are negligible compared to $\partial c_m(z_1)/\partial z_1$ (ref. 12), the following additional approximations hold

$$\frac{\partial c}{\partial r} \approx \frac{\partial c_m(z_1)}{\partial z_1}\frac{dg(r)}{dr} \tag{29a}$$

$$\frac{\partial^2 c}{\partial r^2} \approx \frac{\partial c_m(z_1)}{\partial z_1}\frac{d^2 g(r)}{dr^2} \tag{29b}$$

$$\frac{\partial c}{\partial z_1} \approx \frac{\partial c_m(z_1)}{\partial z_1} \tag{29c}$$

$$\frac{\partial c}{\partial t} \approx 0 \tag{29d}$$

By substituting eqn. 29 into eqn. 25 and neglecting derivatives of $c_m(z_1)$ with respect to z_1 of order two or greater, one obtains the ordinary differential equation

$$v_z(r) - \bar{v} = \frac{1}{r}\frac{d}{dr}\left[rD_r(r)\frac{dg(r)}{dr}\right] \tag{30}$$

which integrates to

$$\int_0^r r[v_z(r) - \bar{v}]dr = rD_r(r)\frac{dg(r)}{dr} \tag{31}$$

where the right-hand side, $rD_r(r)\mathrm{d}g(r)/\mathrm{d}r$, equals zero at $r = 0$ (the lower limit of the integral on the left-hand side), because $\mathrm{d}g(r)/\mathrm{d}r$ equals zero at $r = 0$. (Obviously, the right-hand side is also zero at $r = 0$, because the first factor of this function is r.) The function $\mathrm{d}g(r)/\mathrm{d}r$ equals zero at $r = 0$, because the diffusive flux

$$-D_r(r)\frac{\partial c}{\partial r} = -D_r(r)\frac{\partial c_m(z_1)}{\partial z_1}\frac{\mathrm{d}g(r)}{\mathrm{d}r} \tag{32}$$

is zero at $r = 0$, because of radial symmetry. Because neither $D_r(r)$ nor $\partial c_m(z_1)/\partial z_1$ is zero at $r = 0$, eqn. 32 equals zero at $r = 0$ only if $\mathrm{d}g(r)/\mathrm{d}r$ equals zero at $r = 0$. This function is also zero at $r = a$, because analyte cannot diffuse across the capillary wall. This latter equality will prove most useful later.

If the radial gradient in temperature is the only cause of the radial variation of $D_r(r)$, one can express this variation as[20,25]

$$\frac{D_r(r)\eta(r)}{T(r)} = A' \tag{33}$$

where A' is a constant, whose value depends on the physical properties of the analyte and buffer. The theoretical origin of this expression is the Nernst–Haskell equation, which describes the mutual diffusion coefficient of a salt at infinite dilution[20,25]. Eqn. 33 is also theoretically justified for molecular species by the Stokes–Einstein equation[20,25], which in turn forms the basis of the empirical equations for the mutual diffusion coefficient of Wilke and Chang[20,25]; Tyn and Calus[20]; Nakanishi[20]; King, Hsueh and Mao[25]; and Reddy and Doraiswamy[25].

With eqn. 33, one can express the ratio of $D_r(r)$ to D_{ro}, the value of $D_r(r)$ at the capillary wall, as

$$\frac{D_r(r)}{D_{ro}} = \frac{A'T(r)/\eta(r)}{A'T_o/\eta_o} = \mathrm{f}(r)\frac{T(r)}{T_o} = \mathrm{f}(r)[\theta(r) + 1] \tag{34}$$

from which one concludes

$$D_r(r) = D_{ro}\mathrm{f}(r)[\theta(r) + 1] \tag{35}$$

where $\theta(r)$ is the equivalent of $\theta(y)$, but expressed in terms of r, instead of y.

By substituting eqn. 35 for $D_r(r)$ in eqn. 31, one can show

$$\mathrm{g}(r) - \mathrm{g}(0) = \frac{1}{D_{ro}}\int_0^r \frac{1}{r\mathrm{f}(r)[\theta(r) + 1]}\int_0^r r[v_z(r) - \bar{v}]\mathrm{d}r\mathrm{d}r \tag{36}$$

where $\mathrm{g}(0)$ is the value of $\mathrm{g}(r)$ at $r = 0$. Eqn. 36 alternatively can be expressed in terms of coordinate $y = r/a$ as

$$\mathrm{g}(y) - \mathrm{g}(0) = \frac{a^2\mu_o E}{D_{ro}}\int_0^y \frac{1}{y\mathrm{f}(y)[\theta(y) + 1]}\int_0^y y\left[\mathrm{f}(y) - 2\int_0^1 y\mathrm{f}(y)\mathrm{d}y\right]\mathrm{d}y\mathrm{d}y \tag{37}$$

where $v_z(r)$ is expressed by eqn. 22 and the average zone velocity $\bar{v}$ is

$$\bar{v} = 2\int_0^1 y v_z(y)\mathrm{d}y = [2\mu_o(\int_0^1 y f(y)\mathrm{d}y + \mu_{eo}]E \tag{38}$$

in accordance with this equation. One observes that μ_{eo} subtracts out in this result; the electroosmotic flow causes no dispersion.

A brief outline of the calculation of the non-equilibrium plate height from eqn. 37 may be appropriate here, because Reejhsinghani *et al.*[12] provide little detail in their work, and Grushka *et al.*[11] simply cite their result (actually, its negative). The analysis below differs from that of Reejhsinghani *et al.*[12] as best as the author can tell, but it parallels that of Giddings in his plate-height studies of chromatography[13] and field-flow fractionation[26]. In any case, the result is the same as that derived by Reejhsinghani *et al.* The average convective flux, $<cv_z(r)>$, in the axial direction can be expressed with eqn. 26 as

$$<cv_z(r)> = \frac{2c_m(z_1)}{a^2}\int_0^a r v_z(r)\mathrm{d}r + \frac{2}{a^2}\frac{\partial c_m(z_1)}{\partial z_1}\int_0^a r g(r) v_z(r)\mathrm{d}r \tag{39}$$

The first term in this equation equals the average convective flux, $c_m(z_1)\bar{v}$, which represents the translation of the average zone concentration at the average zone velocity. The second term represents a dispersive flux, which alternatively can be expressed by Fick's first law, $-\mathscr{D}\partial c_m(z_1)/\partial z_1$, where $\mathscr{D}$ is an effective diffusion coefficient equal to

$$\mathscr{D} = -\frac{2}{a^2}\int_0^a r g(r) v_z(r)\mathrm{d}r \tag{40a}$$

$$= -2\int_0^1 y g(y) v_z(y)\mathrm{d}y \tag{40b}$$

and from which the non-equilibrium plate height H is calculated as $2\mathscr{D}/\bar{v}$ (refs. 11, 13 and 26)

$$H = -\frac{4}{a^2\bar{v}}\int_0^a r g(r) v_z(r)\mathrm{d}r = -\frac{4}{\bar{v}}\int_0^1 y g(y) v_z(y)\mathrm{d}y \tag{41}$$

So far, the theory developed here parallels that of Grushka *et al.*[11], except that the radial variation of diffusion coefficient has been included. Now, a slight departure is taken. One does not need to determine the constant of integration g(0) in eqn. 37, as did Grushka *et al.*[11], to evaluate eqn. 41, because this latter equation also equals

$$H = -\frac{4}{\bar{v}}\int_0^1 y[g(y) - g(0)][v_z(y) - \bar{v}]\mathrm{d}y \tag{42a}$$

$$= -\frac{4\mu_o E}{\bar{v}}\int_0^1 y[g(y) - g(0)]\left[f(y) - 2\int_0^1 yf(y)dy\right]dy \tag{42b}$$

To demonstrate this equality, one expands eqn. 42a to the result

$$H = -\frac{4}{\bar{v}}\left[\int_0^1 yg(y)v_z(y)dy - \bar{v}\int_0^1 yg(y)dy - g(0)\int_0^1 yv_z(y)dy + g(0)\bar{v}\int_0^1 ydy\right] \tag{43}$$

The second term in this expansion equals zero, by virtue of eqn. 28. The third and fourth terms respectively equal $-g(0)\bar{v}/2$ and $+g(0)\bar{v}/2$ and cancel one another, regardless of the value of g(0). (In fact, they cancel one another, regardless of the lower limit of the outermost integral in eqn. 37. Advantages accrue if one chooses $y = 0$ as the lower limit, however, as will be shown below.) Only the first term, which equals eqn. 41, remains. This simplification of theory is identical to that developed by Giddings[26] in his non-equilibrium theory of field-flow fractionation.

By combining eqns. 37 and 42b, one can express H as

$$H = -\frac{4(a\mu_o E)^2}{D_{ro}\bar{v}}\int_0^1 y\left[f(y) - 2\int_0^1 yf(y)dy\right]\int_0^y \frac{1}{yf(y)[\theta(y) + 1]}\int_0^y y\left[f(y) - 2\int_0^1 yf(y)dy\right]dydydy \tag{44}$$

This cumbersome result fortunately can be simplified substantially by integration by parts, in a manner identical to that developed by Giddings[27] in the non-equilibrium theory of field-flow fractionation. If one lets

$$U = \int_0^y \frac{1}{yf(y)[\theta(y) + 1]}\int_0^y y\left[f(y) - 2\int_0^1 yf(y)dy\right]dydy \tag{45}$$

and

$$dV = y\left[f(y) - 2\int_0^1 yf(y)dy\right]dy \tag{46}$$

then eqn. 44 can be expressed as

$$H = -\frac{4(a\mu_o E)^2}{D_{ro}\bar{v}}\int_0^1 UdV = -\frac{4(a\mu_o E)^2}{D_{ro}\bar{v}}\left[UV\Big|_0^1 - \int_0^1 VdU\right] \tag{47}$$

where $UV\Big|_0^1$ implies that $U(y = 1)$ and $V(y = 1)$, and $U(y = 0)$ and $V(y = 0)$, are multiplied, and that the latter product is subtracted from the former. The function

$$V = \int y\left[f(y) - 2\int_0^1 yf(y)dy \right]dy \tag{48}$$

is the dimensionless equivalent of eqn. 31, which is zero at both $r = 0$ and $r = a$ ($y = 0$ and $y = 1$), because $dg(r)/dr$ equals zero at both these limits (see discussion immediately following eqn. 31). Therefore, the first term, $UV\Big|_0^1$, equals zero, and eqn. 47 reduces to

$$H = \frac{4(a\mu_o E)^2}{D_{ro}\bar{v}}\int_0^1 V dU = \frac{4(a\mu_o E)^2}{D_{ro}\bar{v}}\int_0^1 \frac{1}{yf(y)[\theta(y)+1]}\left\{\int_0^y y\left[f(y) - 2\int_0^1 yf(y)dy \right]dy\right\}^2 dy \tag{49}$$

where one has now taken advantage of the equality, $V(y = 0) = 0$, to express the product of two integrals as the square of the same integral.

Eqn. 49 can be expressed in the dimensionless form

$$\frac{HD_{ro}\bar{v}}{(a\mu_o E)^2} = 4\int_0^1 \frac{1}{yf(y)[\theta(y)+1]}\left\{\int_0^y y\left[f(y) - 2\int_0^1 yf(y)dy \right]dy\right\}^2 dy \tag{50}$$

which is the desired theoretical result.

In general, eqn. 50 must be evaluated numerically, because $f(y)$ and $\theta(y)$ are computed numerically, as detailed in Part I. For small values of B, however, an analytical solution can be determined by approximating $\theta(y)$ and $f(y)$ in eqn. 50 by eqns. 5 and 13, respectively. In this case, eqn. 50 integrates to the somewhat awkward result

$$\lim_{B\to 0}\frac{HD_{ro}\bar{v}}{(a\mu_o E)^2} = \frac{\alpha}{16} + \frac{2\alpha^2}{B^2(1-\alpha)}\left[\left(1+\frac{B}{4}\right)\ln\left(1+\frac{B}{4}\right) - \frac{B}{4}\right] -$$

$$\frac{2}{B^2\alpha(1-\alpha)}\left[\left(1+\frac{\alpha B}{4}\right)\ln\left(1+\frac{\alpha B}{4}\right) - \frac{\alpha B}{4}\right] \tag{51}$$

where α is defined by eqn. 13b. By using the expansion

$$\left(1+\frac{\gamma}{4}\right)\ln\left(1+\frac{\gamma}{4}\right) - \frac{\gamma}{4} \approx \frac{\gamma^2}{32} - \frac{\gamma^3}{384} + \frac{\gamma^4}{3072} - \frac{\gamma^5}{20480} + \cdots \tag{52}$$

where γ is any real number, one can approximate eqn. 51 by

$$\lim_{B\to 0}\frac{HD_{ro}\bar{v}}{(a\mu_o E)^2} \approx \frac{1}{1536}\left[\frac{\ln(10)\beta_1 T_o B}{(T_o - 168)^2}\right]^2\left\{1 - \frac{3B}{20}\left[1 + \frac{\ln(10)\beta_1 T_o}{(T_o - 168)^2}\right]\right\} \tag{53}$$

where T_o is in degrees Kelvin, α has been explicitly expressed, and β_1 is defined by eqn. 12b.

To test this theory, one should compare eqn. 50 to the analytical result derived by Grushka *et al.*[11]. To make this comparison, one must "turn off" the radial variation of the diffusion coefficient in eqn. 50 by equating the functions f(y) and $\theta(y)$ to one and zero, respectively, in the expression, $\{yf(y)[\theta(y) + 1]\}^{-1}$. In this case, eqn. 50 becomes

$$\lim_{D_r(r)\to D_{ro}} \frac{HD_{ro}\bar{v}}{(a\mu_o E)^2} = 4\int_0^1 \frac{1}{y}\left\{\int_0^y y\left[f(y) - 2\int_0^1 yf(y)dy\right]dy\right\}^2 dy \tag{54}$$

If f(y) in eqn. 54 is now equated to eqn. 16, the approximation to f(y) used by Grushka *et al.*[11], then eqn. 54 integrates to the simple analytical result

$$\lim_{\substack{B\to 0 \\ D_r(r)\to D_{ro}}} \frac{HD_{ro}\bar{v}}{(a\mu_o E)^2} = \frac{1}{1536}\left\{\frac{BB_A}{T_o}\right\}^2 \tag{55}$$

At first glance, eqn. 55 seems quite different from the result of Grushka *et al.*[11], which in dimensionless terms is

$$\lim_{\substack{B\to 0 \\ D_r(r)\to D_{ro}}} \frac{HD_{ro}}{a^2 u_m} = \frac{1}{24}\frac{(BB_A/T_o)^2}{(8 + BB_A/T_o)^2} \tag{56}$$

(This equation, as expressed in ref. 11, actually has a minus sign in the denominator, instead of a plus sign; this appears to be a typographical error.) The apparent difference between eqns. 55 and 56 arises from the neglect of electroosmotic flow in the derivation of eqn. 56, which makes the mean analyte velocity u_m different from the mean analyte velocity $\bar{v}$ described here. One can easily show

$$\lim_{\substack{B\to 0 \\ D_r(r)\to D_{ro}}} \frac{(\mu_o E)^2}{\bar{v}} = \frac{64\ u_m}{(8 + BB_A/T_o)^2} \tag{57}$$

when $\mu_{eo} = 0$ and $\bar{v}$ is calculated from eqns. 16 and 22. By substituting eqn. 57 into eqn. 55, one does obtain eqn. 56, as expected. One should perhaps observe that the inclusion of the electroosmotic flow is essential to an accurate description of plate height, even though it causes no dispersion. The flow does affect the analyte residence time and consequently the number of diffusive steps which partially average out differences in analyte velocity.

In conclusion of this section, one should note that the accuracy of the theory developed by Grushka *et al.*[11] should be substantially improved by substituting the right-hand side of eqn. 17 for B_A in eqns. 55 and 56. This substitution corrects these

authors' otherwise sound work for the shortcomings of the Andrade equation, with the result

$$\lim_{\substack{B\to 0 \\ D_r(r)\to D_{ro}}} \frac{HD_{ro}\bar{v}}{(a\mu_o E)^2} = \frac{1}{1536}\left[(\ln 10)\beta_1 T_o B/(T_o - 168)^2\right]^2 \tag{58a}$$

$$\lim_{\substack{B\to 0 \\ D_r(r)\to D_{ro}}} \frac{HD_{ro}}{a^2 u_m} = \frac{1}{24}\frac{\left[(\ln 10)\beta_1 T_o B/(T_o - 168)^2\right]^2}{\left[8 + (\ln 10)\beta_1 T_o B/(T_o - 168)^2\right]^2} \tag{58b}$$

where β_1 is defined by eqn. 12b. One notes that eqn. 58a is simply the first of the two terms comprising eqn. 53, which approximately corrects for the radial variation of the diffusion coefficient. The percentage error between eqns. 55 and 58a is

$$\lim_{\substack{B\to 0 \\ D_r(r)\to D_{ro}}} \{[B_A(T_o - 168)^2/\ln(10)\beta_1 T_o^2]^2 - 1\}100 \tag{59}$$

and is a function of T_o only.

PROCEDURES

Numerical approximations to $\theta(y)$, eqn. 6a, were computed for specific values of B and T_o as detailed in Part I of the Theory section. Unless otherwise stated, f[T_o, $\theta(y)$] was calculated from eqn. 12. Numerical solutions to $\theta(y)$ were iteratively calculated, until $\theta(y)$ differed by less than one part in two thousand from its predecessor. For small B values (*e.g.*, $B = 0.0001$), only two or three iterations were required; for large B values (*e.g.*, $B = 0.40$), 20 to 25 iterations were required. The dimensionless non-equilibrium plate height, $HD_{ro}\bar{v}/(a\mu_o E)^2$, was then calculated from eqn. 50 with the numerical approximations to f(y) and $\theta(y)$ so determined. For purposes of comparison, $HD_{ro}\bar{v}/(a\mu_o E)^2$ was also computed from eqn. 54, in which the radial variation of the diffusion coefficient is ignored. Here, f(y) was also computed iteratively. This sequence of calculations was then repeated for other values of B and T_o. All numerical integrations were implemented with Simpson's rule and 399 discrete values of y, f(y), h(y), and $\theta(y)$. The computer program prerequisite to these computations was written in double-precision FORTRAN 77 and executed on the IBM 3081-GX computer at Southern Illinois University.

RESULTS AND DISCUSSION

Fig. 1 is a plot of log B *vs.* T_o for select values of radius a and 0.01 and 0.05 M phosphate buffers (pH 7.0), which are representative of those used by Jorgenson and Lukacs in their initial studies[28,29]. These B values were calculated from eqn. 4 with the

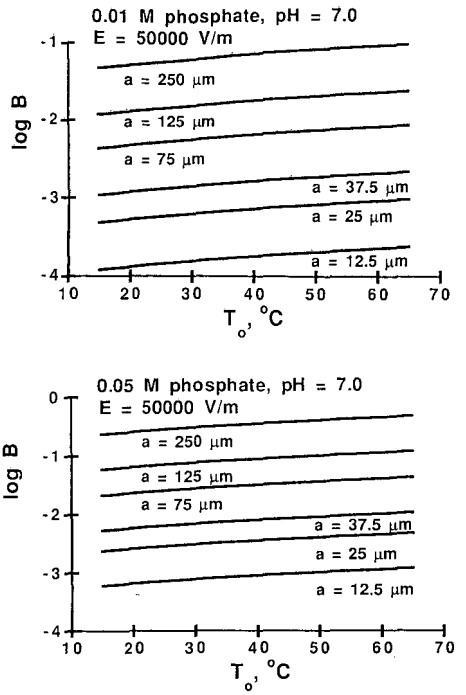

Fig. 1. Plots of log B *vs.* T_o for select capillary radii a, E = 50 000 V/m, and 0.01 and 0.05 M phosphate buffers (pH 7.0). Values of B were calculated from eqn. 4 as detailed in the text.

indicated a values, appropriate values of $k_{to}(T_o)$ and $k_{eo}(T_o)$, and E = 50 000 V/m. In these calculations, $k_{to}(T_o)$ was calculated from eqn. 7c, whereas $k_{eo}(T_o = 25°C)$ was calculated from eqn. 8, the electrophoretic mobilities of the $H_2PO_4^-$, HPO_4^{2-}, and PO_4^{3-} ions at infinite dilution[30], and the concentrations of these ions, which were determined from the acid dissociation constants of phosphoric acid at 25°C[31] and mass balance. The values of k_{eo} at other temperatures were then estimated by correcting k_{eo} (T_o = 25°C) for the variation of viscosity with temperature. Because the relationship between viscosity and temperature is almost exponential, the graphs of log B *vs.* T_o are almost linear. Although the field strength E one uses in these calculations is arbitrary, only a few studies have been carried out with E values greater than 50 000 V/m (ref. 32). Hence, almost all B values actually will be smaller than these, under otherwise identical conditions. These plots show that under typical experimental conditions (*e.g.*, buffer concentrations less than 0.05 M; radii less than 37.5 μm; field strengths less than 50 000 V/m), B is less than 0.01.

Fig. 2 is a plot of $\theta(y)/B$ *vs.* y for select values of B and T_o = 25°C. The lowermost bold curve is a graph of eqn. 5, which applies as B approaches zero. The other curves were computed with the iterative numerical algorithm described in Part I. To confirm this algorithm, the numerical solutions to $\theta(y)$ so computed were compared to the Bessel functions proposed by Coxon and Binder[16], Brown and Hinckley[17], and Jones and Grushka[18]. No substantial difference exists between these solutions, as long as $B < 0.20$; for larger B values, the variation of f(y) with $\theta(y)$ is no longer linear and Bessel functions no longer apply. (These comparisons were actually made by setting

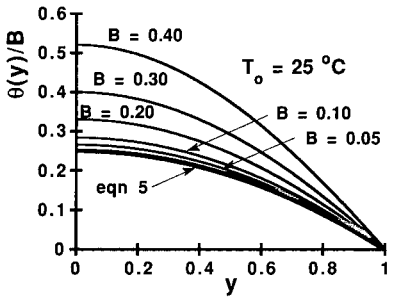

Fig. 2. Plot of $\theta(y)/B$ *vs.* y for select values of B and $T_o = 25°C$. The lowermost bold curve was calculated from eqn. 5; the other curves were computed numerically.

$h[T_o,\theta(y)]$ to unity, since Bessel functions apply when the thermal conductivity is constant. If one allows $h[T_o,\theta(y)]$ to vary with temperature, the Bessel functions are actually acceptable solutions up to $B = 0.30$ or so, because this variation partially compensates for error.) It is unlikely that a flawed algorithm would make predictions that so closely agree with theory. In general, the algorithm always appears to converge to the appropriate global solution to $\theta(y)$; no erroneous local solutions were ever computed in these comparisons.

One can conclude from Fig. 2 that eqn. 5 is a fairly good approximation to $\theta(y)$ for values of B less than 0.01 or so. For much larger B values, however, this solution is clearly inadequate. By comparing the numerical solutions to $\theta(y)/B$ for various B values, one infers that their departure from eqn. 5 is non-linear in B (*e.g.*, the difference between the values of $\theta(y)/B$ at $y = 0$ for $B = 0.40$ and $B = 0.20$ is more than twice the corresponding difference for $B = 0.20$ and eqn. 5, which applies as $B \to 0$). The principal relevance of these departures to this work is the inadequacy of the analytical approximations to $f(y)$, eqns. 13 and 16, when B is greater than 0.01 or so. These approximations are inadequate because they were derived with eqn. 5, which is invalid under these circumstances.

Fig. 3 is a plot of $[f(y)-1]/B$ *vs.* y for select values of B and $T_o = 25°C$. The lowermost bold curve in the upper figure (Fig. 3a) was calculated from eqn. 13, the analytical approximation to $f(y)$ derived here. The dashed bold curve in this figure, and the lowermost bold curve in the lower figure (Fig. 3b), were calculated from eqn. 16 ($B_A = 2400$ K), the analytical approximation to $f(y)$ derived from the Andrade equation. Clearly, these approximations differ at this T_o, and this difference increases with increasing T_o (see below). Because this figure effectively represents the variation of electrophoretic mobility (less the mobility at the wall) with the radial coordinate, one concludes that substantial differences will exist between plate heights calculated from these two functions, even for vanishingly small values of B.

The remaining curves in Fig. 3a and b were computed numerically. In Fig. 3a, $f[T_o,\theta(y)]$ was calculated from eqn. 12, whereas in Fig. 3b, $f[T_o,\theta(y)]$ was calculated from eqn. 15. The numerical solutions to $f(y)$ do not substantially differ from the appropriate analytical one, as long as B is less than 0.01 or so. This finding is perhaps not surprising, because the function $\theta(y)$, on which $f[T_o,\theta(y)]$ depends, can be approximated under these conditions by eqn. 5. For larger values of B, however, the numerical solutions to $f(y)$ differ substantially from the analytical ones. As with $\theta(y)$,

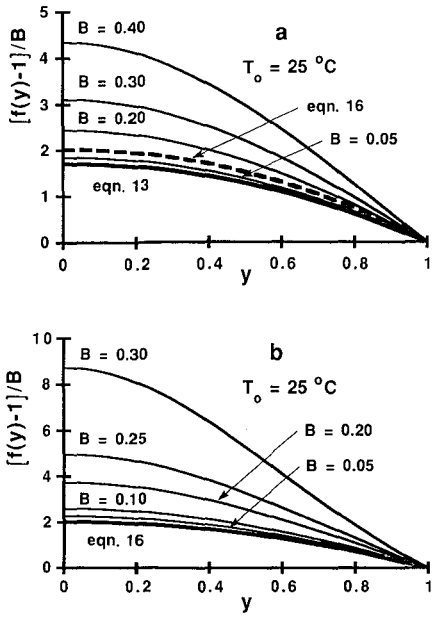

Fig. 3. Plots of $[f(y)-1]/B$ *vs.* y for select values of B and $T_o = 25°C$. The lowermost bold curve in (a) was calculated from eqn. 13; the dashed bold curve in (a), and the lowermost bold curve in (b), were calculated from eqn. 16. The other curves were computed numerically, with $f[T_o,\theta(y)]$ expressed by eqn. 12 for the curves in (a) and by eqn. 15 for those in (b).

the departures of the numerical solutions to $f(y)$ from the analytical ones are non-linear in B. More importantly, significant deviations between Fig. 3a and b are found as B increases. For example, when $B = 0.30$, the value of $[f(y)-1]/B$ at $y = 0$ in Fig. 3a is 3.10, whereas the corresponding value in Fig. 3b is 8.73. These large deviations indicate the necessity of describing η correctly for large B values. The principal origin of these deviations is the overestimation of $f[T_o,\theta(y)]$ by eqn. 15, which in turn causes the functions $\theta(y)$ and $f(y)$ to be overestimated. By the time these functions have converged, after many iterations of the numerical algorithm, these overestimations have been amplified many times.

As another test of the algorithm developed here, a numerical solution to $f(y)$ for $B = 0.0001$ was iteratively computed and compared to the analytical solution, eqn. 13. One would expect little difference between these solutions, since $B \ll 0.01$. In fact, these solutions differed beyond only the seventh or eighth significant figure. In other words, an extremely accurate solution to $f(y)$ was calculated numerically. The author believes that this test confirms this algorithm beyond any reasonable doubt.

Fig. 4 is a plot of the logarithm of the dimensionless plate height, $\log HD_{ro}\bar{v}/(a\mu_o E)^2$, *vs.* $\log B$ for select values of T_o. The abscissa, $\log B$, in each graph is limited by the boiling point of the buffer; therefore, $\log B$ is largest for the smallest T_o values. Because the curves only slightly differ for different T_o values, they are graphed either on different axes or in different plots. The solid curves are graphs of eqn. 50, which corrects for the radial variation of the diffusion coefficient; the dashed curves are graphs of eqn. 54, in which this variation is ignored. For B values less than 0.01 or

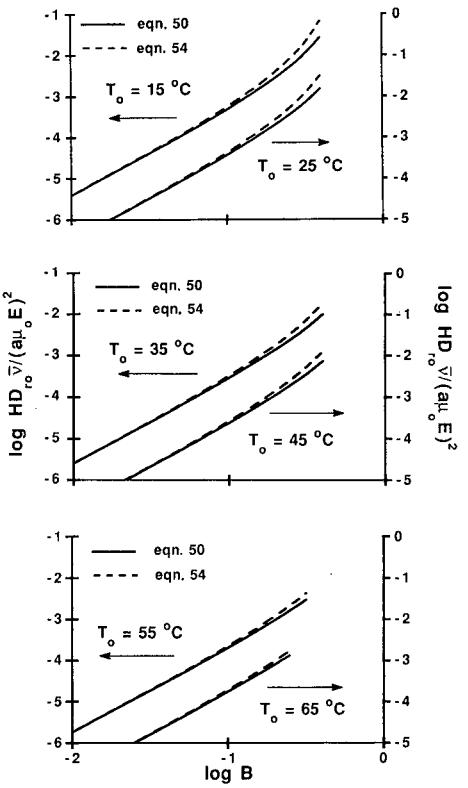

Fig. 4. Plots of log $HD_{ro}\bar{v}/(a\mu_o E)^2$ *vs.* log B for select values of T_o. Solid curves were computed from eqn. 50; dashed curves were computed from eqn. 54. The former equation corrects for the radial variation of the diffusion coefficient; the latter does not.

so, $HD_{ro}\bar{v}/(a\mu_o E)^2$ varies linearly with B^2 (*i.e.*, the slope of the log $HD_{ro}\bar{v}/(a\mu_o E)^2$ *vs.* log B plot is two), although this variation is not shown to avoid the loss of other details. Furthermore, the radial variation of the diffusion coefficient has no significant effect on the plate height. For B values greater than 0.01 or so, however, $HD_{ro}\bar{v}/(a\mu_o E)^2$ varies more rapidly with B than B^2, because $\theta(y)$ and f(y) vary with a power of B greater than one (see above). More importantly, for B values greater than 0.01 or so, the radial variation of the diffusion coefficient also affects the plate height, and this effect increases with increasing B. In these cases, the temperature near the capillary center rises sufficiently above T_o to substantially increase diffusion in this region, relative to that near the wall. Because the time required for analyte ions to diffuse between various positions in the capillary is correspondingly reduced, the differences in analyte velocity at these positions are more effectively averaged out and the plate height decreases.

Because the radial variation of the diffusion coefficient does not significantly affect $HD_{ro}\bar{v}/(a\mu_o E)^2$ unless B is greater than 0.01 or so, one concludes that eqns. 51 and 53, which analytically correct for this variation, have little use. This lack of utility exists, because the analytical approximations to f(y) and $\theta(y)$ with which these equations were derived are themselves not valid, when B is greater than 0.01 or so.

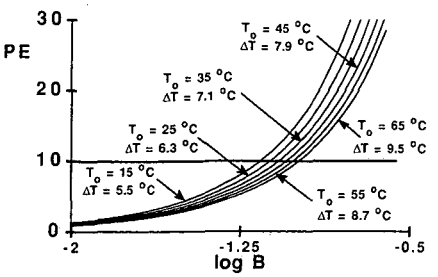

Fig. 5. Plot of percentage error PE between eqns. 50 and 54 *vs.* log B for select values of T_o. The former equation corrects for the radial variation of the diffusion coefficient; the latter does not.

A comparison of the values of $HD_{ro}\bar{v}/(a\mu_o E)^2$ computed numerically from eqn. 50 to those calculated from eqn. 53 confirms this finding. (Much numerical error is encountered in the evaluation of eqn. 51 for small B values, even in double-precision FORTRAN; hence, these results are not compared to eqn. 50.) Unfortunately, with the theory developed here, one cannot determine a simple analytical correction to plate height theory which holds when the radial variation of the diffusion coefficient is important.

The differences between the corrected and uncorrected values of $HD_{ro}\bar{v}/(a\mu_o E)^2$ in Fig. 4 are perhaps underemphasized because of the logarithmic scale. Fig. 5 is a plot of the percentage error, PE, between eqns. 50 and 54 *vs.* log B for select values of T_o. The radial variation of the diffusion coefficient is accounted for in the former equation, whereas this variation is "turned off" in the latter equation. To evaluate both equations, the functions $f(y)$ and $\theta(y)$ were computed numerically, because B is greater than 0.01. The percentage error between these equations is less than one or so, when B is less than 0.01, but rapidly increases with increasing B. The rapid rate of this increase is not apparent from the figure, which is compressed in the vertical direction to avoid loss of detail. For example, the value of PE for $T_o = 15°C$ and $\log B = -0.40$ ($B = 0.40$) slightly exceeds 150.

An arbitrary percentage error, above which one might wish to correct for the variation of the diffusion coefficient, is indicated in Fig. 5 by the horizontal line at PE = 10. The calculated temperature differences ΔT between the capillary center and wall at this threshold are indicated in the figure for the various T_o values. These differences, which are greater than 5°C, are nearly a linear function of T_o (the increment is 0.8°C per 10°C increase in T_o). By and large, this threshold is not crossed, unless B is greater than 0.08 ($\log B > -1.1$) or so. Because experimental values of B almost invariably will be less than this value (see Fig. 1), one can typically neglect the variation of the diffusion coefficient and use the simpler equations for plate height referenced in the Introduction, in which this variation is ignored. Thus, in one sense, the extensive theory derived above may seem somewhat academic. Yet, one must bear in mind that the numerical rigor supporting the conclusion just drawn would not have been possible without it.

Fig. 6 is a plot of $HD_{ro}\bar{v}/(a\mu_o E)^2$ *vs.* log B for select values of T_o. Unlike in Fig. 4, the curves here are not corrected for the variation of the diffusion coefficient. The solid curves, the curves comprised of short dashes, and the curves comprised of long dashes

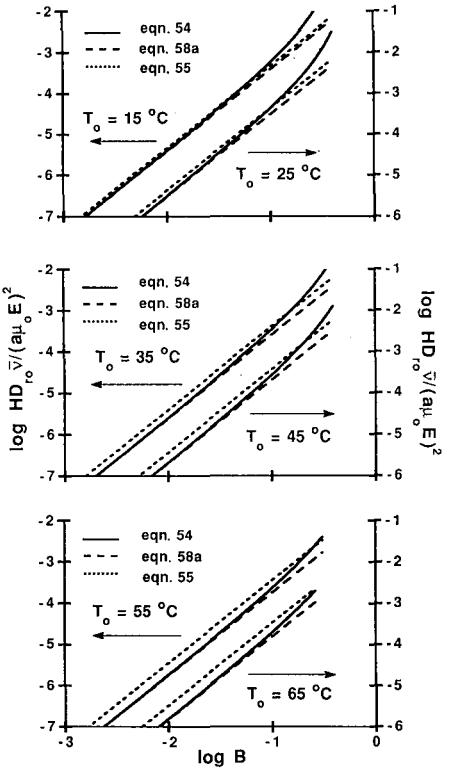

Fig. 6. Plots of log $HD_{ro}\bar{v}/(a\mu_o E)^2$ *vs.* log B for select values of T_o. The solid curves, the curves comprised of short dashes, and the curves comprised of long dashes are graphs of eqns. 54, 55 (B_A = 2400 K) and 58a, respectively. None of these curves corrects for the radial variation of the diffusion coefficient.

are graphs of eqns. 54, 55 (B_A = 2400 K) and 58a, respectively. The last two equations are analytical approximations to the first, which was evaluated numerically. Eqn. 58a, in which f(y) is expressed by eqn. 13, agrees well with this numerical solution, when B is

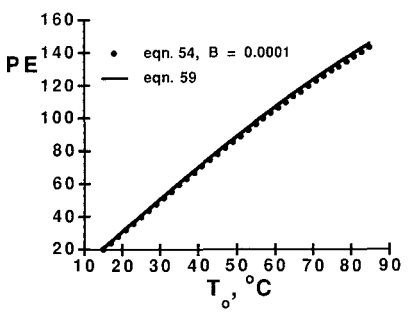

Fig. 7. Plot of percentage error PE between the solutions of Grushka *et al.*[11] and those developed here *vs.* T_o for small B values. Circles represent computations from eqn. 54 and B = 0.0001; the curve is a graph of eqn. 59 (B_A = 2400 K).

less than 0.01 or so, but differs with increasing B. Furthermore, the predictions of eqns. 55 and 58a significantly differ, even when $B \ll 0.01$. (Eqn. 55, in which $f(y)$ is expressed by eqn. 16, is equivalent to the result derived by Grushka *et al.*[11], except that electroosmotic flow is included.) This difference increases with increasing T_0 and originates solely from the choice of the function $f(y)$ with which one evaluates eqn. 54. Because eqn. 16 is greater than eqn. 13 (see Fig. 3a), the values of $HD_{ro}\bar{v}/(a\mu_0 E)^2$ predicted by eqn. 55 are greater than those predicted by eqn. 58a.

The differences between the values of $HD_{ro}\bar{v}/(a\mu_0 E)^2$ derived here and predicted by Grushka *et al.*[11] are perhaps underemphasized in Fig. 6, because of the logarithmic scale. Fig. 7 is a plot of the percentage error PE between these values *vs.* T_0 for $B \ll 0.01$. The circles represent the percentage error computed numerically from eqn. 54, when $B = 0.0001$ and $f[T_0,\theta(y)]$ was alternatively represented by eqns. 12 and 15. The solid curve is a graph of eqn. 59 ($B_A = 2400$ K), which clearly approximates this error. This error substantially increases with increasing T_0 and is greater than 100% for $T_0 > 50$°C or so, a value that is not that uncommon experimentally[33,34].

CONCLUSIONS

The principal significance of this work is its validation of previous analytical solutions to the non-equilibrium plate height in capillary zone electrophoresis. The fairly rigorous treatment developed here, which is based on an iterative solution to the steady-state equation of heat conduction and the inclusion in the continuity equation of the radial variation of diffusion coefficient, does not differ from simpler analytical ones, unless the temperature difference between the capillary center and wall substantially exceeds that encountered in practice. This work also establishes the range of the parameter B over which these analytical solutions apply and suggests that the Andrade equation can mislead one about values of electrophoretic mobility and non-equilibrium plate height, especially at elevated temperatures.

A shortcoming of this work is the lack of any relationship between the temperature T_0 of the capillary wall and the ambient temperature of the capillary surroundings. The latter is easily measured, whereas the former is not. Therefore, some relationship between the two is prerequisite to the testing of this theory. Others have addressed this problem[11,16–18] and their results can be easily adapted here.

No theory is better than the assumptions on which it rests. Most of the assumptions made here (*e.g.*, the absence of thermal diffusion, the absence of heat transfer from electroosmotically induced forced convection, and the independence of chemical equilibria of temperature) are fairly reasonable ones. The assumption of a vanishingly small analyte concentration may be subject to criticism, since in practice one works with detectable levels of analyte, which can affect plate numbers[29]. For better or worse, others have made this assumption and the author has made it as well. Perhaps in this light, this study should be viewed as more comparative than definitive.

One may wish to investigate more closely the assumption of negligible thermal (*i.e.*, free) convection, because the ΔT values reported in Fig. 5 are somewhat substantial. Experiments in wide-bore capillaries have clearly demonstrated the necessity of rotating the capillary contents to minimize dispersion by free convection[7]. A detailed evaluation of the expected amount of free convection is beyond the author's

ability. A rough evaluation is gained by calculating the dimensionless free-convective Nusselt number[14]

$$Nu \approx 0.5(PrGr)^{1/4} \tag{60}$$

where $Pr = C_p\eta/k_t$ and $Gr = a^3g\delta\Delta T/\lambda^2$ are the dimensionless Prandtl and Grashof numbers. (In these definitions, the parameters g, C_p, δ, and λ are the acceleration due to gravity and the constant-pressure heat capacity, thermal coefficient of expansion, and kinematic viscosity of the buffer.) At 25°C, the Prandtl number of dilute aqueous buffers is about 6.16 [$C_p = 4180$ J/kg K, $\eta = 8.90 \cdot 10^{-4}$ kg/ms, and $k_t = 0.605$ W/m K (ref. 35)], whereas the Grashof number can be approximated as $3.16 \cdot 10^9 \Delta T a^3$ [$g = 9.81$ m/s^2, $\delta = 2.57 \cdot 10^{-4}$ K^{-1}, and $\lambda = 8.93 \cdot 10^{-7}$ m^2/s (ref. 35)]. Fig. 5 indicates that ΔT will rarely exceed 10°C = 10 K, whereas a will rarely, if ever, exceed $2.5 \cdot 10^{-4}$ m. Thus, Nu is expected to be less than 0.65 or so. According to the author of ref. 36, this value of Nu indicates that free convection should be minor.

In spite of the rigor of these calculations, they remain at best approximate, because the viscosities of the buffers used in capillary zone electrophoresis are greater than the viscosity of pure water. Furthermore, the variations with temperature of the viscosities of pure water and buffers most probably differ. In these calculations, one has implicitly assumed they are equal. In general, the error so introduced depends on the buffer type and concentration and consequently is difficult to quantify. One can, however, gauge the magnitude of this error by a simple calculation. The viscosity of a 0.051 M solution of phosphoric acid at 20°C is about 1.010 cp (ref. 35), which is 0.008 cp greater than the viscosity of water at this temperature (1.002 cp). If one modifies the numerical algorithm to increment η by 0.008 cp during each iteration, such that $f[T_o, \theta(y)]$ is appropriately adjusted, one finds that the values of $HD_{ro}\bar{v}/(a\mu_o E)^2$ so computed differ from previous computations by less than 4%, when 15°C < T_o < 65°C and $B < 0.01$. Clearly, this calculation is greatly oversimplified. It does suggest, however, that the increased viscosity has only a small effect, as long as the buffer concentration is less than 0.05 M.

SYMBOLS

A_i	f_{ri}/η (m)
A_i^*	$z_i^2 C_i$ (mol/m^3)
A'	$D_r(r)\eta(r)/T(r)$ (kg m/s^2 K)
a	capillary radius (m)
B	$k_{eo}a^2E^2/k_{to}T_o$
B_A	empirical temperature in Andrade equation, commonly equated to 2400 K
c	analyte concentration (mol/m^3)
$c_m(z_1)$	cross sectional average concentration (mol/m^3)
C_i	concentration of ith buffer ion (mol/m^3)
C_p	constant-pressure heat capacity (J/kg K)
$D_r(r)$	radial diffusion coefficient (m^2/s)
D_{ro}	radial diffusion coefficient at inner capillary wall (m^2/s)

D_z	axial diffusion coefficient (m^2/s)
$\mathscr{D}$	effective diffusion coefficient (m^2/s)
e	fundamental electrical charge (C)
E	electric field strength (V/m)
f(y); f(r)	$k_e(y)/k_{eo}$; $k_e(r)/k_{eo}$
f[T_o,$\theta(y)$]	$k_e[T_o,\theta(y)]/k_{eo} = \eta_o/\eta[T_o,\theta(y)]$
f_r; f_{ri}	friction coefficient; friction coefficient of ith ion (kg/s)
F	Faraday (C/mol)
g	acceleration due to gravity (m/s^2)
g(y); g(r)	function defined by eqns. 36 and 37 (m)
g(0)	value of g(y) and g(r) at $y = r = 0$ (m)
h(y)	$k_t(y)/k_{to}$
h[T_o,$\theta(y)$]	$k_t[T_o,\theta(y)]/k_{to}$
H	non-equilibrium plate height (m)
$HD_{ro}\bar{v}/(a\mu_o E)^2$	dimensionless non-equilibrium plate height
$k_e(r)$; $k_e(y)$	electrical conductivity (mho/m)
k_{eo}	electrical conductivity at inner capillary wall (mho/m)
$k_t(r)$; $k_t(y)$	thermal conductivity (W/m K)
k_{to}	thermal conductivity at inner capillary wall (W/m K)
N_r	radial flux (mol/m^2 s)
N_z	axial flux (mol/m^2 s)
r	radial coordinate (m)
t	time (s)
T	temperature (K or °C)
T_o	temperature at inner capillary wall (K or °C)
u_m	average elctrophoretic mobility in theory of Grushka *et al.*[11] (m^2/V s)
$\bar{v}$	average zone velocity (m/s)
v_r	radial velocity (m/s)
$v_z(r)$; $v_z(y)$	axial velocity (m/s)
y	r/a
z	axial coordinate (m)
z_i	unsigned charge number of ith ion
z_1	$z - \bar{v}t$ (m)
α	$\ln(10)\beta_1 T_o/(T_o - 168)^2$
α_1, α_2	coefficients of h(T_o,θ) defined by eqn. 7a and b
β_1, β_2, β_3	coefficients of h(T_o,θ) defined by eqn. 12b–d
δ	coefficient of thermal expansion of buffer (K^{-1})
Δ	thermal conductivity of water (W/m K)
ΔT	temperature difference between capillary center and wall (°C)
ε	electrical permittivity (F/m)
ζ	zeta potential (V)
η	viscosity (kg/m s)
η_o	viscosity at inner capillary wall (kg/m s)
η^*	$\eta e^{-B_\Lambda/T}$ (kg/m s)
$\theta(y)$; $\theta(r)$	$[T(y)-T_o]/T_o$; $[T(r)-T_o]/T_o$
λ	kinematic viscosity (m^2/s)

μ	electrophoretic mobility ($m^2/V\ s$)
μ_{eo}	electroosmotic flow coefficient ($m^2/V\ s$)
μ_o	electrophoretic mobility at inner capillary wall ($m^2/V\ s$)

ACKNOWLEDGEMENT

The author gratefully acknowledges Dr. David W. Kammler of the Department of Mathematics at Southern Illinois University for his suggestion of an iterative numerical solution to eqn. 6a.

REFERENCES

1 B. P. Konstantinov and O. V. Oshurkova, *Sov. Phys.-Techn. Phys.*, 11 (1966) 693.
2 G. Taylor, *Proc. Roy. Soc. (London)*, 219A (1953) 186.
3 G. Taylor, *Proc. Roy. Soc. (London)*, 225A (1954) 473.
4 A. J. P. Martin and F. M. Everaerts, *Proc. Roy. Soc. (London)*, 316A (1970) 493.
5 M. J. E. Golay, in D. H. Desty (Editor), *Gas Chromatography, 1958*, Academic Press, New York, NY, 1958.
6 H. C. Cox, J. K. C. Hessels and J. M. G. Teven, *J. Chromatogr.*, 66 (1972) 19.
7 S. Hjertén, *Chromatogr. Rev.*, 9 (1967) 122.
8 R. Aris, *Proc. Roy. Soc. (London)*, 235A (1956) 67.
9 R. Virtanen, *Acta Polytech. Scand.*, 123 (1974) 7.
10 J. H. Knox and I. H. Grant, *Chromatographia*, 24 (1987) 135.
11 E. Grushka, R. M. McCormick and J. J. Kirkland, *Anal. Chem.*, 61 (1989) 241.
12 N. S. Reejhsinghani, A. J. Barduhn and W. N. Gill, *J. AIChE*, 14 (1968) 100.
13 J. C. Giddings, *Dynamics of Chromatography*, Marcel Dekker, New York, NY, 1965.
14 R. B. Bird, W. E. Stewart and E. N. Lightfoot, *Transport Phenomena*, Wiley, New York, NY, 1960, p. 272.
15 H. S. Carslaw and J. C. Jaeger, *Conduction of Heat in Solids*, Clarendon, Oxford, 2nd ed., 1986.
16 M. Coxon and M. J. Binder, *J. Chromatogr.*, 101 (1974) 1.
17 J. F. Brown and J. O. N. Hinckley, *J. Chromatogr.*, 109 (1975) 218.
18 A. E. Jones and E. Grushka, *J. Chromatogr.*, 466 (1989) 219.
19 R. W. Powell, C. Y. Ho and P. E. Liley, in R. C. Weast (Editor), *CRC Handbook of Chemistry and Physics*, CRC Press, Boca Raton, FL, 69th ed., 1988, p. E-11.
20 R. C. Reid, J. M. Prausnitz and B. E. Poling, *The Properties of Gases and Liquids*, McGraw-Hill, New York, 4th ed., 1987.
21 A. J. Bard and L. R. Faulkner, *Electrochemical Methods*, Wiley, New York, NY, 1980.
22 J. F. Swindells, in R. C. Weast (Editor), *CRC Handbook of Chemistry and Physics*, CRC Press, Boca Raton, FL, 69th ed., 1988, p. F-40.
23 J. R. Coe Swindells, Jr. and T. B. Godfrey, *J. Res.*, 48 (1952) 1.
24 R. J. Hunter, *Zeta Potential in Colloid Science: Principles and Applications*, Academic Press, London, 1981.
25 T. K. Sherwood, R. L. Pigford and C. R. Wilke, *Mass Transfer*, McGraw-Hill, New York, NY, 1975.
26 J. C. Giddings, *J. Chem. Phys.*, 49 (1968) 81.
27 J. C. Giddings, Y. H. Yoon, K. D. Caldwell, M. N. Myers and M. E. Hovingh, *Sep. Sci.*, 10 (1975) 447.
28 J. W. Jorgenson and K. D. Lukacs, *Anal. Chem.*, 53 (1981) 1298.
29 K. D. Lukacs and J. W. Jorgenson, *J. High Resolut. Chromatogr. Chromatogr. Commun.*, 8 (1985) 407.
30 C. M. Mason and J. B. Culvern, *J. Am. Chem. Soc.*, 71 (1949) 2387.
31 D. A. Skoog, D. M. West and F. J. Holler, *Fundamentals of Analytical Chemistry*, Saunders College Publishing, New York, 5th ed., 1988.
32 F. Foret, M. Deml and P. Becek, *J. Chromatogr.*, 452 (1988) 601.

33 S. Terabe, K. Otsuka and T. Ando, *Anal. Chem.*, 57 (1985) 834.
34 J. W. Jorgenson, in J. W. Jorgenson and M. Phillips (Editors), *New Directions in Electrophoretic Methods*, (*ACS Symposium Series*, No. 335), American Chemical Society, Washington, DC, 1987.
35 R. C. Weast (Editor), *CRC Handbook of Chemistry and Physics*, CRC Press, Boca Raton, FL, 69th ed., 1988.
36 H. A. Pohl, *Dielectrophoresis*, Cambridge University Press, Cambridge, 1978.

Journal of Chromatography, 517 (1990) 549–555
Elsevier Science Publishers B.V., Amsterdam

CHROMSYMP. 1978

Micellar electrokinetic chromatography employing sodium alkyl sulfates and Brij 35®[a]

HENRIK T. RASMUSSEN, LISA K. GOEBEL and HAROLD M. McNAIR*
Department of Chemistry, Virginia Polytechnic Institute and State University, Blacksburg, VA 24061 (U.S.A.)

ABSTRACT

Sodium decyl and dodecyl sulfates were evaluated as micellar phases for the micellar electrokinetic chromatographic separation of ASTM test mixture LC-79-2. Selectivity was similar in each system but differed from the selectivity obtained in reversed-phase high-performance liquid chromatography. Despite separation efficiencies of approximately 150 000 theoretical plates per 50 cm, benzene and benzaldehyde coeluted in all concentrations of both surfactants employed. Separation was, however, readily achieved by addition of Brij 35® [polyoxyethylene(23)dodecanol] to the micellar phase.

INTRODUCTION

Micellar electrokinetic chromatography (MEKC), as introduced by Terabe and co-workers[1,2], is a method of microscale chemical separation based on the electrokinetic effects which occur when a buffer-filled fused-silica capillary is subjected to an electric field[3]. The electrokinetic phenomena cause two dissimilar phases (a charged micellar phase and an aqueous buffer) to migrate at different velocities. Specifically, the aqueous phase migrates at a velocity dictated by electroosmotic flow and the micellar phase at a velocity that is the vector sum of the electroosmotic flow and the micelle's electrophoretic mobility. Solutes are separated in such a system based on partitioning between each phase. Therefore, MEKC may be considered analogous to conventional chromatography; the only exception being that the conventional stationary phase is replaced by a micellar phase, which is itself mobile. As a result, modifications must be made to conventional definitions of chromatographic parameters. In MEKC the capacity factor, k', may be expressed as[1]

$$k' = \frac{t_R - t_0}{t_0(1 - t_R/t_{mc})} \quad (1)$$

[a] Brij35® is a Registered Trademark of ICI Americas, Inc.

0021-9673/90/$03.50

where t_R is the retention time of an analyte, t_0 the retention time of a solute which distributes exclusively into the aqueous phase and t_{mc} the retention time of a solute which distributes exclusively into the micellar phase. Accordingly, the master resolution equation for MEKC becomes[2]

$$R_s = \frac{N^{1/2}}{4}\left(\frac{\alpha - 1}{\alpha}\right)\left(\frac{k'_2}{1 + k'_2}\right)\left[\frac{1 - t_0/t_{mc}}{1 + (t_0/t_{mc})k'_1}\right] \quad (2)$$

where R_s is the resolution, N the number of theoretical plates, k'_2 and k'_1 the capacity factors of solutes 2 and 1, respectively, and α the selectivity ($\alpha = k'_2/k'_1$).

By examining the master resolution equation, the mobility of the micellar phase is seen to be detrimental to resolution. However, since electroosmotic flow can be changed via changes in the capillary surface[4–6], buffer pH[7–9] and buffer concentration[10], this limitation may be overcome. The remaining parameters appear favorable in comparison to conventional high-performance liquid chromatography (HPLC). The flat flow profile created by electroosmotic flow[11] can provide for chemical separations with efficiencies in excess of 500 000 theoretical plates per m (ref. 12). Additionally, a vast number of micellar phases are available for optimization of selectivity.

To date most applications have employed sodium dodecyl sulfate (SDS) as the micellar phase[13–17]. However, the use of sodium decyl sulfate (STS), sodium tetradecyl sulfate, sodium dodecanesulfonate, dodecyltrimethylammonium chloride, cetyltrimethylammonium chloride and sodium *n*-dodecanoyl-L-valinate have also been briefly explored[2,18–20]. The addition of tetraalkyl ammmonium salts[21], methanol[22,23] and metal ions[24] to SDS micelles has also been shown to alter selectivity.

The purpose of the research described here is to further characterize SDS and STS micellar phases, and to compare the selectivity obtained in each system with the selectivity observed in reversed-phase HPLC. The influence of Brij 35® [polyoxyethylene(23)dodecanol] on selectivity is also briefly explored.

EXPERIMENTAL

Surfactant solutions of SDS and STS (Aldrich, Milwaukee, WI, U.S.A.) were prepared at the specified concentrations in 0.01 *M* disodium hydrogenphosphate, pH 7.00. To obtain data which can readily be compared with reversed-phase HPLC, ASTM test mixture LC-79-2 (refs. 25, 26), dissolved in each of the surfactant solutions under investigation, was used as the sample. This test mixture contains 1.5 mg/ml benzyl alcohol, 0.02 mg/ml benzaldehyde, 0.025 mg/ml acetophenone, 1.04 mg/ml benzene, 0.4 mg/ml methyl benzoate and 0.054 mg/ml dimethyl terephthalate. To calculate thermodynamic parameters, 1% (v/v) methanol and a small amount of Sudan III were added to the conventional test mix, to mark, respectively, the elution times of completely unretained and completely retained solutes (*i.e.*, t_0 and t_{mc})[2].

MEKC analyses were performed, at ambient temperature, in an 80 cm × 100 μm I.D. fused-silica capillary (Polymicro, Phoenix, AZ, U.S.A.) with a sample introduction–detector distance (effective length) of 50 cm. Separations were performed at +15 kV, as supplied by a Spellman Model RHR 30 high-voltage power supply (Spellman, Plainview, NY, U.S.A.) and monitored by means of an ISCO Model CV4

capillary electrophoresis absorbance detector (ISCO, Lincoln, NE, U.S.A.) set at 254 nm. Samples were introduced into the capillary by siphoning for 10 s at an elevation of 3.8 cm. This provides a sample volume of approximately 10 nl.

To evaluate the effect of Brij 35 on the separation of benzaldehyde and benzene a 0.025 *M* SDS–0.025 *M* Brij 35 (Fisher Scientific, Raleigh, NC, U.S.A.) solution was prepared as above. Benzene (0.84 mg/ml) and benzaldehyde (0.17 mg/ml) were analyzed as described, at a wavelength of 215 nm.

RESULTS AND DISCUSSION

The separation of ASTM test mixture LC-79-2 obtained in 0.05 *M* SDS is shown in Fig. 1. All components with the exception of benzene and benzaldehyde are shown to be adequately resolved. To resolve these coeluting components, optimization in accordance with the master resolution equation for MEKC (eqn. 2) was attempted. An approach similar to that applied in conventional HPLC was employed[27]; thus, initial efforts focused on changing the SDS concentration to effect a more favorable capacity factor for the separation. As seen from the coefficients of correlation in Table I, solute capacity factors are readily predicted as a function of SDS concentration. However, for the range of concentrations utilized (0.025–0.075 *M*), it was not possible to effect the separation of benzene and benzaldehyde.

This observation is in agreement with the master resolution equation. Making the assumption that $k'_1 = k'_2$, the optimum capacity factor for separation of the critical pair is given by the maximum of the function[2]

$$f(k') = \left(\frac{k'}{1+k'}\right)\left[\frac{1 - t_0/t_{mc}}{1 + (t_0/t_{mc})k'}\right] \tag{3}$$

For a t_0/t_{mc} value of 0.291 ± 0.003, as observed for 0.05 *M* SDS, the maximum (0.3) occurs at a capacity factor of approximately 1.85. However, $f(k')$ is constant to within 1% from $k' = 1.6$–2.2; thus the capacity factor is essentially optimized in 0.075 *M* SDS ($k' = 1.63$). This maximum provides an enhancement in resolution by a factor of only 1.08 compared to 0.05 *M* SDS ($k' = 1.03$) and it is therefore not surprising that resolution is not effected by increasing the micellar concentration.

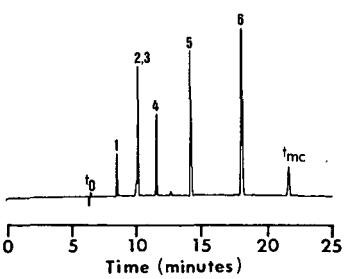

Fig. 1. MEKC separation of ASTM test mixture LC-79-2. Conditions: 80 cm × 100 μm I.D. fused-silica capillary (effective length 50 cm); 0.05 *M* SDS in 0.01 *M* Na_2HPO_4 (pH 7.00); +15 kV applied voltage; UV absorbance detection at 254 nm. Peaks: 1 = benzyl alcohol; 2,3 = benzene and benzaldehyde; 4 = acetophenone; 5 = methyl benzoate; 6 = dimethyl terephthalate.

TABLE I

SOLUTE CAPACITY FACTORS AND t_0/t_{mc} RATIOS *VS.* SDS CONCENTRATION

All values are based on four determinations.

Solute	*SDS concentration*			*r*
	0.025 M	*0.050 M*	*0.075 M*	
Benzyl alcohol	0.28 ± 0.01	0.55 ± 0.02	0.85 ± 0.01	0.99985
Benzene	0.54 ± 0.02	1.09 ± 0.02	1.63 ± 0.03	0.99998
Acetophenone	0.84 ± 0.02	1.71 ± 0.03	2.52 ± 0.03	0.99980
Methyl benzoate	1.67 ± 0.04	3.47 ± 0.05	5.16 ± 0.03	0.99984
DMT[a]	5.38 ± 0.08	10.7 ± 0.3	15.7 ± 0.5	0.99982
t_0/t_{mc}	0.350 ± 0.008	0.291 ± 0.003	0.292 ± 0.003	

[a] Dimethyl terephthalate.

Based on the results of Terabe *et al.*, who noted a decrease in t_0/t_{mc} with an increase in surfactant concentration, it may be argued that as surfactant concentration is increased from 0.05 to 0.075 *M*, an increase in the maximum of $f(k')$ should result. Thus an enhancement in resolution greater than predicted above may be possible. In this work, the experimentally observed t_0/t_{mc} was 0.292 ± 0.003 in 0.075 *M* SDS, indicating that the optimum capacity factor is unaltered. However, in 0.025 *M* SDS the t_0/t_{mc} ratio did increase. By virtue of a decreased t_{mc} value the observed ratio was 0.350 ± 0.008. Reasons for these results are currently under investigation. Speculatively, the variations may be due to a combination of the numerous temperature-dependent parameters which can change as a result of Joule heating as voltage is applied to the capillary. The current drawn and therefore the Joule heat generated, increased with increasing SDS concentration. Under the conditions employed (80 cm × 100 μm capillary; 15 kV applied voltage), the currents drawn in the 0.025, 0.05 and 0.075 *M* SDS solutions were 90, 110 and 135 μA, respectively.

In light of the reduction in resolution caused by the mobility of the micellar phase, it is interesting to compare resolution in MEKC with the resolution obtainable in HPLC. Rewriting eqn. 2 as

$$R_s = \frac{N^{1/2}}{4}\left(\frac{\alpha - 1}{\alpha}\right) f(k') \tag{4}$$

and invoking that the same resolution is required of each separation procedure, it follows that

$$\frac{N_H^{1/2}}{4}\left(\frac{\alpha_H - 1}{\alpha_H}\right) f(k')_H = \frac{N_M^{1/2}}{4}\left(\frac{\alpha_M - 1}{\alpha_M}\right) f(k')_M \tag{5}$$

where the subscripts H and M denote HPLC and MEKC, respectively. When SDS was used as the micellar phase the maximum of $f(k')_M$ was 0.3 and the efficiency (N_M) obtained in a capillary with an effective length of 50 cm approximately 150 000 plates. Assuming that a similar separation can be achieved by HPLC at a capacity factor of 10,

TABLE II

SELECTIVITY (α) BETWEEN SELECTED SOLUTE PAIRS IN 0.05 *M* SDS AND 0.05 *M* STS

All values are based on four determinations.

Solute pair	α *in 0.05 M SDS*	α *in 0.05 M STS*
Benzyl alcohol–benzene	1.97 ± 0.03	1.92 ± 0.01
Benzene–acetophenone	1.569 ± 0.003	1.48 ± 0.02
Acetophenone–methyl benzoate	2.03 ± 0.02	1.91 ± 0.02
Methyl benzoate–DMT	3.09 ± 0.04	2.73 ± 0.04

$f(k')_H = 0.91$. Thus if selectivity is the same in each system (*i.e.*, $\alpha_H = \alpha_M$), the resolution obtained by MEKC is similar to the resolution provided by an HPLC column generating 16 000 theoretical plates.

To improve the resolution provided by MEKC, N_M may be increased by employing a capillary with a longer effective length, or by optimizing the operating parameters governing dispersion[28]. Alternatively, efforts may be made to improve selectivity or decrease the t_0/t_{mc} ratio. In an attempt to obtain these advantages, 0.05 *M* STS was used instead of SDS as the micellar phase. STS provides an extended elution range by virtue of increased electrophoretic mobility (t_0/t_{mc} of STS = 0.235 ± 0.006) and as a result of a shorter alkyl chain length may perhaps be expected to provide different selectivity than SDS. As experimentally observed, 0.05 *M* STS also failed to separate benzene and benzaldehyde. In fact, as shown in Table II, differences in selectivity between SDS and STS are minor. Similar results have been reported by Burton *et al.*[19].

Attempts to improve resolution by employing STS of different concentrations were not feasible. The sample was insoluble in 0.025 *M* STS and 0.075 *M* STS caused an appreciable decrease in the signal-to-noise ratio. The latter is attributed to the generation of Joule heat which is not effectively dissipated by the detector. The current drawn, for an applied potential of 15 kV, was 210 μA for the 0.075 *M* STS solution.

Additional studies showed that other sodium alkyl sulfates are not suitable for MEKC at ambient temperature. Sodium octyl sulfate at a concentration of 0.075 *M* did not dissolve the sample, presumably because this concentration is below the surfactant's critical micelle concentration[29]. Sodium tetradecyl sulfate was insoluble in the operating buffer at a concentration of 0.025 *M*. It should be noted, however, that the solubility increases markedly at elavated temperatures. As shown by Terabe *et al.*[2] 0.05 *M* sodium tetradecyl sulfate may be used at 35°C.

For ASTM test mixture LC-79-2, the selectivity obtained in SDS and STS does however differ from that obtained by conventional reversed-phase HPLC and by reversed-phase HPLC employing Brij 35 as the mobile phase[26]. The orders of elution are listed in Table III. Notably, benzene elutes at different relative times in each separation mode.

Since solvent–micelle partitioning is responsible for part of the selectivity mechanism in micellar chromatography and under the premise that the polar head group changes selectivity in MEKC[19], it is logical to explore the use of Brij 35 as a micellar phase for MEKC. However, because Brij 35 is non-ionic, it cannot migrate

TABLE III

ORDER OF ELUTION OF ASTM LC-79-2 SAMPLE COMPONENTS UNDER VARIOUS LC SEPARATION CONDITIONS

	From ref. 26	*From ref. 26*	*This work*
"Stationary phase":	RP-18	RP-18	SDS and STS
Mobile phase:	30:70 (v/v) acetonitrile–water	6% Brij 35	0.01 *M* Na_2HPO_4 pH 7.00
Elution order:	(1) benzyl alcohol (2) benzaldehyde (3) acetophenone (4) methyl benzoate (5) benzene (6) dimethyl terephthalate	(1) benzyl alcohol (2) benzaldehyde (3) acetophenone (4) benzene (5) methyl benzoate (6) dimethyl terephthalate	(1) benzyl alcohol (2, 3) benzaldehyde and benzene (4) acetophenone (5) methyl benzoate (6) dimethyl terephthalate

electrophoretically. Therefore it is of little use by itself in MEKC. However, the feasibility of adding Brij 35 to a charged micelle, forming charged mixed micelles, remains. The separation of benzene and benzaldehyde obtained in 0.025 *M* SDS–0.025 *M* Brij 35 is shown in Fig. 2. Benzene is retained longer than benzaldehyde, indicating that the nature of the surfactant's polar head group plays an important role in solute retention. It is unclear, however, specifically why selectivity is changed. Several different models for the solubilization of benzene in micelles have been proposed[30].

The specific attributes of SDS–Brij 35 mixed micelles as micellar phases for MEKC will be investigated in a subsequent paper. However, a major advantage of Brij 35, as opposed to charged additives, is that it may be added to the micellar phase without an increase in Joule heating. The current resulting from both the 0.025 *M* SDS and the 0.025 *M* SDS–0.025 *M* Brij 35 solutions was 90 μA. Additionally, as noted previously[26], Brij 35 has a high cloud-point temperature (approximately 100°C) and low molar-absorptivity values in the low UV region. These features allow for Brij 35 to be used at the high temperatures which may result from Joule heating and at the low wavelengths which may be required to effect the detection of many compounds.

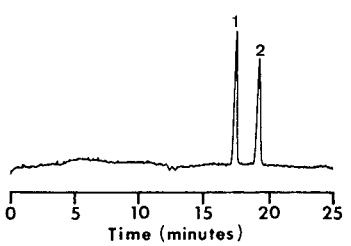

Fig. 2. MEKC separation of benzaldehyde and benzene. Conditions: 80 cm × 100 μm I.D. fused-silica capillary (effective length 50 cm); 0.025 *M* SDS–0.025 *M* Brij 35 in 0.01 *M* Na_2HPO_4 (pH 7.00); +15 kV applied voltage; UV absorbance detection at 215 nm. Peaks: 1 = benzaldehyde; 2 = benzene.

ACKNOWLEDGEMENT

The authors acknowledge J. O. Glanville for helpful discussion.

REFERENCES

1 S. Terabe, K. Otsuka, K. Ichikawa, A. Tsuchiya and T. Ando, *Anal. Chem.*, 56 (1984) 111.
2 S. Terabe, K. Otsuka and T. Ando, *Anal. Chem.*, 57 (1985) 834.
3 J. W. Jorgenson and K. D. Lukacs, *Anal. Chem.*, 53 (1981) 1298.
4 S. Hjerten, *J. Chromatogr.*, 347 (1985) 191.
5 S. Terabe, H. Utsumi, K. Otsuka, T. Ando, T. Inomata, S. Kuse and Y. Hanoaka, *J. High Resolut. Chromatogr. Chromatogr. Commun.*, 9 (1986) 666.
6 A. T. Balchunas and M. J. Sepaniak, *Anal. Chem.*, 59 (1987) 1470.
7 K. D. Lukacs and J. W. Jorgenson, *J. High Resolut. Chromatogr. Chromatogr. Commun.*, 8 (1985) 407.
8 H. T. Rasmussen and H. M. McNair, *J. High Resolut. Chromatogr.*, 12 (1989) 635.
9 K. Otsuka and S. Terabe, *J. Microcolumn Sep.*, 1 (1989) 150.
10 S. Fujiwara and S. Honda, *Anal. Chem.*, 58 (1986) 1811.
11 M. Martin, G. Guiochon, Y. Walbroehl and J. W. Jorgenson, *Anal. Chem.*, 57 (1985) 561.
12 K. H. Row, W. H. Griest and M. P. Maskarinec, *J. Chromatogr.*, 409 (1987) 193.
13 K. Otsuka, S. Terabe and T. Ando, *J. Chromatogr.*, 348 (1985) 39.
14 D. F. Swaile, D. E. Burton, A. T. Balchunas and M. J. Sepaniak, *J. Chromatogr. Sci.*, 26 (1988) 406.
15 D. E. Burton, M. J. Sepaniak and M. P. Maskarinec, *J. Chromatogr. Sci.*, 24 (1986) 347.
16 S. Fujiwara, S. Iwase and S. Honda, *J. Chromatogr.*, 447 (1988) 133.
17 R. A. Wallingford and A. G. Ewing, *J. Chromatogr.*, 441 (1988) 299.
18 K. Otsuka, S. Terabe and T. Ando, *J. Chromatogr.*, 332 (1985) 219.
19 D. E. Burton, M. J. Sepaniak and M. P. Maskarinec, *J. Chromatogr. Sci.*, 25 (1987) 514.
20 A. Dobashi, T. Ono, S. Hara and J. Yamaguchi, *Anal. Chem.*, 61 (1989) 1984.
21 H. Nishi, N. Tsumagari and S. Terabe, *Anal. Chem.*, 61 (1989) 2434.
22 M. M. Bushey and J. W. Jorgenson, *Anal. Chem.*, 61 (1989) 491.
23 J. Gorse, A. T. Balchunas, D. F. Swaile and M. J. Sepaniak, *J. High Resolut. Chromatogr. Chromatogr. Commun.*, 11 (1988) 554.
24 A. S. Cohen, S. Terabe, J. A. Smith and B. L. Karger, *Anal. Chem.*, 59 (1987) 1021.
25 Subcommittee E-19.08 Task Group on Liquid Chromatography of the American Society for Testing and Materials, *J. Chromatogr. Sci.*, 19 (1981) 338.
26 M. F. Borgerding and W. L. Hinze, *Anal. Chem.*, 57 (1985) 2183.
27 L. R. Snyder, J. L. Glajch and J. J. Kirkland, *Practical HPLC Method Development*, Wiley, New York, 1988, ch. 4.
28 S. Terabe, K. Otsuka and T. Ando, *Anal. Chem.*, 61 (1989) 251.
29 M. J. Rosen, *Surfactants and Interfacial Phenomena*, Wiley, New York, 2nd ed., 1989, ch. 3.
30 R. Nagarajan, M. A. Chaiko and E. Ruckenstein, *J. Phys. Chem.*, 88 (1984) 2916.

Journal of Chromatography, 517 (1990) 557–572
Elsevier Science Publishers B.V., Amsterdam

CHROMSYMP. 1971

Electrically driven open-tubular liquid chromatography

G. J. M. BRUIN*, P. P. H. TOCK, J. C. KRAAK and H. POPPE
Laboratory for Analytical Chemistry, University of Amsterdam, Nieuwe Achtergracht 166, 1018 WV Amsterdam (The Netherlands)

ABSTRACT

Electrically driven (ED), as opposed to pressure-driven (PD), open-tubular liquid chromatography (OTLC) was evaluated for different types of open-tubular columns, with inner diameters in the range 5–25 μm. The efficiency of ED-OTLC was found to be better than that of PD-OTLC by a factor of *ca.* 2, in agreement with theory. Injection of the sample in ED-OTLC by electromigration appears to be much simpler than that with the split-injection procedures in PD-OTLC. Electroosmotic mobility was found to depend little on the application of an ODS coating. With the mobile phase used at 60 000 V/m, the maximum linear velocity was 1.4 mm/s. The potential of ED-OTLC in 10–25 μm I.D. capillaries is demonstrated.

INTRODUCTION

Open-tubular liquid chromatography (OTLC) has been extensively investigated both theoretically and experimentally[1–16] in the last 20 years. Efforts have been made in column preparation[3–9] and in developing injection and detection systems[8–16]. Although the performance of OT columns has proved to be much better than that of packed columns, at present OTLC is used only in university laboratories and research institutes. Commercial OTLC instruments are still not available, which can be attributed to the experimental difficulties in efficiently operating OTLC, owing to the extremely small dimensions of the system. It has been found that the inner diameter of OTLC columns should be smaller than 10 μm[2,3] and that the injection and detection volumes should be about 40 and 100 pl, respectively. These small volumes imply the need for a very specialized type of detector, *e.g.*, on-column laser-based optical detectors, electrochemical detectors and mass spectrometric devices[10–16]. Although such detection systems have been tried, the insufficient sensitivity and the low mass loadability of OT columns[9,17] still inhibit the interest of instrument manufacturers in developing an OTLC instrument.

In contrast to the lack of commercial development of OTLC, that of capillary electroseparation techniques has expanded since the introduction of capillary zone electrophoresis around 1980 by Mikkers *et al.*[18] and Jorgenson and Lukacs[19]. Interest in these techniques is growing rapidly, as demonstrated by the enormous increase in

0021-9673/90/$03.50

the number of publications and the introduction of several commercial instruments.

In capillary electroseparation techniques, a high electric potential is applied across a capillary, filled with a buffer, and separations of charged species, based on a difference in charge/mass ratio can be carried out by an electrophoretic process. In addition to charged species, uncharged species can also be transported by the electroosmotic flow, which is induced by the electric field. Currently five capillary electroseparation techniques have been demonstrated experimentally[18–28]:

(i) (free solution) capillary zone electrophoresis (CZE);
(ii) capillary gel electrophoresis;
(iii) capillary micellar electrokinetic chromatography;
(iv) isoelectric focusing; and
(v) capillary electroosmotic chromatography.

These techniques are normally carried out in 10–100 μm I.D. fused-silica capillaries and in most instances on-column detection is used[18–28]. As with OTLC, the detection is one of the major problems. However, considering the great interest in capillary electroseparation techniques, renewed research efforts[27–30] in micro detection will certainly lead in the near future to commercially available ultramicro detectors having better characteristics with respect to sensitivity.

In pressure-driven (PD) OTLC, sample introduction is usually effected by split injection, which requires a relatively large sample volume. When the sample volume is extremely small, the split technique cannot be applied and another means of introducing the sample is necessary, *e.g.*, by disconnecting the column and injecting the sample into the capillary with a microsyringe, as demonstrated by Kennedy and Jorgenson[31,32]. However, this complicates the techniques. In capillary electroseparation techniques the sample introduction is performed by means of electromigration[33,34] or by the vacuum suction method[35]. Both techniques lend themselves to automation. However, the vacuum suction technique may fail with the small I.D. capillaries used in OTLC. Therefore, the electromigration injection is the method of choice for electrically driven (ED) OTLC. The method is very simple, applicable to neutral species and allows manipulations of small sample volumes. Moreover, the method is also applicable to charged species, but the amount of injected solute is affected by the electrophoretic mobility of the solute.

Capillary electroosmotic chromatography in open-tubular columns will henceforth be termed electrically driven OTLC (ED-OTLC). It was first demonstrated in 30–200 μm I.D. columns by Tsuda *et al.*[24] in 1982. They found larger plate heights than expected theoretically and showed some separations of polycyclic aromatics in a 30 μm I.D. capillary. Capillary electroosmotic chromatography in packed fused-silica capillaries was demonstrated by Knox and Grant[36] in 1987. They observed an improvement in plate height by a factor of 2 when comparing ED and PD chromatography in the same column. They also argued that an ED system allows the use of much smaller particles for column packings.

In OTLC, plug flow, as opposed to Poisseuille flow, leads to a smaller contribution from slow equilibration in the mobile phase, the C_m term. We therefore considered it worthwhile to assess the possibilities of using electroosmotic flow as the driving force for OTLC in 10–25 μm I.D. capillaries, and to explore the use of electromigration injection in combination with ED-OTLC.

THEORY

Electroosmosis

The driving force for an ED system is electroosmosis, which results from the existence of the electric double layer. If a surface is in contact with an electrolyte, there will be an excess of charge near that surface. With fused silica, the excess charge is normally positive. Because of the presence of the excess of charge, the application of an electric field will bring about movement of the liquid, which is called the electroosmotic flow. This phenomenon has been treated in more detail by Rice and Whitehead[37] and Van de Goor *et al.*[38]. The electroosmotic flow has a linear velocity v_{eo}, which is given by

$$v_{eo} = E\mu_{eo} = E\varepsilon_o\varepsilon_r \zeta/\eta \tag{1}$$

where μ_{eo} is the electroosmotic mobility, E is the applied electric field, η is the viscosity, $\varepsilon_o\varepsilon_r$ is the dielectric constant of the electrolyte and ζ is the zeta potential near the wall[37,38]. The electroosmotic mobility depends on the viscosity, pH and ionic strength of the electrolyte and on the character (charge density) of the surface of the capillary. The flow profile is virtually rectangular. A deviation from the rectangular shape occurs in the wall region, the size of which is of the order of the size of the diffuse electric double layer, 1–100 nm[39]. Because of the finite size of the double layer, in extremely narrow ($\leqslant 1$ μm) channels and at low ionic strengths, the plug flow and eqn. 1 may not be valid (double-layer overlap)[37,39]. However, such conditions did not occur in our work.

Comparison of plate height between pressure- and electrically driven systems

Axial diffusion and slow equilibration in the mobile and stationary phase are the main processes contributing to band broadening in OTLC. This is expressed in the theoretical plate height equation derived by Golay[40] for a PD system, and by Martin and Guiochon[41] and Giddings[42] for an ED system. These two equations are very similar and deviate only in the function of k', $f(k')_m$. This is attributed to the difference in the flow profiles between the two systems, *viz.*, a plug flow profile in an ED system and a parabolic flow profile in a PD system. The overall plate height equation is valid in both PD and ED systems:

$$H = \frac{2D_m}{u} + f(k')_m \cdot \frac{d_c^2\, u}{D_m} + f(k')_s \cdot \frac{d_f^2\, u}{D_s} \tag{2}$$

where H is the plate height, u is the linear velocity, k' is the capacity factor, D_m and D_s are the diffusion coefficients in the mobile and stationary phase, respectively, d_c is the inner diameter of the column, d_f is the thickness of the stationary phase layer and $f(k')_m$ and $f(k')_s$ are functions of k'.

$f(k')_m$ for the PD system is

$$f(k')_m^{PD} = \frac{(1 + 6k' + 11k'^2)}{96\,(1 + k')^2} \tag{3}$$

and for an ED system, assuming a perfectly flat flow profile,

$$f(k')_m^{ED} = \frac{k'^2}{16\,(1 + k')^2} \tag{4}$$

The main difference between an ED and a PD system is, as mentioned before, the flow profile. This is expressed in different plate height curves, calculated with eqns. 2–4, as shown in Fig. 1A and B for a 25 and a 10 μm I.D. capillary, respectively, for three k' values. As can be seen, for a 25 μm I.D. capillary the gain in efficiency by using an ED system instead of a PD system is by a factor of *ca.* 3. Knox and Grant[36] pointed out that with capillary electroosmotic chromatography in wider bore capillaries, the C_m term, as in OTLC, increases rapidly when retention occurs. For a 10 μm I.D. capillary the same phenomenon occurs but, owing to the smaller inside diameter, the slow mass transfer term is much smaller and less significant. If a 25 μm I.D. capillary in an ED system is compared with a 10 μm I.D. capillary in a PD system, the loss in plate height is by only a factor of 3. This phenomenon opens up the possibility of using larger diameters in ED-OTLC, which has the advantage that there are fewer practical problems with regard to detection, loadability and column preparation.

In Fig. 2, $f(k')_m^{ED}$ and $f(k')_m^{PD}$ are plotted *versus* k'. It is clear that both functions increase with increasing retention. Also, it is clear that $f(k')_m^{ED}$ is always smaller than $f(k')_m^{PD}$. The improvement is very large at low k' values, but is still greater by a factor of 11/6 for k' up to infinity. The lower $f(k')_m^{ED}$ results in a lower plate height for an ED system compared with a PD system.

EXPERIMENTAL

Apparatus

In Fig. 3 an ED-OTLC system is shown, which in principle is similar to a CZE system. It consists of a 0–60 kV d.c. high-voltage power supply (Model R603/05P; Wallis, Worthing, U.K.). Platinum electrodes are used for the connection of the supply with the buffer reservoirs, located at each end of the capillary. The total set-up was placed in a laboratory-built polycarbonate box, which was thermostated in the following way: a radiator, mounted in one of the side walls of the box, was connected to a circulating liquid thermostat (Model TL 1620; Haake, Berlin, F.R.G.), and an air fan was placed in front of the radiator to ensure an air flow of constant temperature around the capillary. On-column detection was carried out at the cathodic side, using laser-induced fluorescence detection as described previously[9]. Sample injection was performed by the electromigration technique[33]. Acetonitrile–phosphate buffer (0.05 or 0.1 *M*, pH 7.0) (2:3, v/v) and methanol–phosphate buffer (0.05 *M*, pH 7.0) (1:1, v/v) were used as mobile phases.

Materials and chemicals

The solvents used were analytical-reagent grade methanol and toluene (Merck, Darmstadt, F.R.G.), acetonitrile (Rathburn, Walkerburn, U.K.) and distilled water, freshly deionized by passage through a PSC filter assembly (Barnstead, Boston, MA, U.S.A.). Prior to use all solvents were filtered by vacuum suction through 0.5-μm

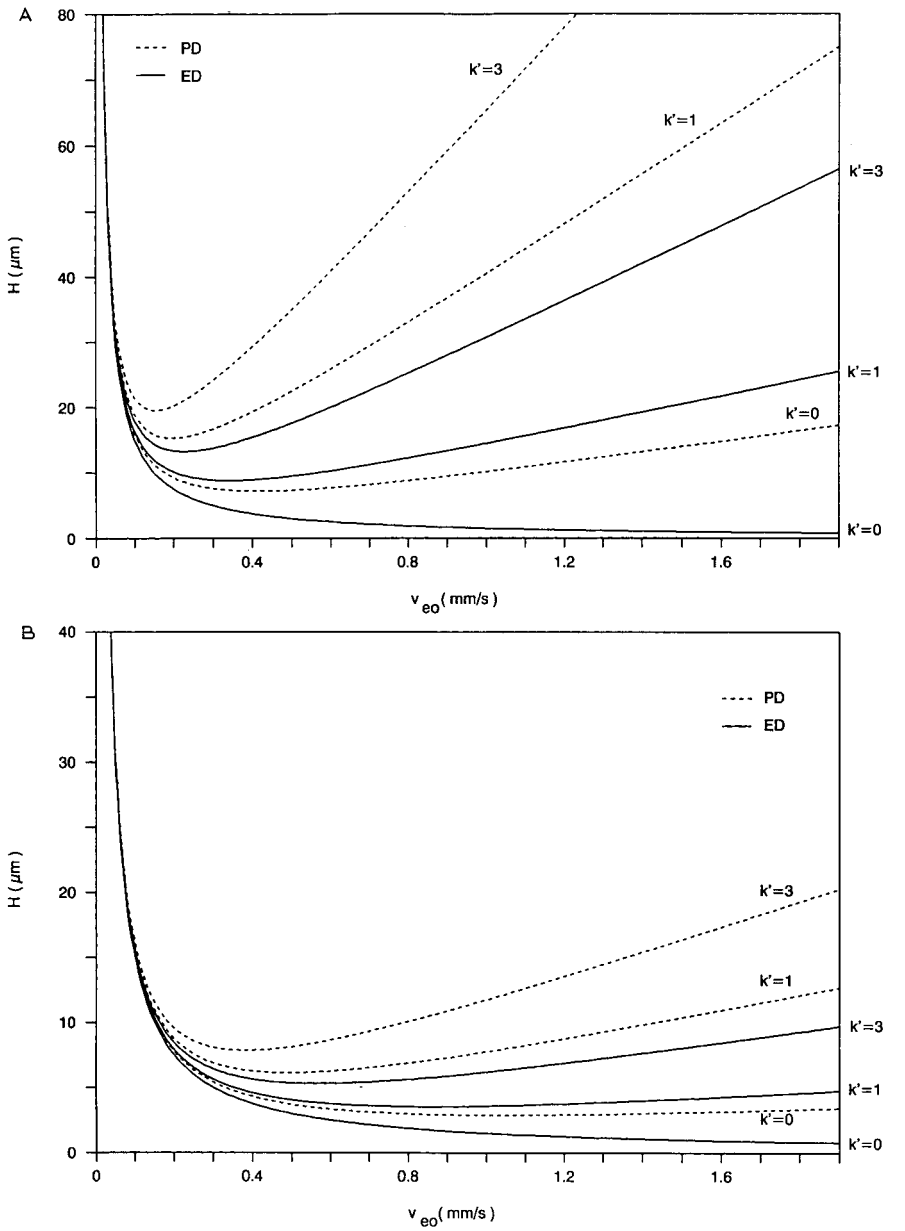

Fig. 1. Theoretical plate height curves for an electrically driven (ED) system (solid lines) and a pressure driven (PD) system (dashed lines) with (A) a 25-μm I.D. capillary and (B) a 10-μm I.D. capillary for three different k' values.

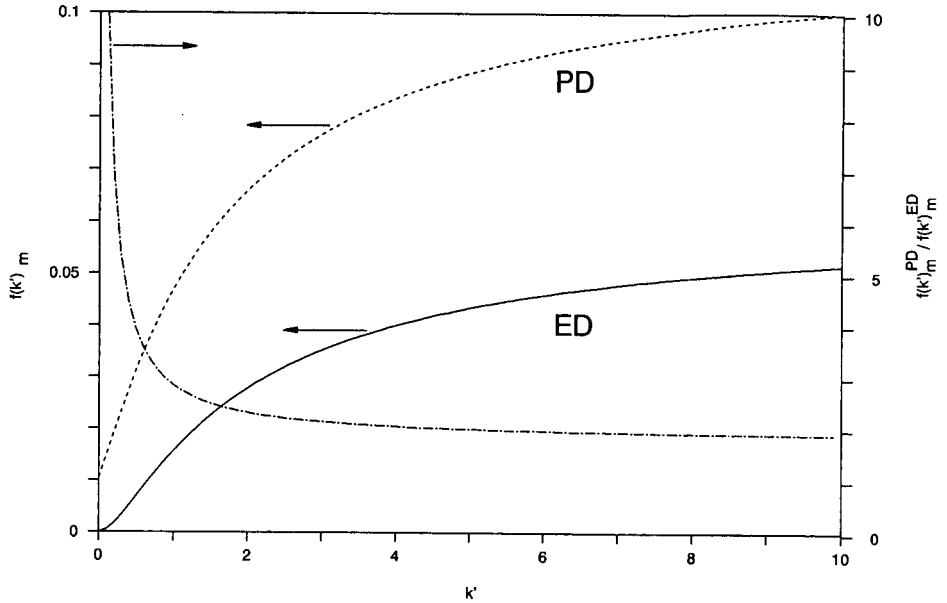

Fig. 2. $f(k')_m$ functions for a pressure-driven system, $f(k')_m^{PD}$ (dashed line), and for an electrically driven system, $f(k')_m^{ED}$ (solid line), plotted *versus* k'. The dot-dashed line represents the $f(k')_m^{PD}/f(k')_m^{ED}$ ratio.

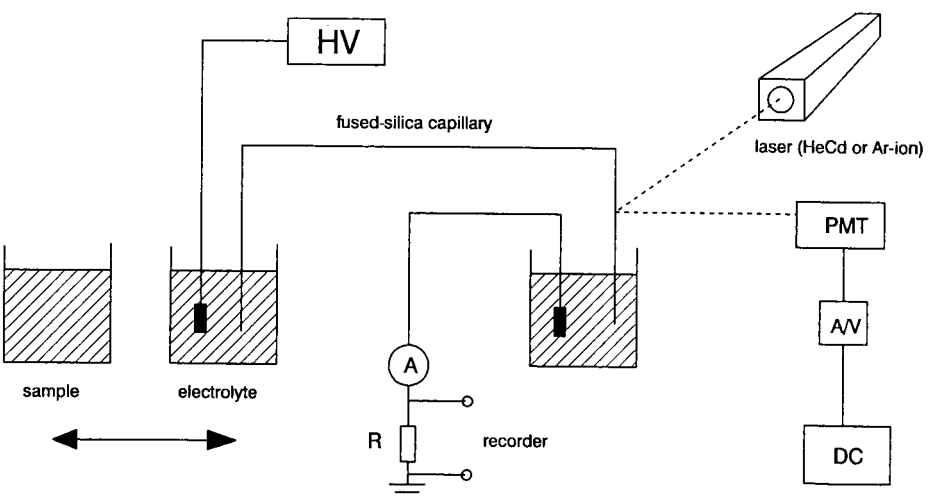

Fig. 3. Experimental set-up. HV = high-voltage power supply; PMT = photomultiplier tube; A/V = current/voltage converter with amplifier; DC = data collection; A = current monitor; R = resistance (= 10 kΩ).

filters (Model FH; Millipore, Bedford, MA, U.S.A.). The polycyclic aromatics used as test compounds were obtained from Janssen (Beerse, Belgium) and Aldrich (Brussels, Belgium). Stock solutions of the test compounds were prepared in the mobile phase. The 10, 25 and 50 μm I.D. fused-silica capillaries were obtained from Polymicro Technology (Phoenix, AZ, U.S.A.). Monochlorodimethyloctadecylsilane (ODS) was obtained from Aldrich (Beerse, Belgium).

Preparation of the capillary

The etched and the porous silica layered (PSL) fused-silica capillaries were prepared according to Tock and co-workers[8,9]. The capillaries were dried at 200°C for at least 2 h while being purged with helium.

Chemical modification

The dried capillary was filled with a 5% (w/v) solution of ODS in toluene. Both ends were sealed in a flame and the capillary was heated at 140°C for 6 h. Finally, the capillary was rinsed with toluene and acetonitrile or methanol before use.

RESULTS AND DISCUSSION

Electroosmotic mobility measurements

One of the most important parameters in ED-OTLC is the electroosmotic mobility in chemically modified capillaries under reversed-phase conditions. These values can be used to predict the accessible linear velocity in ED-OTLC. The electroosmotic flow measurements were carried out according to the method of Huang *et al.*[43]. Briefly, this method is as follows: the used electrolyte is replaced with an electrolyte with a lower conductivity, which results in a gradual decrease in the current when a high voltage is applied until the capillary is completely filled with the new electrolyte. The time, t_m, necessary to reach the new current level can be used to calculate the electroosmotic mobility, μ_{eo}, according to

$$\mu_{eo} = \frac{L}{t_m E} \tag{5}$$

where L is the total length of the capillary. It should be noted that changes in the concentration of the electrolyte must be small (not more than 10%) to avoid changes in the zeta potential during the μ_{eo} measurements, as shown by Zare *et al.*[43]. Table I summarizes the electroosmotic flow measurements in 5–50 μm I.D. capillaries. These measurements were carried out at a sufficiently weak applied electric field to be sure that thermal effects were excluded. It can be seen that μ_{eo} is independent of the inner diameter of the capillary. It can also be observed that μ_{eo} is virtually the same for ODS-treated and bare surfaces, and is not influenced by the presence of porous silica with the mobile phase used. The difference in μ_{eo} observed when methanol and acetonitrile are used as the organic modifier in the electrolyte can be explained by differences in the viscosity and dielectric constant of the electrolytes.

Band broadening due to injection

In order to rule out the possibility of extra-column contributions to band

TABLE I

ELECTROOSMOTIC MOBILITY, μ_{eo}, MEASURED IN VARIOUS CAPILLARIES

Values are averages of at least duplicate measurements.

Capillary		μ_{eo} ($cm^2/V \cdot s$) $\cdot 10^4$	
Type	d_c (μm)	*Acetonitrile–buffer*[a] *(2:3)*	*Methanol–buffer*[a] *(1:1)*
ODS	5	2.40	–
ODS	10	2.38	1.16
PSL-ODS[b]	10	2.18	–
ODS	25	2.49	–
ODS	50	2.43	–
Etched	50	2.37	1.13

[a] 0.1 *M* phosphate buffer (pH 7).
[b] PSL = capillary with a porous silica layer[8,9].

broadening, some conditions governing the injection procedure are discussed.

As shown in Fig. 1A and B, theoretical plate heights for $k' = 0$ as low as 1.5 μm can be obtained. The distance variance, $\sigma^2_{z,col}$ ($= LH$), is 0.75 mm^2 for a 50-cm capillary. When a 5% increase in peak width by external broadening effects is accepted, the following should hold:

$$\sigma^2_{z,tot} \leqslant (1.05\ \sigma_{z,col})^2 \tag{6}$$

or

$$\sigma^2_{z,tot} \leqslant 1.103\ \sigma^2_{z,col} \tag{7}$$

The extra band broadening due to on-column laser-induced fluorescence detection can be neglected[10], and hence $\sigma^2_{z,tot} = \sigma^2_{z,col} + \sigma^2_{z,inj}$, where $\sigma^2_{z,inj}$ is the extra variance caused by the injection zone length. To preserve efficiency, $\sigma^2_{z,inj}$ is not allowed to exceed 0.077 mm^2. The variance $\sigma^2_{z,inj}$ can be expressed as

$$\sigma^2_{z,inj} = \frac{l^2_{inj}}{K^2} \tag{8}$$

where l_{inj} is the length of the injection plug and K^2 is the injection profile factor[44]. This means that the length of the injection plug should be less than 0.96 mm (the injection volume for an unretained solute would be 75 pl in a 10 μm I.D. capillary) when injection of a rectangular plug is assumed with $K^2 = 12$. The restrictions on the injection zone length become even more critical when the injection profile approaches an exponential profile. In this instance one will find a lower K^2 value and thus a smaller maximum acceptable injection zone length.

Using the electromigration technique as described in detail by Rose and Jorgenson[33], it is possible to inject very small sample volumes. For capillary zone electrophoresis, capillary micellar electrokinetic chromatography and capillary gel electrophoresis, discrimination between the sample components appears because charged compounds migrate with a different velocity into the column as a result of

their different electrophoretic mobilities. This implies that the amount of sample components injected depends on their electrophoretic mobility. However, in ED-OTLC electroosmotic chromatography preferably neutral compounds are separated and they all migrate with the same electroosmotic velocity into the capillary. It should be noted that retained components will focus during the sample introduction by a factor of $1 + k'$. Hence for these components larger volumes can be tolerated.

In Fig. 4 the square of the injection volume, V_{inj}^2, is plotted *versus* the column variance, $\sigma_{v,tot}^2$, for a 10 μm I.D. capillary and a pair of solutes with small retention. The column variance is calculated with the measured time standard deviation at 0.6 of the total peak height multiplied by the electroosmotic flow. V_{inj} is varied between 19 and 280 pl by increasing the injection time from 2 to 30 s at a constant injection voltage of 2.4 kV for anthracene ($k' = 0.13$) and 9-anthracenecarbonitrile ($k' = 0.09$). Values for the injection volume were calculated by means of eqn. 1. The electroosmotic flow during the separation was 95 pl/s ($v_{eo} = 1.08$ mm/s). The slope of the plotted lines in the graph of $\sigma_{v,tot}^2$ *versus* V_{inj}^2 equals the reciprocal of K^2 and an average value of $K^2 = 8.0$ was found in this experiment. Various phenomena might be responsible for the deviation in K^2 value from the value for a block, 12. In the first place, the rise and fall times in the voltage[28] may have influenced the amount injected. We also found that the angle at which the capillary is cut is critical: with obliquely cut capillaries K^2 values as low as 3 were found. Finally, Grushka *et al.*[45] found that spontaneous, not electrically induced sample introduction takes place. However, for the present experiments we considered the observed value of 8 to be satisfactory.

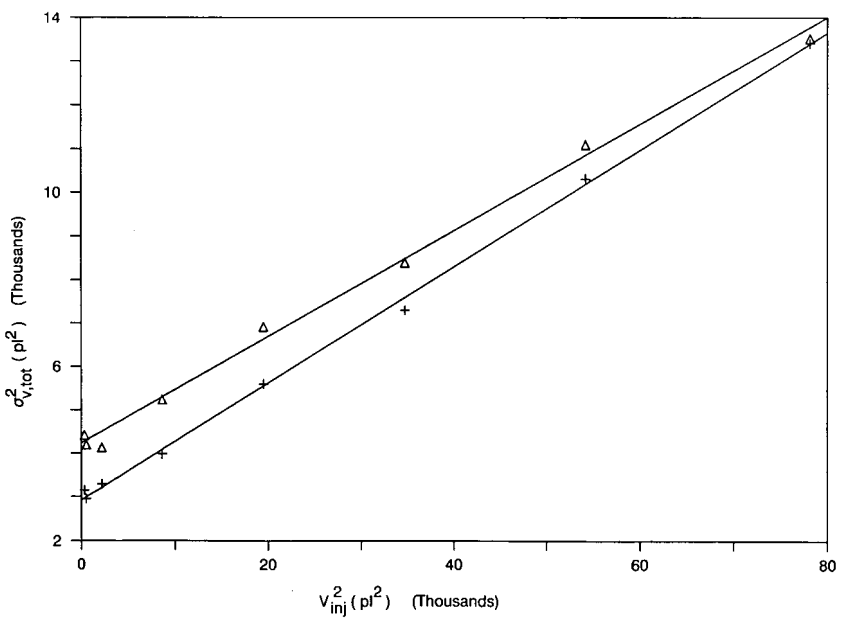

Fig. 4. Total volume variance, $\sigma_{v,tot}^2$, *versus* the square of the injection volume for a 50.0 cm × 10 μm I.D. PSL-ODS capillary. Injection voltage = 2.4 kV; $l_{inj\text{-}det}$ = 25.0 cm; separation voltage = 24.6 kV; current = 2.2 μA. Compounds: +, 9-anthracenecarbonitrile ($k' = 0.09$); △, anthracene ($k' = 0.13$). The lines were drawn from calculations by the linear square root method.

Band broadening by thermal effects

The effects of self-heating on efficiency in an ED system can be expressed as

$$H_{col} = H_{ED} + H_{TH} \tag{9}$$

where H_{ED} is the plate height for an ED system as shown in eqn. 2 and H_{th} is the plate height caused by thermal effects. The latter can be a significant source of band broadening in capillary electroseparation techniques. The magnitude of the temperature gradient from the centre of the capillary to the inner wall, ΔT, can be calculated from[39,46]

$$\Delta T = Q\, d_c^2/16\kappa \tag{10}$$

where κ is the thermal conductivity of the electrolyte, d_c is the inner diameter of the capillary and Q is the power density[39,47]:

$$Q = 4EI/\pi d_c^2 \tag{11}$$

where I is the current. Combination of eqns. 10 and 11 yields a general relationship between the power per unit length (EI) and the temperature gradient:

$$\Delta T = EI/4\pi\kappa \tag{12}$$

Jones and Grushka[46] assumed that a ΔT of less than 1 K across the bore of the capillary will not seriously decrease the efficiency. For $\Delta T = 1$ K and $\kappa = 0.4$ W/(m · K), $EI = 5.02$ W/m. In ED-OTLC, EI is much smaller because of the low current in 10 μm I.D. capillaries. Applying a field of 68.4 kV/m across a 10 μm I.D. capillary filled with, *e.g.*, phosphate buffer (0.1 *M*)–acetonitrile results in a current of 3.42 μA and EI in this instance is 0.23 W/m. Hence it can be said that very small thermal gradients can be expected in 10 μm I.D. capillaries.

Knox[39] derived an expression for H_{TH}:

$$H_{TH} = 10^{-8} \cdot \frac{\varepsilon_o \varepsilon_r\, \zeta}{D_m \eta \kappa^2} \cdot E^5 d_c^6 \lambda^2 c^2 \tag{13}$$

where λ is the equivalent conductivity and c is the concentration of the electrolyte. Using some typical parameters (some of the values are rough estimates) from Table II shows that thermal band broadening caused by heating effects can be neglected for diameters smaller than 100 μm.

Apart from the thermal non-uniformity of the liquid, problems may also arise as a result of the mean temperature rise of the liquid, due to slow heat transfer through the tube material and cooling bath medium. Such temperature increases may affect the reproducibility and stability of components. In contrast to the internal thermal profiles, these effects can be diminished by applying cooling, as shown by various workers[39,47]. The demands on temperature control become more severe when larger inner diameters are used, but even with 25 μm I.D. capillaries in ED-OTLC the entire capillary may heat up by several degrees, as will be shown below.

TABLE II

BAND BROADENING CAUSED BY THERMAL EFFECTS, H_{TH}, AND THE TEMPERATURE EXCESS, θ, OF THE TUBE WALL RELATIVE TO THE SURROUNDING AIR AS A FUNCTION OF THE CAPILLARY DIAMETER FOR ACETONITRILE–BUFFER (2:3)

E = 50 000 V/m, λ = 0.00735 $m^2/\Omega \cdot mol$, c = 60 mol/m^3, $\eta = 1.1 \cdot 10^{-3}$ Pa s, $\varepsilon_o\varepsilon_r = 7.08 \cdot 10^{-10}$ $C^2/N \cdot m^2$, $\zeta = 40 \cdot 10^{-3}$ V, $D_m = 1 \cdot 10^{-9}$ m^2/s, κ = 0.4 W/m · K, Q = 1102 W/cm^3 (calculated with $Q = E^2 \lambda c$), $k' = 0$ and u = 1.5 mm/s.

I.D. *(μm)*	*O.D.* *(μm)*	H_{ED} *(μm)*	H_{TH} *(μm)*	θ *(K)*
10	175	1.33	$9.7 \cdot 10^{-8}$	1.5
25	325	1.33	$2.3 \cdot 10^{-5}$	7.7
50	350	1.33	$1.5 \cdot 10^{-3}$	29.9
100	300	1.33	0.098	125.6
200	500	1.33	6.2	431.0

The temperature increase of the tube relative to the surrounding air, θ, can be calculated from an expression derived by Knox[39] but slightly modified for the fact that formation of heat takes place only in the part of the tube filled with electrolyte:

$$\log \theta = 1.70 \log d_o\ (\mu m) + \log Q[(d_i/d_o)^2]\ (W/cm^3) - 4.20 \qquad (14)$$

where d_i and d_o are the inner and outer diameter of the tube, respectively. It can be concluded from Table II that for a 10 μm I.D. capillary there will be only a very small temperature increase (1.5 K) of the capillary as a whole. This is calculated for

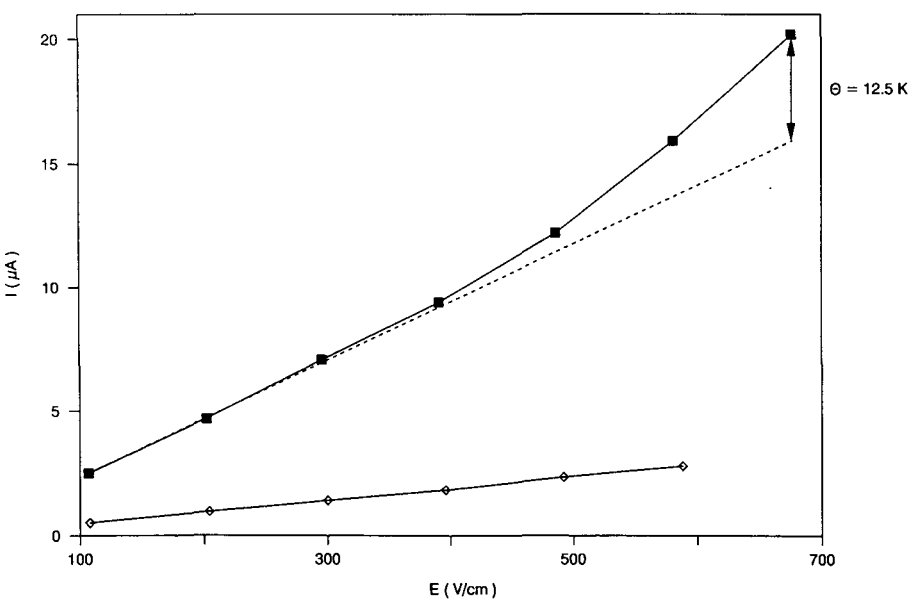

Fig. 5. Plot of current *versus* electric field for natural convection on a 10 μm I.D. × 175 μm O.D. (◇, L = 50.0 cm) and a 25 μm I.D. × 325 μm O.D. (■, L = 50.6 cm) capillary in still air.

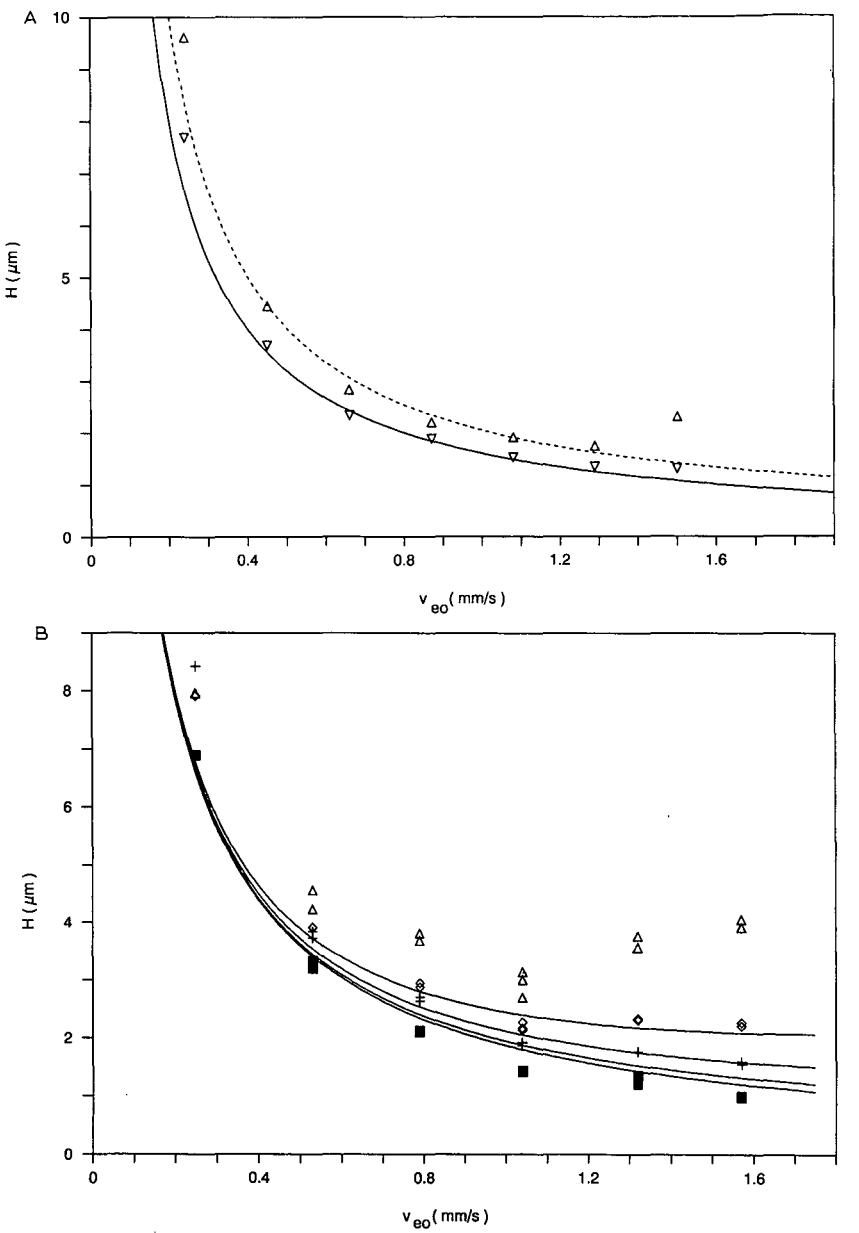

Fig. 6. *H versus* v_{eo} curves for (A) a 10-μm I.D. PSL-ODS capillary and (B) an etched ODS 10-μm I.D. capillary. Mobile phase: phosphate buffer (pH 7.0)–acetonitrile (3:2). V_{inj} = 50 pl; T = 21.0 ± 0.2°C. (A) L = 50.0 cm, $l_{inj\text{-}det}$ = 25.0 cm. ▽, 9-Anthracenecarbonitrile (k' = 0.09); △, anthracene (k' = 0.13); the lines are theoretical lines. (B) L = 45.0 cm, $l_{inj\text{-}det}$ = 22.0 cm. ■, 9-Anthracenemethanol (k' = 0); +, 9-methylanthracene (k' = 0.12); ◇, 1,2-benzanthracene (k' = 0.24); △, 9-phenylanthracene (k' = 0.42).

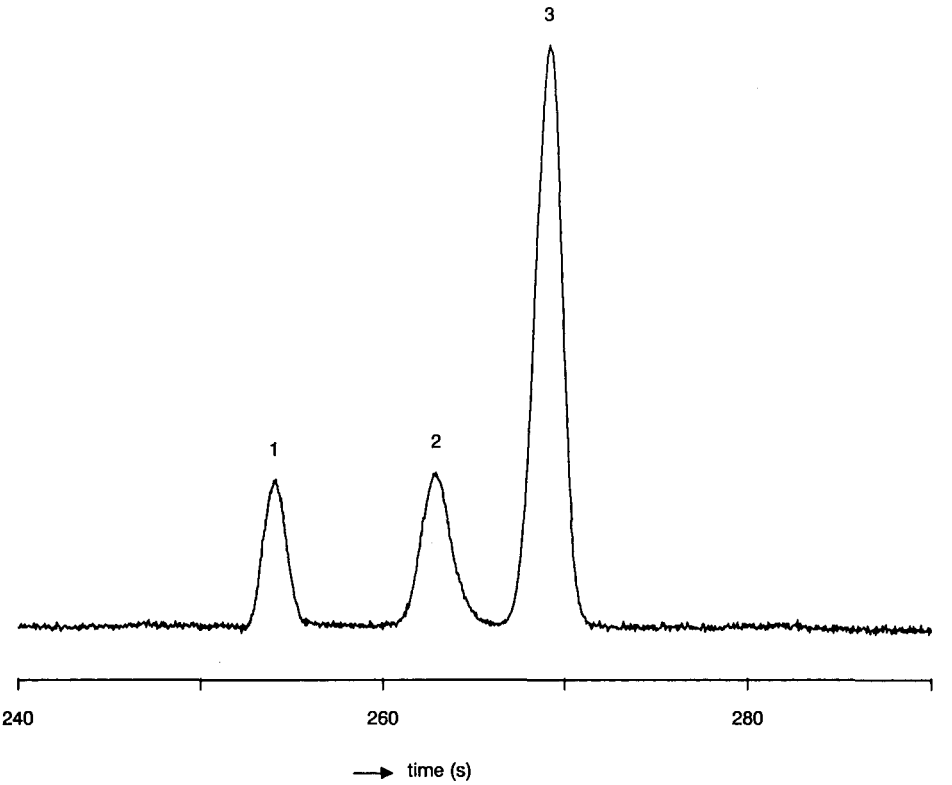

Fig. 7. Chromatogram of three polycyclic aromatics obtained with a 10-μm I.D. ODS-capillary. Applied voltage = 17.5 kV; current = 0.9 μA; L = 45.9 cm, $l_{inj\text{-}det}$ = 22.0 cm. Peaks: 1 = 9-anthracenemethanol (k' = 0); 2 = anthracene (k' = 0.03); 3 = 9-methylanthracene (k' = 0.06). Other details as in Fig. 6.

a situation without a cooling device in the experimental set-up. As shown by Nelson *et al.*[47], the current will increase faster than in proportion to the increase in applied voltage, as a result of poor heat dissipation in still air in 50 μm I.D. and larger capillaries. In Fig. 5 the current, I, is plotted against the applied electric field, E, for 25 and 10 μm I.D. capillaries. It was found that with the 25 μm I.D. capillary there is a small tendency to deviate from linearity, whereas with the 10 μm I.D. capillary a linear relationship holds. Applying a field of 67.6 kV/m ($Q = 2.01 \cdot 10^3$ W/cm^3) in a 25 μm I.D. × 325 μm O.D. capillary gives a calculated value for the temperature increase of θ = 14 K. Fig. 5 shows that a 25% positive deviation from linearity in the current occurs at this electric field strength. It is known that the conductivity changes by 2% per degree[47]. Hence we find an experimental estimate for θ of 12.5 K.

Chromatography

In Fig. 6A a H *versus* v_{eo} curve is shown for a 10-μm I.D. PSL-ODS capillary with an injection volume of about 20 pl. It can be seen that the minimum observed plate heights were 1.4 μm for 9-anthracenecarbonitrile and 1.7 μm for anthracene, and also that good agreement with theory is obtained. Results with another 10 μm I.D. ODS

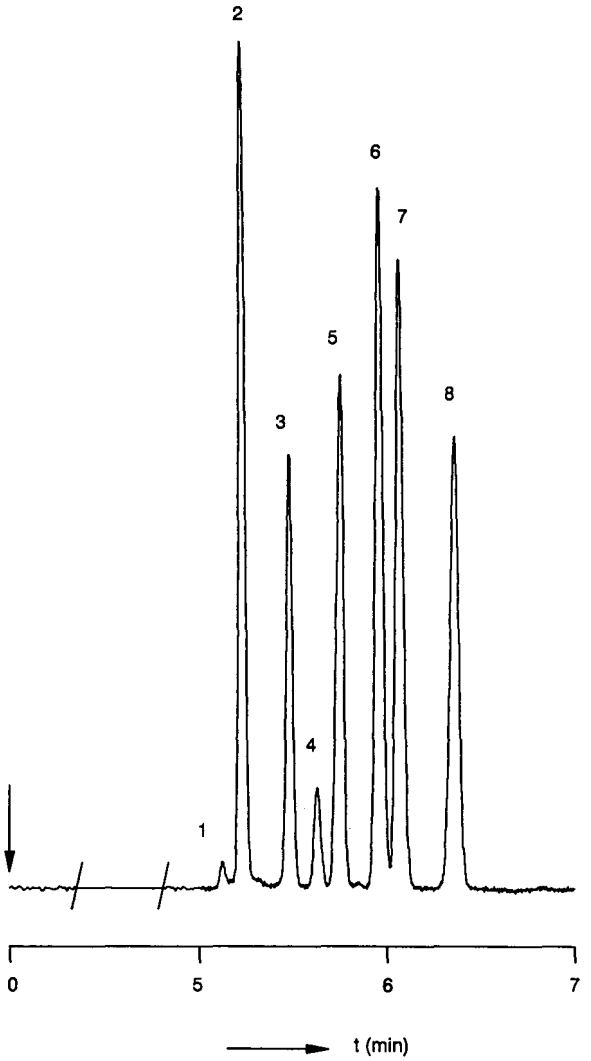

Fig. 8. Chromatogram of eight polycyclic aromatics obtained with a 10-μm I.D. PSL-ODS capillary. Applied voltage = 20 kV; L = 49.0 cm; $l_{inj\text{-}det}$ = 26.5 cm; current = 0.7 μA; T = 25°C; V_{inj} = 9 pl. Mobile phase: 0.05 M phosphate buffer (pH 7.0)–methanol (1:1). Peaks: 1 = naphthoquinone (k' = 0); 2 = 9-anthracenemethanol (k' = 0.03); 3 = 9-anthracenecarbonitrile (k' = 0.06); 4 = anthracene (k' = 0.09); 5 = 7,8-benzoflavone (k' = 0.12); 6 = fluoranthene (k' = 0.16); 7 = pyrene (k' = 0.19); 8 = 9-vinylanthracene (k' = 0.24).

capillary are shown in Fig. 6B. Again, plate heights as low as 1.2 μm could be observed for the unretained 9-anthracenemethanol and 2.3 μm for 1,2-benzanthracene (k' = 0.24). These values correspond to plate numbers of 183 000 and 94 000, respectively. The data in Fig. 6B show good agreement with theory for solutes of low retention. However, at high velocity and retention, a deviation of increasing magnitude occurs, amounting to a factor of nearly 2 in the worst case. This deviation is as yet unexplained.

Some examples of the high performance of ED-OTLC can be seen in Fig. 7, where a sample of three polycyclic aromatics was injected. The peaks show a Gaussian shape and are baseline resolved, despite the small differences in k' values. Another example of a separation is shown in Fig. 8, where eight polycyclic aromatics are separated in less than 400 s, while the group of peaks appears baseline resolved in a time interval of only 90 s.

CONCLUSIONS

It has been shown for the first time that it is possible to perform ED-OTLC in chemically modified 10–25 μm I.D. capillaries near the optimum of the H *versus* v_{eo} curve. An advantage of ED-OTLC is that injection is easier than in a PD-OTLC system, where dynamic or static split injection devices are necessary in order to obtain a sufficiently small injection volume. It is found that very small volumes of uncharged components can be introduced with the electromigration injection technique. It gives the opportunity to analyse very small volumes of sample, *e.g.*, sampling directly from tissue or individual cells. The use of larger I.D. capillaries in ED-OTLC without losing to much efficiency gives better prospects for loadability, optical detection systems and preparation of stationary phases.

The electroosmotic mobility has been found to be independent of the inner diameter of the capillary. Its value in ODS-treated tubes is hardly different from that in untreated tubes and allows adequate mobile phase velocities when typical reversed-phase mobile phases are used.

ACKNOWLEDGEMENTS

The authors thank Miss M. L. V. Pietersen for practical assistance and H. Brugman and T. van Goudoever for the construction of part of the equipment. Support for this work (P.P.H.T.) was provided by the Netherlands Foundation for Chemical Research (SON) with financial aid from the Netherlands Organization for the Scientific Research (NWO) under grant 700-344-003.

REFERENCES

1 J. H. Knox and M. Saleem, *J. Chromatogr. Sci.*, 7 (1969) 614.
2 J. H. Knox and M. T. Gilbert, *J. Chromatogr.*, 186 (1979) 405.
3 J. Jorgenson and E. J. Guthrie, *J. Chromatogr.*, 255 (1983) 335.
4 M. J. Sepaniak, J. D. Vargo, C. N. Kettler and M. P. Maskarinec, *Anal. Chem.*, 56 (1984) 1252.
5 S. Folestad, B. Josefsson and M. Larsson, *J. Chromatogr.*, 391 (1987) 347.
6 O. van Berkel, J. C. Kraak and H. Poppe, *Chromatographia*, 24 (1987) 739.
7 P. R. Dluzneski and J. W. Jorgenson, *J. High Resolut. Chromatogr. Chromatogr. Commun.*, 11 (1988) 332.
8 P. P. H. Tock, G. Stegeman, R. Peerboom, H. Poppe, J. C. Kraak and K. K. Unger, *Chromatographia*, 24 (1987) 617.
9 P. P. H. Tock, C. Boshoven, H. Poppe, J. C. Kraak and K. K. Unger, *J. Chromatogr.*, 477 (1989) 95.
10 H. P. M. van Vliet and H. Poppe, *J. Chromatogr.*, 346 (1985) 149.
11 L. A. Knecht, E. J. Guthrie and J. Jorgenson, *Anal. Chem.*, 56 (1984) 479.
12 M. D. Oates and J. W. Jorgenson, *Anal. Chem.*, 61 (1989) 1977.
13 R. T. Kennedy and J. W. Jorgenson, *Anal. Chem.*, 60 (1988) 1521.

14 A. Manz and W. Simon, *J. Chromatogr.*, 387 (1987) 187.
15 W. M. A. Niessen and H. Poppe, *J. Chromatogr.*, 394 (1987) 21.
16 J. S. de Wit, K. B. Tomer and J. W. Jorgenson, *J. Chromatogr.*, 462 (1989) 365.
17 P. P. H. Tock, P. P. E. Duijsters, J. C. Kraak and H. Poppe, *J. Chromatogr.*, 506 (1990) 185.
18 F. E. P. Mikkers, F. M. Everaerts and Th. P. E. M. Verheggen, *J. Chromatogr.*, 169 (1979) 11.
19 J. W. Jorgenson and K. D. Lukacs, *J. Chromatogr.*, 218 (1981) 209.
20 R. A. Wallingford and A. G. Ewing, *J. Chromatogr.*, 441 (1988) 299.
21 A. S. Cohen and B. L. Karger, *J. Chromatogr.*, 397 (1987) 409.
22 S. Terabe, K. Otsuka and T. Ando, *Anal. Chem.*, 57 (1985) 834.
23 F. Kilar and S. Hjerten, *J. Chromatogr.*, 480 (1989) 351.
24 T. Tsuda, K. Nomura and G. Nakagawa, *J. Chromatogr.*, 248 (1982) 241.
25 J. W. Jorgenson, *Trends Anal. Chem.*, 3 (1984) 51.
26 H. H. Lauer and D. McManigill, *Anal. Chem.*, 58 (1986) 166.
27 M. Yu and N. J. Dovichi, *Appl. Spectrosc.*, 43 (1989) 196.
28 W. G. Kuhr and E. S. Yeung, *Anal. Chem.*, 60 (1988) 2642.
29 R. A. Wallingford and A. G. Ewing, *Anal. Chem.*, 59 (1987) 1762.
30 J. P. Chervet, M. Ursem, J. P. Salzman and R. W. Vannoort, *J. High Resolut. Chromatogr. Chromatogr. Commun.*, 12 (1989) 278.
31 R. T. Kennedy and J. W. Jorgenson, *Anal. Chem.*, 60 (1988) 1521.
32 R. T. Kennedy and J. W. Jorgenson, *Anal. Chem.*, 61 (1989) 436.
33 D. J. Rose and J. W. Jorgenson, *Anal. Chem.*, 60 (1988) 642.
34 R. A. Wallingford and A. G. Ewing, *Anal. Chem.*, 59 (1987) 678.
35 S. E. Moring, J. C. Colburn, P. D. Grossmann and H. H. Lauer, *LC · GC Int.*, 3 (1990) 46.
36 J. H. Knox and I. H. Grant, *Chromatographia*, 24 (1987) 135.
37 C. L. Rice and R. Whitehead, *J. Phys. Chem.*, 69 (1965) 4017.
38 A. A. A. M. van de Goor, B. J. Wanders and F. M. Everaerts, *J. Chromatogr.*, 470 (1989) 95.
39 J. H. Knox, *Chromatographia*, 26 (1988) 329.
40 M. J. E. Golay, in D. H. Desty (Editor), *Gas Chromatography 1958*, Butterworths, London, 1958, pp. 36–55.
41 M. Martin and G. Guiochon, *Anal. Chem.*, 56 (1984) 614.
42 J. C. Giddings, *Dynamics of Chromatography*, Marcel Dekker, New York, 1965.
43 X. Huang, M. J. Gordon and R. N. Zare, *Anal. Chem.*, 60 (1988) 1837.
44 J. C. Sternberg, *Adv. Chromatogr.*, 2 (1966) 205.
45 E. Grushka, R. M. McCormick, J. J. Kirkland, *Anal. Chem.*, 61 (1989) 241.
46 A. E. Jones and E. Grushka, *J. Chromatogr.*, 466 (1989) 219.
47 R. J. Nelson, A. Paulus, A. S. Cohen, A. Guttman and B. L. Karger, *J. Chromatogr.*, 480 (1989) 111.

Journal of Chromatography, 517 (1990) 573–581
Elsevier Science Publishers B.V., Amsterdam

CHROMSYMP. 1986

High-pressure and supercritical capillary electrophoresis

CLEMENT R. YONKER* and RICHARD D. SMITH
Chemical Methods and Separations Group, Chemical Sciences Department, Pacific Northwest Laboratory (Operated by Battelle Memorial Institute), Richland, WA 99352 (U.S.A.)

ABSTRACT

Preliminary results are reported for high-pressure and supercritical capillary electrophoresis. The fluid system investigated was methanol [critical temperature (T_c) = 240°C, critical pressure (P_c) = 80.9 bar] containing a small concentration of background electrolyte. The temperature and pressure regions studied ranged from 25–280°C and 67.1–295.7 bar, respectively, during the course of experimentation. Initial results of electrophoretic separations of 1-naphthol-4-sulfonic acid sodium salt and thymol blue as a function of temperature and pressure will be described and discussed.

INTRODUCTION

Capillary electrophoresis (CE) has proven itself to be a technique of high separation efficiency and of potentially extreme importance in the area of bioseparations[1–5]. The applications of CE to the separation of peptides, proteins and nucleic acids continue to increase. The enhanced separation efficiencies and decreased analysis times for complex solute molecules have proven advantageous for CE as compared to other separation methodologies.

The separation efficiency ultimately obtainable by CE depends upon the ratio of electrophoretic mobility to the diffusion coefficient. Although very high speed separations ($\approx$ 1.5 s) have been demonstrated by capillary zone electrophoresis[6], these have required extremely small sample volumes and have yet demonstrated only limited numbers of theoretical plates. Continued improvement of high-speed separations encounters fundamental limitations. To obtain short analysis times the applied potential across the length of the capillary column should be high[7]; in the absence of heating effects separations improve in direct proportion to electric field strength. However, an excessively high applied potential can lead to deleterious effects due to heating of the capillar buffer solution, causing decreased separation efficiency and possible vaporization of the buffer solution[8]. Decreased separation efficiencies can occur through an increase of the parabolic nature in the electroosmotic velocity flow profile with the increased radial temperature gradient[8,9]. Decreasing the buffer

conductivity to limit heating effects, proportionally limits sample size, due to practical limits placed on the conductivity difference between the buffer and sample.

An increase in the mass transfer characteristics of a solute molecule could improve the separation efficiency in a mass transfer limited system. In a separation which is not mass transfer limited an increase in the diffusion coefficient could prove problematic, leading to increased zone broadening. In capillary electrophoresis where axial diffusion can define the zone broadening limit in some cases, increasing the diffusion coefficient of the solute would not prove beneficial. This could also be true in supercritical-fluid capillary electrophoresis (SCE) for non mass transfer limited situations.

True plug flow is not achieved in electroosmotic flow[9]. Therefore, the shear layer at the capillary wall can contribute to solute zone broadening in capillar electrophoresis. Increasing radial mass transport through this shear layer could decrease the overall zone broadening in the system. This will be dependent on the interplay between ion molecular diffusion in the radial and axial direction in the capillary. SCE could prove to be an interesting technique to study these physicochemical processes for electroosmotic flow.

One might anticipate that electrophoretic mobilities will increase linearly with molecular diffusion coefficients, providing a basis for faster separations. Other secondary benefits might arise from such an experimental approach. For example, increasing pressure in the system would increase the solvent's boiling point, thus decreasing solvent vaporization. Vapor generation during CE separations generally leads to (often dramatic!) failure of the separation. This approach could allow higher electric fields to be used. Therefore, high-pressure capillary electrophoresis (HPCE) and SCE could prove beneficial in mass transfer limited systems and in obtaining shorter analysis times. From a fundamental viewpoint, SCE and HPCE present the novel opportunity to study the effects of fluid density (pressure and temperature) on solute mass transfer in electroosmotic flow. SCE and HPCE can contribute to the understanding of the effect of fluid viscosity changes on electrophoretic and electroosmotic mobilities. Changes in the capillary surface double layer as a function of pressure and temperature can be studied. Any changes in the zeta potential of the surface and the solute molecule with density which can affect solute migration can be studied. Finally, the thermodynamics of equilibrium for the charged solute species as a function of pressure and temperature can be determined.

In this manuscript, we present initial data involving our preliminary experiments with high-pressure and supercritical capillary electrophoresis. The discussion centers on the effects of pressure and temperature on solute selectivity and separation efficiency.

THEORY

Capillary electrophoresis involves the electrophoretic migration of a solute species in a capillary in the presence of an electric field. In the high-pressure or supercritical fluid capillary electrophoresis arrangement we have selected for initial investigation, the electrophoretic migration of the solute occurs in a capillary connected between two high-pressure solvent reservoirs. Therefore, the total velocity of a solute species can be described as

$$v_T^1 = v_{ep}^1 + v_{eo}^1 + v_p^1 \quad (1)$$

where v_T is the total velocity of the solute: v_{ep} and v_{eo} are the electrophoretic and electroosmotic velocity of the solute, respectively: v_p is the velocity of the solute due to a pressure difference (potentially caused by any leakage in the pressurized system and would be detrimental to obtaining high efficiencies): and 1,2... refers to the number of solutes. The electrophoretic velocity of the solute is

$$v_{ep} = \mu_{ep} E \quad (2)$$

where μ_{ep} is the electrophoretic mobility of the solute and E is the electric field strength. The electric field strength is the ratio of the applied voltage to the capillary length (V/L). The electrophoretic mobility of the solute is

$$\mu_{ep} = [\varepsilon\zeta/4\pi\eta] \quad (3)$$

where ε is the dielectric constant, η is the viscosity of the solvent, and ζ is the zeta potential at the solute/solvent interface. These molecular parameters control the electrophoretic mobility for a specific solute molecule. A similar relationship can be described for the electroosmotic mobility; in this case, the zeta potential refers to the potential at the liquid/solid interface on the capillary surface[1,10,11]. In the case of HPCE and SCE, the physicochemical parameters of ε, ζ and η will be a function of temperature, pressure, and fluid density. The dielectric constant and viscosity of a supercritical fluid are clearly a function of temperature and pressure[12–14]. Thus, one can expect to observe changes in the electrophoretic and electroosmotic velocity of the system when using a supercritical fluid compared to conventional liquids.

The separation of two solute molecules will be dependent on differences in their migration velocity. Eqn. 1 describes the total velocity of the solute in a CE experiment. The difference in migration velocities for two solutes (Δ) is determined by subtracting their respectively total velocities. Assuming $v_{eo}^2 = v_{eo}^1$ and $v_p^2 = v_p^1$, then at constant pressure or temperature,

$$\Delta \equiv v_T^2 - v_T^1 = v_{ep}^2 - v_{ep}^1 = \mu_{ep}^2 E - \mu_{ep}^1 E = (\zeta^2 - \zeta^1)E\varepsilon/4\pi\eta \quad (4)$$

The difference in migration velocity (selectivity) is dependent on field strength (E) and two other terms; one term is dependent on molecular differences ($\zeta^2 - \zeta^1$), and the second term is dependent on the solvent ($\varepsilon/4\pi\eta$). The change in selectivity, Δ, as a function of pressure and/or temperature in the supercritical-fluid region could be a sensitive indicator of the change in physical or chemical environment about the solute molecules.

The difference in migration time for two solutes as a function of Δ can be written as,

$$\Delta t = \frac{\Delta L}{\mu^1 \mu^2 E^2} \quad (5)$$

where μ^1 and μ^2 represent the mobility for the two solutes, respectively. The difference in migration time can be related to the fundamental parameters of ζ, E, η and V on appropriate substitution and rearrangement of eqn. 5 yielding,

$$\Delta t = \frac{(\zeta^2 - \zeta^1)\ 4\pi\eta\ L^2}{(\zeta^2\zeta^1)\ \varepsilon V} \tag{6}$$

Therefore, the difference in migration time can be related to the applied potential and specific solute or solvent effects as stated in the above discussion. While the determination of Δt is an oversimplification of the parameters governing solute migration, some insight into the effects of pressure, temperature and applied potential in HPCE and SCE can be obtained from this value.

EXPERIMENTAL

The supercritical capillary electrophoresis system is basically similar to low pressure systems published in the literature[4]. A schematic of the SCE system is shown in Fig. 1. This system has two high-pressure SS316 solvent reservoirs; one at the anode end of the capillary column and one at the grounded end of the column. The system is pressurized using an high-performance liquid chromatography (HPLC) syringe pump (Varian 8500) under microprocessor control. A variable-wavelength UV–visible detector (ISCO) was used for on-line detection of the solute after a section of the polyimide coating of the capillary had been removed. A high-voltage power supply (Glassman) was used to supply the positive potential to the anodic end of the capillary column. A muffle furnace with a temperature controller was used to hold the capillary column at a constant temperature. A hydrostatic line was used between the two high-pressure reservoirs to facilitate sample loading and pressurization. The hy-

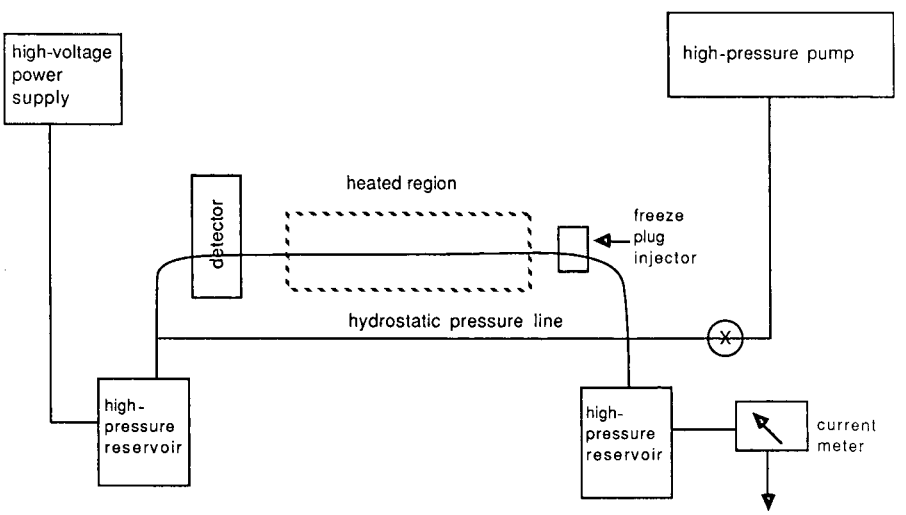

Fig. 1. Schematic of supercritical-fluid capillary electrophoresis system.

drostatic line was connected to the pressurized solvent reservoirs through two high-pressure 1/16-in. stainless-steel 316 tees. These fittings contained connections for the analytical CE column, the hydrostatic line and the solvent delivery line from the pump (see Fig. 1).

Sample injection was accomplished by dipping the end of the analytical capillary column in the solute–electrolyte solution. Then a small section (< 1.5 cm) of the column was frozen using liquid nitrogen. The contraction of the solvent in the capillary pulled a sample plug into the column. The column segment was kept frozen while the system was reconnected to the high-pressure reservoir and then pressurized with the HPLC pump. The hydrostatic line was needed to equalize the pressure on both sides of the frozen column plug, such that on thawing the sample plug would remain positioned at the end of the analytical column. The system temperature and pressure could be equilibrated to the appropriate conditions chosen for study while the column segment was frozen. The "freeze plug" injection technique was necessary because the large volume of typical HPLC sample valves and difficulties arising from the metal and graphite surfaces in these valves which affected the potential gradient down the column. Work is proceeding on the design and construction of more appropriate high-pressure, low dead volume valves for use in the SCE system.

The analytical capillary column used was fused silica, 150 μm I.D. by 360 μm O.D. and *ca.* 100 cm in length. The hydrostatic column was 50 μm I.D. $\times$ 210 μm O.D. fused silica which had a bonded coating of SE-54 on the surface. This organic coating precluded any electroosmotic flow but maintained the two high-pressure reservoirs at a similar pressure value, independent of any electroosmotic flow in the analytical capillary when the system was pressurized. The solvent used was methanol (T_c = 240°C, P_c = 80.9 bar) having an electrolyte concentration of 10 m*M* acetic acid and 10 m*M* sodium acetate. This electrolyte system had a current of *ca.* 40 μA at room temperature and 296 bar at +30 kV applied across the column. The solutes used were 1-naphthol-4-sulfonic acid sodium salt (Kodak Chemical) and thymol blue (Aldrich). Both molecules were soluble in the methanol electrolyte solvent and showed electrophoretic migration at room temperature and pressure. After the determination of the net electroosmotic and electrophoretic flow velocities in the system at room temperature and pressure, initial experiments were undertaken to determine the effect of high-pressure and supercritical conditions on the electrophoretic separation.

RESULTS AND DISCUSSION

There have been several reports of electrochemistry and ion-mobility in supercritical fluids which demonstrate that electrophoretic separations in a supercritical fluid should be feasible[15–20]. This work has entailed voltammetry studies in supercritical carbon dioxide by Wightman and co-workers[16–18] and electrochemical studies in supercritical water and other non-aqueous solvents by Flarsheim *et al.*[19] and Crooks[20]. These studies demonstrate that a supercritical fluid can dissolve an electrolyte and can have sufficient ionic strength (*i.e.*, carry sufficient current) needed for supercritical-fluid capillary electrophoresis.

SCE presents the novel opportunity to study directly the effect of fluid density (*i.e.*, pressure and temperature) on the capillary surface double layer, the zeta potential of the capillary surface and the solute molecule, the effect of changing viscosity on the

mass transport properties of the charged solute in the supercritical fluid, the electrostriction of the solvent about the solute ion[21,22], and the change in equilibrium of the charged solute. In addition, use of high pressures would allow higher electric field gradients to be applied to the analytical column for potentially obtaining shorter analysis times. We note potential difficulties could still arise due to the increased resistive heating of the buffer solution and the effect of the radial temperature gradient on the fluid density and flow velocity profile. In mass transfer limited electrophoretic separations in liquids where the slight parabolic nature of the flow velocity profile leads to decreased separation efficiencies, the use of a supercritical fluid could prove beneficial as shown in supercritical-fluid chromatography. The study of the physicochemical parameters governing SCE could lead to an improved understanding of ion solvation and capillary electrophoresis as practiced today.

Initial data for high-pressure and supercritical capillary electrophoresis are listed in Table I. The change in migration time between the two solutes, Δt, is given as a function of pressure, temperature and voltage potential. At constant pressure and temperature, as the applied potential increases Δt between the two peaks decreases. This decrease in the difference in the migration time between the peaks is due to the increase in potential applied to the system. As shown in eqn. 6, there is a inverse relationship between applied potential (V) and Δt. Therefore, as the potential is increased at constant pressure and temperature, the migration time difference between the solutes would be expected to decrease which is seen in Table I. For HPCE at constant temperature and applied potential, a slight decrease in Δt is noted with increasing pressure. Pressure can effect the solvent viscosity and dielectric constant or the zeta potential between the solute–solvent and solvent–surface. Over the pressure range studied at this temperature, these effects could be expected to be either slight or

TABLE I

SOLUTE SELECTIVITY (Δt) AS A FUNCTION OF POTENTIAL, PRESSURE AND TEMPERATURE

Conditions	*Δt (s)*	*Potential (kV)*	*Atm*	*T(°C)*	*i (μA)*
136 bar, 21°C	270 ± 10	+15			33
	282 ± 20	+20			45
	180 ± 20	+25			57
	180 ± 10	+30			70
21°C, + 20 kV	264 ± 20		67		45
	252 ± 20		137		45
	216 ± 20		206		45
	204 ± 20		278		43
296 bar, + 30 kV	249 ± 9			21	41
	265 ± 9			55	44
	234 ± 9			105	48
	238 ± 9			150	49
	204 ± 9			200	50
	180 ± 9			217	48
	160 ± 18			250	43
	189 ± 9			280	31

negligible. Therefore, the change in Δt would be expected to be very small. At constant pressure and applied potential Δt changes with increasing temperature. This change in Δt is significant and falls outside the experimental error (listed in Table I). In the sub-critical and near-critical regions an increase in temperature would be expected to decrease solvent viscosity which should lead to a decrease in Δt. As temperature increases Δt shows a monotonic decrease. At constant pressure, above the critical temperature, further increases in temperature will decrease solvent viscosity. Therefore, Δt would be expected to decrease based on solvent viscosity arguments as shown in Table I. Density variations in the critical region would affect the zeta potential of the molecules and the viscosity and dielectric constant of the fluid. All these physicochemical parameters would affect the selectivity obtainable between peaks, but at the crude present level of experimental sophistication it is difficult to isolate these individual parameters. Further studies at constant density are planned which will better characterize these physical parameters in HPCE and SCE, but there are some interesting preliminary trends.

The observed electrical current in the analytical column as a function of potential, pressure and temperature is also listed in Table I. Perhaps the most interesting behavior involves the change in current which occurs as a function of temperature at constant pressure. Column current increases with increasing temperature, with a maximum being reached at *ca.* 200°C. Beyond this value the current decreases as one proceeds into the critical region for methanol. This decrease in current could be due to a decrease in solubility of the background electrolyte as temperature increases. In the critical region, the background electrolyte solubility (or dissociation to ionic species for weaker electrolytes) will be a function of fluid density. As the fluid density decreases with increasing temperature at constant pressure, the background current was seen to drop very rapidly.

A representative separation in SCE is shown in Fig. 2. This figure shows the separation of 1-naphthol-4-sulfonic acid sodium salt and thymol blue at room temperature and 280°C at 296 bar and a blank run at 280°C, 296 bar. The blank experiment under supercritical conditions shows a possible "system" peak. If this is

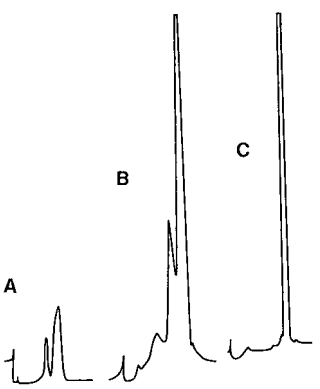

Fig. 2. Supercritical fluid electrophoretic separations of 1-naphthol-4-sulfonic acid sodium salt (first peak) and thymol blue (second peak) at atm 296 and +30 kV; (A) 21°C, 42 μA; (B) 280°C, 30 μA; and (C) blank 280°C, 31 μA.

indeed the case, a systematic study of the "system" peak's migration velocity and its dependence on temperature and pressure could provide information about the surface double layer in the supercritical region. At present it is unclear as to the true nature of this "system" peak, *e.g.*, the "system" peak is not seen at ambient temperatures only at higher temperatures. Further experimental characterization of this "system" peak is being undertaken at this time to determine its exact nature and behavior. Another additional aspect of the results shown in Fig. 2 is the broadening of the peaks in the supercritical fluid as compared to the HPCE separation. One would expect this behavior due to enhanced axial molecular diffusion in a non mass transfer limited separation.

CONCLUSIONS

The preliminary results discussed in this manuscript demonstrate the feasibility of supercritical-fluid electrophoresis. This technique could potentially be used to enhance resolution, separation efficiency, or speed in mass transfer limited systems. Of major interest is the physicochemical study of the surface double layer as a function of pressure and temperature. Specific changes in the zeta potential of the capillary surface and probe molecule with density can also be studied. The effects on the electrophoretic and electroosmotic mobilities by changing fluid viscosity and dielectric constant, and the electrostriction of solvent about an ion in a supercritical fluid can be investigated. Studies of these types should be amenable with SCE, leading to a better understanding of the physicochemical parameters governing solute separation by capillary electrophoresis.

HPCE and SCE are techniques in their infancy and their ultimate usage as analytical separation methodologies is still in question. But, they could prove useful in certain separation schemes. Their use in the investigation of density effects on the physicochemical parameters governing ion mobility in a liquid could prove to be important. Further research characterizing these parameters is continuing at this time.

ACKNOWLEDGEMENTS

The authors acknowledge the support of the U.S. Army Research Office under Contract DAAL03-87-K-0042. The content of this report does not necessarily reflect the position or the policy of the Government, and no official endorsement should be inferred.

REFERENCES

1 J. W. Jorgenson and K. D. Lukacs, *J. Chromatogr.*, 281 (1981) 209.
2 T. Tsuda, G. Nakagawa, M. Sato and K. Yagi, *J Appl. Biochem.*, 5 (1983) 330.
3 H. H. Lauer and D. McManigill, *Anal. Chem.*, 58 (1986) 166.
4 M. J. Gordon, X. Huang, S. L. Pentoney and R. N. Zare, *Science (Washington, D.C.)*, 242 (1988) 224.
5 F. E. P. Mikkers, F. M. Everaerts and Th. P. E. M. Verheggen, *J. Chromatogr.*, 169 (1979) 11.
6 M. A. Mosely, L. J. Deterding, K. B. Tomer and J. W. Jorgenson, *J. Chromatogr.*, 516 (1990) 167.
7 J. W. Jorgenson and K. D. Lukacs, *Science (Washington, D.C.)*, 222 (1983) 266.
8 E. Grushka, R. M. McCormick and J. J. Kirkland, *Anal. Chem.*, 61 (1989) 241.
9 M. Martin and G. Guiochon, *Anal. Chem.*, 56 (1984) 614.
10 V. Pretorius, B. J. Hopkins and J. D. Schieke, *J. Chromatogr.*, 99 (1974) 23.

11 A. S. Cohen, A. Paulus and B. L. Karger, *Chromatographia*, 24 (1987) 15.
12 J. M. St-Arnaud and T. K. Bose, *J. Chem. Phys.*, 71 (1979) 4951.
13 T. K. Bose and R. A. Cole, *J. Chem. Phys.*, 52 (1970) 140.
14 E. U. Franck, *Ber. Bunsen Ges. Phys. Chem.*, 88 (1984) 820.
15 N. Gee and C. R. Freeman, *Can. J. Chem.*, 58 (1980) 1490.
16 M. E. Philips, M. R. Deakin, M. V. Novotny and R. M. Wightman, *J. Phys. Chem.*, 91 (1987) 3934.
17 D. Niehaus, M. Philips, A. Michael and R. M. Wightman, *J. Phys. Chem.*, 893 (1989) 6232.
18 A. C. Michael and R. M. Wightman, *Anal. Chem.*, 61 (1989) 2193.
19 W. M. Flarsheim, Y. Tsow, I. Trachtenberg, K. P. Johnston and A. J. Bard, *J. Phys. Chem.*, 90 (1986) 3857.
20 R. M. Crooks, *Ph. D. Dissertation,* University of Texas at Austin, Austin, TX, 1987.
21 K. R. Atkins, *Phys. Rev.*, 116 (1959) 1339.
22 S. D. Hamann, in R. C. Bradley (Editor), *High Pressure Physics and Chemistry*, Vol. 2, Academic Press, London, 1963, pp. 146–147.

Author Index

Computer-Assisted Method Development for High-Performance Liquid Chromatography

edited by **J.L. Glajch** *and* **L.R. Snyder**

(Spin-off from the Journal of Chromatography Vol. 485 plus an additional chapter, index and glossary)

This book deals with the use of the computer as an aid in selecting adequate or optimum conditions for a given analytical separation. Originally published as Volume 485 of the Journal of Chromatography, it has now been reprinted in book form, since the information is so useful that many chromatographers want a copy readily available in the lab.
An extensive Introduction is added to the book edition. This surveys the field and refers to the pages where particular items are discussed in the book. The addition of a Glossary of Terms, an Author Index and a Subject Index make this book an invaluable source of easily consulted information for the practising chromatographer.
For the purpose of this book, computer-assisted method development will be limited to specific procedures which are intended to be used with a computer - rather than their manually applied precursors. In that sense, the subject can be considered to have begun around 1980.
The ongoing, intense research activity into various forms of computer assisted HPLC method development provides the assurance that this approach can really assist the practical chromatographer working in an industrial laboratory.

1990 xxx + 676 pages
Price: US$ 79.75 / Dfl. 175.00
ISBN 0-444-88748-2

Elsevier Science Publishers
P.O. Box 330, 1000 AH Amsterdam, The Netherlands
In the USA/Canada: P.O. Box 882, Madison Square Station, New York, NY 10159, USA

Journal of Chromatography Library, Volume 45

Chromatography and Modification of Nucleosides

edited by **C.W. Gehrke** *and* **K.C.T. Kuo**, *Department of Biochemistry, University of Missouri-Columbia, and Cancer Research Center, P.O. Box 1268, Columbia, MO, U.S.A.*

Part A

Analytical Methods for Major and Modified Nucleosides - HPLC, GC, MS, NMR, UV and FT-IR

Chromatography and Modification of Nucleosides is a four-volume work which provides state-of-the-art chromatography and analytical methods for use in a wide spectrum of nucleic acid modification research.

The focus of Part A, is the presentation of advanced methods for modification research on tRNAs, mRNAs, mtRNAs, rRNAs and DNAs. HPLC-UV, GC-MS, NMR, FT-IR and affinity chromatography approaches to nucleic acid modification studies are presented, as are nucleoside, oligonucleotide and nucleic acid isolation techniques.

Contents: Introduction and Overview *(C.W. Gehrke, K.C. Kuo)*. 1. Ribonucleoside analysis by reversed-phase high performance liquid chromatography *(C.W. Gehrke, K.C. Kuo)*. 2. HPLC of transfer RNAs using ionic-hydrophobic mixed-mode and hydrophobic-interaction chromatography *(R. Bischoff, L.W. McLaughlin)*. 3. Nucleic acid chromatographic isolation and sequence methods *(G. Keith)*. 4. Affinity chromatography of mammalian tRNAs on immobilized elongation factor Tu from *Thermus thermophilus (M. Sprinzl, K.-H. Derwenskus)*. 5. Structural elucidation of nucleosides in nucleic acids *(C.W. Gehrke et al.)*. 6. Three dimensional dynamic structure of tRNAs by nuclear magnetic resonance spectroscopy *(P.F. Agris, H. Sierzputowska-Gracz)*. 7. Codon recognition: evaluation of the effects of modified bases in the anticodon loop of tRNA using the temperature-jump relaxation method *(H. Grosjean, C. Houssier)*. 8. High-performance liquid chromatography of Cap structures and nucleoside composition in mRNAs *(K.C. Kuo et al.)*. 9. Immunoassays for modified nucleosides of ribonucleic acids *(B.S. Vold)*. 10. Chromatography of synthetic and natural oligonucleotides *(H. Eckstein, H. Schott)*. Subject Index.

1990 liii + 400 pages, ISBN 0-444-88540-4
Price: US$ 141.00 / Dfl. 275.00

Part B

Biological Roles and Function of Modification

Part B, the second of the four-volume work *Chromatography and Modification of Nucleosides*, has as its central theme the modified nucleosides of tRNA and the current analytical means for studying rRNA modifications. Modified nucleoside synthesis, function, structural conformation, biological regulation, and occurrence of modification in a wide range of tRNAs are presented, as is a chapter on DNA modification and a chapter on solid phase immunoassay for determining a particular modification.

The chapters are written by leading scientists in their respective fields and present an up-to-date review on the roles of modified nucleosides in nucleic acids which will be extremely useful for workers in chromatography, molecular biology, genetics, biochemistry, biotechnology and the pharmaceutical industry.

Contents: Introduction and Overview *(D.G. Söll)*. 1. Synthesis and function of modified nucleosides *(G.R. Björk, J. Kohli)*. 2. Biosynthesis and function of queuine and queuosine *(H. Kersten, W. Kersten)*. 3. Codon usage and Q-base modification in *Drosophila melanogaster (E. Kubli)*. 4. Solid phase immunoassay for determining the inosine content in transfer RNA *(E.F. Yamasaki, A.A. Wani, R.W. Trewyn)*. 5. Site directed replacement of nucleotides in the anticodon loop of tRNA: application to the study of inosine biosynthesis in yeast $tRNA^{Ala}$ *(K.A. Kretz, R.W. Trewyn, G. Keith, H. Grosjean)*. 6. tRNA and tRNA-like molecules: structural peculiarities and biological recognition *(R.L. Joshi, A.L. Haenni)*. 7. Mitochondrial tRNAs-structure, modified nucleosides and codon reading patterns *(G. Dirheimer, R.P. Martin)*. 8. The modified nucleotides in ribosomal RNA from man and other eukaryotes *(B.E.H. Maden)*. Modified uridines in the first positions of anticodons of tRNAs and mechanisms of codon recognition *(S. Yokoyama, T. Miyazawa)*. 10. Natural occurring modified nucleosides in DNA *(M. Ehrlich, X.Y. Zhang)*. Subject Index.

1990 xliv + 370 pages, ISBN 0-444-88505-6
Price: US$ 153.75 / Dfl. 300.00

Elsevier Science Publishers
P.O. Box 211, 1000 AE Amsterdam,
The Netherlands

Elsevier Science Publishing Co. Inc.
P.O. Box 882, Madison Square Station,
New York, NY 10159, U.S.A.

Vapor-Liquid Equilibrium Data

by **S. Ohe,** *Department of Applied Chemistry, Tokai University, Kanagawa, Japan*

(Physical Sciences Data, 37)

Vapor-liquid equilibrium (VLE) data are necessary for the design and operation of distillation processes. It is absolutely impossible to determine a distillation process without VLE data.

The author of this book has had much experience designing and constructing distillation processes and towers and knows that VLE data must be easily retrievable, readily comprehensible, and precise. This volume contains the most important VLE data for 1,446 binary systems with Wilson parameters determined by computer processing. The data are also presented graphically.

The Wilson equation, which is known as one of the most applicable to multicomponent systems, is employed for computer-aided determination of the optimum parameters using the non-linear least squares method. The data for each system include the substance names and the chemical formulae for the binary components, literature references, the Antoine vapor pressure constants or vapor pressures of the components, optimized values of the parameters for the Wilson equation, the errors, tables with smoothed values of vapor and liquid compositions and temperatures or pressures, and phase diagrams for visual comparison of the experimental data and calculated values. The systems are arranged according to the Chemical Abstracts system. An alphabetical index of systems is given at the end of the book for convenient retrieval.

Thus the VLE of binary or multicomponent systems can be computed from the Wilson parameters shown in the tables of this book. The book also presents a multicomponent VLE computer program written in BASIC and examples obtained using the program. With the program and parameters provided, VLE can be directly computed on a personal computer. Furthermore, when the Wilson parameters are used as input data for a distillation computer program, the number of theoretical plates (NTP) of distillation columns can be obtained.

Contents: **Part I. Equations for Calculation of the Vapor-Liquid Equilibrium.** 1. Fundamentals Equations for the Vapor-Liquid Equilibrium Relation. 2. Excess Free Energy of Non-Ideal Solutions. 3. Equations for Calculation. 4. Accuracy of Calculation by Wilson's Equation. 5. Examples Executed by Computer Program. References. **Part II. Data Sheets.** Guide to Graphs and Tables. Data Sheets 1-1446. Index.

1989 xxx + 742 pages ISBN 0-444-98876-9
Price: US$ 253.75 / Dfl. 495.00
Exclusive sales rights in Japan: Kodansha Ltd., Tokyo

Vapor-Liquid Equilibrium Data at High Pressure

by **S. Ohe,** *Department of Applied Chemistry, Tokai University, Kanagawa, Japan*

(Physical Sciences Data, 42)

High pressure vapor-liquid equilibrium data are important when very pure compounds are to be prepared, and they are also needed for high pressure liquid or supercritical chromatography.

This volume is a compilation of high pressure vapor-liquid equilibrium data for 700 binary system, processed and plotted by computer for ready inspection of the whole spectrum. The information given for each system comprises: the components' names, chemical formulae, cited literature, and critical temperature, critical pressures, acentric factors of the components, optimized values of the parameters for the Peng-Robinson equations, the errors, and phase diagrams for visual comparison of the experimental data and calculated values.

An alphabetical index by system name is included in the book which will be a useful reference for chemical engineers, research chemists, and graduate students who are interested in the chemical process industry.

Contents: **Part I. Equations for Calculation of the Vapor-Liquid Equilibrium at High Pressure.** 1. Method for Predicting Vapor-Liquid Equilibrium at High Pressure. 2. Prediction Examples for Binary and Multicomponent Vapor-Liquid Equilibria at High Pressure. 3. Prediction Program for Multicomponent Vapor-Liquid Equilibrium at High Pressure. References. **Part II. Data Sheets.** Guide to Graphs and Tables. Data Sheets 1-700. Index.

1990 xxviii + 356 pages ISBN 0-444-98797-5
Price: US$ 202.50 / Dfl. 395.00
Exclusive sales rights in Japan: Kodansha Ltd., Tokyo

ELSEVIER SCIENCE PUBLISHERS

P.O. Box 211, 1000 AE Amsterdam, The Netherlands

P.O. Box 882, Madison Square Station, New York, NY 10159, USA

Selective Sample Handling and Detection in High-Performance Liquid Chromatography

Journal of Chromatography Library, 39

part A

edited by **R.W. Frei**†, *Free University, Amsterdam, The Netherlands, and* **K. Zech**, *Byk Gulden Pharmaceuticals, Konstanz, FRG*

Part A of this two-volume project attempts to treat the sample handling and detection processes in a liquid chromatographic system in an integrated fashion. The need for more selective and sensitive chromatographic methods to help solve the numerous trace analysis problems in complex samples is undisputed. However, few workers realize the strong interdependence of the various steps - sample handling, separation and detection - which must be considered if one wants to arrive at an optimal solution. By introducing a strong element of selectivity and trace enrich- ment in the sample preparation step, fewer demands are placed on the quality of the chromatography and often a simple UV detector can be used. By using a selective detection mode, i.e. a reaction detector, the sample handling step can frequently be simplified and more easily automated. The impact of such a "total system" approach on handling series of highly complex samples such as environmental specimens or biological fluids can be easily imagined.

Contents: 1. On-line sample handling and trace enrichment in liquid chromatography. The determination of organic compounds in water samples. 2. Determination of drugs and their metabolites in biological samples by fully automated HPLC with on-line solid-liquid extraction and pre-column switching. 3. Immobilization of compounds for selective interaction with analytes in liquid chromatography. 4. Design and choice of suitable labelling reagents for liquid chromatography. 5. Photodiode array detection and recognition in high-performance liquid chromatography. 6. Electrochemical techniques for detection in HPLC. 7. Solid-phase reactors in high-performance liquid chromatography. 8. Commercial aspects of post-column reaction detectors for liquid chromatography. Subject Index.

1988 xii + 458 pages
US$ 123.00 / Dfl. 240.00
ISBN 0-444-42881-X

part B

edited by **K. Zech**, *Byk Gulden Pharmaceuticals, Konstanz, FRG, and* **R.W. Frei**†, *Free University, Amsterdam, The Netherlands*

Part B completes the treatment of the handling, separation and detection of complex samples as an integrated, interconnected process. On the basis of this philosophy the editors have selected those contributions which demonstrate that optimal sample preparation leads to a simplification of detection or reduced demands on the separation process. Throughout the book emphasis is on chemical principles with minimum discussion of the equipment required - an approach which reflects the editors' view that the limiting factor in the analysis of complex samples is an incomplete knowledge of the underlying chemistry rather than the hardware available. This lack of knowledge becomes more evident as the demands for lower detection limits grow, as solving complex matrix problems requires a greater understanding of the chemical interaction between the substance to be analysed and the stationary phase.

Contents: I. Preconcentration and Chromatography on Chemically Modified Silicas with Complexation Properties. II. Sample Handling in Ion Chromatography. III. Whole Blood Sample Clean-Up for Chromatographic Analysis. IV. Radio-Column Liquid Chromatography. V. Modern Post-Column Reaction Detection in High-Performance Liquid Chromatography. VI. New Luminescence Detection Techniques. VII. Continuous Separation Techniques in Flow-Injection Analysis. Subject Index.

1989 xii + 394 pages
US$ 136.00 / Dfl. 265.00
ISBN 0-444-88327-4

Written by experienced practitioners, these volumes will be of interest to investigators in many areas of application, including environmental scientists and those active in the clinical, pharmaceutical and bioanalytical fields.

For more information, please write to:

Elsevier Science Publishers
P.O. Box 211, 1000 AE Amsterdam, The Netherlands
P.O. Box 882, Madison Square Station, New York, NY 10159, USA

PUBLICATION SCHEDULE FOR 1990

Journal of Chromatography and Journal of Chromatography, Biomedical Applications

MONTH	J	F	M	A	M	J	J	A	S	O	N	D[a]
Journal of Chromatography	498/1 498/2 499	500 502/1	502/2 503/1 503/2 504/1	504/2 505/1	505/2 506 507 508/1	508/2 509/1 509/2 510	511 512 513	514/1 514/2 515	516/1 516/2 517 518/1	518/2 519/1	519/2 520 521/1 521/2	
Cumulative Indexes, Vols. 451–500		501										
Bibliography Section		524/1		524/2		524/3		524/4		524/5		
Biomedical Applications	525/1	525/2	526/1	526/2 527/1	527/2	528/1 528/2	529/1	529/2 530/1	530/2	531 532/1	532/2 533	

[a] The publication schedule for further issues will be published later.

INFORMATION FOR AUTHORS

(Detailed *Instructions to Authors* were published in Vol. 513, pp. 413–416. A free reprint can be obtained by application to the publisher, Elsevier Science Publishers B.V., P.O. Box 330, 1000 AH Amsterdam, The Netherlands.)

Types of Contributions. The following types of papers are published in the *Journal of Chromatography* and the section on *Biomedical Applications:* Regular research papers (Full-length papers), Notes, Review articles and Letters to the Editor. Notes are usually descriptions of short investigations and reflect the same quality of research as Full-length papers, but should preferably not exceed six printed pages. Letters to the Editor can comment on (parts of) previously published articles, or they can report minor technical improvements of previously published procedures; they should preferably not exceed two printed pages. For review articles, see inside front cover under Submission of Papers.

Submission. Every paper must be accompanied by a letter from the senior author, stating that he is submitting the paper for publication in the *Journal of Chromatography*. Please do not send a letter signed by the director of the institute or the professor unless he is one of the authors.

Manuscripts. Manuscripts should be typed in double spacing on consecutively numbered pages of uniform size. The manuscript should be preceded by a sheet of manuscript paper carrying the title of the paper and the name and full postal address of the person to whom the proofs are to be sent. As a rule, papers should be divided into sections, headed by a caption (*e.g.*, Abstract, Introduction, Experimental, Results, Discussion, etc.). All illustrations, photographs, tables, etc., should be on separate sheets.

Introduction. Every paper must have a concise introduction mentioning what has been done before on the topic described, and stating clearly what is new in the paper now submitted.

Abstract. Full-length papers and Review articles should have an abstract of 50–100 words which clearly and briefly indicates what is new, different and significant. (Notes and Letters to the Editor are published without an abstract.)

Illustrations. The figures should be submitted in a form suitable for reproduction, drawn in Indian ink on drawing or tracing paper. Each illustration should have a legend, all the *legends* being typed (with double spacing) together on a *separate sheet*. If structures are given in the text, the original drawings should be supplied. Coloured illustrations are reproduced at the author's expense, the cost being determined by the number of pages and by the number of colours needed. The written permission of the author and publisher must be obtained for the use of any figure already published. Its source must be indicated in the legend.

References. References should be numbered in the order in which they are cited in the text, and listed in numerical sequence on a separate sheet at the end of the article. Please check a recent issue for the layout of the reference list. Abbreviations for the titles of journals should follow the system used by *Chemical Abstracts*. Articles not yet published should be given as "in press" (journal should be specified), "submitted for publication" (journal should be specified), "in preparation" or "personal communication".

Dispatch. Before sending the manuscript to the Editor please check that the envelope contains four copies of the paper complete with references, legends and figures. One of the sets of figures must be the originals suitable for direct reproduction. Please also ensure that permission to publish has been obtained from your institute.

Proofs. One set of proofs will be sent to the author to be carefully checked for printer's errors. Corrections must be restricted to instances in which the proof is at variance with the manuscript. "Extra corrections" will be inserted at the author's expense.

Reprints. Fifty reprints of Full-length papers, Notes and Letters to the Editor will be supplied free of charge. Additional reprints can be ordered by the authors. An order form containing price quotations will be sent to the authors together with the proofs of their article.

Advertisements. Advertisement rates are available from the publisher on request. The Editors of the journal accept no responsibility for the contents of the advertisements.

(Data Handling in Science and Technology, 5)

PCs for Chemists

edited by: **J. Zupan**, *University of Ljubljana, Yugoslavia*

PCs for Chemists is a handbook on how, when and with what kind of software a chemist should use a PC. Being a beginners' guide, it does not require any specific knowledge about computers. The book covers word processors, spreadsheets, compilers and databases for chemical applications, and it comprises ten contributions each describing one or two different applications and a suggestion for the best choice. Information on how a PC can be linked to instruments, other computers and data networks is also provided.

PCs for Chemists should prove invaluable for all courses covering computer applications to chemistry, pharmacy, biology, and metallurgy.

1990 xvi + 212 pages
Price: US$ 100.00 / Dfl. 195.00
ISBN 0-444-88623-0

Contents:

ELSEVIER SCIENCE PUBLISHERS

P.O. Box 211, 1000 AE Amsterdam, The Netherlands
P.O. Box 882, Madison Square Station, New York, NY 10159, USA